Mitigation of Vibration in Large Electrical Machines

Annabel Shahaj, BEng(Hons)

May 17, 2010

Abstract

In this study two new technologies are investigated with a view to improving the efficiency and reducing the vibrations of large electrical machines. These machines are used for high powered industrial applications.

Individually controlled conductors are part of an *active stator* project that Converteam Ltd are developing. This involves individual conductors located in each stator slot that can be controlled separately. These replace traditional polyphase windings in order to provide a high level of control over the operation of the machine. A linear magneto-mechanical finite element model has been used here to show that this control method can enable a 44% reduction in the copper loss from the machine compared to a sinusoidal supply whilst maintaining the same operational torque. This method introduces extra Fourier harmonics into the excitation pattern supplied to the machine that are not present in the supply current to traditional polyphase windings. These extra harmonics utilize saliency advantageously to produce torque. However, they also increase the vibration of the stator and may increase hysteresis loss in the iron.

The bimorph concept is an idea that is unique to this thesis. This concept involves individually controlled conductors positioned through the root of each stator tooth. On application of a relatively small power input to these conductors a magnetic field is created in the stator which distorts the existing magnetic field. Under certain conditions, the magnetostriction phenomenon causes the teeth to act as a vibration absorber. The effect of this method on the Maxwell forces in the air gap is small. This enables the cancellation of components of vibration of the stator whilst the machine torque is maintained. This is a vibration control method suited to high fre-

quency vibrations where the deformed shape of the stator includes a rocking motion of the teeth and where the resultant stator vibrations lead to tonal noise emission from the machine.

This thesis investigates the two technologies mentioned above with a magneto-mechanical finite element model and two experimental investigations. The thesis also contains background information relevant to this study including an introduction to electrical machines and power electronics, noise radiation and sources of noise in electrical machines, finite element modelling, vibrations of electrical machines and vibration absorbers.

Contents

Acknowledgements

I would like to express my thanks and appreciation to

My supervisor Professor Seamus Garvey for his support throughout this study. His assistance and expert advice has been invaluable.

Dr Karuna Kalita, The University of Nottingham Technicians and The University of Nottingham Support Staff who have assisted me at every stage of the project. Their input enhanced both the content of my work and my journey through the PhD.

Converteam Ltd, The EPSRC and The University of Nottingham for providing the funding for the project. Without this input the project could not have happened.

My family for their constant support. My husband, parents and brother have been there to encourage me throughout the study and have lightened the difficult times.

Nomenclature

$\mathbf{a}$	Nodal Magnetic Potential
A	Cross Sectional Area
$\mathbf{B}$	Matrix of Derivatives of Shape Functions
b	Magnetic Flux Density
C	Damping
$\mathbf{D}$	Mechanical Constitutive Matrix
E	Young's Modulus
f	Supply Frequency
$\mathbf{f}$	Mechanical Forcing Vector
F	Mechanical Force
$\mathbf{G}$	Magnetic Constitutive Matrix
$\mathbf{h}$	Magnetic Field Strength
$\mathbf{H}$	Rotation Transformation Matrix
I	Current
$\mathbf{I}$	Identity Matrix
$\mathbf{i_0}$	Sinusoidal Stator Current Density Pattern
$\mathbf{i_1}$	Stage 1 Stator Slot Current Density Pattern

$\mathbf{i_2}$	Stage 2 Stator Slot Current Density Pattern
$\mathbf{i_3}$	Stage 3 Bimorph Conductor Current Pattern
j	Current Density
$\mathbf{j}$	Vector of Current Density
$\underline{\mathbf{j}}$	Vector of Nodal Current
$\mathbf{J}$	Jacobian Matrix
$\mathbf{K}$	Mechanical Stiffness Matrix
$\underline{\mathbf{K}}$	Magnetic Stiffness Matrix
m	Temporal Harmonic
M	Highest Temporal Harmonic
$\mathbf{M}$	Mechanical Mass Matrix
n	Spatial Harmonic
N	Highest Spatial Harmonic
$\mathbf{N}$	Matrix of Shape Functions
n_{pp}	Number of Pole Pairs
n_s	Synchronous Speed
p	Modal Force
P	Power
R	Resistance

s	Order of Cyclic Symmetry of a Structure
$\mathbf{s}$	Distributed Loading Function
$\mathbf{S}$	Matrix of Partial Differential Operators
s_r	Number of Rotor Slots and Teeth
s_s	Number of Stator Slots and Teeth
t	Time
T	Torque
U	Strain Energy
$\mathbf{U}$	Projection Matrix of Current Density to Nodal Magnetic Potential
V	Kinetic Energy
w	Weighting Function
W	Work Done
$\mathbf{W}$	Transformation Matrix that converts Nodal Magnetic Potential to Magnetostrictive Force
x	Displacement
z	Thickness
$\mathbf{Z}$	Matrix of Derivatives of Shape Functions

α	Constant of Proportionality for Magnetostriction
β	Constant of Proportionality for Magnetostriction
$\mathbf{\Delta}$	Transformation Matrix that Converts Current Density to Modal Force
η	Reference Frame Coordinate Axis
ε	Strain
λ	Magnetostrictive Strain
$\mathbf{\Lambda}$	Spectral Matrix
μ	Permeability
ν	Poisson's Ratio
ω	Frequency
Ω	Rotational Speed
Π	Potential Energy
ϕ	Angle of the Rotor Reference Frame Relative to the Stator
ρ	Density
σ_{RR}	Radial Maxwell Stress
$\sigma_{R\theta}$	Tangential Maxwell Stress
ζ	Reference Frame Coordinate Axis

General Notation

Upper case and bold font indicates a matrix

Lower case and bold font indicates a vector

Italicized characters indicate scalar quantities

The use of $^\top$ as a superscript indicates a transposed matrix or vector

List of Tables

List of Figures

1 Introduction

1.1 Introduction

The main aims of this study are to develop a *magnetic bimorph* concept and *individually controlled conductors* which will together reduce the tonal noise radiated from a large electrical machine and improve the efficiency of the machine. Relevant applications for these machines include military marine vessels, cruise liners and LNG carriers, wind turbines, petroleum and chemical pumps, cooling towers and process machinery.

Alternating magnetic forces in the air gap between the stator and rotor of the machine are essential for the working of the machine. These forces also cause vibrations of the stator which are transmitted through the frame to any adjoining structure. These vibrations are detrimental to the desired running of the machine. At certain frequencies machine vibrations also result in the transmission of unwanted tonal noise. In a commercial situation tonal noise is undesirable. In a military marine vessels it is important that marine vessels do not radiate these signals as they could enable detection of the vessel.

Electrical machines are estimated to use 65% of the total electrical energy produced in developed countries. Electricity demand in 2030 is predicted to be 60% higher than 2000 [9] [56]. This increase in demand is in direct contrast with current legislation to reduce greenhouse gas emission. For example, European Union environment ministers have recently agreed that global emissions from ships should be cut by 20% by 2020 from 2005 levels [98]. Therefore achieving an increase in the efficiency of electrical machines is extremely important.

Much work has been carried out with a view to improving the performance of electrical machines. This has resulted in modern day machines with high power capabilities and efficiencies. However, a trade off is often necessary between operational outputs when improvements are considered. For example with an increase in power often comes a worsening of other features such as increased heat generation or increased vibration. Increasing the efficiency of a machine reduces the versatility of its operation. This study aims to introduce methods to improve machine efficiency and reduce machine vibration so that the overall operation of the machine has not degenerated in any area.

The stator of a radial flux external stator electrical machine is a stack of laminations with a ring shaped back-of-core and teeth that protrude radially inwards. Figure 1 shows a traditionally wound stator in a frame. Currently all stator windings are powered by a single or poly-phase power supply which is most commonly three phase. Oscillating electromagnetic forces are generated in the air gap of the machine between the rotor and the stator and in the stator and rotor iron. The electromagnetic forces that act across the air gap on the stator teeth are Maxwell forces. The magnetostriction effect causes the electromagnetic forces that act within the stator iron. The oscillating Maxwell forces and the magnetostriction effect deform the stator and cause vibrations.

Maxwell and magnetostriction forces can be decomposed into radial and tangential components which are spatially and temporally periodic with many harmonics. In this study, the term frequency can be used to describe the number of oscillations per unit time in both the temporal and spatial domains. The zeroth spatial and temporal harmonic of the tangential component of Maxwell force produces the electromagnetic torque that provides

rotation of the rotor.

Stators of electrical machines exhibit very many vibration mode shapes. Mode shapes that correspond to relatively low natural frequencies exhibit a back of core bending motion and rigid motion of the teeth. At higher frequencies the stator mode shapes include bending motion of the teeth in-phase with the bending motion of the back-of-core. At higher frequencies still the stator mode shapes experience tooth bending motion that is out-of-phase with the back-of-core bending motion. Large electrical machines have a high density of modes that include tooth rocking motion in the frequency range of acoustic interest. The natural frequencies of small machines occur at much higher frequencies than for large machines and so small machines are not relevant to this study.

In large machines some main components of electromagnetic force occur in the frequency range of acoustic interest. The high modal density in this frequency range for large electrical machines means that there is a high likelihood that an electromagnetic force will excite a stator resonance and this will lead to tonal noise emission from the machine. This problem and its elimination provides the focus for this study.

A specific forcing frequency which occurs strongly in electrical machines is the rotor slot passing frequency. This often occurs in the frequency range of acoustic interest and close to mechanical resonances related to tooth rocking motion for large machines. This frequency component occurs as a direct result of the operation of the machine and cannot be prevented. In a large electrical machine there is a high likelihood of the rotor slot forcing exciting one or many tooth rocking resonances.

Noise in electrical machines has three sources; electromagnetic, mechanical and aerodynamic. Electromagnetic has been mentioned above, these sources of noise are the main focus of the work presented in this thesis. The other two sources of noise are covered later in the introduction only.

1.1.1 Ship Propulsion

Traditionally large diesel engines were used for ship propulsion. Utilization of diesel engines for this application required the shaft of a diesel engine to be connected directly to the propeller. Consequently, a long drive shaft, controllable variable pitch propellers and complicated reversible gear boxes were required. Variable propeller speed was needed and therefore the engine speed also needed to be variable, resulting in a system which had poor efficiency.

Diesel-electric propulsion is now predominantly used for ship propulsion. This method utilizes several prime movers (turbines or reciprocating internal combustion engines) which supply power to a number of synchronous generators. Transformers and converters control and convert this power to the synchronous or induction motors which drive the propellers. Utilization of several prime movers instead of one increases drive efficiency significantly as this enables each prime mover to be driven at peak efficiency condition. Power is varied by altering the number of prime movers operating at any one time. Some of the benefits of diesel-electric propulsion over diesel engine propulsion include [13] [16] [22] [93]:

- Synchronous generators supply power at constant voltage and frequency; this constant operating condition increases drive efficiency.
- The location of diesel-electric propulsion systems are very flexible in contrast to diesel engine propulsion systems, which require the engine shaft to be fixed directly to the propeller.

- The electric propulsion system can also be shared with previously separate electric systems on the ship.
- Ship construction is simplified; gearboxes are generally avoided.
- For warships, improvements can be made regarding noise and vulnerability.

The electrical machines that power marine vessels are rated at a few megawatts (MW) with speeds at about $150rpm$. The size of these is typically well over $1m$ in diameter.

1.1.2 The Focus of the Study

The work presented in this thesis focuses on two novel ideas for mitigating the noise of large electrical machines and directly or indirectly improving the operation of the machine. One of the ideas that is considered is the development of electrical machines which have stator conductors in each slot that can be controlled individually. This idea is referred to as the *individually controlled conductor* or ICC method and is being developed by Converteam Ltd [23]. The method which is unique to this thesis is the inclusion of powered electrical conductors through the root of each stator tooth. This is the *magnetic bimorph* method. This method enables control of the motion of the stator teeth to provide vibration absorption to the machine. Both of these methods are described briefly here and are explained in more detail in sections 1.7 and 1.8.

Individually controlled stator conductors are being developed by Converteam Ltd [22]. This method involves complex control and feedback arrangements which enable the excitation of the conductors in each stator slot to be controlled separately. A high level of control will be possible with this configuration, enabling power losses to be reduced and a higher power density

machine achieved. This method may also provide control and elimination of many of the unwanted vibration problems that electrical machines currently experience by preventing troublesome forcing components from being produced. However, it is predicted that the pattern of stator excitation that results in the running of the machine that is smoothest is unlikely to be the same pattern of excitation that gives the highest possible efficiency for the machine. Therefore with this method, a compromise between efficiency and vibration control will still be needed. There will also be noise and vibration problems that this method cannot solve. These problems are due to the electromagnetic forces that directly operate the machine, such as twice supply forcing frequency. These forces will still need to exist and so their potential to cause noise and vibration will still exist.

The bimorph concept is unique to this study and consists of electrical conductors positioned through the root of each tooth in the stator. These conductors are energized creating a magnetic field which distorts the resultant magnetic field in the stator core and so affects the magnetostrictive forcing in the stator iron. Consequently the motion of the stator teeth are affected. The operation of these conductors takes advantage of the magnetostriction effect in ferrous metal to control the motion of the teeth. The excitation to these conductors can be controlled so that the stator teeth act as vibration absorbers and cancel out unwanted vibration of the stator at certain frequencies. There will be specific modes of vibration that cannot be cancelled with this method such as a pure radial expansion and contraction of the stator core. Low frequency vibrations will also not be affected with this method as the bending motion of the tooth is required and at low frequencies the tooth does not deflect in a bending motion.

If the two methods, individually controlled conductors and bimorph con-

ductors are used together to control the operation of an electrical machine, the different benefits that they provide can be combined. The ICCs can be supplied with a current pattern which gives the highest possible efficiency and the bimorph control can be used to eliminate the unwanted vibrations. This enhanced set of controls enables a smooth running, quiet and highly efficient electrical machine.

This thesis develops the bimorph and ICC methods using mainly finite element analysis and some experimental validation. The finite element analysis was carried out with MATLAB and all of the coding was written by the author. The rest of the introduction provides a literature review and background information to set the scene for the rest of the study. Information is given on electrical machine operation and power electronics for speed control. Noise is discussed and descriptions of the types of noise produced by electrical machines is given. The magnetostriction effect and Maxwell forces are described and the bimorph and ICC methods are explained. The other chapters in the thesis are:

Chapter 2: **The Magnetic Bimorph Concept** describes the theory of the magnetic bimorph idea and explains how this can be implemented to cancel components of vibration in large electrical machines by analogy with a vibration absorber. Two experiments are described in order to illustrate the practicality of this concept. The first experiment is a single stator tooth rig. This experiment shows how the presence of bimorph conductors in a stator tooth root can affect the motion of the tooth. The second experiment on a small electrical machine is described. This experiment shows how the magnetic field generated by the bimorph conductors can be used to cancel out the magnetic field generated by the field windings.

Chapter 3: **Coupled Magneto – Mechanical Analysis for Predicting Vibration** presents the calculations that were used in this study to generate a coupled magneto-mechanical model of an electrical machine. Accelerations of these calculations are also described. These were used during the optimization process for finding the ICC current density patterns and bimorph current patterns. These optimization strategies are also described.

Chapter 4: **An Investigation into the Optimum Operation of a Large Electrical Machine** presents the findings of the investigation. This chapter quantifies the vibration and efficiency of the machine when a sinusoidal current pattern is supplied to the stator windings. This information is compared with the vibration and efficiency of a machine when supplied with an ICC current pattern that minimizes the copper loss for the same torque. Another ICC current pattern is investigated that cancels certain components of vibration for the same torque and lowest copper loss. A bimorph current pattern is also analysed to reduce vibration without affecting the torque or increasing the copper loss significantly.

Chapter 5: **The Conclusion** summarizes the main results of the study and presents some areas for further work on this topic.

Appendix A: **Vibration Absorbers** is an overview of vibration absorption technology. The theory behind passive, active and combined vibration absorbers is given with some numerical examples to illustrate the concepts. Developments from the literature are also discussed. This chapter is relevant to the thesis because the magnetic bimorph concepts utilizes the stator tooth as a vibration absorber.

Appendix B: **Finite Element Modelling** covers in general, element gen-

eration, the assembly of each element into the full model, boundary conditions and techniques for dealing with large matrices. The model reduction methods used in this study are explained. Finite element analysis of cyclically symmetric structures is also described.

Appendix C: **The Mechanical FE Model of the Electrical Machine** covers a literature review of techniques that have been used to model electrical machines with a view to predicting vibrations. An explanation is given of the vibrational behaviour of stators of electrical machines due to their cyclically symmetric nature.

Appendix D: **The Magnetic FE Model of the Electrical Machine** has two parts. The first part presents a literature review of techniques for electromagnetic modelling of electrical machines. The second part details the calculations used in this study in a general context.

Appendix E: States Maxwell's equations.

Appendix F: Is a conference paper written by the author

Appendix G: Is a conference paper co-written by the author

1.2 An Introduction to Electrical Machines

Electrical machines are introduced here and relevant background information is given. Electrical machines are characterized as AC or DC machines. This description indicates whether the supply to the machine is alternating current or direct current. DC machines have torque-speed characteristics that can be varied over a wide frequency range and with efficiency values that remain near constant over a wide speed range. Originally, DC ma-

chines were used in the majority of variable speed applications but there are less present day applications for DC machines. Some present day applications where DC machines can be found include in steel mills and mines and on electric trains and cars. All electric utility systems supply alternating current, and so for the majority of industrial applications AC machines are now used. AC machine speed does not vary significantly with load and so when supplied at constant voltage by a constant frequency supply, machine speed remains constant. Originally AC motors were only used in constant speed applications. Early AC machines, by comparison with early DC machines were bulky, heavy and had low efficiency. Advancements in AC drive technology over the last three decades has dramatically increased the utilization of AC machines and they are now far more common than DC machines. Present day AC machines, compared to present day DC machines have high power density, low cost, high efficiency, high reliability and are available in an extremely wide power range [13]. The focus of this work applies only to AC machines because electric ship propulsion systems use mainly AC motors. DC machines are not considered further in this study.

1.2.1 AC Electrical Machines

AC machines are classed as either *synchronous* or *induction* machines. Both synchronous and induction machines are used for high power applications, so both types are equally relevant to this study. In the vast majority of cases both synchronous and induction machines are radial flux machines. Axial flux machines are not considered here. Electrical machines can be used as motors or as generators and many applications require machines to operate as both [36]. Generators are predominantly synchronous machines. The reason for this is that induction machines cannot generate electricity without being connected to an already existing supply. This existing reference voltage is required to induce the generated voltage against. Motors are

mainly induction machines due to their ruggedness, reliability and low cost compared to synchronous machines. However, synchronous machines enable some independent control over the power factor and have higher efficiency. The fundamental components of a machine are the same for both generator and motor operation and so the technology introduced in this study can be applied to both. However, the focus area of this study is for motor operation.

The construction and excitation of the stator of both machines is fundamentally the same but the machines in the two categories have different constructions and excitations for the rotor. For the majority of this study the two types of machines can be considered together. The construction of a cylindrical electrical machine consists of a stator and a rotor separated by an air gap. Motor operation is achieved by an electric current supplied to windings on the stator. A conversion from electrical to mechanical power occurs in the machine which causes mechanical torque to be produced. This torque is transferred to the rotor and drives the connected load [63].

A new technology in the field of electric ship propulsion is the development of high temperature superconductivity wound field synchronous machines (HTS machines). These are essentially AC synchronous machines which have the rotor wound with superconducting wire instead of copper. These rotor windings can conduct more than 150 times the electric current of copper wire with the same dimensions and no resistance. This results in an electrical machine with higher power density and higher efficiency than present day AC machines. The weight and size of HTS machines can be as low as one third of the weight and size of conventional synchronous machines of a corresponding rating, also reducing manufacturing and maintenance costs and increasing design flexibility. The use of superconductor coils eliminates the requirement of the rotor or stator to have teeth, result-

ing in an inherently quieter machine [53].

Machines that exist but are not relevant to this study are:

- Shaded pole motors; these are typically used below 50W
- Split phase machines; these are used in 50W to 500W power applications (such as fans, centrifugal pumps and office equipment)
- Capacitor starter and split capacitor machines (used in high starting torque applications such as air-conditioning and refrigeration)
- Universal motors (used in vacuum cleaners and kitchen appliances) [13]
- Synchronous reluctance machines, switched reluctance machines and stepper motors.

1.2.2 The Stator

The stator of a cylindrical AC machine is formed from a set of identical, highly permeable steel laminations in the shape of a ring with teeth protruding inwards. The laminations combine to form a hollow cylinder. Many turns of wire in the slots between the stator teeth are used to supply current to the machine. Figure 1 shows the stator laminations, windings and casing of a small induction machine. Alternating current is supplied to the stator windings, usually in three phases. Each of the three phases is 120^o out of phase to the others. Some large machines have more than three phases, slotless machines and single and double phase machines also exist, but three phase machines are the most common [13].

The current in the stator windings produces a magnetic field in the stator laminations. The magnetic field rotates around the stator at *synchronous*

speed n_s (Hz), so called because it is synchronized with the supply frequency f (Hz). Synchronous speed also depends on the number of pole pairs n_{pp}:

$$n_s = \frac{f}{n_{pp}} \tag{1}$$

Stator and rotor laminations have good magnetic properties and are also good electrical conductors. Eddy currents exist in the material. These are currents that flow in opposing directions to the required currents, and these cause losses. Laminations are coated with a less conductive, less permeable material. This decreases the effective axial conductivity nearly to zero and so eddy current losses are much reduced. Coating the laminations also slightly increases the reluctance of the global magnetic flux path [63].

1.2.3 Induction Machines

Induction machines are the most common type of AC machine, suitable for both variable and constant speed applications. They are used for a wide range of power requirements from a few watts to several megawatts due to their simplicity, ruggedness, reliability, and low cost. Large induction motors are found on naval vessels, cruise liners and LNG carriers [13] [22].

1.2.3.1 Induction Machine Rotor Construction The rotor of an induction machine is constructed from a dense stack of highly permeable laminations. The laminations are punched to provide slots in which the rotor conductors are situated. The construction of the windings defines the two main types of induction motor, which are wound or squirrel cage.

A squirrel cage rotor has conductive bars embedded in the slots. At each end of the rotor, the bars are connected to end rings which short-circuit the bars together. The bars and end rings of small to medium sized machines are die cast to form an integral block. See Figure 2 for a squirrel cage rotor

with an integral cooling fan.

A wound rotor has windings in a similar construction to the stator. The terminals are connected to slip rings which turn with the rotor. Stationary brushes enable external resistors to be connected in series with the rotor windings which aids start up. During normal operation, the brushes are short-circuited. *Wound* rotor induction machines are less common than their squirrel cage counterparts.

1.2.3.2 Induction Motor Operation The following steps explain the starting of induction motors:

- The current flow through the stator windings produces a magnetic field in the stator laminations.
- The rotating magnetic field in the stator passes through the air gap to the rotor and cuts across the rotor conductors.
- A voltage is induced across the rotor conductors. At the same instant a current flows in the conductors, as described by Faraday's law.
- The induced rotor currents produce magnetic fields around the rotor windings. The magnetic fields from the stator and rotor windings combine to create a distorted magnetic field.
- In accordance with Lenz's law, the resultant magnetic field produces a magnetic force. A small component of this force acts circumferentially around the air gap producing a torque that acts between the rotor and the stator. The main component of magnetic force acts radially on the stator teeth.
- The air gap torque tends to rotate the rotor in the same direction as the magnetic field from the stator windings.

Once the motor is running, there is a difference between synchronous speed n_s and the rotational speed of the rotor Ω. The relative difference is called *slip* (s):

$$s = \frac{100(n_s - \Omega)}{n_s} \tag{2}$$

The presence of slip ensures a torque exists between the rotor and the stator. If the rotor were to rotate at synchronous speed there would be no resultant tangential force in the air gap and consequently no torque to drive the rotor.

The torque developed by an induction motor is dependent on its rotational speed. The relationship between torque and speed is usually illustrated by a plot of a torque-speed curve. The torque-speed curve is unique to every machine and is dependent on the individual properties of the rotor, especially the rotor resistance. The steady state torque-speed curve of a conventional three phase induction motor is shown in figure 3.

At standstill the steady state torque that the motor supplies is called the *locked rotor torque*. A rotor with a high resistance will have a high locked rotor torque and a decrease in speed with increase in load. This is advantageous for starting but results in high losses and low efficiency during operation [13]. The minimum torque that the motor will supply is called the *pull up* torque, this is shown in figure 3 at point 1. The maximum torque that the motor can supply is called the *pull out* torque, this is shown in figure 3 at point 2. If the load applied to the rotor exceeds the pull out torque, the motor will stall and cease running. The motor will accelerate from stand still through the pull up torque and pull out torque until the supply torque falls to equal the load torque. At this point the rotor speed will become constant. If the torque is equal to rated torque, this operating point is called full load and is indicated in figure 3 at point 3. For large machines the slip at this point is usually about 0.5%.

Figure 4 illustrates how varying the supply voltage with constant frequency affects the torque-speed curve. In this figure, two supply-torque against speed curves are shown for a conventional induction motor. A plain solid line indicates supply at rated voltage. A crossed line indicates the same machine supplied at a quarter of the rated voltage. These two lines show that decreasing the supply voltage to the motor reduces the torque supplied by the motor and changes the supply-torque against speed characteristics. A load-torque against speed curve is shown with circular markings, in this case the load torque is proportional to the rotational speed squared and so increasing the speed of the motor increases the load torque. At rated voltage, the motor operates at full load torque, shown in figure 4 at point 1. When the machine is supplied by a quarter of rated voltage, the operating point is shown in the figure at point 2. Varying the supply voltage by any value between rated voltage and a quarter of rated voltage will vary the supply torque within the two supply torque curves shown in the figure. The motor will be driven at the point where the supply torque equals the load torque [13].

Varying the supply voltage and frequency in proportion so that the stator flux remains constant maintains the shape of the torque-speed curve but shifts the curve along the speed axis. This effect is illustrated with the blue lines in figure 5. This graph has three frequency regions; the constant torque region which exists at frequencies from zero Hz up to a base frequency value, the constant power region which occurs at frequencies above the base frequency, and equivalent DC series motor operation at frequencies above this. In the constant torque region, voltage and frequency are varied proportionately; this maintains constant flux and the pull out torque also remains constant. Motors mainly operate in this region. At frequencies

above base frequency, operation is limited by the constant power curve. At frequencies above base frequency, with rated voltage, the air gap flux decreases and so torque decreases; this is DC series motor-like operation [13].

The total current in the machine is split into magnetizing current and rotor current. The magnetizing current is the current required to create the flux in the machine. The rotor current is the additional current required to create the torque. The effect of rotor current on torque is illustrated in figure 6. A rotor current-speed plot is shown with a dashed line. The locked rotor current is the current supplied at stand still. This is high and current decreases as speed increases. At synchronous speed rotor current is zero and so the value of total current is the magnetizing current. When the voltage and frequency is varied so that the stator flux remains constant, the shape of the current-speed curve remains the same but moves along the speed axis with the torque-speed curve. This effect is also shown in figure 6. The locked rotor current is high when the supply voltage is high. When the voltage is reduced so that the stator flux remains constant, the locked rotor current is reduced and the locked rotor torque is high. Therefore, within the limit of rated current a motor can be accelerated from stand still with full rated torque. This results in high efficiency and energy savings and prevents high rotor bar stress.

1.2.4 Synchronous Machines

Synchronous machines are popular for high power applications because most are rated at between $150kW$ and $15MW$ and run at speeds of $150rev/min$ to $1800rev/min$. The vast majority of turbine driven generators in the production of electrical power are synchronous generators [42]. Synchronous machines have higher efficiency than induction machines mainly due to having direct rotor excitation. They are more expensive than induction

motors but in high power applications their life cycle cost can be lower than for induction motors [13] [102]. Synchronous reluctance machines are not considered in this study.

1.2.4.1 Synchronous Machine Rotor Construction The rotor of a synchronous machine may be either wound or have permanent magnet (PM) material. A wound field rotor has one or more windings usually connected together in series. The windings of a wound field synchronous motor are supplied with direct current either from an external exciter through slip rings or from an exciter integral to the rotor so that adjacent poles have opposite polarities [102].

A permanent magnet AC machine has permanent magnets on the rotor instead of one or more windings. These types of rotors can be categorized into axial or radial categories. Radial permanent magnet machines can be either surface or interior, a surface PM rotor is illustrated in figure 7. Surface permanent magnet machines are described as being either trapezoidal or sinusoidal according to the voltage profile which they generate when the machine is open circuited [13].

High energy product magnet material (NdFeB) is often used for permanent magnet motors. High energy magnets enable smaller machines with lower inertia and the same torque. This is presently a very expensive material. However, the cost of this material is falling and so a rise in manufacture and utilization of permanent magnet machines is predicted and the utilization of PM machines may possibly even surpass that of induction machines [13].

1.2.4.2 Synchronous Motor Operation Initially the rotating magnetic field due to supply frequency is too fast to use for start up. Methods used for start up are variable frequency drives, unexcited auxiliary wind-

ings, an additional squirrel cage winding on the rotor or brushless excitation. Very large synchronous motors can be accelerated by an auxiliary motor called a pony motor. During start up no excitation is supplied to the windings of wound rotor synchronous machines [102].

When the rotor is running at close to synchronous speed direct current is supplied through slip rings to the rotor of wound rotor synchronous machines. This produces the rotor poles and the mutual attraction between the rotor and stator poles locks the rotation of the rotor with the rotation of the magnetic field. The torque developed in the air gap at this moment is called the pull in torque. During operation with load torques that are between no load and full load, synchronous motors run at synchronous speed. The synchronous speed of a synchronous motor is also determined by equation (1) [102].

If squirrel cage windings have been used to start the motor, these become redundant as soon as the rotor reaches synchronous speed as no voltage can then be induced in these windings. The squirrel cage windings are also used if there are unwanted fluctuations during the operation of the motor. Any change in rotor speed away from synchronous speed causes currents to be induced in the windings which affects the magnetic field in the machine and consequently the torque acting on the rotor, this acts to dampen the effect of the fluctuations.

The rotor and stator of a synchronous machine have the same number of poles. The axes of the rotor and stator poles directly coincide if the machine is operating with no load. With the application of a mechanical load the rotor poles fall behind the stator poles by an angle α. If the load and therefore α increases, the current increases. The physical angle between

the rotor poles and stator poles α gives rise to an electrical phase shift δ between the induced stator voltage and the rotor voltage:

$$\delta = \alpha n_{pp} \tag{3}$$

Reluctance torque is the torque that is generated by the attraction of the stator poles and unexcited rotor. The maximum value of reluctance torque is usually about 25% of the peak torque generated from the rotor excitation. This occurs when δ is about 45^o. If reluctance torque is neglected the variation of supply torque with respect to δ is a sine wave. The total torque is the sum of the supply torque and reluctance torque. The supply torque, reluctance torque and total torque of a synchronous machine are shown in figure 8. The region of positive total torque indicates motor operation, the negative torque region indicates generator operation. The maximum value of total torque, which occurs when δ is equal to or close to 70^o is the pull out torque [102]. If the load torque exceeds the pull out torque, the rotor poles pull away from the stator poles and jump to the next pole. This is called pole slip and can be extremely damaging to the motor and any equipment connected to it. Therefore, the full load torque is usually around half of the pull out torque.

1.2.5 Machine Losses

Electrical motors transform electrical energy into mechanical energy. During this process some electrical and mechanical energy is lost. This causes an increase in the temperature and a reduction in the efficiency (η) of the motor. Efficiency is given as

$$\eta = \frac{100 P_{out}}{P_{in}} \tag{4}$$

where P_{out} is the machine output power. P_{in} is the machine input power.

1.2.5.1 Mechanical losses Windage P_w and friction P_{fr} are mechanical losses. Windage loss occurs from the air flow through the machine due to cooling. Friction occurs between relatively moving parts. These losses are independent of load and dependent on the speed of the machine.

1.2.5.2 Electrical Losses Rotor and stator copper losses P_{cu} and iron losses P_{fe} are electrical losses. Copper loss is given by

$$P_{cu} = I^2 R \tag{5}$$

where I is the current in the conductors and R is the resistance of the conductors. Resistance is given by

$$R = \frac{\rho L}{A} \tag{6}$$

where L is the length of the conductor and A is the cross-sectional area of the conductor. ρ is the resistivity of copper, this value is dependent on temperature. Copper losses are dependent on supply current and therefore vary with load and speed.

1.2.5.3 Iron losses Hysteresis and eddy currents cause losses in the form of heat in the rotor and stator iron. Hysteresis is the phenomenon of magnetic flux density B lagging behind a varying magnetic field H. A hysteresis loop for iron is shown in figure 9, this curve shows that magnetizing an initially unmagnetized iron specimen causes the magnetic flux density to increase until saturation is reached (from point 1 to 2 on the curve). Reducing the magnetic field strength to zero causes the magnetic flux density to reduce to point 3. The level of magnetic flux density at point 3 is the remanence flux. Supplying the iron with increasing magnetic field strength

in the opposite (negative) direction decreases the magnetic flux density. At point 4 the magnetic flux density is zero, the magnetic field strength at this point is the negative coercive force. For higher negative values of magnetic field strength the magnetic flux density also increases negatively until saturation is reached at point 5. Decreasing the magnetic field strength to zero causes the magnetic flux density to reach negative remanence flux at point 6. Increasing the magnetic field strength in the original direction to the point of coercive force causes the magnetic flux density to decrease to zero at point 7. Further increases in magnetic field strength cause the flux density to increase to the point of saturation (point 2). This is one complete hysteresis loop. If magnetic field strength varies within the unsaturated region, the hysteresis loop is formed within the loop shown. The area enclosed by the hysteresis loop (TAm^{-1}) is proportional to the energy lost (Jm^{-3}) and this varies for different ferromagnetic materials. Silicon steel has a thin hysteresis loop and relatively small area. The iron of the stator and rotor of an electrical machine experiences variations in magnetic field strength at the frequency of the supply current. Therefore, hysteresis losses in electrical machines increase with increasing supply frequency but are independent of load.

Eddy currents are generated in the iron due to the flow of magnetic flux. These currents flow in the iron perpendicular to the direction of the flow of flux causing heat generation in the iron. Both types of iron loss are dependent on the speed of rotation, quality of steel and magnetic flux density.

1.2.5.4 Additional Load Losses All of the losses not covered above are additional load losses P_+ [92]. These are calculated by

$$p_+ = (P_{in} - P_{out}) - (P_{fe} + P_{cu} + P_w + P_{fr}) \tag{7}$$

These are caused by space harmonics and leakage flux at the ends of the windings [9].

1.2.5.5 Overview of Power Losses The losses of one $1.5MW$ synchronous motor are given in table 1 [102]. The efficiency of a motor depends on the load that the motor drives. An efficiency against load curve is shown in figure 10. At no-load, the total power supplied to the machine only needs to be sufficient to overcome friction, windage and iron losses. Therefore, at no-load efficiency is at a minimum. The current required for this is low so copper losses are low and additional load losses are zero. If the load varies but speed remains nearly constant friction, windage and iron losses also remain fairly constant. As the load increases the current supplied to the machine must increase and so the copper losses increase. Efficiency initially increases as the load increases from no-load. There is a range of values of load where efficiency is fairly constant. Above this range efficiency decreases. The temperature of the machine increases with load and the maximum temperature that a machine can withstand defines the *rated* power of the machine. Machine designers aim for maximum efficiency and full load operation to coincide [102].

1.2.6 Discussion and Conclusion of AC Machines

Controlling the rotor excitation of wound field synchronous motors controls whether the power factor is leading, lagging or unity. This results in an improved efficiency machine compared to an induction machine. The highest power factor of induction machines at rated condition is around 0.89. For this reason the rotor and stator of an induction machine needs to be larger than a synchronous machine and so the inertia and mass of an induction machine is greater than for an equivalent synchronous machine. Torque response times are comparable for the two machines but the flux time constant is much faster for wound field synchronous machines [13]. Permanent

magnet motors have no field control but also experience no field loss and so are more efficient, they are more expensive than both wound field synchronous machines and induction machines.

Electrical machines have now been introduced. Both large induction and synchronous machines are relevant to this work. The construction of the stator is the same for both of these two types of machine, although the rotor construction and excitation is different. The resultant equivalent mechanical forcing that causes the torque and vibrations is also essentially the same for both. The two types of machine can largely be discussed and analysed together. Power electronic converters play an important role in the control of machine speed and so they are introduced next.

1.3 Power Electronic Converters

Power electronic converters utilize electronic semiconductor switching devices to convert and control electrical power. It was the introduction of these high power solid switching devices into the speed control of electric motors that facilitated the change from the use of mainly DC motors in variable speed applications to the use of mainly AC motors. They are relevant to this study because these are now used to supply power to electrical machines in very many applications. Power electronic components are also essential for the implementation of the technologies investigated in this study. This section gives an overview of the development of these devices and their characteristics.

Power electronic converters are used in applications such as transport, aerospace, military, residential and commercial. The benefits of power electronics are high efficiency (96% - 99%), ease of cooling, low cost, small size, reliability and longevity. Control is enabled without direct energy dumping such as

throttling of pumps. Therefore, modern day electric motor systems that use power electronic converters for speed control benefit from having low maintenance requirements, high efficiency and superior dynamic performance compared to traditional drive systems [102]. However, this equipment is based on nonlinear switching devices and these generate unwelcome harmonics over a wide frequency range. These feed into the load and supply lines. Electromagnetic interference occurs when switching causes a fast rate of change of voltage and current [13].

A prediction for the near future is that, due to the decreasing cost of converters and their increasing importance in machine drives; all machines will have front end variable frequency converters, even for starting constant speed machines. Intelligent machines will be widely used which have integrated converters and controllers [13].

The next section describes the relevant electronic switching devices.

1.3.1 Semiconductor Switching Devices

Present day power electronic devices for high power applications include:

- Diodes
- Thyristors
- Gate turn-off thyristors (GTOs).
- Insulated gate bipolar transistors (IGBTs).
- Integrated gate commutated thyristors (IGCTs).

Other technologies that are required for the implementation of power electronic devices include semiconductor materials and processing, fabrication and packaging and modelling and simulation [3] [13].

A diode is a semiconductor device that acts like a switch. The diode has an anode and a cathode terminal. If a voltage is supplied so that the anode is positive with respect to the cathode the diode is forward-biased. In this situation the diode acts like a closed switch and current flows. If the diode is reversed biased it acts like an open switch and no current flows. Diodes are used in single phase and three phase bridge rectifiers to convert AC to DC [102].

A thyristor is similar to a diode but in addition to the anode and cathode terminals has a gate terminal. No current flows when the thyristor is reverse-biased. When the thyristor is forward-biased a small current supply to the gate terminal enables the flow of current through the thyristor. Therefore there is more control over power conversion with a thyristor than a diode. Thyristors are capable of switching at frequencies up to about $2kHz$ [102].

Gate turn off thyristors use current control to the gate terminal to enable current to flow through the device when required and also to be blocked when required when the GTO is forward-biased. These are high power switching devices and can operate at thousands of amperes and up to $4000V$. Switching frequencies are possible up to around $400Hz$ but switching losses can be relatively high [13].

Insulated gate bipolar transistors are voltage controlled switches with collector, emitter and base terminals. They provide many benefits over other power electronic technology. They can be powered with hundreds of horsepower. They enable highly efficient, compact, robust converters. They can be used at frequencies up to about $50kHz$, well above the audio frequency

range. This enables the output of low frequency voltages with high control over the waveform and phase. Very low levels of harmonic currents are generated. Subsequently, no harmonic filtering is required and the noise and vibration of the driven motor is reduced to very low levels. IGBTs are used in the majority of applications from several hundred watts to 1-2MW and higher power applications such as with induction motors in ship propulsion systems [13] [22] [102].

IGCTs are voltage controlled, they have comparable switching frequencies to IGBTs and the converter design is simpler than that of GTOs. IGCTs use a high voltage and current so are inherently suitable for multi-megawatt power ratings [13].

1.3.2 Power Electronic Converters

The above devices are used in power electronic converters. Some popular types of power electronic converters are described here.

Static frequency changers convert an input line frequency directly into an output frequency. Cycloconverters are a type of static frequency changer. They are used to start, stop, run, reverse and decelerate slow speed squirrel cage induction and synchronous machines. These utilize thyristors and enable machines to operate with constant stator flux. Cycloconverter fed motors typically run about 10^oC hotter than sinusoidally supplied motors and so require additional cooling or derating [102].

Static voltage controllers are static switches which enable variable voltage speed control. They are used to soft-start induction motors. Static voltage control can be achieved with a three phase autotransformer or three sets of thyristors connected back to back. They are silent and are available

from 1 to thousands of horsepower. Static voltage controllers are preferable to rheostat, autotransformer starters, wye and part winding starters. Autotransformers have lower losses and distortion than thyristors and so thyristors are used only for low power applications [102].

Rectifier-inverter systems with *line commutation* are used to supply rectangular AC waveforms with control over the voltage and frequency. Line commutated systems are used mainly with synchronous motors although they can be used with wound rotor induction motors because the inverter requires reactive power and this is provided by the synchronous motor. A typical rectifier-inverter system is shown in figure 11. The rectifier converts the AC input into DC and this is supplied through a DC link to the inverter which converts the supply into a rectangular AC waveform. Thyristors are suitable for these converters because the current is extinguished naturally when the line voltage changes [102].

Rectifier-inverter systems with $self$ *commutation* are used to generate rectangular AC waveforms to supply squirrel cage induction motors. Induction motors absorb rather than provide reactive power so need self commutated inverters. These utilize similar devices to the line commutated system except for the inverter which can absorb or deliver reactive power and so generates its own frequency. The DC link between the rectifier and inverter is controlled to operate with either almost constant voltage or almost constant current. The constant current link has an inductor as shown in figure 11. The constant voltage link has a capacitor to smooth the current. The inverter frequency is determined by the frequency of the gate pulses. The inverter power depends on the load and the semiconductor switching devices. IGBTs, GTOs or three phase bridge thyristors can be used. Current source converters are used to control individual motors. Voltage source converters

are used to control several motors together [102].

The rectifier-inverter systems described above output rectangular waveforms as shown in figure 12. These contain large third, fifth and seventh harmonics of fundamental frequency. These harmonics generate torque pulsations in the machine which occur at integer multiples of six times fundamental frequency. These pulsations are problematic for low fundamental frequencies but less so at high frequencies. These converters are used in the constant power region of induction motor control where the fundamental frequency is high and so torque pulsations are minimal. These converters are preferable to *pulse width modulation* (PWM) techniques at high fundamental frequencies because PWM techniques have high power losses at high frequencies [102] [104].

Pulse width modulation is a technique that has become popular for converting a DC supply voltage to AC since the development of devices such as GTOs and IGBTs. A PWM system is shown in figure 13. A three phase bridge rectifier with diodes is suitable for converting the AC voltage to DC. An inverter converts the DC supply to a rectangular AC voltage waveform with constant frequency. The frequency of this waveform is called the *carrier* frequency. The proportion of the wave that is positive and negative within one cycle can be controlled. The ratio of the positive period of the pulse to the total period of one pulse is called the *duty cycle* D. If the DC voltage is given the symbol E_1 then the average output voltage E_2 is:

$$E_2 = E_1(2D - 1) \tag{8}$$

By varying the duty cycle and filtering the output the output waveform, average voltage and frequency can be controlled. The inductance of the machine smooths out the high frequency content of current. Figure 14 shows

a sine wave generated with PWM and the variation in duty cycle required to achieve this. The output frequency is called the $fundamental$ frequency. Many shapes of waveform can be generated with PWM techniques. For example low frequencies can be transformed into high frequencies in a fraction of a millisecond. PWM techniques are usually used to control the constant torque operation of the motor under variable voltage variable frequency control. In this region operation can be synchronized or unsynchronized. In unsynchronized mode the carrier frequency is maintained at its upper limit and the fundamental frequency is controlled by altering the number of pulses per fundamental period. Increasing the number of pulses per period decreases the fundamental frequency. This type of operation is used for fundamental frequencies from $0Hz$ to one tenth of the upper limit of the carrier frequency. Synchronized operation is achieved by using a carrier frequency that is an integer multiple (and usually an odd number) of the required fundamental frequency. This operation is preferable for fundamental frequencies that are above one tenth of the upper limit of the carrier frequency in the constant torque region. Carrier frequencies are possible from $1kHz$ to $16kHz$. The higher the carrier frequency the better the wave shape that can be generated and filtering is easier. However, the power loss is also increased. Decreasing the pulse width decreases the average output voltage. [102]. The harmonics of fundamental frequency that are present in the supply from the inverter can be eliminated with PWM but harmonics of the carrier frequency are generated. When electrical machines are supplied by PWM the copper loss and iron loss in the machine is increased. A standard induction motor will therefore run 10^oC to 20^oC higher with a PWM drive than a $50Hz$ sinusoidal supply [102].

The voltage frequency spectrum of these converters consists of discrete frequency components concentrated around multiples of the carrier frequency

rather than the fundamental frequency. Typically, these traditional PWM inverters have carrier frequencies of several kilohertz, which is within the audible range. When PWM is used in the speed control of electrical machines, these distinct frequency components generate tonal acoustic noise in the machine iron. With inverter fed machines, noise generally decreases as the carrier frequency of the inverters increases. This is because in general vibrations at a higher frequency occur where the stator core has higher stiffness and therefore lower response, causing reduced noise and vibration. However, the upper frequency limit that PWM converters can be used effectively is limited by issues of switching losses and efficiency.

Random PWM produces a carrier wave that contains random frequency components. The effect of this is to spread out the acoustic energy over a wide frequency spectrum. The large frequency components that are present in the spectrum of traditional PWM converters disappear with random PWM and so random PWM prevents high levels of tonal noise from being generated. Broadband noise is created and so the use of random PWM does not necessarily reduce the overall noise produced by the connected machine. However, the human perception of broadband noise is that it is far less irritating than tonal noise and so random PWM is used over traditional PWM methods for applications that require low noise emission. Some disadvantages of random PWM compared to traditional PWM include increases in machine harmonic losses and decreases in machine efficiency [17].

1.4 Summary of Electrical Machines, Speed Control and Power Electronics

The previous sections have introduced electrical machines and power electronics as a means of controlling machine speed. A summary of these sections is given here. Electrical machines may be either AC or DC machines.

The vast majority of machines in use today are AC induction machines due to their simplicity, ruggedness, low cost and reliability. Synchronous machines are more suited to high power applications. Their initial cost is higher than that of induction machines but so is their efficiency, resulting in potential for lower long term cost. The construction of a motor is the same as the construction of a generator. The construction and excitation of the stator of an induction machine is essentially the same as the construction and excitation of the stator of a synchronous machine. Recent advances in power electronics technology have led to power electronic converters becoming popular for the speed control of electrical machines. Using power electronic converters to control the speed of electrical machines has many advantages, including vastly increased drive efficiency. However, one disadvantage of converter fed machines is the extra harmonic components that are present in the supply to the machine which can excite noise producing resonances in the machine. The next section addresses noise in general and in electrical machines.

1.5 Noise Radiation

This section discusses some aspects that are related to noise radiation in general. Noise is predominantly caused by unwanted sound radiating through air from a vibrating surface. Noise can be transmitted as pitched or un-pitched. The effect of these two types of noise radiation on the surrounding environment is very different. Un-pitched noise, also known as broadband or white noise, has a well distributed energy spectrum. Broadband noise is generally not irritating to human hearing and does not transmit a characteristic frequency spectrum and so is not considered further in this section [59]. Pitched or tonal noise is created from vibrations of a structure that occur in a fine range around one or very few distinct frequencies. Tonal noise can be extremely irritating to human hearing. Machinery that emits

tonal noise has a characteristic frequency spectrum which is easily detected. Tonal noise is discussed further in the next paragraphs and is the type of noise that this study aims to eliminate.

Assuming that all of the noise emitted by a vibrating structure is caused by sound radiation from the structure, the level of noise radiated by a constant frequency vibration is dependent on the mean-squared velocity of the vibration. High velocity structural vibrations cause high levels of tonal noise to be emitted. The frequency range of interest for acoustic noise is $20Hz$ to $20kHz$, and most importantly between $500Hz$ and $8kHz$ [55]. A high level of tonal noise in this frequency range is considered to be undesirable. Much work has been carried out with the aim of reducing or controlling tonal noise in a vast range of different applications. The usual motivation for the mitigation of tonal noise is for the comfort or health of the people that have to spend time in the vicinity of the noise source. Consequently, various legislation exists that prohibits high levels of tonal noise from being produced, such as *The Control of Noise at Work Regulations 2005*.

The distance from a noise source to the noise detector is important in studies of noise emission. The region surrounding a source of noise can be separated into two zones: The *near field* region and the *far field* region. The far field describes the zone in free space where the *sound pressure* level decreases $6dB$ with each doubling of distance from the source, this relationship is called the inverse-square law. In the far field region the sound pressure and particle velocity are almost exactly in phase. Closer to the source where these two conditions do not hold constitutes the near field region [104].

The level of noise radiated from a structure such as an electrical machine

can be measured and quantified by the sound pressure level and the *sound power* level.

The total sound pressure L_P is (in dB):

$$L_P = \ 10\log_{10}\frac{p^2}{p_{ref}^2} \tag{9}$$

Where p is the rms sound pressure (in Nm^{-2}) at a known point away from the structure and p_{ref} is a reference value, 2x10^{-5} Nm^{-2} [106]. This is approximately equal to the lowest rms sound pressure level that is audible to an average person at $1000Hz$. In order to measure the sound pressure of a machine, many measurements are usually taken at points on an imaginary surface surrounding the noise source and the average rms sound pressure p_{av} of these points is used to calculate the mean sound pressure level $\overline{L}_P$.

$$\overline{L}_P = \ 10\log_{10}\frac{p_{av}^2}{p_{ref}^2} \tag{10}$$

The resulting mean sound pressure level of the noise source will be dependent on the shape and distance of the measuring surface relative to the structure. For example, the value of $\overline{L}_P$ calculated over a hemispherical surface in an anechoic chamber that is a radius of $0.5m$ from the noise source will be $6dB$ greater than $\overline{L}_P$ calculated over a hemispherical surface that is a radius of $1m$ from the noise source if the reverberant field is still weak compared to the direct field. If a sound pressure level is to be used to quantify the noise emitted from a source, the acoustic environment, shape of the measurement surface and the distance of the surface from the noise source must also be given [104].

The total sound power level L_W is (in dB):

$$L_W = 10\log_{10}\frac{P}{P_{ref}} \tag{11}$$

Here P is the sound power emitted by the noise source in $watts$ and P_{ref} is the reference sound power, which is $10^{-12}W$ [106]. The sound power level is related to the mean sound pressure level $\overline{L}_P$ by:

$$L_W = \overline{L}_P + 10\log_{10}S \tag{12}$$

S is the total surface area of the measuring surface (in m^2). The second term of equation (12) accounts for the measurement surface in such a way that the sound power level of a noise source is independent of the shape and radius of the measurement surface. The noise radiated by two noise sources can be compared using the sound power level regardless of differences in the two measurement surfaces used to calculate this.

At a point close to the surface, the radiated sound power caused by a constant frequency acoustic wave is proportional to the velocity of the vibration of the surface that is perpendicular to the plane of the surface. In this case sound power at the measurement point l_W is calculated by.

$$l_W = \overline{v^2}ZA\sigma \tag{13}$$

Z is the characteristic acoustic impedance of air, it has units of *Rayls* and its value is dependent on the acoustic wave frequency and the temperature of the air. A is the area of the vibrating surface, $\overline{v^2}$ is the mean-squared velocity of the vibrating surface. The integral of l_W over the structure's surface gives the total sound power L_W. Not all of the sound that is created by a vibrating surface is radiated away from the surface. The sound radiated

is quantified by the radiation efficiency σ. This is defined as the ratio of the power detected from the radiator to the total power supplied and is dependent on the frequency of the vibration.

1.6 Noise Sources and Reduction Methods in Large Electrical Machines

This section provides important background information for the thesis. The aim of this section is to provide an overview of the factors that contribute to electrical machine noise. The contents of the section are organized as follows:

- Introduction to machine noise
- The vibrational behaviour of the stator
- Electromagnetic noise, which is produced by Maxwell forces and the magnetostriction effect
- Harmonics in the electromagnetic force waves
- Existing electromagnetic noise reduction methods
- Mechanical noise sources in electrical machines
- Mechanical noise reduction methods
- Aerodynamic noise sources in electrical machines
- Aerodynamic noise reduction methods
- Summary of noise in electrical machines

1.6.1 Introduction to Machine Noise

Much work has been carried out over many decades with the aim of understanding the causes of noise in electrical machines and producing quieter

machines. This has resulted in the production of noise becoming a well understood topic. Some noise reduction methods have become standard features of electrical machines. Other methods are more complex to implement and not so practicable.

The noise emitted from electrical machines originates from three main sources; electromagnetic, mechanical and aerodynamic [104]. Each of these sources produce forces which act on the different parts of the machine and cause structural vibrations and noise emission from the machine. Electromagnetic noise dominates at low speeds and medium speeds. At high speeds mechanical and aerodynamic noise dominates [17]. Electromagnetic noise is the main source of noise considered in this study. There are two sources of electromagnetic noise in electrical machines, these are *Maxwell* forces and *magnetostriction* effects. Maxwell forces act in the air gap of the machine, mainly on the tips of the stator teeth and these deform the stator core indirectly. Magnetostriction effects cause direct deformation of the stator iron. The consequence of both of these effects is to cause the stator core and stator teeth to vibrate. Radial vibrations transmitted from the back of the stator core to the frame of the machine cause the radial vibration of the frame, which is the main source of unwanted tonal machine noise. Tangential motion of the stator or frame tends to contribute very little to the overall radiated noise. There are exceptions to this, one is when cooling fins are present because the tangential motion of the frame can cause these to vibrate and consequently radiate noise.

There is a demand for electrical machines to be produced with an ever increasing performance and ever smaller size. These two demands have resulted in modern day machines having thinner frames and operating under higher flux densities than traditional machines. This results in machines

experiencing increased electric and magnetic loading, higher magnetic saturation and an increased need for cooling. These are all factors that lead to a noisy machine [104].

The vibrational characteristics of electrical machines tends to lead to tonal noise being emitted from the machines. The main reason that the tonal noise emitted from electrical machines is undesirable is not for reasons of human comfort: Large electrical machines are used for the propulsion of marine vessels, such as cruise liners, and chemical tankers. Naval vessels, such as navy ships, auxiliary oilers and submarines are also powered by large electrical machines. Any tonal noise emitted by these vessels enables the recognition and detection of the vessels, and it is imperative that this situation be avoided. Therefore, in military marine applications, electrical machines must only produce extremely low levels of vibrations and tonal noise. With this in mind, the aim of this study is to develop a technology for the mitigation of the tonal noise emitted from large electrical machines. This technology would be suitable for use with the type of large electrical machines that are used to power military marine vessels where low noise emission is a priority.

Various methods for reducing the noise emission from electrical machines have been developed. However, the vast majority of the noise producing forces in electrical machines are directly related to the operation of the machine. Thus many noise reduction techniques also negatively affect the performance and increase the cost of the machine. Methods of reduction of electromagnetic noise are usually related to reduction of the magnetic forces, the dynamic vibration level of the machine surface and the radiation efficiency of sound from the surface of the frame [104].

In analysis of the noise production of electrical machines often only the vibrational behaviour of the stator is considered even though the resultant noise is radiated from the surface of the frame. The reason for this is explained here: The frames of electrical machines are usually connected to the stator by ribs, key bars or by shrink fitting the stator into place. The forcing within the machine causes the stator to vibrate, and these vibrations are transmitted to the frame. The resultant tonal acoustic noise is radiated from the surface of the frame. The vibrational response of the stator and frame together will be different to that of the stator alone. Considering the mechanical interaction between the stator and the frame in machine analysis adds to the complication of the analysis significantly. However, if the frame is neglected, the computed vibration levels of the back of the stator core give a reliable indication of the overall level of vibration that the machine produces. The addition of the frame will not increase the overall vibration levels of the machine, and so the level of vibration that is computed without including the frame may over estimate, but will not underestimate the vibration. Therefore a measure of the tonal noise emitted from an electrical machine is given as the radial velocity of the vibration of the back of the stator core.

Rotor vibrations do not usually contribute to the noise produced by electrical machines. The reasons for this are that rotor resonances are not significantly excited by electromagnetic forces and sound radiation from the rotor surface is much lower than from the stator surface [10]. Exceptions to this are external rotor machines which are not considered here and electromagnetic excitation of the first flexural rotor bending mode which transmits vibrations to the bearings and stator.

1.6.2 Vibrations of the Stator

A stator is a cyclically symmetric structure, and this property occurs because a stator can be divided into subsections, with every one of the subsections being identical to every other subsection. Incidently, each subsection includes one tooth, a section of the windings and the corresponding segment of the back of core. Cyclically symmetric structures exhibit unique vibration characteristics and these characteristics are described briefly here. More detail is given on this subject in appendix C.4. The mode shapes of a cyclically symmetric structure can be described by a *mode number* n, the mode number describes the number of complete deformation waves around the circumference that the structure deforms into. At most resonant frequencies of a cyclically symmetric structure there are two corresponding, orthogonal mode shapes with the same mode number.

The majority of noise producing forces within an electrical machine are periodic forces with respect to time and space. These can be decomposed in space into families which correspond to integer mode numbers. The applied forcing is usually made up of travelling waves around the air gap between the rotor and stator. However, radial standing waves are often formed around the circumference of the stator from the interaction of two radial force waves with equal frequency rotating in opposite directions.

At a resonant frequency of the stator, there is a corresponding stator mode shape which dominates the response of the stator. If some forcing is applied to the stator at that resonant frequency, and the force wave has a spatial distribution with the same mode number as that stator mode shape, the stator will resonate [51]. The amplitude of vibration will be large and will depend on the damping in the structure. If the frequency of the force matches the resonant frequency of the stator but the mode number of the force does not

match the mode number of the stator there will be zero net modal excitation at that frequency and the resonance will not be excited. In electrical machines resonance must be avoided if noise and vibration is to be avoided and therefore knowledge of the vibrational response of the stator is required.

The vibration of a structure in a narrow frequency band that is within the range of acoustic interest directly causes tonal acoustic noise to be radiated from the surface of the structure. The different oscillating shapes of the stator produce different levels of noise. The radial vibration of the back of the stator core is the most dominant source of airborne noise. From the point of view of noise emission, the most important force waves are those which have mode numbers between 1 and 10. This is because the flexural rigidity of the stator increases with mode number and so for higher mode numbers the deflections decrease [97]. The surface vibrations from deflected shapes which are described by a high mode number also have low noise radiation efficiency. The natural frequencies of the stator for an n=0 mode number are usually higher than the frequencies of interest [104] [106].

In the range of acoustic interest, a large electrical machine can have thousands of resonant frequencies, whereas a small machine will have only a low number [55]. In a large machine there are also many components of force present at frequencies that are related to noise production. The frequencies and spatial distribution of these force components are likely to coincide with the resonances and mode shapes of the stator and cause high levels of vibration and tonal noise to be emitted.

1.6.2.1 Tooth Rocking Frequency In large electrical machines, a range of important resonant frequencies are the *tooth rocking* frequencies. The corresponding deflected shapes of the stator feature the tangential motion of the stator teeth relative to the stator core. One of these mode shapes

is illustrated in figure 15. If a frequency of the tangential forces that act on the tips of the stator teeth coincides with a tooth rocking frequency, the tangential motion of the teeth can be much larger than the radial motion of the stator. In small machines, this range of resonances occurs at frequencies that are higher than those of interest and so tooth rocking is not important in vibration analysis of small electrical machines. In large electrical machines this frequency range occurs within the frequency range of acoustic interest and so excitation of this resonance causes noise producing vibrations [43].

The lowest tooth rocking frequency corresponds to the tooth rocking in phase with the back of core. This can be found in an FE analysis of a single stator bay where a stator bay consists of one stator tooth, half a slot each side of the tooth and the corresponding section of back-of-core. The back of the stator core is constrained at the boundaries of the bay that join the adjacent bays. The first natural frequency of this model is the lowest tooth rocking frequency of the stator. The corresponding mode shape can be seen in figure 16.

1.6.3 Electromagnetic Noise in Electrical Machines

There are two sources of electromagnetic noise in electrical machines. These are Maxwell forces and magnetostriction effects. This subsection describes the two electromagnetic sources of noise.

Electromagnetic forcing is generated by the flux density wave that rotates around the air gap at synchronous speed. The presence of magnetic flux in the air gap gives rise to Maxwell forces. The presence of magnetic flux in the stator iron gives rise to magnetostriction effects.

1.6.3.1 Maxwell Forces Maxwell forces are generated by the magnetic flux in the air gap between the rotor and stator. The radial component of air gap stress σ_{RR} that leads to the radial components of Maxwell force is:

$$\sigma_{RR} = \frac{b_R^2 - b_\theta^2}{2\mu_0} \tag{14}$$

The radial component of flux density is b_R and the tangential component of flux density is b_θ, μ_0 is the permeability of free space ($\mu_0 = 4\pi \times 10^{-7}\ Hm^{-1}$). The tangential component of air gap stress that leads to the tangential components of Maxwell force is:

$$\sigma_{R\theta} = \frac{2b_R b_\theta}{2\mu_0} \tag{15}$$

The radial component of Maxwell force acts mainly on the tips of the stator teeth and this causes the main source of electromagnetic machine noise [64]. The magnitude of the tangential component of Maxwell force is smaller than the radial component, this acts tangentially on the stator teeth, and provides the working electromagnetic torque that drives the machine [104] [105].

1.6.3.2 Magnetostriction This section describes the phenomenon of magnetostriction in a general context. At the end of the section some information about the effect of magnetostriction on the noise and vibration of electrical machines is given. More specific information about magnetostriction effects in electrical machines and incorporating magnetostriction into FE models of electrical machines is given in appendix D.

Magnetostriction is the phenomenon of a ferromagnetic material changing dimension under the effect of a magnetic field. Magnetostriction is quantified by the mechanical strain it induces in the material in the absence of a

restraint. This strain is given the symbol λ.

The alternating magnetic field in the stator iron of an electrical machine causes alternating magnetostriction. This causes very small non-rigid-body deformations in the stator core and teeth with a high rate of change of deformation. The magnetostriction effect in the stator can cause changes in the vibrations of large stators so that at some frequencies magnetostriction increases vibrations. At other frequencies magnetostriction can dampen vibrations [6] [7].

Magnetostriction can be either spontaneous or forced. Spontaneous magnetostriction occurs in unsaturated iron when subjected to a magnetic field. This occurs from the alignment of atoms within the atomic structure of the material and is a non-linear function of magnetic flux and stress until the point of magnetic saturation. Within unsaturated iron at zero stress, spontaneous magnetostriction is proportional to the square of magnetic flux density. At the point of magnetic saturation of the material, magnetostriction also reaches its saturation value. For magnetic flux levels above the level of saturation the value of spontaneous magnetostriction remains constant.

Forced magnetostriction occurs under the application of an externally applied magnetic field for magnetic flux levels above the point of saturation. This is a linear function of magnetic field for zero stress conditions [12]. The sign of magnetostriction is constant whether the magnetic field is positive or negative [41].

The phenomena of magnetostriction causes the permeability of a ferromagnetic material to be dependent on applied mechanical stress. Applying a

mechanical stress to a ferromagnetic material increases the permeability of the material until a particular stress level is reached. Above this level a further increase in stress will cause a decrease in permeability. Further increases in mechanical stress, cause the permeability to continue to decrease as the material passes through its elastic limit. At each level of stress, the dependence of permeability on magnetic field varies [80].

Different magnetostriction effects can occur in the iron and these have been named [6]:

- Joule magnetostriction
- Volume magnetostriction
- The form effect
- The Δ E effect
- The direct Wiedemann effect
- The Matteuci effect
- The Villari effect

The Joule effect is the principle magnetostriction effect. This is an anisotropic expansion or contraction of the material in the direction of the magnetic field. The deformation of the material in the direction transverse to the magnetic field has half of the amplitude and opposite sign of the deformation in the direction of the magnetic field. With spontaneous Joule magnetostriction the overall volume of the material remains unchanged [76]. In this case the *magnetostrictive Poisson's ratio* will be 0.5 [30].

Forced Joule magnetostriction can lead to a small change in the volume of the material, however, the volume effect is a weak effect [6] [41].

The form effect is dependent on the specimen shape, this is only important in materials that have large demagnetising factors and high saturation intensity [76].

The ΔE effect describes the change in the Young's modulus of the material with magnetic field [30].

The direct Wiedemann effect is a special case of the Joule effect where the material experiences a shear strain due to the magnetic field.

The Matteuci effect is the inverse of the direct Wiedemann effect.

The Villari effect is the inverse of the Joule effect. This describes the interdependency of mechanical strain, magnetic field, material permeability and mechanical stress [30] [41]: Positive magnetostriction describes the expansion of a material under the application of a magnetic field and also the increase in magnetisation with applied tensile mechanical stress. Negative magnetostriction describes the contraction of a material under the application of a magnetic field and also the decrease in magnetisation with applied tensile mechanical stress. Iron can have either positive or negative magnetostriction depending on the strength of the applied magnetic field [6].

The phenomenon of magnetostriction is extremely complex and although the phenomenon is a well known one much research is still being done in this field. Investigations into the effect that magnetostriction has on the noise and vibration of electrical machines focus on the most relevant types of magnetostriction. These are Joule magnetostriction and the Villari effect.

For non saturated iron with no externally applied stress the relationship between magnetostrictive strain and flux density b is simply

$$\lambda \, \alpha \, b^2 \tag{16}$$

and the volume of the iron remains constant. If the iron is saturated or there is externally applied stress, the relationship between strain and flux density is much more complicated. Often the above relationship is assumed in FE analysis of electrical machines for simplicity.

The effect of magnetostriction is negligible in small machines but in large machines has a more prominent effect. Large machines are more susceptible to vibrations from magnetostriction because the small strain caused by magnetostriction leads to large absolute deflections in the larger geometries. In machines magnetostrictive forces are larger than Maxwell forces but their effect on the vibration of the structure is generally less because these forces act within the iron which has high stiffness. Studies have shown magnetostriction to contribute to between 10% and 50% of the noise produced by large electrical machines [6] [7] [54] [71] [80] [81].

Investigations into the effects of magnetostriction on materials and specifically on the effects of noise and vibration on rotating machinery have not been carried out nearly as extensively as the effects of Maxwell forces. This is because accurate magnetostriction data is difficult to obtain. Magnetostriction is dependent on stress and the stress in the stator is difficult to estimate. In the past it has been impractical to include magnetostrictive behaviour in existing FE models [28].

One extensive study into the effect of magnetostriction in electrical machine vibration is [6]. In this study quasi-static and dynamic analyses of

the stator of a large synchronous generator and small induction motor with and without magnetostriction were carried out. Results showed that the presence of magnetostriction changed the vibrational response of the stator. At some frequencies vibrations were decreased by magnetostriction but in the majority of cases magnetostriction increased the vibration of the stator. The differences in vibration with and without magnetostriction were more pronounced for larger stators. Above $1500Hz$ the effect of magnetostriction is negligible. These results were in agreement with results in [7].

1.6.4 Harmonics of Electromagnetic Force

When supplied from a sinusoidal supply the stator currents in an electrical machine induce a flux density wave in the air gap. The initial flux density wave consists of the fundamental time harmonic only. This initial flux density wave induces emf and current waves in the rotor. These induced currents then induce many flux density waves into the air gap. The variation in the geometry of the air gap leads to a resultant flux density wave which has very many spatial harmonics. The flux density wave affects the emf and currents in the rotor and stator. The affected rotor and stator currents further affect the flux density wave in the air gap. The result of this is a flux density wave which consists of very many or even an infinite number of spatial harmonic components. This resultant flux density wave gives rise to an electromagnetic force wave which has many more spatial harmonic components than the initial flux density wave [18].

The spatial harmonic components can be grouped together into components that are generated by the different features of the machine. These are:

- The distribution of the windings in the stator
- The distribution of the windings in the rotor of wound rotor machines,

or the presence of rotor bars in squirrel cage machines

- The interaction of the rotor and stator slots
- Rotor eccentricity
- Magnetic saturation

When the machine is supplied through an inverter, the supply currents are not sinusoidal, and so many time harmonics are present. Each of these time harmonics leads to further sets of space harmonics being induced in the machine and so the electromagnetic supply of an inverter fed machine is infinitely more complex than that fed by a fixed frequency sinusoidal supply [18] [82] [100].

Many different approaches are used to analyse the effects of Maxwell forces and the magnetostriction effect on the vibration of the stator. A basic approach that is often used is to neglect magnetostriction altogether and consider Maxwell force from the radial, fundamental component of the flux density wave only. This approach can be justified because this is by far the largest force component. The tangential component and higher harmonics are therefore neglected. Investigations into the particular harmonics that are important for noise and vibration analysis almost always consider only Maxwell forces. However, the magnetostriction effect as well as Maxwell forces are caused by the presence of magnetic flux density and so the harmonics in the flux density cause harmonics in both types of forcing.

The Maxwell force wave that is created from considering only the radial component of the fundamental flux density wave is proportional at every point to the square of the flux density wave. This can be seen by setting b_θ to equal zero in equation (14). This has a mode number equal to twice the pole pair number, and frequency equal to twice the supply frequency

[1]. This force does not cause predominant airborne noise in small electrical machines because the noise radiation efficiency at this low frequency is relatively poor. For large machines, this force often gives rise to noise and vibration [104].

Within the frequency range of acoustic interest for large machines is the *rotor slot passing* frequency ω_{rsp}. This is given by the rotational speed of the rotor Ω multiplied by the number of rotor slots s_r:

$$\omega_{rsp} = \Omega s_r \tag{17}$$

The shape of this force wave has a distribution around the air gap which is dependent on the combination of the number of rotor and stator teeth s_r and s_s respectively:

$$n = |s_r \pm s_s| \pm 2n_{pp} \tag{18}$$

Radial forcing at rotor slot passing frequency acts on the stator teeth to vibrate the stator. Tangential forcing at rotor slot passing frequency acts to vary the torque as a function of the position of the rotor causing cogging torque. This can also affect the flexural vibrations of the stator. Vibrations caused by the force waves with mode numbers $n = s_r + s_s \pm 2n_{pp}$ are less important because the stator is very stiff to these high spatial frequencies. The lower mode numbers $n =\mid s_r - s_s \mid \pm 2n_{pp}$ are more important [104]. The coincidence of rotor slot passing frequency or rotor slot passing frequency modulated by twice fundamental frequency and a tooth rocking frequency results in noise and vibration of large machines [47] [55] [59].

Rotor eccentricity causes air gap flux density harmonics to be generated. This is often considered to be a mechanical vibration source and so is discussed in section 1.6.6.

Saturation causes extra harmonics to be generated in the air gap flux density. These harmonics may create additional force components or may create force components which magnify force components from other sources. The magnitude of these force components is low but on coincidence with a stator resonant frequency, such as a tooth rocking resonance, can cause stator teeth vibrations to have large amplitudes [100].

1.6.5 Electromagnetic Noise Reduction Methods

Existing methods for reducing electromagnetic noise often focus on

- Controlling forcing frequencies so that they do not coincide with resonant frequencies.
- Reducing the magnetic loading on the machine.
- Reducing the susceptibility of the stator to forced vibrations by changing the geometry and properties of the stator or rotor.
- Utilizing the control available through power electronic converters.

Knowledge of the amplitudes and frequencies of the flux density harmonics in the machine and the forces associated with these are required before alterations to the harmonics can be carried out. Varying the supply current will alter the resultant forces in the machine and make it possible to avoid exciting some of the resonances in the machine [46].

The twice supply frequency forcing component cannot be eliminated by removing imperfections and so where possible the stator should be designed to avoid a resonance at this frequency [104]. If the machine resonant frequencies are found, it may be possible to create exciting forces with frequencies that avoid these frequencies. With variable frequency solid state inverters this is difficult as forcing frequencies vary over a wide frequency range but

bands of frequencies around critical frequency values can be avoided.

Manufacturing a motor with as symmetric a construction as possible reduces the number of resonant frequencies associated with that machine and so reduces the likelihood of a forcing frequency corresponding with a resonant frequency [19].

The radial component of Maxwell force can be reduced by increasing the thickness of the air gap. This is because if all other parameters are equal, the radial component of Maxwell force is inversely proportional to the square of the air gap length. However, increasing the air gap thickness also decreases the efficiency and power factor of the machine and tends to increase the temperature of the machine [104].

Skewing the rotor or stator slots along the axial length of the machine causes the radial forces that act on the individual laminations to change along the length of the machine. This is equivalent to introducing a phase angle between the radial forces that act along the length of the stator. The average radial force that acts on the stator is then decreased from the force that would act with no skew of the slots. Reducing the radial force acting on the stator reduces the excitation of noise vibrations effectively in small machines. However, for machines that are rated above $500kW$, skewing can cause cross currents between the rotor cage bars and introduce torsional vibrations and increase noise. Using a herringbone skew can overcome this problem in induction machines with cast rotor bars [43] [104].

Increasing the pole number of a machine decreases the pole pitch proportionately and reduces the magnetic loading of the back of the stator core enabling the construction of smaller machines. A stator with a thinner

back of core will be less rigid than a stator with a thicker back of core [16] [93]. Increasing stator core thickness can significantly decrease machine noise emission. This is because the vibrational amplitude of the stator is approximately proportional to the inverse of the stator core thickness cubed for frequencies below the corresponding resonance frequency. Noise emission is approximately proportional to stator vibrational amplitude squared. The drawbacks of this method are that this increase would also increase the weight and cost of the machine and affect the natural frequencies of the machine.

A good choice of rotor - stator slot combinations is a well established and essential part of the design of a quiet machine. The aim of the choice of slot combinations is to avoid magnetic flux density space harmonics. Shaping the slot openings to minimize flux pulsations also aids noise reduction [8] [43] [59].

The shape of the magnets in permanent magnet synchronous machines affects the shape of the magnetic force wave in the air gap. Altering the edge shape of the permanent magnets can shift the magnetic forcing frequencies. Transmission of high frequency vibrations is lower than that of low frequency vibrations, and so altering the shape of the permanent magnets to increase the forcing frequencies can reduce vibrations, except at stator resonances [69]. In induction machines, a squirrel cage rotor produces less harmonic components than a wound rotor due to having fully closed slots [18].

Increasing the number of phases from the conventional three gives several benefits including reduced noise and vibration, higher torque density and lower torque pulsations, greater fault tolerance and higher efficiency. The

number of phases is now a design variable for high performance direct drive propulsion motors [93].

Noise emission from a machine is affected by the nature of the power supply to the machine. The use of power electronic components can increase the noise emitted from an electrical machine compared to a pure sinusoidal supply. Noise emission from power electronic devices has been covered in section 1.3.2.

A method for eliminating noise producing components of the Maxwell forces in the air gap has been described in [18]. The method involves injecting small current harmonics into the stator supply current. The injection of one current harmonic creates two force waves with mode numbers 0 and twice the number of pole pairs $2n_{pp}$. If unwanted forces exist that have these mode numbers, and one of the created forces has the same amplitude, angular frequency and opposite phase as the unwanted force this created force will cancel out the unwanted force. This eliminates the vibration and noise that the unwanted force causes. The second created force is supplementary, this could be used to cancel a second unwanted force or it could create extra unwanted noise and vibration. Multiple current injections could be used to cancel many noisy forces. The method requires accurate sensing of the frequency, amplitude and phase of the unwanted force. The frequency, amplitude and phase of the created force is constantly adjusted to oppose the unwanted force. In experiments, Cassoret *et al* [18] used this method on two different machines. At the particular frequency the noise levels were reduced from $50dB$ to $23dB$ and from $47.1dB$ to $24.5dB$. The power that causes the unwanted noise is low and so the power required to cancel the noise is also low (at most 0.002% of the total machine power). The machines used in this experiment were chosen because the mode number and

frequency of the unwanted force was able to be matched by the frequency and mode number of the created force. This method, although effective is only useful at one particular frequency for each created force and for unwanted force waves with particular mode numbers.

This section has reviewed sources of electromagnetic noise and existing methods for ensuring that this type of noise is kept to a minimum. In the next sections, mechanical and aerodynamic noise sources are reviewed.

1.6.6 Mechanical Noise in Electrical Machines

Mechanical noise is negligible at low speeds and increases with speed. Mechanical noise is often caused by eccentricity of the rotor, which can be static or dynamic. Other sources include the bearings and brushes, bad finishing, surface irregularities, too dense grease and rust [17] [83] [104].

Static rotor eccentricity occurs when the axis of rotation of the rotor is located at the centre of the rotor but not at the centre of the stator. This causes the air gap between the rotor and stator to have a minimum and maximum thickness at diametrically opposite points. These points are not changed by the rotation of the rotor. This leads to an uneven flux density distribution in the air gap; which causes an unbalanced magnetic pull on the stator. Static eccentricity of machines that have small air gaps introduces additional harmonics into the magnetic flux density field and therefore additional force components. These forces can give rise to audible noise when their frequencies occur close to the resonant frequencies of the stator. In a three phase two pole induction motor, eccentricity in the air gap causes homopolar alternating fluxes at slip frequency. These excite mechanical forces at double slip frequency [73].

Static eccentricity is most likely to be caused by variations in part dimensions within the manufacturing tolerance limits, this leads to a variation in audible noise data between nominally identical machines. Ovality of the stator core, wear of the bearings and positioning error of the rotor also cause static eccentricity. Changing the number of rotor bars will cause the resulting vibration to occur at different frequencies [25] [26] [60] [73].

Dynamic rotor eccentricity occurs when the rotor is positioned eccentric to the shaft and the bearings are concentric to the stator. As the rotor rotates, the centre of rotation of the rotor changes and so the variation of the magnetic flux density in the air gap also changes, this causes a dynamic unbalanced magnetic pull to act on the stator. The unbalanced magnetic pull acts to decrease the critical speed of the machine, and this increases the likelihood that a supply frequency will correspond with this critical speed. If this does occur, large, dangerous stator vibrations are created. Dynamic eccentricity could occur from a bent shaft, wear of the bearings or movement of the windings and so the effect of dynamic eccentricity can worsen with time [25] [37] [43] [47] [60].

Ball bearing noise is generated from the relative motion between two contacting surfaces and can be due to irregularities of the balls in the races and cages or through ball skidding. Different types of bearing generate different levels and frequencies of noise. The vibratory forces from bearings may have a random frequency spectrum which transmit random vibrations to the structure or may occur in a narrow frequency range and cause tonal noise to be emitted from the bearings [43] [59].

1.6.7 Mechanical Noise Reduction Methods

The likelihood of significant rotor eccentricity occurring in an electrical machine can be reduced by implementing stricter tolerance limits on component dimensions and ensuring static and dynamic balancing of the machine. This increases manufacturing costs but will also increase machine performance, efficiency and life and will decrease torsional and radial vibrations.

Homopolar fluxes in two pole machines caused by static eccentricity can be reduced by inserting non-magnetic rings between the bearings and end shields, or using non magnetic end shields. These both increase the reluctance of the path of the homopolar fluxes and so reduce the flux amplitude. Also, the bearing arrangements of two pole machines should be suitable for the compensation of eccentricities [73].

Parallel paths in the stator windings are another way of reducing noise due to rotor eccentricity. Rotor eccentricity causes the air gap to have a minimum thickness at one angular position and a maximum thickness at another angular position. When the stator windings are connected in series all windings have the same current so the magnetic flux produced in the winding at the angular location of the largest air gap will be less than in the other windings in the series and so a resultant magnetic pull will be generated in the air gap. If the windings are connected in parallel, the current in the windings at the location of the larger air gap increases and acts to offset the unbalanced magnetic flux distribution. The result of this is a reduction in the unbalanced magnetic pull. Yang [104] found that favourable connections for the parallel paths were those with all pole groups in each phase in parallel or all pole groups in each phase in two parallel paths with diametrically opposite pole groups in parallel. There are also advantages to using equalizers to connect the ends of every pair of pole groups [104].

For large and medium machines that have flexible bars linking the outer frame to the inner core, the vibration of the outer frame and inner core can be reduced by altering the stiffness of the connectors and the frame [104].

Bearing noise can be reduced with the use of plain bearings over ball or roller bearings because plain bearings have two contact surfaces of similar radius of curvature and so oil is easily maintained between the surfaces and the likelihood of contact is minimized. Ball or roller bearings are more likely to contact with the housing. Low noise precision bearings, preloaded bearings and journal or sleeve bearings also reduce bearing noise [59].

1.6.8 Aerodynamic Noise in Electrical Machines

Aerodynamic noise occurs from any fast change in the pressure of air flowing through a machine. This can be caused by the fans and ducts that are used for cooling. The noise usually radiates directly from the air flow, but this can also excite resonances in the structure and cause structure borne vibration and noise. Cooling fans are usually mounted on the shaft of small machines and have the same speed. At speeds above rated speed, audible noise is dominated by the aerodynamic noise of the fan [82]. The power density of electrical machines has significantly increased over the last few decades and the space available for cooling has also decreased. This necessitates higher air velocities for improved surface heat transfer coefficients, which also cause increased noise [59]. Noise from ventilation is usually broadband in nature, caused by the irregular flow of air through ducts with sharp changes in cross section or direction. Pure tones are also superimposed on this. The pure tones are caused by the periodic disturbances of the rotating fan blades, obstructions in the air stream and resonances in cavities [100].

1.6.9 Aerodynamic Noise Reduction Methods

Aerodynamic audible noise from the fan can be counteracted by using a separate fan or by optimisation of the motor and fan construction [82]. For example, a decrease in noise can be achieved by an increased clearance at the ends of the fan blades and contouring stationary obstructions. Changing the number of fan blades can also decrease the noise level. Duct design is also important in reducing pitched aerodynamic noise [59]. White noise can be decreased by avoiding sharp corners and sudden changes in cross sections in air passages. Acoustic insulating materials can help to reduce aerodynamic and structure borne noise [59]. Distributing the air stream away from the machine can move the noise to a place where it is less important [43].

1.6.10 Summary of Machine Noise and Reduction Methods

This section has introduced the sources of noise in electrical machines. These are categorized as electromagnetic, mechanical and aerodynamic. The electromagnetic forcing in the air gap of the machine and in the stator iron that causes noise to be emitted from the machine is the focus of this study. This study aims to create a technology that will either eliminate these forces or control the resulting vibration. Electromagnetic noise is generated by two varying forces, these are Maxwell forces and the magnetostriction effect. Maxwell forces have been studied in depth by many researchers. Magnetostriction effects are less well understood and more complex. In large electrical machines the magnetostriction effect is important. Also in large electrical machines, analysis of noise vibrations is complex. This is because of their high modal density in the range of acoustic interest and the presence of forcing frequencies in this range which are essential to the operation of the machine. Reduction of electromagnetic noise is difficult to achieve because many of the techniques that could potentially reduce any noise produced by an electrical machine adversely affect the performance of

the machine.

The next sections describe the specific methods that are proposed in this study for reductions in vibrations and increases in efficiency of electrical machines.

1.7 The Magnetic Bimorph Concept

The magnetic bimorph concept is unique to this thesis. This is a new idea for eliminating some of the electromagnetic noise produced by electrical machines. This idea consists of an electrical conductor placed through the root of each tooth of a large stator. Control of the excitation to these conductors will control the motion of the teeth and the resulting vibration of the stator in a manner that uses the teeth as inherent vibration absorbers. This concept utilizes the magnetostriction phenomenon in iron. The following paragraphs explain this concept in more detail.

The magnetic bimorph concept has electrical conductors through the root of each stator tooth. If there is no other source of excitation to the machine, exciting the bimorph conductor will create a circular magnetic field around the conductor in the stator iron at the root of each tooth.

The excitation provided to the standard stator windings in an electrical machine causes magnetic flux lines to flow circumferentially around the stator core and radially through a large proportion of the stator teeth. The lines of flux that flow in the teeth are fairly straight and are uniformly distributed. This is shown for a single stator tooth in figure 17. Exciting the bimorph conductor along with the stator winding excitation will cause the magnetic fields to interact. The magnetic field from the bimorph conductor will act to divide the previously uniform flux unevenly in the teeth so that

flux lines become more concentrated on one side of the conductor than the other. This effect is shown for the stator tooth in figure 18. Due to the magnetostriction effect, the tooth will expand or contract along one side and bend as if there is a mechanical moment acting on the tooth. This is shown in figure 19. The bimorph conductors can be controlled so that the equivalent moment acting on the tooth is controlled. This moment can then counteract the Maxwell forces that act tangentially on the tooth tips and the magnetostriction caused by the stator windings. This cancels out the motion of the teeth and prevents the noise that would occur from the tooth rocking motion. The cancelling of unwanted periodic forces by imposing further periodic forces is called vibration cancellation. This concept is described in appendix A.

Predictions for this concept are that force cancellation will be effective at high forcing frequencies but not effective at low frequencies. This is because the concept relies on the bending motion of the tooth. At frequencies below the tooth rocking frequency the tooth exhibits rigid body motion and the stator back of core expands and contracts. At tooth rocking frequencies the teeth bend relative to the stator core. This bending motion also occurs at frequencies above the lower limits for tooth rocking frequency. Therefore vibration at forcing frequencies above tooth rocking frequency can be cancelled by this method.

A positive feature of this concept is that it can be used in conjunction with a machine that is supplied by mains electricity, although feedback control components and power electronic converters will be required for control of the bimorph conductors.

The vibration modes that feature a radial contraction and expansion of

the stator core will not be cancelled by this method since those modes have zero participation from tooth bending. However this motion is unlikely to cause high levels of noise.

1.8 The Individually Controlled Conductors Method

Machines that are supplied by mains electricity are only three phase machines. Machines that are supplied by power electronic converters are mainly three phase machines. However, these have the potential to be supplied with more than three phases. Increasing the number of phases that a machine is supplied with increases the level of control over the machine. The amount by which three phase machines can be controlled is relatively limited. The maximum control that is possible over an electrical machine is achieved by controlling the total currents in the conductors in each of the stator slots individually.

Electrical machines with individually controlled conductors (ICCs) in the stator slots are a technology that is currently being investigated with a view to implementation by Converteam Ltd as part of an *Active Stator* project [23]. This technology involves conductors in the slots of the stator each connected to a supply that is provided through busbar ring assemblies and sets of semiconductor switching devices at one or both ends of the stator. Figure 20 illustrates this construction. The conductors can be connected in pairs with a control arrangement located at one end of the stator so that the current supplied to one conductor flows along the length of the stator and back in the other conductor in the opposite direction. The conductors can also be connected so that sets of semiconductor switching devices and power supply busbar ring assemblies are situated at each end of the stator. With this configuration every conductor can be controlled individually. This method of power supply and control is considered in this thesis. This

construction straight away provides one advantage over traditionally wound stator constructions, and that is the use of ring assemblies instead of end windings. This is advantageous because, although the overall efficiency of traditionally wound electrical machines is high, some power is still lost during operation. Copper loss is usually a large source of power loss. This is proportional to the length of the windings if all other values are constant. Replacing the end windings from the stator with ring assemblies can eliminate a large proportion of the copper material and therefore the copper loss from the machine.

The main benefit of the ICC method is the high level of control that this method provides. Controlling the conductors in each slot results in control over the electromagnetic forces that are created in the machine. This control can be utilized so that the machine is supplied with a current pattern that results in the least power losses possible and therefore, leads to the most efficient operation of the machine. This will then enable higher power density machines to be produced and operators can benefit from lower life-cycle costs.

Another aspect where this method may be of use is in the control of vibrations. It has already been established that electromagnetic forcing is essential to provide the working electromagnetic torque that turns the rotor. However, electromagnetic forcing also produces vibrations in the stator and these transmit to the connecting components of the machine. At certain frequencies stator vibrations cause noise to be emitted from the machine. The ICC idea works by controlling the forces that are produced in the machine. This method therefore has the potential to control the troublesome components of force so that those components are reduced. This method of vibration reduction is predicted to be effective in the majority of cases.

However, there will also be drawbacks to this method; some of the electromagnetic force components that cause unwanted vibrations are essential to the running of the machine and so cannot be reduced by this method. One example of this is the twice supply frequency force that occurs as a direct result of the fundamental supply frequency. Elimination of this component of force would prevent the machine from running. Also, the pattern of current which is required for a smooth running machine is unlikely to be the same pattern of current that gives the highest efficiency. The method will be suitable for one of these criteria but not both of them together.

The bimorph controls described in the previous section can be used in a stator in conjunction with individually controlled conductors. These two methods used together have the potential to create an extremely efficient machine which also produces a very low level of noise and vibration. Including the bimorph controls in a machine supplied with ICCs means that the ICCs can be powered with the current pattern that provides the machine with the most efficient operation and the vibration control can be provided by the bimorph conductors. The unwanted force components will be produced but they will be cancelled by equal and opposite force components produced from the bimorph conductors.

1.9 Conclusion to the Introduction

The introduction has set out the aims for the thesis, given the background information relevant to this topic and described the proposed methods for achieving the aims. The remainder of the thesis will develop these ideas further and illustrate how effective these methods can be.

The aim of the study is to develop a method of reducing electromagnetic noise in large electrical machines. The motivation for this work is for the

marine industry where military vessels are required to be silent so that signals are not generated which enable the unwanted detection of the vessels.

The methods that are proposed to achieve this are called bimorph conductors and individually controlled conductors. The magnetic bimorph concept is unique to this study. This concept utilizes electrical conductors in the root of each tooth in the machine stator. Control over the excitation to these conductors leads to control over the movement of the stator tooth and the ability to use the movement of each stator tooth as a vibration absorber. This method takes advantage of the magnetostriction phenomenon in iron to create this motion. The method is a realistic proposal for cancellation of unwanted forcing frequencies close to and higher than the tooth rocking frequency. This method is suitable for large machines where the tooth rocking frequency occurs at a relatively low frequency and the magnetostriction effect is significant. However, low frequency vibrations caused by the deformation of the stator core and not the teeth cannot be controlled by this method.

The individually controlled conductor method consists of windings in the stator slots which replace traditional stator windings. The conductors in each stator slot are controlled individually, which provides a high level of control over the current fed to the machine. This method can be utilized to achieve an extremely efficient machine. This construction also eliminates end windings and so eliminates the copper losses that occur in these. Drawbacks of this method include the inability to affect force components that are essential to the running of the machine even if these also cause noise and vibration. Also, a trade-off is required between the excitation pattern which provides the most efficient machine and the excitation pattern that provides the quietest operation.

Combining the bimorph and ICC method results in a level of control over the machine which enables both high efficiency and low noise. Efficiency is provided by the ICC controls and vibration absorption by the bimorph controls. This idea is developed further in the rest of the thesis.

Windage and Friction	0.57
Stator Copper Loss	0.69
Rotor Copper Loss	0.28
Stator Core Loss	0.74
Stray Load Losses	0.27
Total Loss	2.55

Table 1: Losses from a $1492kW$ Synchronous Motor (%)
Taken from [102]

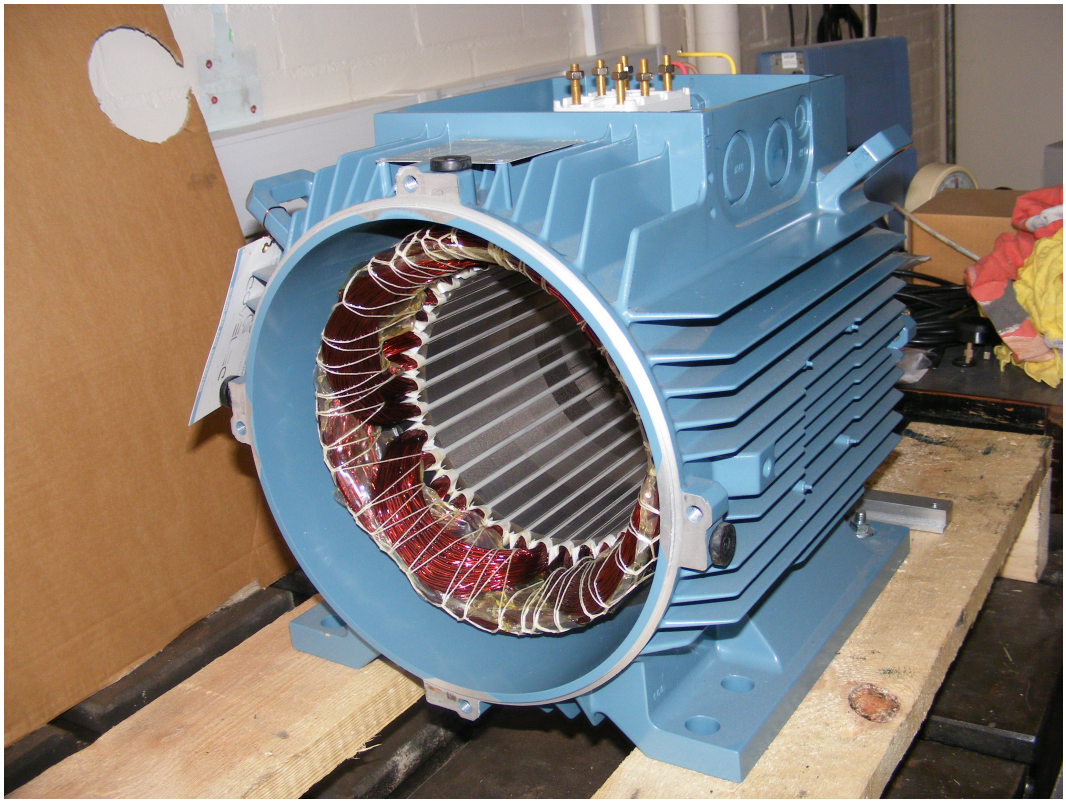

Figure 1: An Induction Motor Stator and Casing

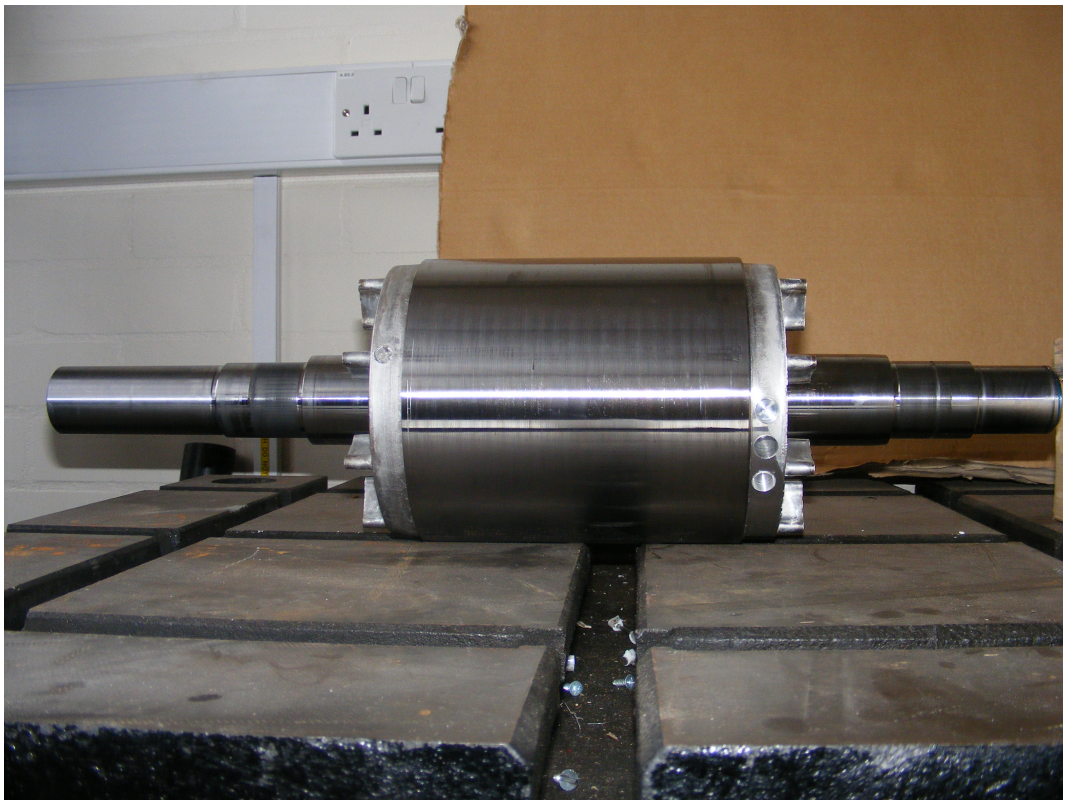

Figure 2: An Induction Motor Rotor

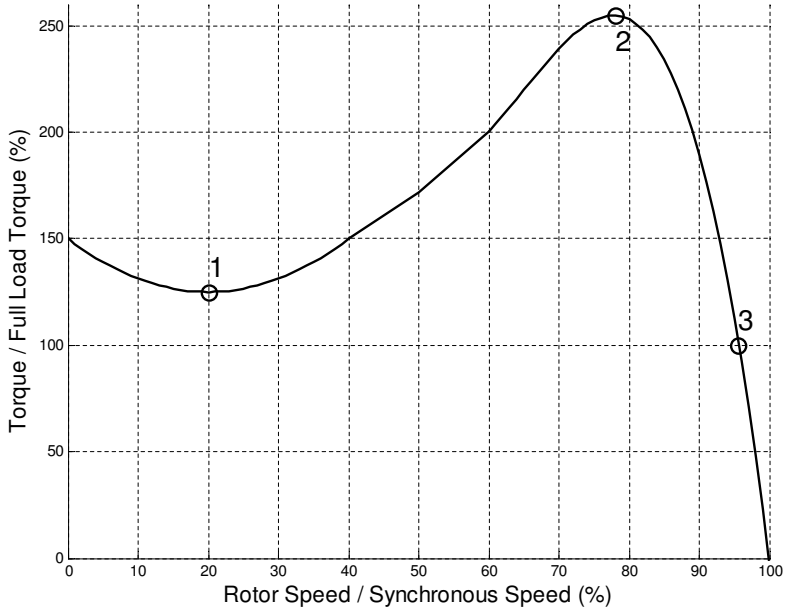

Figure 3: The Torque Speed Curve of a Conventional AC Induction Motor
1: Pull Up Torque
2: Pull out Torque
3: Full Load

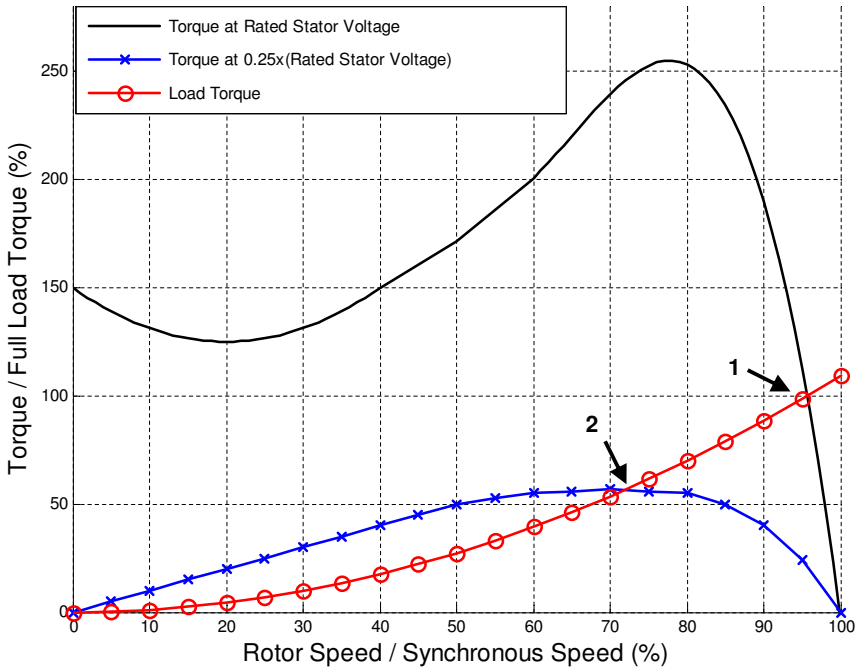

Figure 4: The Torque against Speed Curves for Rated Voltage, $\frac{1}{4}$ Rated Voltage and Load Torque

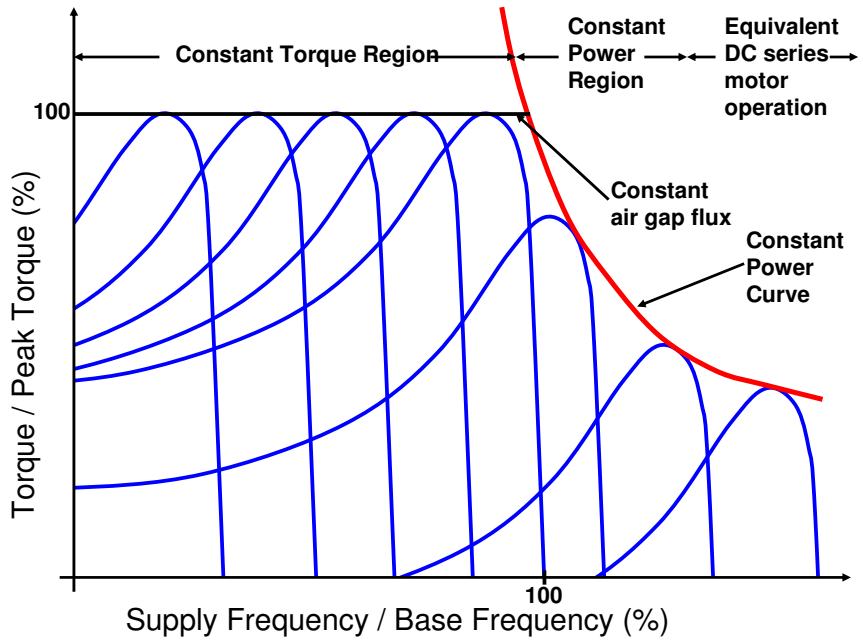

Figure 5: The Torque against Speed Curves with Variable Voltage and Variable Frequency

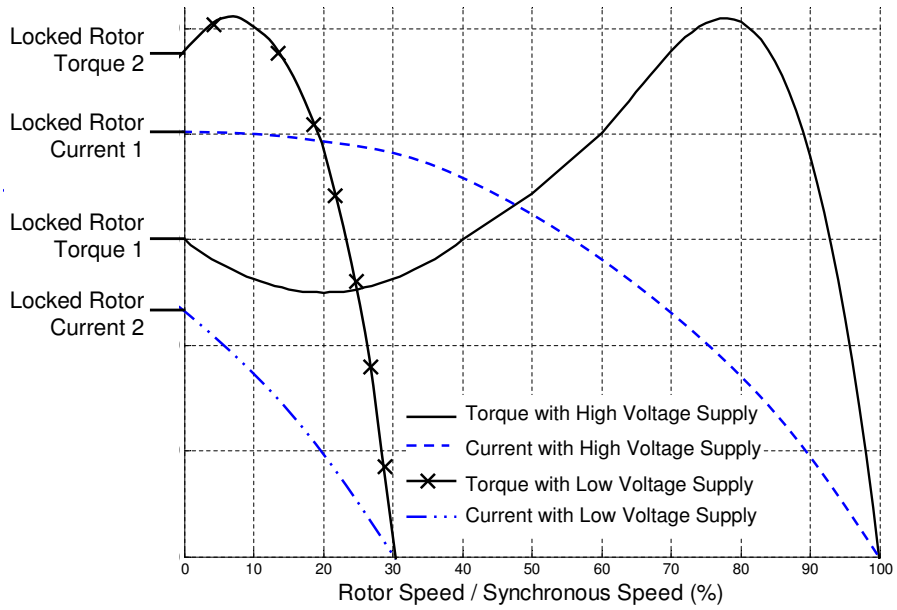

Figure 6: Torque and Rotor Current against Speed Curves

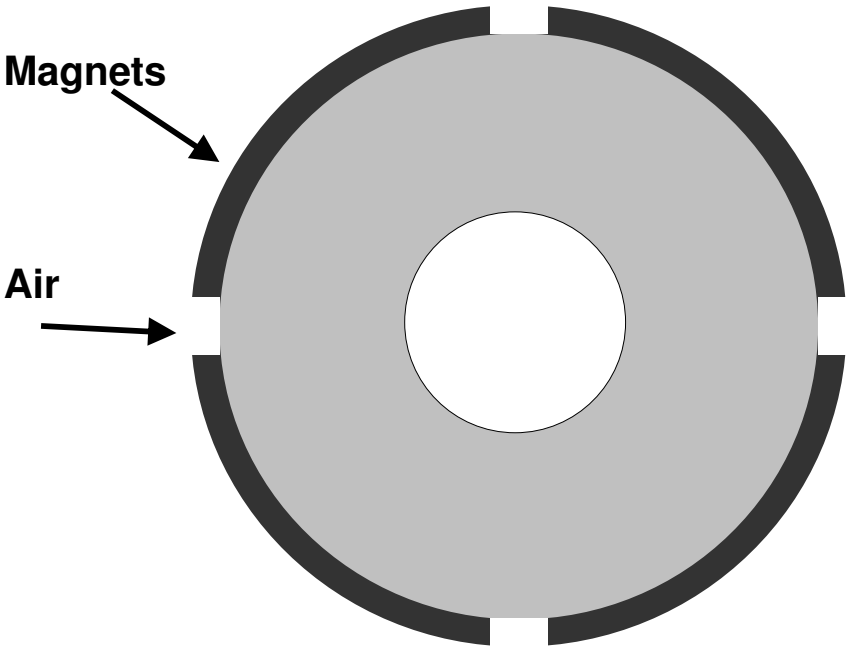

Figure 7: A Surface Permanent Magnet Rotor

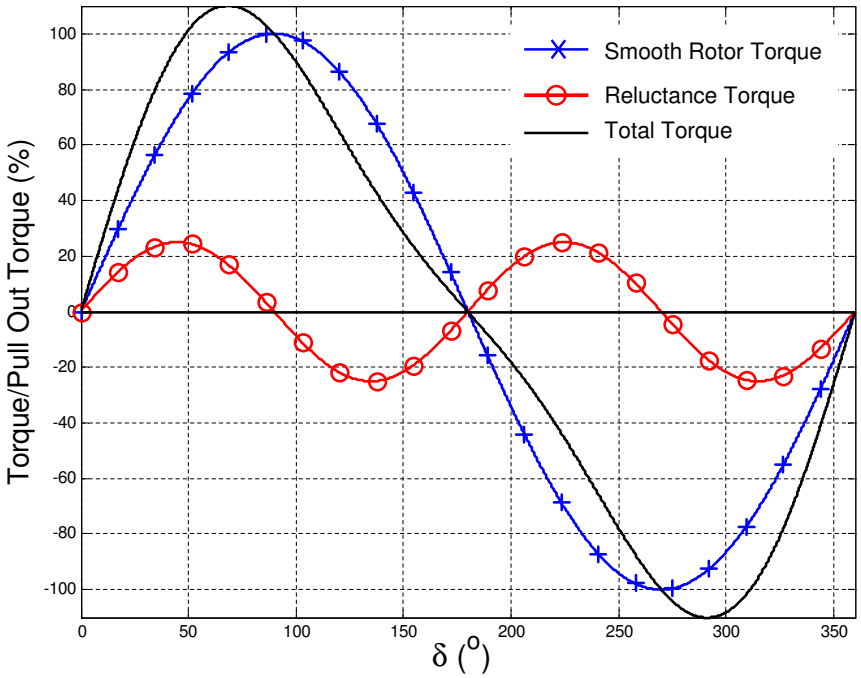

Figure 8: The Torque against δ Curve for a Synchronous Machine

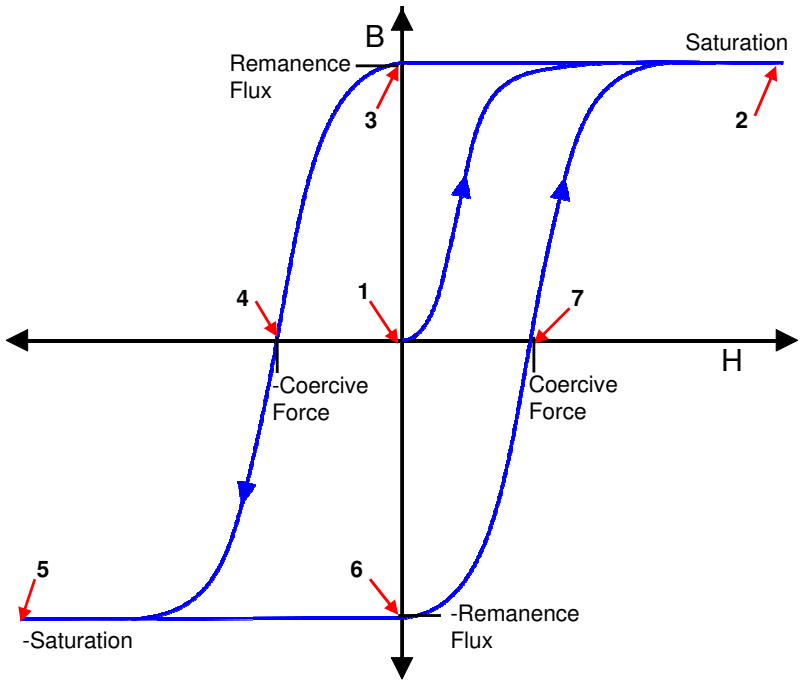

Figure 9: Hysteresis Loop

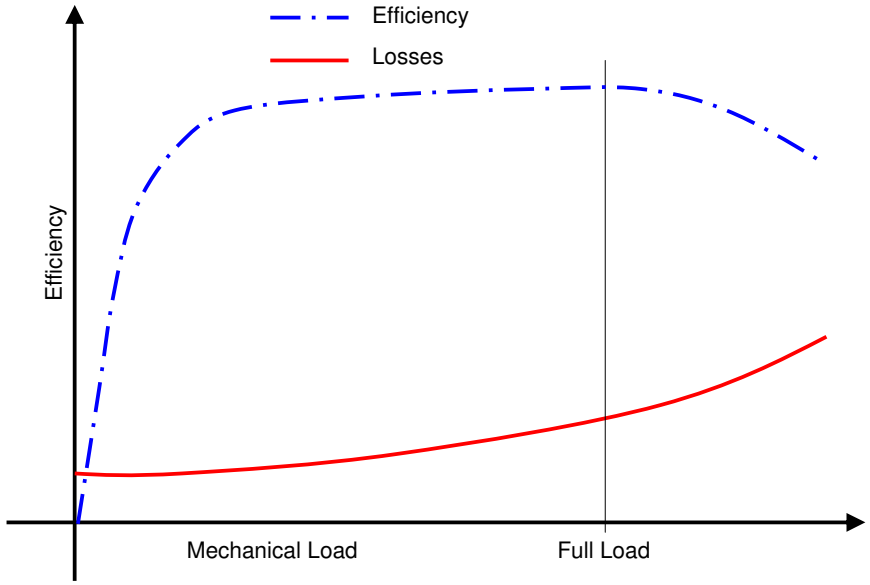

Figure 10: Machine Efficiency against Load

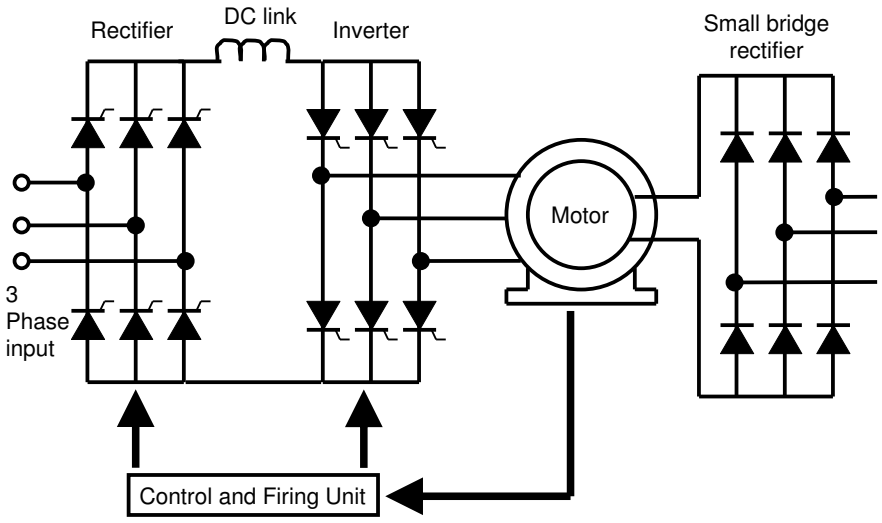

Figure 11: A Typical Rectifier-Inverter System

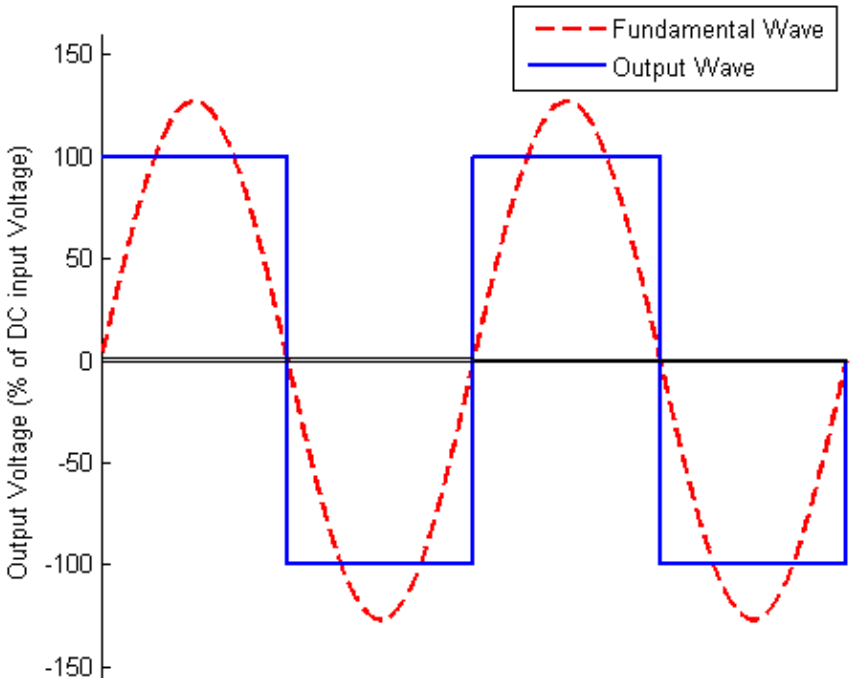

Figure 12: Output Wave Form From a Rectifier - Inverter System

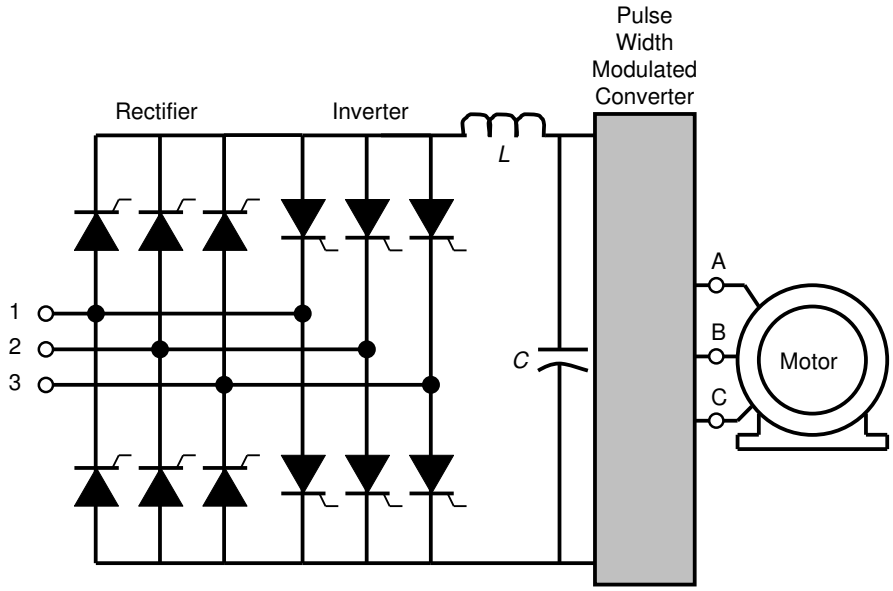

Figure 13: A Typical Pulse Width Modulation System

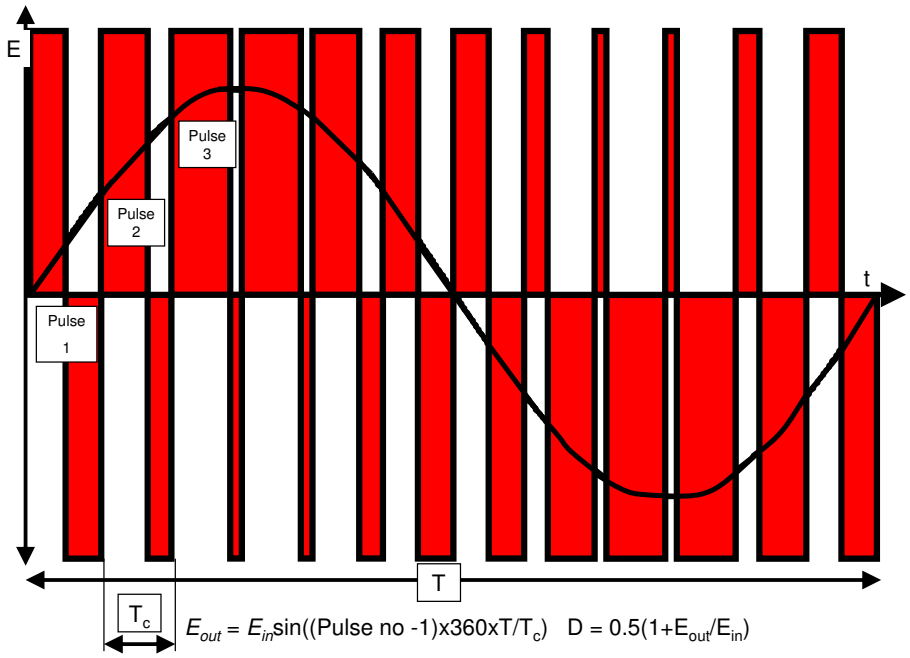

Figure 14: PWM: Generating a Sine Wave From a DC Supply

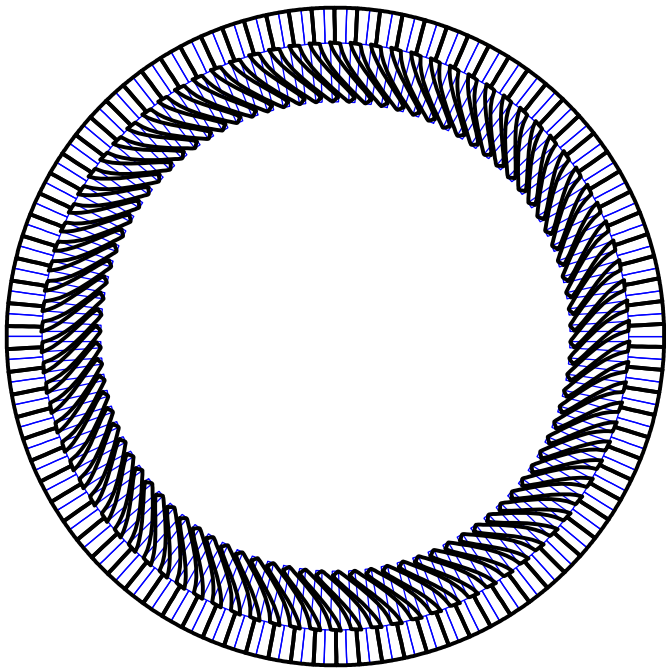

Figure 15: A $n = 0$ *Tooth Rocking* Mode

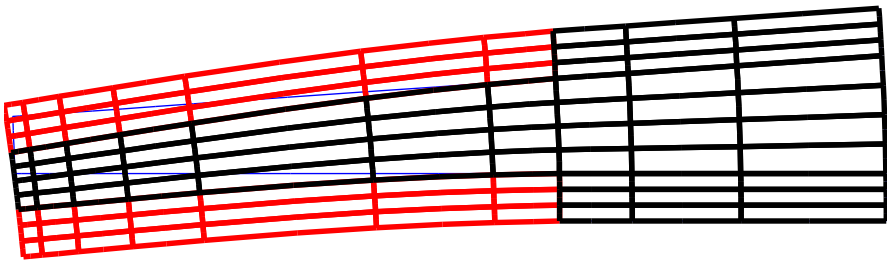

Figure 16: The Lowest Tooth Rocking Frequency Mode Shape

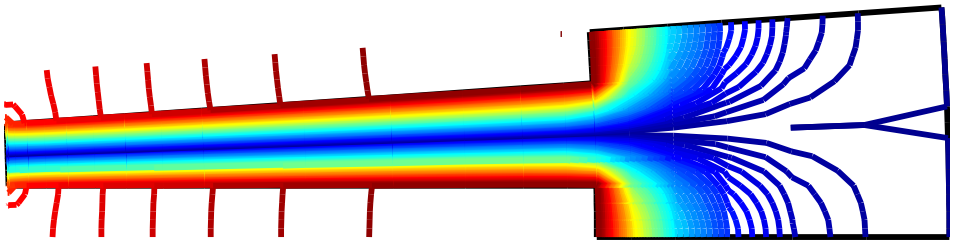

Figure 17: Uniform Magnetic Flux in a Stator Tooth

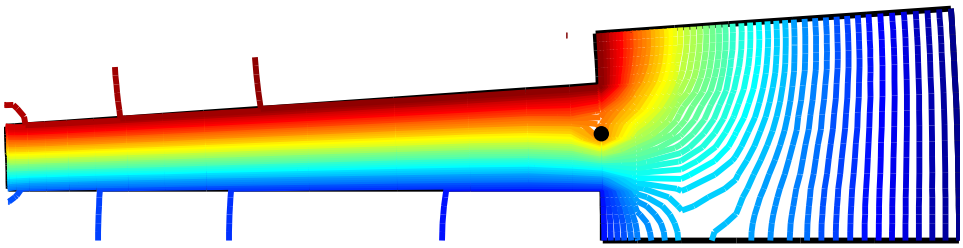

Figure 18: The Magnetic Bimorph Effect on the Magnetic Flux in a Stator Tooth

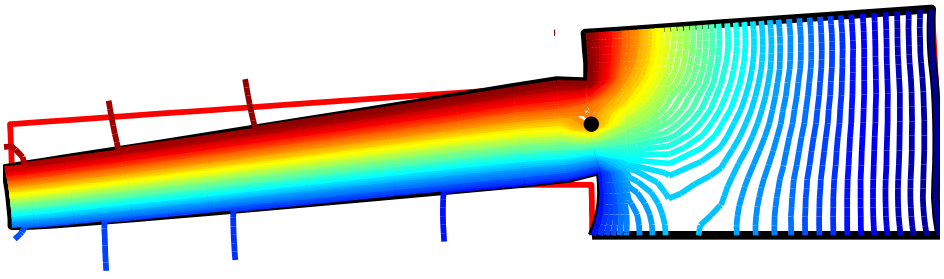

Figure 19: The Magnetic Bimorph Effect on the Motion of a Stator Tooth

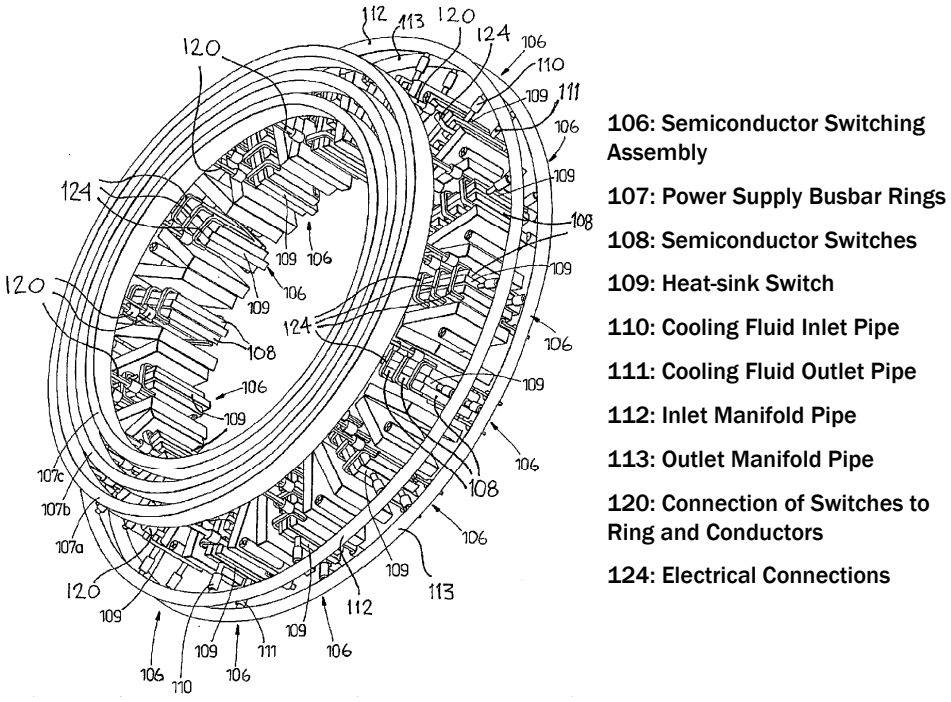

Figure 20: Individually Controlled Conductor Power Supply and Control Arrangement
Taken from [23]

2 The Magnetic Bimorph Concept

2.1 Introduction to the Magnetic Bimorph Concept

This chapter describes the theory of the magnetic bimorph concept and two experimental investigations that were carried out to investigate the potential of using this method in practice. The first experimental investigation illustrates the physical ability of *bimorph conductors* to create a tooth rocking motion in a single stator tooth. The second experimental investigation illustrates the effect of the bimorph magnetic field on the vibration of an electrical machine.

A simple bimorph actuator or sensor usually refers to a cantilever beam that consists of two active layers. An input causes an extension of one layer of the beam and this causes the beam to deflect. The layers are usually formed from two materials with different coefficients of thermal expansion or from one active and one inactive piezoelectric strip. They are activated by a thermal or electrical input. These are used as actuators and sensors in applications that include thermostats, fuel injection valves and optical positioning.

The magnetic bimorph effect that is investigated in this study requires a ferromagnetic material cantilever beam to carry a longitudinal flux. The bimorph effect is generated with an electrical conductor through the root of the beam and perpendicular to the longitudinal axis of the beam. On application of an electrical current in the conductor a magnetic field is generated in the beam around the conductor. The magnetic field from the conductor acts to distort the already existing magnetic field. This causes the flux density on one side of the beam to become more dense than the flux density on the other side. The magnetostriction effect causes an instantaneous strain

to occur in a ferromagnetic material under the application of a magnetic field. The distorted magnetic field in the beam causes a high strain in the beam along the side of the beam of high density magnetic flux. This strain acts to bend the beam. This has an effect on the beam comparable to a mechanical moment applied to the free end of the beam. A single stator tooth is comparable to a cantilever beam fixed to the stator back of core. This effect is shown on a single stator tooth in figures 17, 18 and 19 in Chapter 1.

This study aims to show the potential of the bimorph effect as a method of vibration absorption in large electrical machines. There are certain conditions that occur during the operation of large electrical machines that give the bimorph effect this potential. One condition is that at any instant during operation of the machine a substantial proportion of all of the stator teeth have flux flowing from the tooth root to the tooth tip or vice versa. This flux mainly flows uniformly along the length of the teeth. Another condition occurs in the nature of the vibration of the stator core and teeth. The deflected shape of the stator at a particular frequency consists of a contribution from many mode shapes. Many of the deflected shapes of the stator include a rocking motion of some or all of the teeth and a deflection of the back of the stator core. The bimorph effect can control the flow of flux through those stator teeth that have an existing longitudinal flux. Subsequently this controls the rocking motion of those teeth. This can be used to cancel some of the vibration of the stator. Vibration modes that do not have a tooth rocking motion cannot be cancelled by the bimorph effect.

In order to implement the bimorph concept of vibration control in electrical machines, it is proposed that conductors be positioned through the root of each stator tooth. These are to be controlled individually so that the magnetic flux that flows through the root of each tooth is optimized

for the most effective control over the motion of the tooth. At an instant in time when no flux flows through the tooth, exciting the bimorph conductor in that tooth will generate flux around the conductor but will not generate a flow of flux along the length of the tooth. A large current would be required through that conductor if this magnetic field was to affect the bending of that tooth. This is unnecessary because at an instant when flux flows through the tooth the magnetic field can be distorted by exciting the bimorph conductor with only a small amount of current. At one instant in time a large proportion of the stator teeth will have a flow of longitudinal flux and so the motion of these teeth will be controlled by the bimorph conductors. Practical implementation of this control would require measurement of the flux in the teeth with a search coil.

2.2 Using Stator Teeth as Vibration Absorbers

This section describes the theoretical application of the magnetic bimorph concept to an electrical machine. An analogy with a vibration absorber is used. Vibration absorbers have been described in appendix A.

A single DoF mass-spring-damper primary system and attached vibration absorber is shown in figure 21. The stator teeth are represented by the single DoF mass-spring-damper absorber system. The corresponding part of stator back of core is represented by the primary mass-spring-damper system. The spring stiffness and damping factor K_{teeth} and C_{teeth} respectively represent the dynamic characteristics of the stator teeth with no bimorph control. The spring stiffness and damping factor K_{core} and C_{core} respectively represent the dynamic characteristics of the stator back of core. The intrinsic electromagnetic forces from Maxwell forces and the magnetostriction effect due to the excitation in the field windings are collectively represented by F_{em}. The equivalent magnetostrictive forcing that occurs as a result of the

bimorph control is denoted $F_{bimorph}$ and is applied to the stator teeth and core in equal magnitude but with opposite sign. $F_{bimorph}$ acts on the stator teeth with the same sign as F_{em}. This force is controlled via control of the currents in the bimorph conductors. The equation of motion for this system is:

$$\begin{bmatrix} M_{core} & 0 \\ 0 & M_{teeth} \end{bmatrix} \begin{Bmatrix} \ddot{x}_{core} \\ \ddot{x}_{teeth} \end{Bmatrix} + \begin{bmatrix} (C_{core} + C_{teeth}) & -C_{teeth} \\ -C_{teeth} & C_{teeth} \end{bmatrix} \begin{Bmatrix} \dot{x}_{core} \\ \dot{x}_{teeth} \end{Bmatrix} + ...$$

$$\begin{bmatrix} (K_{core} + K_{teeth}) & -K_{teeth} \\ -K_{teeth} & K_{teeth} \end{bmatrix} \begin{Bmatrix} x_{core} \\ x_{teeth} \end{Bmatrix} = \begin{Bmatrix} F_{em} + F_{bimorph} \\ -F_{bimorph} \end{Bmatrix} \quad (19)$$

2.2.1 Cancelling a Modal Force

The vibration absorber system considered here will experience unwanted vibration when excited with the original electromagnetic force F_{em} and no bimorph excitation. In this case the right hand side of equation (19) will be:

$$\mathbf{f} = \begin{Bmatrix} F_{em} \\ 0 \end{Bmatrix} \quad (20)$$

The unwanted vibration can be cancelled by cancelling out a modal force. If a mode shape of the system is

$$\mathbf{u} = \begin{Bmatrix} u_{11} \\ u_{21} \end{Bmatrix} \quad (21)$$

The modal force from the original electromagnetic forcing is:

$$p_{em} = \mathbf{u}^{\top}\mathbf{f} = u_{11}F_{em} \quad (22)$$

The modal force generated from the bimorph conductors can be created to eliminate the modal force produced by the electromagnetic forces in the

stator. The force created when the bimorph excitation is also considered is the right hand side of equation (19):

$$\mathbf{f} = \left\{ \begin{array}{c} F_{em} + F_{bimorph} \\ -F_{bimorph} \end{array} \right\} \tag{23}$$

The modal force in this case is therefore

$$p = u_{11}F_{em} + (u_{11} - u_{21})F_{bimorph} \tag{24}$$

In order to eliminate this modal force the control force must be:

$$F_{bimorph} = \frac{-u_{11}F_{em}}{u_{11} - u_{21}} \tag{25}$$

Modal forces are independent of frequency. This method prevents resonances from being excited when an excitation frequency equals a resonant frequency that corresponds to the unwanted mode $\mathbf{u}$.

In order to implement this method in an electrical machine a control loop and an external power input to the bimorph conductors would be required in the manner of an active vibration controller. However, the actuation for this method is provided by the teeth which are an inherent part of the machine design. This method is therefore a combination of passive and active vibration control methods. This aspect of the bimorph concept could be implemented in practice and is investigated further in an FE investigation. The results of this investigation are given in chapter 4.

2.2.2 Combined Vibration Control

An alternative approach to the above is to consider the teeth to have variable stiffness which is controlled by the bimorph conductors. With no bimorph control the teeth act as a passive vibration absorber and have stiff-

ness K_{teeth}. The bimorph control can be used to increase or decrease this stiffness. Therefore the force from the bimorph conductors can be written

$$F_{bimorph} = \delta K_{bimorph}(x_{core} - x_{teeth}) \tag{26}$$

then the equation of motion (19) becomes

$$\begin{bmatrix} M_{core} & 0 \\ 0 & M_{teeth} \end{bmatrix} \begin{Bmatrix} \ddot{x}_{core} \\ \ddot{x}_{teeth} \end{Bmatrix} + \begin{bmatrix} (C_{core} + C_{teeth}) & -C_{teeth} \\ -C_{teeth} & C_{teeth} \end{bmatrix} \begin{Bmatrix} \dot{x}_{core} \\ \dot{x}_{teeth} \end{Bmatrix} + ...$$

$$\begin{bmatrix} (K_{core} + K_{teeth} + \delta K_{bimorph}) & -(K_{teeth} + \delta K_{bimorph}) \\ -(K_{teeth} + \delta K_{bimorph}) & (K_{teeth} + \delta K_{bimorph}) \end{bmatrix} \begin{Bmatrix} x_{core} \\ x_{teeth} \end{Bmatrix} = \begin{Bmatrix} F_{em} \\ 0 \end{Bmatrix} \tag{27}$$

This is combined vibration absorption which is explained in appendix A.4. By controlling the currents in the bimorph conductors, the effective stiffness of the teeth can be altered. This alters the dynamic stiffness of the structure so that the tooth rocking frequency shifts to higher or lower frequency values. This enables the tooth to act as a vibration absorber over a range of frequencies around the tooth rocking frequency.

In the suggested application for magnetic bimorph conductors through the teeth of an electrical machine, x_{teeth} is a function of the deflection of the tooth and the flux in the tooth. In order to utilize the variable stiffness properties of the tooth and bimorph conductor, online measurements of the tooth flux and deflection would be required. Measuring the deflection of the tooth is not practical and so the idea of varying the stiffness properties of the teeth is a theoretical notion only. This particular aspect of the bimorph concept is not developed further. However, using the bimorph conductors to cancel a modal force is a simpler and more practical idea. This idea has been investigated further in the following sections of this chapter and in the

following chapters in this thesis.

The following sections describe two practical investigations into the magnetic bimorph concept.

2.3 Demonstration of the Bimorph Effect on a Single Stator Tooth Rig

An experimental rig was designed, built and modelled in order to demonstrate the effect that bimorph conductors could have on the stator teeth of a large electrical machine. The design and dimensions of the structure are shown in figure 22. The test structure consisted of laminations of electrical steel in the shape of a tooth inside a rectangular shaped surround. The tooth represented a single stator tooth. The surrounding material provided for the magnetic flux path. A $2mm$ air gap between the tooth tip and the surround represented the air gap between the stator tooth and rotor in an electrical machine. On each length of the surround were two coils of wire. Direct current was supplied to these to provide the field excitation to the rig. A thick conducting wire was threaded through eighteen holes in the tooth root in a spiral configuration. All loops were connected in series. This was the bimorph conductor. Alternating current was supplied to the bimorph conductor with all currents supplied in the same direction through the tooth. The aim of this experiment was to demonstrate that on application of the bimorph current the tooth rocking motion of the rig could be excited. This structure has reflection symmetry about the axis through the centre of the tooth.

The tooth has a narrow rectangular section close to the root and a wider rectangular section for the main body. This geometry was chosen so that the natural frequency of the tooth rocking motion occurred at a frequency

that could be excited and measured with the available equipment. An impulse test was carried out on the rig and the response was measured. The equivalent response was modelled and the two results compared. A response was also measured and modelled for AC bimorph excitation. Figure 23 shows the location of the impulse and accelerometer on the mechanical and magnetic meshes.

2.3.1 Finite Element Modelling of the Tooth Rig

The stator tooth rig was modelled with 2D mechanical and magnetic models in MATLAB. The modelling techniques are explained in appendices B and D.6 The scripts used were written by the author. The models were coupled using an indirect weak coupling method which is explained in appendix D.2. The mesh of the mechanical model consisted of the iron and windings. The mesh of the magnetic model had the same geometry for the iron and windings but also included the air gap inside the rig and a layer of air outside the rig. Eight noded quadrilateral elements were used in a structured mesh. The magnetic and mechanical meshes are shown in figure 23.

2.3.1.1 The Magnetic Model The stiffness matrix of the magnetic model was constructed. No reduction was required for this because only one DoF exists per node and so the model was not too large to construct and analyse in full. The excitation vector included the distributed excitation from the field coils and point excitation from the bimorph conductors. This model was solved to give the values of magnetic potential at each node in the structure.

Initially only DC excitation to the field windings was considered. In this case the magnetic flux flowed down the tooth and back around both sides of the surround. The symmetric nature of the geometry and excitation ensured that the same amount of flux flowed around each side of the rig

and there was an equal amount of flux each side of the tooth. The lines of constant magnetic potential for this case are shown in figure 24.

The problem was then solved with field excitation and bimorph excitation together. The bimorph excitation caused a magnetic field to be generated around each conductor in the iron. This magnetic field interacted with the magnetic field from the field windings and distorted the previously uniform field in the tooth. The lines of constant magnetic potential due to the field windings and excitation in the bimorph conductors with a magnitude of $2.2A$, $1.1A$, $-1.1A$ and $-2.2A$ are shown in figures 25 to 28 respectively. The nodal magnetic potential values in the iron were used to calculate equivalent nodal magnetostriction forces that act on the mechanical model. Maxwell forces exist in the air gap due to leakage flux, however, the magnitude of these forces is negligible compared to the magnetostrictive forces and so are not considered here.

2.3.1.2 The Mechanical Model The mechanical mass and stiffness matrices were created with the merge and reduction process that is explained in appendix B.12. The FE mesh of the tooth rig is relatively coarse around the root of the tooth and this has the effect of stiffening the model. In order to overcome this effect the value of Young's modulus of the tooth and surround that have been used in the model are much lower than the standard value for steel ($200GPa$). The surround and thick part of the tooth has a Young's modulus of $160GPa$ and the tooth root has a Young's modulus of $116GPa$. All of the material property values that were used are given in table 3. The model was initially undamped. Modal damping was introduced so that around the first natural frequency of the rig the response from the model matched the experimental response.

The eigenvalue problem was solved and the first non rigid body mode shape

is shown in figure 29. This is a bending motion of the tooth. Equivalent magnetostriction forces were calculated from the nodal potentials due to field and bimorph excitation. These were reduced and applied to the mechanical model to generate a frequency response which is discussed alongside the experimental results in the next section. The deflected shapes from the application of magnetostriction forces are shown in figures 25 to 28 for different levels of excitation to the bimorph conductors.

2.3.2 Experimental Setup and Results

2.3.2.1 Rig Construction The rig was constructed as follows: Large sheets of electrical steel were bonded together to form stacks of laminations roughly 10mm thick. Each stack was cut to the shapes shown in figure 22 at a waterjet machining centre. The shapes were then bonded together to form the rig. The lower edge of the rig was cut separately so that fully formed coils could be located on the lengths of the rig. Holes in the corners of the rig were drilled and bolts were inserted to hold the laminations together and to bolt the lower edge to the sides. The holes in the tooth root were drilled and the bimorph conductors were inserted. Each one of four field coils had equal numbers of turns and wire diameter. This information is given in table 2. The whole rig was suspended by a bungee cord to approximate free boundary conditions. An accelerometer was attached to one side of the rig to measure the horizontal motion of the surround. The location of this is given by point 2 in figure 23. Figure 30 is a photograph of the completed structure.

2.3.2.2 Impulse Tests Impulse tests were carried out on the rig. The locations of the impulse and response are shown with point 1 and point 2 in figure 23. Figure 31 shows the frequency response function of one impulse test. The response is the acceleration of the rig per unit force of impulse and so has units of kg^{-1}. This test was modelled and the result is also given

in figure 31. At low frequencies the modelled response is constant with respect to frequency but the measured response includes some oscillation. The average measured response is 15% higher than the average modelled response. The experimental results show that an antiresonance occurs at $71.37Hz$, the model predicts this antiresonance to occur at $70.80Hz$. These frequency values differ by only 0.8%. A resonance occurs at $78.2Hz$. The response from the model and the experiment are in agreement at this frequency and at frequencies above this. The resonance is dominated by the first bending mode of the tooth relative to the surround which moves in the opposite way. This mode is shown in figure 29.

2.3.2.3 Excitation of the Bimorph Conductors The field coils had 400 turns each. The coils on each side of the rig were connected in series and excited with $0.5A$ direct current to provide the field excitation. The field excitation would have caused magnetic flux to flow down the tooth and back around both sides of the surround as shown in figure 24. The magnetostriction effect would have caused a small strain in the stator tooth rig. $2.2A$ peak alternating current was supplied to the bimorph conductor in the root of the tooth. As the current varied, the distribution of the magnetic field in the root of the tooth and through the length of the tooth would have varied and alternated from side to side in the tooth. The strain in the material due to magnetostriction under the influence of the magnetic field also alternated from one side of the tooth to the other. This had the effect of bending the tooth. The alternating magnetic field and corresponding bending motion of the tooth are shown in figures 25 to 28. The response from this experiment and the response that the model predicts are shown in figure 32. At frequencies above $55Hz$ the modelled and measured responses are in agreement. A resonance can clearly be seen at $78.2Hz$, at this frequency the deflected shape of the rig is shown in figures 25 to 28. This proves that the excitation of the conductors through the root of the

tooth has excited the bending motion in the structure. Below $55Hz$ the modelled and experimental data do not coincide. The predicted response goes to zero at $0Hz$. This is because the bimorph conductors do not excite any rigid body motion and therefore, this is likely to be the correct response of the two. The experimental results appear to decrease with decreasing frequency from $78.2Hz$ to $40Hz$ and then increase with decreasing frequency from $40Hz$ to $0Hz$. An accelerometer cannot measure $0Hz$ and so it is likely that at low frequencies the accelerometer has picked up a reading of flux through the accelerometer and this is interfering with the true reading.

2.3.3 Conclusion to the First Bimorph Demonstration

The experiment and FE model used in this investigation have together shown that the bimorph concept has successfully utilized the magnetostriction effect to excite the tooth rocking motion of the rig. This effect can accurately be predicted by a finite element model.

2.4 Demonstration of the Bimorph Effect on a Small Electrical Machine

The concept of providing vibration absorption in electrical machines by using bimorph conductors through the root of the stator teeth has been investigated through experimentation on a small electrical machine. This section describes the steps that were carried out and the results of the investigation. The aim of this experiment was to verify the effect that the magnetic field from the bimorph conductors had on the vibration of a stator.

2.4.1 Construction of the Stator and Rotor

An $11kW$ 4 pole induction motor was adapted for the purpose of this investigation. The stator and rotor were both removed from the casing and the stator was subsequently used in the experiment but the rotor was not. The

stator is shown in figure 1 in Chapter 1. The dimensions of the stator of this machine are given in table 4. The original stator windings were removed and the stator lamination stack was split into several shorter stacks. Holes were drilled through the root of each tooth and the stator was reassembled as shown in figure 33. The bimorph conductors were then threaded through these holes in a six pole, three phase pattern that is shown in figure 34. This differs from the suggested application for bimorph control which is that each tooth be fitted with an independently controlled bimorph conductor. The top of the casing was removed and the stator was positioned in the lower half of the casing. An accelerometer was placed on the top of the stator to measure the radial vibration response.

A six pole wound salient rotor was constructed from laminations of electrical steel. The main dimensions of the rotor are given in table 5. The rotor was created by bonding twelve sheets of laminations. A number of rotor shapes were cut from the sheets with a waterjet machine to produce a number of stacks of laminations in the required form. The rotor shape is shown in figure 35. These small stacks were then bonded together to form the complete rotor. Each pole on the rotor was wound with a concentrated winding. The rotor was then fixed in the centre of the stator. The completed machine is shown in figure 36.

2.4.2 The Bimorph Conductors

The proposal for the bimorph concept is to excite individual conductors through the root of each stator tooth with a small amount of current which would not significantly affect the flux in the air gap. The bimorph conductors in this experiment differ from the proposed configuration as the test machine was constructed with the bimorph conductors in a three phase winding configuration. Exciting one of these phases would have generated

a large amount of flux in the air gap of the machine. This flux would affect the radial Maxwell forces in the air gap of the machine. In order that the bimorph currents had as little effect as possible on the air gap field, one single conductor through the root of one tooth was used for the experiments.

2.4.3 Field Excited and Bimorph Excited Stator Vibration

The vibration that the field windings caused was recorded: Windings on the rotor pole pair on the horizontal axis were connected in parallel. These were excited with DC. One phase of the stator field windings was excited with alternating current. The bimorph circuits were all open for this test. The response from the accelerometer is given in figure 37.

The vibration that the bimorph conductors caused was recorded: An AC supply was connected across a single bimorph conductor. This stator tooth was located directly in line with the centre of one of the excited rotor poles. The rotor winding was excited with DC. No excitation was supplied to the stator field windings. The response from the accelerometer is given by the red line in figure 38.

The response in figure 37 and the response in figure 38 show that resonances at $997Hz$ and $2645Hz$ were excited by the stator field alone and also by the bimorph field with current supplied to the rotor pole pair but with no current supplied to the stator conductors. The stator field excited a resonance at $4888Hz$ this was not excited by the bimorph conductors. The bimorph conductors excited resonances at $4674Hz$ and at $7243Hz$ which were not excited by the stator field. At $7243Hz$ the response could be dominated by a bending motion of the stator teeth.

2.4.4 Using the Bimorph Conductors in Vibration Control

The bimorph conductors were used at a single frequency to cancel the vibration from the stator field. The method that was chosen for this involved exciting the bimorph and stator fields at close but not identical frequencies with excitation levels that caused the magnitude of the response from both sources individually to be the same. The response that is predicted in theory for this method has been generated with two sine waves and is shown in figure 39. This shows that at set intervals the two waves interfere destructively to cancel out the response. The experimental results were achieved with one stator phase excited at $1000Hz$ and the bimorph conductor excited at $1000.5Hz$. The response is shown in figure 40. This response shows that the vibration from the bimorph conductor cancels out the vibration from the field conductor at intervals of $2s$ as required.

2.4.5 The Effect of the Bimorph Conductors on the Air Gap Flux

Two short investigations were carried out in order to verify that the above responses were caused by the bimorph effect and not by the interaction of radial Maxwell forces from the field and bimorph conductors. One investigation presented the measured response of the stator from the bimorph excitation firstly without the rotor field and secondly with the rotor field excited. The first measured response was achieved with the bimorph conductors excited, without excitation applied to the stator field windings or to the rotor windings. The second measured response was achieved with the bimorph conductors excited and one pole of the rotor field excited with no stator field excitation. The response of the stator under these two conditions is given in figure 38. Figure 38 shows that at most frequencies the response of the stator from the bimorph conductors alone is substantially lower than the response from the bimorph conductors and rotor field together. This shows that the effect of the radial Maxwell forces in the air gap from the

bimorph conductors is lower than the effect of the interaction between the flux generated by the bimorph and rotor excitation.

The second short investigation into the effect of the flux from the bimorph conductors considered the mmf in the air gap due to the stator windings and bimorph conductor for the situation at $1000Hz$ where the bimorph field cancelled the stator winding field. This investigation discovered that the mmf in the air gap due to the bimorph conductor alone is much lower than the mmf in the air gap from the stator field. This investigation is described here: The teeth numbers in the stator and the relative stator phase location is shown in figure 41. The mmf acting on the teeth tips is presented relative to this. The bimorph conductor that was excited is located in tooth 0. The current supplied to the bimorph conductor was $3A$. The current supplied to the stator field windings was $0.7A$ and the number of turns in one stator coil was 75. Therefore the mmf from a single stator field coil was $52.5Aturns$. The mmf waveform from the bimorph conductor alone is shown in figure 42. The mmf waveform from the stator field is shown in figure 43 along with the mmf waveform from the bimorph conductor. The field from the rotor is not considered here. The figures clearly show that the mmf that the bimorph conductor generates is very small relative to the stator field mmf and therefore the bimorph conductors have little effect on the Maxwell forces in the air gap. The cancelled vibration signal that has been achieved at $1000Hz$ is due to the effect that the bimorph conductors have on the magnetostrictive forces in the stator iron.

2.4.6 Conclusion to the Second Bimorph Demonstration

This experiment has shown that the magnetostrictive forcing generated from the bimorph field can cancel the electromagnetic forcing generated from the stator field in an electrical machine.

2.5 Conclusion to the Chapter

The magnetic bimorph concept can be used to prevent electrical machine resonances from being excited by cancelling the dominating modal forces of those resonances. This method is independent of frequency and will also reduce vibrations away from resonance where those cancelled modes dominate. This idea has been illustrated in theory and could also be implemented in practice. A finite element investigation into the magnetic bimorph concept in large electrical machines has examined this idea further and the results are given in chapter 4.

Theoretically the magnetic bimorph effect can eliminate machine vibrations at any frequency above the lowest value of tooth rocking frequency by cancelling the operating shape at that frequency using a combined vibration absorption technique. However, this idea would be impractical to actually implement.

The experimental investigations have shown that the bimorph concept has the potential to be a practical solution to vibration problems in electrical machines. The bimorph conductors have proven to excite the rocking motion of a single stator tooth by affecting the magnetostriction phenomenon in the iron. It has also been proven that a small amount of excitation of these conductors can cancel the vibration of a machine and this only affects the air gap mmf slightly. Therefore the magnetic bimorph concept has the potential to reduce vibrations in large electrical machines with the requirement of a relatively small input of energy and with negligible effect on the operation of the machine.

Lamination Thickness	0.35	mm
Number of Laminations	96	
Rig Axial Thickness	41	mm
Rig Length	280	mm
Number of Turns per Coil	400	
Field Wire Diameter	0.3	mm
Cross Sectional Area of Coil	520	mm^2
Number of Turns in the Bimorph Conductor	18	
Bimorph Conductor Diameter	2.0	mm
Mass	5.3	kg

Table 2: The Stator Tooth Rig

Density of the Main Body	ρ	8000	kgm^{-3}
Young's Modulus of the Main Body	E	160	GPa
Density of the Tooth Root	ρ	7900	kgm^{-3}
Young's Modulus of the Tooth Root	E	119	GPa
Density of the Tooth	ρ	7900	kgm^{-3}
Young's Modulus of the Tooth	E	160	GPa
Poisson's Ratio	ν	0.27	
Magnetostrictive Constants	p	1×10^{-5}	
	q	-3×10^{-7}	
Relative Permeability of steel	μ_r	2000	
Current density in field windings	j_{DC}	$\frac{5\times10^6}{13}$	Am^{-2}
Peak Current in the bimorph conductors	j_b	2.2	A

Table 3: Assumed Material Properties of the Stator Tooth Rig Model

STATOR		
Number of Stator Teeth	36	
Outer Radius	127.5	mm
Radius to Tooth Tips	82.5	mm
Radius to Tooth Root	101.5	mm
Length	180.0	mm
Number of turns per coil	75	
Number of Pole Pairs	2	

Table 4: Dimensions of the Test Machine Stator

ROTOR	
Number of Pole Pairs	3
Outer Radius	$81.0mm$
Total stack length	$165mm$
Lamination Thickness	$0.5mm$
Number of Laminations	300
Electrical Steel Grade	M400-50A
Coating	SURALAC 7000
Bonding Varnish	Ultimeg U2002L Epoxy
Number of turns per coil	250

Table 5: The New Rotor Information

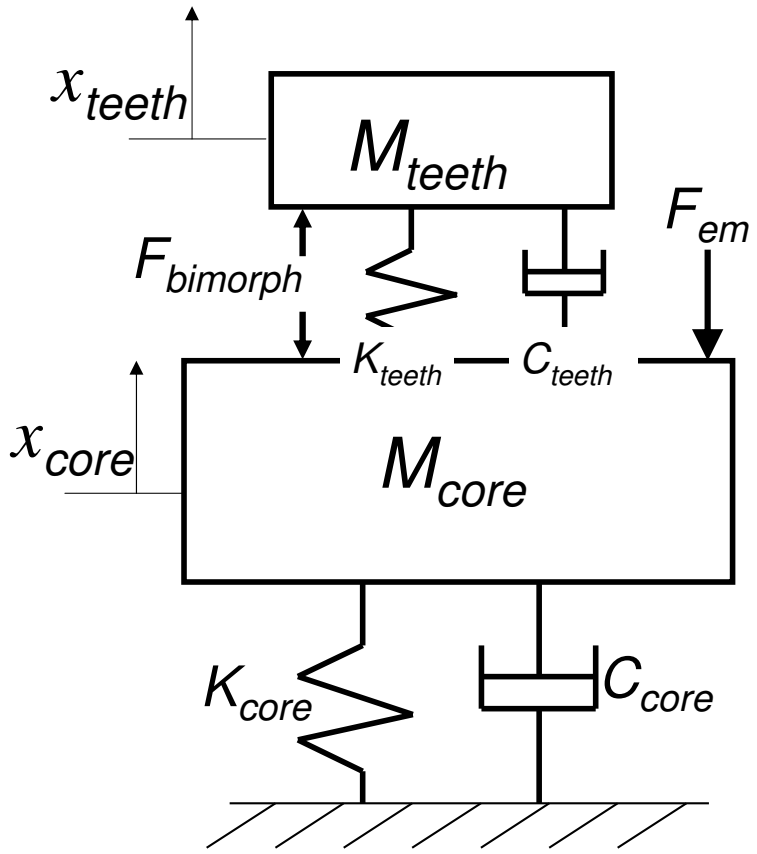

Figure 21: The Stator Tooth as a Vibration Absorber

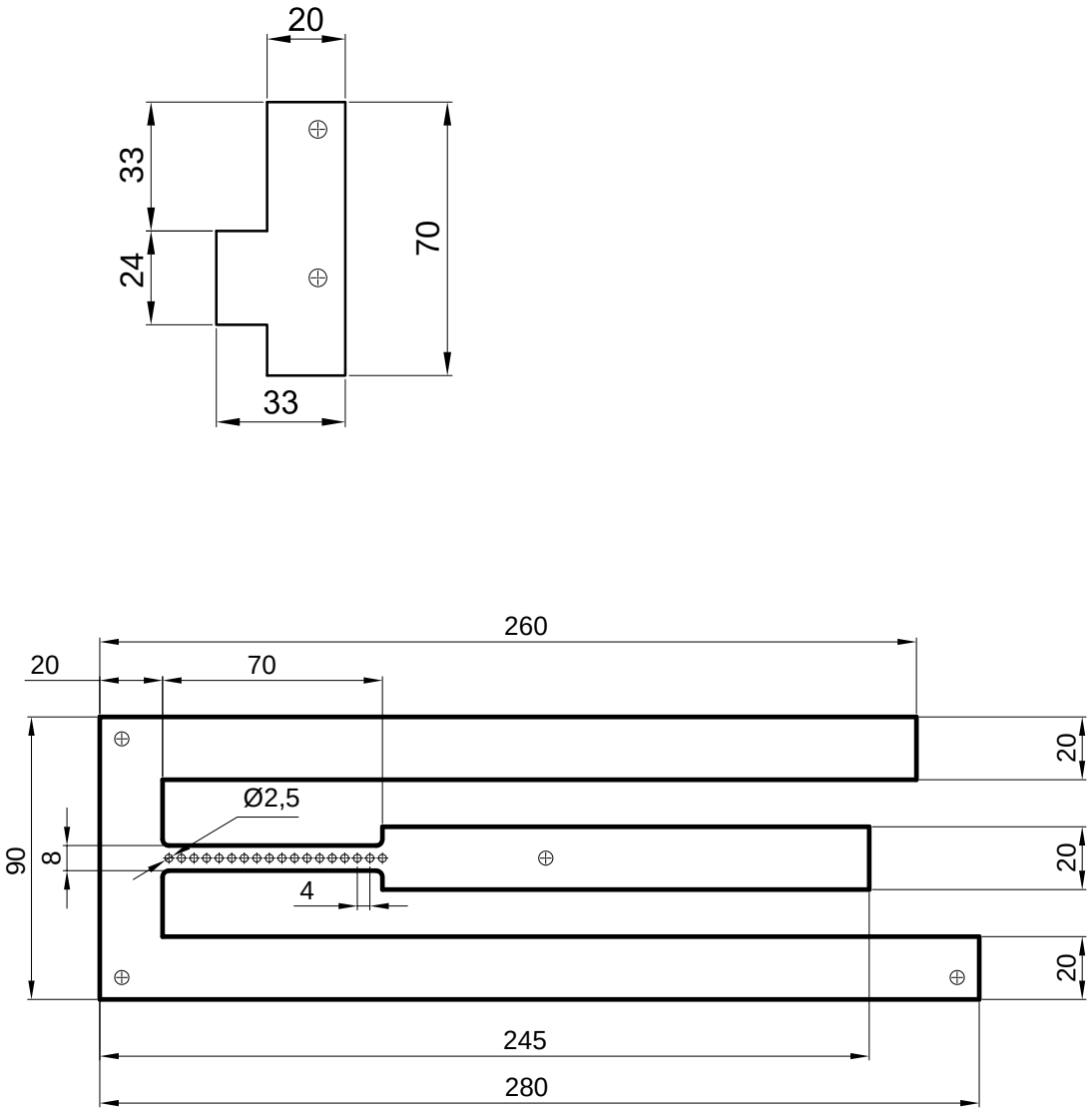

Figure 22: The Stator Tooth Rig (mm)

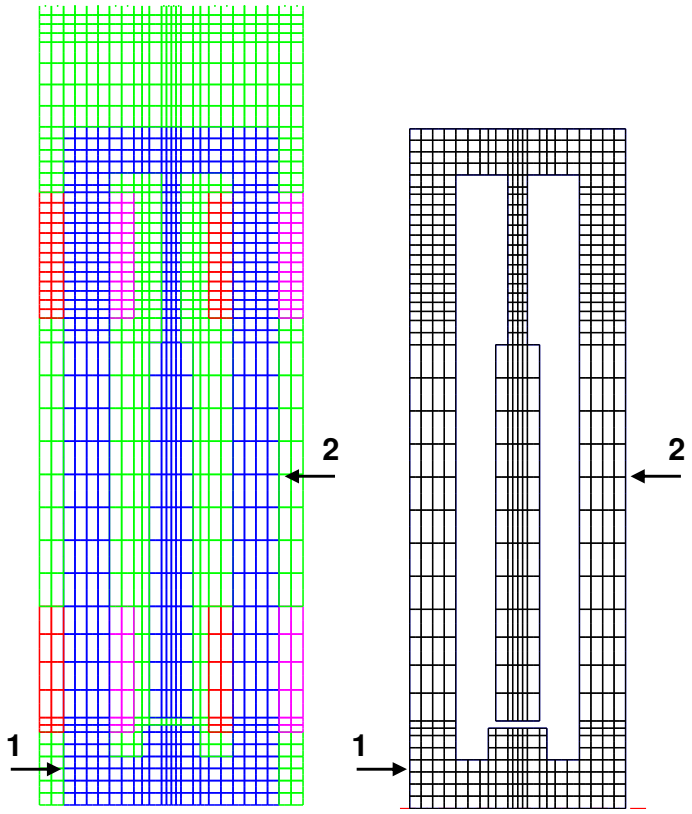

Figure 23: The Magnetic and Mechanical Mesh of the Tooth Rig Model
1: Location of Impulse
2: Location of Accelerometer

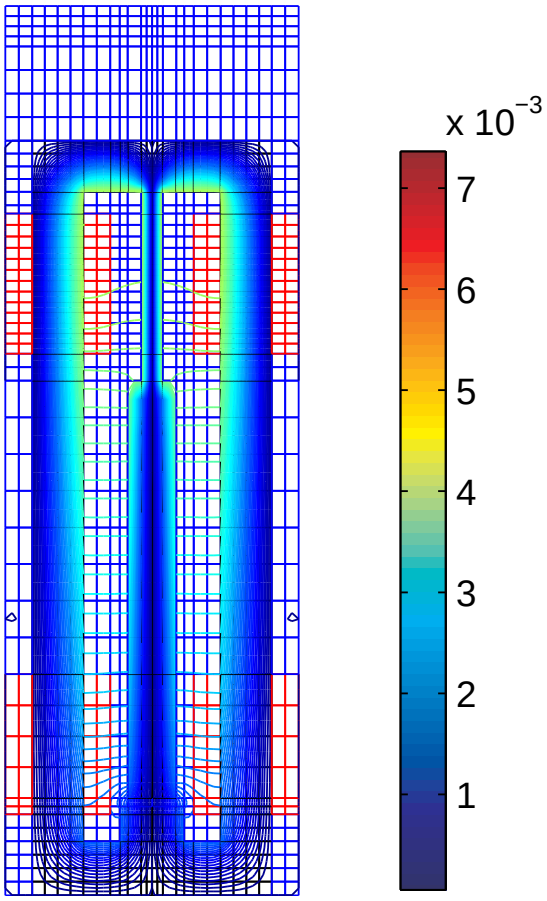

Figure 24: Contour Lines of Magnetic Potential from the Field Excitation

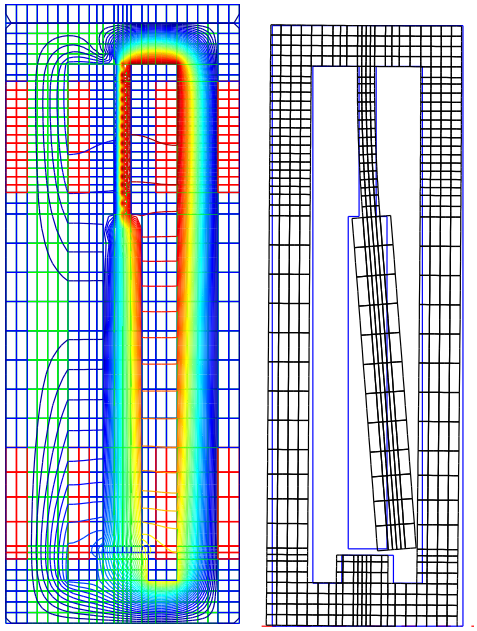

Figure 25: Magnetic Field and Corresponding Mechanical Deformation: 2.2A Bimorph Current

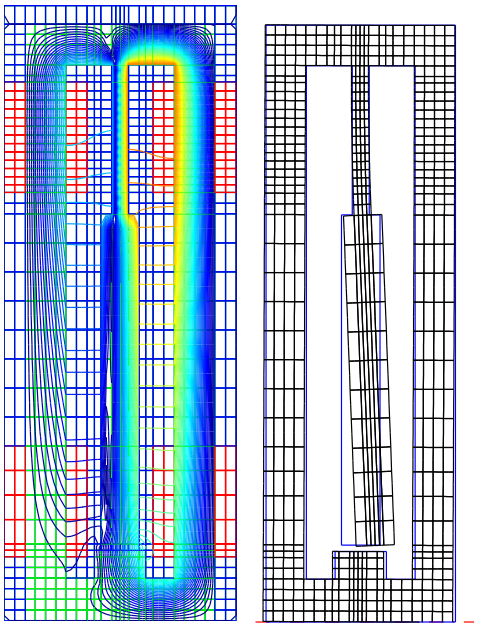

Figure 26: Magnetic Field and Corresponding Mechanical Deformation: 1.1A Bimorph Current

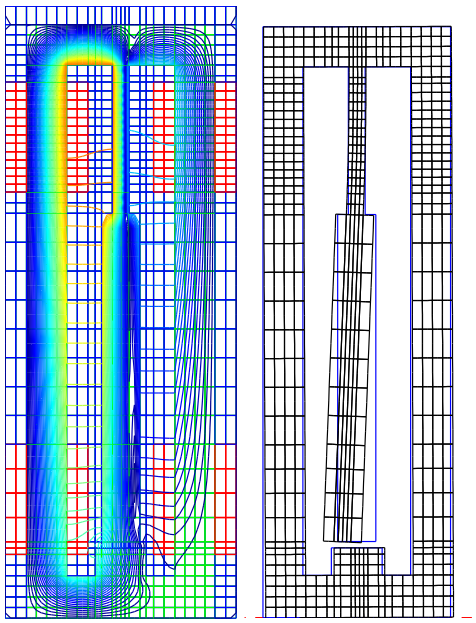

Figure 27: Magnetic Field and Corresponding Mechanical Deformation: - 1.1A Bimorph Current

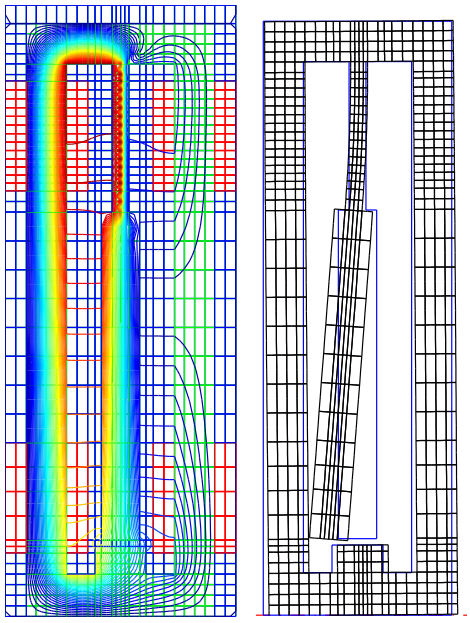

Figure 28: Magnetic Field and Corresponding Mechanical Deformation: - 2.2A Bimorph Current

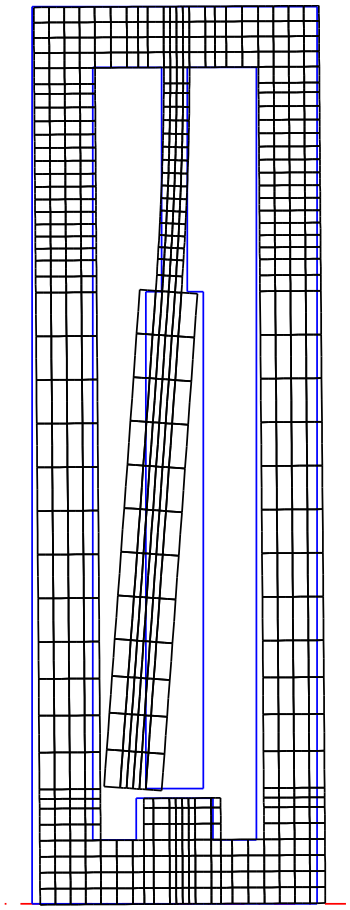

Figure 29: First Non Rigid Body Mode of the Tooth Rig

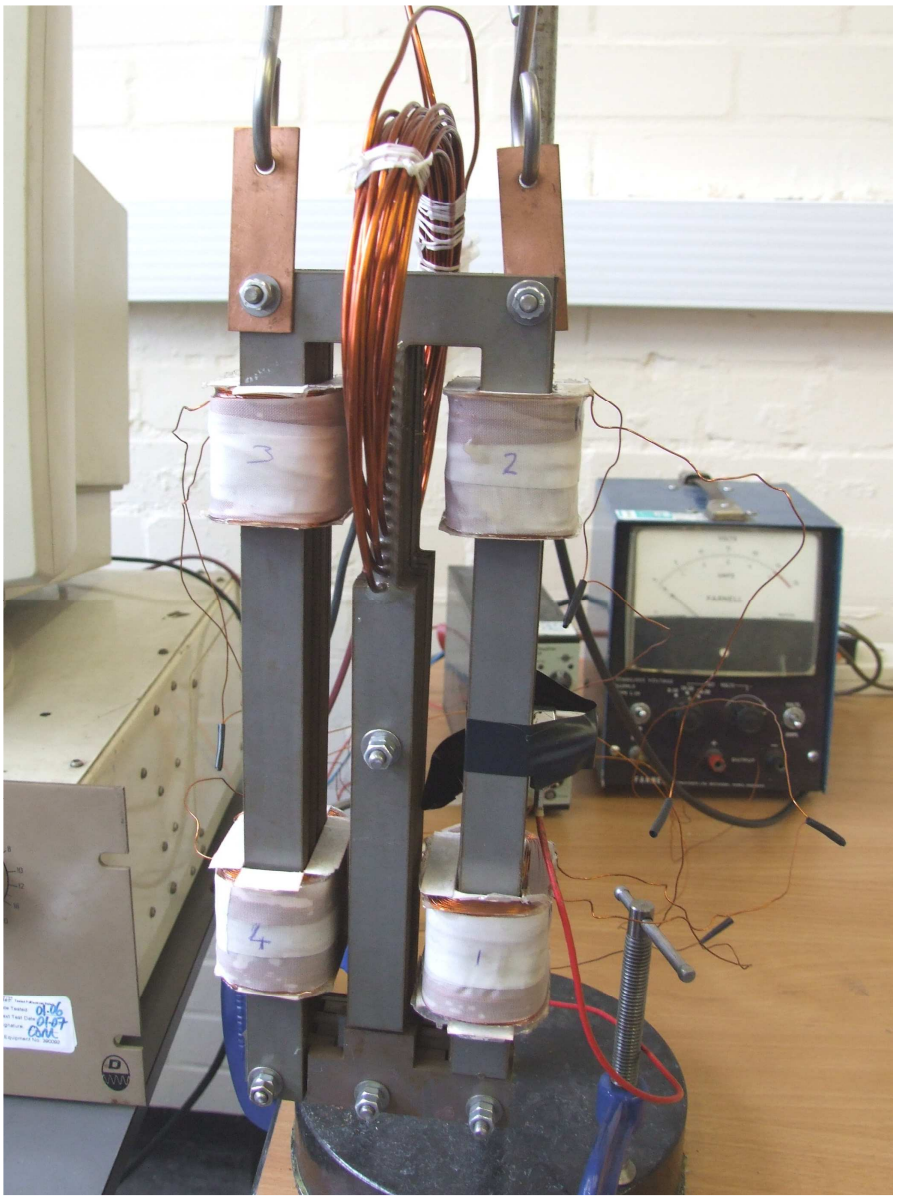

Figure 30: The Stator Tooth Rig

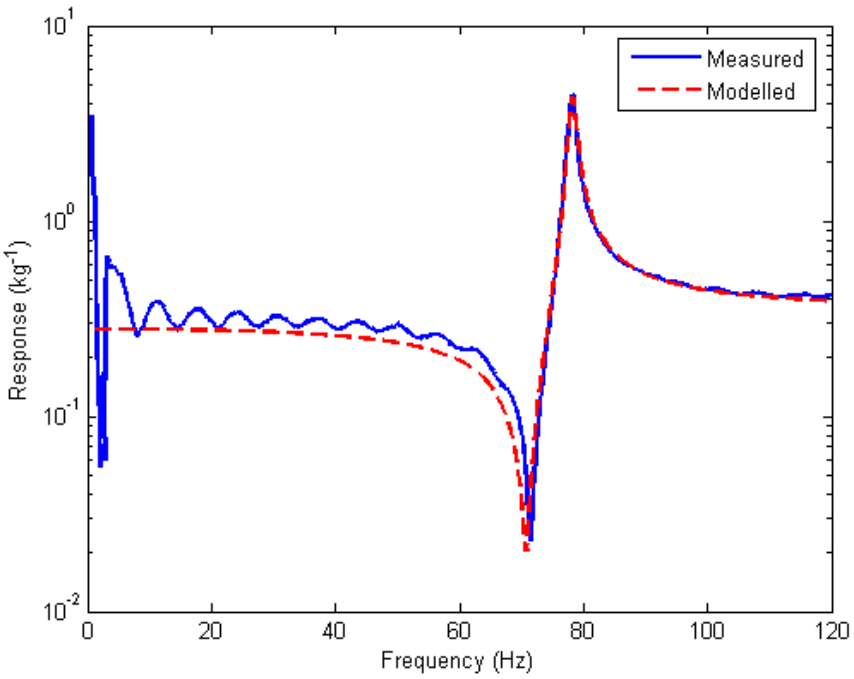

Figure 31: Frequency Response Function due to an Impulse to the Rig

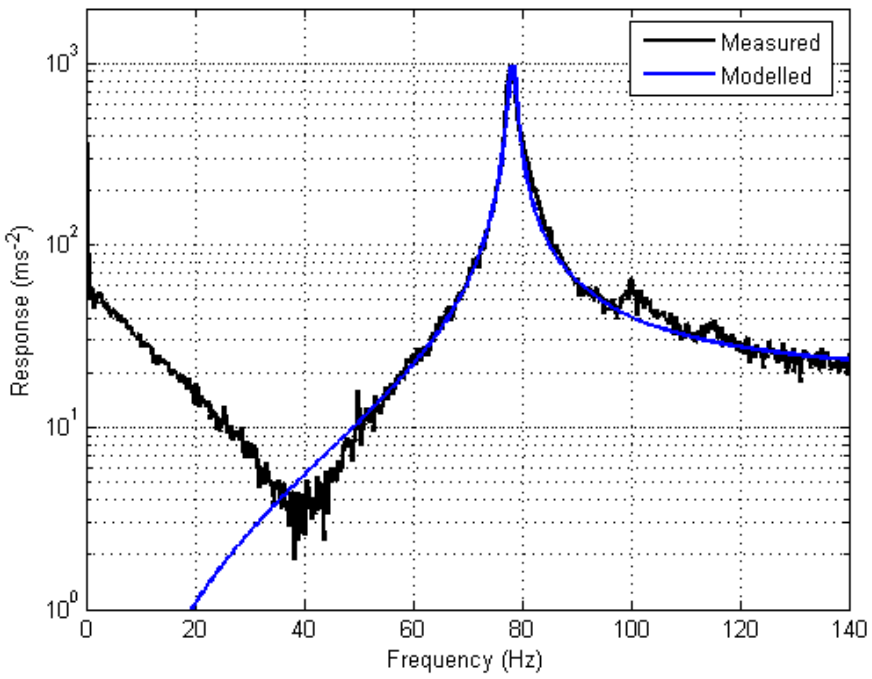

Figure 32: Response of the Tooth Rig to Field and Bimorph Excitation: Measured and Modelled Response

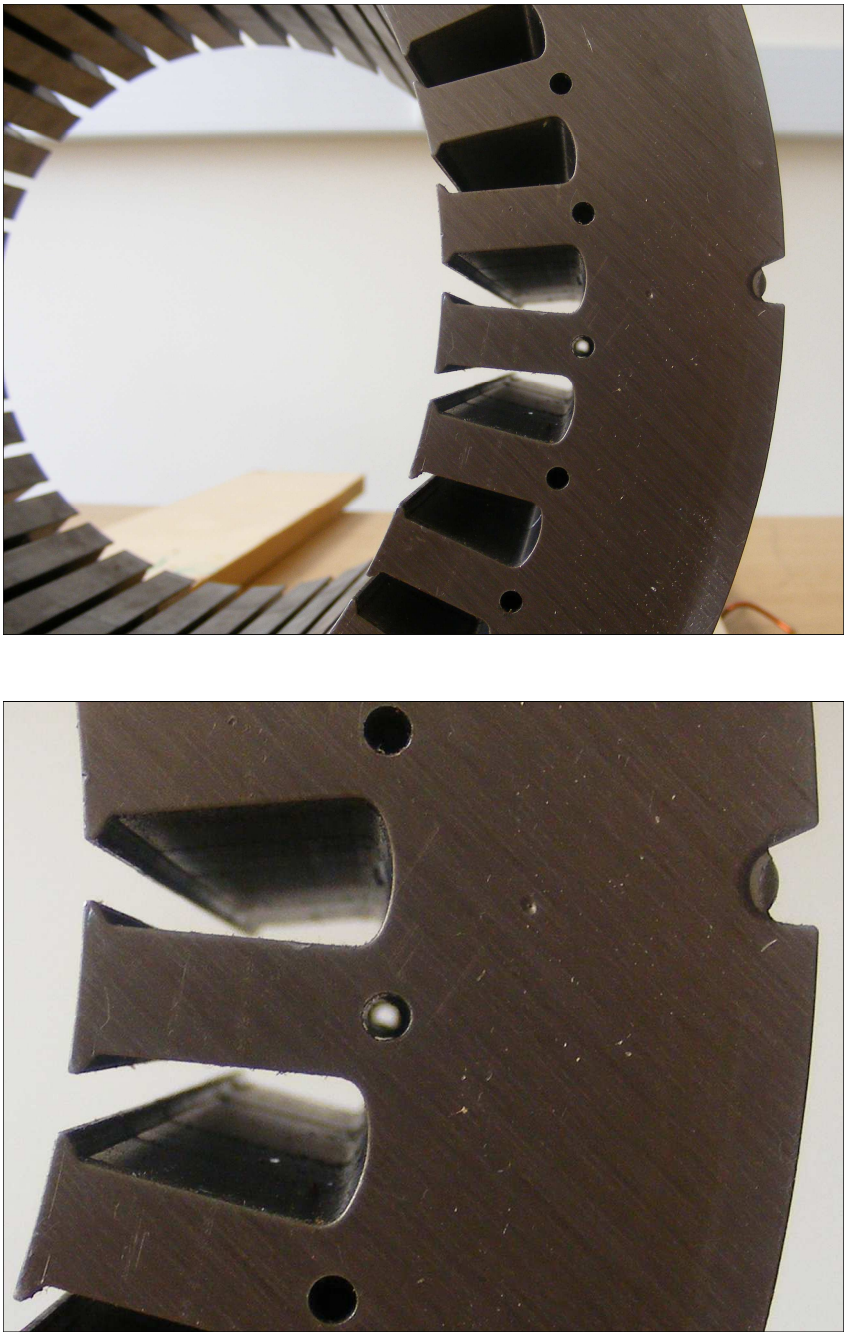

Figure 33: The Holes in the Stator Teeth for the Bimorph Conductors

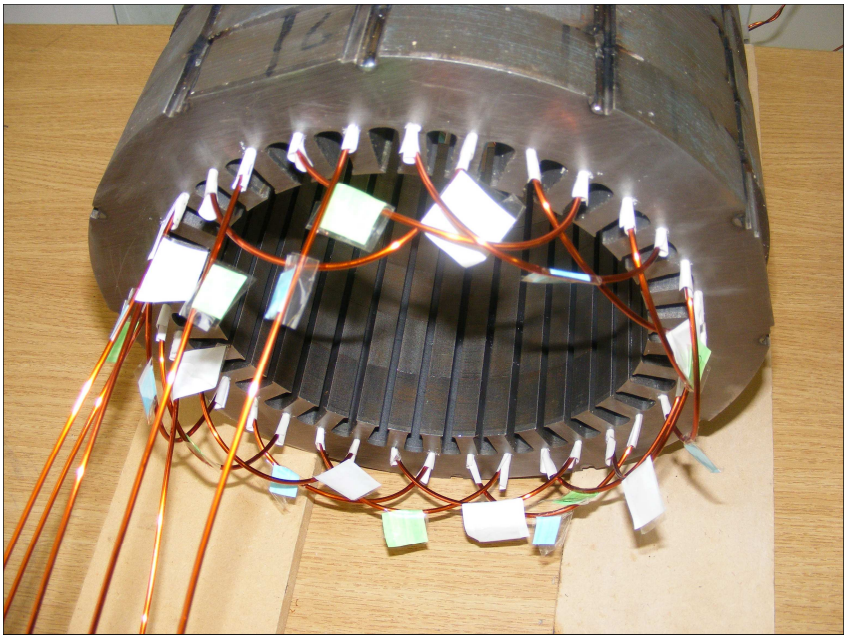

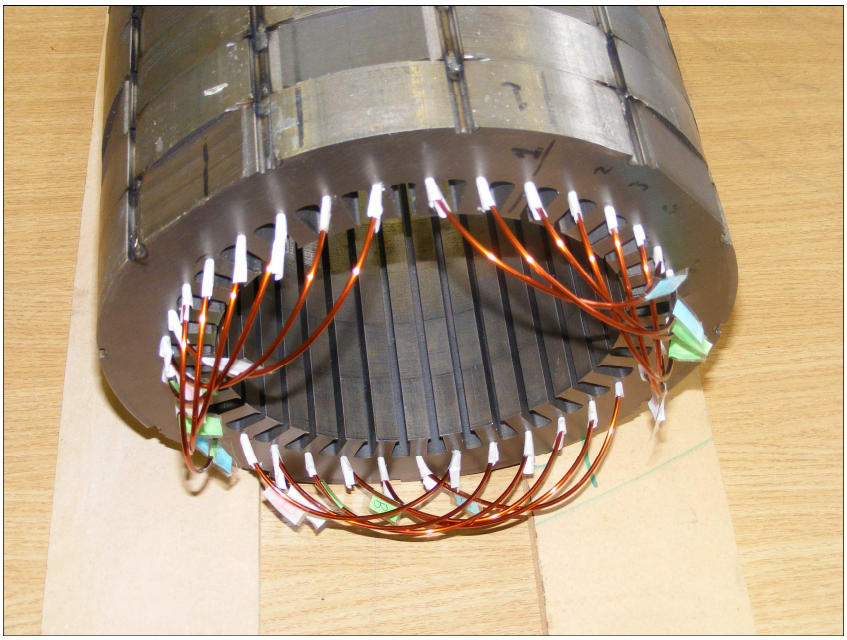

Figure 34: The Bimorph Conductors

Figure 35: Small Rotor Stacks

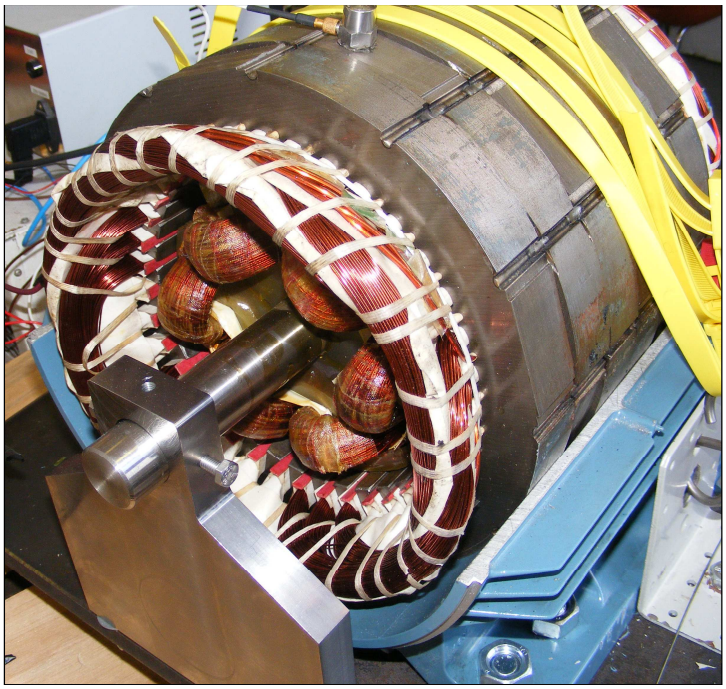

Figure 36: The Test Machine

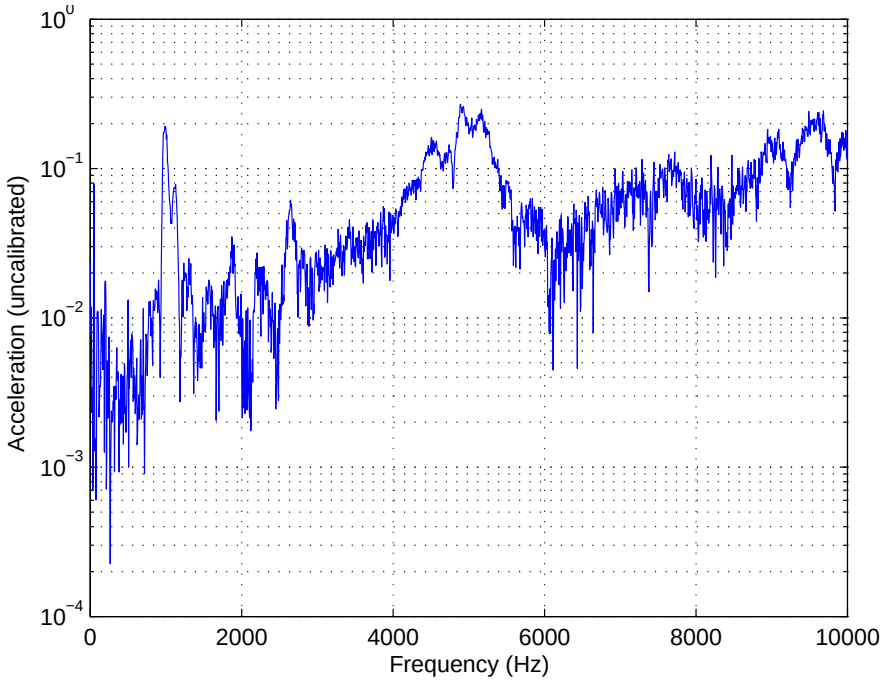

Figure 37: Response from Stator Field Excitation

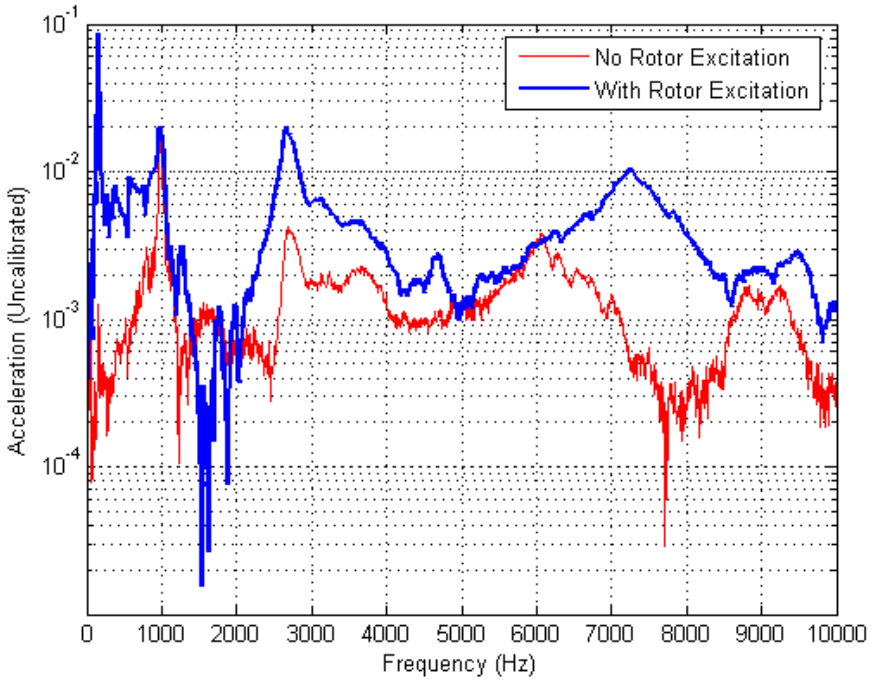

Figure 38: Response from a Single Bimorph Conductor

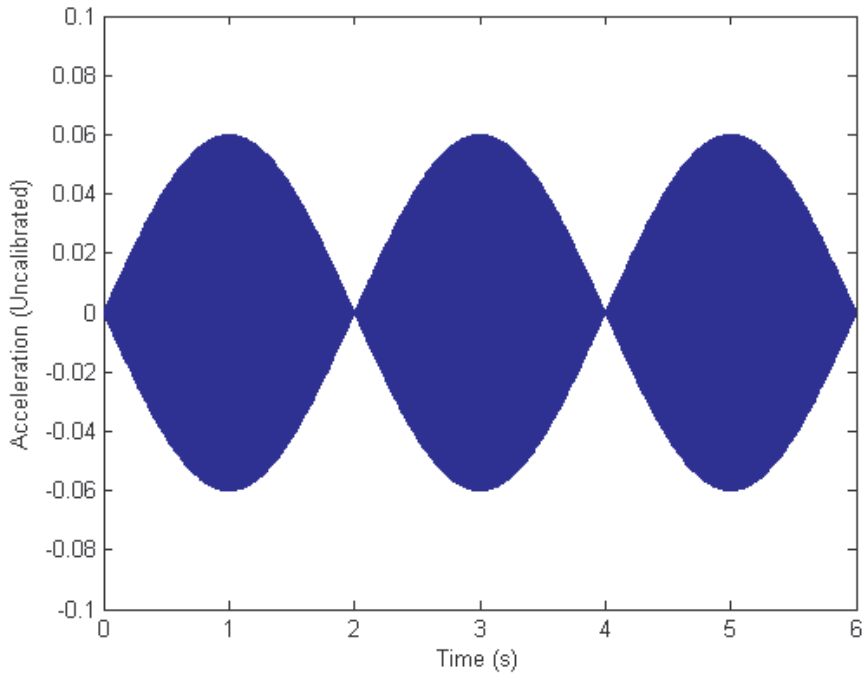

Figure 39: The Calculated Sum of a 1000Hz Sine Wave and a 1000.5Hz Sine Wave

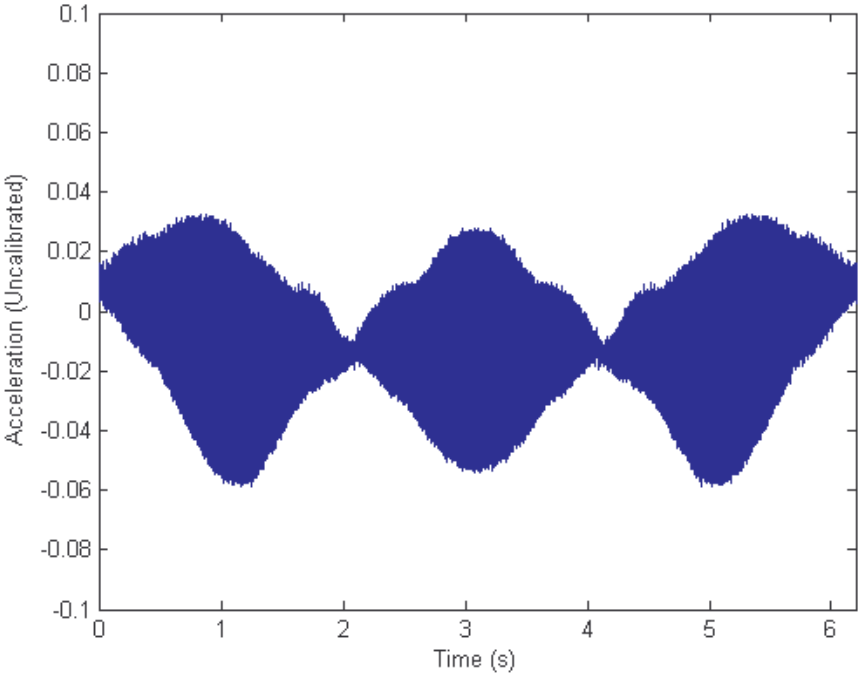

Figure 40: A Measured Time Domain Response of the Stator at $1000Hz$ from the Bimorph Conductor and Stator Field Windings

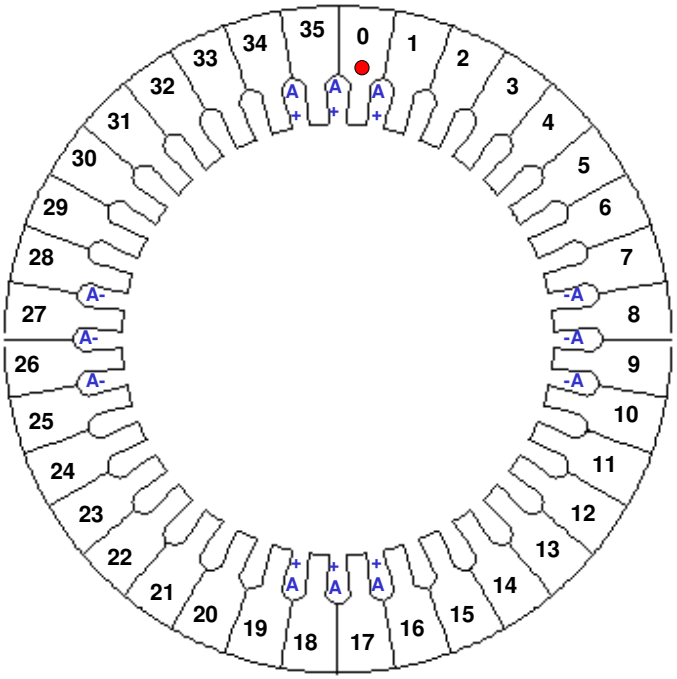

Figure 41: Relative Location of Stator Field Phase, Bimorph Conductor and Teeth Numbers

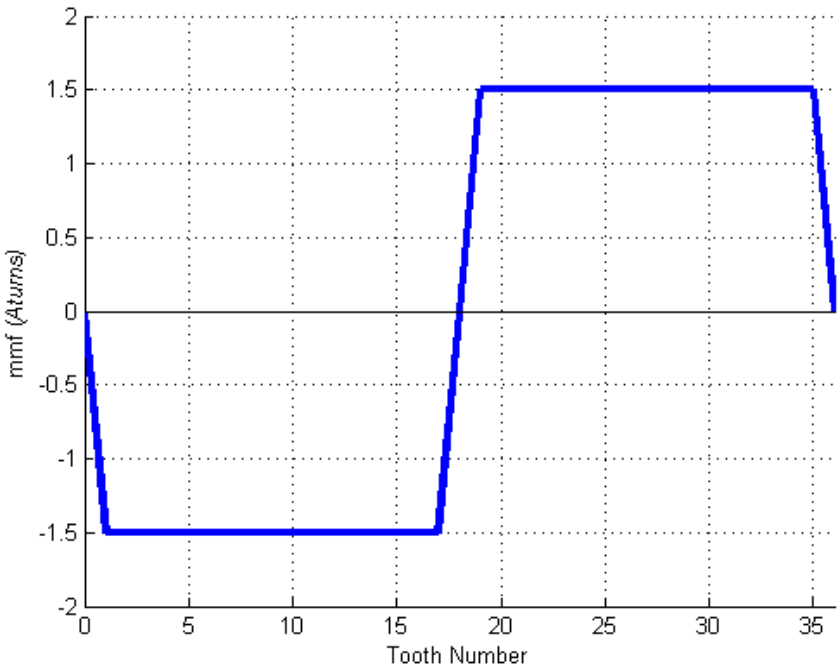

Figure 42: MMF Waveform from the Bimorph Conductor

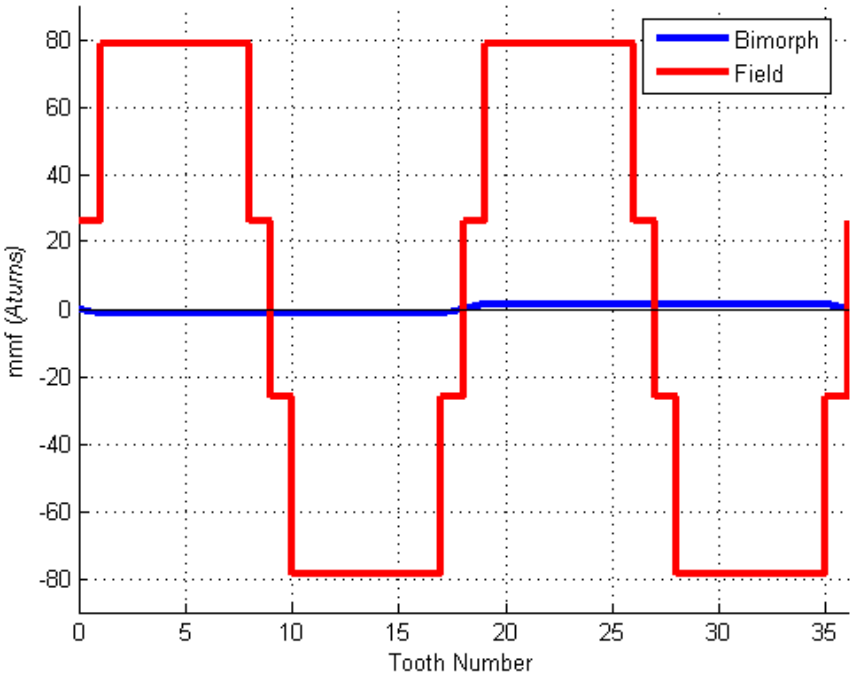

Figure 43: MMF Waveform from the Stator Field Windings

3 Coupled Magneto-Mechanical Analysis for Predicting Vibration

3.1 Introduction

This chapter describes a coupled magneto-mechanical analysis for predicting the torque and vibration of an electrical machine with individually controlled conductors and with bimorph conductors. There are four stages in this study which relate to the type of excitation applied to the stator of the machine. These excitation patterns are investigated in the next chapter to discover the effect they have on the torque and vibration levels of the machine. The stator excitation types that are investigated are:

Stage 0: A sinusoidal current pattern

Stage 1: An individually controlled stator slot current pattern that minimizes the copper loss but does not affect the torque

Stage 2: An individually controlled stator slot current pattern that cancels some components of noise, does not affect the torque and has the minimum possible copper loss

Stage 3: An individually controlled stator slot current pattern that minimizes the copper loss but does not affect the torque with currents in bimorph conductors that cancel some components of noise

This chapter explains the modelling methods used in a general context. The specific values that were used and the results of the investigation are given in the next chapter. This chapter is organized as follows:

- Section 3.2 describes the magneto-mechanical model generation and full calculations that were required to calculate the torque and vibration of an electrical machine from known currents.

- Section 3.3 describes alternative computationally efficient methods for carrying out this analysis.

- The constrained optimization methods that were used for calculating the current patterns are given in section 3.4.

The calculations described here consider the instantaneous currents in the rotor slots, stator slots and bimorph conductors to be known variables. A fixed sinusoidal current pattern was supplied to the rotor and this pattern was maintained for all of the types of stator excitation. Induced currents were not considered. The current density was constant throughout each stator and rotor slot. The currents in all of the stator slots were independent of one another. The currents in all of the bimorph conductors were independent of one another.

3.2 Quantifying Torque and Vibration

3.2.1 The Mechanical FE Model

A structured mesh was generated for one bay of the stator. This consisted of the stator tooth, half a slot either side of the tooth and the corresponding part of the back of core. The element mass and stiffness matrices were assembled using the method described in appendix B.7. The merge and reduction process was used to generate super-elements for each bay of the stator as described in sections B.8, B.11 and B.12 of the appendices. These super-elements were then used in a second merge and reduction process to generate the reduced mass and stiffness matrices for the whole stator. This process is described in appendix B.14. The information for this specific system is described in appendix 4.2.3.

The eigenvalue problem was solved for the reduced system to give the mode shapes and natural frequencies of the structure. The mode shapes of the

stator were categorized into families of modes. This process is explained in appendix C.4.2. The mode shapes were also mass normalized using the method described in appendix C.3.

3.2.2 The Magnetic FE Model

The complete magnetic mesh included the stator iron, stator slot-fill, rotor iron, rotor slot-fill and the air gap between the stator and rotor. The process of generating the complete magnetic model initially required the mesh and matrices to be generated separately for the rotor and for the stator. These separate models were then coupled together.

The stator mesh included the stator iron and slot-fill and the geometry of these nodes and elements matched that of the mechanical mesh. Some of the air gap was also included in the stator model. The nodes on the inner-most boundary of the air gap in the stator model were the stator *central circle* nodes. The mesh of the rotor included the rotor iron, slot-fill and layers of air gap. The nodes on the outer boundary of the air gap in the rotor model were the rotor *central circle* nodes. The rotor and stator central circle nodes sat on the same circle. The circumferential position of these nodes did not necessarily coincide.

The element stiffness matrices were generated as described in appendix B.6.1. In the magnetic model the magnetic stiffness matrix for each bay could be fully assembled using *the merge* described in appendix B.8. This is because only one DoF exists for each node and so the magnetic stiffness matrix is considerably smaller than the mechanical system matrices. Boundary values were required in order to achieve a unique solution. The outer circumference of the stator and inner circumference of the rotor were taken as the boundaries. The values of magnetic potential of these nodes

were set to zero. The merge of the stiffness matrices was completed without including the boundary nodes. The stiffness matrices for a single rotor and stator bay were then reduced in a single transformation. This reduction is explained in appendix B.13. The specific DoFs retained in the matrix are described in section 4.2.4. These super-elements were used to create the magnetic stiffness matrix for the rotor and stator with the merge and reduction described in appendix B.14.

The elemental excitation vector was created using the method described in appendix B.6.2. A sinusoidal rotor current pattern was assigned to the rotor. This pattern was fixed relative to the rotor coordinate axis and was maintained for all angles of rotation of the rotor and for all stator current patterns. The current density j_{Rk} in rotor slot k was calculated by

$$j_{Rk} = J_R \cos(n_{pp}\theta_{Rk}) \tag{28}$$

where J_R is the peak rotor current density, n_{pp} is the number of pole pairs and

$$\theta_{Rk} = \frac{2\pi k}{s_R} \tag{29}$$

The slot number k is counted anti-clockwise from the positive x axis of the rotor reference frame and s_R is the number of rotor slots.

The initial sinusoidal current density pattern that was assigned to the stator rotated around the stator. This pattern leads the rotor excitation by an angle α. The angle α that was chosen generated maximum possible torque. The current density j_{Sk} in stator slot k is

$$j_{Sk} = J_S \cos(n_{pp}(\theta_{Sk} - \phi + \alpha)) \tag{30}$$

J_S is the peak stator current density, ϕ is the rotational angle of the rotor reference frame relative to the stator reference frame and

$$\theta_{Sk} = \frac{2\pi k}{s_S} \tag{31}$$

The slot number k is counted anti-clockwise from the positive x axis of the stator reference frame and s_S is the number of stator slots.

Master nodes were maintained in the location of the bimorph conductors in the stator teeth. These currents were included in the excitation vector as point currents applied to those nodes.

The full excitation vectors for the rotor and stator bays were generated and then reduced using the transformation described in appendix B.13. The merge and reduction was used to create the excitation vectors for the reduced rotor and stator models.

In order to solve the governing equation for the whole structure the rotor and stator models were coupled together using the central circle method described in appendix D.7. During the reduction the air gap nodes were retained which enabled this coupling method to be achieved without further complicated transformations. Once the nodal magnetic potentials of the reduced model were found, these were expanded to give the nodal magnetic potentials for the whole of the rotor and stator. The boundary nodes were excluded from this expansion as the magnetic potential of these nodes had already been assigned to zero.

3.2.3 Calculating Maxwell Forces Acting at the Tooth Tips

The middle circle is a circle through the middle of a ring of elements in the air gap in the stator model. The magnetic flux density at every point on the

middle circle in the air gap was calculated using the values of nodal potential of the nodes on the elements situated on the middle circle. This method is described in appendix D.8. These values were then used to calculate the shear and tangential stress at every point on the middle circle. The product of the average of these values and the length of the middle circle in a bay gives the Maxwell forces that act on the tooth tips of that bay. This method is described in appendix D.9. The result of this method is a local x and y component of force that acts at the centre of each tooth tip. The central tooth tip nodes were kept as masters in the mechanical model and so these forces could be applied directly to the reduced mechanical model.

3.2.4 Calculating Equivalent Magnetostriction Forces

Calculating the equivalent magnetostriction forces required a larger amount of computation than calculating the Maxwell forces. The values of magnetic potential for the nodes in each element in the stator iron of the magnetic model were used to calculate a vector of equivalent magnetostriction forces for the corresponding DoFs in the mechanical model. This method is described in appendix D.10. The elemental force vectors were merged and reduced to create vectors for each bay in the local coordinates of the bay. The force vectors for each bay were then used in the second merge and reduction process to create a reduced forcing vector for the whole stator. The merge and reduction processes that were used on the forcing vectors were the same processes that were used on the mass and stiffness matrices of the mechanical system. The entries in the reduced vector of magnetostrictive forces corresponded directly to the entries in the reduced mechanical mass and stiffness matrices.

3.2.5 Calculating the Vibration of the Stator for each Temporal and Spatial Component of Force

The excitation and response of the machine was temporally and spatially periodic. A single period needed to be analysed in both domains in order to gather all of the required information for the analysis. Two dimensional Fourier decomposition was used on the electromagnetic forcing. This enabled the response of the machine to be found from each individual Fourier component of force.

Time was taken as a non dimensional periodic quantity. One complete rotation of the rotor corresponded to one period in time. The rotor positions were discretized into many equally spaced steps. These rotor positions represented the time steps in a single period in the time domain.

One period in the space domain corresponded to 360^o around the air gap circumference. Therefore, the whole of the stator was analysed. The angle subtended by each bay provided the steps in the space domain.

The Maxwell forces acting at the tooth tips and the equivalent magnetostrictive forces depend on the rotational position of the rotor. These values were calculated for every time step in one period. Each vector of nodal forces was combined into a matrix with rows corresponding to the DoFs in the reduced mechanical system and columns corresponding to each time step. These were decomposed in time and space using the method illustrated in appendix B.16.

For each combination of spatial and temporal harmonic n and m there

exists a 2x2 block in the Fourier map of coefficients of those harmonics:

$$\begin{bmatrix} \cos(n\theta)\cos(mt) & \cos(n\theta)\sin(mt) \\ \sin(n\theta)\cos(mt) & \sin(n\theta)\sin(mt) \end{bmatrix} \tag{32}$$

These blocks can be extracted from the map and expanded to give nodal forces in the temporal frequency domain. This is described in appendix B.16.

The vector of nodal forces in the temporal frequency domain for all spatial components can be found if the nodal forces in the time domain are decomposed only once into the temporal frequency domain.

Modal forces are found from:

$$\mathbf{P} = \mathbf{Q}^{\top}\mathbf{F} \tag{33}$$

Where $\mathbf{F}$ is the nodal forcing in the time or temporal frequency domain and $\mathbf{Q}$ is a matrix of mass-normalized mode shape vectors (appendix C.3). The entries in the rows of the modal force vector represent the magnitude of the force applied to each mode of the structure. Using the normalized system and transformations described in appendix C.3, the mass matrix is transformed to give the identity matrix. Proportional damping is used so the damping matrix can be transformed to give a diagonal matrix. The entries on the diagonal can be extracted into the vector $2\gamma\boldsymbol{\omega}$ where γ is the damping factor and $\boldsymbol{\omega}$ is a vector of natural frequencies. The stiffness matrix is transformed to give the spectral matrix $\boldsymbol{\Lambda}$ which is diagonal so the entries on the diagonal can be turned into the vector $\boldsymbol{\lambda}$ which is a vector of eigenvalues. Modal displacements $\mathbf{q}$ are given in the frequency domain, by:

$$\mathbf{q} = [(\boldsymbol{\lambda} - \omega_f^2) + 2\gamma\omega_f\boldsymbol{\omega}i]^{-1}\mathbf{P} \tag{34}$$

i is the imaginary number. The forcing frequency is ω_f, for a force with temporal harmonic m and a rotor rotational speed of Ω (rads^{-1}) this is:

$$\omega_f = m\Omega \tag{35}$$

The mode shape vectors are taken as dimensionless quantities so that the units of the identity and spectral matrices are kg and Nm^{-1} respectively and the unit of modal force is N.

The vibration level of the machine is quantified by K the root-mean-squared radial velocity of the nodes on the back of the stator core. In order to calculate this, the modal displacement vector $\mathbf{q}$ is transformed to give the nodal displacement of all DoFs in the mechanical structure (appendix C.3). This is found by using the local x y deflection of these nodes $\mathbf{x}_c$ and $\mathbf{y}_c$ and transforming into radial and tangential components $\mathbf{r}_c$ and $\mathbf{t}_c$. The root-mean-squared vibration velocity is calculated as the square root of the sum of the radial deflections multiplied by the forcing frequency squared:

$$K = \sqrt{\mathbf{r}_c^\top \mathbf{r}_c \omega_f^2} \tag{36}$$

This measure has been chosen because when all other values are constant, sound power is proportional to radial velocity squared and so this measure allows for a comparison of the noise emitted from the machine by each excitation method considered.

3.2.6 Calculating Electromagnetic Torque and Copper Loss

The torque is calculated as the product of the line integral of the tangential Maxwell stress of the middle circle points and the mean radius of those points as described in appendix D.11. This calculation is carried out for every time step.

The copper loss from a machine is proportional to current squared if resistance is constant. The mean-squared current supplied to the machine therefore gives an indication of the magnitude of the copper loss from the machine.

3.2.7 Calculating Root-Mean-Squared Values

The root-mean-squared (rms) value of a variable quantity is a useful single measure of that quantity. The rms values of torque, modal force and current are given in the next chapter as measures of the successfulness of each stage in the analysis. The calculation of rms current is described here:

The rms current is calculated for every time step as

$$i_{rms} = \sqrt{\frac{\mathbf{i}^\top \mathbf{i}}{s}} \tag{37}$$

where $\mathbf{i}$ is the vector of current in each slot and s is the number of slots. A value for i_{rms} exists for every time step. A vector of these values can be created and an overall rms value calculated for the whole analysis by repeating equation (37). In this case $\mathbf{i}$ is a vector of rms current for every time step and s is the number of time steps.

A single value of torque and modal force for each mode in one mode pair exist for every time step and so the rms value of these is calculated with $\mathbf{i}$ as a vector of these values for each time step and s as the number of time steps.

3.3 Accelerations of the Calculations

The computer capacity and time required for the full analysis described above is acceptable when a low number of computations are required. However, in order to calculate the current patterns for stages 1 2 and 3 optimizations were used which required many repeats of the calculations. The full calculation methods were far too time consuming to be used in the optimization process and so accelerations of these methods were developed.

The analysis can be separated into linear and non-linear sections. If saliency is neglected the magnetic potential, magnetic flux density and torque are linearly dependent on current. The Maxwell stresses, Maxwell forces and equivalent magnetostriction forces are related to magnetic flux density squared and so the relationship between these and current is non linear. Projection methods are used for accelerating the calculations of these quantities. The methods used for accelerating the linearly related quantities are described next. The methods used for accelerating the calculation of magnetostrictive forces is described in section 3.3.2. This method can also be used to accelerate the calculation of Maxwell forces although the full calculation method for this is not time consuming if the calculation of magnetic flux density is accelerated. This is because the calculation of Maxwell forces at the tooth tips only requires simple manipulations of magnetic flux density on the middle circle.

3.3.1 Accelerations for Linearly Related Variables

In the electrical machine structure the values of magnetic potential are calculated for each node and the values of magnetic flux density are calculated at every point around the middle circle for every time step. This results in very many values for both of these quantities. However, these values are not all independent. They are related to the excitation applied to the stator.

The cumulative number of stator slots and bimorph conductors gives the number of independent variables in the current pattern. This is also the number of possible independent variations in the magnetic potential and magnetic flux density. The vector of nodal magnetic potentials can be projected onto a subspace. The dimension of the subspace equals the number of independent variations in potential. This is considerably smaller than the size of the full vector and so a projection transformation provides a reduction transformation. The reduced vector can be used in the analysis and the results expanded back onto the full space. The excitation variables provide the constraints for this transformation. These constraints exist inherently in the analysis and so this method does not introduce errors into the analysis above the numerical errors that occur from the computation.

Projection matrices are not unique. Any one projection matrix post multiplied by an invertible matrix will also give a projection matrix for the same subspace. Mathematically either of these matrices will work. However, numerically a well conditioned projection matrix is required. The columns in a well conditioned projection matrix are distinct from each other.

A sensitivity study was used to generate the projection matrices for the quantities that are linearly related to current. In general this method can be explained by considering any linearly related vector quantities $\mathbf{a}$ and $\mathbf{b}$. A change from the original vector $\mathbf{a_0}$ of $\mathbf{\Delta a}$ leads to the new vector $\mathbf{a_1}$:

$$\mathbf{a_1} = \mathbf{a_0} + \mathbf{\Delta a} \tag{38}$$

The corresponding change from $\mathbf{b_0}$ to $\mathbf{b_1}$ is captured by the sensitivity matrix $\mathbf{S}$:

$$\mathbf{b_1} = \mathbf{b_0} + \mathbf{S\Delta a} \tag{39}$$

The number of rows in $\mathbf{S}$ is the number of entries in $\mathbf{b_0}$. The number of columns in $\mathbf{S}$ is the number of entries in $\mathbf{a_0}$. Sensitivity matrices are created using a central difference method for every entry in the vector in turn. Initially

$$\mathbf{b_0} = \begin{Bmatrix} b_{01} \\ b_{02} \\ b_{03} \end{Bmatrix} \qquad \mathbf{\Delta a} = \begin{Bmatrix} 0 \\ 0 \\ 0 \\ 0 \end{Bmatrix} \tag{40}$$

The first entry in $\mathbf{\Delta a}$ is increased by a relatively small amount and the new vector $\mathbf{b}^+$ is calculated

$$\mathbf{\Delta a} = \begin{Bmatrix} \Delta a \\ 0 \\ 0 \\ 0 \end{Bmatrix} \qquad \mathbf{b}^+ = \begin{Bmatrix} b_1^+ \\ b_2^+ \\ b_3^+ \end{Bmatrix} \tag{41}$$

The entry in $\mathbf{\Delta a}$ is then set back to zero. Then the first entry in $\mathbf{\Delta a}$ is decreased by the same amount and $\mathbf{b}^-$ is calculated

$$\mathbf{\Delta a} = \begin{Bmatrix} -\Delta a \\ 0 \\ 0 \\ 0 \end{Bmatrix} \qquad \mathbf{b}^- = \begin{Bmatrix} b_1^- \\ b_2^- \\ b_3^- \end{Bmatrix} \tag{42}$$

The central difference is then

$$\mathbf{s_1} = \frac{\mathbf{b}^+ - \mathbf{b}^-}{\Delta a - (-\Delta a)} = \begin{Bmatrix} \frac{b_1^+ - b_1^-}{2\Delta a} \\ \frac{b_2^+ - b_2^-}{2\Delta a} \\ \frac{b_3^+ - b_3^-}{2\Delta a} \end{Bmatrix} \tag{43}$$

$\mathbf{s_1}$ becomes the first column in the sensitivity matrix $\mathbf{S}$. The other columns in $\mathbf{S}$ are calculated by changing those corresponding entries in $\mathbf{\Delta a}$ in the same manner.

In this study the sensitivity matrices were used to accelerate the calculation of nodal magnetic potential, magnetic flux density and torque with change in current density in the slots and change in current in the bimorph conductors. A sensitivity matrix was required for each quantity for each time step.

Torque is a scalar quantity and so the sensitivity of torque to current density in the stator slots is a transposed vector. The number of entries in this vector equals the number of bays in the stator. $\mathbf{b_0}$ is the torque from the initial sinusoidal current pattern in the stator and rotor. $\mathbf{\Delta a}$ is the change in stator current away from the initial pattern.

The sensitivity matrix of nodal magnetic potential to current density in the stator slots is a matrix with the number of rows equal to the number of nodes in the magnetic stator model and the number of columns equal to the number of stator slots. $\mathbf{b_0}$ is the nodal magnetic potential from the initial sinusoidal current pattern in the stator and rotor. $\mathbf{\Delta a}$ is the change in stator current away from the initial pattern.

The sensitivity matrix of magnetic flux density on the middle circle has the number of rows equal to the number of points on the middle circle and number of columns equal to the number of stator slots. $\mathbf{b_0}$ is the magnetic potential of these points from the rotor excitation only. $\mathbf{\Delta a}$ is the current pattern in the stator.

Once the sensitivity matrices are calculated, the governing equations of the magnetic model need not be solved again. This is a large matrix equation which requires large computational capacity. This projection method eliminates the need to calculate the full vector of magnetic nodal excitation and removes the time taken for expanding from the central circle method and the merge and reduction. The time consuming calculation of magnetic flux density at the many points on the middle circle is also removed.

3.3.2 An Acceleration for Calculating Equivalent Magnetostriction Forces

Calculating the equivalent nodal magnetostriction forces from a known current pattern can be split into linear and non linear stages. The linear stage is the calculation of nodal magnetic potential from the stator slot current density and bimorph current patterns. The computation of this stage is accelerated with the sensitivity matrices described above.

The non linear stage is the calculation of equivalent nodal magnetostriction forces for every DoF in the stator iron from values of potential for every node in the stator iron. This computation can be accelerated with a method that captures the non linear relationship within a matrix transformation. This method considers every element in the stator in turn and within every element every node is considered in turn. Two matrices $\mathbf{W}_{xie}$ and $\mathbf{W}_{yie}$ exist for every node i in every element e in one bay of the stator iron of the mechanical model. These provide the transformation from the nodal potential of every node in the element to magnetostriction forces for the x and y DoFs in the element. The equivalent magnetostriction forces for the x and y DoFs of one node in an element due to magnetostriction in

that element are found from:

$$f_{\lambda xie} = \mathbf{a}_e^\top \mathbf{W}_{xie} \mathbf{a}_e \qquad\qquad f_{\lambda yie} = \mathbf{a}_e^\top \mathbf{W}_{yie} \mathbf{a}_e \tag{44}$$

The matrices $\mathbf{W}_{xie}$ and $\mathbf{W}_{yie}$ are calculated as described in section 3.3.4. The x and y components of force for all nodes in one element are found with the above equation with the same vector of nodal potentials $\mathbf{a}_e$ and different transformation matrices $\mathbf{W}_{xie}$ and $\mathbf{W}_{yie}$ for each node. The scalar values $f_{\lambda xie}$ and $f_{\lambda yie}$ are combined into a vector of elemental forces. The set of $\mathbf{W}_{xie}$ and $\mathbf{W}_{yie}$ matrices that are used for one bay are used to convert nodal potentials to nodal forces for all bays. The elemental forcing vectors are merged and reduced into forcing vectors for each bay. This results in vectors of force for all bays in the local coordinates of the bay. These vectors can then be used in the merge and reduction process to create the reduced forcing vector to apply to the reduced mechanical model.

These matrix transformations robustly capture the non linearity of the magnetic potential - magnetostriction force relationship. Once these matrices have been computed they can be used whenever required and do not need to be calculated again. The previous method required Gaussian integration of each element in the structure every time the elemental forces were calculated. This method replaces the previous method with the simple multiplication in equation (44) but does not eliminate the need for the merge and reduction processes.

3.3.3 Accelerations for Calculating Modal Forces

The complete calculation of modal force from stator slot current density and bimorph conductor current can be reduced down into one set of matrix

multiplications:

$$p_{1M} = \mathbf{b}^\top \mathbf{\Delta}_{1M} \mathbf{b} \qquad p_{2M} = \mathbf{b}^\top \mathbf{\Delta}_{2M} \mathbf{b}$$
$$p_{1\lambda} = \mathbf{b}^\top \mathbf{\Delta}_{1\lambda} \mathbf{b} \qquad p_{2\lambda} = \mathbf{b}^\top \mathbf{\Delta}_{2\lambda} \mathbf{b} \tag{45}$$

Here $\mathbf{b}$ is a vector that represents the currents in the machine. This has three partitions. The first is a single entry 1 or 0, which defines whether or not the rotor excitation is considered. The entries in the second partition correspond to each of the stator slot current densities. The entries in the third partition correspond to each of the bimorph conductor currents:

$$\mathbf{b} = \left\{ \begin{array}{c} b_r \\ \hline b_{s1} \\ \vdots \\ b_{ss} \\ \hline b_{b1} \\ \vdots \\ b_{bs} \end{array} \right\} \tag{46}$$

The number of stator bays is s and so $\mathbf{b}$ has $2s+1$ entries.

The matrices $\mathbf{\Delta}_{1M}$ and $\mathbf{\Delta}_{2M}$ are used for the modal force calculation for Maxwell forces p_{1M} and p_{2M} for the first and second mode in the mode pair respectively. The matrices $\mathbf{\Delta_{1\lambda}}$ and $\mathbf{\Delta_{2\lambda}}$ are used for the modal force calculation for equivalent magnetostriction forces $p_{1\lambda}$ and $p_{2\lambda}$ for the first and second mode in the mode pair. The total modal forces for each of the two modes in the mode pair are then:

$$p_1 = p_{1M} + p_{1\lambda} \qquad p_2 = p_{2M} + p_{2\lambda} \tag{47}$$

These are calculated as follows:

In order to compute the $\mathbf{\Delta}$ matrices, a projection matrix $\mathbf{U}$ is created that relates $\mathbf{b}$ to nodal magnetic potential $\mathbf{a}$:

$$\mathbf{a} = \mathbf{U}\mathbf{b} \tag{48}$$

The first column of $\mathbf{U}$ is the nodal magnetic potential in the stator from the rotor excitation only. The next s columns are the sensitivity of magnetic potential to stator slot current. The next s columns are the sensitivity of magnetic potential to bimorph currents. Sensitivity matrices are explained in section 3.3.1. A matrix $\mathbf{U}$ exists for each time step. This is one construction method for $\mathbf{U}$. Other methods are possible which are equivalent because of the non-uniqueness of a projection matrices as noted in section 3.3.1.

The $\mathbf{\Delta}$ matrices are square with dimensions $2s+1$. Their entries are calculated with the method described in section 3.3.4. These four matrices are required for all time steps. Once they are computed the calculation of modal force is simply equation (45).

3.3.4 A Transformation Matrix to Relate Vector Entries Squared to a Scalar

The $\mathbf{\Delta}$ matrices given in section 3.3.3 and the $\mathbf{W}$ matrices given in section 3.3.2 are constructed with the same method which is explained here. These matrices provide an acceleration of the calculation of a single variable f if this is related to the entries in a vector $\mathbf{a}$ squared. The accelerated calculation is given in the form:

$$f = \mathbf{a}^\top \mathbf{W}\mathbf{a} \tag{49}$$

W provides the transformation between the vector information in **a** and the single variable f. If **a** has eight entries then:

$$\mathbf{W} = \begin{bmatrix} w_{11} & w_{12} & \dots & w_{18} \\ w_{12} & w_{22} & \dots & w_{28} \\ \vdots & \vdots & \ddots & \vdots \\ w_{18} & w_{28} & \dots & w_{88} \end{bmatrix} \tag{50}$$

Note that this matrix is symmetric. In order to build **W**, the diagonal entries of the transformation matrix are considered first. The vector **a** is initialized with zeros and the j^{th} entry is set to unity. With this **a** the value of f can be found through the full calculation method. (For magnetostriction forces this is the method described in section D.10.) Substituting **a** into equation (49) leads to:

$$w_{jj} = f \tag{51}$$

The vector **a** is initialized again and the next entry is set to unity. All diagonal entries are found this way.

The off-diagonal entries can be found once the diagonal entries are known. Two entries in **a** are populated with the value 1. These are entry j and k ($j \neq k$). The required value is found with the full calculation method. If j=1 and k=2 then

$$\mathbf{a} = \begin{Bmatrix} 1 \\ 1 \\ 0 \\ \vdots \\ 0 \end{Bmatrix} \tag{52}$$

and substituting (52) into equation (49) leads to

$$f = w_{11} + 2w_{12} + w_{22} \tag{53}$$

In general terms

$$f = w_{jj} + 2w_{jk} + w_{kk} \tag{54}$$

The values w_{jj}, w_{kk} are known and so w_{jk} is easily found. The vector $\mathbf{a}$ is initialized again and the next entries are set to unity. This process is carried out until all values in $\mathbf{W}$ are found.

Section 3.2 has described the full calculation methods that are required for the investigation of the operation of the machine described in the next chapter. Section 3.3 has explained how much of these calculation methods can be reduced into simple matrix transformations. The next section describes the optimization processes and constraints that are required to calculate the current patterns for each stage in the investigation.

3.4 Constrained Optimizations

The current patterns for stages 1, 2 and 3 are found using least squares optimization processes described here. Stages 1 and 2 utilize the individually controlled conductor (ICC) method. There are s slots in the stator. If no constraints are imposed then there are s possible independent variables in the current density vector. Constraints on the current patterns are imposed to achieve the required operation of the machine. Each constraint that is imposed reduces the number of independent current variables by one.

3.4.1 Optimization for Stage 1

For stage 1 the requirement was to find a stator slot current pattern that minimized the copper loss but did not affect the torque. This was achieved by writing torque as

$$T = T_0 + \mathbf{s}^\top \boldsymbol{\Delta}\mathbf{i_1} \tag{55}$$

were T_0 is the nominal torque that was generated with the sinusoidal current pattern $\mathbf{i_0}$ from stage 0. T is the new torque generated from the result of the stage 1 current density pattern $\mathbf{i_1}$. $\mathbf{s}$ is the sensitivity of torque to change in current and $\boldsymbol{\Delta}\mathbf{i_1}$ is the change in slot current density from $\mathbf{i_0}$.

$$\mathbf{i_1} = \mathbf{i_0} + \boldsymbol{\Delta}\mathbf{i_1} \tag{56}$$

The constraint that torque should not change with a change in current from $\mathbf{i_0}$ to $\mathbf{i_1}$ reduces the amount of possible variables in $\mathbf{i_1}$ from s to $(s-1)$. This constraint is imposed by setting $\boldsymbol{\Delta}\mathbf{i_1}$ to

$$\boldsymbol{\Delta}\mathbf{i_1} = \mathbf{T}\boldsymbol{\Delta}\mathbf{i}_R \tag{57}$$

so that equation (55) becomes

$$T = T_0 + \mathbf{s}^\top \mathbf{T}\boldsymbol{\Delta}\mathbf{i}_R \tag{58}$$

and equation (56) becomes

$$\mathbf{i_1} = \mathbf{i_0} + \mathbf{T}\boldsymbol{\Delta}\mathbf{i}_R \tag{59}$$

The transformation matrix $\mathbf{T}$ has s rows and $(s-1)$ columns, so $\boldsymbol{\Delta}\mathbf{i}_R$ has $(s-1)$ entries. $\mathbf{T}$ is orthogonal to $\mathbf{s}$ so that

$$\mathbf{s}^\top \mathbf{T} = \mathbf{0} \tag{60}$$

This provides the constraint that the torque does not change with change in current. Substituting equation (60) into equation (58) leads to $T = T_0$. The construction of the matrix $\mathbf{T}$ is explained in appendix B.15.1.

The optimum current is then found by minimizing the sum of the squares of currents. The sum of the squares of currents is:

$$\mathbf{i_1}^\top \mathbf{i_1} = \mathbf{i_0}^\top \mathbf{i_0} + \mathbf{2i_0}^\top \mathbf{T\Delta i}_R + (\mathbf{T\Delta i}_R)^\top \mathbf{T\Delta i}_R \tag{61}$$

This is minimized by differentiating with respect to $\mathbf{\Delta i}_R$ and setting this to zero so that

$$\mathbf{\Delta i}_R = -(\mathbf{i_0}^\top \mathbf{T}(\mathbf{T}^\top \mathbf{T})^{-\mathbf{1}})^\top \tag{62}$$

Once $\mathbf{T}$ and $\mathbf{s}$ are known $\mathbf{\Delta i}_R$ can be found from equation (62) and $\mathbf{\Delta i_1}$ can be found from equation (57).

This method linearizes torque with respect to current. If torque and current were linearly related then implementing the above method once for every time step would immediately achieve the optimized current density vector. However, saliency causes the linear relationship to break down. Over small changes in current, the non linear effect due to saliency is negligible and a linear assumption is adequate. For large changes in current, saliency has a large effect, the magnetic field variables predicted with a linear assumption do not equal the actual magnetic field variables. Consequently the actual torque also differs from the torque predicted with a linear model. The above calculation correctly calculates the direction for the change in current density in each slot. However if 100% of $\mathbf{\Delta i_1}$ was to be implemented, the current pattern would be forced to change by a relatively large amount and the torque predicted with equation (55) would not be correct. This problem is overcome by implementing a change in the current density pattern that

is a proportion γ of $\mathbf{\Delta i_1}$, and so equations (55) and (56) are rewritten:

$$T = T_0 + \gamma \mathbf{s}^\top \mathbf{\Delta i_1} \qquad \mathbf{i_1} = \mathbf{i_0} + \gamma \mathbf{\Delta i_1} \tag{63}$$

Once this value of $\mathbf{i_1}$ has been found the torque is calculated. If this has varied from the required value, $\mathbf{i_1}$ is scaled so that the torque is kept constant. The sensitivity vector $\mathbf{s}$ is recalculated and the current is optimized again. This process is continued until the values in $\mathbf{\Delta i_1}$ converge. See figure 44 for a flow chart of this optimization process. The proportion of $\mathbf{\Delta i_1}$ that is used in this iteration could be a single arbitrary value such as 0.1. However, this could be a very time consuming approach to the optimization. A more efficient approach is to use a line search method.

3.4.1.1 Line Search Line search provides a means of calculating the fraction γ of the change in $\mathbf{\Delta i_1}$ that gives the result that is closest to the required result. Here, the required result is a minimized sum of squares of currents. Line search achieves this by defining a range of values for γ, for example 0, 1/2 and 1. The sum of squares of currents is calculated for each of these values and the value of γ that gives the minimum result is found. If this is 0 or 1 then the range of values of γ is extended until the minimum result does not occur at a limiting value. Figures 45 and 46 illustrate this. The value of γ that gives the minimum result and the values either side of this are taken and a polynomial is fitted through these values as shown in figure 47. From this the value of γ that results in the minimum sum of squares of current in that step in the iteration can be found and used.

3.4.2 Optimization for Stage 2

In stage 2 a stator slot current pattern is required that cancels some components of noise, does not affect the torque and has the minimum possible copper loss. In order to implement this the above method was extended to

also cancel out a pair of modal forces. This optimization starts with the current pattern $\mathbf{i_1}$ found in stage 1. The change in current density from $\mathbf{i_1}$ to $\mathbf{i_2}$ is $\mathbf{\Delta i_2}$:

$$\mathbf{i_2} = \mathbf{i_1} + \mathbf{\Delta i_2} \tag{64}$$

Three equations describe the relationship between change in current and torque and change in current and modal force: The torque provided by $\mathbf{i_2}$ is:

$$T = T_0 + \mathbf{s}^\top \mathbf{\Delta i_2} \tag{65}$$

The modal force due to current pattern $\mathbf{i_2}$ and the first mode in the mode pair is p_{12}.

$$p_{12} = p_{11} + \mathbf{s_{11}^\top} \mathbf{\Delta i_2} \tag{66}$$

The modal force due to current density pattern $\mathbf{i_1}$ and the first mode in the mode pair is p_{11}. The modal force due to current pattern $\mathbf{i_2}$ and the second mode in the mode pair is p_{22}.

$$p_{22} = p_{21} + \mathbf{s_{21}^\top} \mathbf{\Delta i_2} \tag{67}$$

The modal force due to current density pattern $\mathbf{i_1}$ and the second mode in the mode pair is p_{21}. The vectors $\mathbf{s_{11}}$ and $\mathbf{s_{21}}$ are the sensitivities of the first and second modal force to current.

The three constraints that must be met are:

Constant torque with respect to change in current $T = T_0$:

$$\mathbf{s}^\top \mathbf{\Delta i_2} = 0 \tag{68}$$

Elimination of the first modal force $p_{12} = 0$:

$$\mathbf{s_{11}^\top \Delta i_2} = -p_{11} \tag{69}$$

Elimination of the second modal force $p_{22} = 0$:

$$\mathbf{s_{21}^\top \Delta i_2} = -p_{21} \tag{70}$$

The change in current $\mathbf{\Delta i_2}$ can be set to

$$\mathbf{\Delta i_2} = \mathbf{T_2 g} + \mathbf{h} \tag{71}$$

$\mathbf{T_2}$ is a matrix with s rows and $(s-3)$ columns. $\mathbf{g}$ is a vector with $(s-3)$ entries and this term is used to minimize the sum of squares of current. $\mathbf{h}$ is a vector with s entries and this term cancels the modal forces.

Equations (65), (66) and (67) then become:

$$T = T_0 + \mathbf{s}^\top(\mathbf{T_2 g} + \mathbf{h}) \tag{72}$$

$$p_{12} = p_{11} + \mathbf{s_{11}^\top}(\mathbf{T_2 g} + \mathbf{h}) \tag{73}$$

$$p_{22} = p_{21} + \mathbf{s_{21}^\top}(\mathbf{T_2 g} + \mathbf{h}) \tag{74}$$

In order to achieve the constraints in equations (68), (69) and (70) the following must hold:

$$\begin{bmatrix} \mathbf{s}^\top \\ \mathbf{s_{11}^\top} \\ \mathbf{s_{21}^\top} \end{bmatrix} \mathbf{T_2} = \mathbf{0} \tag{75}$$

$\mathbf{T_2}$ can be found with the construction method given in appendix B.15.1.

Substituting equation (75) into equations (72), (73) and (74) leads to the

following requirements for $\mathbf{h}$:

$$\mathbf{s}^\top \mathbf{h} = 0 \tag{76}$$

$$\mathbf{s_{11}}^\top \mathbf{h} = -p_{11} \tag{77}$$

$$\mathbf{s_{21}}^\top \mathbf{h} = -p_{21} \tag{78}$$

The vector $\mathbf{h}$ enables the constraints to be met. This vector is found by noticing that equation (76) can be written using $\mathbf{T}$ from equation (60). If

$$\mathbf{h} = \mathbf{T}\mathbf{j} \tag{79}$$

equation (76) becomes:

$$\mathbf{s}^\top \mathbf{T}\mathbf{j} = 0 \tag{80}$$

$\mathbf{j}$ can be found from the constraints in equations (77) and (78).

$$\begin{bmatrix} \mathbf{s_{11}}^\top \\ \mathbf{s_{21}}^\top \end{bmatrix} \mathbf{T}\mathbf{j} = \begin{Bmatrix} -p_{11} \\ -p_{21} \end{Bmatrix} \tag{81}$$

The solution to $\mathbf{j}$ is not unique. A pseudo-inverse approach can be applied to equation (81) to find one acceptable vector $\mathbf{j}$.

From equation (79) $\mathbf{h}$ can be found. This has ensured the torque does not change with change in current and that the modal forces are cancelled.

The vector $\mathbf{g}$ is required to minimize the sum of squares of current. The sum of squares of current is given by

$$\mathbf{i_2}^\top \mathbf{i_2} = (\mathbf{i_1} + \mathbf{h})^\top (\mathbf{i_1} + \mathbf{h}) + \mathbf{2}(\mathbf{i_1} + \mathbf{h})^\top \mathbf{T_2 g} + (\mathbf{T_2 g})^\top \mathbf{T_2 g} \tag{82}$$

Differentiating this with respect to $\mathbf{g}$ and setting to zero gives

$$\mathbf{g} = -((\mathbf{i_1} + \mathbf{h})^\top \mathbf{T_2} (\mathbf{T_2}^\top \mathbf{T_2})^{-\mathbf{1}})^\top \tag{83}$$

This process also linearizes torque and modal force with respect to current. The linearity assumed in these equations breaks down with relatively large $\mathbf{\Delta i_2}$ values. Therefore, calculating the optimum $\mathbf{i_2}$ requires an iterative procedure. This iteration involves cancelling the modal forces in small steps instead of attempting to find a current density pattern that completely cancels the modal forces in one step. The current density pattern that cancels the proportion of modal force under consideration may cause the resultant torque to change. The current density is scaled so that the torque is kept constant. The sensitivity matrices $\mathbf{s}$, $\mathbf{s_{11}}$ and $\mathbf{s_{21}}$ must be recalculated in every step in the iteration. The optimum $\mathbf{i_2}$ occurs when the full values of modal force have been reduced to negligible values. This process is illustrated in figure 48.

3.4.2.1 Consideration of Modal Forces Modal forces are mentioned in appendices C.3 and section 3.2.5. A modal force is found from

$$p = \mathbf{Q}^\top \mathbf{f} \tag{84}$$

Where $\mathbf{f}$ is a vector of nodal forces, $\mathbf{Q}$ is a matrix of orthogonalized mode shapes and p is the modal force. This calculation can be carried out with $\mathbf{f}$ in the time domain or in the frequency domain. In this study $\mathbf{f}$ is a vector of electromagnetic forcing in the time domain. A vector $\mathbf{f}$ exists for every time step and so a modal force p also exists for every time step. Cancelling the modal force instantaneously cancels that particular spatial harmonic for all temporal harmonics. There are s slots in the stator and T time steps so there are $s \times T$ unknowns in this problem.

If equation (84) was carried out in the frequency domain then an extra layer of computation would be required. This would enable the modal force from a combination of specific temporal as well as spatial harmonics to be eliminated. However, in order to achieve this all time steps would need to be analysed together in order to cancel the specific temporal component. This would need to be repeated for all time steps. This creates a problem with $s \times T \times T$ unknowns which would be far more complex to implement but may produce a more effective result.

3.4.3 Optimization for Stage 3

In stage 3 the stator slot current density pattern that was found in stage 1 is used. This minimizes the copper loss but does not affect the torque. Currents in bimorph conductors were required to cancel some components of vibration. This method results in the required torque being produced with minimum copper loss from the stator conductors with extra current fed into the bimorph conductors to reduce vibration. In order to achieve this a pair of modal forces from the electromagnetic force caused by the $\mathbf{i_1}$ current pattern were cancelled out by the electromagnetic force generated by the bimorph conductors. The force generated by the bimorph conductors is mainly magnetostrictive. The effect of this excitation method on Maxwell forces in the air gap is much less than the effect on magnetostriction. The current in the bimorph conductors is $\mathbf{i_3}$. This is a vector of nodal current with s entries, one for every tooth in the stator. There are two constraints to this problem:

$$p_{13} = p_{11} + \mathbf{s_{13}^{\top} i_3} \tag{85}$$

$$p_{23} = p_{21} + \mathbf{s_{23}^{\top} i_3} \tag{86}$$

The modal forces p_{11} and p_{21} are the modal forces from the first and second mode of a mode pair and electromagnetic forcing from the $\mathbf{i_1}$ current density pattern. This might be a different mode pair to that is cancelled in section 3.4.2. The modal forces p_{13} and p_{23} are the modal forces from the $\mathbf{i_3}$ bimorph current pattern and the mode pair. The vectors $\mathbf{s_{13}}$ and $\mathbf{s_{23}}$ are the sensitivities of modal force to bimorph currents. Both Maxwell forces and magnetostriction forces are included in this analysis. However, the bimorph currents are predicted to be relatively small and so are not expected to affect the torque. Torque is therefore neglected from this analysis. The constraints are

$$\mathbf{s_{13}}^\top \mathbf{i_3} = -p_{11} \tag{87}$$

$$\mathbf{s_{23}}^\top \mathbf{i_3} = -p_{21} \tag{88}$$

The bimorph currents can be rewritten:

$$\mathbf{i_3} = \mathbf{T_b}\mathbf{d} + \mathbf{c} \tag{89}$$

$\mathbf{T_b}$ is a matrix with s rows and $s-2$ columns, $\mathbf{d}$ is a vector with $s-2$ entries and $\mathbf{c}$ is a vector with s entries. Equations (85) and (86) then become

$$p_{13} = p_{11} + \mathbf{s_{13}}^\top(\mathbf{T_b}\mathbf{d} + \mathbf{c}) \tag{90}$$

$$p_{23} = p_{21} + \mathbf{s_{23}}^\top(\mathbf{T_b}\mathbf{d} + \mathbf{c}) \tag{91}$$

In order to achieve the constraints in equations (87) and (88) the following must hold:

$$\begin{bmatrix} \mathbf{s_{13}}^\top \\ \mathbf{s_{23}}^\top \end{bmatrix} \mathbf{T_b} = \mathbf{0} \tag{92}$$

$\mathbf{T_b}$ can be found with the construction method given in appendix B.15.1.

Substituting equation (92) into equations (90) and (91) leads to the following requirements for $\mathbf{c}$ which enables $\mathbf{c}$ to be found and the constraints to be met.

$$\left\{ \begin{array}{c} \mathbf{s}_{13}^{\top} \\ \mathbf{s}_{23}^{\top} \end{array} \right\} \mathbf{c} = \left\{ \begin{array}{c} -p_{11} \\ -p_{21} \end{array} \right\} \tag{93}$$

A pseudo-inverse approach is used to calculate $\mathbf{c}$. The vector $\mathbf{d}$ is required to minimize the sum of squares of current. The sum of squares of current is given by

$$\mathbf{i_3^{\top} i_3} = \mathbf{c}^{\top}\mathbf{c} + \mathbf{2c}^{\top}\mathbf{T_b d} + (\mathbf{T_b d})^{\top}\mathbf{T_b d} \tag{94}$$

Differentiating this with respect to $\mathbf{d}$ and setting to zero gives

$$\mathbf{d} = -\mathbf{c}^{\top}\mathbf{T_b}(\mathbf{T_b^{\top} T_b})^{-\mathbf{1}} \tag{95}$$

This enables $\mathbf{i_3}$ to be found for all time steps. The bimorph currents that are required are small and so linearity holds and iterations are not required for this analysis. This process is illustrated in figure 49.

3.5 Conclusion to the Chapter

This chapter has introduced the main methods used for an investigation of a large electrical machine. This investigation aims to quantify the vibration of the back of the stator core and the power loss that occurs from four types of excitation applied to the stator. Information that is given in the appendices in a general context is brought together in this chapter and referred specifically to this investigation.

The development of the magneto-mechanical model of the large electrical machine has been described. This consists of separate magnetic and mechanical models. The magnetic model calculations are carried out in the

time domain. These include calculations of Maxwell forces that act at the tooth tips of the stator and equivalent magnetostriction forces that act at the nodes in the stator iron. These electromagnetic forces are calculated from known slot current densities and bimorph conductor currents. Analysis of a complete spatial and temporal period of the machine is required in order to decompose the forces into temporal and spatial frequency components. The magnetic and mechanical models are coupled by applying the electromagnetic forces to the mechanical model in the frequency domain. The torque, sum of the squares of currents and the resulting vibration of the back of the stator core provide the measure of success for each excitation method considered.

These calculation methods require large computational capacity and time. Accelerations were developed which enable certain values to be calculated without the need for the full lengthy calculation methods. These accelerations were based mainly on projection methods and have been described in this chapter.

Now that the calculation methods have been described, the results of the investigation can be presented. These are given in the next chapter.

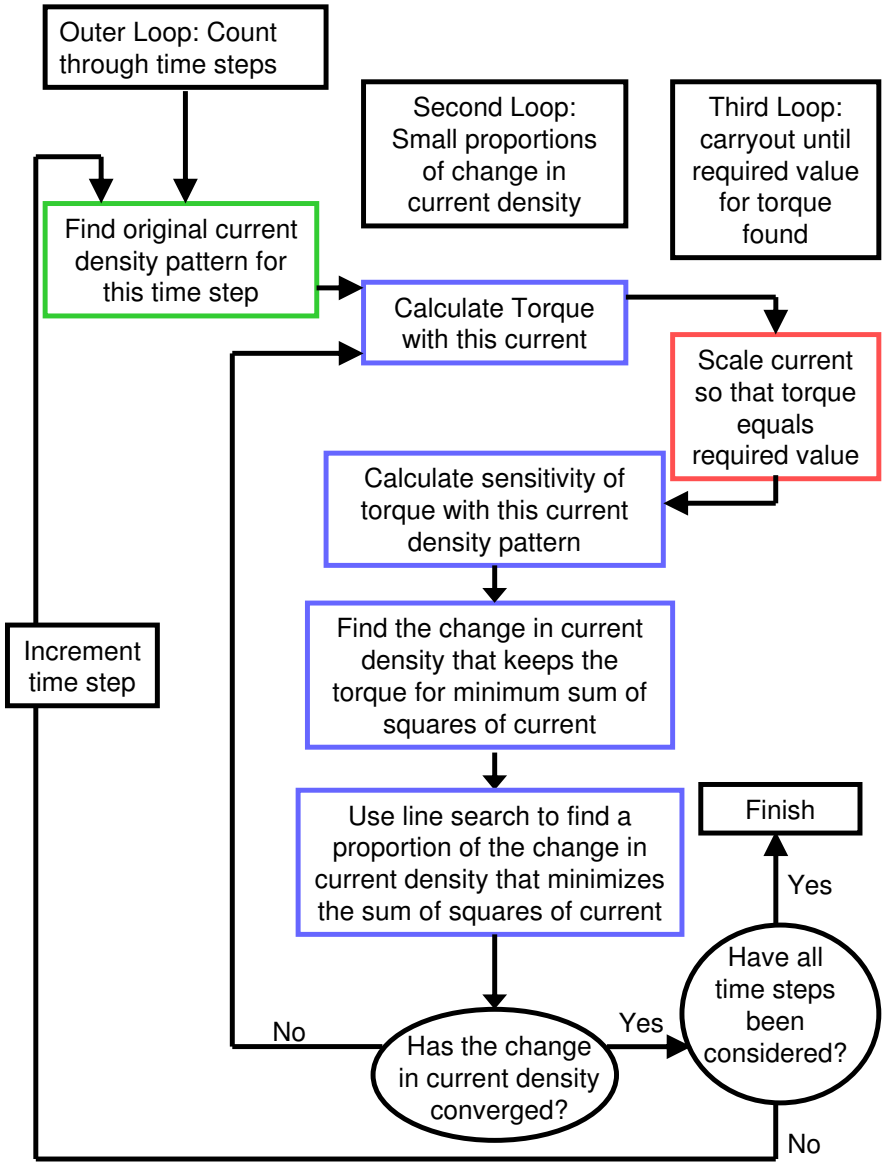

Figure 44: Iteration Process for Achieving Stage 1 Current Density Pattern

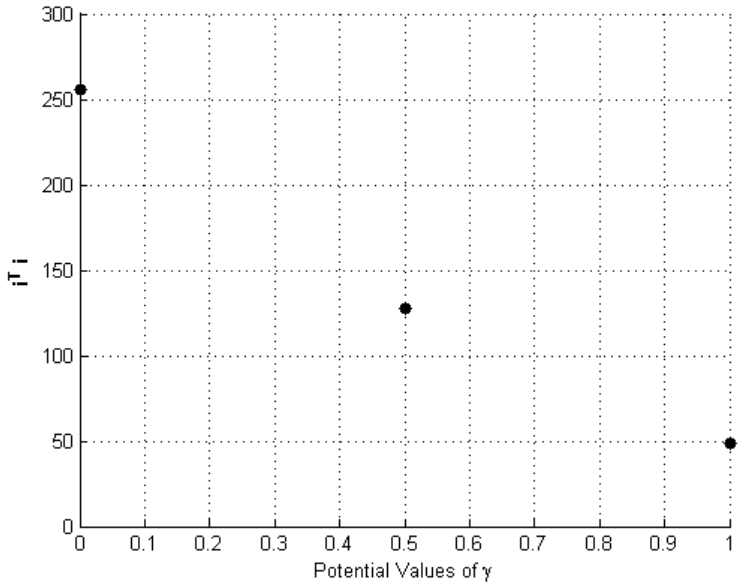

Figure 45: Example Sum of Squares of Current for Different γ Values

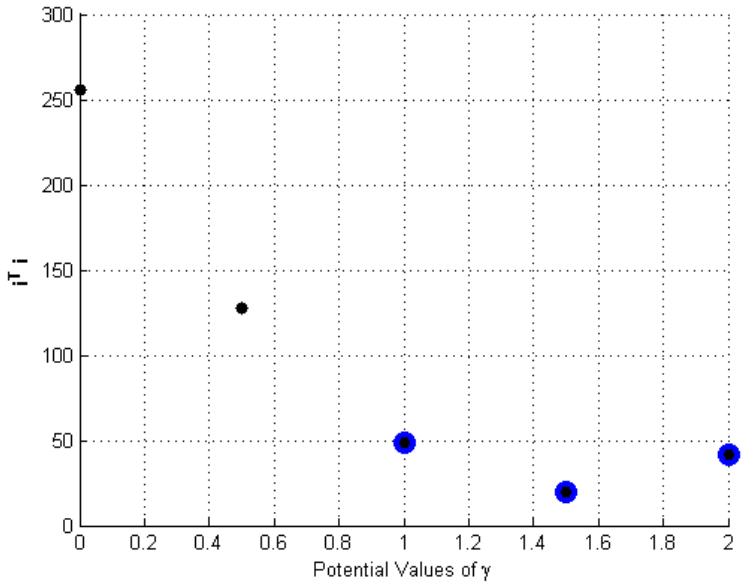

Figure 46: Example Sum of Squares of Current for Extended γ Values

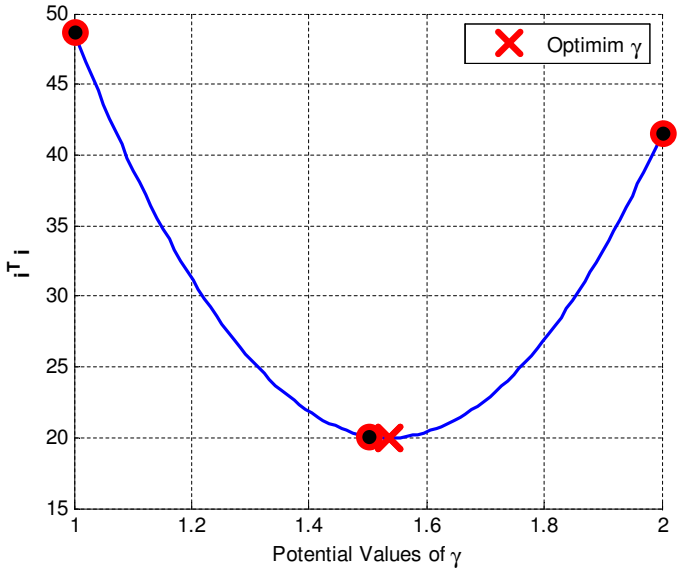

Figure 47: Example Curve Fit of the Sum of Squares of Current for Three γ Values

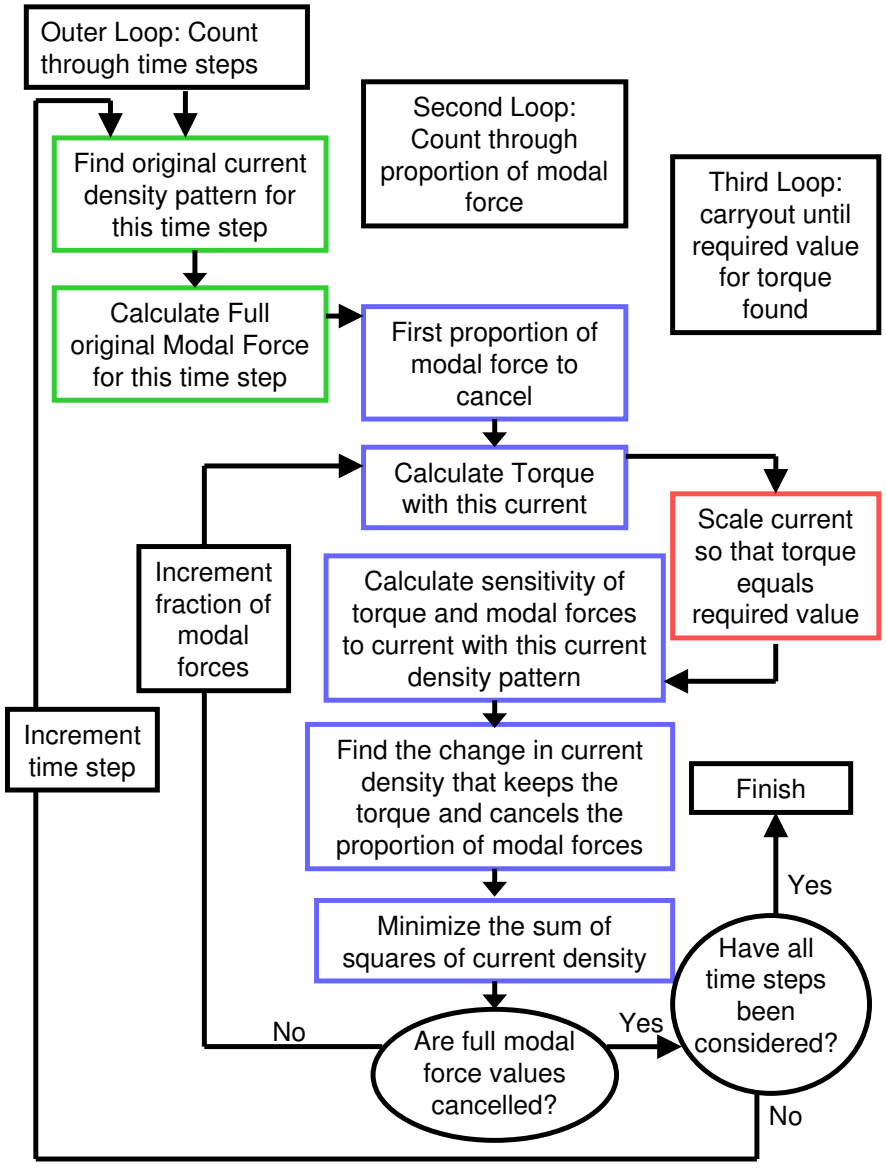

Figure 48: Iteration Process for Achieving Stage 2 Current Density Pattern

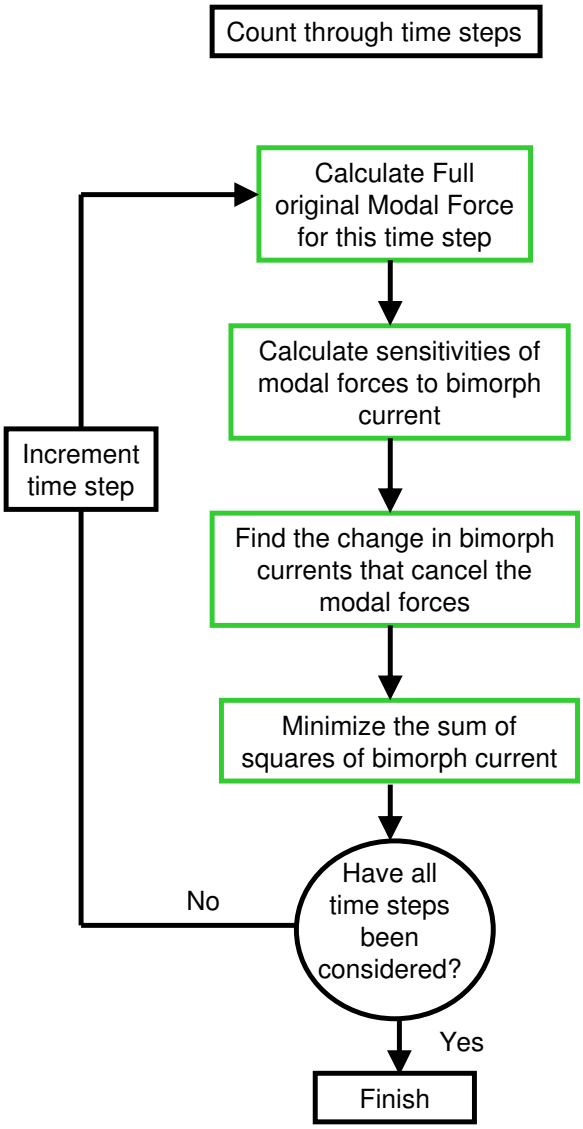

Figure 49: Iteration Process for Achieving Stage 3 Bimorph Current Pattern

4 An Investigation into the Optimum Operation of a Large Electrical Machine

4.1 Introduction

The aim of this study is to investigate the effect of two new technologies on the noise and vibration of a large electrical machine. One technology is a method of controlling each stator slot conductor individually. This is the ICC method and this method is part of Converteam Ltd's active stator project [23]. ICCs give a large amount of control over the supply current waveform and so enable some manipulation of the spatial and temporal harmonics of current. This advanced level of control can be used to minimize the power loss from the machine and reduce vibration causing components of current.

The second technology is unique to this thesis. This is the magnetic bimorph concept. Conductors threaded through the root of each stator tooth and energized individually can alter the magnetic field in the stator teeth and core. At forcing frequencies above and around tooth rocking frequency this concept can be used to manipulate the motion of the stator teeth. This causes the stator teeth to act as vibration absorbers and cancel some components of vibration.

These methods have been investigated using a 2D FE model of a large electrical machine. The modelling was carried out in MATLAB, the scripts were written by the author. The results of this investigation is presented in this chapter. A mechanical FE model was created of the stator and a magnetic FE model was created of the stator, rotor and air gap. The effect

that the ICC and magnetic bimorph technologies have on the efficiency and vibration of the machine is investigated and quantified.

This investigation is split into four stages which relate to the type of excitation applied to the stator of the machine. These stages are:

Stage 0: A sinusoidal current density pattern. This is used to set a reference value for torque and to estimate a corresponding total copper loss.

Stage 1: An ICC current density pattern that minimizes the copper loss but does not affect the torque.

Stage 2: An ICC current density pattern that cancels some components of noise, does not affect the torque and has the minimum possible copper loss subject to the vibration cancellation requirement.

Stage 3: An ICC current density pattern that minimizes the copper loss but does not affect the torque with currents in bimorph conductors that cancel some components of noise.

In each of these sections the electromagnetic forcing that occurs as a result of the current pattern is analysed. This is the sum of the Maxwell forces that act on the teeth tips and the equivalent magnetostriction forces that act within the stator iron. Each combination of spatial and temporal Fourier harmonic of force is extracted and applied to the mechanical stator model. The vibration caused by these components of force is given as the radial vibration of the back of the stator core. The level of vibration of the machine for running speeds between $20Hz$ and $30Hz$ is given with attention paid to the rotational speeds where resonances occur that are to be cancelled out by the stage 2 and stage 3 current patterns. The mean-squared current required for each of these situations and the resultant vibration of the stator are used as measurements of the effectiveness of each technology.

The structure of this chapter is as follows:

In section 4.2 the model of the machine is described. Assumptions that were used in order to implement the analysis are given. The details of the mechanical and magnetic machine are also given.

In section 4.3 the results of the mechanical FE investigation alone are presented. This includes the natural frequencies and mode shapes of the machine.

Section 4.4 presents the results of the initial investigation into the performance of the machine under a sinusoidal stator current pattern. This indicates the nominal performance of the machine and these results are used for comparison purposes in the subsequent sections.

Section 4.5 delivers the results from stage 1. This is an ICC stator current density pattern that provides the same torque as the sinusoidal current density pattern but minimizes the mean-squared current. The effect of this excitation pattern on the vibration of the stator is also described.

Section 4.6 describes the results from stage 2. This is an ICC stator current density pattern that cancels the modal forces from the first pair of n=4 modes. (The spatial mode number is given by n). This also maintains the nominal torque and minimizes the mean-squared current. The effect of this current pattern on the vibration of the stator is shown compared to the nominal and stage 1 excitation patterns.

Section 4.7 gives the results from stage 3. This has the stage 1 ICC current

density pattern in the slots and a current pattern in the bimorph conductors. The bimorph conductor currents are controlled to cancel the modal forces from the first pair of non rigid body n=1 modes. The magnitude of current in these is small compared to the current in the stator slots so this method is not expected to change the torque. This combination of excitation methods minimizes the mean-squared current in the slots and cancels some components of vibration. The effect of this excitation method on the overall vibration of the stator is described.

Section 4.8 provides the conclusion to the chapter.

4.2 The FE Model of a Large Electrical Machine

4.2.1 Assumptions and Simplifications

The requirement of the investigation is to quantify the vibration and mean-squared current from the different excitation methods. Therefore the results from each method must be comparable. Simplifications and assumptions are required to create the model with feasible computational methods, capacity and time. These may introduce inaccuracies into the results, however the results are consistent for each of the methods considered and so do not prevent a comparison between the results. The magnetic and mechanical models are two dimensional. In the magnetic model, saturation and eddy currents are neglected. The currents in the stator and rotor are allocated known values and induced currents are not considered.

The magnetic and mechanical models are coupled together with a weak indirect coupling method. A weak coupling approach calculates only the effect of the magnetic model on the mechanical model. The reverse relationship is not considered unlike strong coupling methods which do consider the reverse effect. Direct coupling methods take into account the effect

of magnetisation on elasticity and the effect of deformation on permeability. These interdependencies are neglected in the chosen indirect coupling method because the deflections in the structure are assumed to be small and so the consequential changes in material properties should be negligible. The coupling method chosen simplifies the relationship between the magnetic and mechanical models significantly compared to strong and direct coupling methods. Coupling methods are explained in detail in appendix D.2.

4.2.2 Details of the Machine

The large machine is created with ninety bays in the stator and the whole stator is analysed. Each calculation is carried out for 360 time steps. The rotor is rotated anticlockwise by 1^o in each step. This generates results for a complete spatial and temporal period.

The same mesh of the stator iron and slot fill is used in the mechanical and magnetic model. The radius to the machine air gap is $0.6m$. All of the dimensions of the stator are given in table 6. Eight noded quadrilateral elements are used to generate the mesh. One bay is shown in figure 50. One stator bay includes one tooth, a half slot either side of the tooth and the corresponding segment of back of core. This is generated so that fine elements are formed around the tooth root and tip with coarser elements in the centre of the tooth length and back of core. Fine elements at the tooth root are required in the mechanical model to capture the bending motion of the tooth. Fine elements at the tooth tip are required in the magnetic model so there is a gradual change in element size towards the air gap which is very fine.

4.2.3 The Mechanical FE Model of the Large Electrical Machine

The number of nodes and elements in the full and reduced mechanical stator model are given in table 7. The assumed material properties are given in table 8. The Young's modulus of the slot fill is a fraction of the standard value of the Young's modulus of copper because much of a stator slot is taken up with the insulating material and adhesive which has a relatively low Young's modulus. A damping factor γ of 0.01 has been used.

The reduced stator model retains both the x and y DoFs for all master nodes and the same master nodes are retained in each bay of the stator. This leaves the master nodes shown in figure 51. Therefore, the cyclic symmetry of the structure is maintained. Maxwell forces can be applied directly to the tooth tips of the reduced stator. The deflection of the back of the stator core can be found directly from the reduced model.

4.2.4 The Magnetic FE Model of the Large Electrical Machine

The geometry of the full mesh of the stator iron from the mechanical model is also used for the magnetic model. The analysis of the magnetic stator model from this point onward is independent of the analysis of the mechanical model. Four layers of air gap elements and nodes are added to the magnetic stator mesh. The numbers of nodes and elements in the full and reduced models are given in table 9. The assumed material properties are given in table 10. The master nodes in one bay of the reduced stator model are shown in figure 52. These include the node in the location of the bimorph conductors, the nodes on the elements on the middle circle and one node in each half slot which represents the distributed current throughout the half slot.

The discretization of the mesh of the magnetic model is important for gen-

erating accurate results. The mesh that has been used is as fine as was feasible for the computation. If the mesh is made even finer then the results of the magnetic model will change slightly. This mesh is considered acceptable and any errors that are present in the results are consistent for all stages in the analysis so the results for each stage can be compared to each other.

The rotor is modelled with 83 bays. The dimensions of the rotor are given in table 11. One bay of the rotor consists of a slot and half a tooth either side of the slot and the corresponding rotor core. This model also has one layer of air gap elements. The mesh of one rotor bay is shown in figure 53. The number of nodes and elements in the full and reduced model are given in table 11. The assumed material properties are given in table 12. The master nodes of the reduced rotor model include the nodes on the elements on the central circle and one node in each slot which represents the distributed current across the slot. These are shown in figure 54.

The rotor was initially modelled as an induction motor. The mesh shown in figure 53 had the same relative permeability for the rotor teeth as the core. The mean-squared current for the initial sinusoidal current pattern in the stator slots is $1.11\times10^5 A^2$. When the currents in the stator model were optimized in stage 1 of the analysis they reduced by 96% to a mean-squared value of $4.40\times10^3 A^2$. The current pattern that resulted from this optimization would not work in a realistic situation because the induced currents in the rotor would be too low to generate any torque. This situation was not predicted by the model because the rotor currents in the model were maintained at fixed values. For this reason, the relative permeability of the rotor teeth was changed to 5 which is a very low value. The excitation to the rotor was increased so that the flux in the machine remained the

same as for the original induction motor. A sinusoidal current pattern was applied to the rotor with an mean-squared value of $9.51\times10^6 A^2$ and this was maintained for all stages of the analysis. The large decrease in relative permeability of the rotor changed the magnetic model of the rotor so that this closely models either a slotless wound rotor with iron that is saturated or a surface mounted permanent magnet rotor of a synchronous machine.

4.3 The Vibrational Characteristics of the Machine

The lower limit of tooth rocking frequency is calculated as described in section 1.6.2.1. For the model analysed this is $519Hz$. The rocking motion of the teeth exists in mode shapes at this frequency and higher frequencies than this.

The natural frequencies for the first 10 mode numbers are given in tables 13 and 14 along with descriptions of the corresponding mode shapes. These frequencies are also shown on a plot of natural frequency against mode number for the stator in figure 55. Some mode shapes of interest are shown in figure 58 to 57. Appendix C.4 gives information on stator vibrations and the relevance of figure 55.

The first n=4 mode pair and first non rigid body n=1 mode pair are important in this study. The natural frequency that corresponds to the n=4 mode pair is $372Hz$. This mode consists of the back of the stator core expanding radially in four locations 90^o to each other and contracting in four locations 45^o to these. This results in the square-like deflected shape shown in figure 61. The first non rigid body n=1 mode pair occurs at $858Hz$. This has the mode shape shown in figure 62. This mode mainly involves the rocking motion of the teeth.

4.4 Stage 0 Results: The Sinusoidal Current Density Pattern

4.4.1 Stage 0 Current and Torque

A sinusoidal current pattern was assigned to the stator and rotor slots. At the first time step the rotor and stator reference frame were aligned. At this instant the current density distribution around the stator is shown in figure 70. Figure 70 also shows the current density in the first slot throughout one complete time period. The mean-squared current for this stage is $1.11\times10^5 A^2$. This stator excitation pattern contains only the 2^{nd} temporal and spatial harmonics of current. Contour lines of magnetic potential are shown in figure 71. As the rotor rotates with respect to the stator the magnetic field also rotates. If the air gap was shaped like a ring with no irregularities there would be no saliency and the magnetic flux density in the air gap would only consist of the 2^{nd} spatial and temporal harmonics. The Maxwell force created in the air gap is related to magnetic flux density squared and so would consist only of a 4^{th} temporal and spatial harmonic. However, temporal and spatial frequency variations occur in the magnetic field due to the changing geometry of the air gap as the rotor rotates and so extra spatial and temporal harmonics are present in the magnetic field in the air gap. The distributions of radial and tangential magnetic flux density around the air gap at the first time step are shown in figures 72 and 73. The distributions of radial and tangential Maxwell stress around the air gap at the first time step are shown in figures 74 and 75. The harmonics that have been induced in the magnetic field are shown with a contour plot in figure 76 for the tangential Maxwell force in the air gap. This plot shows large harmonics with a red colour, followed by orange, green and then low value non-zero harmonics in blue. In addition to (n=4,m=4) the large harmonics are (n=0,m=0), (n=1,m=1), (n=5,m=5), (n=23,m=23),

(n=24,m=24), (n=27,m=27), (n=28,m=28), (n=29,m=29), (n=31,m=31) and (n=32,m=32). These coefficients are on the diagonal of the map in figure 76. Low value, non-zero contour lines also exist in many places away from these diagonal values.

The tangential component of Maxwell force has generated a torque in this machine of $8066Nm$. This value of torque is due to all of the harmonics that have been generated in the magnetic field not just the main (n=4,m=4) component.

4.4.2 Stage 0 Modal Forces

The modal force from the electromagnetic force and one of the n=4 modes from the first n=4 mode pair is shown in figure 77. The contributions from the equivalent magnetostriction force and Maxwell force are also shown. The total modal force oscillates four times in the time period with rms value $1.6 \times 10^4 N$. The modal forces from magnetostriction and Maxwell force are exactly out of phase and the modal force from Maxwell force is larger than magnetostriction. A second modal force exists due to the electromagnetic force and the second n=4 mode. The modes are orthogonal and so this modal force leads the modal force that is displayed by $2\pi/4n$. At the instant in time when the magnitude of one modal force is maximum the other is zero.

The modal force from the electromagnetic force and one of the n=1 modes from the first n=1 non rigid body mode pair is shown in figure 78. The total modal force has one complete cycle in the one time period. The rms value is $0.029N$. The modal forcing on the n=4 modes is therefore many magnitudes higher than the n=1 modal forcing.

4.4.3 Stage 0 Vibration

The stator vibration that is caused by electromagnetic forcing from the sinusoidal stator current density pattern used in this stage provides the benchmark for comparison with the subsequent stages. The vibration is quantified by the magnitude of the rms radial velocity of the back of the stator core (equation (36) in chapter 3). The vibration has been analysed at rotor rotational speeds between $20Hz$ and $30Hz$. The vibration caused by each combination of spatial (n) and temporal (m) harmonic of electromagnetic force is given in figure 79. This plot shows that many resonant peaks appear in this frequency range. The plot also shows some responses that are fairly constant with speed across the whole of this frequency range. Forcing frequency is the product of rotational speed and temporal harmonic. The resonances that have been excited in this speed range occur for a particular combination of temporal and spatial harmonic where the forcing frequency caused by the temporal harmonic equals a resonant frequency of the mode family defined by the spatial harmonic.

The spatial harmonics that are important to this study are the n=4 and n=1 harmonics. The maximum value for each n=4 response has been marked with a square in figure 79. The maximum value for each n=1 response has been marked with a circle. The response from the fourth temporal and fourth spatial harmonics of EM force (n=4, m=4) is large and fairly constant with speed. This is shown on the graph with a green line. The rms vibration velocity from this combination of harmonics varies from $9.6 \times 10^{-6} ms^{-1}$ at rotor speed $20Hz$ to $1.5 \times 10^{-5} ms^{-1}$ at rotor speed $30Hz$. The response from the n=1 and m=1 component of force is also large and fairly constant with speed. This is shown on the graph with a pink line. The vibration from this combination of harmonics varies from $1.4 \times 10^{-5} ms^{-1}$ at $20Hz$ to $9.1 \times 10^{-6} ms^{-1}$ at $30Hz$. The responses from the (n=1, m=1) and (n=4,

m=4) components of force are fairly constant with change in rotor speed because the resonances of the n=4 and n=1 modes are much higher than the forcing frequencies caused by the m=4 and m=1 temporal harmonics. There are twelve combinations of temporal and spatial harmonic having responses above the flat (n=1, m=1), (n=4, m=4) responses. Table 15 gives the rotational speed, spatial harmonic, temporal harmonic, forcing frequency and resulting back of core radial velocity at the speed where each resonance occurs for each of these responses. In the speed range considered, the resonances dominate the vibration of the stator at specific frequencies. The frequency range around these frequencies where the response is high is extremely narrow. Therefore, at most frequencies across the speed range considered the vibration of the stator is caused by either the (n=4, m=4) or (n=1, m=1) components of force.

The vibration of the back of the stator core from the 4^{th} spatial harmonic and each temporal harmonic that is present in figure 79 is shown in figure 80. It can be seen clearly from this figure that six n=4 resonances have been excited in this speed range. The rotational speed, temporal harmonic, magnitude and forcing frequency of these resonances are given in table 20.

The vibration of the back of the stator core from the 1^{st} spatial harmonic and each temporal harmonic in the rotor speed range between $20Hz$ and $30Hz$ is shown in figure 81. Fourteen n=1 resonances have been excited in this speed range. The response of twelve of these are higher than the flat (n=1, m=1) response. The rotational speed, temporal harmonic, magnitude and forcing frequency of these is given in table 21.

Three particular running speeds have been investigated to demonstrate how the different combinations of temporal and spatial harmonic of force con-

tribute to the vibration of the stator at resonance condition and away from a resonance. A typical running speed of an electrical machine is $25Hz$. The forcing frequencies at this running speed do not correspond with any of the resonances of the stator. Therefore, this speed has been chosen for the demonstration. At $24.8Hz$ a resonance is excited by the (n=4, m=15) combination of harmonics of force. The fourth spatial harmonic is of interest to the ICC excitation pattern in stage 2. At $25.2Hz$ is a resonance that is excited by the (n=1, m=34) combination of harmonics of force and n=1 is a spatial harmonic of interest for the bimorph concept in stage 3. These two speeds have been chosen to illustrate the effect of the subsequent excitation patterns on the response of the stator at resonances that are excited by the targeted harmonics of force and by other harmonics of force that are not targeted.

Figure 82 shows that at a running speed of $25.0Hz$ the (n=4, m=4) and (n=1, m=1) combinations of harmonics contribute the most to the vibration of the machine. These are the flat responses that have been mentioned previously.

Figure 83 shows that at $24.8Hz$ the flat (n=4, m=4) response causes the highest level of vibration followed by the (n=1, m=1) response and then the response excited by the (n=4, m=15) harmonics. The resonance excited by the (n=4, m=15) harmonics of force occurs because the forcing frequency of this component of force is $24.8 \times 15 = 372Hz$ which is the resonant frequency of the first n=4 mode pair. Figure 84 shows that at $25.2Hz$ the resonance excited by the (n=1, m=34) harmonics of force causes the most vibration followed by (n=4, m=4) and (n=1, m=1).

4.4.4 Summary of Stage 0

This section has laid out the quantities of interest such as the torque generated by the machine and the mean-squared current required to deliver this torque from nominal sinusoidal stator and rotor current patterns. The magnetic field has been enriched with Fourier harmonics that are due to the stator and rotor excitation pattern and the geometry of the air gap. The electromagnetic force provides the torque and also causes the vibration of the stator. Modal forces and vibration levels have been quantified from this nominal current pattern. In the next sections a comparison of the torque, mean-squared current, modal forces and vibration caused by the new technologies will enable a quantification of the effectiveness of each technology.

4.5 Stage 1 Results: The ICC Pattern that Maintains Torque with Minimum Copper Loss

4.5.1 Stage 1 Current and Torque

The result of the optimization described in section 3.4.1 is the ICC stator slot current density pattern shown in the time and space domain in figure 85. The torque that is generated is $8066Nm$. The mean-squared current is $6.21\times10^4A^2$. This is a decrease of 44% from stage 0. The torque has therefore been maintained as required with a much lower mean-squared current value.

An explanation of how the above reduction in current is possible can be found by looking at the Fourier coefficients of the current pattern and the resultant tangential component of Maxwell force. The stage 1 current pattern is decomposed into spatial and temporal frequency components and a contour plot of this information is given in figure 86. The largest compo-

nent is from (n=2,m=2) but extra harmonics have also been introduced at (n=1,m=1), (n=3,m=3), (n=25,m=25), (n=26,m=26), (n=29,m=29) and (n=30,m=30). The nominal stator current density pattern in stage 0 was entirely (n=2,m=2). The stage 0 forces were largely (n=4,m=4) but many other harmonics were introduced in the force through saliency. Large harmonics have now been introduced purposefully into the excitation pattern and these have led to harmonics in the tangential component of Maxwell force which are shown in figure 87. Comparing figure 87 with figure 76 clearly shows that the main components of harmonics that were present on the diagonal of the contour plot in stage 0 have also been produced by the stage 1 current pattern. However, away from the diagonal there are less resultant harmonics in the tangential Maxwell force pattern for stage 1 than for stage 0. Therefore, this current pattern creates some harmonics in the magnetic field that are useful for torque generation and eliminates other harmonics that are not useful for torque generation. Plots of the radial and tangential Maxwell forces exerted on each stator tooth are shown in figures 93 and 94 for the first time step. From these figures it can be seen that the spatial pattern of Maxwell force has been largely unaffected by the change in current density in the slots.

4.5.2 Stage 1 Modal Forces

Figures 88 and 89 show the modal force for the n=4 and n=1 modes. The n=4 modal force has varied by less than 1% from the n=4 modal force from stage 0. The rms value for this is $1.63 \times 10^4 N$. The n=1 modal force has increased significantly. The rms value of this modal force is now $5.86N$.

4.5.3 Stage 1 Vibration

The vibration caused by each combination of spatial and temporal harmonic of electromagnetic force at rotational speeds between $20Hz$ and $30Hz$ is pre-

sented in figure 90. The maximum value for each n=4 response has been marked with a square. The maximum value for each n=1 response has been marked with a circle. The number of large responses that occur at rotational speeds between $20Hz$ and $30Hz$ that are larger than the flat (n=1, m=1), (n=4, m=4) responses is 29. Table 16 gives the rotational speed, spatial harmonic, temporal harmonic, forcing frequency and resulting back of core radial velocity for each of these 29 large responses. The number of responses with magnitudes above $1 \times 10^{-4} ms^{-1}$ is 23. This has increased from none in stage 0 where sinusoidal current patterns were used on the rotor and stator. The vibration from the (n=4, m=4) combination of harmonics varies from $4.56 \times 10^{-5} ms^{-1}$ at rotor speed $20Hz$ to $7.29 \times 10^{-5} ms^{-1}$ at rotor speed $30Hz$. This is an increase of 375% from the (n=4, m=4) response in stage 0. The response from the n=1 and m=1 component of force varies from $2.74 \times 10^{-5} ms^{-1}$ at $20Hz$ to $1.83 \times 10^{-5} ms^{-1}$ at $30Hz$. This is an increase of 100% from the (n=1, m=1) response in stage 0. All of the responses at resonance have increased compared to the responses in stage 0.

The vibration of the back of the stator core from the 4^{th} spatial harmonic and each temporal harmonic is shown in figure 91. There are still six large n=4 responses in this speed range and three of these are higher than the flat response from the (n=4, m=4) harmonics of force. The rotational speed, temporal harmonic, magnitude and forcing frequency of these responses are given in table 20. Table 22 shows that all of these responses have increased in magnitude from stage 0 by amounts between 212% to 1790%.

The vibration of the back of the stator core from the 1^{st} spatial harmonic and each temporal harmonic in the speed range between $20Hz$ and $30Hz$ is shown in figure 92. There are still fourteen n=1 resonances that have been excited in this speed range. All of these have magnitudes higher than

the flat (n=1, m=1) response. The rotational speed, temporal harmonic, magnitude and forcing frequency of these 14 resonances is given in table 21. Table 23 shows that these responses have all increased in magnitude from stage 0 by between 433% to 1837%. The other responses that are present in the speed range that are shown in figure 90 have also increased by similar amounts to the n=1 and n=4 responses. These can be seen by comparing table 16 with table 15.

At running speeds of $25.0Hz$, $24.8Hz$ and $25.2Hz$ the magnitude of vibration has increased at all three speeds compared to stage 0. The components of force that cause these vibrations are the same components that caused the vibration in stage 0. Figure 82 shows that the vibration at a running speed of $25.0Hz$ is mainly from the (n=4, m=4) harmonics, the second contributor is the (n=1, m=1) combination of force harmonics. At $24.8Hz$ the (n=4, m=4) combination of harmonics contributes the most to the vibration followed by (n=4, m=15) and (n=1, m=1). This is shown in figure 83. At $25.2Hz$ the (n=1, m=34) combination of harmonics causes the highest vibration followed by (n=4, m=4) and (n=1, m=1). This is shown in figure 84.

4.5.4 Summary of Stage 1

This method has implemented ICCs that enable independent values of current density in each slot. The resulting current pattern has optimized the spatial and temporal harmonics of current so that the coefficients of electromagnetic force that produce the torque are increased and the components of force that restrict the torque are cancelled out. The required torque has been maintained with a substantial decrease in the mean-squared current from the nominal sinusoidal current density pattern.

The improvement of lower copper loss for the same torque has had a detrimental effect on the vibration of the machine. In the $10Hz$ rotor speed range around $25.0Hz$ the number of resonances that are excited has increased due to the extra harmonics in the current density pattern. This increases the chance of the machine experiencing a troublesome resonance at an operating speed in this range. The magnitude of the velocity of the stator from each combination of spatial and temporal harmonics has also increased. This increases the frequency range around each resonant frequency where the response of the machine will be high. The steady responses from the (n=4, m=4) or (n=1, m=1) components of force have also increased. Consequently there is a higher level of vibration and noise emission from the machine across the entire speed range with this excitation pattern.

4.6 Stage 2 Results: The ICC pattern that Maintains Torque and Reduces Vibration with Minimum Copper Loss

4.6.1 Stage 2 Current and Torque

The stator current pattern that cancels a pair of n=4 modes as well as maintaining the torque and minimizing the copper loss is shown in figure 95. The mean-squared current for this stage is $8.40\times10^5A^2$. This is a 655% increase from the nominal sinusoidal current pattern and a 1251% increase from the stage 1 current pattern, which is a vast increase. The torque that is generated is $8066Nm$. The torque has therefore been maintained as required.

This current density pattern is decomposed into spatial and temporal frequency components and a contour plot of these coefficients is given in figure 96. There is an increase from stage 1 in the number of significant harmonics

of current. The (n=6,m=6) combination of harmonics of current has the largest coefficient. The other combinations of harmonics that are also introduced include among others (n=2,m=2), (n=10,m=10), (n=14,m=14), (n=22,m=22), (n=26,m=26) and (n=34,m=34). The coefficients of the harmonics of tangential Maxwell force that this excitation has generated are shown in figure 97. There are many more large coefficients in this figure than for stage 0 or stage 1. The largest coefficient is (n=4,m=4) followed by (n=0,m=0). Plots of the radial and tangential Maxwell forces exerted on each stator tooth are shown in figures 93 and 94 for the first time step. From these figures it can be seen that the pattern of Maxwell force has been affected from stage 0 and 1 by the change in current density in the slots.

4.6.2 Stage 2 Modal Forces

Figure 98 shows the modal force for the n=4 modes. This excitation pattern has caused the modal force from magnetostriction to equal the modal force from Maxwell force with opposite sign. This cancels out the total n=4 modal force. The total modal force is shown in figure 99 the rms value of this is now $0.0039N$ compared to 1.63×10^4N in stage 1.

The modal force for the n=1 mode is shown in figure 100 this has a combination of low and high frequency variations with time. The rms value is 6.80×10^4N this has increased from $5.86N$ in stage 1.

4.6.3 Stage 2 Vibration

The vibration caused by each combination of spatial and temporal harmonic of electromagnetic force is given in figure 101. The number of resonances that are excited at rotor speeds between $20Hz$ and $30Hz$ with responses larger than the flat (n=1, m=1), (n=4, m=4) responses is 63. All of these 63 resonances have magnitudes above $1 \times 10^{-4}ms^{-1}$. This is nearly three times

the number of significant resonances excited in the stage 1 analysis. Tables 17 and 18 give the rotational speed, spatial harmonic, temporal harmonic, forcing frequency and resulting back of core radial velocity at the speed where each resonance occurs for each of these responses.

4.6.4 The Effect of the Stage 2 Current Pattern on Excitation of the Targeted Resonances

The vibration from the (n=4, m=4) combination of harmonics due to this excitation pattern varies from $1.70 \times 10^{-6} ms^{-1}$ at rotor speed $20Hz$ to $2.55 \times 10^{-6} ms^{-1}$ at rotor speed $30Hz$. This is a decrease of 83% from stage 0 and 96% from stage 1. Compared to the reponses from the other combinations of harmonics this response is now negligible and can barely been seen in figure 101.

The vibration of the back of the stator core from the 4^{th} spatial harmonic and each temporal harmonic is shown in figure 102. There are still six n=4 resonances that have been excited in this speed range and all of these have higher magnitudes than the flat response from the (n=4, m=4) harmonics of force. This is because the response from (n=4, m=4) has decreased significantly. Table 22 shows that the responses at the n=4 resonances have decreased by up to 93% compared to stage 1. Table 22 also shows that compared to stage 0 the response of only one n=4 resonance has been reduced, the other five are up to 191% higher. The rotational speed, temporal harmonic, magnitude and forcing frequency of these responses are given in table 20. Figure 101 shows that compared to the responses from the other combinations of harmonics that are now present in the vibration spectrum, the magnitude of the n=4 responses are low.

Figure 83 shows the vibration from the stator at $24.8Hz$. This excita-

tion pattern has managed to reduce considerably the response of the n=4 responses. At this speed, with this excitation pattern the responses from the (n=4,m=15) and the (n=4,m=4) harmonics are much lower than the responses from the (n=1,m=1) and (n=8,m=8) harmonics. The vibration from these responses has increased from stage 1.

4.6.5 The Effect of the Stage 2 Current Pattern on the Other Resonances

The responses from the n=1 harmonics of force are used here to demonstrate the effect that the stage 2 current pattern has on the uncontrolled harmonics of response. The flat response from the n=1 and m=1 combination of harmonics varies from $4.64 \times 10^{-4} ms^{-1}$ at $20Hz$ to $3.09 \times 10^{-4} ms^{-1}$ at $30Hz$. This is an increase of 3,290% from stage 0 and 1,591% from stage 1.

The vibration of the back of the stator core from the 1^{st} spatial harmonic and each temporal harmonic in the speed range between $20Hz$ and $30Hz$ is shown in figure 103. There are still fourteen n=1 resonances that have been excited in this speed range, all of which have magnitudes greater than the flat (n=1,m=1) response. The rotational speed, temporal harmonic, magnitude and forcing frequency of these resonances is given in table 21. Table 23 shows that the responses at these resonances have all increased in magnitude from stage 0 by between 16,000% and 317,000% and from stage 1 by 2,000% to 24,000%. These are extremely high increases. The other resonances that are present in the speed range that are shown in figure 101 have also increased by similar amounts to the n=1 responses. These can be seen by comparing tables 17 and 18 with tables 15 and 16 and figure 101 with figures 79 and 90.

Figure 82 shows that at rotor speed $25.0Hz$ the overall vibration of the stator has increased significantly compared to stage 1. The combinations of temporal and spatial harmonics that cause this high vibration level have changed from the previous stages. The (n=4, m=4) harmonics no longer show up but the (n=1, m=1) response has increased to a level far higher than the (n=4, m=4) response in stage 1. The second highest contribution to vibration is now (n=0, m=23) and the third highest is (n=8, m=8).

Figure 84 shows that at rotor speed $25.2Hz$ the overall level of vibration is much higher with the stage 2 excitation than stage 1. This is the frequency where the (n=1,m=34) resonance is excited. The stage 2 excitation increases the (n=1,m=34) response considerably compared to stage 1. The second largest contribution to vibration is from the (n=1,m=1) harmonics and then the (n=8,m=8) harmonics.

4.6.6 Summary of Stage 2

This excitation pattern has reduced the excitation of the n=4 resonances as required. However, in order to achieve this, many extra harmonics were included in the pattern of excitation and these have led to many extra harmonics of force. This has doubled the number of resonances that are excited significantly in the stator between rotor speeds of $20Hz$ and $30Hz$. The mean-squared current has also increased considerably from stage 1 and even from stage 0. This higher magnitude of current has led to higher responses of vibration from spatial harmonics other than n=4. Therefore, the excitation pattern that is required to reduce one spatial component of vibration has led to an increase in both the overall vibration of the stator and in the copper loss from the machine. The overall operation with this current pattern is therefore worse than with the uncorrected pattern from stage 0.

Changing the components of current in the stator slots in a way that torque is maintained has two effects on the operation of the machine. One is a change in the vibration of the stator and one is a change in the copper loss. The change in vibration is a first order effect and the change in copper loss is a second order effect. When targeted components of current are reduced so that targeted vibration components are reduced, other components of current are increased in order for the constraint on torque to be met. These increased current components cause an increase in vibration components other than the targeted vibration components. The results that have been presented above show an overall worsening of the vibration of the stator. This occurs because the modal forces that excite the n=4 mode pair have been reduced to negligible values and this has required a large change in the current pattern compared to stage 1. This large change in the current pattern has increased the vibration of the other components dramatically. However, the large reduction in the n=4 component of vibration is unnecessary. This component of vibration needs only to be reduced to levels that are equivalent to the other vibration components at that speed. An optimum current pattern will exist that reduces the levels of vibration from the n=4 mode pair slightly and increases the other vibration components slightly so that the overall vibration level is lower than the vibration level with no vibration correction. The decrease in vibration will be small but this small change in the components of current will not affect the copper loss as this is a secondary effect of the change in current. Therefore it is possible to use the ICCs to provide a current pattern to the stator that maintains the required torque, reduces the copper loss and results in vibration levels lower than those presented.

4.7 Stage 3 Results: The Magnetic Bimorph Concept for Vibration Control with the Stage 1 ICC Current Pattern

4.7.1 Stage 3 Current and Torque

This stage aims to implement bimorph excitation to cancel the modal forces of the first n=1 non rigid body mode pair. The current pattern from stage 1 is implemented in the stator slots. The bimorph excitation is calculated with the optimization explained in section 3.4.3. The resulting bimorph excitation is shown in figure 104. The mean-squared current through the bimorph conductors is $2.82\times10^{-4}A^2$. This is $2.54\times10^{-7}\%$ of the nominal mean-squared sinusoidal current pattern. This current pattern is decomposed into spatial and temporal harmonics and contour lines of these are shown in figure 105. This plot shows that the largest combination of harmonics in the bimorph conductors is (n=1, m=1), and then (n=3, m=3). Other large combinations of harmonics are (n=25, m=25), (n=27, m=27), (n=29, m=29) and (n=31, m=31). There are contour lines around all of the n=1 and n=3 spatial harmonics that are not present in previous excitation patterns.

The torque that is generated is $8066Nm$. The torque is unaffected by the bimorph excitation.

4.7.2 Stage 3 Modal Forces

Figure 106 shows the modal force for the n=1 mode. This excitation pattern has caused the modal force from magnetostriction to equal the modal force from Maxwell force with opposite sign. This cancels out the total n=1 modal force. The total modal force is shown in figure 107 the rms value of this is now $1.70 \times 10^{-5}N$.

The modal force for the n=4 mode is shown in figure 108. The rms value is $1.63 \times 10^4 N$. This has not changed from stage 1.

4.7.3 Stage 3 Vibration

The vibration caused by each combination of spatial and temporal harmonic of electromagnetic force is given in figure 109. The number of significant resonances that occur at rotor speeds between $20Hz$ and $30Hz$ with responses larger than the flat (n=1, m=1), (n=4, m=4) responses is 28. Table 19 gives the rotational speed, spatial harmonic, temporal harmonic, forcing frequency and resulting back of core radial velocity at the speed where each resonance occurs for each of these responses. There are 11 resonances with magnitudes above $1 \times 10^{-4} ms^{-1}$. This is a decrease from 23 in stage 1.

4.7.4 The Effect of the Stage 3 Current Pattern on Excitation of the Targeted Resonances

The response from the n=1 and m=1 component of force varies from $3.10 \times 10^{-5} ms^{-1}$ at rotor speed $20Hz$ to $2.06 \times 10^{-5} ms^{-1}$ at rotor speed $30Hz$. This is an increase of 126% from stage 0 and 13% from stage 1. This is a small change from stage 1 and at this rotational speed the deflected shape of the stator is unlikely to include any rocking motion of the teeth. Therefore this flat response is not expected to be altered by the bimorph conductors.

The vibration of the back of the stator core from the 1^{st} spatial harmonic and each temporal harmonic in the speed range between $20Hz$ and $30Hz$ is shown in figure 111. There are still fourteen n=1 resonances that have been excited in this speed range. The rotational speed, temporal harmonic, magnitude and forcing frequency of these resonances is given in table 21. The response of only six of these is higher than the flat (n=1, m=1) re-

sponse. Table 23 shows that the response of nine of these resonances have increased in magnitude from stage 0 by up to 149% and five have been reduced in magnitude by up to 38%. Compared to stage 1 the magnitude of the response of the stator at all resonances has decreased by up to 96%.

Figure 84 shows that at rotor speed $25.2Hz$ the overall level of vibration is lower with the stage 3 excitation than stage 1 and stage 2. This is the frequency where the (n=1,m=34) resonance is excited and the modal force that excites this resonance has been reduced significantly so the magnitude of the response of this resonance is reduced. However, this resonance is still the largest cause of vibration at this rotational speed. The second largest contribution to vibration is from the (n=4,m=4) harmonics. This has also been reduced compared to stage 1, which is a fortunate coincidence and not a planned outcome. The (n=1,m=1) harmonics cause the third largest contribution to vibration at this speed and as mentioned above this response has not changed considerably from stage 1.

To be effective this concept requires that significant rocking motion of the teeth occurs in the modes of interest. The only resonances in the speed range between $20Hz$ and $30Hz$ that have been excited that include some rocking motion of the teeth are the n=1 modes. The other excited resonances all have mode shapes that are on the first trend line of the graph in figure 55. These modes all exhibit expansions and contractions of the back of the stator core and no tooth rocking motion. Therefore, the excitation of the other resonances in this frequency range cannot be eliminated with this method. Tables 15 to 19 includes an indication of whether or not the tooth rocking motion exists for every resonance.

4.7.5 The Effect of the Stage 3 Current Pattern on the Other Resonances

The responses from the n=4 harmonics of force are used here to demonstrate the effect that the bimorph current pattern has on the uncontrolled harmonics of response. The vibration from the (n=4, m=4) combination of harmonics varies from $3.68 \times 10^{-5} ms^{-1}$ at rotor speed $20Hz$ to $5.88 \times 10^{-5} ms^{-1}$ at rotor speed $30Hz$. This is an increase of 284% from stage 0 and a decrease of 19% from stage 1. This has advantageously reduced the vibration of the stator although this outcome is purely coincidental.

The vibration of the back of the stator core from the 4^{th} spatial harmonic and each temporal harmonic is shown in figure 110. There are still six n=4 resonances in this speed range that have been excited and five of these are higher than the flat response from the (n=4, m=4) harmonics of force. Table 22 shows that the responses at the n=4 resonances have increased by up to 1,125% compared to stage 0. Compared to stage 1 three responses have been increased by up to 228%, two have been reduced by up to 49% and one has not changed. The rotational speed, temporal harmonic, magnitude and forcing frequency of these resonances are given in table 20. The other resonances that are excited in the speed range that are shown in figure 109 have also changed by similar amounts to the n=4 resonances. Some have been increased, some have been decreased. These can be seen by comparing table 19 with tables 15 and 16 and figure 109 with figure 79 and 90.

At rotor speed $25.0Hz$ the largest contribution to the vibration of the stator is from the (n=4, m=4) harmonics of force. Figure 82 shows that the vibration with the bimorph excitation has been reduced slightly from stage 1.

Figure 83 shows the vibration from the stator at rotational speed $24.8Hz$. At this speed the (n=4,m=15) resonance exists. The figure shows that the response from this resonance is largely unchanged compared to stage 1. The second largest contribution to vibration is from (n=4,m=4) and then (n=1,m=1). Therefore, the cancellation of the n=1 resonances has had little effect on the vibration from other harmonics.

4.7.6 Summary of Stage 3

This stator slot excitation pattern has the lowest stator slot copper loss possible to generate the required level of torque. The magnitude of current that is required through the bimorph conductors is small compared to the currents in the slots and so does not increase the copper loss significantly. This bimorph current pattern has negligible effect on the torque. The n=1 resonances are reduced by this method. However, the flat response from the (n=1,m=1) harmonics of force is increased slightly. The response from the other harmonics that are not controlled by this method are affected only slightly because the increase in excitation is only slight compared to stage 1. The vibration levels from some are increased and from others are decreased and some are not affected at all. Overall the number of resonances with high magnitude in the speed range is reduced from stage 1 by 12. Therefore, the likelihood that a rotational speed will cause a resonance to be excited is decreased with this method. Overall, figure 109 shows that with this excitation method, for the majority of the speed range the (n=4,m=4) harmonics contribute the most to the vibration. At the specific speeds where the n=1 resonances exist this concept is successful at reducing the excitation of these modes without affecting the torque or requiring a large increase in power. There is also no significant detrimental affect to the other resonances in the speed range.

4.8 Conclusion to the Chapter

This chapter has presented the results of the investigation into the optimum operation of a large electrical machine. Two technologies were investigated in four steps. The *zeroth* step gave the reference information so that the performance of the machine with ICCs and bimorph conductors could be compared and to find the nominal torque of the machine. This step involved implementing a four pole sinusoidal current pattern on the stator. The torque that this excitation provided was maintained in the subsequent steps.

The first stage implemented an ICC current pattern on the stator slots that provided the same torque as the nominal sinusoidal current pattern but minimized the mean-squared current in the stator. This was achieved by including additional spatial and temporal harmonics in the current pattern that were not present in the sinusoidal current pattern. These harmonics led to additional harmonics in the electromagnetic force and these aided the torque production from the machine whilst the mean-squared current was reduced. This was possible due to saliency which is the non uniform geometry of the air gap between the rotor and stator which alters the magnetic field in the air gap. The mean-squared current was reduced from the nominal value by 44%. However, the additional harmonics in this slot excitation pattern led to additional significant harmonics in the electromagnetic force and additional resonances from the stator in the speed range between $20Hz$ and $30Hz$. The magnitude of the vibration of the stator at resonance and away from resonance was also increased. Therefore, this method has proved successful in its main aim of reducing the copper loss from the machine but this is achieved at the expense of higher noise and vibration levels from the machine. Hysteresis losses in electrical machines increase with frequency and so the extra harmonics that have been introduced into this

current pattern are likely to increase the hysteresis loss from the machine. It is predicted that if hysteresis was taken into account in the modelling an optimal ICC current pattern would exist that is a slight variation from that presented here in stage 1.

The second stage implemented another ICC stator slot current pattern which cancelled the first n=4 modal forces and maintained the nominal value of torque. The results showed that the torque had been maintained and the responses due to these modal forces had been reduced significantly at and away from resonance. However, in order to achieve this the mean-squared current was increased by 655% compared to the nominal current pattern. In addition to the unfeasibly high current that this method requires, the number of important resonances that were present in the speed range of interest more than doubled from the number of resonances in stage 0. This is due to the extra harmonics that were required in the excitation pattern to cancel the modal forces. The magnitude of the response of the stator due to spatial harmonics other than the n=4 harmonic also increased dramatically at resonance and away from resonance. Therefore, this excitation pattern has had a detrimental affect on the operation of the machine in all areas considered. The decrease in n=4 vibrations is overshadowed by the extreme increase in vibrations due to the other spatial harmonics and requires a far too great amount of input power to be feasible. A small change in current pattern from stage 1 is likely to achieve an optimum solution that results in a slight suppression of the vibration caused by the n=4 component of force and a slight increase in the other vibration components so that the overall vibration level is reduced slightly and the mean-squared current and torque are unaffected.

The third stage utilized the ICC current pattern from stage 1 in the sta-

tor slots. An excitation pattern was supplied to the bimorph conductors so that the resulting magnetic field from the combination of the two excitations cancelled out the modal forces from the first non rigid body n=1 mode pair. The magnitude of current required by the bimorphs was small so resultant changes in torque were negligible. The magnitude of the response of the stator at resonances that were due to the n=1 harmonics were reduced. This was possible because this mode includes the rocking motion of the teeth. Away from resonance the large response of the stator that was due to the n=1 and m=1 harmonics of force was not altered by this method. This is due to the absence of rocking of the teeth from this deflected shape. The n=1 resonances were the only resonances that were excited in the speed range of interest that the bimorph conductors could have been used to control. The magnitude of the resonances that were caused by spatial harmonics other than the first were altered slightly, some were increased and some were decreased, some were not affected. Overall this method led to a decrease in the number of high magnitude resonances in total in the speed range.

The ICC method has successfully enabled a reduction in copper loss from the machine compared to a traditional sinusoidal current pattern. However, this method on its own has not proved successful in reducing vibration from the machine. The bimorph concept has successfully reduced the vibration of the targeted modes. This method does not significantly increase losses from the machine or alter the torque or vibration from other modes. However, this method is constrained to work only for modes that include substantial rocking motion of the teeth and cannot be used to eliminate any other resonances that occur.

Number of Stator Bays	90	
Outer Radius	0.8400	m
Radius to Tooth Tips	0.6000	m
Radius to Tooth Root	0.7500	m
Tooth Tip Thickness	0.0157	m
Tooth Root Thickness	0.0261	m
Half-Slot Thickness	0.0131	m
Half-Slot Length	0.1500	m
Radius to Bimorph Node	0.7500	m
Half Slot Area	0.00197	m^2
Whole Slot Area	0.00393	m^2
Area of All Slots	0.35370	m^2

Table 6: Dimensions of the Stator

Nodes in the Full Model	28800
DoFs in the Full Model	57600
Number of Elements	9000
Nodes in One Full Bay	341
Nodes in the Reduced Model	810
DoFs in the Reduced Model	1620
Nodes in One Reduced Bay	11

Table 7: The Stator Mechanical Model

Stator Core Young's Modulus	200×10^9	Nm^{-2}
Stator Teeth Young's Modulus	200×10^9	Nm^{-2}
Stator Slot Fill Young's Modulus	5×10^9	Nm^{-2}
Stator Core Density	7800	Kgm^{-3}
Stator Teeth Density	23400	Kgm^{-3}
Stator Slot Fill Density	4450	Kgm^{-3}
Stator Core Poisson's Ratio	0.270	
Stator Teeth Poisson's Ratio	0.270	
Stator Slot Fill Poisson's Ratio	0.300	

Table 8: Mechanical Material Properties of the Stator

Nodes in the Full Model	39600
Number of Elements	12600
Nodes in One Bay	469
Number of Boundary Nodes	1800
Number of Central Circle Nodes	1800
Number of Current Carrying Nodes	12420
Number of Air Gap Layers	4
Nodes in the Reduced Model	4770
Fourier harmonics in Central Circle Transformation	332

Table 9: The Stator Magnetic Model

Stator Core Relative Permeability	1000
Stator Teeth Relative Permeability	1000
Stator Slot Fill Relative Permeability	1
Number of Pole Pairs	2

Table 10: Magnetic Material Properties of the Stator

Description	Value	Units	Description	Number
Number of Rotor Bays	83			
Inner Radius	0.3000	m	Full Model Nodes	10624
Radius to Tooth Tips	0.5996	m	Full Model Elements	3320
Radius to Tooth Root	0.4498	m	Nodes in One Bay	149
Tooth Tip Thickness	0.0284	m	Boundary Nodes	664
Tooth Root Thickness	0.0170	m	Central Circle Nodes	664
Slot Thickness	0.0170	m	Current Carrying Nodes	4399
Slot Length	0.1498	m	Air Gap Layers	1
Slot Area	0.00255	m^2	Reduced Model Nodes	1743
Area of All Slots	0.21137	m^2		

Table 11: Dimensions of the Rotor and Magnetic Model Information

Rotor Core Relative Permeability	1000
Rotor Teeth Relative Permeability	5
Rotor Slot Fill Relative Permeability	1
Number of Pole Pairs	2

Table 12: Magnetic Material Properties of the Rotor

	Rigid Body Modes	Back-of-Core Bending	Tooth Rocking In-Phase with Back-of-Core	Tooth Rocking Out-of-Phase Back-of-Core
		Figs 59 to 61	Figs 63 to 64	Figure 65
n=1	0		858	1,718
n=2		78	1,264	2,031
n=3		207	1,529	2,586
n=4		372	1,735	3,229
n=5		564	1,937	3,865
n=6		780	2,146	4,442
n=7		1,017	2,365	4,928
n=8		1,271	2,593	5,310
n=9		1,540	2,827	5,602
	Back-of-Core Bending & Tooth Expansion	Back-of-Core Bending & Tooth Rocking In-Phase	Only Tooth Rocking	Back-of-Core Bending & Tooth Rocking Out-of-Phase
	Figure 66	Figure 67	Figure 68	Figure 69
n=1	7,732	8,388	13,597	23,757
n=2	7,632	8,621	13,654	23,523
n=3	7,563	8,919	13,752	23,305
n=4	7,551	9,262	13,895	23,106
n=5	7,617	9,641	14,092	22,926
n=6	7,783	10,050	14,353	22,766
n=7	8,069	10,480	14,693	22,629
n=8	8,475	10,920	15,129	22,513
n=9	8,977	11,355	15,678	22,422

Table 13: Natural Frequencies of the Stator (Hz)

Frequency (Hz)	Description	
0	Rigid Body Mode	
575	Breathing Mode	Figure 56
1,634	1^{st} Tooth Rocking Mode	Figure 57
7,791	Tooth elongation and contraction	
8,285	2^{nd} Tooth Rocking Mode	
13,578	3^{rd} Tooth Rocking Mode	
23,961	4^{th} Tooth Rocking Mode	

Table 14: Natural Frequencies (Hz) and Descriptions of the n=0 Modes of the Stator

	Rotor Speed	Spatial Harmonic	Temporal Harmonic	Forcing Frequency	Back of Core Velocity	Tooth Rocking
	Hz	n	m	Hz	ms^{-1}	?
1	20.4	1	42	858	1.62E-05	Yes
2	20.9	1	41	858	6.34E-05	Yes
3	21.5	1	40	858	1.53E-05	Yes
4	22.0	1	39	858	1.35E-05	Yes
5	23.2	1	37	858	1.61E-05	Yes
6	23.5	5	24	564	1.31E-05	No
7	23.8	1	36	858	2.76E-05	Yes
8	24.5	1	35	858	2.11E-05	Yes
9	25.2	1	34	858	3.77E-05	Yes
10	26.8	1	32	858	1.40E-05	Yes
11	27.7	1	31	858	2.47E-05	Yes
12	28.6	1	30	858	6.43E-05	Yes

Table 15: Stage 0 Rotational Speeds, Spatial and Temporal Harmonics, Forcing Frequency and Vibration Magnitudes of Resonances

	Rotor Speed	Spatial Harmonic	Temporal Harmonic	Forcing Frequency	Back of Core Velocity	Tooth Rocking
	Hz	n	m	Hz	ms^{-1}	?
1	20.4	1	42	858	8.71E-05	Yes
2	20.6	0	28	575	1.39E-04	No
3	20.6	4	18	372	5.75E-05	No
4	20.7	3	10	207	1.13E-04	No
5	20.9	1	41	858	4.13E-04	Yes
6	21.1	6	37	780	6.16E-05	No
7	21.5	1	40	858	1.18E-04	Yes
8	21.9	4	17	372	1.37E-04	No
9	22.0	1	39	858	1.92E-04	Yes
10	22.1	0	26	575	7.98E-05	No
11	22.6	1	38	858	1.65E-04	Yes
12	23.0	3	9	207	7.37E-05	No
13	23.2	1	37	858	1.81E-04	Yes
14	23.8	1	36	858	1.47E-04	Yes
15	24.0	0	24	575	1.30E-04	No
16	24.5	1	35	858	1.37E-04	Yes
17	25.0	0	23	575	8.68E-05	No
18	25.2	1	34	858	3.02E-04	Yes
19	25.4	7	40	1017	1.30E-04	No
20	25.9	3	8	207	1.49E-04	No
21	26.0	1	33	858	1.76E-04	Yes
22	26.2	0	22	575	3.49E-04	No
23	26.5	4	14	372	1.27E-04	No
24	26.8	1	32	858	1.26E-04	Yes
25	27.7	1	31	858	2.64E-04	Yes
26	28.2	7	36	1017	1.83E-04	No
27	28.6	1	30	858	5.39E-04	Yes
28	29.6	3	7	207	1.46E-04	No
29	29.6	1	29	858	1.35E-04	Yes

Table 16: Stage 1 Rotational Speeds, Spatial and Temporal Harmonics, Forcing Frequency and Vibration Magnitudes of Resonances

	Rotor Speed	Spatial Harmonic	Temporal Harmonic	Forcing Frequency	Back of Core Velocity	Tooth Rocking
	Hz	n	m	Hz	ms^{-1}	?
1	20.01	6	39	780	2.01E-03	No
2	20.15	5	28	564	6.40E-03	No
3	20.43	1	42	858	5.77E-03	Yes
4	20.54	6	38	780	2.97E-03	No
5	20.55	0	28	575	1.66E-03	No
6	20.71	3	10	207	4.39E-03	No
7	20.90	5	27	564	2.00E-02	No
8	20.93	1	41	858	9.39E-02	Yes
9	21.09	6	37	780	7.63E-03	No
10	21.31	0	27	575	1.78E-02	No
11	21.45	1	40	858	9.91E-03	Yes
12	21.68	6	36	780	2.11E-03	No
13	21.70	5	26	564	6.08E-03	No
14	22.00	1	39	858	9.75E-03	Yes
15	22.13	0	26	575	6.77E-02	No
16	22.30	6	35	780	1.29E-03	No
17	22.57	5	25	564	1.01E-02	No
18	22.58	1	38	858	1.17E-02	Yes
19	22.95	6	34	780	6.65E-03	No
20	23.01	3	9	207	3.47E-03	No
21	23.02	0	25	575	9.09E-03	No
22	23.19	1	37	858	2.64E-02	Yes
23	23.51	5	24	564	7.15E-03	No
24	23.65	6	33	780	3.97E-03	No
25	23.65	7	43	1017	1.36E-03	No
26	23.84	1	36	858	1.03E-02	Yes
27	23.98	0	24	575	1.39E-03	Yes
28	24.21	7	42	1017	1.81E-03	No
29	24.39	6	32	780	3.23E-03	No
30	24.52	1	35	858	1.88E-02	Yes
31	24.53	5	23	564	7.74E-03	No
32	24.80	7	41	1017	5.89E-03	No
33	25.02	0	23	575	2.47E-02	No

Table 17: Stage 2 Rotational Speeds, Spatial and Temporal Harmonics, Forcing Frequency and Vibration Magnitudes of Resonances (Part 1)

	Rotor Speed	Spatial Harmonic	Temporal Harmonic	Forcing Frequency	Back of Core Velocity	Tooth Rocking
	Hz	n	m	Hz	ms^{-1}	?
34	25.18	6	31	780	9.55E-03	No
35	25.24	1	34	858	6.24E-03	Yes
36	25.42	7	40	1017	7.57E-03	No
37	25.65	5	22	564	5.83E-03	No
38	25.88	3	8	207	3.35E-03	No
39	26.00	1	33	858	8.95E-03	Yes
40	26.01	6	30	780	2.44E-03	No
41	26.08	7	39	1017	4.87E-03	No
42	26.16	0	22	575	1.89E-02	No
43	26.17	2	3	79	2.41E-02	No
44	26.76	7	38	1017	3.07E-03	No
45	26.82	1	32	858	2.16E-02	Yes
46	26.87	5	21	564	1.15E-02	No
47	26.91	6	29	780	9.72E-04	No
48	27.40	0	21	575	2.87E-03	No
49	27.49	7	37	1017	9.65E-03	No
50	27.68	1	31	858	2.18E-02	Yes
51	27.87	6	28	780	3.37E-03	No
52	28.21	5	20	564	4.01E-03	No
53	28.25	7	36	1017	8.95E-03	No
54	28.60	1	30	858	2.84E-02	Yes
55	28.77	0	20	575	2.49E-02	No
56	28.91	6	27	780	3.63E-03	No
57	29.06	7	35	1017	8.63E-03	No
58	29.41	2	43	1264	1.34E-02	No
59	29.56	8	43	1271	2.72E-03	No
60	29.58	3	7	207	1.02E-02	No
61	29.59	1	29	858	3.19E-02	Yes
62	29.70	5	19	564	4.18E-03	No
63	29.91	7	34	1017	1.64E-03	No

Table 18: Stage 2 Rotational Speeds, Spatial and Temporal Harmonics, Forcing Frequency and Vibration Magnitudes of Resonances (Part 2)

	Rotor Speed	Spatial Harmonic	Temporal Harmonic	Forcing Frequency	Back of Core Velocity	Tooth Rocking
	Hz	n	m	Hz	ms^{-1}	?
1	20.55	0	28	575	8.25E-05	No
2	20.64	4	18	372	7.10E-05	No
3	20.71	3	10	207	1.10E-04	No
4	20.90	5	27	564	4.47E-05	No
5	20.93	1	41	858	1.51E-04	Yes
6	21.09	6	37	780	5.32E-05	No
7	21.31	0	27	575	9.08E-05	No
8	21.85	4	17	372	6.90E-05	No
9	22.13	0	26	575	1.49E-04	No
10	23.01	3	9	207	6.21E-05	No
11	23.02	0	25	575	8.17E-05	No
12	23.51	5	24	564	6.69E-05	No
13	23.98	0	24	575	2.14E-04	No
14	24.77	4	15	372	5.29E-05	No
15	24.80	7	41	1017	5.73E-05	No
16	25.02	0	23	575	2.35E-04	No
17	25.24	1	34	858	5.36E-05	Yes
18	25.42	7	40	1017	1.06E-04	No
19	25.88	3	8	207	1.48E-04	No
20	26.16	0	22	575	5.34E-04	No
21	26.54	4	14	372	1.07E-04	No
22	27.49	7	37	1017	7.61E-05	No
23	28.25	7	36	1017	1.72E-04	No
24	28.58	4	13	372	6.17E-05	No
25	28.60	1	30	858	5.85E-05	Yes
26	28.77	0	20	575	9.08E-05	No
27	29.58	3	7	207	1.44E-04	No
28	29.70	5	19	564	6.27E-05	No

Table 19: Stage 3 Rotational Speeds, Spatial and Temporal Harmonics, Forcing Frequency and Vibration Magnitudes of Resonances

	Rotor Speed	m	Forcing Frequency	Back of Core Velocity			
				Stage 0	Stage 1	Stage 2	Stage 3
	Hz		Hz	ms^{-1}	ms^{-1}	ms^{-1}	ms^{-1}
1	20.6	18	372	6.84E-06	5.75E-05	7.91E-06	7.10E-05
2	21.9	17	372	7.22E-06	1.37E-04	1.01E-05	6.90E-05
3	23.2	16	372	6.12E-06	1.92E-05	4.16E-06	3.78E-05
4	24.8	15	372	8.66E-06	5.28E-05	1.42E-05	5.29E-05
5	26.5	14	372	8.74E-06	1.27E-04	2.55E-05	1.07E-04
6	28.6	13	372	6.03E-06	1.88E-05	1.01E-05	6.17E-05

Table 20: n=4 Resonances at Rotational Speeds between $20Hz$ and $30Hz$

	Rotor Speed	m	Forcing Frequency	Back of Core Velocity			
				Stage 0	Stage 1	Stage 2	Stage 3
	Hz		Hz	ms^{-1}	ms^{-1}	ms^{-1}	ms^{-1}
1	20.4	42	858	1.62E-05	8.71E-05	5.77E-03	1.96E-05
2	20.9	41	858	6.34E-05	4.13E-04	9.39E-02	1.51E-04
3	21.5	40	858	1.53E-05	1.18E-04	9.91E-03	1.38E-05
4	22.0	39	858	1.35E-05	1.92E-04	9.75E-03	8.31E-06
5	22.6	38	858	1.04E-05	1.65E-04	1.17E-02	1.97E-05
6	23.2	37	858	1.61E-05	1.81E-04	2.64E-02	4.01E-05
7	23.8	36	858	2.76E-05	1.47E-04	1.03E-02	2.15E-05
8	24.5	35	858	2.11E-05	1.37E-04	1.88E-02	3.72E-05
9	25.2	34	858	3.77E-05	3.02E-04	6.24E-03	5.36E-05
10	26.0	33	858	9.09E-06	1.76E-04	8.95E-03	7.22E-06
11	26.8	32	858	1.40E-05	1.26E-04	2.16E-02	2.09E-05
12	27.7	31	858	2.47E-05	2.64E-04	2.18E-02	4.70E-05
13	28.6	30	858	6.43E-05	5.39E-04	2.84E-02	5.85E-05
14	29.6	29	858	1.00E-05	1.35E-04	3.19E-02	1.79E-05

Table 21: n=1 Resonances at Rotational Speeds between $20Hz$ and $30Hz$

	Rotation Speed	m	Forcing Frequency	Change Stage 0 to 1	Controlled Change		Uncontrolled Change	
					Stage 1 to 2	Stage 0 to 2	Stage 1 to 3	Stage 0 to 3
	Hz		Hz	%	%	%	%	%
1	20.6	18	372	741	-86	16	24	938
2	21.9	17	372	1790	-93	40	-49	855
3	23.2	16	372	213	-78	-32	97	518
4	24.8	15	372	510	-73	64	0	511
5	26.5	14	372	1352	-80	191	-16	1125
6	28.6	13	372	212	-46	68	228	923

Table 22: Changes in the Magnitude of the n=4 Resonances

	Rotation Speed	m	Forcing Frequency	Change Stage 0 to 1	Controlled Change Stage 1 to 3	Controlled Change Stage 0 to 3	Uncontrolled Change Stage 1 to 2	Uncontrolled Change Stage 0 to 2
	Hz		Hz	%	%	%	%	%
1	20.4	42	858	438	-77	21	6,525	35,557
2	20.9	41	858	551	-63	138	22,644	147,979
3	21.5	40	858	668	-88	-10	8,323	64,575
4	22.0	39	858	1,320	-96	-38	4,978	72,024
5	22.6	38	858	1,485	-88	90	6,977	112,036
6	23.2	37	858	1,023	-78	149	14,472	163,567
7	23.8	36	858	433	-85	-22	6,922	37,321
8	24.5	35	858	551	-73	76	13,572	88,850
9	25.2	34	858	700	-82	42	1,965	16,424
10	26.0	33	858	1,837	-96	-21	4,984	98,362
11	26.8	32	858	796	-83	49	17,095	153,911
12	27.7	31	858	970	-82	90	8,137	88,057
13	28.6	30	858	739	-89	-9	5,178	44,159
14	29.6	29	858	1,239	-87	78	23,587	317,087

Table 23: Changes in the Magnitude of the n=1 Resonances

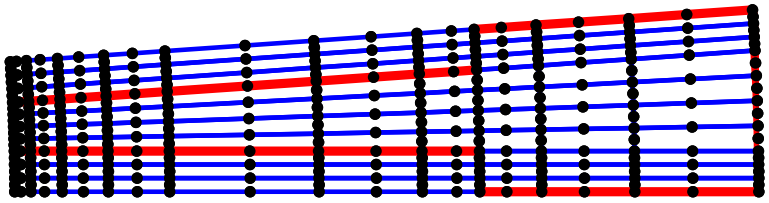

Figure 50: The Full Mesh For One Stator Bay

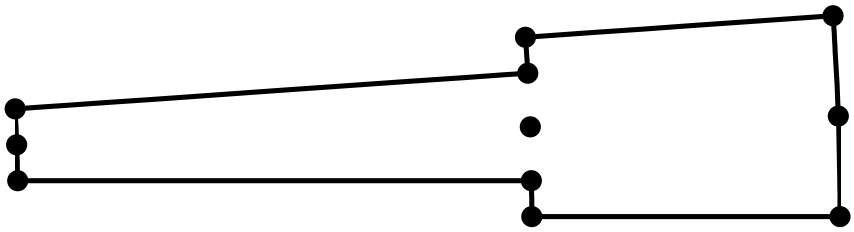

Figure 51: One Stator Bay with Master Nodes After the Complete Merge and Reduction of the Stator

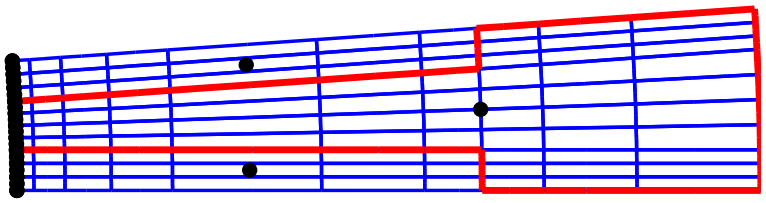

Figure 52: The Master Nodes in One Magnetic Stator Bay

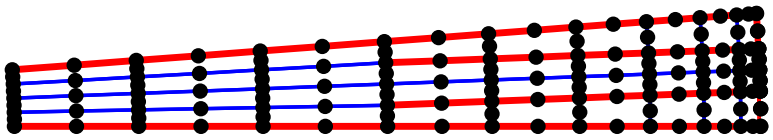

Figure 53: The Full Mesh For One Rotor Bay

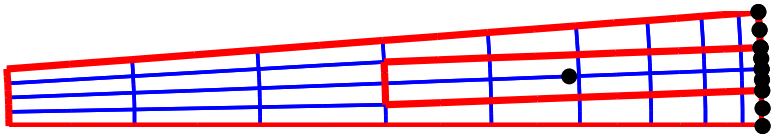

Figure 54: The Master Nodes in One Rotor Bay

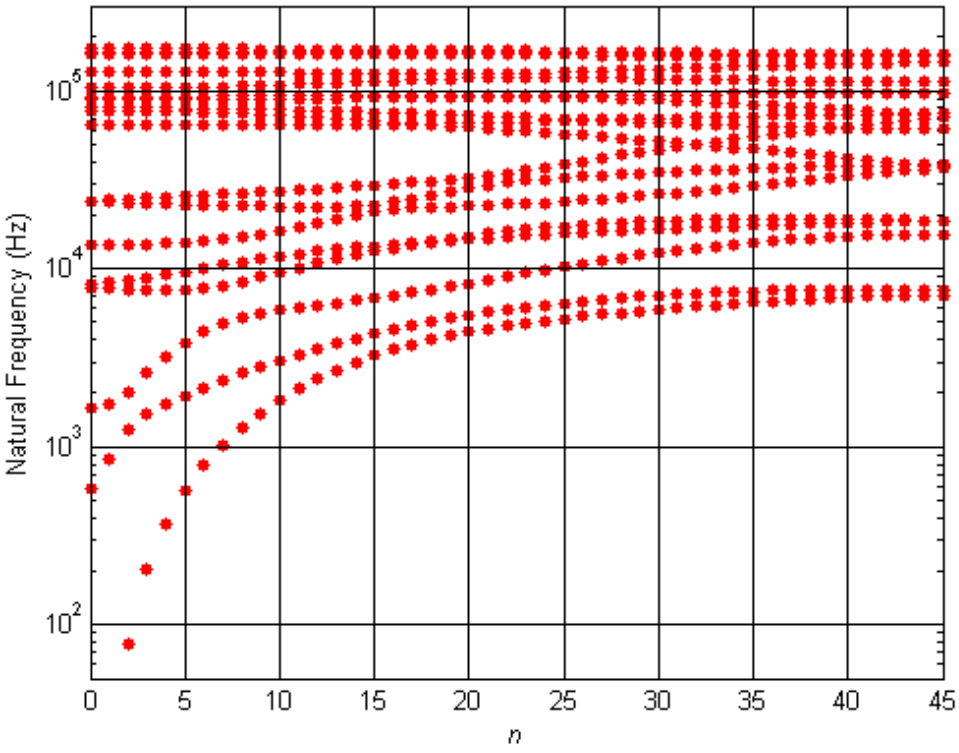

Figure 55: Natural Frequencies against Mode Number n

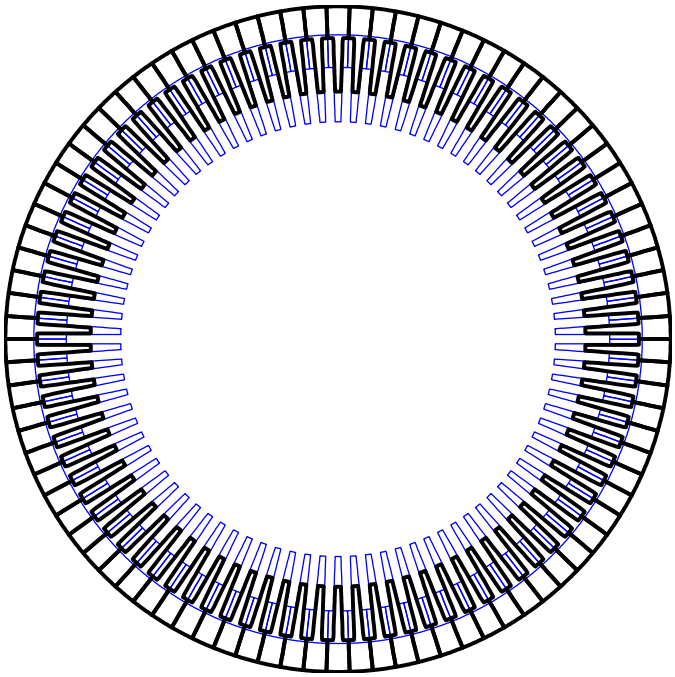

Figure 56: A $n = 0$ *Breathing* Mode

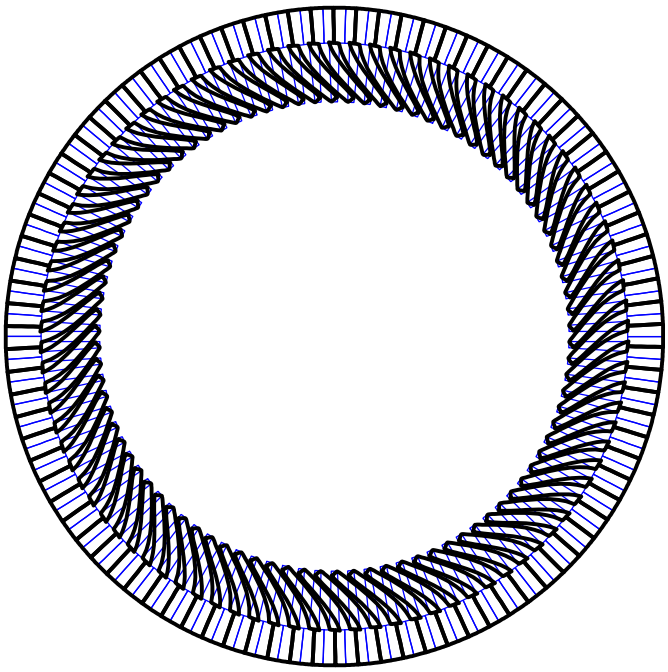

Figure 57: A $n = 0$ *Tooth Rocking* Mode

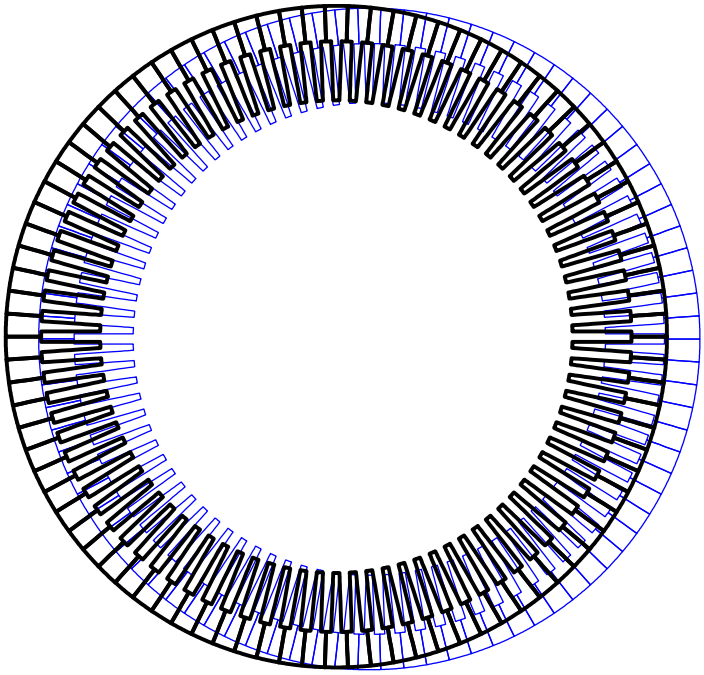

Figure 58: A $n = 1$ *Translational* Mode

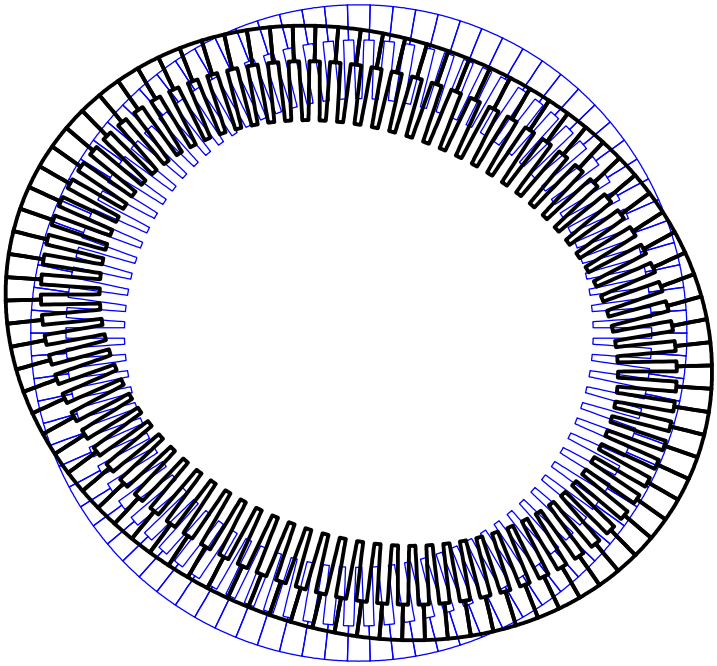

Figure 59: A $n = 2$ Back-of-Core Bending Mode

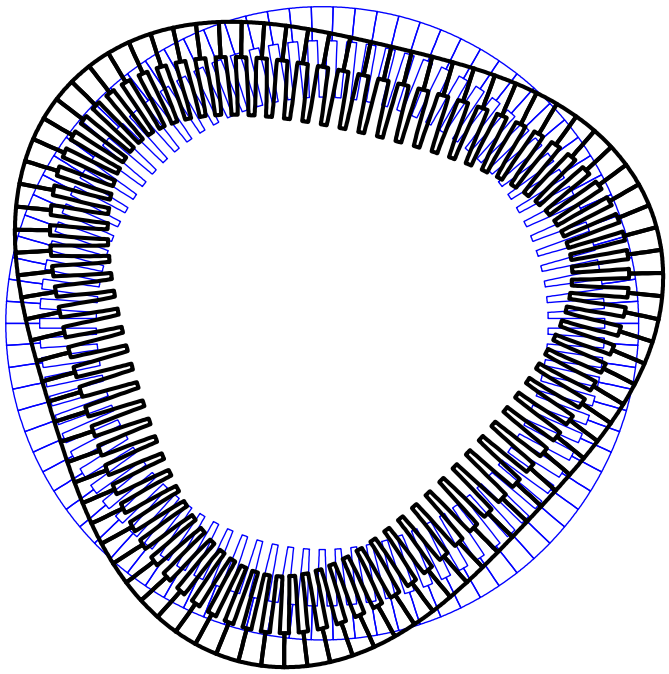

Figure 60: A $n = 3$ Back-of-Core Bending Mode

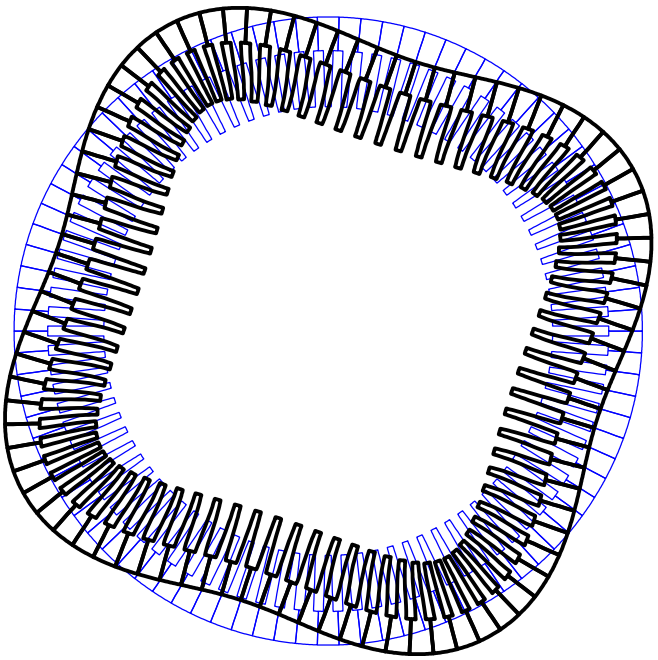

Figure 61: A $n = 4$ Back-of-Core Bending Mode

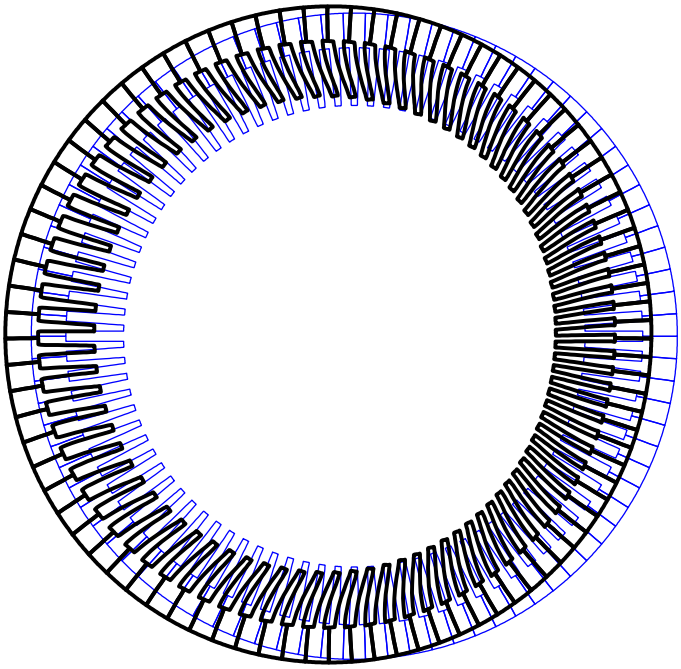

Figure 62: A $n = 1$ Tooth Rocking Mode

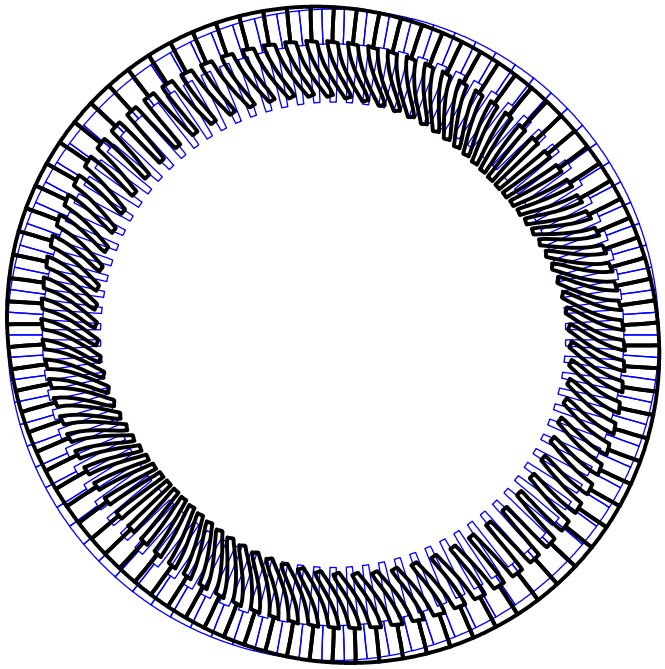

Figure 63: $n = 2$ Tooth Rocking In-Phase with Back-of-Core

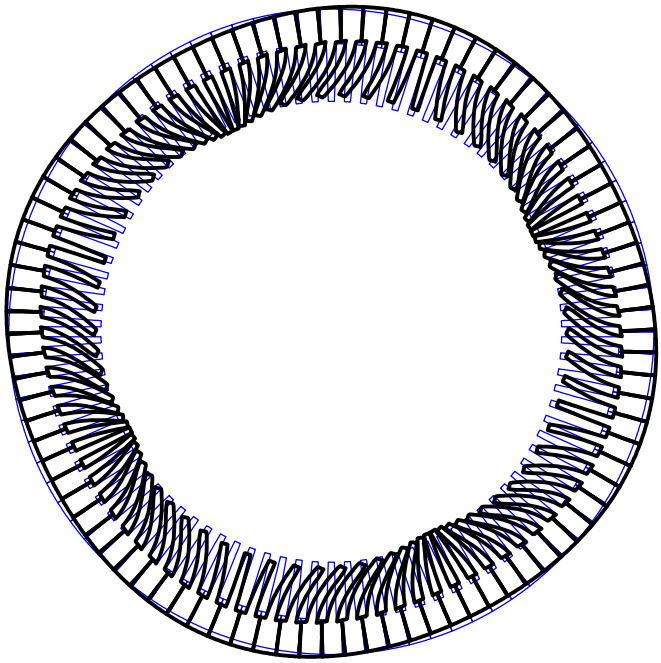

Figure 64: $n = 4$ Tooth Rocking In-Phase with Back-of-Core

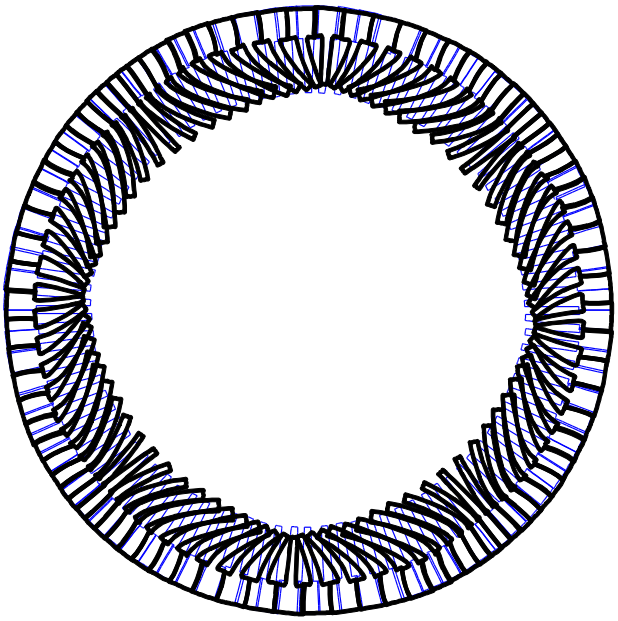

Figure 65: $n = 4$ Tooth Rocking Out-of-Phase with Back-of-Core

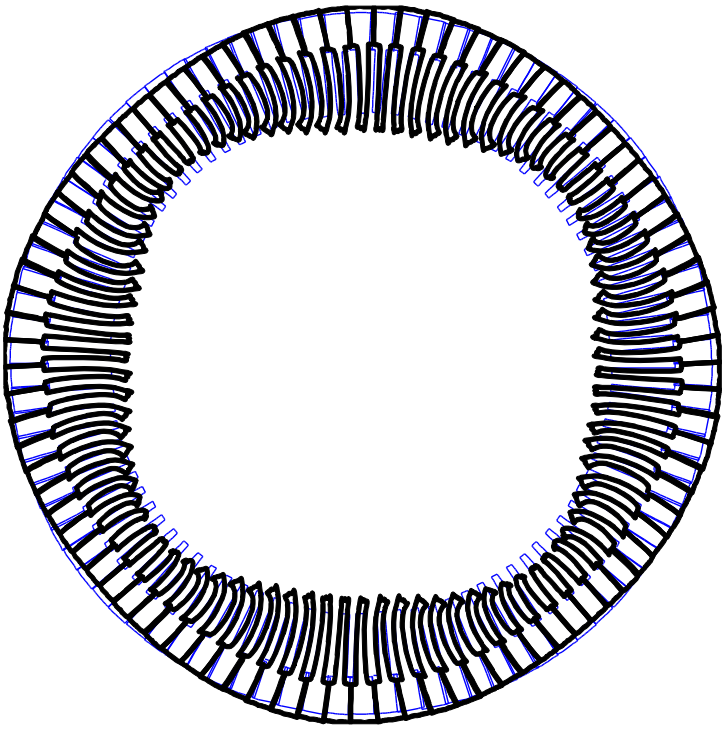

Figure 66: $n = 4$ Back-of-Core Bending and Tooth Expansion

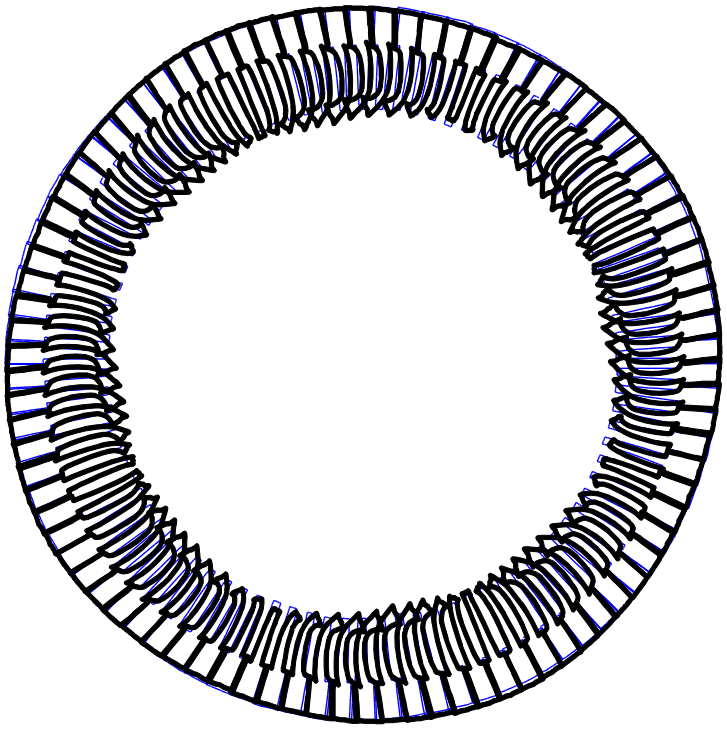

Figure 67: A $n = 4$ Back-of-Core Bending and Tooth Rocking Mode

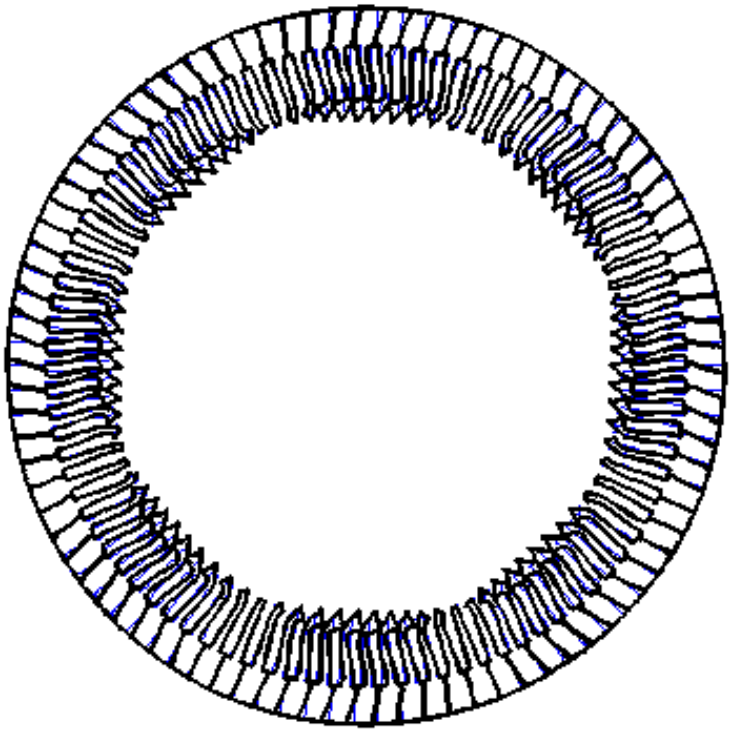

Figure 68: A $n = 4$ Tooth Rocking Mode

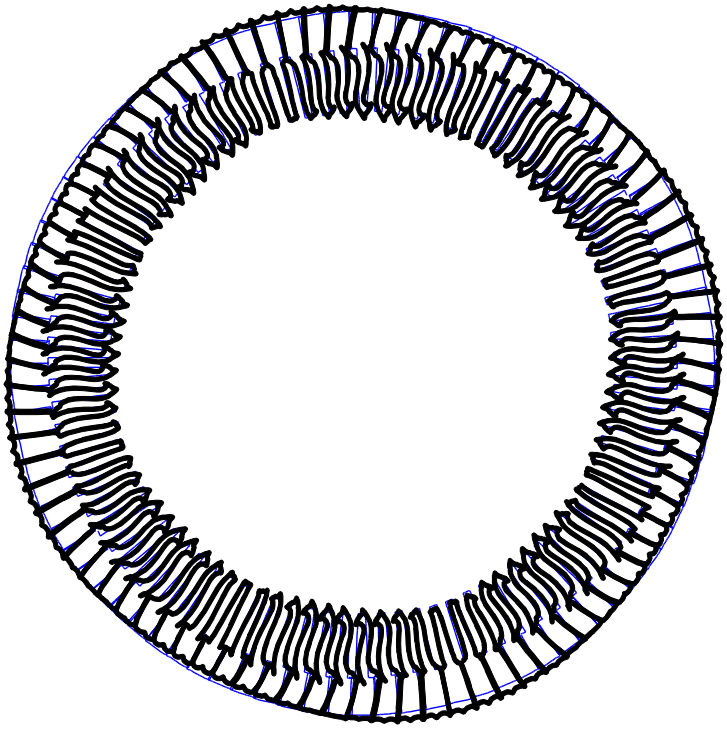

Figure 69: Second $n = 4$ Back-of-Core Bending and Tooth Rocking Mode

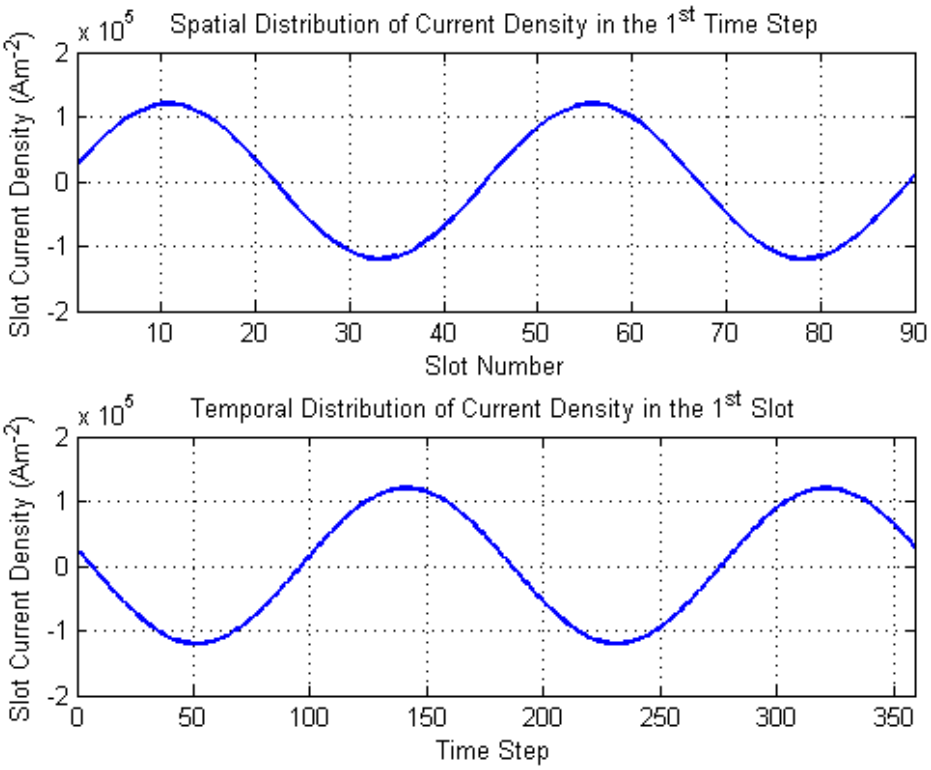

Figure 70: Sinusoidal Stator Current Density Pattern

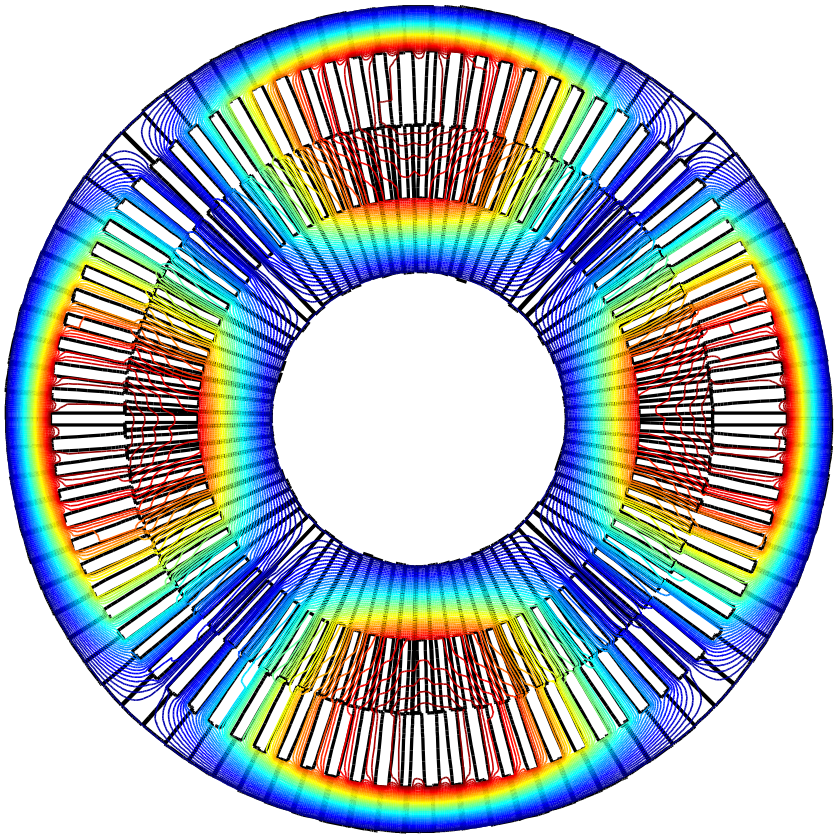

Figure 71: Contours of Magnetic Potential from a Sinusoidal Stator Current Pattern

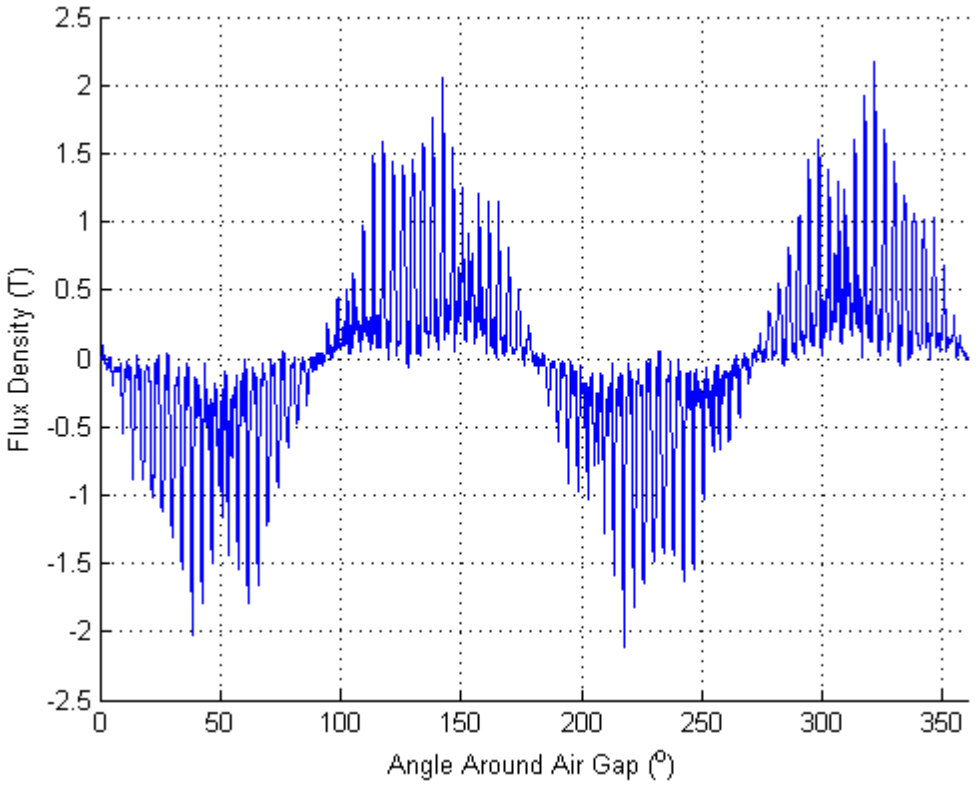

Figure 72: Radial Magnetic Flux from a Sinusoidal Stator Current Pattern

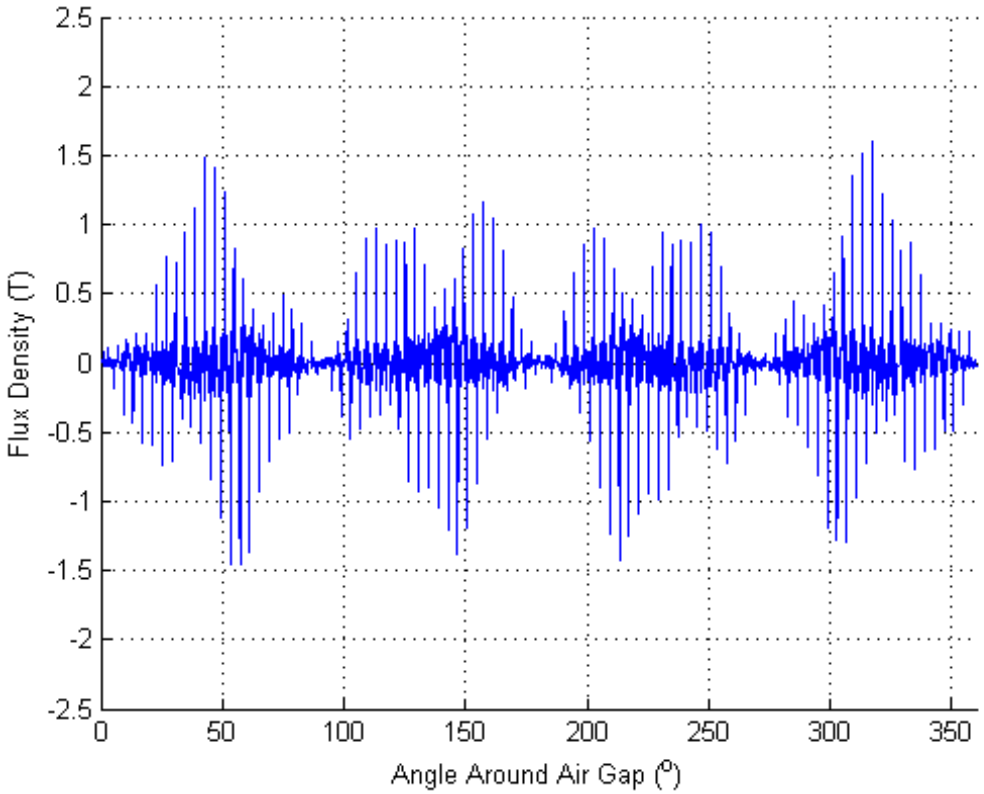

Figure 73: Tangential Magnetic Flux from a Sinusoidal Stator Current Pattern

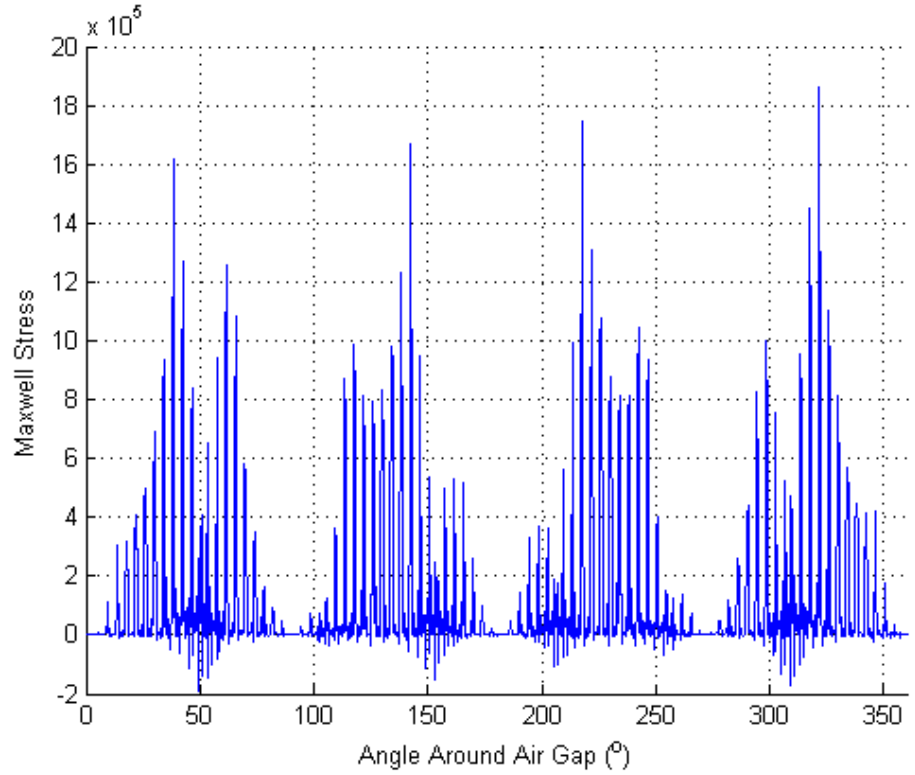

Figure 74: Radial Maxwell Stress from a Sinusoidal Stator Current Pattern

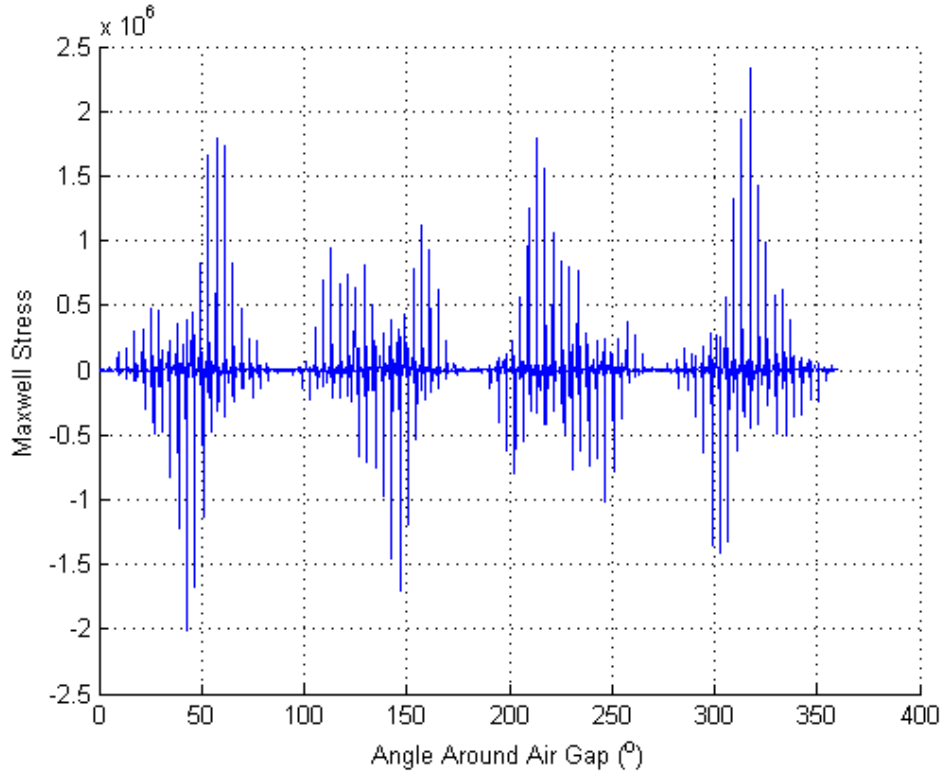

Figure 75: Tangential Maxwell Stress from a Sinusoidal Stator Current Pattern

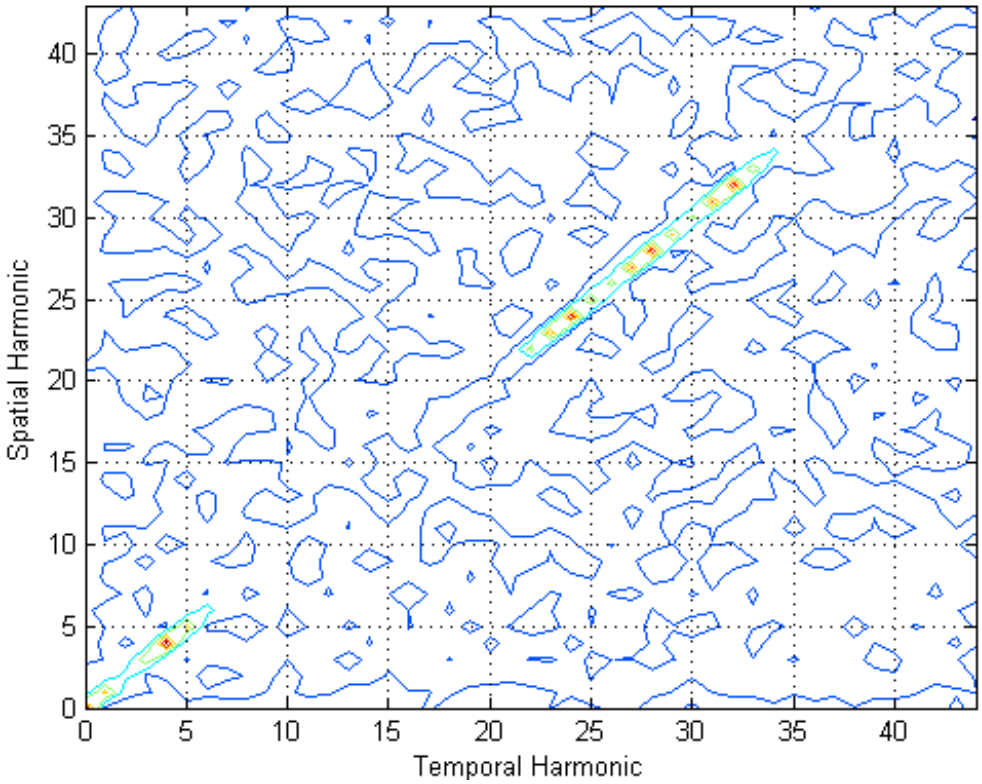

Figure 76: Contours of Tangential Maxwell Force from a Sinusoidal Stator Current Pattern

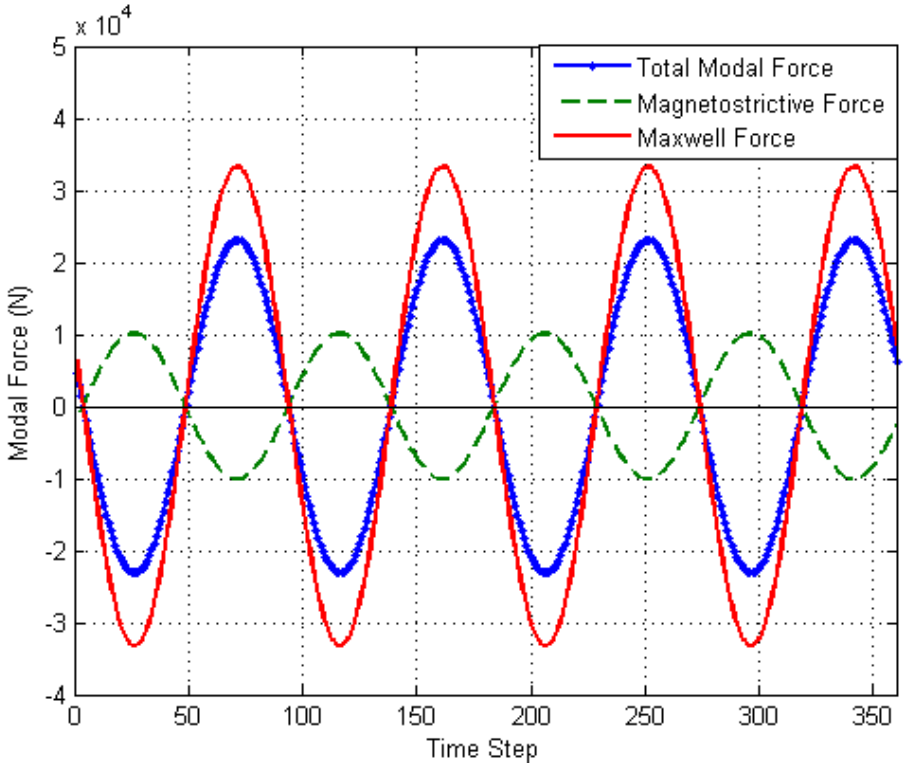

Figure 77: Modal Force from One n=4 Mode and Stage 0 Electromagnetic Force

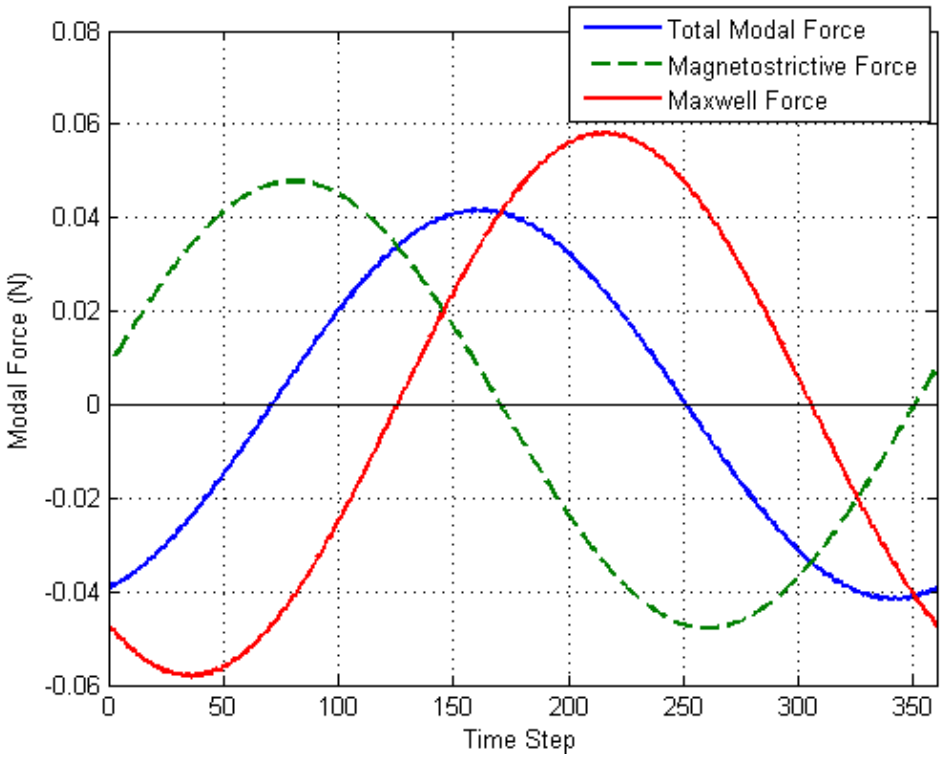

Figure 78: Modal Force from One n=1 Mode and Stage 0 Electromagnetic Force

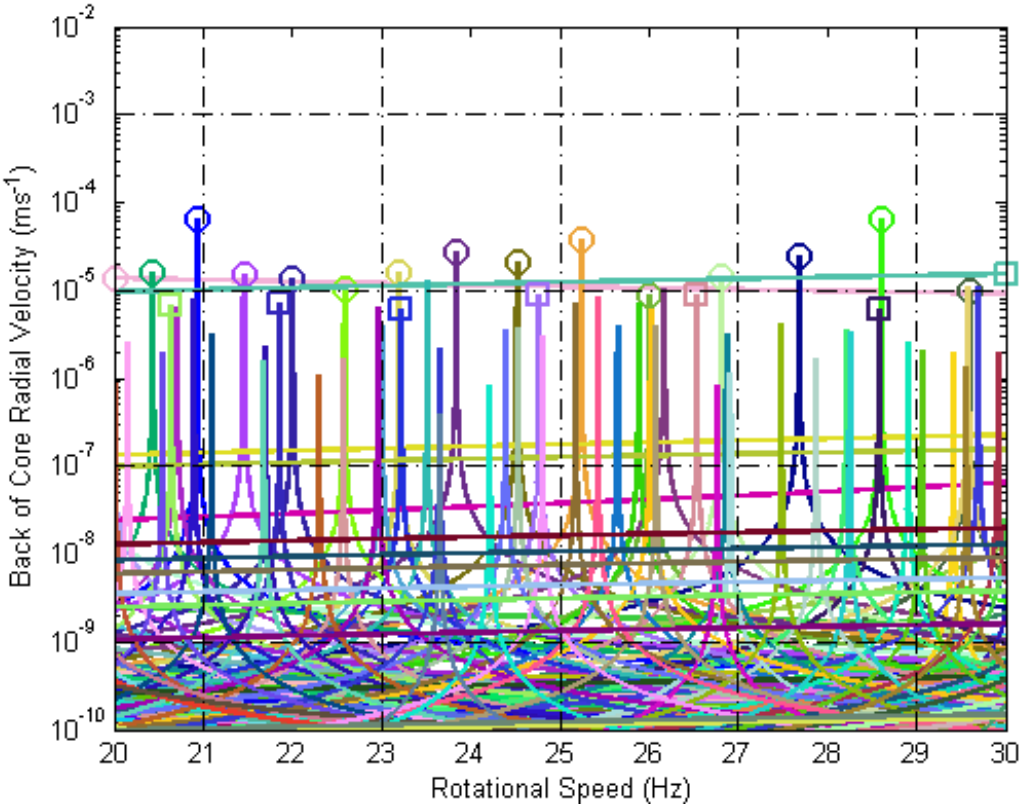

Figure 79: Stage 0 Vibration for Rotor Speeds Between $20Hz$ and $30Hz$ for all Combinations of Spatial and Temporal Harmonics

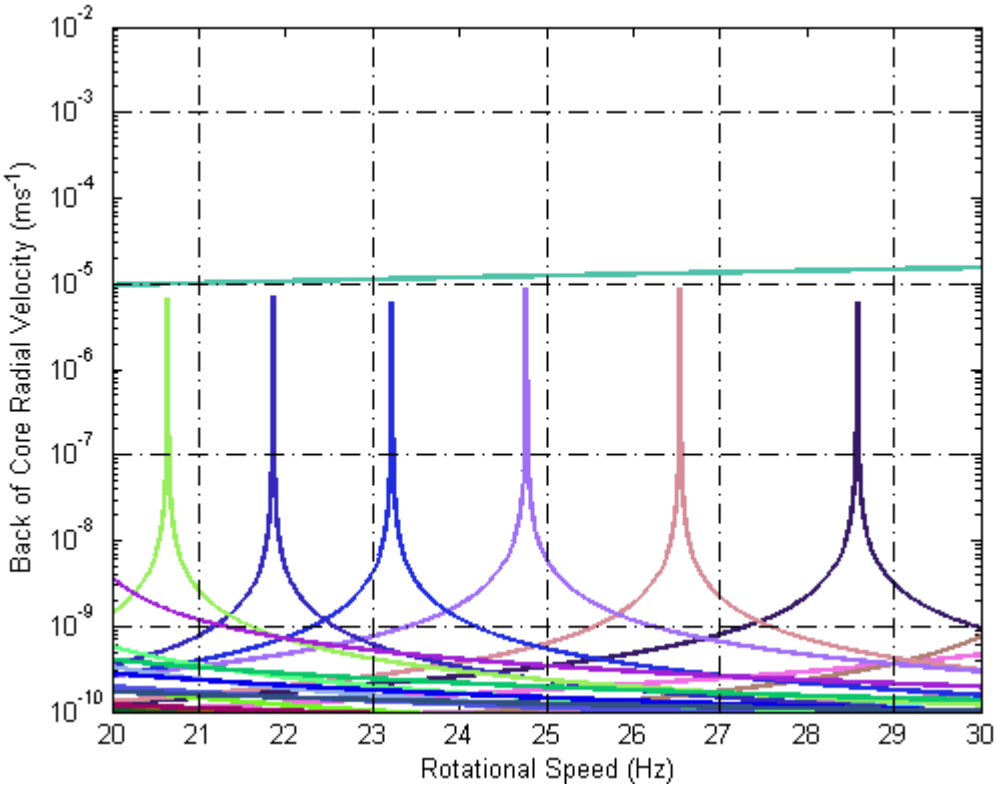

Figure 80: Response from n=4 Fourier Components of EM Forcing from Stage 0 Excitation

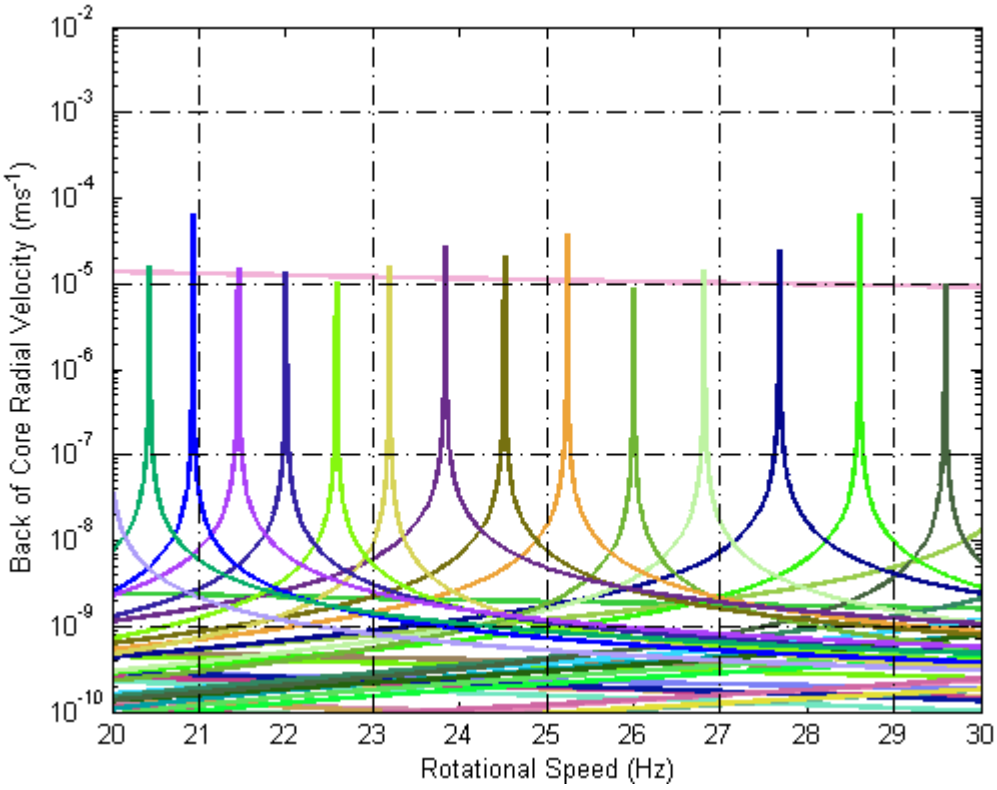

Figure 81: Response from n=1 Fourier Components of EM Forcing from Stage 0 Excitation

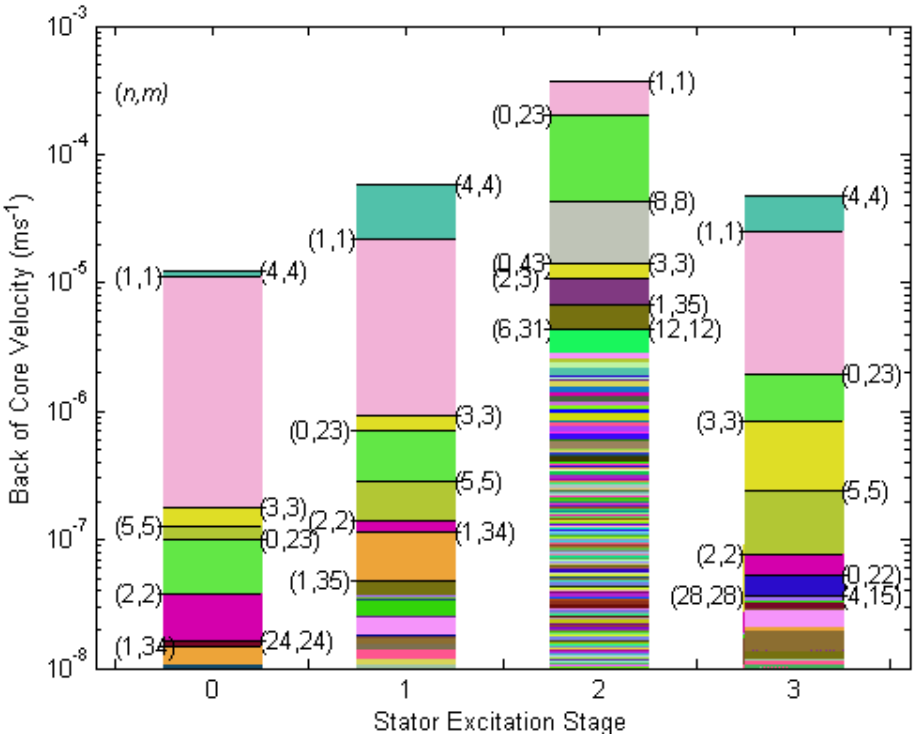

Figure 82: Contributions to Noise from Spatial and Temporal Harmonic combinations for Each Stage of Stator Excitation at Rotational Speed 25.0Hz

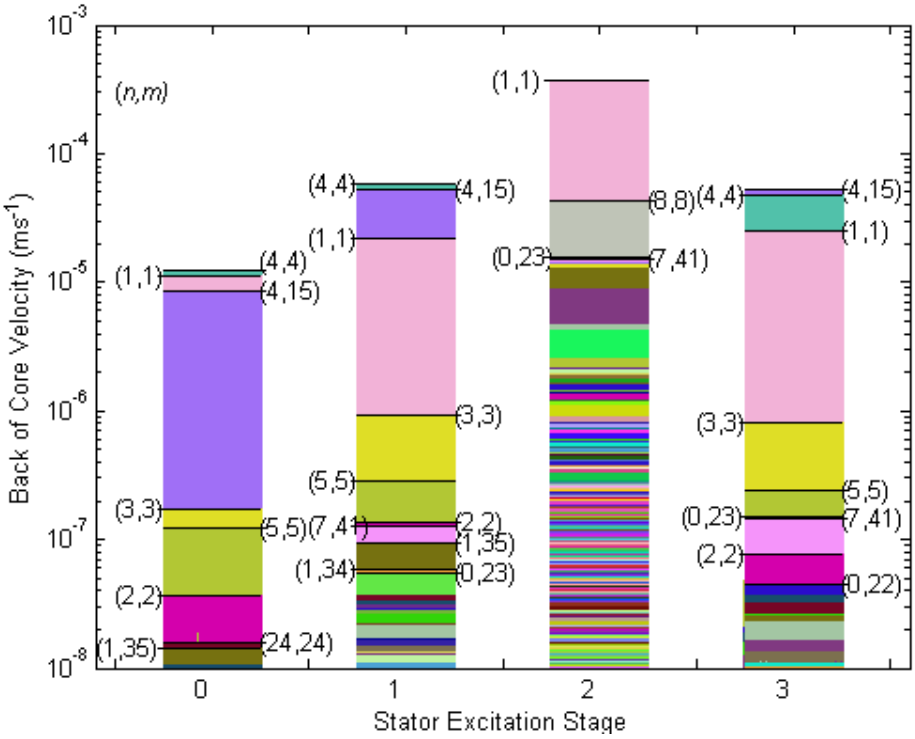

Figure 83: Contributions to Noise from Spatial and Temporal Harmonic combinations for Each Stage of Stator Excitation at Rotational Speed 24.8Hz

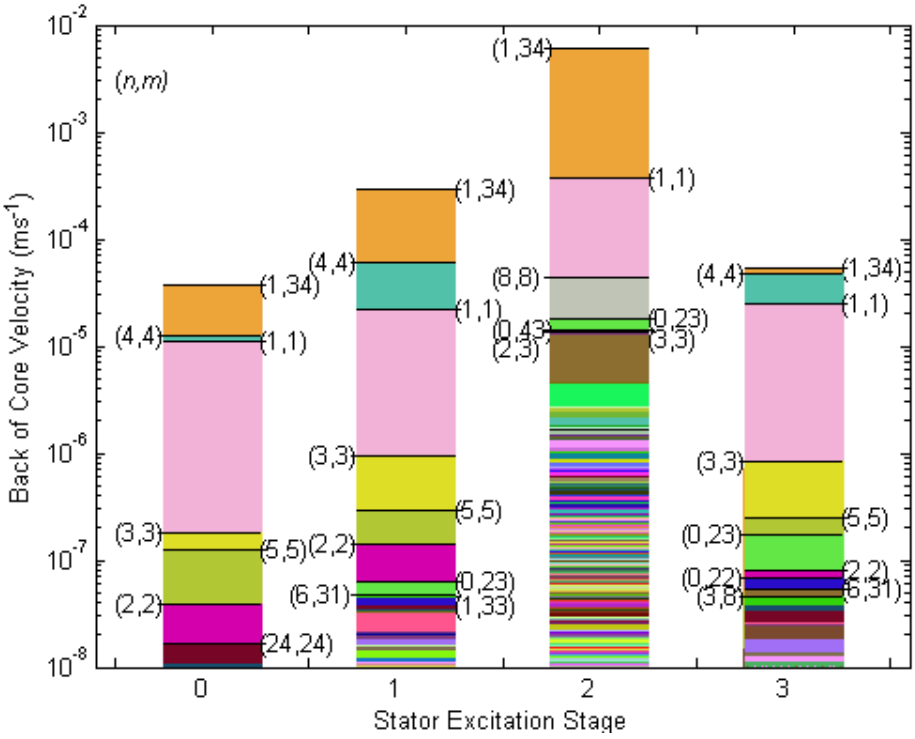

Figure 84: Contributions to Noise from Spatial and Temporal Harmonic combinations for Each Stage of Stator Excitation at Rotational Speed 25.2Hz

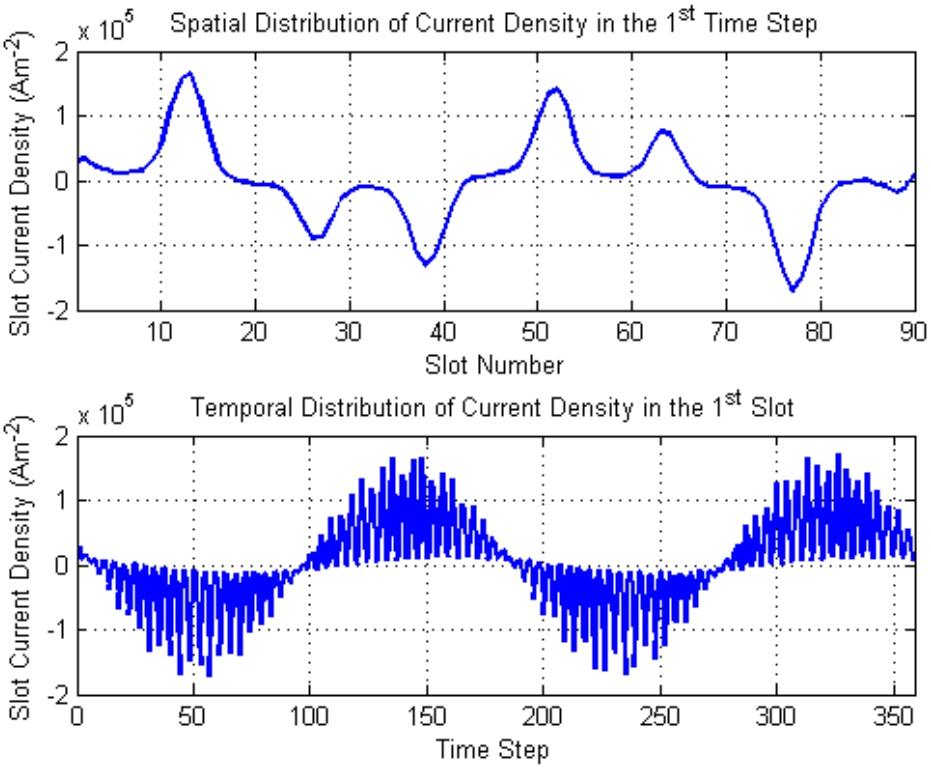

Figure 85: Stage 1 Stator Current Density Pattern

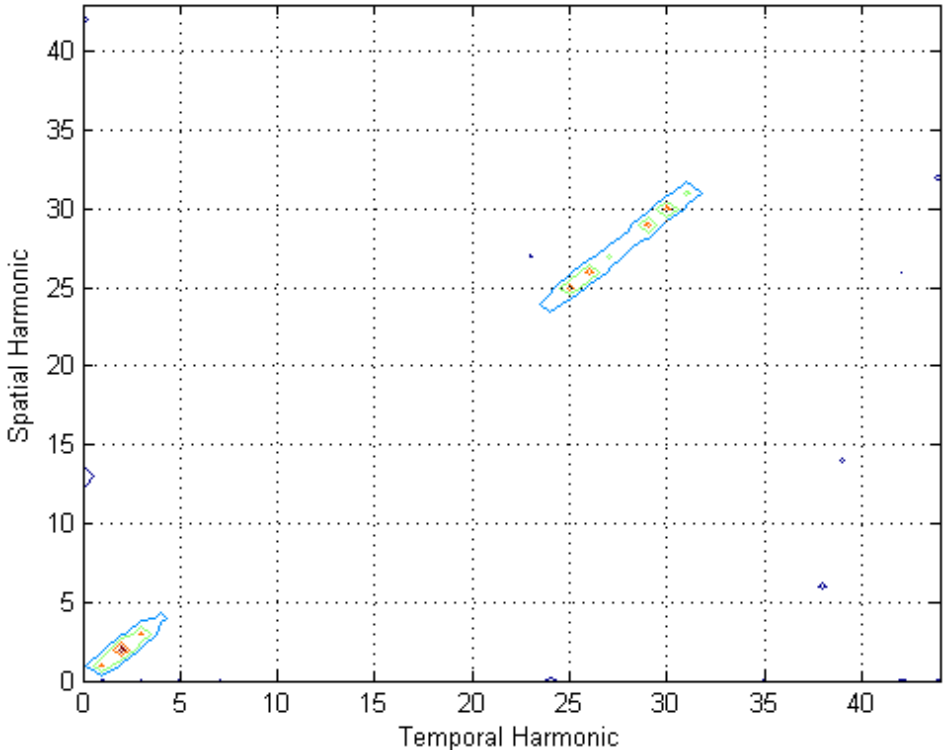

Figure 86: Stage 1 Spatial and Temporal Harmonics of Current Density

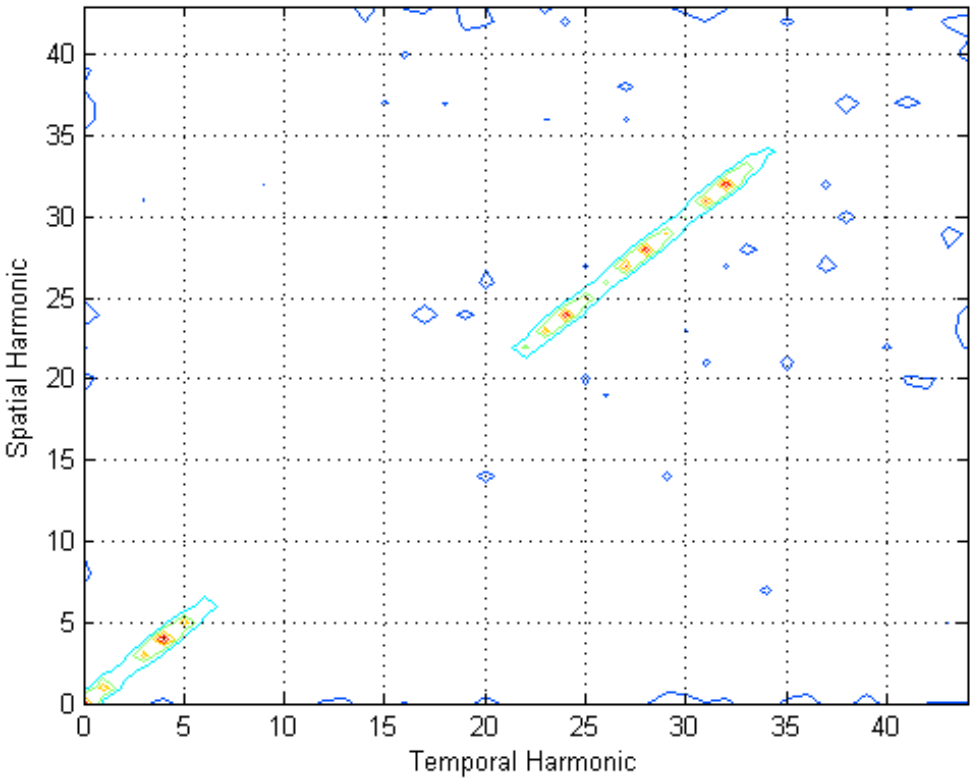

Figure 87: Stage 1 Contours of Tangential Maxwell Force

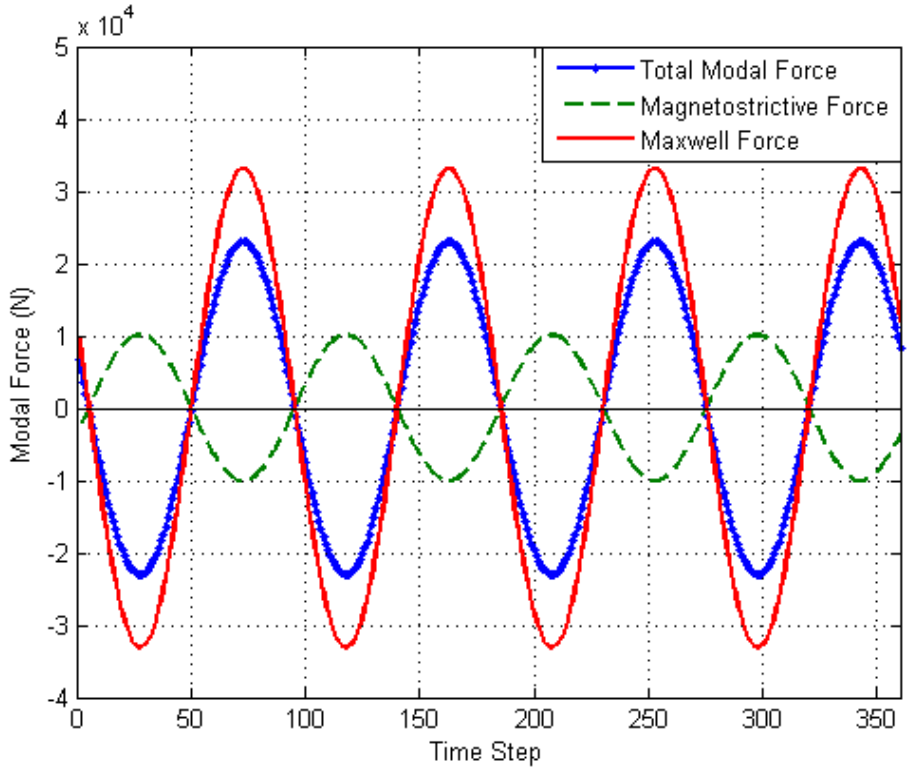

Figure 88: Modal Force from One n=4 Mode and Stage 1 Electromagnetic Force

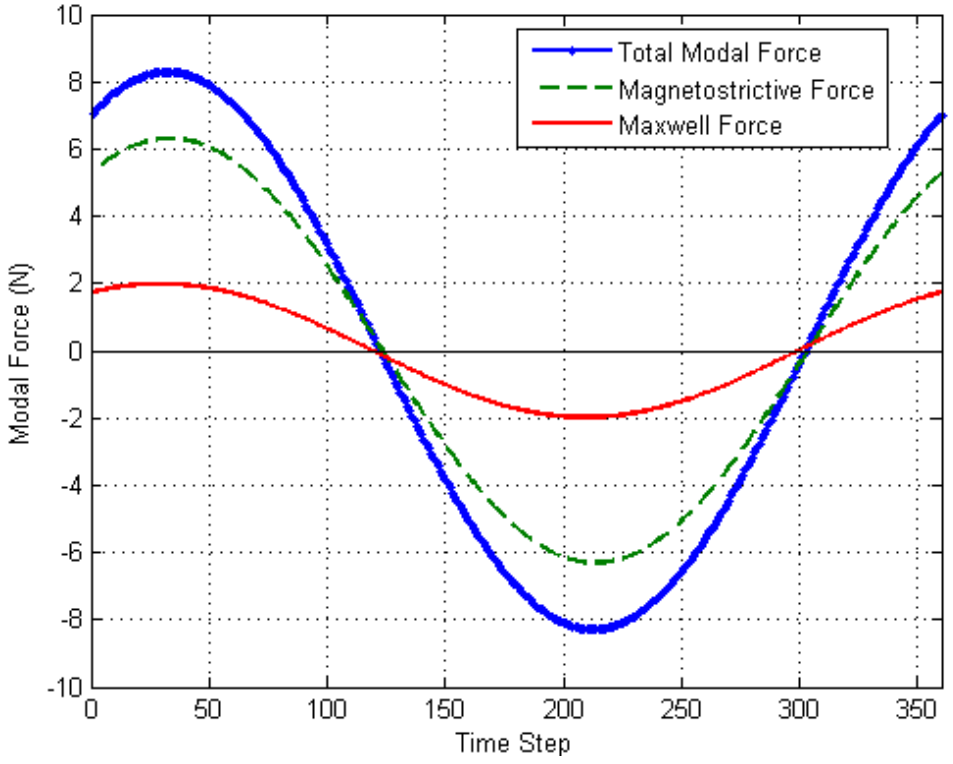

Figure 89: Modal Force from One n=1 Mode and Stage 1 Electromagnetic Force

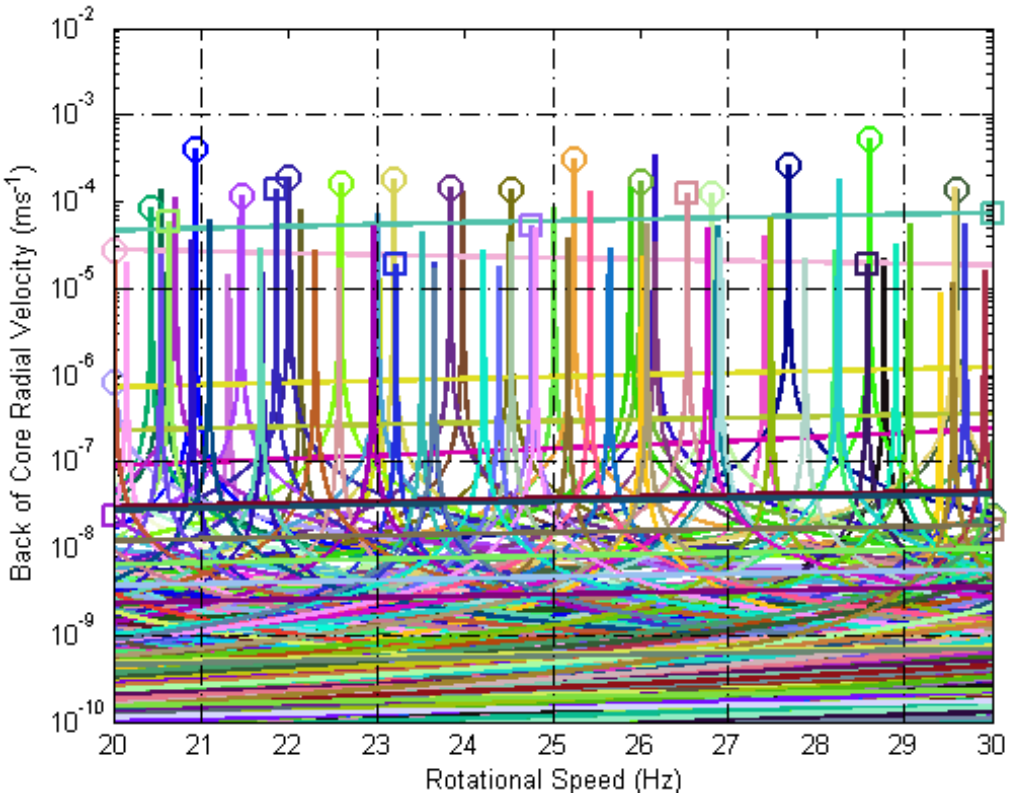

Figure 90: Stage 1 Vibration for Rotor Speeds Between $20Hz$ and $30Hz$ for all Combinations of Spatial and Temporal Harmonics

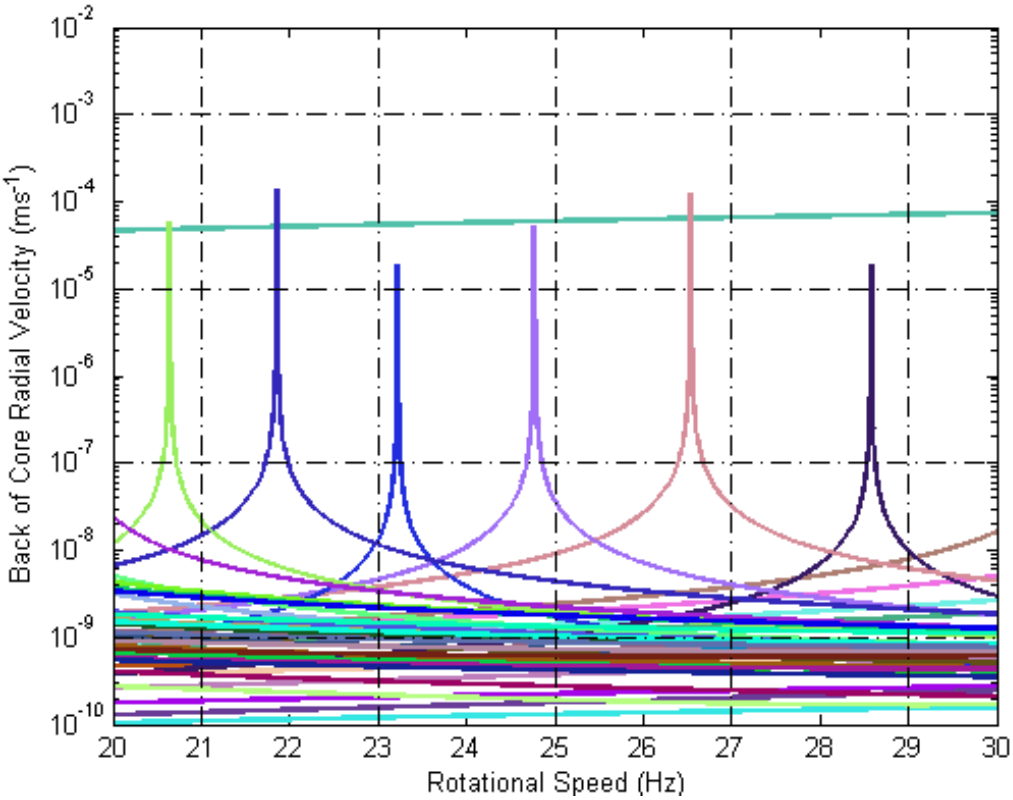

Figure 91: Response from n=4 Fourier Components of EM Forcing from Stage 1 Excitation

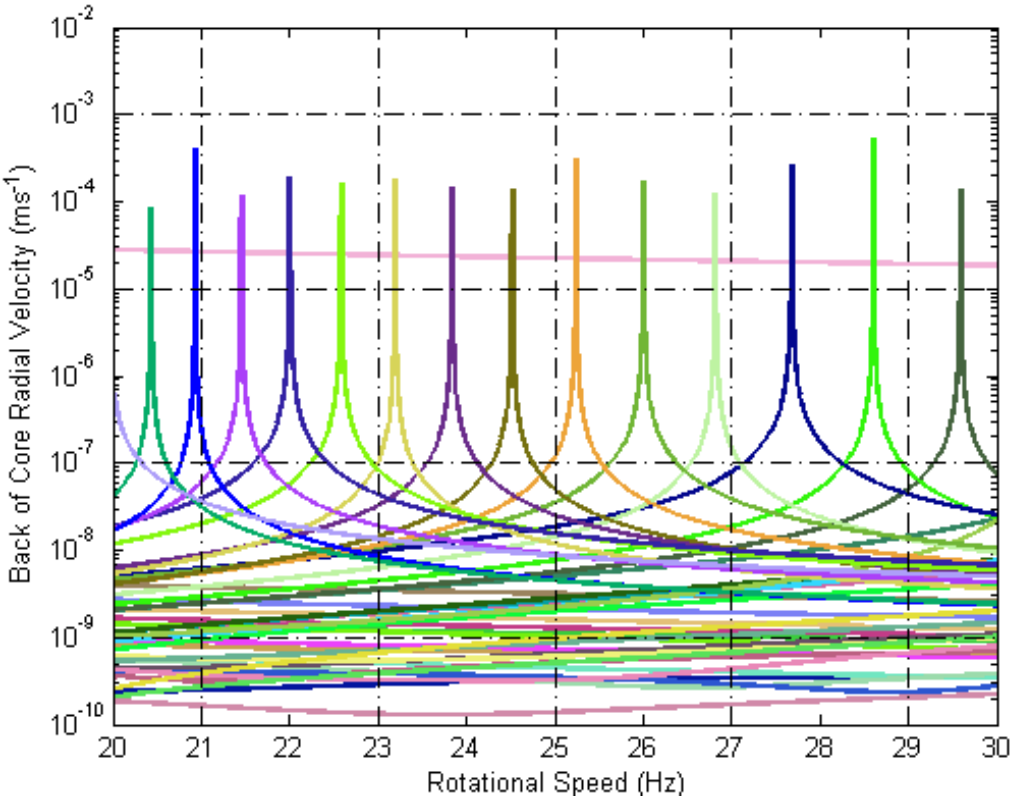

Figure 92: Response from n=1 Fourier Components of EM Forcing from Stage 1 Excitation

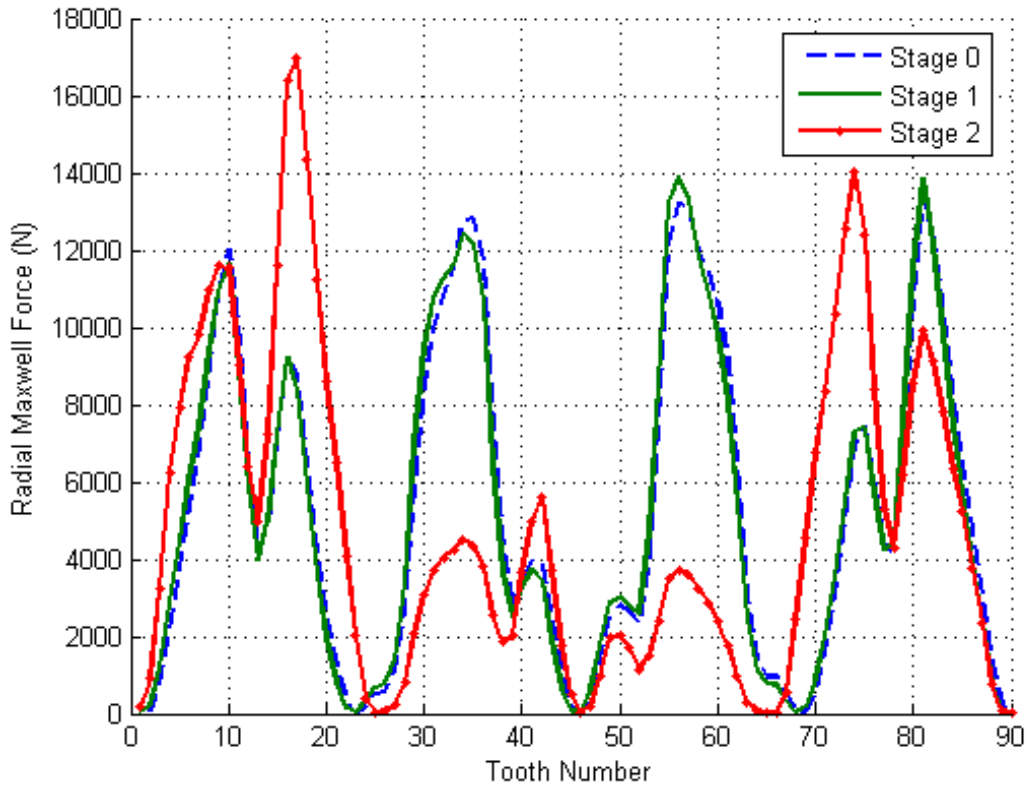

Figure 93: Radial Maxwell Force at each Tooth Tip for Each Stage in the Analysis

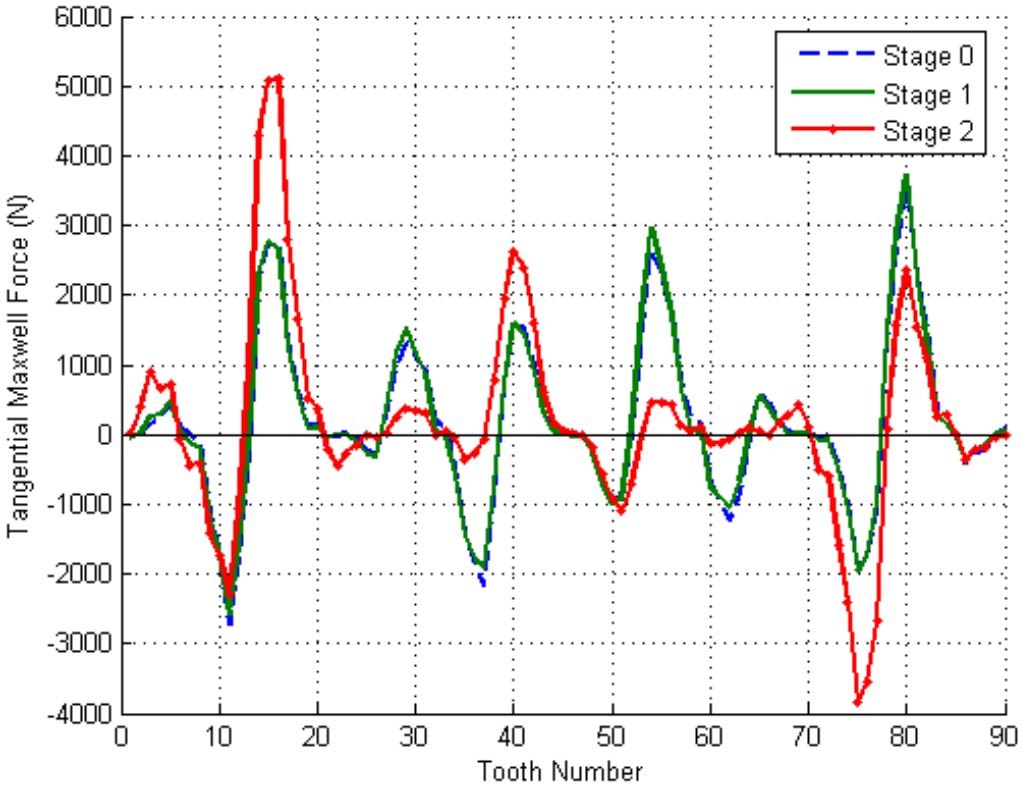

Figure 94: Tangential Maxwell Force at each Tooth Tip for Each Stage in the Analysis

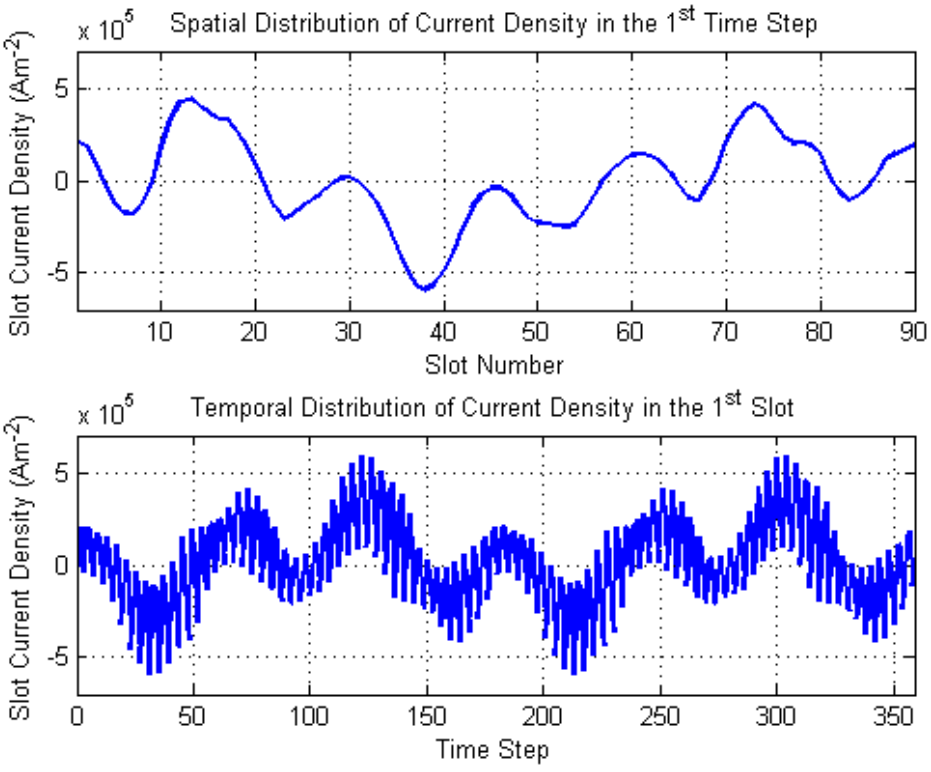

Figure 95: Stage 2 Stator Current Density Pattern

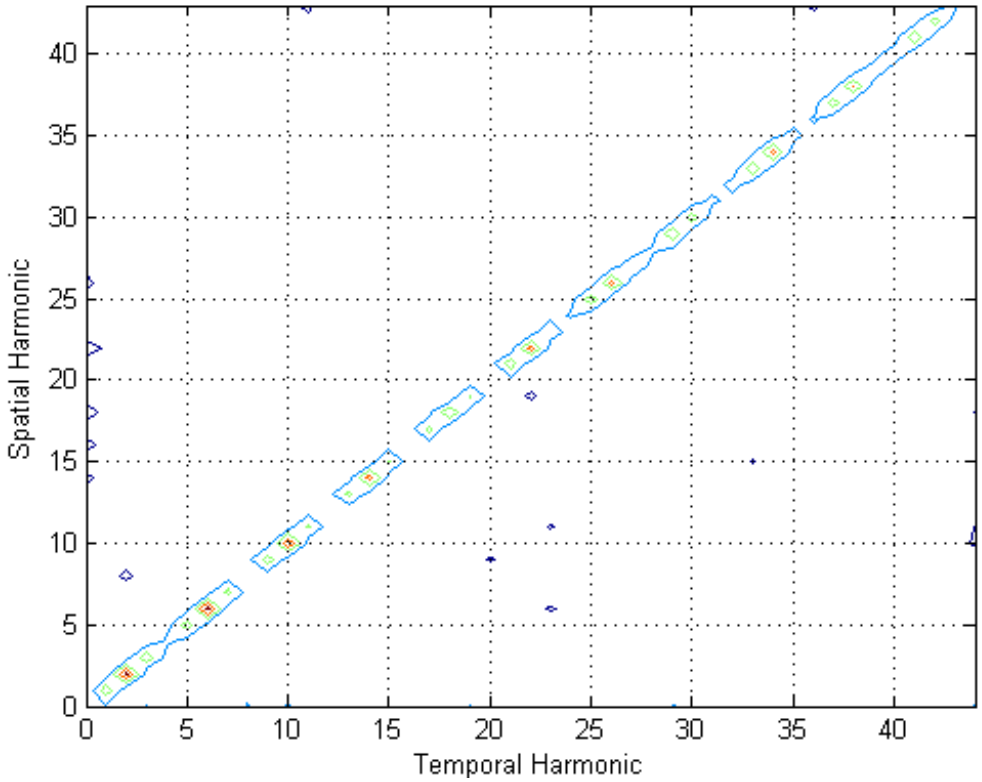

Figure 96: Stage 2 Spatial and Temporal Harmonics of Current Density

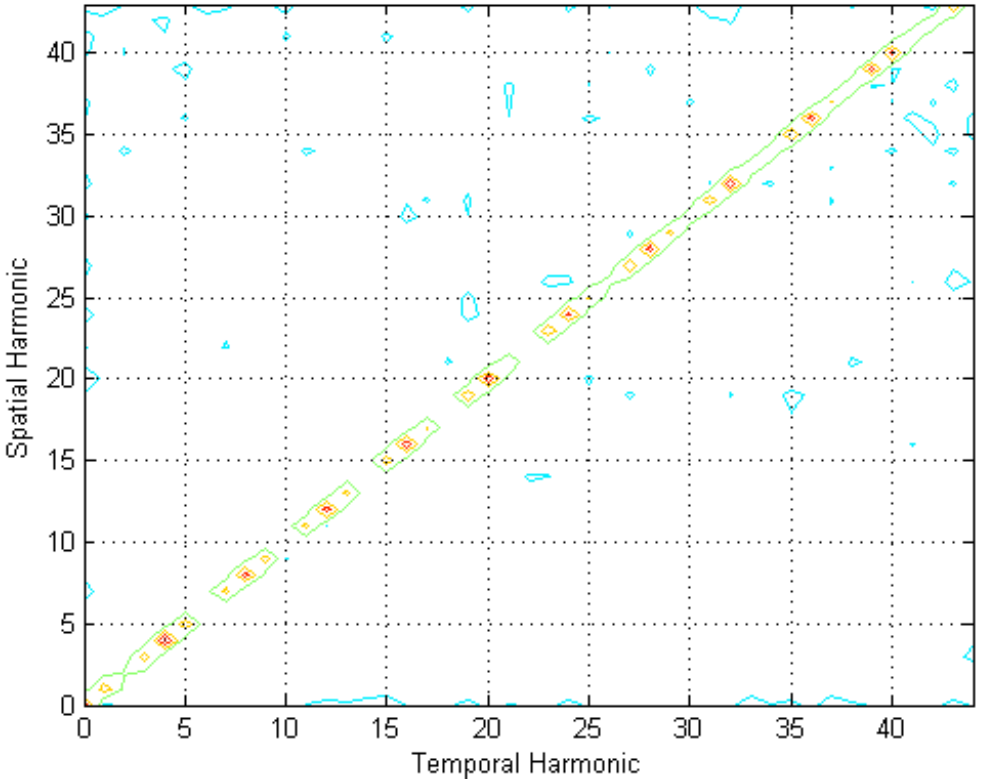

Figure 97: Stage 2 Contours of Tangential Maxwell Force

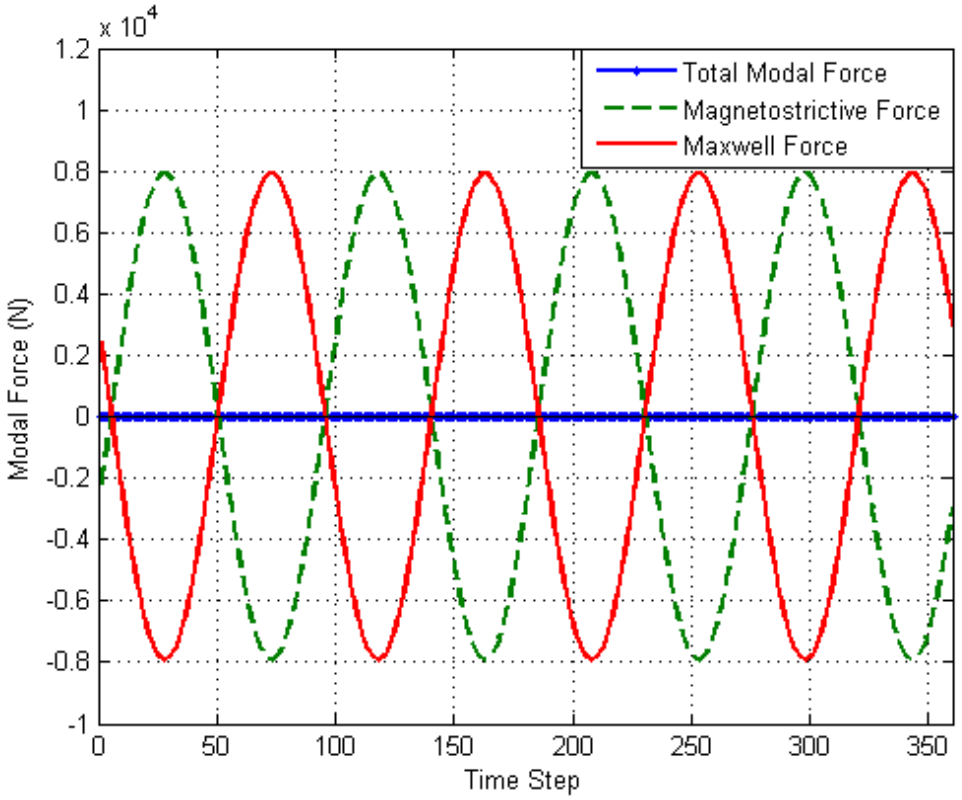

Figure 98: Modal Force from One n=4 Mode and Stage 2 Electromagnetic Force

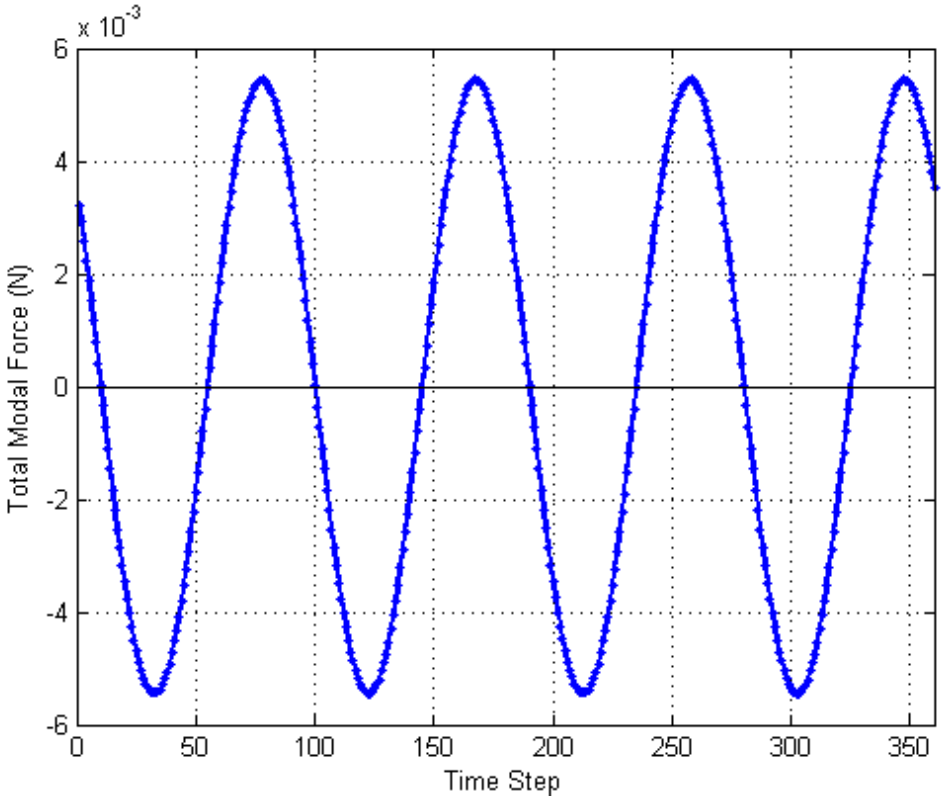

Figure 99: Total Modal Force from One n=4 Mode and Stage 2 Electromagnetic Force

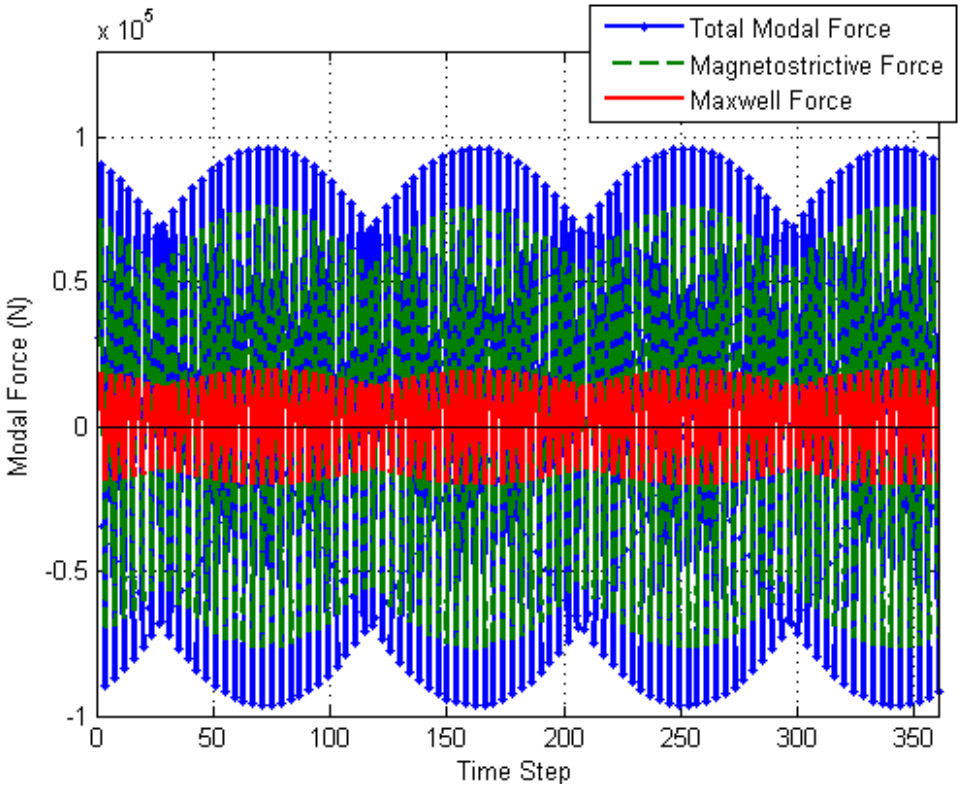

Figure 100: Modal Force from One n=1 Mode and Stage 2 Electromagnetic Force

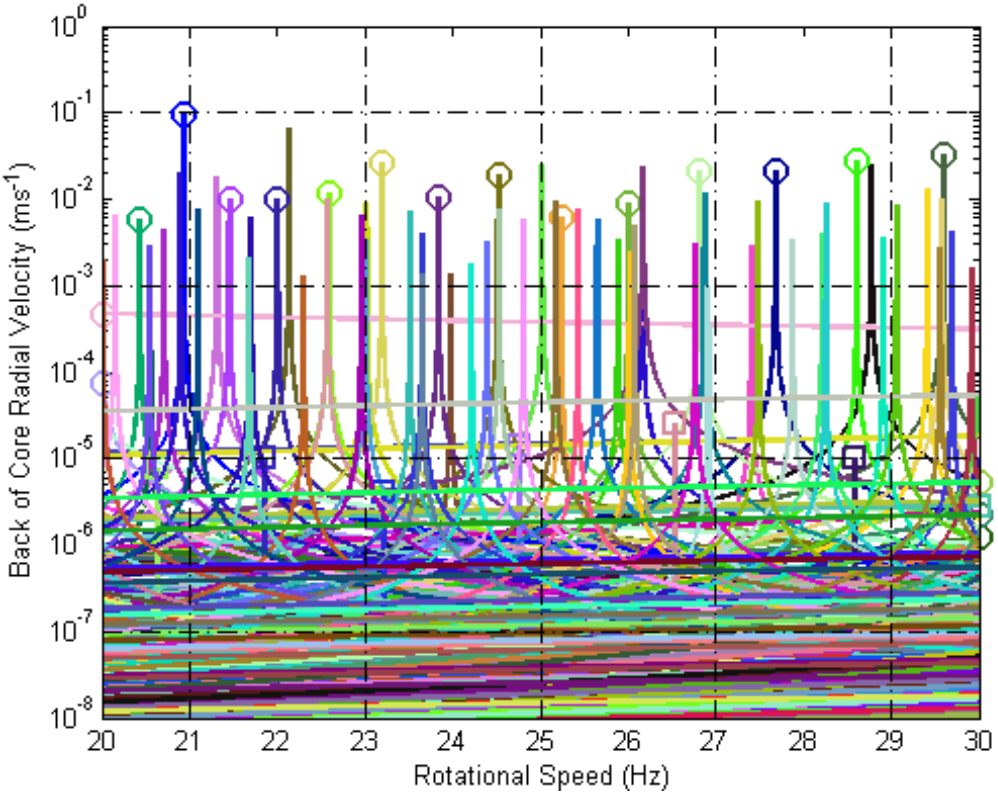

Figure 101: Stage 2 Vibration for Rotor Speeds Between $20Hz$ and $30Hz$ for all Combinations of Spatial and Temporal Harmonics

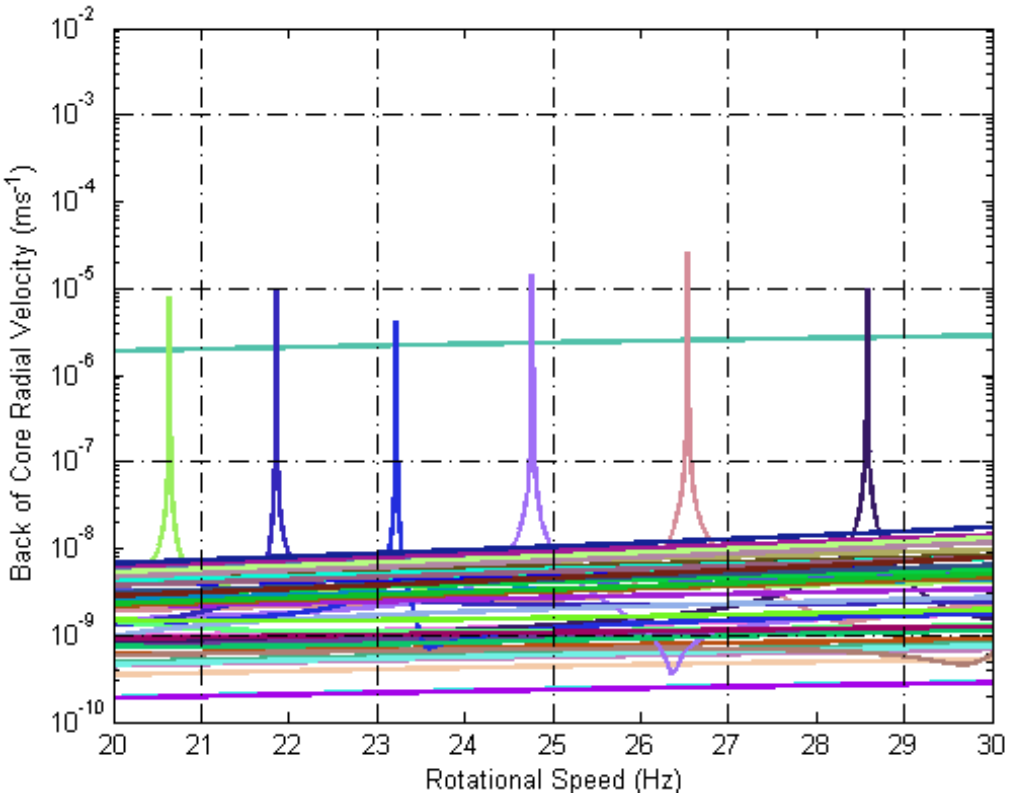

Figure 102: Response from n=4 Fourier Components of EM Forcing from Stage 2 Excitation

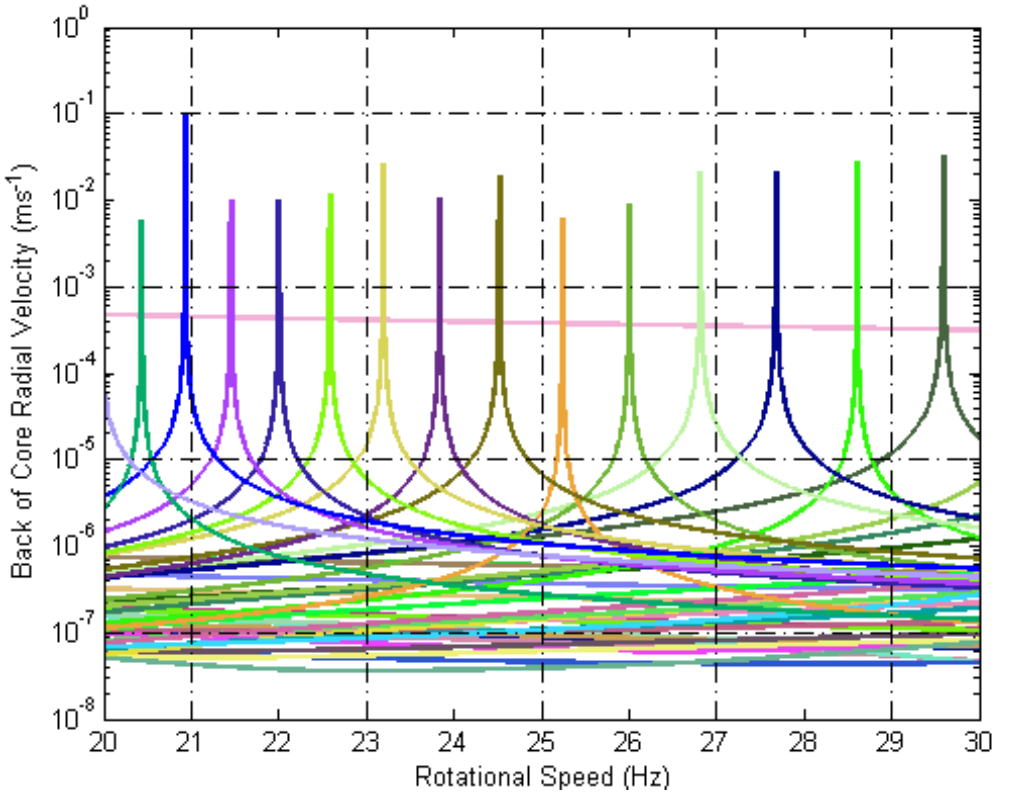

Figure 103: Response from n=1 Fourier Components of EM Forcing from Stage 2 Excitation

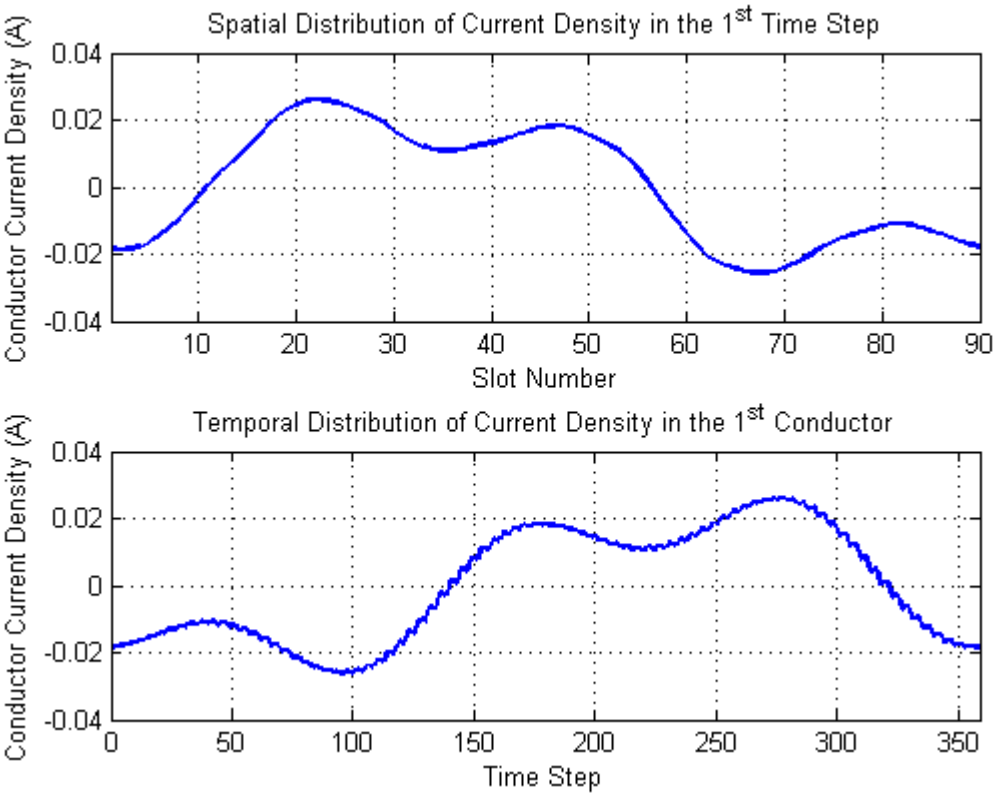

Figure 104: Stage 3 Bimorph Current Pattern

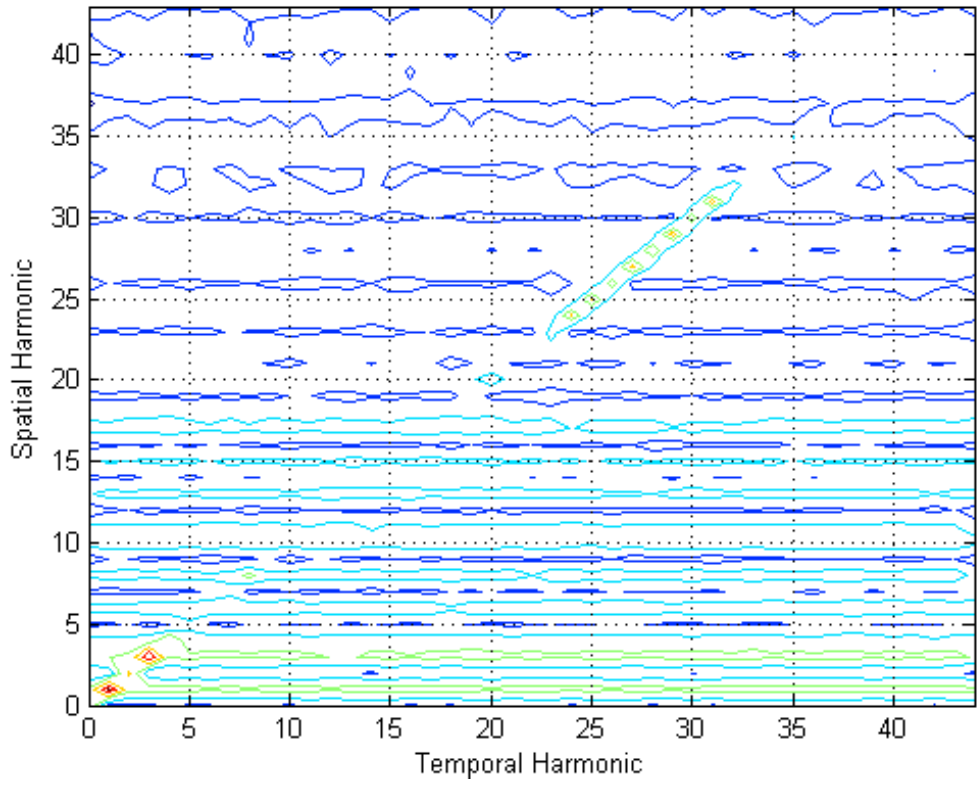

Figure 105: Stage 3 Spatial and Temporal Harmonics of Current Density

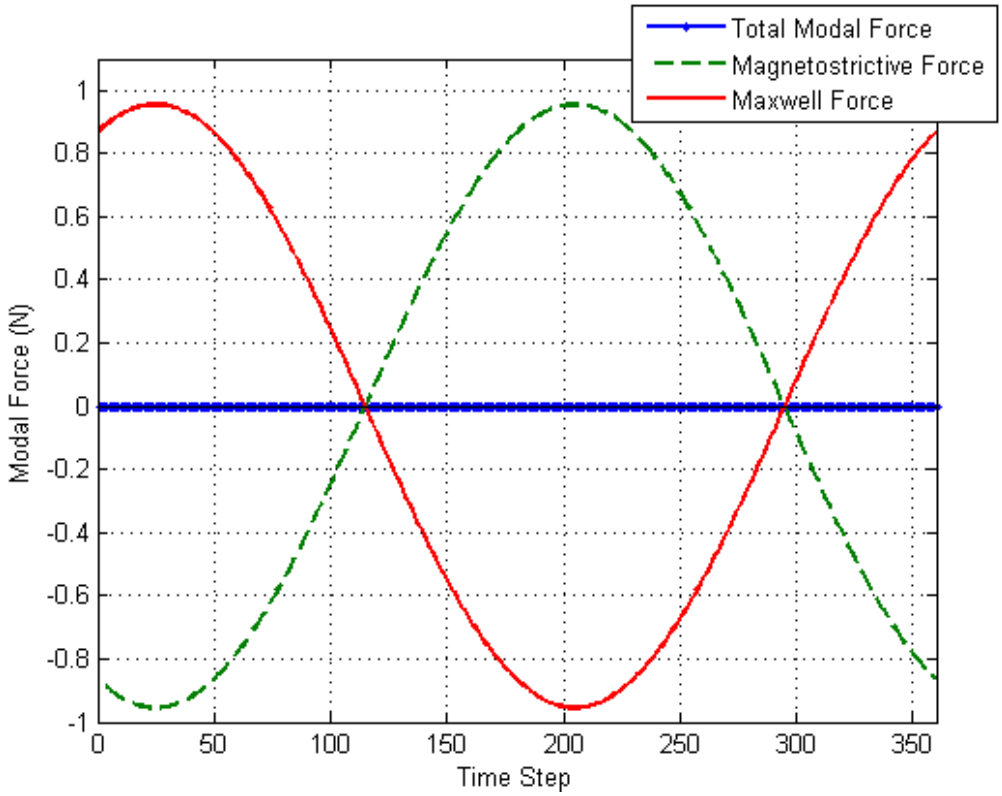

Figure 106: Modal Force from One n=1 Mode and Stage 3 Electromagnetic Force

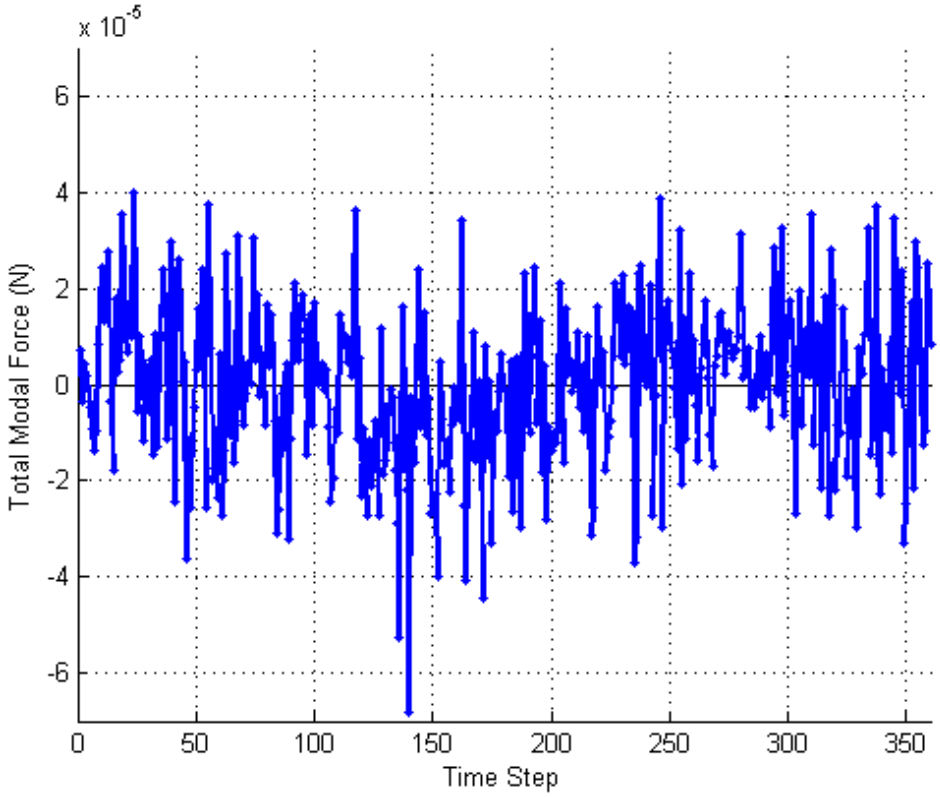

Figure 107: Total Modal Force from One n=1 Mode and Stage 3 Electromagnetic Force

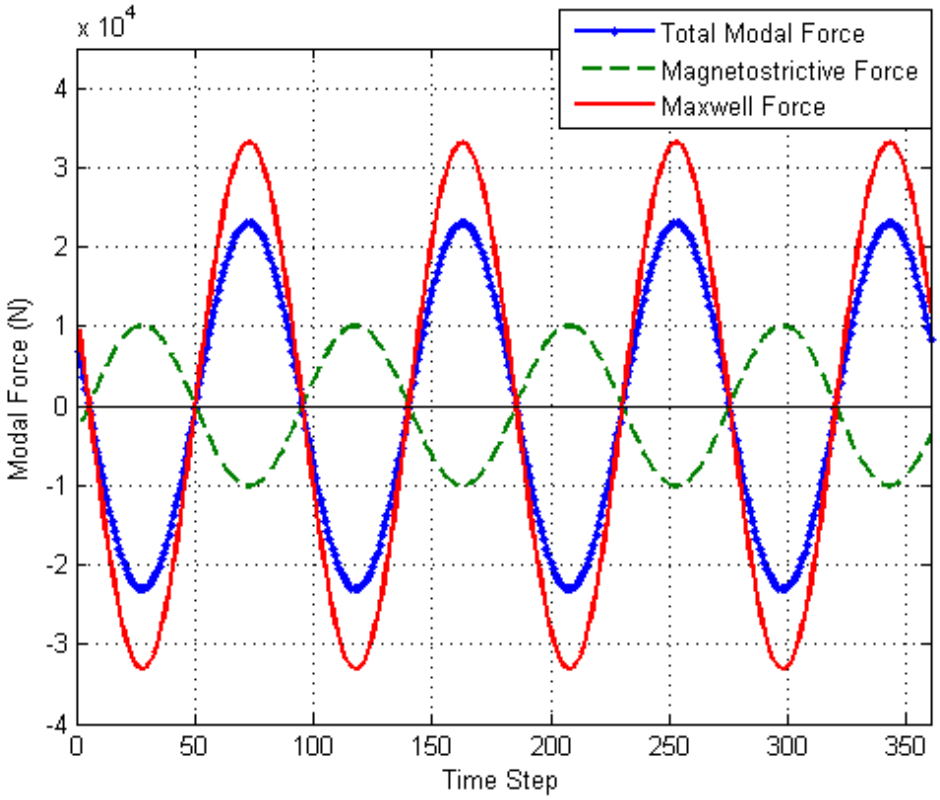

Figure 108: Modal Force from One n=4 Mode and Stage 3 Electromagnetic Force

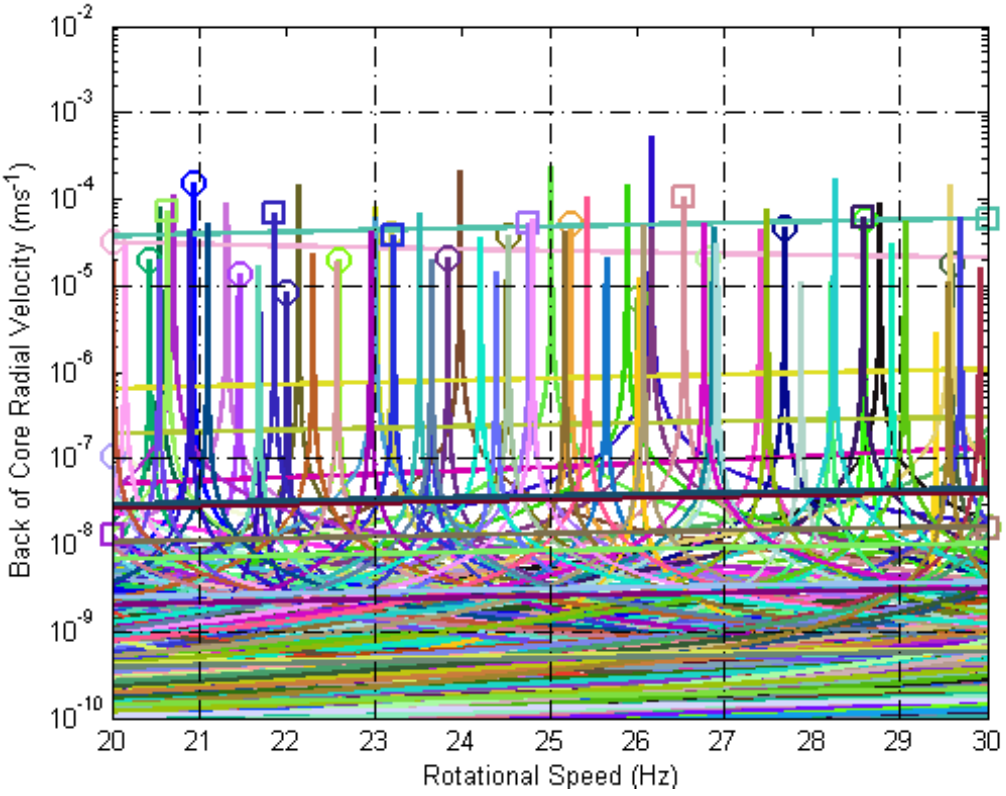

Figure 109: Stage 3 Vibration for Rotor Speeds Between $20Hz$ and $30Hz$ for all Combinations of Spatial and Temporal Harmonics

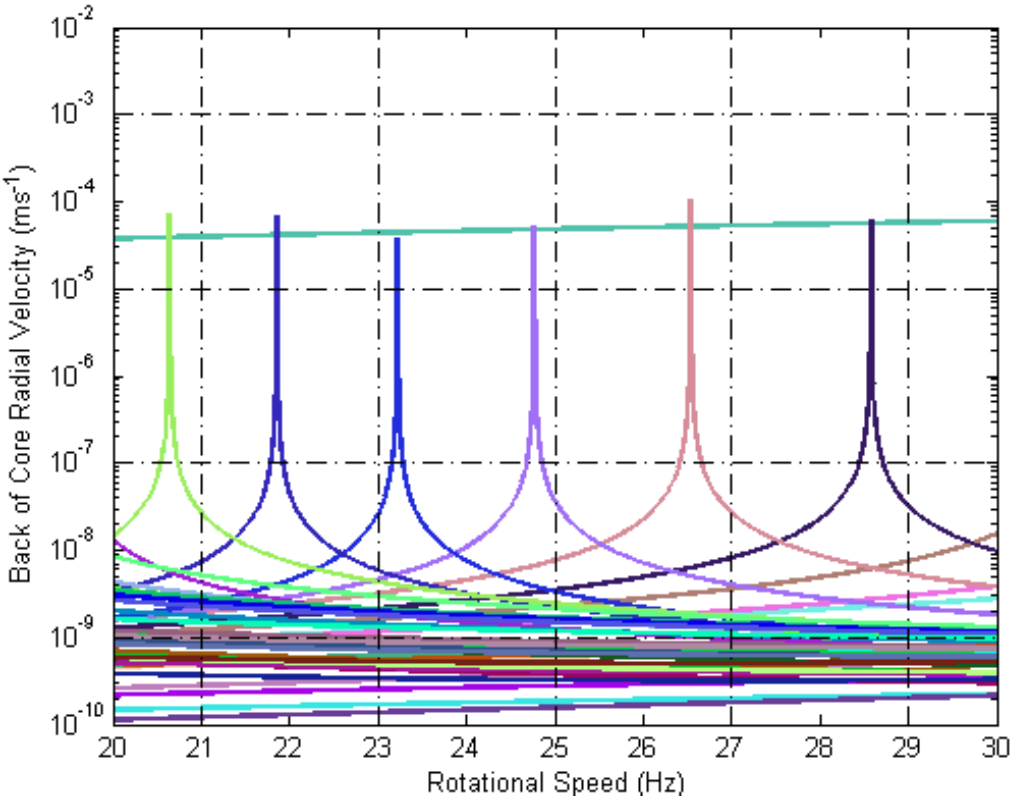

Figure 110: Response from n=4 Fourier Components of EM Forcing from Stage 3 Excitation

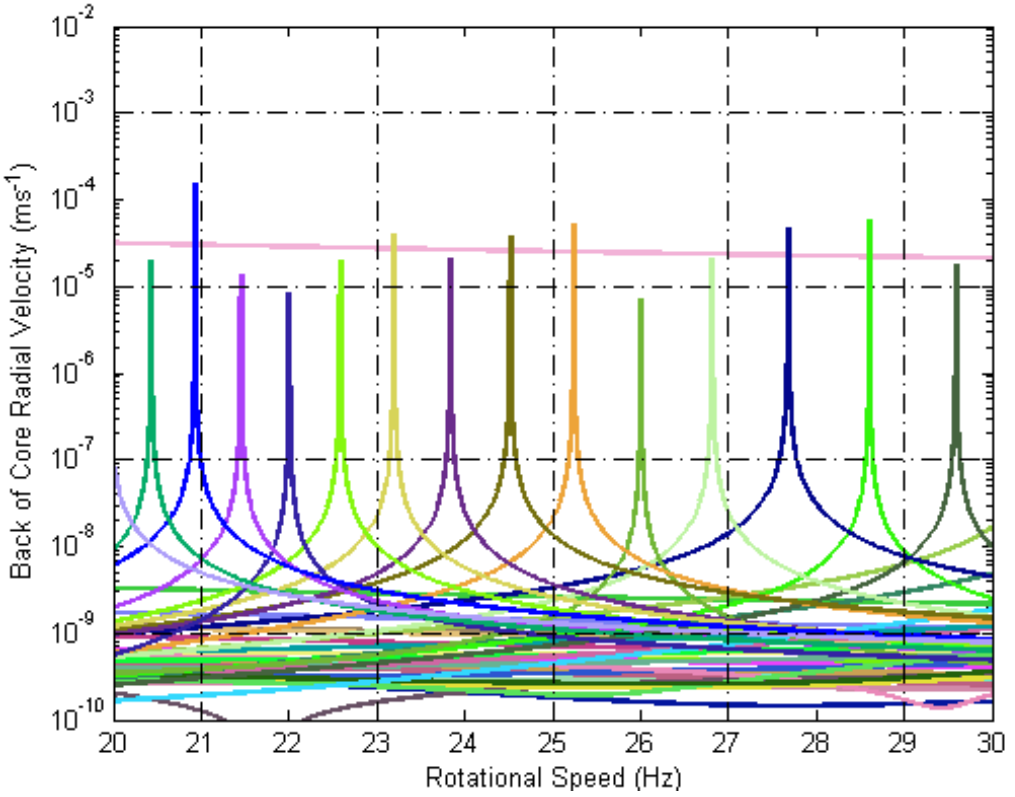

Figure 111: Response from n=1 Fourier Components of EM Forcing from Stage 3 Excitation

5 The Conclusion

5.1 Conclusion

The aim of this study was to investigate two new technologies in the field of noise and vibration in large electrical machines. The technologies that were investigated were individually controlled conductors ($ICCs$) and the *bimorph* effect. The main feature of the study was a 2D magneto-mechanical FE model of a large electrical machine. This model was used to understand the effects of the two technologies on the copper loss and vibration of a large machine. Two experimental investigations were also carried out. These investigated the practicality of the bimorph effect.

5.1.1 Sinusoidal Stator Excitation

A large electrical machine was modelled with a 2D magneto-mechanical FE model. Initially a four pole sinusoidal excitation pattern was supplied to the rotor and stator. The torque, mean-squared current, vibration of the back of the stator core and modal forcing on the first n=4 mode pair and first n=1 non rigid body mode pair were found. These values were used as benchmarks for comparison with the investigation of the ICC and bimorph concepts.

5.1.2 Individually Controlled Conductors

The individually controlled conductor method describes the use of individual conductors positioned in each stator slot with separate control over each conductor. This enhanced set of controls allows for higher versatility in the excitation pattern supplied to the stator of the machine than traditional polyphase excitation patterns. The construction of these conductors also replaces end windings with ring assemblies which reduce the source of much of the copper loss from traditionally wound machines.

This method has been investigated with a view to reducing the copper loss from the stator conductors and eliminating components of vibration. The investigation found that extra spatial and temporal harmonics of current can be included in the current pattern which tend to eliminate non-productive harmonics from the tangential component of Maxwell force and produce other harmonics that utilize saliency advantageously to generate torque. This results in a relatively low requirement for mean-squared stator current compared to a traditional sinusoidal current pattern. This current pattern is richer in harmonics than a sinusoidal current pattern and therefore produces extra components of electromagnetic force. The resulting vibration from the stator is increased by the application of these forces.

The investigation also utilized this method to eliminate the modal forces from the electromagnetic force and the first pair of n=4 modes. The torque was maintained and the copper loss was minimized. The direct vibration of the targeted modal forces was reduced. However, many extra harmonics were required in the current pattern and these led to many extra harmonics in the force and vibration of the stator. The overall level of vibration was much increased by this method and the mean-squared current that was required to achieve this result was much higher than the sinusoidal mean-squared current. This result has been caused by a large change in the current pattern from stage 1 in order to zero the n=4 component of force.

A suggestion for reducing the overall vibration of the system with the ICCs would be to manipulate the harmonics of current so that the unwanted component of force decreased by a small amount. The vibration caused by the other components of force would increase slightly. The minimum vibration level would occur when the vibration from the targeted component of force

equaled the vibration from the other components of force. This suggested method would reduce the overall vibration level slightly and would not increase the copper loss significantly.

Overall the ICC method is effective at minimizing the copper loss from the machine although this method has a detrimental effect on the vibration of the stator. The ICC method could be used for reducing the vibration of the machine very slightly. In applications where high efficiency is a priority the benefit that this method provides may outweigh the disadvantages of increased vibration.

5.1.3 The Bimorph Effect

The bimorph effect occurs in a ferromagnetic beam structure due to the magnetostriction effect. A longitudinal flux through the beam is affected by a current supplied to a conductor which is positioned through the beam perpendicular to the longitudinal axis. The magnetic flux from the conductor and the longitudinal magnetic flux interact to produce a magnetic field with higher flux density on one side of the beam than the other. A strain is produced in the beam due to magnetostriction associated with the magnetic flux. The value of strain is higher on one side of the beam than the other causing the beam to deflect. Controlling the combination of the longitudinal flux and the current in the conductor enables control of the motion of the beam.

Controlling the motion of the stator teeth by using the bimorph effect to reduce the vibration of an electrical machine is at least in one view, a vibration absorption technique. Vibration absorbers have been investigated in this study in order to provide the background information for this technology.

The bimorph effect can be implemented in electrical machines by inserting conductors through the root of each tooth and supplying current to each conductor individually. This affects the flow of magnetic flux through the machine so that the rocking motion of the teeth can be controlled. This effect can be utilized for vibration control of stator vibrations that involve a rocking motion of the teeth. This motion occurs at relatively high frequencies. The power required to excite the conductors is extremely low compared to the power supply to the field windings and the bimorph concept could provide an efficient means of vibration absorption in electrical machines with very few practical disadvantages.

Vibration modes exist at frequencies below tooth rocking frequency that do not include the tooth rocking motion. The bimorph effect cannot be used to control these lower frequency vibrations. The presence of unexcited bimorph conductors in the stator teeth has very little effect on the flow of flux through the teeth and so the existence of these conductors is not detrimental to the nominal running of the machine.

The bimorph effect was investigated with the magneto-mechanical FE machine model. The bimorph conductors were excited so that the modal force of the first n=1 non rigid body mode pair was cancelled. The investigation showed that the excitation required to achieve this vibration suppression was relatively low. This level of excitation reduced the responses of the required resonances and did not significantly affect the torque. Many other resonances were excited in the speed range considered that were not dominated by n=1 modes. The responses of these were affected only slightly so that over the speed range considered the level of vibration with the bimorph conductors was lower than without. The uncontrolled responses could not

be reduced with the bimorph effect because none of the corresponding deflected shapes included substantial tooth rocking motion.

The bimorph effect was investigated with two experiments. A single stator tooth rig was developed to represent the bimorph effect on a single stator tooth. Field and bimorph windings on the rig were excited and the resulting motion of the rig was recorded. This investigation proved that the motion of a stator tooth can be caused by the current in the bimorph conductors. Another experiment was carried out on a small electrical machine with bimorph conductors threaded through the root of the stator teeth. The experiment showed that the magnetic field from a small supply current to the bimorph conductors can cancel out the vibration caused by the magnetic field from the stator windings with little effect on the air gap mmf.

The FE model has shown that theoretically the bimorph concept is an effective, efficient method of achieving vibration suppression in large electrical machines. The experimental investigations have illustrated that this concept is also practical to implement. The method effectively suppresses stator resonances that are governed by the tooth rocking motion. This method does not completely suppress all vibration components but it also does not introduce any detrimental effects into the machine operation. When used in conjunction with the ICC method for minimizing copper loss the result is a highly efficient machine with reduced vibration levels compared to operation under the same ICC method with no bimorph control.

5.2 Further Work

5.2.1 The Bimorph Concept

The magnetic bimorph concept is an entirely new idea for the control of electrical machine vibration. This investigation provides the only study

into this effect. Further work is needed to fully authenticate this idea and bring it to realization as a vibration control method.

The next major step should be a demonstration that illustrates every aspect related to implementation of the magnetic bimorph concept. This will involve an electrical machine with individual bimorph conductors in each stator tooth root. The bimorph conductors should be controlled to cancel the vibration of the machine. In order to achieve this a relatively large machine will be required in order to excite the rocking motion of the stator teeth. Control to each of the bimorph conductors needs to be developed so that the input to the conductors efficiently and effectively cancels the vibration of the machine. Sensor and control techniques need to be investigated in order to implement the most effective method. The tooth flux and back of core displacement would ideally need to be known for each tooth in order to implement the required control. The effect of the bimorph controls on the different running conditions of the machine should be investigated including start up and shut down and different speed and load levels.

A detailed model of this machine is also required in order to carry out an in-depth FE investigation of the demonstration. The vibration of the machine needs to be predicted and investigated without bimorph control. Three dimensions and eddy currents could be included in more computationally intense models.

5.2.2 Individually Controlled Conductors

The ICC method has proved to be an effective method for increasing machine efficiency with the modelling techniques used. The modelling techniques should be developed further in order to appreciate the effectiveness of this technology with particular constructions of electrical machine.

The ICC method relies on the saliency of the machine. Saliency is affected by saturation and rotor and stator geometry. Different types of rotor could be investigated so that the effect of rotor geometry can be seen.

The effect of saturation on copper loss could be investigated. Saturation can be modelled by rounding the corners of the stator and rotor teeth. In the investigation presented here, the relative permeability of the rotor teeth was decreased significantly compared to that of iron. The effect of the decreased permeability is similar to the effect of rotor teeth that are saturated and so modelling saturation in the rotor is unlikely to change the results significantly. By including saturation in the stator model it is expected that the reduction of copper loss in the machine will not be as dramatic as shown when saturation is neglected.

An induction machine could not be modelled effectively in this study as induced rotor currents were not included. The reduced mean-squared current that is enabled with the ICC method affects the magnetic field and the induced rotor currents. Therefore induced currents should be included in order to appreciate fully the affect that this change in current pattern has on the overall operation of the machine.

5.2.3 Modal Force Cancellation

The study reported here achieved vibration suppression by cancellation of specific spatial harmonics of modal force. The modal forces were considered in the time domain. This had the effect of cancelling all of the temporal harmonics of force for each spatial harmonic of force that was targeted. An alternative method to this would be to cancel specific temporal harmonics as well as spatial harmonics of force. In order to achieve this, the modal

force would be considered in the frequency domain. This would involve a set of scalar equations:

$$\int_{t=0}^{t=T} \mathbf{f}(t)^\top \mathbf{v_1} \cos(\frac{2\pi t m}{T}) dt = 0$$
$$\int_{t=0}^{t=T} \mathbf{f}(t)^\top \mathbf{v_1} \sin(\frac{2\pi t m}{T}) dt = 0$$
$$\int_{t=0}^{t=T} \mathbf{f}(t)^\top \mathbf{v_2} \cos(\frac{2\pi t m}{T}) dt = 0$$
$$\int_{t=0}^{t=T} \mathbf{f}(t)^\top \mathbf{v_2} \sin(\frac{2\pi t m}{T}) dt = 0$$

where t is time, T is the time period, $\mathbf{f}$ is the electromagnetic force, $\mathbf{v_1}$ is a symmetric mode, $\mathbf{v_2}$ is an anti-symmetric mode and m is the temporal harmonic under consideration. The four equations would exist for every time step and these hundreds of equations would need to be solved. The computation of this would be intense. However, this approach is likely to lead to improved results compared to the results that have been presented here because the modal force under consideration would cancel the single required combination of temporal and spatial harmonics of force rather than all temporal harmonics of force for each single spatial harmonic of force.

References

[1] Philip L Alger and Edward Erdelyi. Calculation of the Magnetic Noise of Polyphase Induction Motors. *The Journal of the Acoustical Society of America*, 28(6):1063–1067, 1956.

[2] George B Arfken and Hans J Weber. *Mathematical Methods for Physicists*. Elsevier Academic Press, Burlington, USA, sixth edition, 2005.

[3] Malcolm Barnes. *Variable Speed Drives and Power Electronics*. Practical. Newnes Publications, Oxford, 2003.

[4] C Bastiaensen, W Deprez, J Driesen, and R Belmans. Influence of Parameter Distributions on Electromechanical Torque of Induction Motors. In *3rd IEEE Benelux Young Researchers Symposium in Electrical Power Engineering*, Ghent, Belgium, 2006. IEEE.

[5] Anouar Belahcen. Magnetoelastic Coupling and Rayleigh Damping. *COMPEL: The International Journal for Computation and Mathematics in Electrical and Electronic Engineering*, 23(3):647–654, 2004.

[6] Anouar Belahcen. *Magnetoelasticity, Magnetic Forces and Magnetostriction in Electrical Machines*. PhD thesis, Helsinki University of Technology, 2004.

[7] Anouar Belahcen. Vibrations of Rotating Electrical Machines Due to Magnetomechanical Coupling and Magnetostriction. *IEEE Transactions on Magnetics*, 42(4):971–974, 2006.

[8] R Belmans, K J Binns, W Geysen, and A Vandenput. *Vibrations and Audible Noise in Alternating Current Machines*, volume 148 of *Nato Advanced Science Institutes Series, Series E: Applied Sciences*. Kluwer Academic Publishers, Dordrecht, 1988.

[9] Ronnie Belmans, Wim Deprez, and Ozdemir Gol. Increasing Induction Motor Drives Efficiency: Understanding the Pitfalls. In *Proceedings of Electrotechnical Institute*, pages 7–25, Warsaw, Poland, 2005.

[10] M E H Benbouzid, G Reyne, S Derou, and A Foggia. Finite Element Modelling of a Synchronous Machine: Electromagnetic Forces and Mode Shapes. *IEEE Transactions on Magnetics*, 29(2):2014 – 2018, 1993.

[11] Abhijit Bhattacharyya, James Brown, Sheldon Samborsky, Lyle Sweeney, Osmar Zaiane, Kevin Andrusky, Marta Gawel, and Chelsea Rieger. S.M.A/M.E.M.S Research Group, University of Alberta, 2001 http://www.cs.ualberta.ca/ database/MEMS/sma_mems/sma.html.

[12] Robert Raymond Birss. *The Magnetostriction of Some Ferromagnetic Metals*. PhD thesis, University of Nottingham, 1958.

[13] Bimal Bose. *Power Electronics and Motor Drives*. Advances and Trends. Academic Press, Burlington, 2006.

[14] M J Brennan, J Garcia-Bonito, S J Elliott, A David, and R J Pinnington. Experimental Investigation of Different Actuator Technologies for Active Vibration Control. *Smart Materials and Structures*, 8:145–153, 1999.

[15] John E Brock. A Note on the Damped Vibration Absorber. *Journal of Applied Mechanics*, 68:A284, 1946.

[16] R M Calfo, J A Fulmer, and J E Tessara. Generators for Use in Electric Marine Ship Propulsion Systems. In *Power Engineering Society Summer Meeting*, volume 1, pages 254–259. IEEE, 2002.

[17] Stefan Laurentiu Capitaneanu, Bernard de Fornel, Maurice Fadel, and Fabrice Jadot. On the Acoustic Noise Radiated by PWM A.C Motor Drives. *AUTOMATIKA*, 44(3):137 – 145, 2003.

[18] Bertrand Cassoret, Rodolphe Corton, Daniel Roger, and Jean-Francois Brudny. Magnetic Noise Reduction of Induction Machines. *IEEE Transactions on Power Electronics*, 18(2):570–579, 2003.

[19] S C Chang and R Yacamini. Experimental Study of the Vibrational Behaviour of Machine Stators. *IEE Procedings Electric Power Applications*, 143(3):242–250, 1996.

[20] Yi-De Chen, Chyun-Chau Fuh, and Pi-Cheng Tung. Application of Voice Coil Motors in Active Dynamic Vibration Absorbers. *IEEE Transactions on Magnetics*, 41(3):1149 – 1154, 2005.

[21] F Claeyssen, N Lhermet, and T Maillard. Magnetostrictive Actuators Compared to Piezoelectric Actuators. *European Workshop on Smart Structures in Engineering and Technology*, 4763(1):194–200, 2003.

[22] www.converteam.com Converteam: The Power Conversion Company.

[23] Allan David Crane. Rotary Electrical Machines, Converteam Ltd, US patent application US 2003/0178896, 2003.

[24] K Delaere, W Heylen, R Belmans, and K Hameyer. Strong Magneto-mechanical F.E Coupling Using Local Magnetostriction Forces. *The European Journal of Applied Physics*, 13(2):115–119, 2001.

[25] Koen Delaere, J Fransen, Kay Hameyer, and Ronnie Belmans. Manufacturing Tolerances as a Cause for Audible Noise of Induction Motors. In *International Seminar on Vibrations and Acoustic Noise of Electric Machinery*, pages 223–227, Bethune, France, 1998.

[26] Koen Delaere, Kay Hameyer, and Ronnie Belmans. Static Eccentricity as a Cause for Audible Noise of Induction Motors. In *Proceedings of the International Conference on Electrical Machines*, volume 1, pages 502–506, Istanbul. Turkey, 1998.

[27] Koen Delaere, Kay Hameyer, and Ronnie Belmans. Local Magnetostriction Forces for Finite Element Analysis. *IEEE Transactions on Magnetics*, 36(5):3115–3118, 2000.

[28] Koen Delaere, Ward Heylen, Ronnie Belmans, and Kay Hameyer. Comparison of Induction Machine Stator Vibration Spectra Induced by Reluctance Forces and Magnetostriction. *IEEE Transactions on Magnetics*, 38(2):969–972, 2002.

[29] Koen Delaere, Ward Heylen, Kay Hameyer, and Ronnie Belmans. Strong Coupling of Magnetic and Mechanical Finite Element Analysis. *Journal of Magnetism and Magnetic Materials*, 226-230 part 2:1226–1228, 2001.

[30] Koen Delaere, Michele Iadevaia, Ward Heylen, Ronnie Belmans, and Kay Hameyer. Finite Element Analysis of Electrical Machine Vibrations Caused by Lorentz, Maxwell and Magnetostriction Forces. In *IEE Seminar on Current Trends in the Use of Finite Elements (FE) in Electromechanical Design and Analysis*, pages 9/1–9/4, London, UK, 2000. IEE.

[31] Koen Delaere, Michele Iadevaia, Paul Sas, Ronnie Belmans, and Kay Hameyer. Coupling of Numerical Magnetic and Experimental Vibration Analysis for Electrical Machines. In *3rd Chinese International Conference on Electrical Machines. Edition 3*, pages 475 – 478, Xian, China, 1999.

[32] Koen Delaere, Paul Sas, Ronnie Belmans, and Kay Hameyer. Weak Coupling of Magnetic and Vibrational Analysis Using Local Forces. In *IEEE International Electric Machines and Drives Conference. IEMDC'99*, pages 514–516, Seattle, WA, USA, 1999. IEEE.

[33] J P Den Hartog. Vibration of Frames of Electrical Machines. *Transactions of the ASME*, APM-50-6, 1927.

[34] J P Den Hartog. Vibration of Frames of Electrical Machines. *Transactions of the ASME*, APM-50-11, 1928.

[35] J P Den Hartog. *Mechanical Vibrations*. McGraw-Hill Book Company, 4th edition, 1956.

[36] W Deprez, A Dexters, C Bastiaensen, F Parasiliti, and R Belmans. Induction Machine Efficiency in Four Quadrants. In *EEMODS '07: Energy Efficiency in Motor Driven Systems*, Beijing, China, 2007.

[37] M Didden, J Driesen, and Ronnie Belmans. Possible Problems and Solutions When Introducing Variable Speed Drives. In *EEMODS*, Treviso, Italy, 2002.

[38] C Dingyue, L Xia, C Hongsheg, X Hui, and D Jianjia. Study of Vibration Suppression in Discrete Domain. *Acta Mechanica*, 158(1-2):57–66, 2002.

[39] David G Dorrell, Mircea Popescu, and Malcolm I McGilp. Torque Calculation in Finite Element Solutions of Electrical Machines by Consideration of Stored Energy. *IEEE Transactions on Magnetics*, 42(10):3431–3433, 2006.

[40] Nelson Dunford and Jacob T Schwartz. *Linear Operators Part 1: General Theory*, volume 7 of *Pure and Applied Mathematics. A Series of Texts and Monographs*. Interscience Publishers Inc, New York, 1958.

[41] N B Ekreem, A G Olabi, T Prescott, A Rafferty, and M S J Hashmi. An Overview of Magnetostriction, Its Use and Methods to Measure These Properties. *Journal of Materials Processing Technology*, 191(1-3):96 – 101, 2007.

[42] Electric Power Generators Electronics Information Online. Http://www.electronics-manufacturers.com/info/electrical-components/electric-power-generators.html, 2006.

[43] A J Ellison and C J Moore. Acoustic Noise and Vibration of Rotating Electric Machines. *Proceedings of the IEE*, 115(11):1633–1640, 1968.

[44] A J Ellison and S J Yang. Natural Frequencies of Stators of Small Electric Machines. *Proceedings of the IEE*, 118(1):185–190, 1971.

[45] Hakan Elmali, Mark E Renzulli, and Nejat Olgac. Experimental Comparison of Delayed Resonator and PD Controlled Vibration Absorbers Using Electromagnetic Actuators. *Journal of dynamic systems, measurement, and control*, 122(3):514–520, 2000.

[46] A A Fahim, T A Lipo, and C J Slavik. Electromagnetic Model for Evaluation of Flux Harmonics and Resulting Magnetic Forces in Induction Motors. In *Sixth International Conference on Electrical Machines and Drives (Conference Publication Number 376)*, London, UK, 1993. IEE.

[47] William R Finley, M M Hodowanec, and W G Holter. An Analytical Approach to Solving Motor Vibration Problems. *IEEE Transactions on Industry Applications*, 363(5), 1999.

[48] M I Friswell, S D Garvey, and J E T Penny. Model Reduction Using Dynamic and Iterated IRS Techniques. *Journal of Sound and Vibration*, 186(2):311–323, 1995.

[49] M I Friswell, J E Penny, S D Garvey, and A W Lees. *Dynamics of Rotating Machines*. Cambridge University Press, 2009.

[50] C R Fuller, S J Elliott, and P A Nelson. *Active Control of Vibration*. Academic Press Limited, London, 1996.

[51] C R Fuller and A H Von Flotow. Active Control of Sound and Vibration. *Control Systems Magazine, IEEE*, 15(6):9–19, December 1995.

[52] Aurel Galantai. *Projectors and Projection Methods*, volume 6 of *Advances in Mathematics*. Kluwer Academic Publishers, Boston, 2004.

[53] Bruce Gamble. Super Conductor Motors for High Speed Ship Propulsion. *American Superconductor, Sea Technology*, 2005.

[54] S D Garvey and C N Glew. Magnetostrictive Excitation of Vibration in Machines -. A Modal Approach. In *Ninth International Conference on Electrical Machines and Drives*, Canterbury Christ Church College, UK, 1999. IEE.

[55] S D Garvey, J E Penny, M I Friswell, and C N Glew. Modelling the Vibrational Behaviour of Stator Cores of Electrical Machines with a View to Successfully Predicting Machine Noise. Digest No: 1997/166. In *IEE Colloquium on Modeling the Performance of Electrical Machines*, pages 3/1–3/13, Savoy Place, London, 1997. IEE.

[56] Jacek F Gieras, Chong Wang, and Joseph Cho Lai. *Noise of Polyphase Electric Motors*. Electrical and Computing Engineering. CRC Press, Columbus, 2006.

[57] R S Girgis and S P Verma. Method for Accurate Determination of Resonant Frequencies and Vibration Behaviour of Stators of Electrical Machines. *Electric Power Applications, IEE Proceedings B*, 128(1):1–11, 1981.

[58] Victor Giurgiutiu, Craig A Rogers, and Zaffir Chaudhry. Energy-Based Comparison of Solid-State Induced-Strain Actuators. *Journal of Intelligent Material Systems and Structures*, 7(1):4–14, 1996.

[59] B L Goss. Electric Motor Noise: Control of Noise at the Source. *American Industrial Hygiene Association Journal*, pages 16–21, 1970.

[60] Hanifi Guldemir. Detection of Airgap Eccentricity Using Line Current Spectrum of Induction Motors. *Electric Power Systems Research*, 64:109–117, 2003.

[61] Robert J Guyan. Reduction of Stiffness and Mass Matrices. *American Institute of Aeronautics and Astronautics Journal*, 3(2):380, 1965.

[62] K Hameyer and R Belmans. *Numerical Modelling and Design of Electrical Machines and Devices*, volume 1 of *Advances in Electrical and Electronic Engineering*. WIT Press, Southampton, 1999.

[63] Kay Hameyer. Numerical Techniques for Electrical Machines: A Personal View. *ELECTROMOTION*, 7:115–126, 2000.

[64] Kay Hameyer, Francois Henrotte, and Koen Delaere. Electromagnetically Excited Audible Noise in Electrical Machines. *Journal of KSNVE*, 13(2):109–118, 2003.

[65] Simon G Hill and Scott D Snyder. Design of an Adaptive Vibration Absorber to Reduce Electrical Transformer Structural Vibration. *Journal of Vibration and Acoustics*, 124(4):606–611, 2002.

[66] Kenneth H Huebner, Earl A Thornton, and Ted G Byrom. *The Finite Element Method for Engineers*. John Wiley and Sons Inc, New York, third edition, 1995.

[67] Douglas Ivers, Robert Wilson, and Donald Margolis. Whirling-Beam Self-Tuning Vibration Absorber. *Journal of Dynamic Systems, Measurement, and Control*, 130(3):031009–1–031009–11, 2008.

[68] Nader Jalili. A Comparative Study and Analysis of Semi-Active Vibration-Control Systems. *Journal of Vibration and Acoustics*, 124(4):593 – 605, 2002.

[69] G H Jang and D K Lieu. The Effect of Magnet Geometry on Electric Motor Vibration. *IEEE Transactions on Magnetics*, 27(6):5202 – 5204, 1991.

[70] Karuna Kalita. *Integrating Rotodynamic and Electromagnetic Dynamic Models for Flexible-Rotor Electrical Machines*. PhD thesis, University of Nottingham, 2007.

[71] Katsumi Kamimoto, Fuminori Ishibashi, Shinichi Noda, Shunji Yanase, and Tadashi Sasaki. Magnetostriction and Motor Vibration. *Electrical Engineering in Japan*, 148(2):8–13, 2004.

[72] M R F Kidner and M J Brennan. Varying the Stiffness of a Beam-Like Neutralizer under Fuzzy Logic Control. *Journal of Vibration and Acoustics*, 124(1):90–99, 2002.

[73] K P Kovacs. Two-Pole Induction-Motor Vibrations Caused by Homopolar Alternating Fluxes. *IEEE Transactions on Power Apparatus and Systems*, 96(4):1105 – 1108, 1977.

[74] Alois Kufer and Jan Kadlec. *Fourier Series*. The Butterworth Group and co. (publishers) ltd, London, 1st edition, 1971.

[75] Byeong Woo Lee and Eon Jong Lee. Effects of Complex Doping on Microstructural and Electrical Properties of PZT Ceramics. *Journal of Electroceram*, 17:597–602, 2006.

[76] Eric Walter Lee. *The Magnetostriction of Ferromagnetic Alloys*. PhD thesis, The University of Nottingham, 1952.

[77] Jie Liu, Kefu Liu, and Hao Bai. Application of a Time-Delayed Control System in Vibration Suppression. In *International Conference on Mechatronics and Automation*, volume 1, pages 230 – 235, Niagara Falls, Canada, 2005. IEEE.

[78] Kefu Liu and Jie Liu. The Damped Dynamic Vibration Absorbers: Revisited and New Results. *Journal of Sound and Vibration*, 284:1181–1189, 2005.

[79] C May, K Kuhnen, P Pagliarulo, and H Janocha. Magnetostrictive Dynamic Vibration Absorber (D.V.A) for Passive and Active Damping. In *Euronoise*, Naples, 2003.

[80] O A Mohammad. Numerical Prediction of Magnetostrictive Behaviour in Non-Oriented Electrical Steel Sheets. In *Southeast Conference*, pages 179–182, Clemson, SC, USA, 2001. IEEE.

[81] O A Mohammad, T Calvert, and R McConnell. Coupled Magnetoelastic Finite Element Formulation Including Anisotropic Reluctivity Tensor and Magnetostriction Effects for Machinery Applications. *IEEE Transactions on Magnetics*, 37(5):3388 – 3392, 2001.

[82] J Muster, P K Budig, R Belmans, W Geysen, and P K Sattler. Audible Noise in Speed-Controlled Inverter-Fed Medium-Sized Induction Motors. *ETEP*, 5(1):5 – 13, 1995.

[83] Joe Nevelsteen. Vibrations, Causes and Effects on Large Electric Motors. In *IEEE 25th Annual Petroleum and Chemical Industry Conference*, pages 214–217, Tulsa, Oklahoma, USA, 1978.

[84] Eiichi Nishida and G H Koopmann. A Method for Designing and Fabricating Broadband Vibration Absorbers for Structural Noise Control. *Journal of Vibration and Acoustics*, 129:397–405, 2007.

[85] Nejat Olgac and B T Holm-Hansen. A Novel Active Vibration Absorption Technique: Delayed Resonator. *Journal of Sound and Vibration*, 176(1):93 – 104, 1994.

[86] Mehmet Bulent Ozer and Thomas J Royston. Extending Den Hartog's Vibration Absorber Technique to Multi-Degree-of-Freedom Systems. *Journal of Vibration and Acoustics*, 127(4):341–350, 2005.

[87] PAFEC. *Theory Manual*. PAFEC Limited, Strelley Hall, Strelley, Nottingham, 1984.

[88] Mircea Popescu. Prediction of the Electromagnetic Torque in Synchronous Machines through Maxwell Stress Harmonic Filter (HFT) Method. *Electrical Engineering*, 89(2):117–125, 2006.

[89] Andre Preumont. *Responsive Systems for Active Vibration Control*, volume 85 of *N.A.T.O Science Series. Series 2: Mathematics, Physics and Chemistry*. IOS Press, Amsterdam Kluwer Academic Publishers, Amsterdam, 2002.

[90] Jingqiu Qiao and William Cai. Calculation and Error Analysis of Electromagnetic Torque for a Wheel Permanent-Magnet Motor. *IEEE Transactions on Industry Applications*, 42(5):1155 – 1161, 2006.

[91] Mark E Renzulli, Rajiv Ghosh-Roy, and Nejat Olgac. Robust Control of the Delayed Resonator Vibration Absorber. *IEEE Transactions on Control Systems Technology*, 7(6):683 – 691, 1999.

[92] B Slaets, P Van Roy, and R Belmans. Determining the Efficiency of Induction Machines, Converters and Softstarters. *ELECTROMOTION*, 7(2):73 – 80, 2000.

[93] A C Smith, S Williamson, and C G Hodge. High Torque Dense Naval Propulsion Motors. In *Electric Machines and Drives Conference IEMDC*, volume 3, pages 1421 – 1427. IEEE, 2003.

[94] J Q Sun, M R Jolly, and M A Norris. Passive, Adaptive and Active Vibration Absorbers: A Survey. *Journal of Mechanical Design*, 117(B):234–242, 1995.

[95] D L Thomas. Dynamics of Rotationally Periodic Structures. *International Journal For Numerical Methods in Engineering*, 14(1):81–102, 1979.

[96] E G Thomas and A J Meadows. *Maxwell's Equations and Their Applications*. Student Monographs in Physics. Adam Hilger Ltd, Sussex, 1st edition, 1985.

[97] Laszlo Peregrin Timar. Recent Trends in the Noise and Vibration Investigations of Asynchronous Motors. *Periodica Polytechnica*, 27(3-4):259–266, 1983.

[98] Alessandro Torello. Update: EU Mins Propose Global CO2 Cuts for Aviation, Shipping, The Wall Street Journal, 21st October 2009.

[99] Manish T Valoor, K Chandrashekhara, and Sanjeev Agarwal. Self-Adaptive Vibration Control of Smart Composite Beams Using Recurrent Neural Architecture. *International Journal For Solids and Structures*, 38:7857–7874, 2001.

[100] S P Verma. Noise and Vibrations of Electrical Machines and Drives; Their Production and Means of Reduction. In *Proceedings of the 1996 International Conference on Power Electronics, Drives and Energy Systems for Industrial Growth*, volume 2, pages 1031–1037, New Delhi, India, 1996. IEEE.

[101] Huan Wang and Keith Williams. The Vibrational Analysis and Experimental Verification of a Plane Electrical Machine Stator Model. *Mechanical Systems and Signal Processing*, 9(4):429–438, 1995.

[102] Theodore Wildi. *Electrical Machines, Drives, and Power Systems*. Pearson Education Inc, 5th edition, 2002.

[103] Keith A Williams, George TC Chiu, and Robert J Bernhard. Nonlinear Control of a Shape Memory Alloy Adaptive Tuned Vibration Absorber. *Journal of Sound and Vibration*, 288:1131–1155, 2005.

[104] S J Yang. *Low-Noise Electrical Motors*. Monographs in Electrical and Electronic Engineering. Oxford Science Publications, Oxford, 1981.

[105] Shenbo Yu and Renyuan Tang. Electromagnetic and Mechanical Characterizations of Noise and Vibration in Permanent Magnet Synchronous Machines. *IEEE Transactions on Magnetics*, 42(4):1335–1338, 2006.

[106] Z Q Zhu and David Howe. Improved Methods for Prediction of Electromagnetic Noise Radiated by Electrical Machines. *IEE Procedings - Electric Power Applications*, 141(2):109 – 120, 1994.

[107] O C Zienkiewicz and R L Taylor. *The Finite Element Method*, volume 1 Basic Formulation and Linear Problems. McGraw-Hill Book Company (UK) ltd, 4th edition, 1989.

[108] Lei Zuo and Jean-Jacques E Slotine. Robust Vibration Isolation Via Frequency-Shaped Sliding Control and Modal Decomposition. *Journal of Sound and Vibration*, 285:1123–1149, 2005.

A Vibration Absorbers

The motivation for this part of the study is the requirement to eliminate noise producing vibrations in large electrical machines. Vibrations in electrical machines are produced mainly by periodic electromagnetic forces in the machine. These forces act on the stator and the stator vibrates.

The magnetic bimorph concept has been introduced in section 1.7. This is a method of vibration absorption suitable for large electrical machines. The magnetic bimorph effect is brought about by the presence of a conductor through the root of each tooth in the stator. The current supplied to the bimorph conductors can be controlled so that the magnetostriction forces in the stator are controlled and cause the stator teeth to act as vibration absorbers.

A.1 Vibration Absorption

Vibration absorption and vibration isolation are used to reduce or eliminate the vibrations of a structure. Vibration absorption eliminates the effect of the force that causes the unwanted vibrations. Vibration isolation reduces the transmission of unwanted forces to the system or prevents the resultant displacement of the system [35]. Vibration isolation is often considered alongside vibration absorption, but in this chapter vibration absorption alone is considered.

Vibration absorbers can be categorized into three sections. *Passive* vibration absorbers, *active* vibration controllers and *combined* passive and active absorbers. Passive vibration absorbers are so named because they require no external energy input. Active vibration control utilizes actuators, sensors and controllers and these usually require an external energy source.

Combined absorbers are nominally passive absorbers with some additional active control. These three types are described in more detail in the following sections.

Vibrations of structures such as space craft and buildings have lasting transient behaviour which consists of rapidly changing disturbances. Active vibration control is used for absorption of these disturbances. The vibrations associated with acoustic noise have short transient behaviour and so are largely steady. Recently improvements in digital signal processing chips have increased the feasibility of vibration absorption technologies for use with relatively steady disturbances. These technologies are used in structures that produce vibrations at acoustic frequencies [51]. Structures that emit unwanted acoustic noise and vibration are often rotating machines. These experience force and response patterns with multiple periodic frequencies which are the fundamental frequency and higher harmonics of this frequency. The result of this force and response pattern is multiple pure tones emitted from the structure [51]. Periodic excitation is much simpler to control than broadband excitation and both passive and active methods exist that are suitable only for the suppression of periodic excitation [51]. These methods are discussed in this chapter.

Noise and vibration problems can be spatially distributed or spatially concentrated problems. Interior aircraft cabin noise is an example of a spatially distributed noise problem. These types of problems require elimination by multiple complex control systems. Spatially concentrated problems have a disturbance or response region which is small compared to the wavelength of the structure. These problems are less complex because actuators and sensors can be located at a low number of specific locations in order to eliminate the unwanted excitation or response [51]. Spatially concentrated

problems are considered in this chapter.

In this chapter the machinery or component that is the source of unwanted vibration is called the *primary* system. The vibration absorber is attached to the primary system in order to suppress the unwanted vibration. For the examples given in this chapter the primary system is a single DoF mass-spring-damper system as shown in figure 112 with the properties given in table 24. The equation of motion of this is

$$M_P\ddot{x}_1 + C_P\dot{x}_1 + K_P x_1 = F \tag{96}$$

where M_P is the mass of the primary system, C_P and K_P are the damping constant and the spring stiffness of the damper and spring that ground the primary system. F is the periodic force that is applied to the primary system and x_1 is the response of the system. The frequency response function (FRF) of the primary system is shown in figure 113. It can be seen from figure 113 that there is a single resonant frequency where the amplitude of the response of the system is high. Away from this resonance the response of the system is much lower.

This system is designed to operate at frequency ω_d. The frequency axis of figure 113 is given relative to this design frequency and the response axis is relative to x_d which is the unabsorbed response of the primary system at ω_d. Vibration absorption of this system will now be considered.

The excitation frequency or the properties of the combined primary and absorber system may vary over a long or short time period. This factor must be taken into account when designing or choosing a vibration absorber. Short term variations include variable running speeds, variable forcing frequencies and the variation in speed during start up and shut down. Long

term variations in system properties which may detune the system include temperature changes during operation and the deterioration of the structure over its life cycle. With this in mind the following paragraphs describe how passive DVAs are designed.

A.2 Passive Absorption

A.2.1 Passive Vibration Absorption Theory

A passive absorber will now be attached to the primary system to reduce the response of the primary system at a design frequency ω_d.

Passive vibration absorption is provided by a dynamic vibration absorber (DVA). A DVA is a simple mass-spring-damper system which is attached to the primary system as shown in figure 114. This is used to suppress the vibration of a primary system caused by harmonic forcing at a single frequency. The equation of motion of the combined primary and absorber system is:

$$\begin{bmatrix} M_P & 0 \\ 0 & M_A \end{bmatrix} \begin{Bmatrix} \ddot{x}_1 \\ \ddot{x}_2 \end{Bmatrix} + \begin{bmatrix} (C_P + C_A) & -C_A \\ -C_A & C_A \end{bmatrix} \begin{Bmatrix} \dot{x_1} \\ \dot{x_2} \end{Bmatrix} + \begin{bmatrix} (K_P + K_A) & -K_A \\ -K_A & K_A \end{bmatrix} \begin{Bmatrix} x_1 \\ x_2 \end{Bmatrix} = \begin{Bmatrix} F \\ 0 \end{Bmatrix} \tag{97}$$

The symbols M_A, C_A and K_A represent the mass, damping and stiffness of the absorber system respectively. No forcing is applied to the absorber and x_2 is the response of the absorber.

The resonant frequency of a single DoF DVA is given by:

$$\omega_A = \sqrt{\frac{K_A}{M_A}} \tag{98}$$

The values of K_A and M_A can be chosen so that the absorber resonant frequency is equal to the design frequency:

$$\omega_A = \omega_d \tag{99}$$

The design frequency is usually the excitation frequency of the force that is causing the unwanted vibration. Sometimes absorbers are used to attenuate a resonance of the primary system and in this case the design frequency is the resonant frequency of the primary system. Attaching the tuned DVA to the primary system results in the suppression of the response of the primary system at the point of attachment of the absorber at the tuned resonant frequency of the absorber. An extra resonance is introduced into the response of the primary system by the presence of the single DoF DVA. Attaching the DVA to the single-DoF primary system will cause the FRF of the primary system to have two resonant frequencies. These are either side of the anti-resonant frequency which occurs at the tuned resonant frequency of the absorber. This is illustrated in figure 115 for an undamped absorber with the properties given in table 25.

The effect that the absorber mass has on the response of the primary system is shown in figure 116 where the response of the primary system is given with absorber mass values of 1%, 10% and 100% of the primary mass. This absorber system is undamped. The design frequency is the same for all mass values and so the stiffness values are chosen so that equation (99) holds. The line that shows the response of the primary system with an absorber mass which is 1% of the primary system mass shows that the primary system response is low at the design frequency but is high at frequencies that deviate only slightly from this. There is also a resonance at a frequency very close to the design frequency. This figure shows that as the absorber mass increases, the range around the design frequency where the primary response is low

increases and the distance between resonant frequencies also increases. The response of the primary system at the resonant frequency of the absorber decreases as the absorber mass increases. If only a small absorber mass is used the effect of a variation in operating speed or absorber properties during operation is that the primary system could operate with vibration levels worse than those without the absorber and could even resonate. In order to obtain a passive vibration absorber that can provide vibration absorption in a broad frequency range, a relatively heavy absorber mass is required [38] [68] [78] [103].

At the resonant frequencies of the combined system, the amplitude of the primary response depends on the damping in the primary system. Using a damped DVA has the effect of decreasing the response of the primary system at the resonant frequencies and increasing the response of the primary system at the anti-resonant frequency. Therefore, damping is often used to achieve robust vibration absorption but a damped DVA will not achieve complete vibration suppression at any frequency. A perfect passive vibration absorber which is tuned so that the primary system operates at a single constant frequency will be undamped. Zero damping in the absorber enables the absorber mass to be the smallest mass possible that will reduce the response of the primary system to zero at the tuned resonant frequency of the DVA. However, at the resonant frequency the response of a vibration absorber approaches infinity as the absorber system damping goes to zero. In practical situations a small amount of damping is required or will occur naturally in the vibration absorber structure.

The effect of damping in the absorber system is shown in figure 117. The response of the primary system is plotted for absorber damping ratios of 0, 0.05 and 0.1. The primary system properties are given in table 24. The

absorber system mass and stiffness are given in table 25. Figure 117 shows that two points exist on the FRF of a single-DoF primary system with attached damped DVA which are independent of damping in the DVA. These are called invariant points and were investigated by Den Hartog [35]. He used these points to find a so-called *optimum* damped absorber system. This optimum absorber causes the primary system response to have a minimum amplitude at the resonant frequencies and consequently gives a close to flat but non zero response across the frequency spectrum. Any tuning of the absorber system other than this leads to an increase in the response of the primary system at some frequency within the frequency range of interest. Two criteria are used to tune the absorber frequency and optimize the damping values for this absorber system. The absorber mass and stiffness values are tuned so that:

$$\beta = \frac{1}{1+\mu} \tag{100}$$

where $\beta = \omega_A/\omega_P$, $\omega_P = \sqrt{K_P/M_P}$ and $\mu = M_A/M_P$. To find the optimum damping value the second criterion is that one of the resonant frequencies must occur at an invariant point. This is the same as forcing the FRF to pass horizontally through this point. An expression for this damping ratio γ was given in [15] and is:

$$\gamma = \sqrt{\frac{3\mu}{8(1+\mu)^3}} \tag{101}$$

The damping constant C_A found from [78] is then:

$$C_A = 2\gamma M_A \omega_P \tag{102}$$

For the primary system values given in table 24, an optimum absorber has the properties given in table 26. The FRF of this system is shown in figure 118.

Changing the absorber stiffness K_a has the effect of moving the absorber resonant frequency. This effect is used in combined passive and active absorbers and so is described in section A.4.

The features of passive absorber systems that have been described in this section were illustrated with a single DoF primary system with translational motion. However, the effect of a vibration absorber can be extended to rotational motion and multi-DoF systems. Rotational vibration absorbers utilize torsional springs. The analysis of multi-DoF systems is more complicated than for single-DoF systems but the trends that have been described for single-DoF systems still apply. The equations for finding the optimum damped vibration absorber can be extended to multi-DoF systems so that the FRF of the primary system will have a near flat response across a wide frequency range. Details of a method for achieving this are described in [86].

A.2.2 Passive Absorber Designs

Different structures have been utilized as passive vibration absorbers. Structures such as pendulums, beams, electro-rheological fluids, rings and magnetic materials have been used as single DoF absorbers [94]. Several multi-DoF absorbers are described in the next paragraphs in more detail.

Hill *et al* [65] developed a multi-DoF passive absorber which absorbed the response of the primary system at three excitation frequencies and in a small frequency range either side of these frequencies. The absorber consisted of two pairs of rods. Each pair of rods supported a mass either side of a centre section, mounted on the primary system. This configuration displayed six distinct, predictable mode shapes. The mass, material properties, rod

diameters and lengths were tuned so that two absorber resonant frequencies occurred either side of each of the three excitation frequencies. This resulted in a passive absorber system which was slightly more robust than an absorber system would be if three absorber resonant frequencies were tuned exactly to the primary system excitation frequencies.

In [84] a passive multi-DoF absorber was analysed and tested. This consisted of a centre mass and 12 cantilever beams with bolts in the ends. The beams each represented a stiffness and the bolts represented a mass. The beams had three degrees of freedom, one vertical translation, and two rotations. This configuration of vibration absorber is suitable for suppressing the vibration of a shell structure which exhibits rotational and translational degrees of freedom.

A.3 Active Controllers

Active vibration control is provided in the form of an actuator, sensor and control system. Sensors are available in the form of transducers such as accelerometers and strain gauges, piezoelectric material, magnetostrictive material, optical fibres, shape memory alloys and laser vibrometers [50].

Actuators for vibration control are available in different forms including

- Electromagnetic
- Pneumatic
- Hydraulic
- Piezoelectric
- Magnetostrictive
- Shape Memory Alloys

An actuator can potentially exert forces on the primary system over a wide range of frequencies. Active control can therefore provide for the suppression of broadband excitation but the actuator and control arrangements can be complex and expensive [20] [68]. Actuators can be characterized by the blocked force, free displacement, power and operating frequency range that they cater for. The blocked force is the force exerted when the actuator is constrained not to move and the free displacement is the stroke of the actuator when unconstrained. Actuators have an associated dynamic stiffness that causes their blocked force and free displacement to be dependent on frequency. At frequencies below the resonant frequency of the device the dynamic stiffness is fairly constant with respect to frequency and so the free displacement is also constant. Below the device resonant frequency the force of voltage controlled actuators is constant. The force of current controlled actuators in this frequency range decreases with increasing frequency due to electrical loss [14]. The free displacement of the actuator is magnitudes higher at the device resonant frequency than away from the resonance. At frequencies above the resonant frequency of the absorber the free displacement becomes frequency dependent and generally decreases with increasing frequency [14]. The frequency of the absorber resonance depends on the stiffness of the actuator. An actuator formed from a material with a high Young's modulus will have a high resonant frequency and high blocked force and an actuator with a low Young's modulus will have a low resonant frequency and high free displacement. Some actuators are operated at the resonant frequency of the device to achieve the high stroke that occurs only at the resonant frequency. The mechanisms and advantages and disadvantages of some specific actuator types are discussed next and then some control arrangements are described.

A.3.1 Electromagnetic Actuators

Electromagnetic actuators consist of two ferromagnetic or permanent magnet material parts which are separated by a gap which is usually air. Some relative movement is required between the parts. Lines of magnetic flux must flow in a loop and these lines generally flow from one part to the other across the air gap. The lines of flux that cross the air gap generate a Maxwell force which provides the actuation. Electromagnetic actuators can be categorized as either linear or rotational depending on the resulting motion of the actuator.

The majority of rotational electromagnetic actuators are cylindrical motors. The stroke of rotational actuators is not related to the air gap thickness and so a high stroke can be achieved. The configuration of rotational actuators allows for the same line of magnetic flux to cross the air gap at a number of different points. A force is generated at each of these points and this generates an overall actuation force that is higher than the force generated by linear electromagnetic actuators. However, the power density of rotational actuators is reduced if a gear set is required to convert the rotational motion into linear motion as this adds to the weight of the unit.

Voice coil motors, shakers, magnetic bearings and solenoids are examples of linear actuators. Linear actuators directly output linear motion so extra gear sets are not required to convert this. The stroke length is directly related to the length of the air gap and so if a large stroke is required a large actuator is needed. The configuration of linear actuators requires that the actuation force is generated across one air gap and the ferromagnetic material needs to provide for the magnetic return path.

In general electromagnetic motors have fast response times and high preci-

sion is possible, they are also relatively cheap. An advantage of electromagnetic actuators is that they convert electrical energy directly into mechanical energy and so do not require extra power units which are required by hydraulic or pneumatic actuators. However, they can have low power density and are nonlinear so are complex to control. They are used in applications that require rapid, controlled motion [14] [20] [58].

A.3.2 Hydraulic and Pneumatic Actuators

Hydraulic and pneumatic actuators are considered together here because the only main difference between the two is the fluid that is used. The majority of linear actuators on the market are hydraulic and pneumatic cylinders. Advantages of these are high force and large displacements. If servovalves are included in the actuator configuration a variable stroke is enabled over a wide frequency range. Servovalve equipped hydraulic cylinders are used in aerospace, automotive and robotic applications. One disadvantage of using hydraulic and pneumatic actuators is that a separate power supply unit is required to supply the cylinder with fluid, this requires additional electric motors and pumps. This adds to the weight of the device and prevents these types of actuators being used in certain situations such as on rotating blades [58].

A.3.3 Piezoelectric Actuators

The piezoelectric effect is the strong phenomenon of a voltage difference produced across the ends of a ferroelectric material that is compressed. This effect can be used for sensing. The inverse of this effect also exists so that a mechanical strain is produced in a ferroelectric material on application of an electrical field. This effect is used to create actuation. A ferroelectric material is a material that has a spontaneous polarization which can be reversed under application of an external magnetic field. A common material used in

piezoelectric actuators is lead zirconium titanate or PZT. This is described as soft or hard depending on the dopant that is combined with the pure PZT. Generally, a soft PZT is created by donar doping which introduces metallic vacancies and results in increased strain being possible but also leads to higher losses. Acceptor dopants introduce oxygen vacancies which results in hard PZT which has lower strains and lower losses [75]. Hard PZT exhibits strain of $200ppm$ to $300ppm$, soft PZT has associated strain values of around $1250ppm$ [21].

The advantages of piezoelectric ceramics are that they have good shape versatility, are easy to control, have a high electro-mechanical coupling factor and have a higher power density than electromagnetic and magnetostrictive actuators. They are voltage controlled which results in efficiency being independent of frequency and so they perform well at high as well as low frequencies [14] [21]. However, the stroke possible from piezoelectric actuators is considered to be low compared to the stroke that is possible with electromagnetic and shape memory actuators. In some applications mechanical amplification is required to increase the length of stroke. However, this is done at the expense of the blocked force. Piezoelectric actuators can also be arranged in a stack configuration in order to amplify the strains.

A.3.4 Magnetostrictive Actuators

Magnetostriction is the phenomenon of an induced strain in a ferromagnetic material under the influence of an external magnetic field. The inverse effect also holds. This phenomenon has been covered in section 1.6.3.2 of The Introduction of this thesis. The most common magnetostrictive material is Terfenol-D ($Tb_{0.3}Dy_{0.7}Fe_{1.9}$). This material can achieve strains up to $2000ppm$ and is therefore classed as a giant magnetostrictive material (GMM) [21]. Magnetostrictive material only produces strain in one direc-

tion and so to use both compressive and tensile strains in actuation applications the material must be pre-stressed.

Magnetostrictive actuators have similar properties to piezoelectric actuators. However, magnetostrictive actuators are required to have energizing coils around the magnetostrictive material and a corresponding magnetic circuit armature which are not required by piezoelectric devices. This results in these actuators being heavier than piezoelectric actuators [21]. The Young's modulus of magnetostrictive materials is lower than that of piezoelectric materials and so magnetostrictive actuators have a lower resonant frequency, higher strain and lower force than piezoelectric actuators. Magnetostrictive devices are current controlled and electrical loss increases with increasing frequency so they are more efficient at low frequencies [14]. At resonance the dynamic strain is higher than for piezoelectric actuators and so they are often used as low frequency, compact resonators. These actuators can still require mechanical amplification in the same way as piezoelectric actuators [21]. Above resonance, the upper frequency limit that magnetostrictive actuators can operate at is defined by the eddy currents induced in the material. Constructing these actuators from laminations could reduce this disadvantage however this would significantly increase the cost [21]. Advantages of magnetostrictive actuators include precise control over the resultant motion, high blocked force, a high magneto-mechanical coupling factor, high efficiency and long life span. An application for magnetostrictive vibration control actuators is for the vibration control in helicopter rotors [14].

A.3.5 Shape Memory Alloy Actuators

The three main types of shape memory alloys (SMAs) are copper-zinc-aluminium (CuZnAl), copper-aluminium-nickel (CuAlNi), and nickel-titanium

(NiTi). These alloys have properties of the shape memory effect, pseudo-elasticity and super-elasticity. These properties exist due to a phase change of the alloy between a Martensite phase and an Austensite phase which is caused by a temperature change of around 10^oC. This phase change causes the arrangement of the molecules in the alloy to change, although they remain closely packed and the alloy remains solid. The shape memory effect is the ability to remember and return to a certain shape after experiencing a large deformation. This is achieved by utilizing the different properties of the alloy in the different phases. Below a transition temperature the alloy is in the Martensite phase and in this phase is relatively soft and so can be easily deformed. Heating the alloy above the transition temperature transforms the alloy into the Austensite phase and the alloy returns to the original shape. Pseudo-elasticity occurs in the material at constant temperature in the Austensite phase when a load is applied. As the load increases, the phase is changed from Austensite to Martensite and the load is absorbed by the softer material. When the load is removed the phase returns to Austensite and the material returns to its original shape [11]. The property of super-elasticity enables strains of up to 5% or to be experienced by the alloy with full recovery to the original shape [21].

In engineering applications nickel-titanium (NiTi) alloy is most commonly used. Higher forces are possible with SMA actuators than magnetostrictive or piezoelectric actuators but they operate at only a few Hz [21]. The mechanical and electrical properties of SMAs are good. They have a long fatigue life and high corrosion resistance. These alloys exhibit high internal damping which is generated by hysteresis in the transition to and from the Martensite and Austensite phases. This property is useful in vibration damping applications. If a SMA is to be used as a damper the only control that is required is the variation in temperature around the transition

temperature. A control unit for a SMA damper may therefore be lighter and less complicated than a piezoelectric control unit as no electronics or control loop are required.

A.3.6 Actuator Summary

Type	Displacement	Power Density	Comment
Linear Motors	limited by actuator length	Low	Rapid, controlled movement
Rotational Motors	not limited by actuator length	Very low if gears required	Rapid, controlled movement
Pneumatic Hydraulic	Variable with servo-valve	Low as motor & pump required	Make up majority of linear actuators
Piezoelectric PZT	Low	High	High resonant frequency
Magnetostrictive Terfenol – D	Medium	Low due to energizing coils	Low resonant frequency
SMAs NiTi	High	High	Very low frequency operation

A.3.7 Actuator Control

Different control strategies exist for use in an active vibration control system. These can be feedback or feedforward. Both feedback and feedforward control strategies aim to decouple the controlled output from the disturbance. This requires knowledge of the structure's dynamics especially at the excitation frequencies [51].

Feedback control uses the response of the primary system and the actuator. This signal is fed back to the actuator [50]. Types of feedback control include linear time invariant feedback and adaptive feedback. The first of

these is used much more than the second in noise vibration control applications. Different methods exist for feedback control of periodic disturbances. All of these methods implement high feedback gains only at the excitation frequency. This decouples the response from the excitation at the excitation frequency but does not affect sensor noise and instability at other frequencies [51].

Feedforward methods are simple and effective and are used often in vibration control of periodic disturbances [51]. Feedforward control can be used when the excitation of the primary system is observed. To achieve this a reference signal is often derived from the excitation. This signal is fed forward to the actuator. A sensor can be used to detect the response of the primary structure. This monitors the performance of the controller and can be used to adapt the feedforward control system. This signal is not directly used to generate the control signal as for feedback control. Feedforward control relies on careful selection of the amplitude and phase of the controller. Types of feedforward control include adaptive feedforward of velocity, acceleration or force signals. Adaptive feedforward cancellation can be used to estimate the magnitudes of unknown sinusoidal disturbances [20].

Control loops can be open or closed. Open loop control approaches are simple but not necessarily robust. Closed loop control is robust enough to accommodate changes and uncertainties of a system [103]. One method of active vibration control available for suppression of vibration caused by sinusoidal forcing is called the internal model principle. This requires a model of the system generating the disturbance to be included in the feedback system. This method is based on notch filtering. A notch filter reduces a system response at an assigned frequency and only affects the response at that frequency [20]. Other control strategies include linear quadratic

Gaussian regulator (LQG), H_α, μ-synthesis and sliding mode control [108].

A.4 Combined Active and Passive Absorption

A combined vibration absorber is a term used here to describe hybrid and adaptive or semi-active vibration absorbers. Adaptive and semi-active vibration absorbers are passive absorber structures with an active spring or damper in parallel with the passive spring or damper. Both the passive and active springs and dampers support a reaction mass. The passive spring stiffness is constant and the active spring stiffness is controllable. This acts to tune the resonant frequency of the absorber. Hybrid vibration absorbers are structures which combine a passive part and an active part into the one structure. These can have two modes of operation, a passive mode and an active mode [94].

Some combined vibration absorbers utilize controllable damping. However, the presence of damping in an absorber prevents the absorber from achieving complete vibration suppression of the primary system. The most common adaptive absorber is therefore a DVA with variable stiffness. In this case the passive absorber mass can be the minimum that is required to reduce the response of the primary system to the desired level at a single, nominal frequency only. Adaptation of the absorber stiffness enables the resonant frequency of the absorber to vary. On-line tuning of the absorber stiffness enables the resonant frequency of the absorber to track the excitation frequency and ensures that the response of the primary system remains low with deviations in the excitation frequency away from the nominal frequency [103]. The active component of combined vibration absorption requires vibration measurements, feedback control, an external power supply and actuation. Therefore, one disadvantage of combined absorption systems is that changing the effective stiffness of a system to track a wide frequency range

can require a high input of energy. A low power variable stiffness technique will result in the ability to absorb vibrations over a small frequency range only [68]. Nevertheless the energy input of a combined system is lower than that required for full active control and so there are many advantages to using combined absorption. These include the potential to achieve a system which has the simplicity, reliability and stability of a passive absorber without requiring a heavy passive absorber mass and the robust ability of an active device without the high energy and therefore high expense incurred from full active control [68] [89].

The following sections describe combined vibration absorber technology in more detail. These sections consist of:

- An Example of a Combined Absorber
- Variable Stiffness Technologies
- Self Tuning Vibration Absorbers
- Delayed Resonators
- Variable Damping Absorbers
- Multi-DoF Combined Vibration Absorbers
- Combined Vibration Absorber Control

A.4.1 An Example of a Combined Absorber

An adaptive vibration absorber with active stiffness consists of a passive mass-spring-damper system with an active spring in parallel with the passive spring as shown in figure 119. The equation of motion of this system is:

$$\begin{bmatrix} M_P & 0 \\ 0 & M_A \end{bmatrix} \begin{Bmatrix} \ddot{x}_1 \\ \ddot{x}_2 \end{Bmatrix} + \begin{bmatrix} (C_P + C_A) & -C_A \\ -C_A & C_A \end{bmatrix} \begin{Bmatrix} \dot{x}_1 \\ \dot{x}_2 \end{Bmatrix} + ...$$

$$\begin{bmatrix} (K_P + K_A + \delta k) & -(K_A + \delta k) \\ -(K_A + \delta k) & K_A + \delta k \end{bmatrix} \begin{Bmatrix} x_1 \\ x_2 \end{Bmatrix} = \begin{Bmatrix} F \\ 0 \end{Bmatrix} \tag{103}$$

In this example the response of a primary system with the properties given in table 24 is reduced using a combined absorber. The combined absorber has been designed so that the response of the primary system is reduced to 10% of the unabsorbed response x_d at a design frequency ω_d. This low response is maintained over a frequency range which is the same range that is achieved with a passive vibration aborber which has mass equal to the primary system mass. The FRF of the primary system with a passive absorber of equal mass is shown in figure 116 with a red line.

The passive part of the absorber is designed first. The mass and passive spring values are chosen so that the response of the primary system is reduced to 10% of x_d at a nominal frequency ω_n within the required frequency range. The nominal frequency is chosen so that the increase in stiffness to absorb the primary system at the higher frequency limit is the same as the decrease in stiffness from the nominal to absorb the primary system at the lower frequency limit. The nominal mass that is required to achieve this reduction at ω_n is only 0.130% of the mass of the primary system. The passive stiffness is 0.106% of the primary system stiffness.

The active spring acts to tune this resonance away from ω_n. At frequencies below ω_n the active spring opposes the passive spring and so the addition of the active spring reduces the effective spring stiffness of the absorber and tunes the resonant frequency of the absorber to a lower frequency. The FRF of the primary and absorber system tuned to the lower frequency limit is shown in figure 120. At frequencies above the nominal resonant frequency of the absorber the active spring acts with the passive spring. The increased spring stiffness acts to tune the absorber to resonate at higher frequencies.

The response of the primary and absorber system tuned to the upper frequency limit is shown in figure 121. In this case the response is lower than required because the mass is not altered. The change in stiffness at the extremes of the frequency range is ±0.0289% of the primary system spring. This is ±27.264% of the nominal, passive absorber stiffness. The combined absorber properties are given in table 27.

The equivalent entirely passive absorber system which would be required to reduce the response of the primary system by the same levels in the same frequency range requires an absorber mass 100% of the primary mass and stiffness 7.426% of the primary system stiffness. Whereas the mass of the combined absorber is 0.130% of the primary mass, the passive spring stiffness is 0.106% of the primary spring stiffness and the active spring stiffness is ±0.0289% of the primary spring stiffness. The fact that the passive system property values are much higher than the equivalent values for the combined absorber illustrates the potential of combined vibration absorption technology as a method for suppressing variable frequency vibrations. These values are for illustrative purposes only. Passive vibration absorbers that require the mass to be the same as the primary system would not be considered as a feasible solution to vibration absorption.

In an electrical machine a range of resonances are associated with the teeth rocking relative to the stator core. In large electrical machines the natural frequencies associated with this tooth rocking motion correspond to some frequencies of excitation of the stator. The aim of the magnetic bimorph concept is to utilize the motion of the teeth to achieve vibration absorption in large electrical machines. This is a combined vibration absorption method where the teeth provide the passive part. The bimorph conductors provide the excitation that is required to utilize the motion of the teeth.

The details of this concept are explained in chapter 2.

A.4.2 Variable Stiffness Technologies

The above vibration absorption theory has described how combined vibration absorbers can effectively reduce vibrations over a very wide frequency range by implementing a variable stiffness technique. However, practical methods for realizing this idea are more challenging. The active part is often achieved with an actuator and control loop in a similar manner to full active control. The actuator is often an electromagnetic, piezoelectric, magnetostrictive or shape memory alloy actuator. These have been described in section A.3. The passive part can be achieved with a physical mass-spring-damper set. Beam structures are frequently used in investigations of combined absorption. The rest of this section describes in more detail some of the arrangements of combined vibration absorber systems that have been used in the literature for achieving robust vibration suppression.

Beams are utilized for this application because of the simplicity of the structure and the inherent mass, stiffness and damping values they possess. The equivalent material properties of a beam can be altered with active control. Some methods for achieving this are:

- The application of piezoelectric strips at the root of a cantilever beam. Under the influence of an electric field the stiffness and strain of the strip will change which will affect the overall stiffness of the beam.

- A composite beam manufactured from strips of material which includes piezoelectric strips. This results in a beam with a built in sensor and actutator [99].

- A beam with a mass that can be moved along the beam. Different locations of the mass will result in different resonant frequencies of

the structure.

- A beam constructed from plates which are constrained relative to each other but separated by a gap of controllable distance will have a controllable second moment of area. One example of this is shown in figure 122. This is four beams connected in a diamond shape. The frequency of the structure is dependent on the total width of the diamond and the thickness of the individual beams used. The lowest frequency that is possible with this configuration occurs with zero separation of the beams. This configuration among other similar configurations were investigated in [72]. Swept sinusoidal excitation was applied to the primary system initially at the passive tuned resonant frequency of the absorber. This was altered to equal the resonant frequency of the primary system. Robust absorption was provided by changing the beam geometry and consequently altering the beam stiffness and resonant frequency. Fuzzy logic control enabled this geometry change to track the excitation frequency.

- Shape memory alloys such as NiTi are also utilized for combined vibration absorption. Tuning is achieved through heating and cooling of the material which alters the Young's modulus of the beam and therefore controls the resonant frequencies of the beam [103].

- An absorber developed and tested in [79] consisted of two backing plates separated by a magnetostrictive rod. Elastic suspension arms were attached between the two plates and these provided a 90^o rotation and $\times 6$ amplification of motion from the elongation of the rod. The absorber mass was made up of the magnetostrictive rod, the coils for excitation and the plates and suspension arms. The passive resonant frequency was tuned to $100Hz$ and the absorber acted actively over the range $50Hz$ to $400Hz$. The absorber was also required to ex-

ert specific forces at $100Hz$, $200Hz$ and $300Hz$ and this was achieved with the developed absorber.

A.4.3 Self Tuning Vibration Absorbers

Self tuning combined vibration absorbers are devices which use energy from the primary system to change the tuned frequency of the absorber to match the primary system's excitation frequency [67]. No external power, sensors or actuation are required to tune a self tuning vibration absorber. A mechanical feedback loop exists which is created from the motion of the primary system. When the excitation frequency differs from the absorber's nominal resonant frequency, the motion of the primary system tunes the absorber's resonant frequency in the direction of the excitation frequency until the absorber's resonant frequency equals the excitation frequency.

Ivers *et al* [67] simulated, designed and tested a self tuning vibration absorber. The active part of the absorber featured a threaded cantilever beam with a fitted threaded mass. The fixed end of the cantilever beam was attached to an L shaped base. Two unequal dampers at 45^o to the base attached the free end of the beam to the base. The base was attached to the primary system by a passive spring and damper in parallel. The beam sat perpendicular to the line of motion of the primary system. The overall resonant frequency of the absorber was controlled by the stiffness of the cantilever beam as well as the attachment spring and the location of the threaded mass along the beam. When the primary system oscillated at a frequency other than that which the passive absorber was tuned to, the cantilever responded in a whirling motion which wound the mass along the length of the beam. The authors showed that correct choice of absorber parameters ensure this structure behaves successfully as a self tuning vibration absorber. However, with this particular design a large time delay

exists between the change in excitation frequency and change in absorber frequency. This particular setup is also only sufficient for suppression of vibration along a single axis.

A.4.4 Delayed Resonators

A particular type of combined vibration absorber has been named the *delayed resonator* [85]. The delayed resonator can achieve complete vibration suppression at any desired frequency within a wide frequency range. A simple control loop is utilized which is closed within the absorber and so the absorber is a stand-alone device. The structure of the resonator is based on a passive damped DVA with a proportional feedback control with a time delay in parallel with the nominal passive spring and damper. A schematic of this system is shown in figure 123. The introduction of a time delay into a system has the effect of destabilizing the system. In the majority of situations this destabilizing effect is undesired and so compensated for or eliminated. In a delayed resonator this affects the absorber so that it resonates at a controlled frequency and therefore, the steady state behaviour of the delayed resonator is an ideal vibration absorber. The force that this absorber exerts on the primary system F_D can be equated with the force exerted by a spring which has stiffness equal to the control gain g, but retarded by a time delay τ. When the control gain is zero, the absorber acts as a passive DVA. The equation of motion of a primary system with attached delayed resonator is:

$$\begin{bmatrix} M_P & 0 \\ 0 & M_A \end{bmatrix} \begin{Bmatrix} \ddot{x}_1(t) \\ \ddot{x}_2(t) \end{Bmatrix} + \begin{bmatrix} (C_P + C_A) & -C_A \\ -C_A & C_A \end{bmatrix} \begin{Bmatrix} \dot{x_1}(t) \\ \dot{x_2}(t) \end{Bmatrix} + ...$$

$$\begin{bmatrix} (K_P + K_A) & -K_A \\ -K_A & K_A \end{bmatrix} \begin{Bmatrix} x_1(t) \\ x_2(t) \end{Bmatrix} + g \begin{bmatrix} 1 & -1 \\ -1 & 1 \end{bmatrix} \begin{Bmatrix} x_1(t-\tau) \\ x_2(t-\tau) \end{Bmatrix} = \begin{Bmatrix} F(t) \\ 0 \end{Bmatrix} \tag{104}$$

The characteristic equation of the delayed resonator is transcendental and so has infinitely many roots. Within the frequency range of operation the values of g and τ must be chosen so that the system exhibits marginal stability. In order to achieve this two of the roots of the characteristic equation must lie on the imaginary axis of the complex plane and all other roots must lie in the stable left half plane of the complex space [85]. The feedback control determines the stability of the system and depends only on the operating frequency. Therefore, in order to maintain marginal stability, prior knowledge of the operating frequency range is required. Theoretically, the highest frequency that the delayed resonator can be tuned to corresponds to zero time delay. In reality the sampling rate of the controller sets the upper frequency limit that this system can be used for [38] [85]. The delayed resonator can be tuned in real time. When the desired frequency is changed, the new resonance occurs after a settling time which is dependent on the system dynamics [85]. In order to tune the delayed resonator one of; the relative displacement, velocity or acceleration between the absorber and primary system must be recorded. No further information regarding the primary system is needed and so this control is considered to be decoupled from the primary system. This is one advantage of this method over other methods such as proportional derivative (PD) control because PD control also requires knowledge of the velocity of the primary system [45].

Renzulli *et al* [91] investigated a delayed resonator. The authors initialized gain and time delay values with a model of the absorber. The final values were found with an iteration of a gradient search method. The authors carried out experiments to verify the model. A feedback signal was supplied from an accelerometer. The delayed resonator was shown to successfully suppress the response of the beam at the point of the absorber for a single excitation frequency. Using an automatic tuning algorithm, the

delayed resonator also suppressed time varying excitation frequencies, although to a lesser degree than for constant frequencies. The presence of the delayed resonator also introduced residual oscillations into the system at second and third harmonics of excitation frequency.

Dingyue *et al* [38] and Liu *et al* [77] also investigated similar systems. In [38] simulations of their delayed damper resulted in reduction of the magnitude of the response by 98% in the range $80Hz$ to $960Hz$. Disturbances at frequencies of multiples of just below $80Hz$ are magnified within the band pass. Experimentation gave up to 80% reduction in response magnitude. The authors of both papers concluded that this type of absorber system can suppress vibration response of a system at a range of frequencies limited only by hardware constraints. The delayed damper is effective at suppressing frequencies at a reference frequency and integer harmonics of that frequency.

A.4.5 Variable Damping Absorbers

Broadband excitation can be suppressed to some extent with damping control. The presence of damping in the absorber system introduces a phase shift between the response of the primary system and the response of the absorber system. Including damping in a system reduces the peak responses of the system and increases the response of the system at anti-resonances. Variable dampers are used in applications such as buildings, bridges, trains and tanks. Examples of variable dampers include traditional devices such as variable orifice dampers and controllable friction braces and isolators. Recent advances in smart material technology has led to electro-rheological fluid dampers and magneto-rheological fluid dampers becoming widely used. Electro-rheological fluid dampers experience instantaneous reversible changes in material characteristics, especially shear modulus, when

supplied with an electric potential. These require a high voltage electric field. Magneto-rheological fluids consist of magnetically polarizable particles in a carrier medium. Under application of a magnetic field, the fluid becomes a semi-solid. These can operate from a battery such as that in a vehicle [68].

A.4.6 Multi-DoF Combined Vibration Absorbers

Principles of combined vibration absorption can be extended from single frequency suppression to consider absorbing the response of a primary system due to excitation forces with multiple frequencies. This is a concept that is useful in many situations as machinery often experiences excitations that comprise a fundamental frequency as well as integer harmonics of that frequency.

Active absorption was attempted on an initially passive 6DoF vibration absorber in [65]. This absorber consisted of a main mass and two pairs of rods which each supported a mass. Adaptive absorption was achieved with a stepper motor. This wound the masses in and out and therefore changed the resonant frequencies of the absorber. However, in practice the presence of the motor increased the number of absorber resonances and decreased the effectiveness of the absorber at the required frequencies.

A.4.7 Combined Vibration Absorber Control

Williams *et al* [103] developed a proportional integral (PI) controller to tune an adaptive - passive vibration absorber. The indicator used by the controller of the required tuning direction of the absorber frequency is the cosine of the difference in phase between the excitation and absorber frequencies. If this value is below zero, the absorber resonance is below the excitation frequency. If this value is above zero the absorber resonance is

above the excitation frequency. This measure is exact when no damping exists in the absorber system and has been shown to be sufficiently accurate in a system with a lightly damped absorber. The developed system was stable in the absence of control signal saturation. In the case of a saturated control signal a nonlinear controller with an anti-windup algorithm was developed.

A.4.8 Summary of Combined Vibration Absorbers

This section has described combined vibration absorbers with theoretical examples and descriptions of practical devices. Both single and multi-DoF structures have been covered. The theory clearly illustrates that the advantages of these devices over full passive and full active systems is the ability for robust absorption with low weight and relatively low power input. Implementing this idea in practice is more challenging but still feasible and many studies have achieved this.

A.5 Conclusion

This chapter has described passive, active and combined vibration absorbers. The theory that is often used to explain these absorbers has been given, practical devices and the work of other authors in this field has been discussed. Passive devices require no external input of energy. However, in order for these to provide robust absorption a heavy mass is required. Active control methods provide vibration suppression over a wide frequency range but complicated sensors, controllers and actuators are required to achieve this and an external power source is required. Combined passive and active vibration absorbers provide robust vibration control with a relatively small mass and passive spring. However, these systems usually require sensors, controllers and an external energy source.

This chapter has provided background information on vibration absorbers

because this information is relevant to the magnetic bimorph concept. This concept is explained in chapter 2 and in this chapter an analogy with a combined vibration absorber is made.

Mass	M_P	40	kg
Stiffness	K_P	50,000	N/m
Damping Constant	C_P	20	Ns/m
Applied Force	F	100	N
Design Frequency	ω_d	4.85	Hz
Response at ω_d	x_d	7.8	mm

Table 24: Primary System Properties

Mass	M_A	4.000	kg
Stiffness	K_A	3713.000	N/m
Damping Constant	C_A	0	Ns/m

Table 25: Passive Absorber System Properties

Mass	M_A	4.000	kg
Stiffness	K_A	4132.231	N/m
Damping Constant	C_A	56.916	Ns/m

Table 26: Optimum Passive Absorber System Properties

Nominal Resonant Frequency	ω_n	31.952	rads^{-1}
Absorber Mass	M_A	0.052	kg
Absorber Damping Constant	C_A	0	Ns/m
Nominal Absorber Stiffness	K_A	53.087	N/m
Lower Resonant Frequency	ω_1	27.250	rads^{-1}
Change in Stiffness (to achieve ω_1)	δk	-14.474	N/m
Upper Resonant Frequency	ω_2	36.045	rads^{-1}
Change in Stiffness (to achieve ω_2)	δk	+14.474	N/m

Table 27: Combined Absorber System Properties

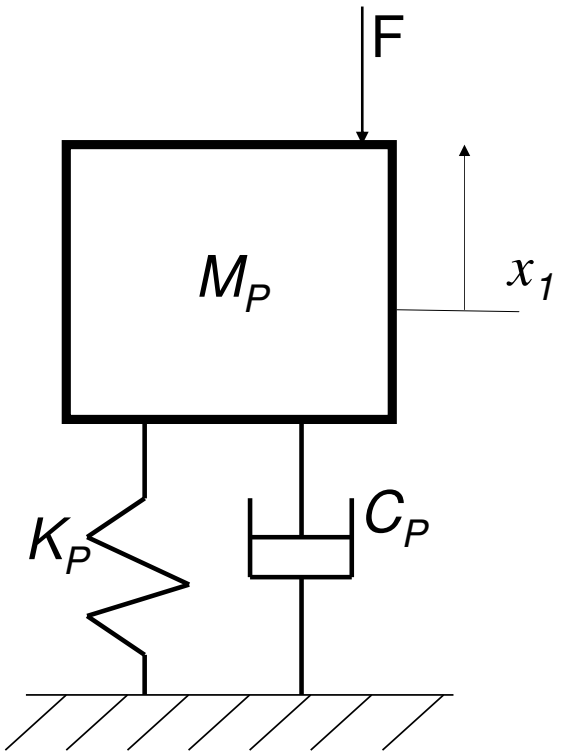

Figure 112: A Primary Mass - Spring - Damper System

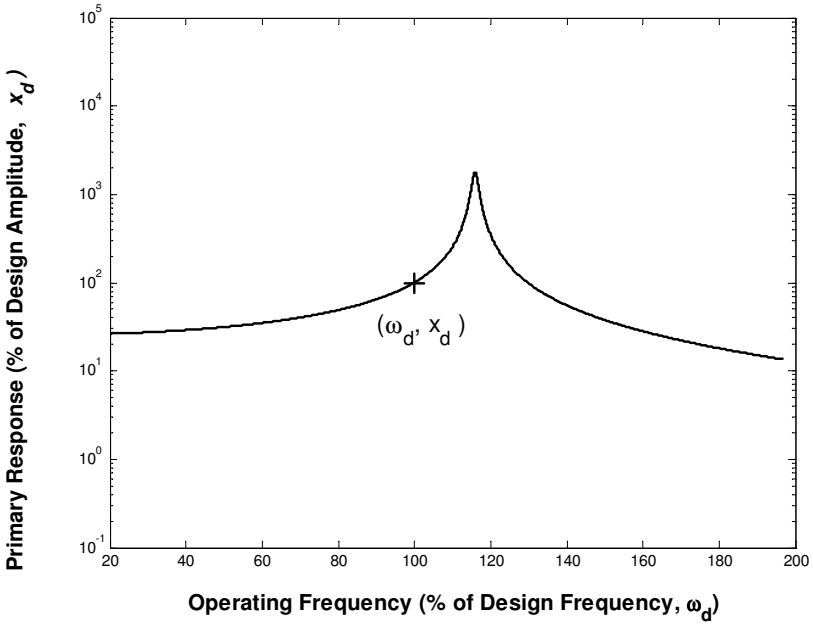

Figure 113: The Frequency Response Function of the Primary System

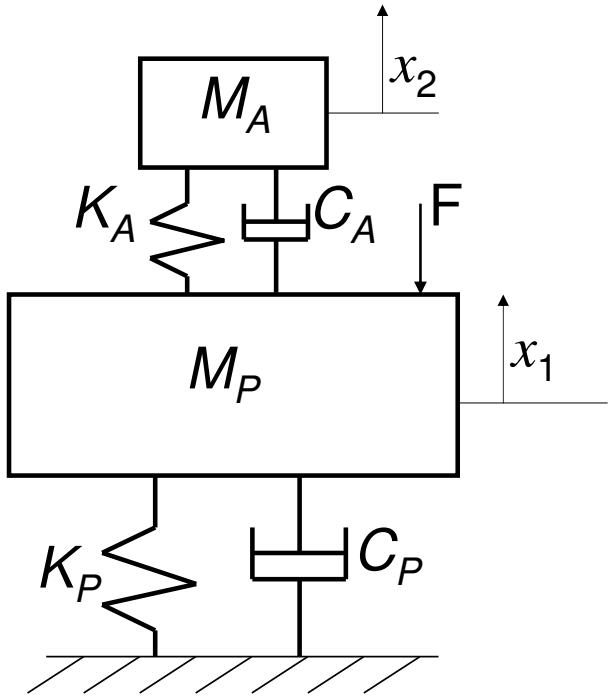

Figure 114: The Primary System with Attached Passive Absorber

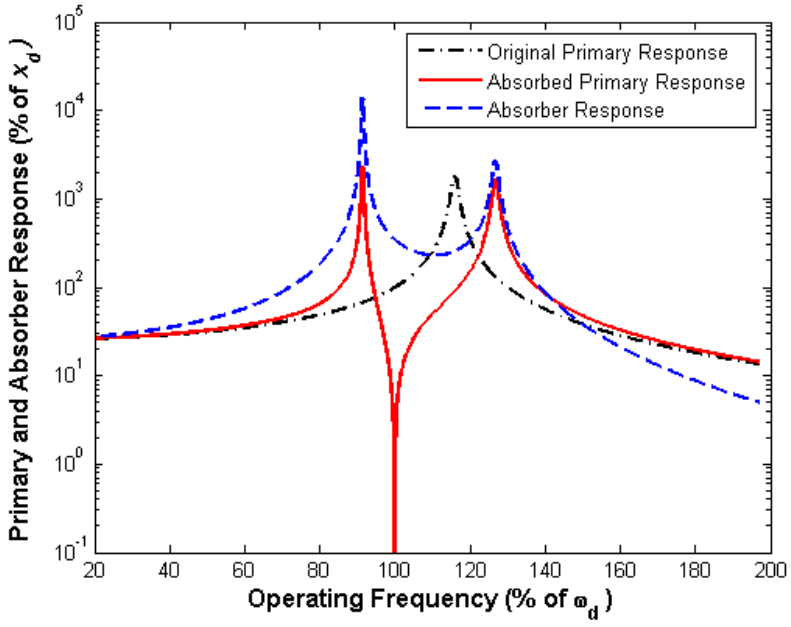

Figure 115: The Frequency Response Function of the Primary and Absorber System

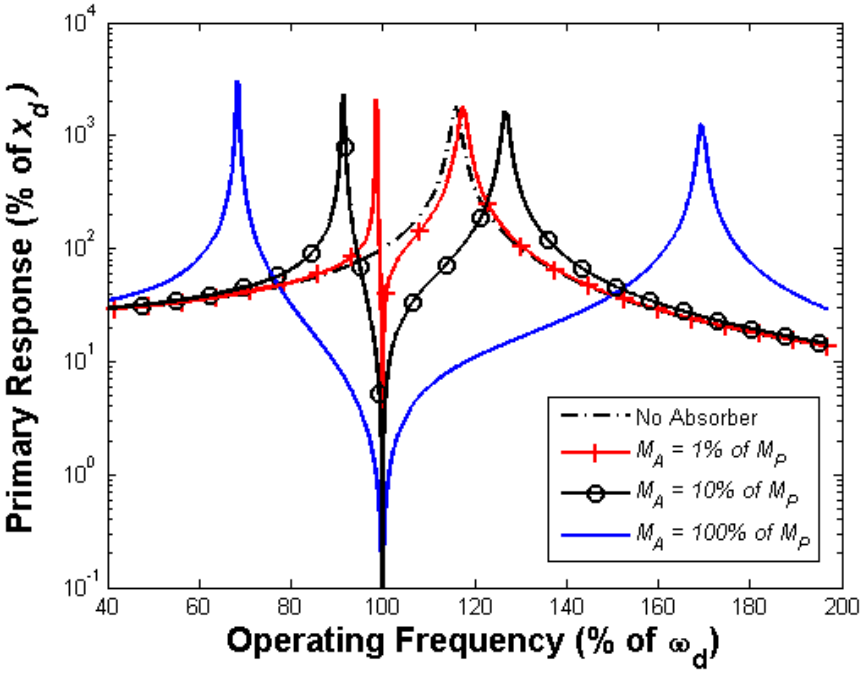

Figure 116: The Frequency Response Function of the Primary System with Different Passive Absorber Mass Values

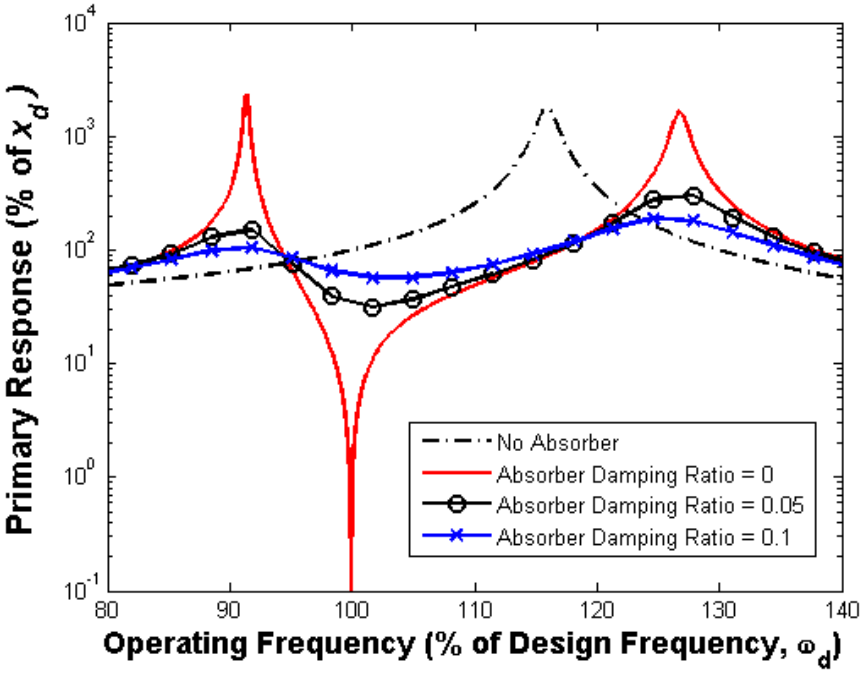

Figure 117: The Frequency Response Function of the Primary System with Different Passive Absorber Damping Ratios

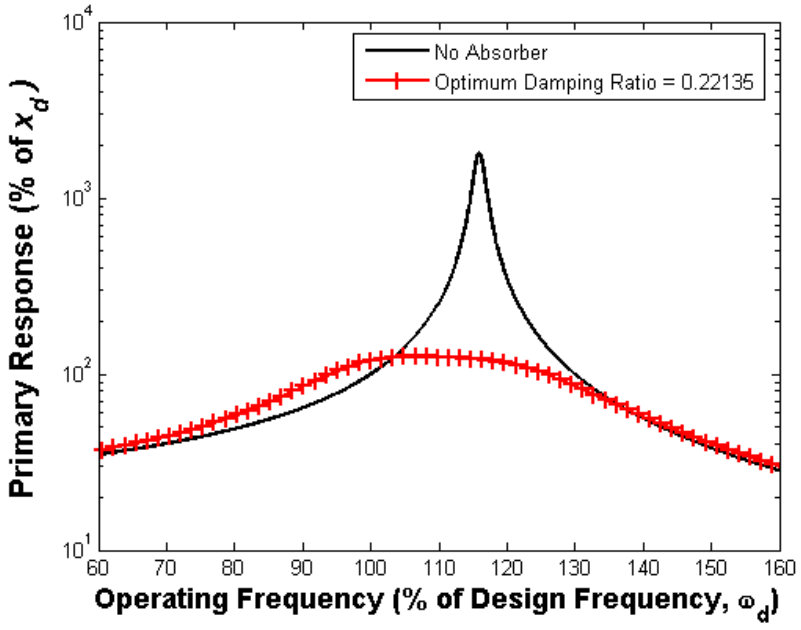

Figure 118: The Frequency Response Function of the Primary System with Optimum Absorber Properties

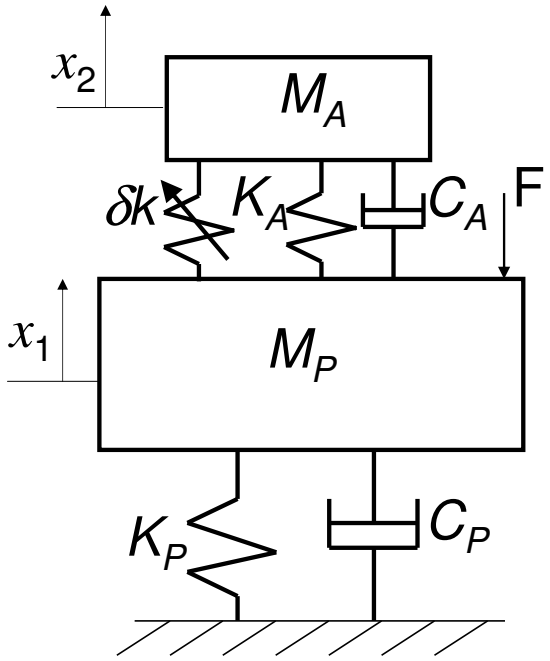

Figure 119: The Primary System with Attached Combined Vibration Absorber

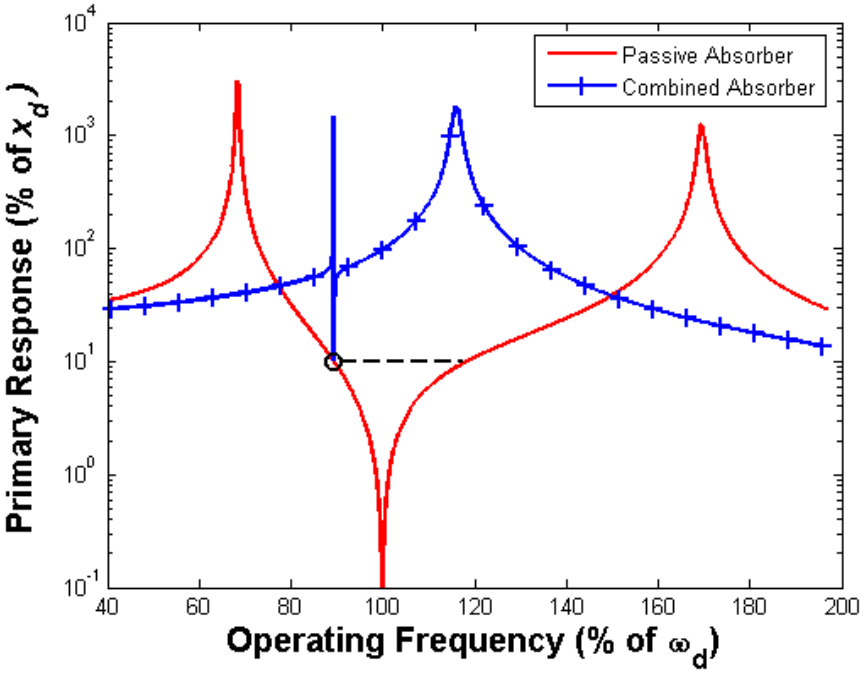

Figure 120: The Primary System and Combined Absorber FRF Tuned to a Low Frequency

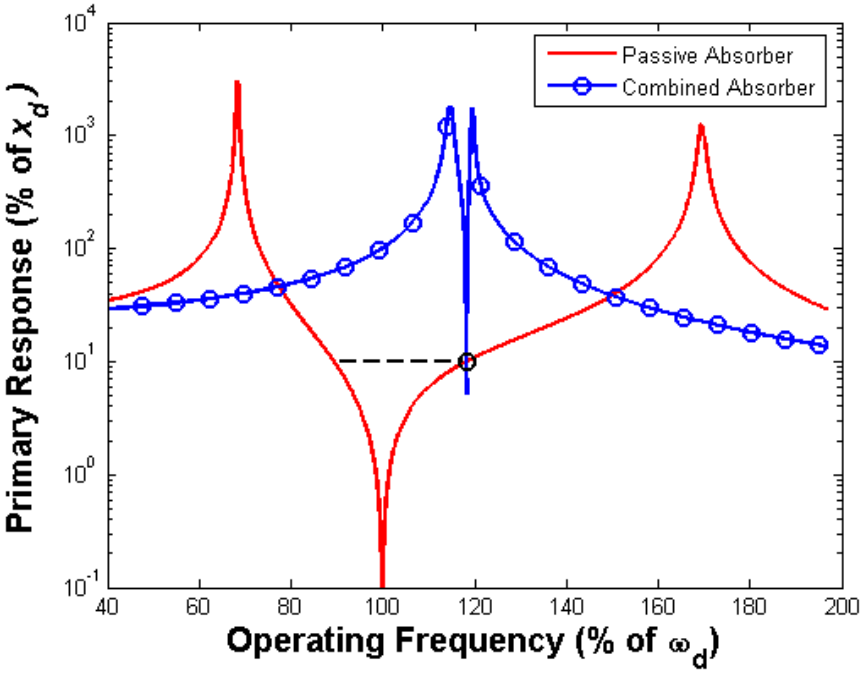

Figure 121: The Primary System and Combined Absorber FRF Tuned to a High Frequency

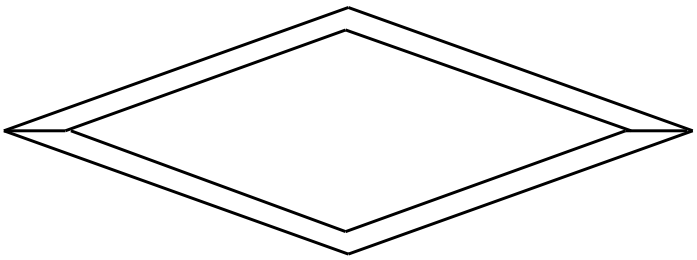

Figure 122: A Variable Geometry Structure for use as a Combined Vibration Absorber

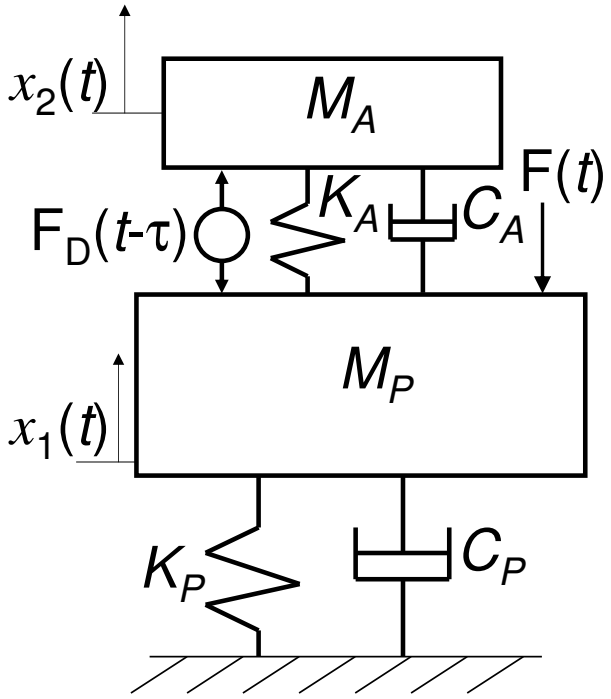

Figure 123: The Primary System with Attached Delayed Resonator

B Finite Element Modelling

This chapter provides the background information about finite element (FE) modelling that is relevant to this study. The first sections within the chapter cover the general formulation of the FE problem. This involves discretizing the geometry of the structure under consideration into elements and choosing interpolation functions to map from the coordinates of the global structure to elemental coordinates. The generation of the element is given in general terms and then the FE problem is illustrated for the situations that are used in this study. These are a magnetic model and a mechanical model. The assembly of element matrices into global matrices is then explained briefly and boundary conditions are considered. Methods for dealing with large matrices are described because the global matrices created by FE analysis are often too large to be manipulated directly. Guyan reduction is one of these techniques and this is described in more detail. This reduction technique can also be used during the merge of the element matrices into the global matrices. This method is described here because the merge and reduction method was used in this study.

If a structure under analysis has a cyclically symmetric geometry, this feature can be used advantageously in FE analysis. The last sections in this chapter explain how cyclic symmetry can be used in the assembly and reduction of the global matrices. An alternative means of assembling the global matrices of cyclically symmetric structures is also given.

B.1 Introduction to Finite Element Analysis

This section explains the formulation of the FE problem.

A field problem in a continuum region has an infinite number of field vari-

ables since a continuum region is composed of an infinite number of points and a field variable exists at each of the points. The FE method discretizes a continuum region into finite elements. The finite element problem has a finite number of field variables which are piecewise approximations to the governing equations. Nodes lie on the elements, usually on the element boundaries. There may be more than one field variable or degree of freedom (DoF) per node. The solution to the governing equation is given in terms of the values of the field variables at the nodes. Interpolation functions are defined in terms of the values of the unknown field variables at the nodes. The interpolation functions approximate the values of the field variables across the region of the element. The nodal values and interpolation functions fully define the field variable within the element [107].

Finite element models can be *linear* or *nonlinear*. In a linear model, an increase in the input by a certain multiplication factor will lead to an increase in the response by that same multiplication factor. Nonlinear problems have more complicated relationships between the input and the solution. Nonlinear field problems are modelled by a system of nonlinear equations which cannot be solved in a closed form. An iteration technique is required to solve the field problem such as Newton iteration. In every step of the iteration a series of linear equations is solved, the convergence of the solution of these local linear equations gives the solution to the nonlinear problem. In this study only linear systems are considered.

Finite element models can be used to describe either static or dynamic situations. A static FE problem has a governing equation of the form:

$$\mathbf{Kx} = \mathbf{f} \tag{105}$$

All static field equations have this structure. $\mathbf{K}$ is a stiffness matrix, $\mathbf{x}$ is a vector of field variables and $\mathbf{f}$ provides the input of the problem. Where the system has nonlinearity, $\mathbf{K}$ itself may depend on $\mathbf{x}$. This work focuses on linear problems where $\mathbf{K}$ is concerned. Often, the terms in a FE problem are referred to in the context of mechanical analysis and this terminology is adopted here. The terms $\mathbf{x}$ and $\mathbf{f}$ are therefore referred to as displacement and nodal force vectors respectively. In specific cases these vectors may not actually hold values of displacement or force; for example in the case of electromagnetic fields these are vectors of magnetic potential and nodal current respectively.

An undamped dynamic problem has the form:

$$\mathbf{M}\ddot{\mathbf{x}} + \mathbf{K}\mathbf{x} = \mathbf{f} \tag{106}$$

The definitions of $\mathbf{K}$, $\mathbf{x}$ and $\mathbf{f}$ remain the same for the dynamic case as for the static case. An inertia or mass matrix $\mathbf{M}$ and acceleration vector $\ddot{\mathbf{x}}$ are also included in dynamic systems. Damping has been neglected in this analysis.

The transformation of the field variables from the continuous problem to the finite problem also applies to the forcing. Values of forcing in a continuum can exist at each of the infinite number of points in the solution region. The distributed forces act to cause a deflection in the structure. The product of the force and resulting incremental deflection of the structure is the incremental work done to the system. In a FE problem, the continuous forcing is discretized and nodal force values are given at every DoF in the structure. The work done by the nodal forces is set to be equal to the work done by the distributed forces and from this the nodal forces can be calculated. The force at any point within an element can be estimated by the values

of the nodal forces of that element and the interpolation functions. This procedure is described in more detail in section B.4.

B.2 Discretizing the Continuum into Elements

The continuum region must be completely covered by the mesh of elements. The accuracy of the final solution is strongly dependent on an accurate choice of the discretization of the region, which can be in two or three dimensions. There are various shapes of elements and numbers of nodes per element that can be chosen to generate the mesh. Nodes can lie internally in the element as well as on the element boundaries. The boundary or external nodes provide the connection between adjacent elements. The direct representation of the continuum region is given in real space. In real space in two dimensions global Cartesian coordinate axes are used and these are labelled (x, y).

In two dimensions, the most simple element is a triangle with three nodes; one in each corner. Triangle elements with six nodes have a node situated on each edge as well as each corner. Quadrilateral elements with four nodes; one at each corner of the element, and with eight nodes; situated on the mid sides of the element as well as on the corners, are also common in two dimensional FE analysis. Elements with nodes on the edges as well as the corners allow for curved boundaries to be approximated more accurately and these problems require less elements for the same solution accuracy than for problems that use elements with corner nodes only. In three dimensions tetrahedron, wedge and hexahedron shapes are used. These can have nodes located on the corners, edges, surfaces and sometimes within the volume [66].

A FE mesh can be *structured* or *unstructured*. A structured mesh is built

up from meshable regions. The meshable regions cover and separate the structure according to its different materials and major geometrical features. The level of discretization is defined for each meshable region and elements are generated to comply with this. The level of discretization defined for each region in a structured mesh is not flexible. This is because the element borders generated by the discretization are continuous across the structure and so compatibility must usually be maintained across the borders of the meshable regions. The resulting mesh has quadrilateral and or triangle elements arranged in a regular pattern.

At the mesh generation stage, a material property label is assigned to each meshable region and the material properties of the region are assigned to that label. All elements in that region are generated with those same material properties. The process of deriving the element matrices is carried out for each individual element in turn. The resulting element matrices are square with dimensions equal to the number of DoFs in the element.

In an unstructured mesh, elements are generated as required to fit to the geometric shape of the structure and the discretization requirements of the solution. Usually elements in unstructured meshes are triangle shaped, but quadrilateral elements can also be generated either directly or by combining two adjoining triangular elements.

In order to solve the FE problem accurately, a fine discretization is often required in certain parts of the mesh. This requires smaller elements and many nodes to be generated in those regions. In a structured mesh, in order to maintain continuity of the element boundaries, a fine mesh may have to be created in areas where this is not required, increasing the size of the problem. In an unstructured mesh, the size of the problem is kept to a

minimum because fine discretization is used only in the specific areas where this is required.

In order to generate a three dimensional mesh, a mesh extrusion or solid modelling method can often be used. Mesh extrusion extrudes a two dimensional mesh along a third direction. Solid modelling generates the mesh within the volume from a discretization of the surface of the structure.

The following sections are written specifically concerning two dimensional meshes but much of the information given can easily be extended to three dimensional models. Figure 124 illustrates an example eight noded, quadrilateral element in real space with global coordinates and specifies an option for the ordering of the eight nodes around the element boundary. The node ordering given in figure 124 is the node ordering used in subsequent sections.

B.3 Interpolation Functions

Interpolation or shape functions provide an approximation of the values of the field variables at any point within the element. The shape functions are required to ensure continuity of the field variable within the element. They must allow for convergence of the correct solution with increasing levels of discretization. They must possess geometric isotropy, which means they must be invariant under a coordinate transformation. Polynomials are normally used as shape functions as they are easy to integrate and differentiate and have geometric isotropy. The total number of coefficients in the polynomial is given by the number of DoFs in the element which is the product of the number of nodes in the element and the number of DoFs per node.

Elements are usually derived in a reference space. The 2D reference coordinate system, sometimes called the natural coordinates are a Cartesian

coordinate set labelled (ζ, η). The purpose of the reference coordinate system is to describe the location of points in the element in terms of the coordinates of the nodes in the reference coordinate system. Regardless of the geometry of a quadrilateral element in real space, the corresponding reference element always forms a square with its boundaries on lines of $\zeta = 1$, $\zeta = -1$, $\eta = 1$, and $\eta = -1$ and its centre located at the origin of the coordinate frame. There is a one-to-one mapping between each node in the reference element and the corresponding node in the real element. See figure 125 for an illustration of a reference element.

Elements can be described as *isoparametric* if the interpolation functions that interpolate the field variables at any point within the element from the field variables at the nodes are the same as the interpolation functions that provide the transformation from reference to global coordinates [66]. All of the elements considered in this study are isoparametric.

B.4 Element Properties

FE analysis has been introduced, the generation of the governing equations of the problem are now described.

The governing equation of the FE problem is transformed into a matrix equation which is solved to give the solution to the problem. The properties of the elements are described in the matrices of the governing equation. Different methods exist for generating these element matrices and these are described here.

The Direct Approach is the earliest approach used to create a finite element model. This method uses direct physical reasoning to establish the element equations and so is limited to simple problems, such as the force

and displacement relationships of beam members of rigidly jointed frames.

The Variational Approach is the most conventional approach when a classical variational statement exists for the given problem. This can be used to formulate the element properties for the simplest shapes as well as for sophisticated problems. A function and boundary conditions exist which describe the problem. Appropriate differential equations maximise, minimise or make stationary the function using the same boundary conditions. These equations are the governing partial differential equations of the problem.

The Weighted Residual Approach is used if classical variational principles are unknown. Estimates of the field variables and boundary conditions are used in the partial differential equations. This gives a residual or error of the estimates. Weighting the residual drives the estimate of the function to converge to the solution [66].

B.4.1 The Static Problem

In static problems the change in potential energy $\Delta\Pi$ stored in a structure is equal to the change in strain energy ΔU minus the change in the work done on the structure by the external forces ΔW.

$$\Delta\Pi = \Delta U - \Delta W \tag{107}$$

For equilibrium to be ensured, the total potential energy must be stationary, in stable elastic situations this is also the minimum potential energy. This is the variational problem for static situations:

$$\frac{\partial\Delta\Pi}{\partial\Delta\mathbf{x_e}} = \frac{\partial\Delta U}{\partial\Delta\mathbf{x_e}} - \frac{\partial\Delta W}{\partial\Delta\mathbf{x_e}} = 0 \tag{108}$$

The change in strain energy ΔU is given by:

$$\Delta U = \frac{1}{2}\Delta \mathbf{x_e}^\top \mathbf{K_e} \Delta \mathbf{x_e} \tag{109}$$

$\mathbf{K_e}$ is the element stiffness matrix and $\Delta \mathbf{x_e}$ is a vector of displacements of the DoFs in the element.

An increment of the work done by external nodal forces ΔW_{equ} is equal to the work done by the distributed forces ΔW:

$$\Delta W_{equ} = \Delta W \tag{110}$$

The work done by the nodal forces $\mathbf{f_e}$ is:

$$\Delta W_{equ} = \mathbf{f_e}^\top \Delta \mathbf{x_e} \tag{111}$$

Castigliano's theorem states that the derivative of strain energy with respect to displacement gives the force in the direction of the displacement. This can also be seen from differentiating equations (109) and (111) with respect to $\Delta \mathbf{x_e}$ and substituting into equations (110) and (108):

$$\mathbf{f_e} = \mathbf{K_e} \Delta \mathbf{x_e} \tag{112}$$

This gives the governing equation of a static FE problem for a single element.

The formulation of the stiffness matrix can be found by considering the stress-strain relationship of linearly elastic materials:

At any point within an element, the incremental displacement is given as

$\Delta\mathbf{u}$, in reference coordinates (ζ, η):

$$\Delta\mathbf{u} = \mathbf{N}\Delta\mathbf{x_e} \tag{113}$$

The matrix of shape functions $\mathbf{N}$ interpolates the displacements of the nodes to displacements at any point within the element in terms of the reference coordinates:

$$\mathbf{N} = \begin{bmatrix} N_1 & 0 & N_2 & 0 & \cdots & \cdots & N_8 & 0 \\ 0 & N_1 & 0 & N_2 & \cdots & \cdots & 0 & N_8 \end{bmatrix} \tag{114}$$

The shape functions are:

$$\begin{aligned} N_1 &= -\frac{1}{4}(\eta - 1)(\zeta - 1)(\eta + \zeta + 1) & N_5 &= \frac{1}{2}(\zeta^2 - 1)(\eta - 1) \\ N_2 &= \frac{1}{4}(\eta - 1)(\zeta + 1)(\eta - \zeta + 1) & N_6 &= \frac{1}{2}(\zeta - 1)(\eta^2 - 1) \\ N_3 &= -\frac{1}{4}(\eta + 1)(\zeta - 1)(\eta - \zeta - 1) & N_7 &= -\frac{1}{2}(\zeta + 1)(\eta^2 - 1) \\ N_4 &= \frac{1}{4}(\eta + 1)(\zeta + 1)(\eta + \zeta - 1) & N_8 &= -\frac{1}{2}(\zeta^2 - 1)(\eta + 1) \end{aligned} \tag{115}$$

The numbering of the shape functions corresponds to the nodes on the real element which are illustrated in figure 124.

The incremental strain at any point in the element is given as:

$$\Delta\boldsymbol{\varepsilon} = \mathbf{S}\Delta\mathbf{u} \tag{116}$$

$\mathbf{S}$ provides the derivatives of displacement. This is a matrix of partial differential operators. In mechanical analysis $\mathbf{S}$ is:

$$\mathbf{S} = \begin{bmatrix} \frac{\partial}{\partial x} & 0 \\ 0 & \frac{\partial}{\partial y} \\ \frac{\partial}{\partial y} & \frac{\partial}{\partial x} \end{bmatrix} \tag{117}$$

By substituting equation (113) into equation (116) the strain in terms of nodal displacements is found to be:

$$\Delta\boldsymbol{\varepsilon} = \mathbf{B}\Delta\mathbf{x_e} \tag{118}$$

$$\mathbf{B} = \mathbf{SN} \tag{119}$$

The $\mathbf{B}$ matrix is in terms of reference coordinates. The stress caused by the distributed force in reference coordinates is given by:

$$\boldsymbol{\sigma} = \mathbf{D}\Delta\boldsymbol{\varepsilon} \tag{120}$$

$\mathbf{D}$ is the constitutive matrix. The constitutive matrix is dependent on the material or substance in question and provides a relation between two physical quantities.

Equation (118), substituted into equation (120) gives the stress caused by the distributed force, in terms of nodal displacements:

$$\boldsymbol{\sigma} = \mathbf{DB}\Delta\mathbf{x_e} \tag{121}$$

The incremental work done by the distributed loading across the element ΔW neglecting work done by internal stresses, strains and body forces is:

$$\Delta W = \int_{A_e} z\boldsymbol{\sigma}\Delta\boldsymbol{\varepsilon}dA \tag{122}$$

A_e is the area of the element and z is the thickness of the element. The incremental work done by the nodal forces ΔW_{equ} is given in equation (111), this must be equal to the incremental work done by the distributed loading across the element:

$$\mathbf{f_e}^{\top}\Delta\mathbf{x_e} = \int_{A_e} z\boldsymbol{\sigma}\Delta\boldsymbol{\varepsilon}dA \tag{123}$$

Substituting equation (118) and equation (121) into equation (123) and simplifying results in:

$$\mathbf{f_e} = \left[\int_{A_e} z\mathbf{B}^\top \mathbf{D}\mathbf{B} dA\right] \Delta\mathbf{x_e} = \left[\int_{-1}^{1}\int_{-1}^{1} z\mathbf{B}^\top \mathbf{D}\mathbf{B}|\mathbf{J}| d\zeta d\eta\right] \Delta\mathbf{x_e} \tag{124}$$

Elements are created in reference space. Coordinate transformations from reference space to real space use the determinant of the Jacobian matrix $|\mathbf{J}|$. The Jacobian matrix is:

$$\mathbf{J} = \begin{bmatrix} \dfrac{\partial x}{\partial \zeta} & \dfrac{\partial y}{\partial \zeta} \\ \dfrac{\partial x}{\partial \eta} & \dfrac{\partial y}{\partial \eta} \end{bmatrix} \tag{125}$$

Equating equation (112) with equation (124) gives the formulation of a two-dimensional FE stiffness matrix for an element.

$$\mathbf{K}_e = \int_{A_e} z\mathbf{B}^\top \mathbf{D}\mathbf{B} dA = \int_{-1}^{1}\int_{-1}^{1} z\mathbf{B}^\top \mathbf{D}\mathbf{B}|\mathbf{J}| d\zeta d\eta \tag{126}$$

B.4.2 The Dynamic Problem

The variational statement for a dynamic situation is the minimum of the Lagrangian ΔL:

$$\Delta L = \Delta V - \Delta U \tag{127}$$

The incremental kinetic energy ΔV is given by:

$$\Delta V = \frac{1}{2}\Delta\dot{\mathbf{x}}_\mathbf{e}^\top \mathbf{M_e} \Delta\dot{\mathbf{x}}_\mathbf{e} \tag{128}$$

The differentiation of kinetic energy with respect to displacement gives the inertia force required to cause the acceleration in a direction that opposes the motion:

$$\mathbf{f_{acc}} = -\mathbf{M_e}\ddot{\mathbf{x}}_\mathbf{e} \tag{129}$$

The governing equation of motion for the element of a dynamic system is:

$$\mathbf{f_e} = \mathbf{M_e}\ddot{\mathbf{x}}_\mathbf{e} + \mathbf{K_e}\mathbf{x_e} \tag{130}$$

The element mass matrix $\mathbf{M_e}$ is given by:

$$\mathbf{M_e} = \int_{A_e} \rho \mathbf{N}^\top \mathbf{N} dA = \int_{-1}^{1}\int_{-1}^{1} \rho \mathbf{N}^\top \mathbf{N} |\mathbf{J}| d\zeta d\eta \tag{131}$$

ρ is the density of the element.

The governing equations for static and dynamic problems (112) and (130) respectively can be used for both individual elements and for the structure as a whole. The assembly of the element mass and stiffness matrices $\mathbf{M_e}$ and $\mathbf{K_e}$ into global mass and stiffness matrices $\mathbf{M}$ and $\mathbf{K}$ is explained in section B.8.

B.4.3 Numerical Integration of the Element Matrices

The integration of the element mass and stiffness matrices is carried out using a numerical integration method, which is most frequently *Gaussian* integration. This method estimates the integration of a function by finding the value of that function at a chosen number of discrete points and multiplying these values by predefined weighting values. A one dimensional polynomial of order n will be integrated exactly by Gaussian integration if the number of points used q is $\frac{1}{2}(n+1)$.

For quadrilateral elements, the formulation of the mass and stiffness matrices in reference coordinates, using Gaussian integration is given by:

$$\mathbf{M}_e = \rho \sum_{i=1}^{q}\sum_{k=1}^{q} w_i w_k \mathbf{N}(\zeta_i, \eta_k)^\top \mathbf{N}(\zeta_i, \eta_k) |\mathbf{J}| \tag{132}$$

$$\mathbf{K}_e = z \sum_{i=1}^{q} \sum_{k=1}^{q} w_i w_k \mathbf{B}(\zeta_i, \eta_k)^\top \mathbf{D}\mathbf{B}(\zeta_i, \eta_k)|\mathbf{J}| \tag{133}$$

The symbols w_i and w_k are weighting functions and the values of the product $w_i w_k$ are given in table 28. Alternative integral expressions exist for triangle elements.

B.5 The Element Forcing Vector

This section describes the external excitation applied to a FE structure. The explanation is given in terms of a mechanical loading but is relevant to any form of applied excitation, such as electrical current in an electromagnetic model.

The element vector of nodal forces $\mathbf{f_e}$ holds the loading applied to the DoFs of the element. This can be from point loads applied to a localized region or from a distributed load acting over a wider area.

Point loads applied to a structure can be represented by situating nodes at the location of the forcing. The rows in the forcing vector then correspond to the DoFs that have forcing applied to them. The appropriate entries of the forcing vector can then be populated directly with the amplitude and direction of the point loads.

Distributed loading is discretized and represented as equivalent nodal forcing. The equivalent nodal forces are calculated by considering the work done on the system by the distributed loading. The incremental work done by the equivalent nodal forces ΔW_{equ} must be equal to the incremental work done on the system by the distributed loading ΔW.

If the distributed loading is given by a function $\mathbf{s}$ in natural coordinates,

the resultant displacement at any point in the element is given by $\Delta\mathbf{u}$; and the work done by the distributed load ΔW is:

$$\Delta W = \int_{A_e} \mathbf{s}^\top \Delta\mathbf{u} dA \tag{134}$$

By substituting equation (113) into equation (134), the work done by the distributed force, in terms of the equivalent nodal displacements $\Delta\mathbf{x_e}$ is:

$$\Delta W = \left[\int_{A_e} \mathbf{s}^\top \mathbf{N} dA\right] \Delta\mathbf{x_e} = \left[\int_{-1}^{1}\int_{-1}^{1} \mathbf{s}^\top \mathbf{N}|\mathbf{J}| d\zeta d\eta\right] \Delta\mathbf{x_e} \tag{135}$$

Equating the work done by the distributed loading (equation (135)) to the work done by the equivalent nodal forces (equation(111)) gives the equivalent nodal force vector for the element:

$$\mathbf{f_e} = \int_{A_e} \mathbf{s}\mathbf{N} dA = \int_{-1}^{1}\int_{-1}^{1} \mathbf{s}\mathbf{N}|\mathbf{J}| d\zeta d\eta \tag{136}$$

Numerically this is found from:

$$\mathbf{f_e} = \sum_{i=1}^{q}\sum_{k=1}^{q} w_i w_k \mathbf{s}\mathbf{N}(\zeta_i, \eta_k)|\mathbf{J}| \tag{137}$$

B.6 The Element Properties of a Magnetic Model

Section B.4 gave the element formulation for general static and dynamic problems. This section gives the formulation specifically for a magnetic FE analysis.

B.6.1 The Element Stiffness Matrix

The governing equation for a single element in electromagnetic problems is:

$$\underline{\mathbf{j}}_\mathbf{e} = \underline{\mathbf{K}}_\mathbf{e}\mathbf{a_e} \tag{138}$$

$\underline{\mathbf{K_e}}$ is the element magnetic stiffness matrix, $\underline{\mathbf{j}}_\mathbf{e}$ is a vector of nodal currents and $\mathbf{a_e}$ is a vector of nodal magnetic potentials.

The magnetic vector potential $\mathbf{a}$ at a single node has the form:

$$\mathbf{a} = 0\mathbf{i} + 0\mathbf{j} + a\mathbf{k}$$

for an element in two dimensions $\mathbf{i}$ and $\mathbf{j}$ indicate perpendicular (x, y) directions in the plane of the model and $\mathbf{k}$ is in the z direction, perpendicular to the plane of the model. For the magnetic FE problem the DoFs in the x and y directions can be neglected, and only one field variable or DoF per node needs to be considered [70].

The element magnetic stiffness matrix $\underline{\mathbf{K_e}}$ is created from:

$$\underline{\mathbf{K_e}} = \int_{A_e} \mathbf{B}^\top \mathbf{J}^{-\top} \mathbf{G} \mathbf{J}^{-1} \mathbf{B} dA = \int_{-1}^{1} \int_{-1}^{1} \mathbf{B}^\top \mathbf{J}^{-\top} \mathbf{G} \mathbf{J}^{-1} \mathbf{B} |\mathbf{J}| d\zeta d\eta \qquad (139)$$

$\mathbf{N}$ is given in equations (114) and (115), and $|\mathbf{J}|$ is the determinant of the Jacobian matrix given in equation (125). Recall from equation (119) that $\mathbf{B} = \mathbf{SN}$. For this one dimensional situation, $\mathbf{S}$ is given as:

$$\mathbf{S} = \begin{bmatrix} \frac{\partial}{\partial x} & 0 \\ 0 & \frac{\partial}{\partial y} \end{bmatrix}$$

For magnetic situations, the constitutive matrix $\mathbf{G}$ relates the magnetic field strength $\mathbf{h}$ to magnetic flux density $\mathbf{b}$ and holds information about material permeability;

$$\mathbf{G} = \begin{bmatrix} \frac{1}{\mu_{yy}} & 0 \\ 0 & \frac{1}{\mu_{xx}} \end{bmatrix} \qquad (140)$$

μ_{xx} is the permeability in the x direction and μ_{yy} is the permeability in the y direction, where x and y are the principle axes of the magnetic material.

Normally these two values are equal.

The numerical computation of equation (139) using q integration points is given by:

$$\underline{\mathbf{K}_\mathbf{e}} = \sum_{i=1}^{q}\sum_{k=1}^{q} w_i w_k \mathbf{B}(\zeta_i, \eta_k)^\top \mathbf{J}^{-\top} \mathbf{G} \mathbf{J}^{-1} \mathbf{B}(\zeta_i, \eta_k) |\mathbf{J}| \tag{141}$$

The values of the product $w_i w_k$ are given in table 28.

B.6.2 The Element Nodal Current Vector

Magnetic excitation is provided by the flow of current through the structure. A 2D magnetic model considers the regions in the plane of the model in which current flows perpendicular to the plane. In these current carrying regions, the current density j is assumed constant and is found by dividing the total amount of current in the region by the cross sectional area of the region. The element vector of nodal currents $\underline{\mathbf{j_e}}$ is then formulated by:

$$\underline{\mathbf{j_e}} = j \int_{A_e} \mathbf{N} dA = j \int_{-1}^{1}\int_{-1}^{1} \mathbf{N} |\mathbf{J}| d\zeta d\eta \tag{142}$$

Numerically, $\underline{\mathbf{j}}_\mathbf{e}$ is:

$$\underline{\mathbf{j}}_\mathbf{e} = j \sum_{i=1}^{q}\sum_{k=1}^{q} w_i w_k \mathbf{N}(\zeta_i, \eta_k) |\mathbf{J}| \tag{143}$$

This method is used where current flows through windings with a number of turns which cover a discrete area of the model. A single current carrying wire with a small cross sectional area compared to the area of the element, passing through the structure is modelled by a point current at the location of the wire. In this situation, the vector of nodal currents can be populated directly with the value of current in the wire by locating a node at the position of the wire.

B.7 The Element Properties of a Mechanical Model

This section describes specifically FE analysis in structural dynamics problems. For structural dynamics problems, the governing equation of motion for a single element is:

$$\mathbf{M_e}\ddot{\mathbf{x}}_\mathbf{e} + \mathbf{K_e}\mathbf{x_e} = \mathbf{f_e} \tag{144}$$

Each node in the 2D model has displacement coordinates in the x and y directions, so there are two DoFs per node. The mass and stiffness matrices are created for each element using the required element material information and shape functions as follows:

B.7.1 The Element Mass Matrix

The general formulation of a 2D element mass matrix is:

$$\mathbf{M_e} = \int_{A_e} \rho \mathbf{N}^\top \mathbf{N} dA = \int_{-1}^{1}\int_{-1}^{1} \rho \mathbf{N}^\top \mathbf{N} |\mathbf{J}| d\zeta d\eta \tag{145}$$

All of these matrices and symbols have already been defined in section B.4.

B.7.2 The Element Stiffness Matrix

The general formulation of an element stiffness matrix is:

$$\mathbf{K_e} = \int_{A_e} z\mathbf{B}^\top \mathbf{D}\mathbf{B} dA = \int_{-1}^{1}\int_{-1}^{1} z\mathbf{B}^\top \mathbf{D}\mathbf{B} |\mathbf{J}| d\zeta d\eta \tag{146}$$

The constitutive matrix $\mathbf{D}$ provides the transformation from strain to stress. Well known matrices exist for $\mathbf{D}$ for *plane stress* and *plane strain* problems.

Plane stress situations occur in thin flat plates and when loading occurs only in the $x - y$ plane of the structure and not transverse to the plane, and when no constraints exist on the strain in the direction of the thickness

of the structure. For plane stress approximations the constitutive matrix is:

$$\mathbf{D} = \frac{E}{1-\nu^2}\begin{bmatrix} 1 & \nu & 0 \\ \nu & 1 & 0 \\ 0 & 0 & \frac{1-\nu}{2} \end{bmatrix} \tag{147}$$

The material properties; Young's modulus E and Poisson's ratio ν are assumed to be constant in the element.

Plane strain problems approximate long solids whose geometry and loading are constant in the longest dimension. The stress along the length of the structure is not zero and the strain in the transverse direction is negligible. For plane strain approximations the constitutive matrix is:

$$\mathbf{D} = \frac{E}{(1+\nu)(1-2\nu)}\begin{bmatrix} 1-\nu & \nu & 0 \\ \nu & 1-\nu & 0 \\ 0 & 0 & \frac{1-2\nu}{2} \end{bmatrix} \tag{148}$$

The formulation of the mechanical mass and stiffness matrices in reference coordinates, using Gaussian integration is given by:

$$\mathbf{M_e} = \rho \sum_{i=1}^{q}\sum_{k=1}^{q} w_i w_k \mathbf{N}(\zeta_i, \eta_k)^\top \mathbf{N}(\zeta_i, \eta_k)|\mathbf{J}| \tag{149}$$

$$\mathbf{K_e} = z \sum_{i=1}^{q}\sum_{k=1}^{q} w_i w_k \mathbf{B}(\zeta_i, \eta_k)^\top \mathbf{D}\mathbf{B}(\zeta_i, \eta_k)|\mathbf{J}| \tag{150}$$

Equivalent expressions exist for triangle elements.

B.8 The Assembly Procedure

A process called *the merge* is used to assemble the properties from the element matrices of each individual element into global matrices which hold the properties of all of the DoFs in the entire structure. It is this global system that can then be solved for the field variable of each DoF. This section describes the process of the merge.

For each DoF in the element there is a corresponding row and column pair in the element matrices that contains the numerical values of the properties that are associated with that DoF. Call the total number of DoFs in a single element $ndof$. The DoFs in a single element are numbered with local labels, these are the numbers from 1 to $ndof$. The rows and columns of the element matrices are also numbered 1 to $ndof$. The link between the DoFs in the element and the entries in the matrices can then be traced through the labelling of both the DoFs in the element and the row and column pairs in the matrix, see figure 126 for a representation of this.

The material properties of the entire structure are quantified by values that correspond to the DoFs in the structure. These values populate the global matrices in the row and column pairs that correspond to the DoFs in the structure. The DoFs in the structure will be numbered with global labels from one up to the total number of DoFs in the structure $NDOF$. Each row and column pair of the global matrices will also be labelled from one up to $NDOF$. The global label of a DoF in the structure links that DoF to its corresponding row and column pair in the global matrices.

During the merge each element is taken in turn. The element DoF labels are mapped to the global DoF labels, see figure 127 for an illustration. Each of the $ndof$ rows and columns in the element matrices use this mapping to

transfer from their location in the element matrices to their location in the global matrices. The properties from the element matrices are superposed onto the global matrices at the location of the global labels, see figure 128.

Once all of the element matrices have been merged into the global matrices, the global matrices hold the combined information from all of the individual element matrices. These global matrices are square and of size $NDOF$.

The global equation of motion for the structural dynamics problem is given as:

$$\mathbf{M}\ddot{\mathbf{x}} + \mathbf{K}\mathbf{x} = \mathbf{f} \tag{151}$$

$\mathbf{M}$, is the global mass matrix, $\mathbf{K}$ is the global stiffness matrix, $\ddot{\mathbf{x}}$ is the acceleration, $\mathbf{x}$ is the displacement and $\mathbf{f}$ is the global forcing vector.

The global static magnetic FE problem is given as:

$$\underline{\mathbf{K}}\mathbf{a} = \underline{\mathbf{j}} \tag{152}$$

The stiffness matrix is $\underline{\mathbf{K}}$, $\underline{\mathbf{j}}$ is the vector of nodal currents and $\mathbf{a}$ is a vector of magnetic potentials.

B.9 Boundary Conditions

Most field problems have a governing equation of the form $\mathbf{K}\mathbf{x} = \mathbf{f}$. The stiffness matrix $\mathbf{K}$ is singular and so the solution cannot be uniquely determined. Boundary conditions are applied to the field problem in order to ensure a unique solution to the problem. The solutions for the remaining DoFs in the structure are given relative to the boundary values. The boundary conditions are generally applied to the global matrices after the

assembly procedure has been completed. *Dirichlet* and *Neumann* boundary conditions are important boundary conditions [62].

Dirichlet boundary conditions set the unknown function to a known function on the boundary of the differential problem. Dirichlet boundary conditions are essential boundary conditions because they do not characterize the space of the solution.

Neumann boundary conditions prescribe the value of the derivative of the unknown function at the boundary, in the direction normal to the boundary. If the Neumann boundary conditions are constant then flux lines can pass through the boundary. The Neumann boundary conditions are natural boundary conditions as they do not influence the definition of the space of the problem.

Mixed boundary conditions include both Dirichlet and Neumann boundary conditions [66].

In situations where a zero solution has been imposed on a single DoF or a range of DoFs, the rows and columns in the matrices that correspond to those DoFs can be removed from the assembled matrices or the matrices can be assembled without including those DoFs.

Once the boundary conditions have been imposed, the set of matrix equations can be solved for the field variables.

B.9.1 Boundary Conditions in the Magnetic FE Problem

In the magnetic problem, the nodes on the boundary of the structure are assigned values of zero potential. As well as ensuring a unique solution to

the problem they prevent flux from crossing the boundary. This constrains the magnetic flux lines to remain within the region of the model. Lines of magnetic flux are the contour lines of constant vector potential, found from the solution of the governing equation.

B.10 Manipulation of Large Matrices

The solution to a FE problem converges to the exact solution as the level of discretization of the mesh increases. A finely discretized mesh contains many elements, nodes and DoFs. The matrices of a complex or large structure will therefore need to be large if an accurate solution to the problem is to be found. Limitations to computational capacity prevent the direct use of large matrices in calculations. Matrix transformations and manipulation techniques are available to enable the manipulation, solution and storage of matrices that are too large to store or solve directly [87]. Some of these techniques are:

- Sparse matrices
- Banded techniques
- Prescribed displacements and reaction loads
- Model reduction techniques

Sparse matrices are advantageous to use if the matrices are mainly populated with zeros. Only the non zero values of a matrix and their location in the full matrix are stored in the sparse matrix, which compresses the matrix and reduces the amount of memory required to store the information considerably. However, operations that are designed to utilize standard matrix structures can be slow and consume large amounts of memory when applied to sparse matrices. Specialized algorithms can often be used that take advantage of the sparse nature of the matrices. Matrices that do not contain a

large proportion of zero entries have no advantages to being stored as sparse.

Power methods are algorithms for finding the largest eigenvalue from a very large sparse system without the need to solve the eigenvalue problem. From a given matrix, the power methods algorithm uses matrix-vector multiplication in an iteration until the largest eigenvalue and corresponding eigenvector of that matrix have converged. The iteration to find the highest eigenvalue and eigenvector pair can sometimes be slow.

The *Lanczos* algorithm is an extension of the power methods and uses the solution for the largest eigenvalue and eigenvector to iterate to find an estimate of the other eigenvalues and eigenvectors in the system. Errors are present in the first solution, which may be negligible for the initial result but are magnified by rounding in subsequent calculations.

A *simultaneous iteration* method for eigenvalues of very large systems starts with an estimate of the first p mode shapes of the system. p is less than the total number of DoFs in the system. The estimate of the mode shapes is used to reduce the full mass and stiffness matrices to dimensions of p. The eigenvalue problem of this reduced system can be found and the mode shapes expanded back to represent the next estimate of the mode shapes of the full system. This estimate is then used in the next iteration until the change in eigenvalues between the iteration steps converges.

Banded techniques require matrices to be ordered so that all the non zero entries in the matrix only appear on the diagonal and in a band above and below the diagonal. The entries in the bands above and below the diagonal must also be symmetric. The entries on the diagonal and on the band under the diagonal are stored as a rectangular array of mainly non zero values.

The full solution can be approximated by implementing a series of transformations on this rectangular array. A *Partitioned Banded* technique can be used for very large problems by storing only a partition of the diagonal and the lower band of entries.

Prescribed displacements and reaction loads: Setting the boundary conditions of a problem decreases the number of unknowns in the problem and enables the single large matrix equation to be split into two smaller equations. The displacements of DoFs on the boundary of a structure $\mathbf{x_b}$ with prescribed boundary conditions are known. The forcing applied to these DoFs $\mathbf{f_b}$ is unknown. The forcing applied to all internal DoFs $\mathbf{f_i}$ is known and initially the displacements of these DoFs $\mathbf{x_i}$ is unknown. The governing equations of motion can be partitioned:

$$\begin{bmatrix} \mathbf{K_{ii}} & \mathbf{K_{ib}} \\ \mathbf{K_{bi}} & \mathbf{K_{bb}} \end{bmatrix} \begin{Bmatrix} \mathbf{x_i} \\ \mathbf{x_b} \end{Bmatrix} = \begin{Bmatrix} \mathbf{f_i} \\ \mathbf{f_b} \end{Bmatrix} \tag{153}$$

and separated into two smaller equations of motion. One equation considers the unknown displacements and known forcing of the internal DoFs:

$$\mathbf{K_{ii}x_i} = \mathbf{f_i} - \mathbf{K_{ib}x_b} \tag{154}$$

The other considers the known displacements and unknown forcing of the boundary nodes:

$$\mathbf{f_b} = \mathbf{K_{bi}x_i} + \mathbf{K_{bb}x_b} \tag{155}$$

Equation (154) can be solved for the unknown internal displacements and then equation (155) can be solved for the unknown boundary forcing. For a large problem with, for example a much higher number of internal than boundary DoFs, equation (154) will be only slightly smaller than equation (153). But equation (155) will be much smaller and easier to solve.

Guyan reduction is a model reduction method that reduces matrices to a manageable size. The solution of the remaining DoFs in the reduced matrices to the static problem are solved exactly. This option for dealing with large matrices is explained in detail in section B.11.

Substructuring is also a model reduction method. This method partitions a large structure into substructures and creates the system matrices for the substructures. The substructure matrices can be partitioned into two sections. The first section holds the DoFs that are internal to that substructure and do not connect to any other substructure. The second section holds the DoFs which provide the coupling between adjoining substructures. The internal DoFs can be eliminated from the substructure matrices. Two reduced substructure matrices that represent adjacent substructures can be merged together to create a new substructure, the internal DoFs of the new substructure can then be eliminated. This process is carried out for all of the substructures until a much reduced system of matrices has been created for the whole structure [87].

B.11 Guyan Reduction

Guyan reduction is a model reduction technique that provides a means of reducing the dimensions of FE mass and stiffness matrices [61]. This method does not compromise the accuracy of the final solution too greatly provided that the set of master DoFs is chosen well and the range of frequencies of interest is not too high. Guyan reduction can be used on a dynamic system of the form $\mathbf{M}\ddot{\mathbf{x}} + \mathbf{K}\mathbf{x} = \mathbf{f}$ which consists of a static (stiffness) term and an inertia (mass) term. The transformations used neglect the inertia of the slave DoFs and so the solution is exact only when used in static analysis. Guyan reduction is also applicable to equations of the form: $\underline{\mathbf{K}}\mathbf{a} = \underline{\mathbf{j}}$ which

contain only a static term and no inertia term.

The transformation that is used on the mass and stiffness matrices reduce certain DoFs out of the matrices. These DoFs are called slaves and the remaining DoFs are masters. The elimination of the slave DoFs reduces the system matrices to a manageable size. The static and dynamic responses to forcing of the reduced system can be found by solving the equation of motion of the reduced system. Mode shapes and natural frequencies are found by solving the eigenvalue problem of the reduced system. This gives an accurate approximation of the low natural frequencies. For sufficiently low frequencies, the errors arising from the model reduction are proportional to the square of the frequency. Errors caused by neglecting the inertia are larger for higher frequencies [48].

The same transformation used to reduce the matrices can also be used to expand the mode shapes and responses of the reduced system. This provides an estimate of the mode shapes and the responses of the full system as linear functions of the mode shapes and responses of the master DoFs.

The choice of the DoF that should be reduced from a range of eligible DoFs that have been merged into the matrices is made by considering the contribution of each of those DoFs to the kinetic energy of the system. A measurement of this contribution is found by calculating the *internal natural frequencies* of the eligible DoFs. The internal natural frequencies are the square roots of the ratios of the individual diagonal entries in the global stiffness matrix to the corresponding diagonal entries in the global mass matrix. A low internal natural frequency indicates a DoF which has a large inertia effect and therefore a large contribution to the kinetic energy of the system and should be kept as a master DoF. The response of the

reduced system is accurate in a frequency range from 0Hz to some large fraction of the internal natural frequency of the slave DoF. Selecting the DoF with the highest internal natural frequency to be the slave DoF ensures a large frequency range where the response of the reduced system is accurate [87].

Guyan reduction is carried out as follows:

The equation of motion of the system $\mathbf{M}\ddot{\mathbf{x}} + \mathbf{K}\mathbf{x} = \mathbf{f}$ can be structured in this way:

$$\begin{bmatrix} \mathbf{M_{mm}} & \mathbf{M_{ms}} \\ \mathbf{M_{sm}} & \mathbf{M_{ss}} \end{bmatrix} \begin{Bmatrix} \ddot{\mathbf{x}}_\mathbf{m} \\ \ddot{\mathbf{x}}_\mathbf{s} \end{Bmatrix} + \begin{bmatrix} \mathbf{K_{mm}} & \mathbf{K_{ms}} \\ \mathbf{K_{sm}} & \mathbf{K_{ss}} \end{bmatrix} \begin{Bmatrix} \mathbf{x_m} \\ \mathbf{x_s} \end{Bmatrix} = \begin{Bmatrix} \mathbf{f_m} \\ \mathbf{f_s} \end{Bmatrix} \tag{156}$$

$\mathbf{M}$, $\mathbf{K}$, $\ddot{\mathbf{x}}$, $\mathbf{x}$ and $\mathbf{f}$ are mass and stiffness matrices and acceleration, displacement and force vectors respectively. The subscript **mm** indicates the master DoFs, the subscript **ss** indicates the slave DoFs, subscripts **ms** and **sm** indicate the DoFs that provide the coupling between the slave and master DoFs. The lower block row in equation (156) ensures equilibrium in the slave DoFs that are reduced out. Note that the ordering of the entries in (156) is for illustrative purposes only and is not necessary when carrying out the computation.

Neglecting the inertia of the slave DoFs, the lower block row in equation (156) becomes:

$$\mathbf{K_{sm}x_m} + \mathbf{K_{ss}x_s} = \mathbf{f_s} \tag{157}$$

By rearranging equation (157), the slave and master DoFs can be written as:

$$\left\{ \begin{array}{c} \mathbf{x_m} \\ \mathbf{x_s} \end{array} \right\} = \left[\begin{array}{cc} \mathbf{I} & \\ \mathbf{-K_{ss}^{-1}} & \mathbf{K_{sm}} \end{array} \right] \mathbf{x_m} + \left[\begin{array}{cc} 0 & \\ \mathbf{K_{ss}^{-1}} & \mathbf{f_s} \end{array} \right] \tag{158}$$

The transformation matrix $\mathbf{T_s}$ is defined as:

$$\mathbf{T_s} = \left[\begin{array}{cc} \mathbf{I} & \\ \mathbf{-K_{ss}^{-1}} & \mathbf{K_{sm}} \end{array} \right] =: \left[\begin{array}{c} \mathbf{I} \\ \mathbf{t_s} \end{array} \right] \tag{159}$$

The reduced mass and stiffness matrices and forcing vector are then found from:

$$\mathbf{M_R} = \mathbf{T_s^\top M T_s} \tag{160}$$

$$\mathbf{K_R} = \mathbf{T_s^\top K T_s} \tag{161}$$

$$\mathbf{f_R} = \mathbf{T_s^\top f} \tag{162}$$

A more computationally effective way to calculate the reduced matrices is:

$$\mathbf{M_R} = \mathbf{M_{mm}} + \mathbf{t_s^\top M_{sm}} + \mathbf{M_{ms} t_s} + \mathbf{t_s^\top M_{ss} t_s} \tag{163}$$

$$\mathbf{K_R} = \mathbf{K_{mm}} + \mathbf{t_s^\top K_{sm}} + \mathbf{K_{ms} t_s} + \mathbf{t_s^\top K_{ss} t_s} \tag{164}$$

$$\mathbf{f_R} = \mathbf{f_m} + \mathbf{t_s^\top f_s} \tag{165}$$

The equation of motion of the reduced system is given by:

$$\mathbf{M_R \ddot{x}_m} + \mathbf{K_R x_m} = \mathbf{f_R} \tag{166}$$

The reduced system consists of master DoFs only and so the matrices of the reduced system are significantly smaller than the full system matrices.

Equation (166) can easily be solved to find the response of the master DoFs. The response of the slave DoFs can be estimated using:

$$\mathbf{x_s} = -\mathbf{K_{ss}^{-1}K_{sm}x_m} + \mathbf{K_{ss}^{-1}f_s} \tag{167}$$

which is extracted from equation (158). The response of the master and slave DoFs together make up the response of the full system.

B.12 Guyan Reduction In The Merge

Guyan reduction can be used in conjunction with the merge of the global mass and stiffness matrices. Using Guyan reduction in the merge prevents the global matrices from becoming too large to process during the merge.

B.12.1 Choosing the Master and Slave DoFs

Before the merge and reduction begins, some DoFs that are required to be present in the final, reduced matrices can be prevented from being reduced out. This is done by creating a *flag* vector which indicates which of the DoFs need to be retained as masters and which DoFs can be used as slaves. The flag vector is consulted for each DoF present in the global matrices whenever the global matrices are reduced. A reason for preventing certain DoFs from being reduced may be if external forces are known to be applied to these DoFs. In a case where the applied forcing occurs to few DoFs, computation is more straightforward if the DoFs to which forcing is applied are not reduced. The same is also true if the responses of a small number of specific DoFs are required. In this case, applying the force directly to the reduced system and calculating the response gives the required results. No expansion transformations are required and no reduction of the forcing vector is required.

B.12.2 The Merge and Reduction Process

The elements are ordered by their location in the structure so that as the elements are merged into the global matrices and the DoFs are reduced, the size that is required of the global matrices is kept to a minimum. The number of DoFs present in the matrices at each step in the merge and reduction process is the front size. As the element matrices are merged in, the front size increases and as the DoFs are reduced out the front size decreases. A dummy run of the merge and reduction process is used to calculate the maximum front size that is reached and the size of the global matrices is initially set by this value. During the dummy run no matrices are manipulated. The dummy run uses the DoF labels and the mapping of the position of each DoF from the element matrices to the global matrices. In each of the steps in the merge and reduction, the dummy run records the front size [87]. Figure 129 illustrates the element merge in the dummy run for a system with two DoFs per node. The front size for this example is illustrated in figure 130.

When the global matrices have been initialized after the dummy run has been completed, the element matrices are merged into the global matrices until the global matrices are fully populated. By this time, a range of DoFs are then eligible to be reduced. Eligible DoFs are those that are not flagged to be kept and for which all the element matrices that contain entries which contribute mass and stiffness properties to that DoF have been merged into the global matrices. The slave DoF is chosen to be the DoF with the highest internal natural frequency of all eligible DoFs and it is reduced from the global matrices using equations (163) to (165). The next slave DoF is chosen and Guyan reduction is carried out again until the global matrices have been reduced to a size which allows for further element matrices to be merged in. Each row and column pair in the global matrices are initially al-

located to a particular DoF and those rows and columns in the matrices are populated with the values of that DoF. Once a DoF has been reduced out of the global matrices, that row and column pair are allocated to another DoF whose properties populate the matrices when that DoF is merged in.

The merge and reduction is carried out until all element matrices have been merged into the global matrices. If required, the final reduction can eliminate all entries except those corresponding to the DoFs which have been flagged to be kept. In this case, it is unnecessary to choose the slave DoFs from their internal natural frequencies and the order of reduction is unimportant. The slave DoF with the lowest internal natural frequency will define the frequency range within which the solution of the reduced system will be accurate. The frequency range where results are accurate can be found by noting each internal natural frequency as the slave DoFs are reduced.

On completion of the merge and reduction of the structure, a solution is found for the reduced system. The solution of the reduced system gives, for the master DoFs; the static response to forcing, the dynamic response at a frequency of interest and the mode shapes. Information for the master DoFs alone may be all of the information that is required, and if so, no further transformations are needed.

B.12.3 Expanding the Results

If the responses or mode shapes are required for the full system, these can be estimated as linear functions of the responses or mode shapes of the master DoFs using equation (167). A fully populated vector of responses or a mode shape vector is generated using an expansion of the reduced vector and a transfer of DoFs from the reduced vector to the global vector. The

reduced system is transformed in steps which are carried out in the reverse of the order that the merge and reduction was carried out in. The expansion process is explained here by assuming that the final steps in the merge and reduction reduced out a number of DoFs and the steps previous to this merged in a number of elements.

Before the expansion begins, the response of the reduced system is found and an unpopulated global response vector is initialized. This has the same number of rows as there are DoFs in the full structure. The expansion process then goes back through the steps that were carried out in the merge and reduction, starting with the final step. For the purposes of this example this was a reduction. The responses of the master DoFs are used to estimate the response of the slave DoF that was reduced in the final reduction, using equation (167). That slave DoF response now becomes a master DoF response and is located in the reduced response vector in the position it occupied in the matrices before it was reduced out. This new reduced response vector is used to estimate the response of the next slave DoF and this is located in the reduced response vector at the relevant location. This expansion process continues until the response of the slave DoFs have been estimated that were reduced out after the last element was merged in.

The last element that was merged in is then considered. The responses that correspond to the DoFs of that element are transfered out of the reduced response vector into the the global response vector. The location of these entries in the global vector correspond to the location of those same DoFs in the global structure. The next element is then considered until another expansion is required.

The process of estimating the slave DoF responses and transferring the

information to the global response vector continues until all responses have been entered into the global vector. This response vector contains the exact responses of the master DoFs and estimates of the slave DoFs as linear combinations of the responses of the master DoFs [87].

B.13 Reducing a Matrix in a Single Transformation

System matrices that are not too large to generate and store but are too large to manipulate can be created using the merge process described in section B.8 and reduced in a single transformation. For the governing equation

$$\underline{\mathbf{j}}_{\mathbf{1}} = \underline{\mathbf{K}}_{\mathbf{1}}\mathbf{a_1} \tag{168}$$

the reduction transformation is:

$$\mathbf{a_1} = \mathbf{T}\mathbf{a_2} \tag{169}$$

The reduced stiffness matrix and excitation vector are found from

$$\underline{\mathbf{K}}_{\mathbf{2}} = \mathbf{T}^{\top}\underline{\mathbf{K}}_{\mathbf{1}}\mathbf{T} \qquad\qquad \underline{\mathbf{j}}_{\mathbf{2}} = \mathbf{T}^{\top}\underline{\mathbf{j}}_{\mathbf{1}} \tag{170}$$

and the reduced equation of motion becomes

$$\underline{\mathbf{j}}_{\mathbf{2}} = \underline{\mathbf{K}}_{\mathbf{2}}\mathbf{a_2} \tag{171}$$

The transformation matrix $\mathbf{T}$ is created by considering each master DoF in turn and applying a unit of excitation to that DoF only. The response of the structure to that excitation becomes one column in $\mathbf{T}$. For example if

the first DoF in the structure is a master DoF then

$$\underline{\mathbf{j}}_{\mathbf{1}} = \begin{Bmatrix} 1 \\ 0 \\ \vdots \\ 0 \end{Bmatrix} \tag{172}$$

and substituting (172) into equation (168) leads to

$$\mathbf{a_1} = \mathbf{k_{1i}} \tag{173}$$

where $\mathbf{k_{1i}}$ is the first column in $\underline{\mathbf{K}}_{\mathbf{1}}^{-\mathbf{1}}$. $\mathbf{k_{1i}}$ becomes the first entry in $\mathbf{T}$. The next master DoF is then considered and this result becomes the second column of $\mathbf{T}$. This is carried out for all master DoFs in the structure.

Areas of distributed excitation can be reduced so they are represented by a single value. This value is then treated in the same way as any other DoF is treated in the analysis. This is achieved by finding the response of the structure to the excitation of that area and including that response in a column of $\mathbf{T}$. $\underline{\mathbf{j}}_{\mathbf{2}}$ can be found with equation (170). The corresponding entry in $\underline{\mathbf{j}}_{\mathbf{2}}$ will be the single value that represents the excitation of that area.

If the columns in $\mathbf{T}$ generated by this method are all similar, for example if the master nodes are located close together, then this method will not give a good solution. The condition of $\mathbf{T}$ can be improved if, when applying unit excitation to each master DoF the remaining master DoFs are clamped. This will force the structure into a unique response for each master node and improve the condition of $\mathbf{T}$.

If the reduction matrix $\mathbf{T}$ provides a combination of reductions of DoFs with distributed excitation and reductions of other slave DoFs then the

columns of **T** may be badly conditioned. Conditioning **T** can be achieved by scaling the columns so that the sum of the squares of the entries equals unity.

The sections in this chapter so far can be applied generally to structures of any shape. The next sections apply only to structures with rotational periodicity.

B.14 Cyclic Symmetry Using Super Elements

This section shows how the feature of cyclic symmetry can be used in the merge and reduction process. Section B.15 describes an alternative method of assembling the mass and stiffness matrices of a cyclically symmetric structure which decouples the mode families. Section B.16 describes the decomposition of a periodic quantity into Fourier components. A more detailed description of cyclically symmetric structures is given in section C.4.

A two dimensional cyclically symmetric structure is composed of m identical substructures or bays in global (x, y) coordinates. Each bay also has a local (x_L, y_L) coordinate reference frame. A simple coordinate transformation converts the local coordinates to global coordinates.

The merge and reduction processes described in sections B.11, B.12 and B.13 are extended here to two stages which create a cyclically symmetric FE model. The first stage creates a *super element*. This is achieved through the merge and reduction methods described in sections B.12 and B.13 to create the reduced mass and stiffness matrices for a single bay. The master DoFs which remain in the super element matrices must include all DoFs for all of the nodes on the boundaries of the bay that provide the connection to adjacent bays and any other internal DoFs which are advantageous to keep

for the subsequent analysis of the structure. For example, the master nodes of one mechanical stator bay, after the first merge and reduction stage are shown in figure 132.

The master DoFs in the super element are sorted so that for nodes with two DoFs in the (x, y) directions, they occur in the order x then y for each node, for increasing radius along the positive x-axis, then with increasing angle anticlockwise from the positive x-axis. This arrangement ensures that the DoFs in the super element matrices are ordered so that all the DoFs on the lower side of the bay are contiguous (call this *side A*). All DoFs between the upper and lower sides are contiguous (call this *partition I*) and all DoFs on the upper side are contiguous (call this *side B*). Figure 131 shows where these DoF occur in the stator bay example and the local coordinates of the bay. The super element mass and stiffness matrices that are created for the one bay are identical to the mass and stiffness matrices for all the other bays, in the local coordinates for each bay.

During the merge of the super elements, the DoFs on *side B* of one bay will connect to the DoFs on *side A* of the adjacent bay. In order for the displacement coordinates of the DoFs on the sides of two adjoining bays to coincide; a transformation is needed on *side B* of each bay. The transformation matrix rotates the DoF coordinates about an angle θ so that the x and y displacement coordinates for *side B* correspond to the x and y displacement coordinates for *side A* of the next bay. The rotation transformation matrix $\mathbf{H}$ is a square matrix with length equal to the number of DoFs on *side B*. $\mathbf{H}$ is mainly populated with zeros but has blocks on the diagonal in the form:

$$\begin{bmatrix} \cos(\theta) & \sin(\theta) \\ -\sin(\theta) & \cos(\theta) \end{bmatrix} \tag{174}$$

The transformed mass and stiffness matrices and forcing vector for one bay are in the form:

$$\mathbf{M}_{BAY} = \begin{bmatrix} \mathbf{M}_{AA} & \mathbf{M}_{AI} & \mathbf{M}_{AB}\mathbf{H} \\ \mathbf{M}_{IA} & \mathbf{M}_{II} & \mathbf{M}_{IB}\mathbf{H} \\ \mathbf{H}^\top\mathbf{M}_{BA} & \mathbf{H}^\top\mathbf{M}_{BI} & \mathbf{H}^\top\mathbf{M}_{BB}\mathbf{H} \end{bmatrix} \tag{175}$$

$$\mathbf{K}_{BAY} = \begin{bmatrix} \mathbf{K}_{AA} & \mathbf{K}_{AI} & \mathbf{K}_{AB}\mathbf{H} \\ \mathbf{K}_{IA} & \mathbf{K}_{II} & \mathbf{K}_{IB}\mathbf{H} \\ \mathbf{H}^\top\mathbf{K}_{BA} & \mathbf{H}^\top\mathbf{K}_{BI} & \mathbf{H}^\top\mathbf{K}_{BB}\mathbf{H} \end{bmatrix} \tag{176}$$

$$\mathbf{f}_{BAY} = \begin{Bmatrix} \mathbf{f}_A \\ \mathbf{f}_I \\ \mathbf{H}^\top\mathbf{f}_B \end{Bmatrix} \tag{177}$$

The second stage of the merge and reduction sees the super element matrices merged into the global matrices and further DoFs reduced out. The process creates the reduced mass and stiffness matrices for the whole stator as follows: Global matrices are initialized and each super element matrix is merged into the global matrices in the manner described in section B.12.2. The global stiffness matrix and forcing vector with two bays merged in before any reduction is carried out are:

$$\mathbf{K} = \begin{bmatrix} \mathbf{K}_{AA1} & \mathbf{K}_{AI1} & \mathbf{K}_{AB1}\mathbf{H} & 0 & 0 & \dots \\ \mathbf{K}_{IA1} & \mathbf{K}_{II1} & \mathbf{K}_{IB1}\mathbf{H} & 0 & 0 & \dots \\ \mathbf{H}^\top\mathbf{K}_{BA1} & \mathbf{H}^\top\mathbf{K}_{BI1} & \mathbf{H}^\top\mathbf{K}_{BB1}\mathbf{H} + \mathbf{K}_{AA2} & \mathbf{K}_{AI1} & \mathbf{K}_{AB1}\mathbf{H} & \dots \\ 0 & 0 & \mathbf{K}_{IA2} & \mathbf{K}_{II2} & \mathbf{K}_{IB2}\mathbf{H} & \dots \\ 0 & 0 & \mathbf{H}^\top\mathbf{K}_{BA2} & \mathbf{H}^\top\mathbf{K}_{BI2} & \mathbf{H}^\top\mathbf{K}_{BB2}\mathbf{H} + \dots & \dots \\ \vdots & \vdots & \vdots & \vdots & \vdots & \ddots \end{bmatrix} \tag{178}$$

$$\mathbf{f} = \begin{Bmatrix} \mathbf{f}_{A1} \\ \mathbf{f}_{I1} \\ \mathbf{H}^{\top}\mathbf{f}_{B1} + \mathbf{f}_{A2} \\ \mathbf{f}_{I2} \\ \mathbf{H}^{\top}\mathbf{f}_{B2} + ... \\ \vdots \end{Bmatrix} \tag{179}$$

The global mass matrix has the same form as the global stiffness matrix.

The element matrices are merged into the global matrices until the global matrices are fully populated. At this point, some DoFs must be reduced out of the global matrices before more element matrices can be merged in. Of the DoFs in the global matrices, a number will be eligible to be used as slave DoFs in the reduction. The slave DoFs are reduced out of the global matrices. When enough DoFs have been reduced, more element matrices can be merged into the global matrices. This process continues until all of the element matrices have been merged in and only the required master DoFs remain. An example of the DoFs that are kept as masters in one bay of a mechanical stator model, after the second merge and reduction, is shown in figure 133. The reduced structure maintains properties of cyclic symmetry.

B.15 Cyclic Symmetry Analysis

This section describes a method of generating the global mass and stiffness matrices of a cyclically symmetric structure from the mass and stiffness matrices of a single bay. The order of symmetry of a cyclically symmetric structure gives the number of identical bays that make up the structure. The method utilizes the spatial harmonic n of each mode family and constraints at the edges of two adjoining bays to create reduced mass and stiffness matrices for the whole structure in terms of the mass and stiffness

matrices for one bay [55].

The solution to the eigenvalue problem of the reduced system gives only the mode shapes and frequencies that correspond to the mode family number n which was used to create the mass and stiffness matrices. Therefore, a different mass and stiffness matrix exist for each value of n that is analysed.

Two transformations are used on the original mass and stiffness matrices of the bay, either of these transformations could be used first. One order of assembly is described here:

An individual, unconstrained bay has the equation of motion:

$$\mathbf{M_{bay}}\ddot{\mathbf{x}}_{\mathbf{bay}} + \mathbf{K_{bay}}\mathbf{x_{bay}} = \mathbf{f_{bay}} \tag{180}$$

$\mathbf{M_{bay}}$ and $\mathbf{K_{bay}}$ are the mass and stiffness matrices, $\ddot{\mathbf{x}}_{\mathbf{bay}}$, $\mathbf{x_{bay}}$ and $\mathbf{f_{bay}}$ are acceleration, displacement and force vectors for the individual, unconnected bay respectively. Each bay has identical material properties, and so mass and stiffness matrices can be assembled for the whole unconnected structure, which consists of s unconnected bays. The equation of motion for the unconnected structure is:

$$\mathbf{M_u}\ddot{\mathbf{x}}_{\mathbf{u}} + \mathbf{K_u}\mathbf{x_u} = \mathbf{f_u} \tag{181}$$

where

$$\mathbf{M_u} = \mathbf{I_s} \otimes \mathbf{M_{bay}}, \qquad \mathbf{K_u} = \mathbf{I_s} \otimes \mathbf{K_{bay}} \tag{182}$$

The Kronecker product $\otimes$ provides a way of presenting matrices with equal entries in blocks in the matrix. For example:

$$\begin{bmatrix} A & B \\ C & D \end{bmatrix} \otimes \begin{bmatrix} 1 & 1 \\ 1 & 1 \end{bmatrix} = \begin{bmatrix} A & A & B & B \\ A & A & B & B \\ C & C & D & D \\ C & C & D & D \end{bmatrix} \tag{183}$$

The identity matrix $\mathbf{I_s}$ has length s and

$$\mathbf{x_u} = \begin{Bmatrix} \mathbf{x_{bay_1}} \\ \mathbf{x_{bay_2}} \\ \mathbf{x_{bay_3}} \\ \vdots \\ \mathbf{x_{bay_s}} \end{Bmatrix}, \qquad \mathbf{f_u} = \begin{Bmatrix} \mathbf{f_{bay_1}} \\ \mathbf{f_{bay_2}} \\ \mathbf{f_{bay_3}} \\ \vdots \\ \mathbf{f_{bay_s}} \end{Bmatrix} \tag{184}$$

The first transformation on this unconnected system utilizes the categorization of each mode family by the spatial harmonic n:

$$\mathbf{x_u} = \mathbf{T_N x_N} \tag{185}$$

$$\mathbf{T_N} = \begin{bmatrix} \cos(0(\frac{2n\pi}{s})) & \sin(0(\frac{2n\pi}{s})) \\ \cos(1(\frac{2n\pi}{s})) & \sin(1(\frac{2n\pi}{s})) \\ \cos(2(\frac{2n\pi}{s})) & \sin(2(\frac{2n\pi}{s})) \\ \vdots & \vdots \\ \cos((s-1)(\frac{2n\pi}{s})) & \sin((s-1)(\frac{2n\pi}{s})) \end{bmatrix} \otimes \mathbf{I} \tag{186}$$

This identity matrix $\mathbf{I}$ has dimensions equal to the number of DoFs in an unconstrained bay.

The new displacement coordinates can be partitioned:

$$\mathbf{x_N} = \left\{ \begin{array}{c} \mathbf{x_c} \\ \mathbf{x_s} \end{array} \right\} \tag{187}$$

Substituting equation (185) into equation (181) gives the equation of motion of the system after the first transformation:

$$\mathbf{M_N}\ddot{\mathbf{x}}_\mathbf{N} + \mathbf{K_N}\mathbf{x_N} = \mathbf{f_N} \tag{188}$$

$\mathbf{M_N}$ and $\mathbf{K_N}$ are:

$$\mathbf{M_N} = \frac{s}{2}\begin{bmatrix} \mathbf{M_{bay}} & 0 \\ 0 & \mathbf{M_{bay}} \end{bmatrix} \text{ and } \mathbf{K_N} = \frac{s}{2}\begin{bmatrix} \mathbf{K_{bay}} & 0 \\ 0 & \mathbf{K_{bay}} \end{bmatrix} \tag{189}$$

Two special cases exist where $n = 0$ and $n{=}s/2$. In these cases the mass and stiffness matrices $\mathbf{M_N}$ and $\mathbf{K_N}$ are:

$$\mathbf{M_N} = s\mathbf{M_{bay}} \text{ and } \mathbf{K_N} = s\mathbf{K_{bay}} \tag{190}$$

In the case of equation (190), the number of DoFs in $\mathbf{M_N}$ and $\mathbf{K_N}$ is half that of the number of DoFs in $\mathbf{M_N}$ and $\mathbf{K_N}$ in equation (189) for all other values of n.

The second transformation is created from the constraints which exist between two adjacent bays. The general form of the constraints is:

$$\mathbf{Q}^\top\mathbf{x_{bay}}_{(i)} + \mathbf{R}^\top\mathbf{x_{bay}}_{(i+1)} = 0 \tag{191}$$

This constraint will be satisfied for all i if:

$$\mathbf{C_N^\top}\mathbf{x_N} = \mathbf{0} \tag{192}$$

Where $\mathbf{C_N^\top}$ is:

$$\mathbf{C_N^\top} = \begin{bmatrix} \mathbf{Q}^\top + \mathbf{R}^\top \cos(\frac{2n\pi}{s}) & \mathbf{R}^\top \sin(\frac{2n\pi}{s}) \\ -\mathbf{R}^\top \sin(\frac{2n\pi}{s}) & \mathbf{Q}^\top + \mathbf{R}^\top \cos(\frac{2n\pi}{s}) \end{bmatrix}$$

The second transformation is given by:

$$\mathbf{x_N} = \mathbf{T_R} \mathbf{x_r} \tag{193}$$

The matrix $\mathbf{T_R}$ is constructed as described in section B.15.1. By substitution of equation (193) into equation (188); the final equation of motion for the structure is:

$$\mathbf{M_r} \ddot{\mathbf{x}}_\mathbf{r} + \mathbf{K_r} \mathbf{x_r} = \mathbf{f_r} \tag{194}$$

The resulting system matrices $\mathbf{M_r}$ and $\mathbf{K_r}$ have dimensions equal to twice the total of the number of DoFs in one bay minus the number of constraints between the bays. This method results in a final matrix equation which is a significantly reduced problem compared to the full matrix equation.

Solving the eigenvalue problem for equation (194) gives the mode shapes and eigenvalues for the reduced structure for all modes described by the spatial harmonic n. The mode shape vectors can be expanded with the transformations given in equation (193) and equation (185) to give the mode shapes for the unconnected structure. Note that the coordinate system used for each bay in this case is the local coordinate system.

B.15.1 Constructing the Transformation Matrix

The transformation matrix $\mathbf{T}$ that satisfies two conditions:

$$\mathbf{C}^\top \mathbf{T} = \mathbf{0} \tag{195}$$

$$[\mathbf{CT}] \text{ is invertible} \tag{196}$$

is found here. The matrix $\mathbf{C}$ is known. Each row in $\mathbf{C}^\top$ represents a constraint. The constraints are counted with the letter k. To construct $\mathbf{T}$ each constraint is considered in turn. The relevant row $\mathbf{c}_k^\top$ is extracted from $\mathbf{C}^\top$ [49]. For example

$$\mathbf{c}_1^\top = \begin{bmatrix} 1 & 4 & 9 & 3 \end{bmatrix} \tag{197}$$

A matrix $\mathbf{T}_k$ is initialized as the identity matrix with dimensions the same as the number of entries in $\mathbf{c}_k^\top$:

$$\mathbf{T}_1 = \begin{bmatrix} 1 & 0 & 0 & 0 \\ 0 & 1 & 0 & 0 \\ 0 & 0 & 1 & 0 \\ 0 & 0 & 0 & 1 \end{bmatrix} \tag{198}$$

The largest value in $\mathbf{c}_k^\top$ is found and the index of this entry noted (in the example entry 3 has the largest value 9). The column of $\mathbf{T}_k$ with that index is removed. The row in $\mathbf{T}_k$ with that index is replaced so that

$$\mathbf{C}_k^\top \mathbf{T}_k = 0 \tag{199}$$

In the example

$$\mathbf{T}_1 = \begin{bmatrix} 1 & 0 & 0 \\ 0 & 1 & 0 \\ -\frac{1}{9} & -\frac{4}{9} & -\frac{3}{9} \\ 0 & 0 & 1 \end{bmatrix} \tag{200}$$

If only one constraint is applied to the system $\mathbf{T} = \mathbf{T}_1$ and this is used in the required transformation.

If there is more than one constraint then the next constraint is considered.

$\mathbf{C}^\top$ is transformed in order to continue building $\mathbf{T}$:

$$\mathbf{C}_k^\top = \mathbf{C}_{k-1}^\top \mathbf{T}_{k-1} \tag{201}$$

$\mathbf{C}_k^\top$ has one less column than $\mathbf{C}_{k-1}^\top$. The entries in $\mathbf{C}_k^\top$ in the rows $< k$ are zero. $\mathbf{T}_k$ is initialized as the identity matrix this also has one less row and column than $\mathbf{T}_{k-1}$. The relevant row and column of $\mathbf{T}_k$ is replaced as described above so that equation (199) holds.

The transformation matrix is then:

$$\mathbf{T}_k = \mathbf{T}_{k-1}\mathbf{T}_k \tag{202}$$

This process is repeated for each constraint. When all constraints have been considered $\mathbf{T} = \mathbf{T}_k$. $\mathbf{T}$ is a matrix with the number of rows equal to the number of columns in $\mathbf{C}^\top$ and the number of columns equal to the number of rows minus the number of constraints. $\mathbf{T}$ is not unique. $\mathbf{T}$ can be post-multiplied by any invertible matrix and the result will also satisfy equation (195).

B.16 Cyclic Symmetry: Decomposing Quantities in Time and Space

This section explains the steps involved in two dimensional Fourier transforms. This section is relevant to any quantity that is periodic in two dimensions. The two dimensions that are described here are space and time. The quantity that is used in this description is force $\mathbf{f}$ but the Fourier transforms can be used for any quantity such as displacement and stress as long as the quantities have two dimensional periodicity.

Time is dealt with here as a non dimensional quantity with period 2π. The

force vector is found for many equally spaced steps in time between 0 and 2π.

Space is periodic in this study because the structure under consideration is circular and separated into s bays. In the local coordinates of each bay the geometry of the bays is identical. The spatial period is one complete revolution around the structure. Force is found for many points in the structure. The distribution of these points is either continuous or discrete and this feature must be taken into account in the Fourier decomposition. The decomposition requires use of a vector of angles $\boldsymbol{\theta}$.

If forcing values are known at many closely spaced points around the structure the forcing can be considered to be continuously variable in the space domain. The values of force are given at each point in polar coordinates. Two vectors of force exist and these are decomposed separately. One vector holds the radial values of force at each point $\mathbf{f_r}$, the other holds the tangential values of force at each point $\mathbf{f_\theta}$. The vector of angles $\boldsymbol{\theta}$ holds the angle to each point from the positive global x axis. In this case there are s points and s entries in $\mathbf{f_r}$, $\mathbf{f_\theta}$ and $\boldsymbol{\theta}$.

$$\mathbf{f_r} = \begin{Bmatrix} f_{r1} \\ f_{r2} \\ \vdots \\ f_{rs} \end{Bmatrix} \qquad \mathbf{f_\theta} = \begin{Bmatrix} f_{\theta 1} \\ f_{\theta 2} \\ \vdots \\ f_{\theta s} \end{Bmatrix} \qquad \boldsymbol{\theta} = \begin{Bmatrix} \theta_1 \\ \theta_2 \\ \vdots \\ \theta_s \end{Bmatrix} \tag{203}$$

Values that are discretely variable, such as nodal forcing are accounted for as follows. Each of the nodes in a bay are considered separately. For the node j in a bay, the forcing is considered for the same (jth) node in all bays. For this set of nodes there will be a vector which holds the forces in the

local x direction and another that holds the forces in the local y direction for those nodes. The angles in $\boldsymbol{\theta}$ are the angles to the local x axis of each bay from the positive global x axis. The bays are counted with the symbol k from 1 to s. If there are J nodes in a bay there will be $2J$ force vectors considered. If there are s bays there will be s entries in each vector.

$$\mathbf{f_{jx}} = \begin{Bmatrix} f_{jx1} \\ f_{jx2} \\ \vdots \\ f_{jxk} \\ \vdots \\ f_{jxs} \end{Bmatrix} \qquad \mathbf{f_{jy}} = \begin{Bmatrix} f_{jy1} \\ f_{jy2} \\ \vdots \\ f_{jyk} \\ \vdots \\ f_{jys} \end{Bmatrix} \qquad \boldsymbol{\theta} = \begin{Bmatrix} \theta_1 \\ \theta_2 \\ \vdots \\ \theta_k \\ \vdots \\ \theta_s \end{Bmatrix} \tag{204}$$

The angle to the k^{th} bay is:

$$\theta_k = (k-1)\frac{2\pi}{s} \tag{205}$$

The above describes the organization of force in space. The vectors of force will be calculated for every time step within one period of time. There are T time steps so there will be T sets of these force vectors.

B.16.1 Finding a Quantity from Fourier Coefficients

First the forward relationship for Fourier analysis is described. This involves composing the force from known values of Fourier coefficients [74]:

$$\begin{aligned} \mathbf{f}(\theta,t) = \sum_{n=0}^{N}\sum_{m=0}^{M} & \mathbf{a}_{nm}\cos(n\theta)\cos(mt) + \mathbf{b}_{nm}\cos(n\theta)\sin(mt) \\ & + \mathbf{c}_{nm}\sin(n\theta)\cos(mt) + \mathbf{d}_{nm}\sin(n\theta)\sin(mt) \end{aligned} \tag{206}$$

$$\mathbf{a}_{nm} = \frac{1}{\pi^2}\int_{\theta=-\pi}^{\theta=\pi}\int_{t=-\pi}^{t=\pi}\mathbf{f}(\theta,t)\cos(n\theta)\cos(mt)\,d\theta\,dt \tag{207}$$

$$\mathbf{b}_{nm} = \frac{1}{\pi^2} \int_{\theta=-\pi}^{\theta=\pi} \int_{t=-\pi}^{t=\pi} \mathbf{f}(\theta, t) \cos(n\theta) \sin(mt) d\theta dt \tag{208}$$

$$\mathbf{c}_{nm} = \frac{1}{\pi^2} \int_{\theta=-\pi}^{\theta=\pi} \int_{t=-\pi}^{t=\pi} \mathbf{f}(\theta, t) \sin(n\theta) \cos(mt) d\theta dt \tag{209}$$

$$\mathbf{d}_{nm} = \frac{1}{\pi^2} \int_{\theta=-\pi}^{\theta=\pi} \int_{t=-\pi}^{t=\pi} \mathbf{f}(\theta, t) \sin(n\theta) \sin(mt) d\theta dt \tag{210}$$

$$\mathbf{c}_{0m} = \mathbf{d}_{0m} = 0 \text{ for all } m$$

$$\mathbf{b}_{n0} = \mathbf{d}_{n0} = 0 \text{ for all } n$$

The spatial index is given by n and N is the total number of spatial components $N \leq s/2$. If force is a discrete quantity then s is the order of cyclic symmetry of the structure. If the force is a continuous quantity s is the number of points in $\mathbf{f}$. The temporal index is m and M is the total number of spatial components $M \leq T/2$. $\mathbf{a}_{nm}, \mathbf{b}_{nm}, \mathbf{c}_{nm}$ and $\mathbf{d}_{nm}$ are the magnitudes of force of each component.

B.16.2 Decomposing the Quantity into Fourier Coefficients

The reverse of the relationship for Fourier analysis involves decomposing a known force into Fourier coefficients.

The forcing vector is initially given in the *time* and *space* domain. Two transformation calculations convert the forcing vector into a two dimensional Fourier map. The Fourier map is an array of values in the *temporal frequency* and *spatial frequency* domain. The values in the Fourier map are the coefficients $\mathbf{a}_{nm}$, $\mathbf{b}_{nm}$, $\mathbf{c}_{nm}$ and $\mathbf{d}_{nm}$ introduced in the previous section. The order that the transformations are carried out in is not important but the order described here first converts from the time and space domain into the spatial frequency and time domain and secondly into the temporal frequency and spatial frequency domain. The coefficients in the spatial fre-

quency and time domain $\boldsymbol{\vartheta_1}(\theta)$ are created from any of the vectors of forces $\mathbf{f}$ mentioned above using the transformation:

$$\boldsymbol{\vartheta_1}(\theta) = (\mathbf{B_1}^\top \mathbf{B_1})^{-1}(\mathbf{B_1}^\top \mathbf{f}) \tag{211}$$

$$\mathbf{B_1} = \begin{bmatrix} \cos(0\boldsymbol{\theta}) & \cos(1\boldsymbol{\theta}) & \sin(1\boldsymbol{\theta}) & \cdots & \cos((N-1)\boldsymbol{\theta}) & \sin((N-1)\boldsymbol{\theta}) & \cos(N\boldsymbol{\theta}) \end{bmatrix} \tag{212}$$

If the points of force in $\mathbf{f}$ are equally spaced then the columns in $\mathbf{B_1}$ are orthogonal and the product $(\mathbf{B_1}^\top \mathbf{B_1})$ is a diagonal matrix.

The transformation in equation (211) is carried out for all of the vectors of forcing that have been calculated for all T time steps resulting in T vectors of coefficients $\boldsymbol{\vartheta_1}(\theta)$. Combining these vectors into a single array results in a matrix $\boldsymbol{\Psi_1}(\theta)$ which has $2N$ rows and a column for each time step. Each row holds the coefficients of the spatial harmonics.

The transformation from the spatial frequency and time domain into the temporal frequency and spatial frequency domain uses M temporal coefficients.

$$\boldsymbol{\Psi_2}(\theta, t) = ((\mathbf{B_2}^\top \mathbf{B_2})^{-1}(\mathbf{B_2}^\top \boldsymbol{\Psi_1}(\theta)^\top))^\top \tag{213}$$

$$\mathbf{B_2} = \begin{bmatrix} \cos(0t_1) & \cos(1t_1) & \sin(1t_1) & \cdots & \cos((M-1)t_1) & \sin((M-1)t_1) & \cos(Mt_1) \\ \cos(0t_2) & \cos(1t_2) & \sin(1t_2) & \cdots & \cos((M-1)t_2) & \sin((M-1)t_2) & \cos(Mt_2) \\ \vdots & \vdots & \vdots & \ddots & \vdots & \vdots & \vdots \\ \cos(0t_T) & \cos(1t_T) & \sin(1t_T) & \cdots & \cos((M-1)t_T) & \sin((M-1)t_T) & \cos(Mt_T) \end{bmatrix} \tag{214}$$

The value of time at each step is t_1 to t_T. For equally spaced time steps the product $(\mathbf{B_2}^\top \mathbf{B_2})$ is diagonal because the columns of $\mathbf{B_2}$ are orthogonal.

The columns of the resulting matrix $\boldsymbol{\Psi_2}(\theta, t)$ correspond to coefficients of the different temporal harmonics with constant spatial harmonic and the

rows correspond to coefficients of different spatial harmonics with constant temporal harmonic:

$$\begin{bmatrix} \cos(0\theta)\cos(0t) & \cos(0\theta)\cos(1t) & \cos(0\theta)\sin(1t) & \cdots & \cos(0\theta)\cos(Mt) \\ \cos(1\theta)\cos(0t) & \cos(1\theta)\cos(1t) & \cos(1\theta)\sin(1t) & \cdots & \cos(1\theta)\cos(Mt) \\ \sin(1\theta)\cos(0t) & \sin(1\theta)\cos(1t) & \sin(1\theta)\sin(1t) & \cdots & \sin(1\theta)\cos(Mt) \\ \cos(2\theta)\cos(0t) & \cos(2\theta)\cos(1t) & \cos(2\theta)\sin(1t) & \cdots & \cos(2\theta)\cos(Mt) \\ \sin(2\theta)\cos(0t) & \sin(2\theta)\cos(1t) & \sin(2\theta)\sin(1t) & \cdots & \sin(2\theta)\cos(Mt) \\ \vdots & \vdots & \vdots & \ddots & \vdots \\ \cos(N\theta)\cos(0t) & \cos(N\theta)\cos(1t) & \cos(N\theta)\sin(1t) & \cdots & \cos(N\theta)\cos(Mt) \end{bmatrix} \tag{215}$$

For each combination of spatial and temporal harmonic n and m there exists a 2x2 block in the Fourier map of coefficients of those harmonics:

$$\begin{bmatrix} \cos(n\theta)\cos(mt) & \cos(n\theta)\sin(mt) \\ \sin(n\theta)\cos(mt) & \sin(n\theta)\sin(mt) \end{bmatrix} \tag{216}$$

Sin(0) is zero so these components are neglected from the map. The 2x2 block for the 0^{th} spatial harmonic is created with the relevant entries from the first and last row:

$$\begin{bmatrix} \cos(0\theta)\cos(mt) & \cos(0\theta)\sin(mt) \\ \cos(N\theta)\cos(mt) & \cos(N\theta)\sin(mt) \end{bmatrix} \tag{217}$$

The 2x2 block for the 0^{th} temporal harmonic is created with the relevant entries from the first and last column:

$$\begin{bmatrix} \cos(n\theta)\cos(0t) & \cos(n\theta)\cos(Mt) \\ \sin(n\theta)\cos(0t) & \sin(n\theta)\cos(Mt) \end{bmatrix} \tag{218}$$

B.16.3 Expanding Back into the Temporal Frequency Domain

In order to find the forcing from a particular combination of temporal m and spatial n harmonic the two rows and columns in $\mathbf{\Psi_2}$ that correspond to those harmonics are extracted and denoted Ψ_2:

$$\begin{bmatrix} \cos(n\theta)\cos(mt) & \cos(n\theta)\sin(mt) \\ \sin(n\theta)\cos(mt) & \sin(n\theta)\sin(mt) \end{bmatrix} \tag{219}$$

Whether the initial forcing vector contained continuous or discrete variables in the time and space domain, the expansion is used to find discrete nodal values of force. This is achieved by transforming into nodal forces $\mathbf{f}_\omega$ for the same node in each bay in the temporal frequency domain:

$$[\mathbf{f}_{\omega 1}, \mathbf{f}_{\omega 2}] = \mathbf{B_3}\Psi_2 \tag{220}$$

$$\mathbf{B_3} = \begin{bmatrix} \cos(n\theta_1) & \sin(n\theta_1) \\ \cos(n\theta_2) & \sin(n\theta_2) \\ \vdots & \vdots \\ \cos(n\theta_s) & \sin(n\theta_s) \end{bmatrix} \tag{221}$$

The angles θ_1, θ_2 and θ_s are the angle to the x axis of the 1st, 2nd and last bay (s) respectively from the global positive x axis of the structure.

The matrices $[\mathbf{f}_{\omega 1}, \mathbf{f}_{\omega 2}]$ have s rows and these hold the values of force for each bay. There are 2 columns, the first for the cosine component and the second for the sine component of forcing. These must be combined using the imaginary number i to give the total force that corresponds to each bay:

$$\mathbf{f}_\omega = \mathbf{f}_{\omega 1} - i\mathbf{f}_{\omega 2} \tag{222}$$

This expansion process can be carried out for all nodes in the bay and inserted into a global vector for the whole structure. If the initial vectors of forces contained force values in polar coordinates then the resultant force vectors will also hold values in polar coordinates. If the vectors of force in the time and space domain contained force values in local Cartesian coordinates then the resultant force vectors will also hold values in local Cartesian coordinates.

B.17 Conclusion to the Finite Element Modelling Chapter

This chapter has introduced and illustrated the finite element method in general terms and in terms that are specifically relevant to this study. The generation of the element matrices has been given for the magnetic model and the mechanical model. The specific magnetic and mechanical models that have been developed for this study were generated with the methods described in this chapter.

Cyclically symmetric structures have been described. Methods for utilizing this feature for generating the FE matrix equations have also been given. Periodic forcing has also been considered. This chapter has set out the methods that were used to generate the models that are described in the following sections.

ζ	η	$w_i w_k$
-0.86213631159495	-0.86213631159495	0.12100299328560
-0.33998104358486	-0.86213631159495	0.22685185185185
0.33998104358486	-0.86213631159495	0.22685185185185
0.86213631159495	-0.86213631159495	0.12100299328560
-0.86213631159495	-0.33998104358486	0.22685185185185
-0.33998104358486	-0.33998104358486	0.42529330301069
0.33998104358486	-0.33998104358486	0.42529330301069
0.86213631159495	-0.33998104358486	0.22685185185185
-0.86213631159495	0.33998104358486	0.22685185185185
-0.33998104358486	0.33998104358486	0.42529330301069
0.33998104358486	0.33998104358486	0.42529330301069
0.86213631159495	0.33998104358486	0.22685185185185
-0.86213631159495	0.86213631159495	0.12100299328560
-0.33998104358486	0.86213631159495	0.22685185185185
0.33998104358486	0.86213631159495	0.22685185185185
0.86213631159495	0.86213631159495	0.12100299328560

Table 28: Gaussian Integration Weightings

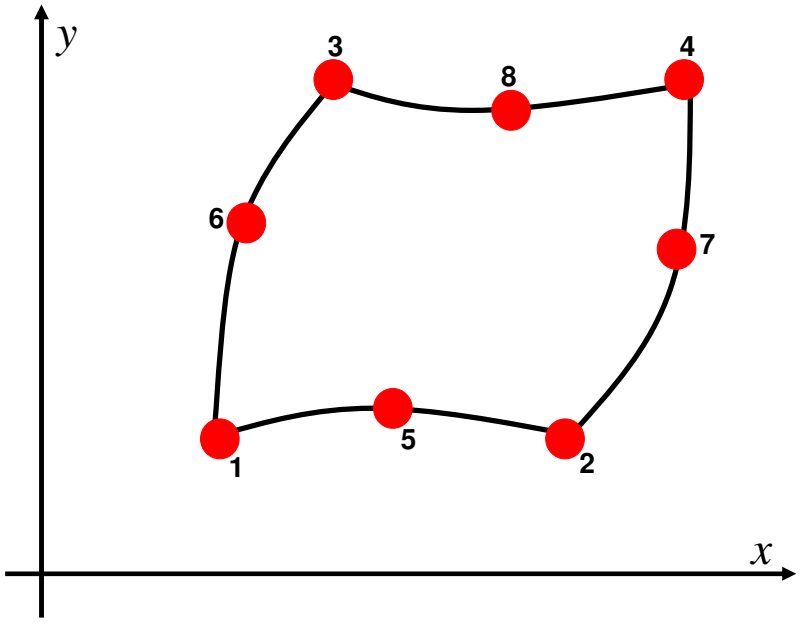

Figure 124: An 8 Noded Quadrilateral Element in Real Space

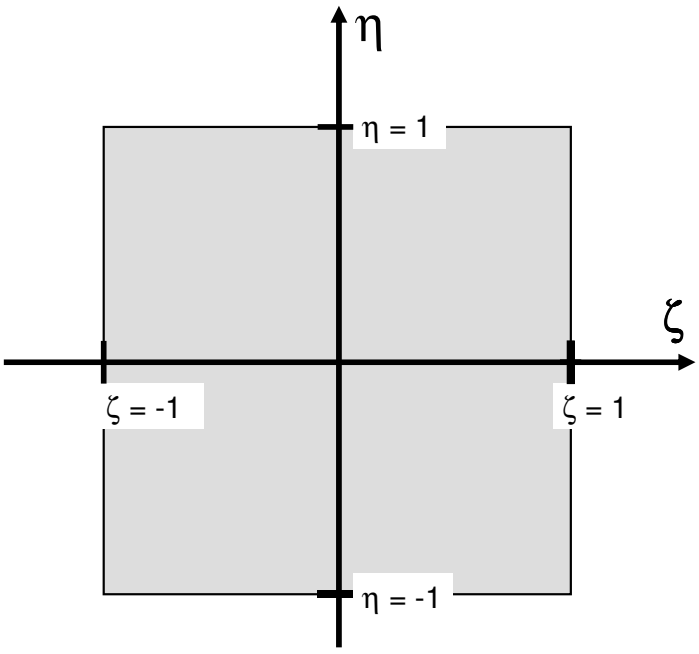

Figure 125: An Element in Reference Space

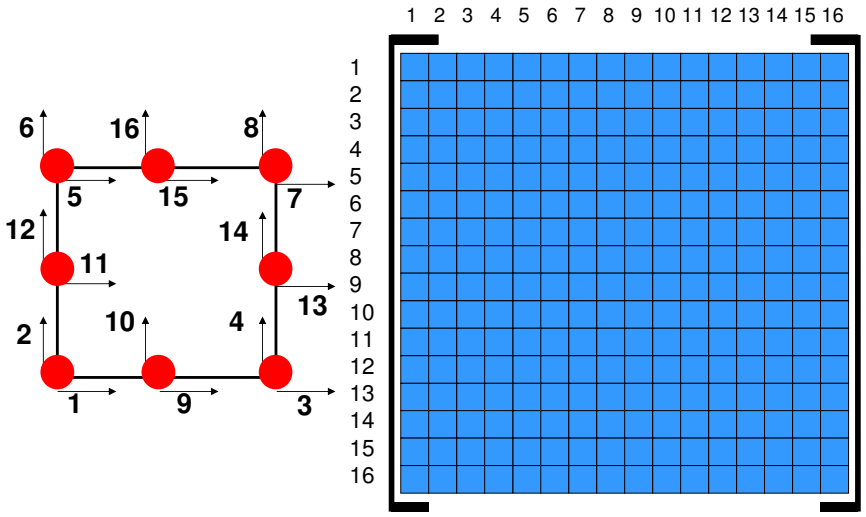

Figure 126: A Single Element with Local DoF Labels and the Corresponding Element Matrix

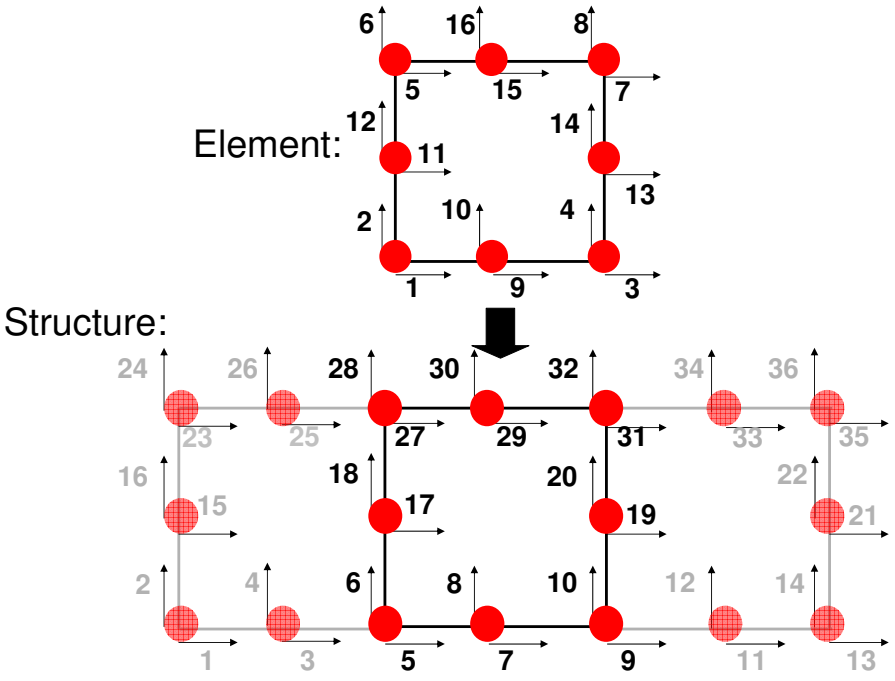

Figure 127: An Element with Local DoF Labels and in the Structure with Global DoF Labels

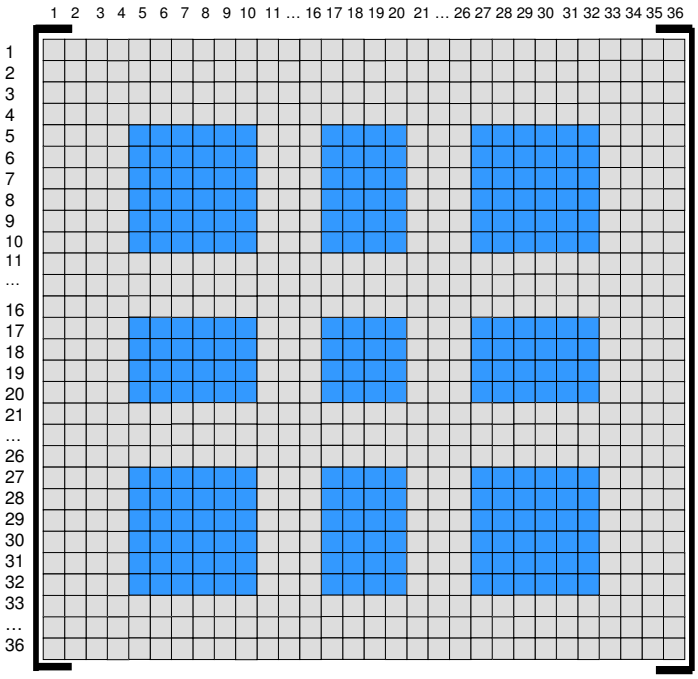

Figure 128: The Element Matrix Merged Into The Global Matrix

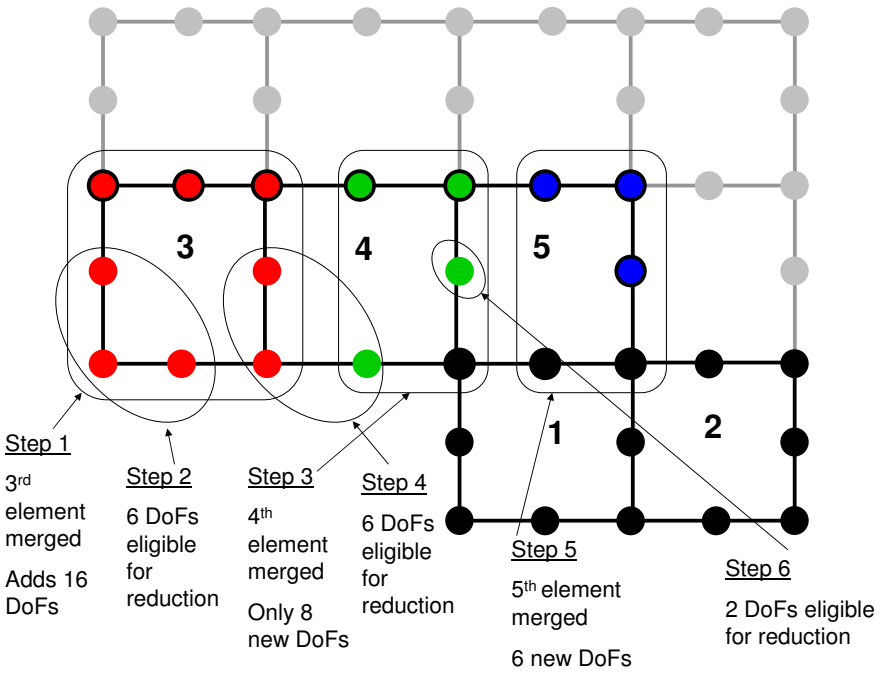

Figure 129: An Example of a Dummy Run of the Element Merge and Reduction

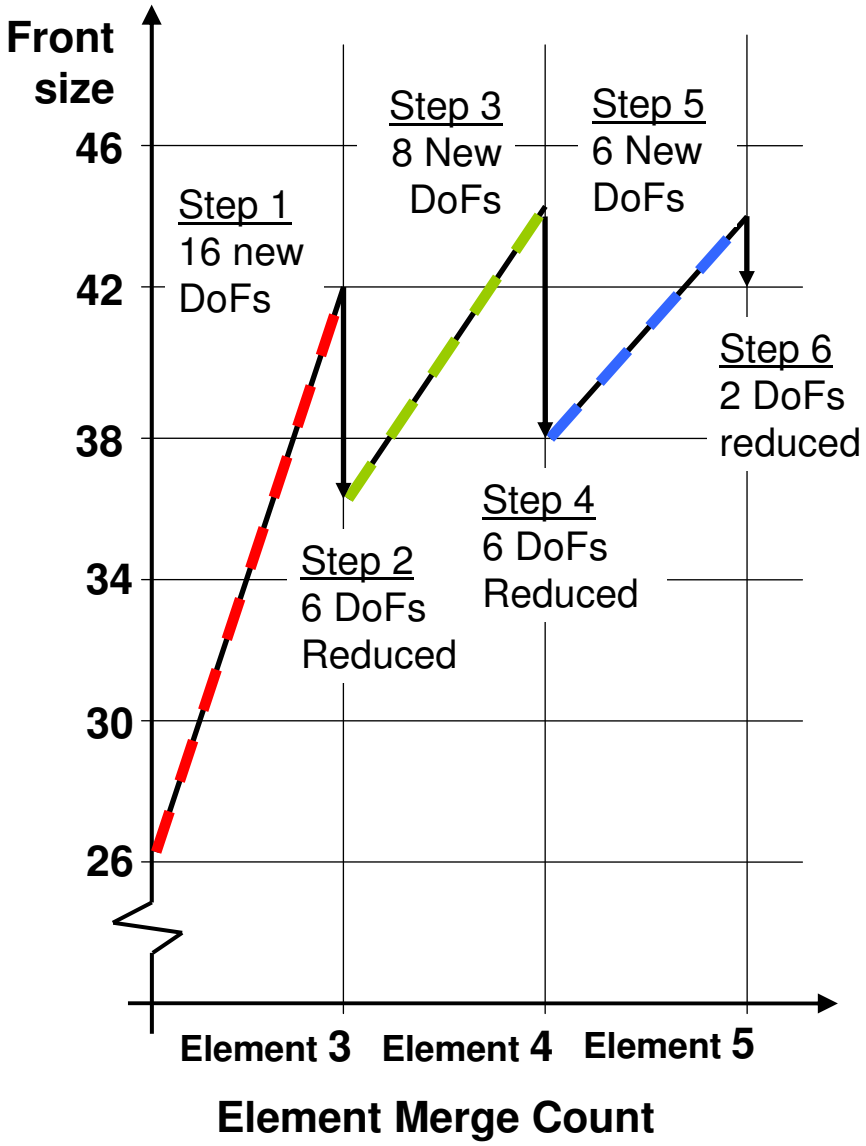

Figure 130: How the Front Size is Counted During the Dummy Run

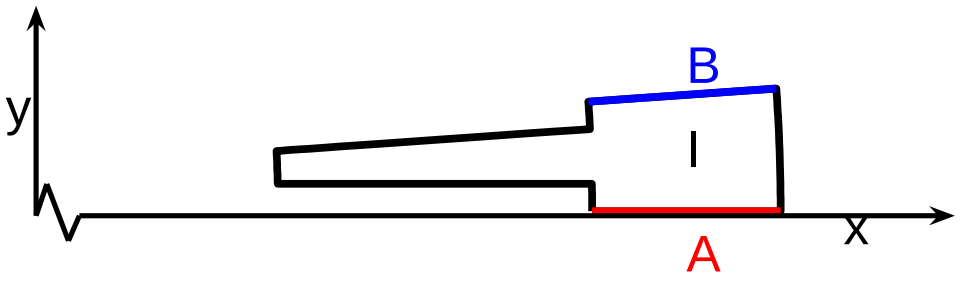

Figure 131: The Boundary of One Stator Bay

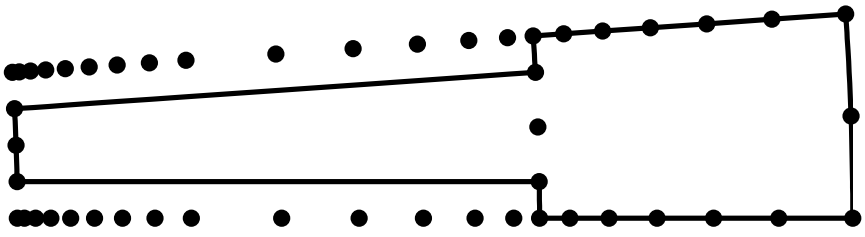

Figure 132: One Stator Bay with Master Nodes After the Merge and Reduction of One Bay

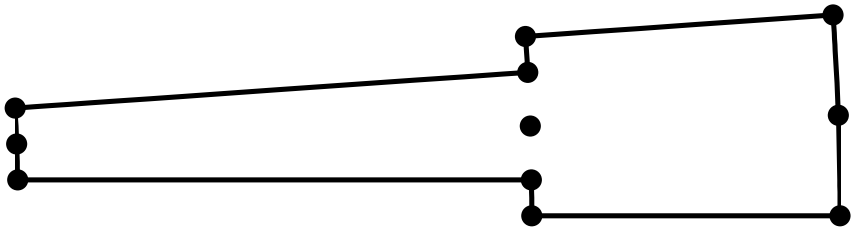

Figure 133: One Stator Bay with Master Nodes After the Complete Merge and Reduction of the Stator

C The Mechanical FE Model of the Electrical Machine

C.1 Mechanical FE Analysis Introduction

This chapter gives some background information related to mechanical finite element analysis of electrical machines and the mode shapes of the stator. The first section describes briefly some of the methods that have been used to model electrical machines and shows how these methods have developed over the years. The second section explains how the mode shapes of a cyclically symmetric structure can be categorized into families of modes. Much of this section is relevant to any cyclically symmetric structure, however the examples given in this section are of the stator of an electrical machine.

C.2 Machine Modelling

Electromagnetic machine noise is largely caused by the response of the stator of an electrical machine under applied electromagnetic forcing across the air gap and in the stator iron. The resultant vibrations from these applied forces are highly dependent on the vibrational characteristics of the stator and so analysis of noise emission from electrical machines requires knowledge of the mode shapes and natural frequencies of the stator. This section discusses some of the methods that have been used to analyse the vibrational behaviour of a machine with most of this work concentrated on the stator.

The computer power and capacity available for computational analysis sets limits for the size of the analysis that can be carried out. Assumptions, simplifications and model reduction techniques are often required in order to carryout accurate analysis of a physical situation. Stator modelling

has been carried out since at least the 1950s. Vast simplifications of the stator geometry were required for the early models and the number of techniques available for analysis were limited. The introduction of finite element analysis and improvements in computer capacity have enabled techniques for modelling to be developed and improved significantly since these early models.

Early stator modelling techniques applied energy methods to simple geometries such as ring models and calculated the natural frequencies of these. Further work introduced double ring models with the two rings separated by key bars representing a stator core and frame [1]. The teeth and windings were then included as cantilever beams joined to the stator core [57]. Modern day finite element techniques allow for complex geometric structures to be analysed and as a result far more realistic stator models can be generated and analysed [19]. However, assumptions are still required to simplify complex situations. The different levels of complexity and different features that are often included in electrical machine analysis result in the following common types of models:

- Two dimensional models
- Three dimensional models
- Ring models
- Double ring models or ring and frame models
- Solid cylinder models
- Laminated cylinder models
- Symmetrical and asymmetrical models
- Stator models with the frame included

- Models of the stator core, teeth and windings
- Damped and undamped models

C.2.1 Two and Three Dimensional Models

Some studies into the vibrations of electrical machines use models that are two dimensional and some studies use models that are three dimensional. A three dimensional model has the ability to account for the properties and response of the machine along the length. A two dimensional model can only account for a single cross section of the machine. An accurate three dimensional model requires a larger amount of computer storage and computation than a two dimensional plane model.

C.2.2 Ring and Cylinder Models

The simplest two dimensional stator model that has been used in the literature is a ring model and the simplest three dimensional model is a solid cylinder. Often, the properties of the ring and cylinder models are developed by assuming that the teeth and windings contribute to the inertia but not to the stiffness of the structure.

The vibrations within a machine transmit to the frame of the machine and a large amount of electrical machine noise is emitted from the frame. In 1927 Den Hartog [33] investigated the vibration of the frame by modelling this as both a ring with rigid feet and a ring with hinged feet. The first natural frequency for both of these models was calculated. The results showed that the first natural frequency of a frame with rigid feet is higher than that of a frame with hinged feet. In a follow up paper in 1928 [34] Den Hartog showed that the natural frequencies calculated for a ring with fixed and hinged feet were the upper and lower limits respectively for the first natural frequency of a machine frame. This second paper narrowed down the frequency range

by quantifying the flexibility of the feet and the corresponding first natural frequency of the frame [34]. The mode shape at the first natural frequency of the frame shows that the sides of the frame vibrate radially and the top of the frame has a mainly tangential displacement. The first natural frequency of the frame of a small example machine was shown to be close to the rotor slot passing frequency of the machine which could lead to the production of tonal noise. It was stated that a coincidence of frequencies could occur in a large machine with a more flexible frame and the higher magnetic force harmonics. The higher natural frequencies of the frame could be of importance in the noise emission from a machine but these were not calculated in these papers due to the complexity of the calculations [33] [34].

Modelling of the stator was carried out in 1956 by Alger *et al* in [1] who developed a 2D model of a stator which consisted of two concentric rings. A thin outer ring represented the stator frame. The inner ring represented the stator core, teeth and stator windings. The teeth contributed to the inertia but not the strength of the structure. The inner ring was connected to the outer ring by ribs which allowed for the transmission of vibrations from the inner to the outer ring. Electromagnetic forcing was considered to act on the inner ring and cause this to vibrate. The resultant vibration of the outer ring represented the level of noise that was emitted. This model was used to estimate the frequency, mode number and amplitude of the force waves for steady deflections of an example machine. This information was then used to indicate the sound pressure level of the machine [1].

In 1968 Ellison *et al* [43] showed that by modelling the stator as a cylinder and neglecting its shear energy and rotary inertia, the static response of the cylinder can easily be found. This can be multiplied by a dynamic magnification factor to give the dynamic response. However, when modelling

stators with thick cores or few poles, or thin cores vibrating at high mode numbers, the rotary inertia and shear energy of the cylinder must also be taken account of. For long stators, vibrations with axial variation should also be considered. Ellison *et al* also stated that machines which have the stator and frame connected with an interference fit can be considered as a single cylinder. But stators that are connected to the frame by ribs or key bars have a more complicated transmission of vibration between the stator and frame. If the contact between the stator and frame is not assumed to be solid, the frame can be assumed not to affect the vibration of the stator [43].

C.2.3 Laminated Models

A stator is built up of many identical laminations of electrical steel in order to prevent the flow of eddy currents in the iron. A consequence of this construction of the stator is that a small amount of relative movement is allowed for between adjacent laminations and this affects the mechanical response of the stator compared to an equivalent solid structure. The effective modulus of rigidity of a stack of laminated steel can be as low as 0.25% of the modulus of rigidity of solid steel [55].

In [101] Wang *et al* investigated the effects of laminations and clamping pressure on stator vibrations. Lamination thickness was first investigated on four solid ring models of varying thickness. Theoretical models using 3D block finite elements were created and experimental tests were also carried out. Both experimental and theoretical results showed that the in-plane radial vibrations were independent of the thickness of the ring. Out of plane vibrations were dependent on ring thickness and these frequencies increased as the ring thickness increased. The study continued to analyse the effect of the number of laminations in experimental ring models formed

from lamination stacks. Results from impact tests showed that, for transverse vibrations, the vibrational behaviour of a laminated stack was different to that of a solid ring of the same thickness as the stack. The resonant frequencies of the transverse modes of each laminated stack were close to the resonant frequencies of the single ring which had the same thickness as the individual laminations in the stack. These results showed that the transverse vibrational behaviour of a lamination stack is dominated by the vibrational behaviour of the individual laminations in the stack. The reason for this is that adjacent laminations do not have an elastic connection between them and so a small amount of slip is allowed for between the laminations in a single stack. The magnitudes of the transverse responses of the laminated stacks were lower than those of the corresponding solid rings and so the laminations cause a reduction in the FRF of the ring model. The in-plane vibration modes and frequencies were independent of the number of laminations in the stack. The clamping pressure was also investigated experimentally. The results showed that the transverse responses of the lamination stacks decreased with increasing clamping pressure and started to disappear. The responses of the in-plane vibrations were not affected by the clamping pressure. The authors concluded that stators exhibit mainly in-plane vibrations and so a plane model is sufficient for modelling the vibrations of a stator. A solid cylinder model predicts extra transverse vibrations that are not present in the vibrational response of the laminated model and the errors in the resonant frequencies of the radial vibrations are large compared to the predictions of the plane model [101].

C.2.4 Cyclically Symmetric Models

Usually the stator of an electrical machine is a cyclically symmetric structure. This feature is often exploited in electrical machine analysis as it allows for the complexity of the structure to be reduced and the analysis

simplified. Studies that took advantage of this feature are mentioned here briefly. An electrical machine will have geometric features such as feet and fins which cause asymmetries in the structure. One study is mentioned here of the effect that asymmetries have on the frequency spectrum of an otherwise cyclically symmetric structure.

In 1997 [55] Garvey *et al* used a model which exploited the cyclic symmetry of the stator core and the categorization of mode shapes into families. The mass and stiffness matrix for a single bay, which incorporates a stator tooth and the corresponding back of core was generated. Transformations carried out on these matrices resulted in a system which could be solved to find the different resonant frequencies for an individual mode number.

Chang *et al* [19] carried out numerical analysis and experimental tests on a ring model and a ring with a notch indented into it. The aim of this work was to investigate the effect of geometric irregularities in otherwise cyclically symmetric structures by observing the difference in their frequency response functions (FRFs). The calculated and experimentally measured FRF for the notched ring were compared to those for a perfectly symmetric ring. The study showed that a FRF for the notched ring consisted of resonant peaks which coincided almost exactly with the resonant peaks for the regular ring. Extra peaks which did not occur on the FRF for the regular ring were also present in the FRF for the notched ring. The extra peaks occurred at close frequencies to the peaks for the regular ring but with lower amplitude. This phenomenon of natural frequency pairs occurring with asymmetrical shapes is sometimes known as frequency splitting or dual resonances [57]. In order to investigate the effects of realistic asymmetries, impact tests were carried out on a stator core and frame. The resulting FRF consisted of many more resonant peaks than for the ring model and many of the peaks occurred

in pairs. Analysis of these resonances showed that where pairs occurred, the two corresponding radial and axial mode shapes were of the same mode order. The authors concluded that the FRF of a machine with geometric irregularities has an enriched FRF. If a symmetric model is to be used to predict the vibrational behaviour of a machine stator, some resonances will not be predicted. A similar conclusion was drawn by Yang in [104] and Girgis *et al* in [57].

C.2.5 Stator Models with Teeth and Windings

In 1972 in [44] Ellison *et al* calculated the natural frequencies of the radial vibration of a stator and frame. The frame was modelled with a thin ring. The stator had a thick core, teeth and windings. An interference fit between the stator core and frame was modelled with key bars. Equations of energy were used; the total kinetic energy of the machine was given as the sum of the kinetic energy of the frame, core, teeth and windings due to rotational and translational motion. The total bending energy of the machine was given by the sum of the bending energies of the frame, core and ribs. The sum of the shear energy of the core, the extensional energy of the core and the ribs and the total bending energy gave the total potential energy of the system. The total potential energy and total kinetic energy were used in Lagrange's equation of motion to derive the equation of motion of the system and calculate the natural frequencies. The calculated natural frequencies only differed from measured values by up to 3%. This result was an improvement on previous similar methods which had neglected shear, extension and rotational inertia, the authors showed that these assumptions resulted in errors of up to 20% compared with experimental measurements [44].

In 1982 in [57] Girgis *et al* developed a method for determining the resonant

frequencies and mode shapes of a three dimensional stator. The model that was developed consisted of a thick stator core, teeth and windings and a thin frame which was connected to the stator by cooling ribs. Equations of energy were applied to the different features of the stator separately. The teeth, windings and cooling ribs were treated as cantilevers fixed to the stator and the stator was treated as a cylinder. Numerical methods were needed to solve the resulting complex system of equations and initial estimates of the mode shapes were required. The solution gave mode shapes and natural frequencies for radial vibrations, axial vibrations and torsional vibrations of the stator and frame. The study also found that the axial length of the stator can be neglected in simulations of short machines to simplify the analysis and still give a reasonable estimate of the in-plane vibrations of the stator. The relationship between size and frequency was also considered with the conclusion that the natural frequencies of stators are inversely proportional to the stator diameter, causing a high modal density in the frequency range of acoustic interest for large machines [57].

Benbouzid *et al* [10] in 1993 investigated the effect of the presence of the teeth, windings and wedges on the natural frequencies of a stator model. In this paper, the natural frequencies of four undamped finite element models of a stator were found. The different models had increasing levels of complexity in the geometry. The first model represented a stator core only (a ring model). The second model was a stator core with teeth. The third model was a stator with teeth and impregnated windings. The fourth model was of a stator with teeth, impregnated windings and wedges. A comparison of the first two models showed clearly that the presence of teeth affected the calculated resonant frequencies of the stator as explained here. For most of the mode shapes that correspond to low frequency resonances, bending occurs in the stator core but the teeth exhibit rigid motion, this affects the

resonant frequencies only slightly compared to the ring model. At higher resonant frequencies the motion of the teeth includes some bending which is opposite to the bending of the back of the stator. This motion of the teeth contributes to the rotational inertia of the stator and acts to decrease the natural frequencies compared to the ring model. The bending motion of the teeth increases at higher frequencies. The effect that the teeth have on the natural frequencies in comparison with the ring model becomes more prominent at higher frequencies. In the third model the contact between the teeth and windings was assumed to be perfect. The actual non-homogeneous, non-isotropic windings were modelled by homogeneous, non-isotropic material. This and the fourth model which included wedges gave higher natural frequencies compared to the second model of the stator core and teeth. This effect is due to the presence of the windings and wedges which suppress the lateral vibrations of the teeth. This showed that the windings and wedges contribute stiffness properties to the stator model as well as additional mass and it is important to include the effects of these in stator vibration analysis [10].

In [100], in 1996 various models were analysed by numerical FE modelling and experimentation. The different models had varying degrees of complexity from a laminated cylindrical shell, a stator with teeth and no windings to a stator with teeth and windings. The laminated cylindrical model was used to verify the numerical analysis. Several resonances were noticed from the experimental results that were not predicted by the theory, most of these resonances were multiple resonances with the same circumferential mode number but higher order longitudinal mode numbers. These were thought to be caused by the inhomogeneousness of the laminated model axially due to the laminations. Some of the multiple resonances were dual resonances caused by irregularities in the plane of the cylinder from holding bolts and

end plates. Comparing a FRF from a smooth cylinder to a stator core with teeth shows that the motion of the teeth causes extra sharp resonant peaks that are not present in the FRF of the smooth cylinder. A long stator model with teeth and windings had resonances additional to those that were predicted which were caused by irregularities in the structure and windings. The windings were not impregnated and this flexibility added extra resonances. The study concluded that the main effect of the windings is to add damping to the stator and restrict the motion of the teeth [100].

C.2.6 Quasi-Static and Dynamic Models

Mechanical models can be classed as *quasi-static* or *dynamic*. Quasi-static models account only for the stiffness and neglect the mass and damping. Dynamic models account for the mass and can have non-zero damping or zero damping. Quasi-static models are much simpler to analyse and require less computational memory than dynamic models. Dynamic situations cannot be accurately simulated with quasi-static models [6].

C.2.7 Damped Models

Different methods exist for including damping in mechanical analysis. Belahcen [5] used an FE model to investigate the effect of Rayleigh damping factors ξ and δ on the vibrational behaviour of the stator core of a synchronous generator. Raleigh damping is given by $\mathbf{D_R} = \xi\mathbf{M} + \delta\mathbf{K}$, in the equation of motion $\mathbf{M}\ddot{\mathbf{x}} + \mathbf{D_R}\dot{\mathbf{x}} + \mathbf{K}\mathbf{x} = \mathbf{f}$. The applied forcing was from Maxwell forces and the resultant vibration of the stator was calculated for different values of the Rayleigh damping factors. In [6] Belahcen compared the results of two dynamic models, one included realistic damping values, the other had no damping. Both studies found that away from the resonant frequencies there were little differences in the amplitude of displacements between models with reasonable damping and undamped models.

When an exciting force is equal to or close to a structure's natural frequency, the amplitude of vibration is determined by the damping capacity of the structure. Thus damping should be considered when calculating the amplitude of vibration at resonance [104].

C.2.8 Stator Modelling Summary

This section has described some of the methods that have previously been used to analyse electrical machines. It has been shown that the most accurate results are achieved by including as many of the features of the machine as possible. With modern day computational capacity and FE analysis methods realistic models are possible. However, a few simplifications can be made to FE analysis of electrical machine stators. One simplification is the use of a 2D model to predict the frequency response of the 3D structure. This is possible because the stator is constructed from laminations. Relative movement occurs between the laminations and the radial vibration characteristic of the stack is dominated by that of the individual plates. The other simplification is the use of cyclic symmetry in the analysis. There are methods used in FE analysis which take advantage of this feature to simplify the model construction and reduce the size of the model. However, assuming a structure is cyclically symmetric may result in some natural frequencies being missed by the analysis.

The presence of the teeth and windings are important and must be considered. At low frequencies the teeth have little effect on the frequencies. At the higher natural frequencies the rotational inertia of the teeth becomes important. The bending motions of the teeth cause the natural frequencies of the stator to be lower than that of an equivalent ring and cause extra natural frequencies to occur. The windings act to dampen the motion of

the teeth.

The next points provide a summary of each type of model that has been considered here:

- **Two dimensional models**
  - Cannot predict out-of-plane motion
  - Less computational capacity required
- **Three dimensional models**
  - Can account for all degrees of motion
  - Computationally intense
- **Single and double ring and cylinder models**
  - Simple to analyse
  - Neglect the rotational inertia of the teeth
  - Estimate low frequency responses
  - Neglect the effect of features such as windings and frame
- **Laminated models**
  - Account for relative movement between laminations
  - Predict lower vibration magnitudes than a solid cylinder
  - Stator vibrations occur mainly in-plane
  - In-plane response of a laminated stack independent of clamping pressure and number of laminations
  - In-plane response of a laminated stack can be captured by a 2D model
  - Transverse responses decrease with increasing clamping pressure

- **Cyclically Symmetrical models**
  - Model reduction techniques take advantage of cyclic symmetry
  - Neglects asymmetrical features
  - Could miss actual resonances of the structure
  - Geometric irregularities in an otherwise cyclically symmetric structure cause dual resonances
- **Models of the stator core, teeth and windings**
  - Use energy methods or finite element analysis
  - Computationally intense
  - Account for rotational inertia of the teeth
  - Teeth and wedges contribute important stiffness and mass properties
  - Windings mainly contribute damping properties
  - Accurate results possible
- **Quasi static and dynamic models**
  - Quasi-static models account only for the stiffness
  - Quasi-static models are much simpler to analysis but not suitable for dynamic situations
  - Dynamic models account for mass and damping as well as stiffness
- **Damped and undamped models**
  - Response at resonance determined by damping of the structure
  - Away from resonant conditions damping has little effect

C.3 Transforming a System into Modal Coordinates

A forced, multi-DoF system with N DoFs has an equation of motion for each of the DoFs in the system. These equations are coupled and so require solving simultaneously. The equation of motion for the whole structure is represented in the following matrix equation

$$\mathbf{M}\ddot{\mathbf{x}} + \mathbf{D}\dot{\mathbf{x}} + \mathbf{K}\mathbf{x} = \mathbf{f} \tag{223}$$

where $\mathbf{M}$ is the mass matrix, $\mathbf{D}$ is the damping matrix, $\mathbf{K}$ is the stiffness matrix, $\mathbf{f}$ is the force vector, $\mathbf{x}$ is a vector of displacements, $\dot{\mathbf{x}}$ is a vector of velocities and $\ddot{\mathbf{x}}$ is a vector of accelerations of the DoFs in the system. Each row in these matrices and vectors corresponds to a DoF in the corresponding system. In vibration analysis the equation of motion of the system is often transformed into modal coordinates. This transformation uncouples the mass and stiffness matrices of the multi-DoF system so that the resulting *modal mass* and *modal stiffness* matrices are diagonal. In modal coordinates the system can be treated as N individual single-DoF systems. The analysis of the system in modal coordinates is therefore much simpler than the analysis of the original system. A simple transformation of the solution in modal coordinates leads to the solution of the original multi-DoF system. If proportional damping is assumed the resulting damping matrix is also diagonal. In the case of proportional damping $\mathbf{D} = a_1\mathbf{M} + b_1\mathbf{K}$ where a_1 and b_1 are scalar values.

Mode shapes can be scaled by any arbitrary value. Modal mass and stiffness matrices are usually scaled to unit modal mass, or *mass normalized*. The modal mass matrix is then equal to the identity matrix and the modal stiffness matrix is given by the spectral matrix. The spectral matrix is a matrix mainly populated with zeros, the eigenvalues of the system are the

only entries and these are located on the diagonal of the matrix.

The orthonormalization process is described here:

The matrix of mode shapes of the original system can be denoted $\mathbf{U}$:

$$\mathbf{U} = \left[\begin{array}{cccc} \mathbf{u}_1, & \mathbf{u}_2, & \ldots, & \mathbf{u}_N \end{array} \right] \tag{224}$$

The mode shapes of the undamped system have the property of orthogonality. This property enables the modal mass $\mathbf{M_m}$ and stiffness $\mathbf{K_m}$ matrices to be found from the original mass and stiffness matrices:

$$\mathbf{M_m} = \mathbf{U}^\top \mathbf{M} \mathbf{U} \qquad\qquad \mathbf{K_m} = \mathbf{U}^\top \mathbf{K} \mathbf{U} \tag{225}$$

$$\mathbf{M_m} = \begin{bmatrix} m_{m1} & 0 & 0 & 0 \\ 0 & m_{m2} & 0 & 0 \\ 0 & 0 & \ddots & 0 \\ 0 & 0 & 0 & m_{mN} \end{bmatrix}, \quad \mathbf{K_m} = \begin{bmatrix} k_{m1} & 0 & 0 & 0 \\ 0 & k_{m2} & 0 & 0 \\ 0 & 0 & \ddots & 0 \\ 0 & 0 & 0 & k_{mN} \end{bmatrix} \tag{226}$$

To scale mode j to unit modal mass $\mathbf{q}_j$, the original mode $\mathbf{u}_j$ is divided by the square root of the modal mass value of that mode m_{mj}.

$$\mathbf{q}_j = \frac{\mathbf{u}_j}{\sqrt{m_{mj}}} \tag{227}$$

The matrix of all vectors scaled to unit modal mass $\mathbf{Q}$ can be used to scale the mass, proportional damping and stiffness matrices to unit modal mass:

$$\mathbf{Q}^\top \mathbf{M} \mathbf{Q} = \mathbf{I} \qquad \mathbf{Q}^\top \mathbf{D} \mathbf{Q} = 2\gamma\mathbf{\Omega} \qquad \mathbf{Q}^\top \mathbf{K} \mathbf{Q} = \mathbf{\Lambda} \tag{228}$$

$\mathbf{I}$ is the identity matrix, γ is the damping factor, $\mathbf{\Omega}$ is a matrix of natural frequencies and $\mathbf{\Lambda}$ is the spectral matrix:

$$\mathbf{\Omega} = \begin{bmatrix} \omega_1 & 0 & 0 & 0 \\ 0 & \omega_2 & 0 & 0 \\ 0 & 0 & \ddots & 0 \\ 0 & 0 & 0 & \omega_{mN} \end{bmatrix} \qquad \mathbf{\Lambda} = \begin{bmatrix} \lambda_1 & 0 & 0 & 0 \\ 0 & \lambda_2 & 0 & 0 \\ 0 & 0 & \ddots & 0 \\ 0 & 0 & 0 & \lambda_{mN} \end{bmatrix} \tag{229}$$

$$\omega_j = \sqrt{\lambda_j} \tag{230}$$

ω_j is the natural frequency that corresponds to the j^{th} mode of the system, λ_j is the eigenvalue that corresponds to the j^{th} mode of the system.

The displacement of the DoFs can be related to the modal displacement vector $\mathbf{y}$ by:

$$\mathbf{x} = \mathbf{Q}\mathbf{y} \tag{231}$$

By substituting equation (231) into equation (223) and pre-multiplying by $\mathbf{Q}^\top$ the equation of motion becomes:

$$\mathbf{I}\ddot{\mathbf{y}} + 2\gamma\mathbf{\Omega}\dot{\mathbf{y}} + \mathbf{\Lambda}\mathbf{y} = \mathbf{p} \tag{232}$$

The modal force vector is $\mathbf{p}$:

$$\mathbf{p} = \mathbf{Q}^\top\mathbf{f} \tag{233}$$

The matrices in equation (232) are diagonal and so this matrix equation can easily be solved as a vector equation:

$$\ddot{\mathbf{y}} + 2\gamma\boldsymbol{\omega}\dot{\mathbf{y}} + \boldsymbol{\lambda}\mathbf{y} = \mathbf{p} \tag{234}$$

Where

$$\boldsymbol{\omega} = \left\{ \begin{array}{cccc} \omega_1, & \omega_2, & \ldots, & \omega_{mN} \end{array} \right\}^\top \quad \boldsymbol{\lambda} = \left\{ \begin{array}{cccc} \lambda_1, & \lambda_2, & \ldots, & \lambda_{mN} \end{array} \right\}^\top \tag{235}$$

Once equation (234) has been solved. The nodal displacements can be found with equation (231).

C.4 Cyclically Periodic Structures and Families of Modes

This thesis has already shown that there are advantages to recognizing when structures posses cyclic symmetry. This feature can be utilized in FE analysis to simplify the computations. It can also be used to understand and predict the vibration characteristics of the structure. This section describes the geometry and behaviour of cyclically symmetric structures.

C.4.1 Cyclic Symmetry Mode Shape Behaviour

Cyclic symmetry occurs in a structure if the geometry of the structure at an angle θ is identical to the geometry of the structure at angle $(\theta + 2\pi k/s)$ where s is the order of cyclic symmetry of the structure and k is any integer [95]. The geometry of a cyclically symmetric structure can therefore be decomposed into s identical substructures or *bays*, each joined to the adjacent bay at the boundaries of the bay. The complete structure can be described within a global coordinate frame. Each bay can be considered within its own local coordinate frame. A simple transformation can convert from the local coordinate frame to the global coordinate frame. The stator of an electrical machine is a cyclically symmetric structure, with the number of teeth indicating the order of symmetry of the structure. Features such as clamping bolts can disrupt this and decrease the order of symmetry, however these are not considered here.

The mode shapes of any cyclically symmetric structure occur in families. Each mode family is categorized by the spatial harmonic number n, also called the mode number. The mode number is the number of complete sinusoidal waves around the circumference that the structure deflects by. Note that the deflections in each bay are measured in the local coordinates of the bay. Two orthogonal mode shapes exist for each resonant frequency of a cyclically symmetric structure, except for n=0 and $n = s/2$ when only one single mode shape exists. The angle between two orthogonal mode pairs is $\pi/2n$ radians.

C.4.2 Categorization of Cyclically Symmetric Mode Shapes

It is possible to categorize mode shape families with a graphical representation of the waves around the circumference of the structure. This is done in the following manner: The eigenvalue problem for the completed system is solved. One DoF is chosen, the deflection of this same DoF in each bay, in local coordinates is plotted against bay number. The resulting shape is a sinusoidal wave form with n complete waves. An n=0 plot is a straight horizontal line.

An analytical method of categorizing modes utilizes a projection of each mode onto a subspace using a projection matrix [40][52]. The projection matrix in question is created using the matrix $\mathbf{P}$ spanning the subspace of interest:

$$\mathbf{P} = \begin{bmatrix} 1 & 0 \\ \cos(\frac{2(1)n\pi}{s}) & \sin(\frac{2(1)n\pi}{s}) \\ \vdots & \vdots \\ \cos(\frac{2(k)n\pi}{s}) & \sin(\frac{2(k)n\pi}{s}) \\ \vdots & \vdots \\ \cos(\frac{2(s-1)n\pi}{s}) & \sin(\frac{2(s-1)n\pi}{s}) \end{bmatrix} \otimes \mathbf{I} \tag{236}$$

In (236) the length of the identity matrix $\mathbf{I}$ is equal to the number of DoFs in one bay. The number of block rows in $\mathbf{P}$ is s; the order of cyclic symmetry in the structure, k is an integer that increases from 0 in the first block to s-1 in the last block.

The projection matrix $\mathbf{T}$ is created from:

$$\mathbf{T} = \mathbf{P}(\mathbf{P}^\top\mathbf{P})^{-1}\mathbf{P}^\top \tag{237}$$

A mode $\mathbf{w}$ is classified by a particular mode number n if the following relationship holds:

$$(\mathbf{I} - \mathbf{T})\mathbf{w} = 0 \tag{238}$$

C.4.3 Orthonormalization

In FE analysis of a cyclically symmetric structure, the two modes in a mode pair will be calculated independently and so are unlikely to be given as orthogonal. Section C.3 explains that it is advantageous to make all modes orthonormal before carrying out further analysis as use of orthonormal equations of motion simplifies analysis immensely. Orthonormal modes are modes that are orthogonal and normalized according to some fixed inner-product. The Gram Schmidt process orthogonalizes and normalizes a set of linearly independent functions with respect to an arbitrary weighting matrix $\mathbf{A}$ as follows [2]:

If $\mathbf{v}$ and $\mathbf{w}$ are two mode shape vectors, a scale factor κ can be found from:

$$\kappa = \frac{\mathbf{v}^\top\mathbf{A}\mathbf{w}}{\mathbf{w}^\top\mathbf{A}\mathbf{w}} \tag{239}$$

An orthogonal mode is produced by scaling $\mathbf{w}$ by κ and subtracting from $\mathbf{v}$:

$$\mathbf{u} = \mathbf{v} - \mathbf{w}\kappa \tag{240}$$

This is normalized by:

$$\mathbf{u} = \frac{\mathbf{u}}{\sqrt{\mathbf{u}^\top \mathbf{u}}} \tag{241}$$

The modes $\mathbf{u}$ and $\mathbf{w}$ are now orthonormal.

C.5 Discussion of Stator Mode Shapes

Figure 134 shows a plot of the natural frequencies of a stator against the mode number of the corresponding mode. The order of cyclic symmetry of this structure is 90 and so the n=0 and n=45 modes have only one mode shape for each natural frequency. Every other point on the graph represents a pair of modes for each natural frequency.

A cyclically symmetric structure constrained to move only within a plane will always have three rigid body modes at $0Hz$. One of the rigid body modes is an n=0 mode, which is a rigid body rotation about the centre. Two are orthogonal n=1 modes, which are rigid body translations in perpendicular directions as shown in figure 135. Modes at $0Hz$ are not shown in figure 134.

From the plot in figure 134 trend lines can be seen. The points which indicate the lowest natural frequency for each mode pair for mode numbers $n = 2$ and above make up the first trend line. The mode shapes for every mode family on this trend line have a characteristic deflected shape which is the expansion and contraction of the back of core. The first n=2 mode pair has an ovaling of the structure, where an expansion occurs along one diameter line and a compression occurs along a line perpendicular to

this, see figure 136. The first n=3 mode pair deflects radially outwards at three angles $2\pi/3$ radians to each other and radially inwardly at angles $2\pi/6$ radians to these, see figure 137. The first n=4 mode pair deflects into a square-like shape, so deflects radially outwards at four angles $2\pi/4$ radians to each other and inwardly at angles $2\pi/8$ radians to these, see figure 138. No n=0 or n=1 modes appear on this trend line because there are no corresponding mode shapes for these mode numbers.

The second natural frequency for each mode pair makes up the second trend line on figure 134. This line includes an n=1 mode but does not include an n=0 mode. These frequencies are the lower frequencies associated with tooth rocking. All mode shapes on this line include some tooth rocking motion which is in phase with the motion of the back of the stator core. These tooth rocking modes include the shapes shown in figures 139 and 140. The mode shapes of the trend line for the third lowest natural frequencies all have some tooth movement that is out of phase with the back of the stator core such as that shown in figure 141.

The n=0 modes are special cases which do not necessarily belong on the trend lines. The first non rigid body n=0 mode appears to sit on the second trend line, however, this is a breathing mode not a tooth rocking mode. This is shown in figure 142. The second n=0 mode that appears to sit on the third trend line is the tooth rocking mode shown in figure 143. The lowest tooth rocking frequency that can be found with a FE model is by considering a single stator bay with the edges of the bay clamped. The first mode shape of this analysis gives the closest representation that can be modelled of the first n=0 tooth rocking mode that corresponds to the second trend line in figure 134.

C.6 Conclusion to the Chapter

This chapter has given an overview of some of the methods used in the literature to model electrical machines. Simple models exist for this however, the more features that can be included in the model the more accurate the results will be. Modern FE techniques enable complicated and accurate numerical modelling of electrical machines.

A stator is a cyclically symmetric structure and this feature leads to vibrational behaviour which can be categorized by trends lines and mode families. The n=0 family of modes are an exception to this. Tooth rocking is an important vibrational characteristic in this study.

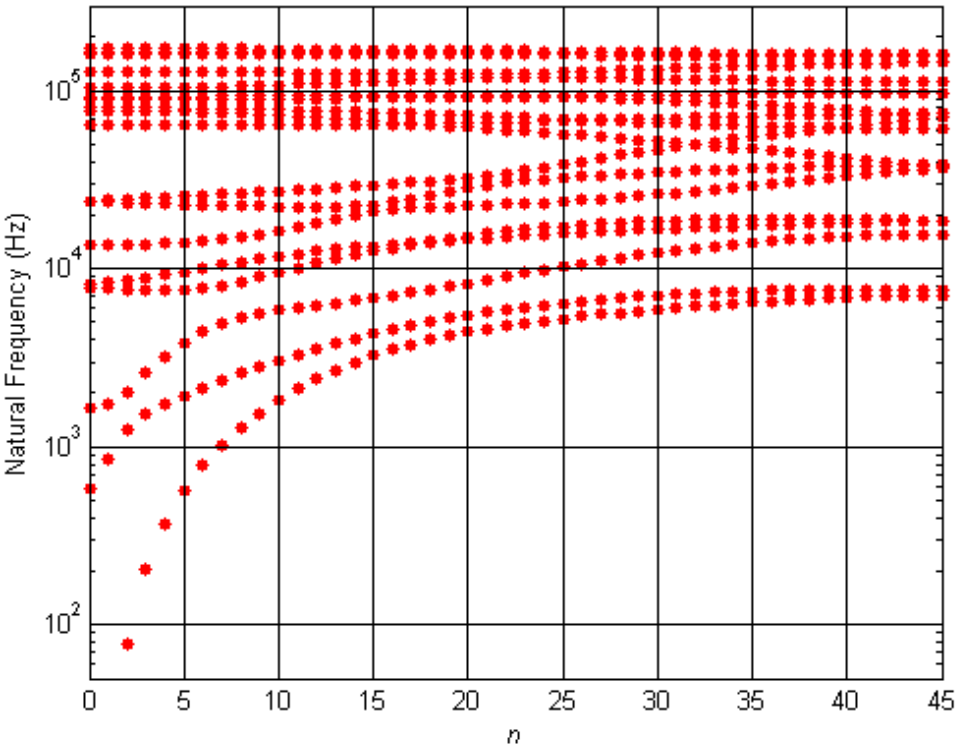

Figure 134: Natural Frequencies against Mode Number n

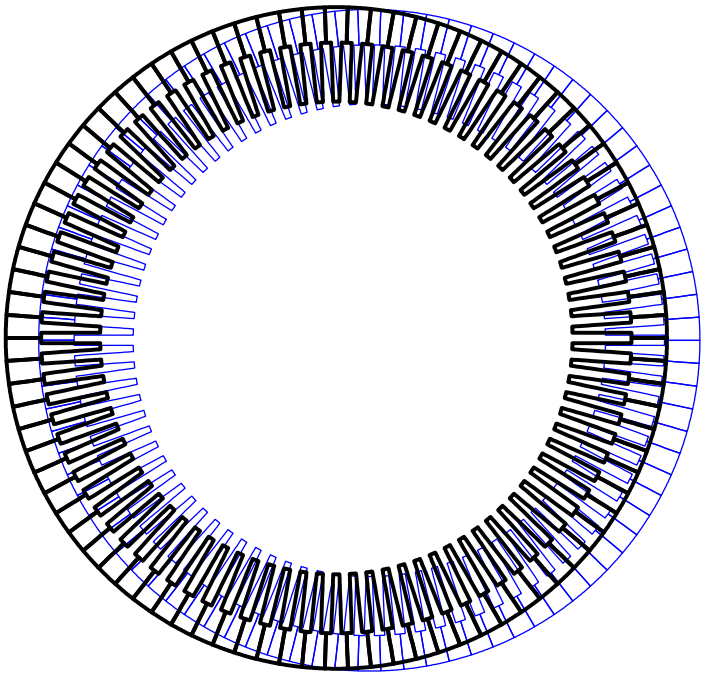

Figure 135: A $n = 1$ *Translational* Mode

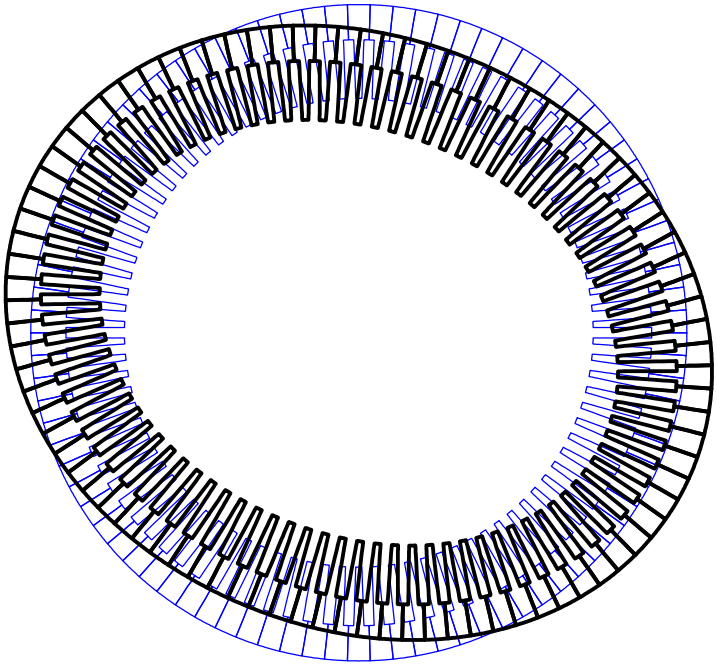

Figure 136: A $n = 2$ Mode

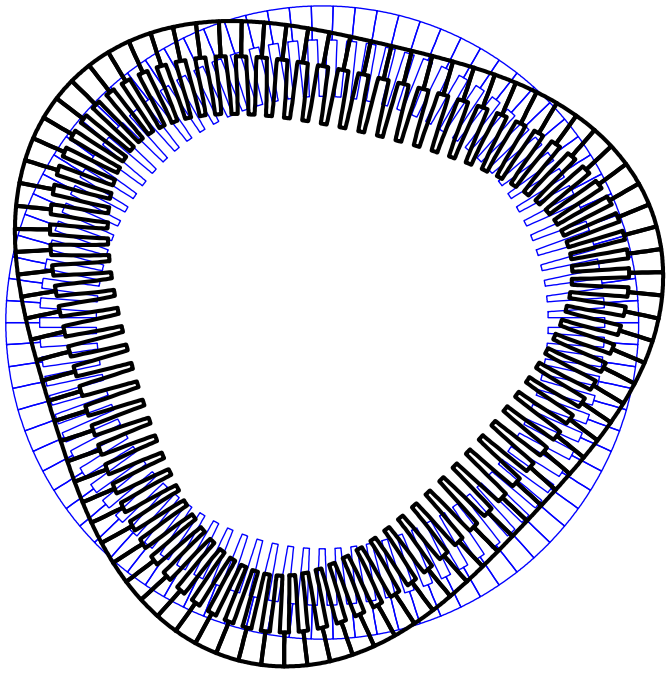

Figure 137: A $n = 3$ Mode

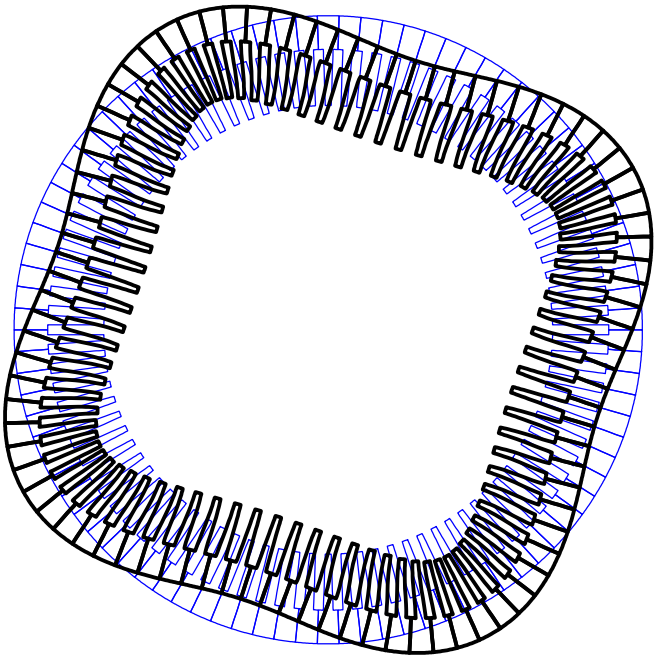

Figure 138: A $n = 4$ Mode

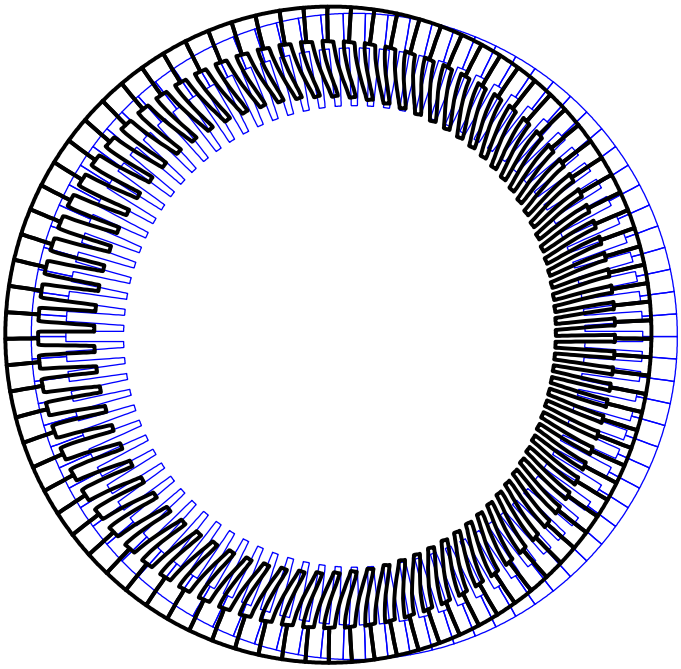

Figure 139: A $n = 1$ Mode

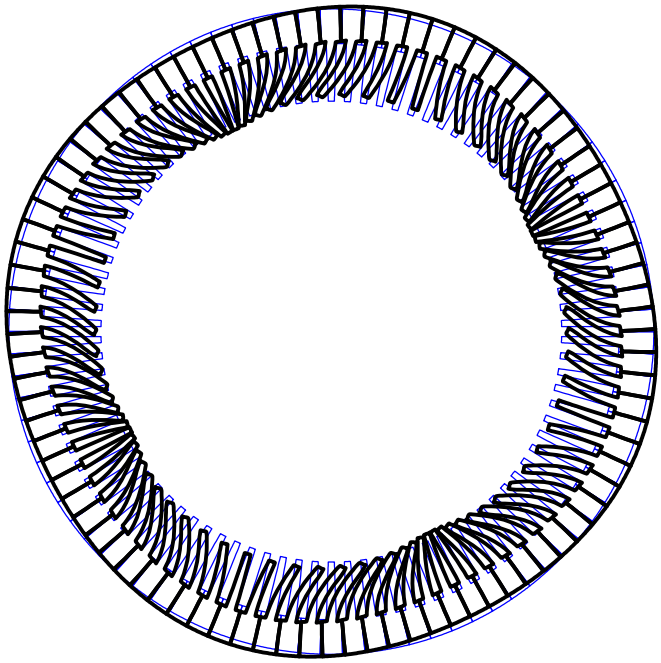

Figure 140: A $n = 4$ Mode

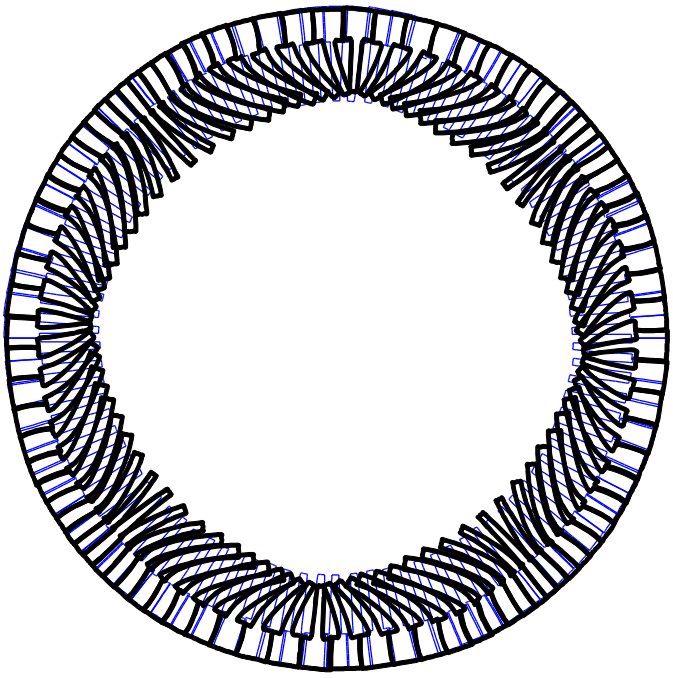

Figure 141: A $n = 4$ Mode

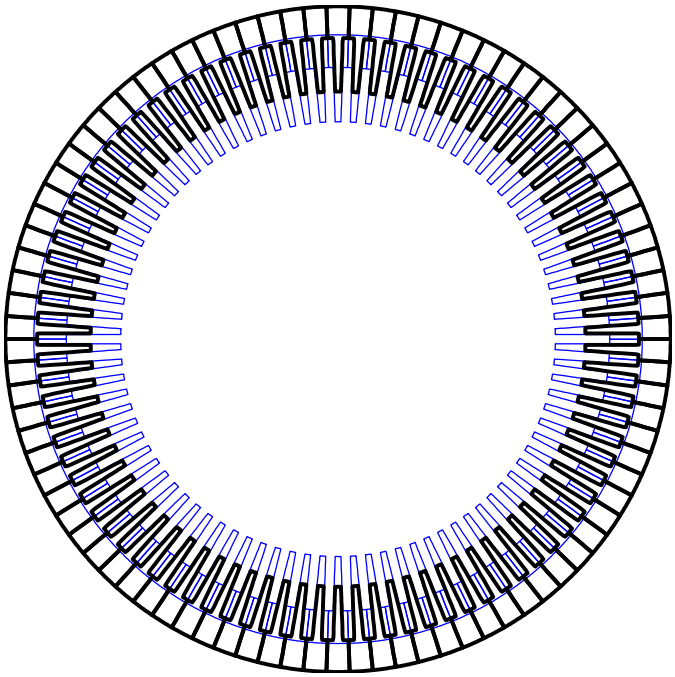

Figure 142: A $n = 0$ *Breathing* Mode

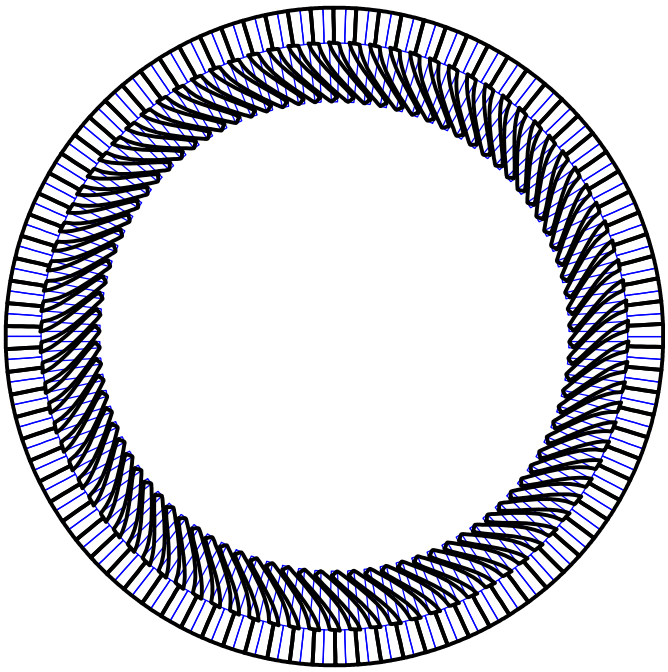

Figure 143: A $n = 0$ *Tooth Rocking* Mode

D The Magnetic FE Model of the Electrical Machine

D.1 Part 1: The Literature Review

This chapter provides background information regarding magnetic FE modelling techniques and describes the methods that were used in this study for magnetic FE analysis. The chapter is organized into two parts. The first part consists of sections D.2 to D.5. These describe some of the techniques that are available for magnetic finite element analysis of electrical machines. This is a vast topic and these sections only give an overview of some of the literature that has investigated and used these technologies. This includes:

- An explanation of the levels of coupling between magnetic and mechanical models
- Methods of calculating Maxwell forces.
- A discussion of magnetostriction.
- Methods for calculating electromagnetic torque.

The discussion of magnetostriction is given in more detail than for Maxwell forces as the magnetostriction phenomenon is more complex than the analysis of Maxwell forces. The methods that are discussed in the first part are alternative to the methods that were actually used in this study. Part 2 comprises sections D.6 to D.12, these explain the calculations that were used in this study.

D.2 Different Methods of Coupling the Magnetic and Mechanical Models

Mechanical and electrical field problems are usually analysed independently. The material properties of the variables of the two field problems are in-

dependent if the magnetostriction effect and Maxwell forces are neglected. Inclusion of the magnetostriction phenomenon causes the variables in the mechanical and electrical fields to be dependent upon one another. The strain of ferromagnetic materials is not only dependent on the mechanical stress of the material, but also on the external magnetic field in which the material is located. The magnetisation of the material in the magnetic field is dependent on the magnetic field and the stress of the material. Therefore, strain and magnetisation both depend on stress and magnetic field [12]. This interdependency of field variables is dealt with in FE analysis by using coupled models. Coupled models take into account the effect of the solution of one set of field equations on the other field. Different levels of coupling between the magnetic and elastic models can be used.

The different levels of coupling that can be used in the analysis between the mechanical and magnetic models can be categorized as [6]:

- Weak indirect
- Strong indirect
- Direct
- Local
- Global

Indirect coupling (strong and weak) couples two otherwise separate models; one for the magnetic field and one for the elastic field. The material properties of these two fields are independent of the other field. This method does not take into account any change in mechanical material properties (Young's modulus and Poisson's ratio) due to changes in the magnetic field or changes in the magnetic material properties (permeability) due to changes in the mechanical model. This method is useful if the dependence of the

material properties on the magnetic or elastic fields is negligible or if the relationship between the material properties and fields is not known [6].

Weak coupling describes a unidirectional dependency of the elastic field on the magnetic field. With this level of coupling the equivalent electromagnetic forces are calculated from the magnetic field and are then applied to the mechanical model. There is no further consideration of the effect that the resulting mechanical deformation has on the magnetic field or magnetic properties of the material [6]. Weak coupling has been used in the FE investigation into a single stator tooth rig in chapter 2 and in the investigation into a large electrical machine in chapter 4.

Strong coupling accounts for the effect of the magnetic field on the elastic field and also the effect of the elastic field on the magnetic field. This method is required when the magnetostrictive strain is large enough that the corresponding geometric changes have an effect on the magnetic field. This method is carried out using an iterative approach that calculates the strain in the mechanical model and then uses this information to find the effect of this on the magnetic field [6].

Directly coupled models take into account the effect that the magnetic and elastic fields have on each other and also account for the interdependency of the material properties of each field on the other field. In order to achieve this either the constitutive equations for each field are coupled to the variables of the other field or the field equations are coupled. This method requires data for the material dependent parameters and this information requires complicated measurements to be taken for the material in question. The relationship between nodal magnetic vector potential and elastic nodal displacement is also needed which requires the use of an iterative method

similar to the strong indirect coupled method [6].

Local coupling describes the use of coupled constitutive equations. The variables of one field are coupled to the variables of the other field. So for example the magnetic stiffness matrix is dependent on the deflections in the mechanical model as well as the magnetic potentials in the magnetic model. This is achieved with an iterative procedure which solves the field equations using the initial variable values. The solution is then used to update the values of the variables. The updated variables are then used to update the solution.

Global coupling describes the use of coupled field equations. The variables of both fields are present in both field equations. Within this the constitutive equations may also be coupled. This also uses an iterative technique to find the solution [6].

D.3 Approaches to Calculating Maxwell Forces

D.3.1 The Air Gap Permeance Method

A simple method of calculating the radial magnetic flux distribution in the air gap is to multiply an expression for the winding magneto-motive force (mmf) by an expression for air gap permeance [18]. The mmf and permeance waves are usually represented by a Fourier series and the terms in the Fourier series account for the features of the machine that generate spatial harmonics in the force waves [43]. These are the rotor slots, the stator slots, eccentricity of the rotor, asymmetries in the rotor and stator and magnetic saturation [104]. If the permeance and mmf harmonics are of a similar order the accuracy of this method is low. However, the most important harmonic components of mmf waves are usually large compared to the slot pitch, where predominant magnetic noise components are concerned [104].

Induced rotor currents are difficult to take account of with this method [46]. Once the radial magnetic flux density b_R in the air gap is known the radial force F_R acting over some small area A can be estimated:

$$F_R \approx \frac{b_R^2}{2\mu_0} A \tag{242}$$

D.3.2 Weak Coupling and The Principle of Virtual Work

Maxwell and Lorentz forces were found in a FE analysis with a weakly coupled approach by Delaere *et al* in [31] and [32] using *the principle of virtual work*. In this method an expression for the elastic energy in the material U and an expression for the magnetic energy in the material W are given as:

$$U = \frac{1}{2}(\mathbf{\Delta x})^\top \mathbf{K}(\mathbf{\Delta x}) \qquad W = \frac{1}{2}(\mathbf{\Delta a})^\top \underline{\mathbf{K}}(\mathbf{\Delta a}) \tag{243}$$

where $\mathbf{\Delta x}$ is the nodal deformation, $\mathbf{\Delta a}$ is the change in nodal magnetic vector potential, $\mathbf{K}$ is the mechanical stiffness matrix and $\underline{\mathbf{K}}$ is the magnetic stiffness matrix. The sum of these two expressions gives the total magneto-elastic energy in the system [32].

For a weakly coupled system the symbol $\mathbf{\Sigma}$ provides the coupling between the two systems and represents the dependency of mechanical energy variation on magnetic energy variation [31]. The electromagnetic forces from the magnetic field are found by minimizing the magnetic energy with respect to nodal displacement. For a linear system, this is:

$$\frac{\partial W}{\partial(\mathbf{\Delta x})} = \frac{1}{2}\frac{\partial((\mathbf{\Delta a})^\top \underline{\mathbf{K}}(\mathbf{\Delta a}))}{\partial(\mathbf{\Delta x})} = -\mathbf{f}_{em} = \mathbf{\Sigma \Delta a} \tag{244}$$

In equation (244) the change in magnetic potential $\mathbf{\Delta a}$ must be constant with respect to $\partial(\mathbf{\Delta x})$ [32].

In a nonlinear or saturated system, the magnetic stiffness matrix is dependent on permeability [30]. In this situation electromagnetic force is:

$$\mathbf{f}_{em} = -\frac{\partial W(\mathbf{\Delta x}, \mathbf{\Delta a})}{\partial(\mathbf{\Delta x})} = -\int_0^{\mathbf{\Delta a}} (\mathbf{\Delta a})^\top \frac{\partial \underline{\mathbf{K}}(\mathbf{\Delta x}, \mathbf{\Delta a})}{\partial(\mathbf{\Delta x})} d(\mathbf{\Delta a}) \tag{245}$$

The magnetic source term $\mathbf{j}$ is given by:

$$\frac{\partial W}{\partial(\mathbf{\Delta a})} = \underline{\mathbf{K}}\mathbf{\Delta a} = \mathbf{j} \tag{246}$$

The force from the mechanical source $\mathbf{f}$ is given by:

$$\frac{\partial U}{\partial(\mathbf{\Delta x})} = \mathbf{K}\mathbf{\Delta x} = \mathbf{f} \tag{247}$$

Combining equations (244), (246) and (247) leads to

$$\begin{bmatrix} \underline{\mathbf{K}} & 0 \\ \mathbf{\Sigma} & \mathbf{K} \end{bmatrix} \begin{Bmatrix} \mathbf{\Delta a} \\ \mathbf{\Delta x} \end{Bmatrix} = \begin{Bmatrix} \mathbf{j} \\ \mathbf{f} \end{Bmatrix} \tag{248}$$

where $\mathbf{f}$ is a vector of total external nodal excitation forces. This can be uncoupled by moving the vector of electromagnetic force to the right hand side:

$$\begin{bmatrix} \underline{\mathbf{K}} & 0 \\ 0 & \mathbf{K} \end{bmatrix} \begin{Bmatrix} \mathbf{\Delta a} \\ \mathbf{\Delta x} \end{Bmatrix} = \begin{Bmatrix} \mathbf{j} \\ \mathbf{f} + \mathbf{f}_{em} \end{Bmatrix} \tag{249}$$

The solution of the magnetic system allows for the calculation of the electromagnetic forces and then the mechanical system can be solved to find the resulting displacements [32].

D.4 Approaches to Calculating Equivalent Magnetostriction Forces

In order to incorporate magnetostriction into an electro-mechanical analysis, a method is needed to quantify the phenomenon. Studies into the effects of magnetostriction have used different methods and these are reviewed here. Much work has been carried out by Belahcen [6] and [7] and Delaere [27] to [32] on the effect of magnetostriction as well as Maxwell forces in electrical machines.

Magnetisation data for electrical steel is available from manufacturers for material under no externally applied stress. However, the application of stress to iron changes the magnetisation characteristics of the material and data for magnetisation against stress is not readily available. Data for magnetostrictive strain as a function of flux density is also not readily available [80]. Therefore, in many analytical and numerical studies into the effect of magnetostriction gaps exist in the data that is required for these studies. The studies overcome this problem either by experimental measurements, such as in [6] or by analytical techniques, such as in [80].

Measured data for magnetostrictive strain is complex to obtain due to the required values being difficult to capture and due to the variation of strain with both applied stress and flux density. A ferromagnetic material in an electrical field will experience the largest absolute amount of magnetostrictive strain in the direction of the flux. It is in this direction that measured values of strain are usually captured.

Studies that calculate the values of magnetostrictive strain as oppose to measuring them assume a relationship for the behaviour of the material. If the magnetostriction in the direction of the magnetic field is either calcu-

lated or measured, the magnetostriction perpendicular to the magnetic field is often estimated. Two assumptions are often used to do this. These are that no shear stress or strain occurs perpendicular or parallel to the magnetic field and that no volume magnetostriction occurs. The result of these assumptions is that the magnitude of the magnetostriction in the direction perpendicular to the magnetic field is estimated at half of the magnitude of the magnetostriction parallel to the magnetic field but with the opposite sign. This is the equivalent of a magnetostrictive Poisson's ratio of 0.5 compared to the mechanical Poisson's ratio of iron which is 0.3 [6].

Models for magnetostriction can be elongation-based or force-based. Elongation -based models find the elongation that is caused by the magnetostriction as a function of the magnetic induction of the material. These models are less common than force-based models and are not considered further. With force-based models, an equivalent magnetostriction force is calculated. Applying this equivalent force causes the same strain in the material as is caused by the magnetostriction effect.

D.4.1 A Weak Coupling Approach

Delaere *et al* in [29] and [30] showed that equivalent magnetostriction forces can be incorporated into the weakly coupled system in equation (249). The resulting mechanical deflection of the nodes in the system when magnetostriction is included $\mathbf{\Delta x}_\top$ is the sum of the elastic deflection $\mathbf{\Delta x}$ and the deflection caused by magnetostriction $\mathbf{\Delta x}_\lambda$:

$$\mathbf{\Delta x}_\top = \mathbf{\Delta x} + \mathbf{\Delta x}_\lambda \tag{250}$$

Magnetic flux density is found from the solution to the magnetic field equation. The direction of the magnetic flux density is taken as the x axis and the y axis is perpendicular to this. Using either known magnetostriction

characteristics or assumed magnetostrictive strain as a function of magnetic flux density, the magnetostriction of each element can be calculated. The magnetostriction of the element in the x direction is λ, magnetostriction perpendicular to this is λ_t. For plane stress and isotropic magnetostriction the magnetostrictive strain in the x and y directions is [28]:

$$\begin{aligned} \lambda_x &= \lambda \\ \lambda_y &= \lambda_t = -\tfrac{\lambda}{2} \\ \lambda_z &= \lambda_t = -\tfrac{\lambda}{2} \end{aligned} \tag{251}$$

In the local coordinates of each element, the centre of gravity is taken to be a fixed point with coordinates (x_m^e, y_m^e). The nodal displacements of the element $\mathbf{\Delta x}_\lambda^e = (u_{ei}, v_{ei})$ are found with respect to this fixed point:

$$u_{ei} = (x_{ni} - x_m^e)\lambda_x \tag{252}$$

$$v_{ei} = (y_{ni} - y_m^e)\lambda_y \tag{253}$$

where (x_{ni}, y_{ni}) are the coordinates of the ith node. Elemental nodal displacements cannot be summed, but the elemental nodal forces can be. The elemental nodal forces $\mathbf{f}_\lambda^e$ are found simply using the element stiffness matrix:

$$\mathbf{f}_\lambda^e = \mathbf{K}^e(\mathbf{\Delta x})_\lambda^e \tag{254}$$

The vector of nodal forces for the whole structure is the sum of the elemental forces:

$$\mathbf{f}_\lambda = \sum_e \mathbf{f}_\lambda^e \tag{255}$$

These forces are incorporated into equation (249) as follows:

$$\begin{bmatrix} \underline{\mathbf{K}} & 0 \\ 0 & \mathbf{K} \end{bmatrix} \begin{Bmatrix} \mathbf{a} \\ \mathbf{\Delta x}_\top \end{Bmatrix} = \begin{Bmatrix} \mathbf{j} \\ \mathbf{f} + \mathbf{f}_{em} + \mathbf{f}_\lambda \end{Bmatrix} \tag{256}$$

This result can also be obtained by substituting equation (250) into equation (249) and minimizing the mechanical energy with respect to the total nodal deformation $\mathbf{\Delta x}_\top$.

D.4.2 A Strong Coupling Approach

A strong coupling approach was used in [81] to develop a numerical model of an electrical machine using energy equations for the mechanical and magnetic systems. The strong coupling accounted for magnetic saturation, change in permeability with stress and the dependence of magnetic force on magnetic vector potential and mechanical deformation.

In [24] and [29] Delaere *et al* incorporate magnetostriction in a strong coupling analysis. In this case the system of equations can be written as:

$$\begin{bmatrix} \underline{\mathbf{K}} & \mathbf{\Lambda} \\ \mathbf{\Sigma} & \mathbf{K} \end{bmatrix} \begin{Bmatrix} \mathbf{\Delta a} \\ \mathbf{\Delta x}_\top \end{Bmatrix} = \begin{Bmatrix} \mathbf{j} \\ \mathbf{f} \end{Bmatrix} \tag{257}$$

Here the symbol $\mathbf{\Lambda}$ represents the dependency of permeability on strain. The product $\mathbf{\Lambda \Delta x}_\top$ represents the change in elastic energy U due to a change in the magnetic field:

$$\frac{\partial U}{\partial(\mathbf{\Delta a})} \approx \mathbf{\Lambda \Delta x}_\top \tag{258}$$

There will also be terms independent of $\mathbf{\Delta x}_\top$ in this expression. An analytical expression for $\frac{\partial U}{\partial(\mathbf{\Delta a})}$ is given in [24] by considering a change in flux density ΔB which causes a change in deformation $\Delta \mathbf{x}_\lambda$ due to magnetostriction. No external stresses are applied so the change in mechanical energy is zero but the change in deflection is not zero. The external work that is required to shrink the structure back to its original shape gives the change in mechanical energy ΔU that the magnetostriction causes. For an isotropic

material under plane stress [24]:

$$\frac{\partial U}{\partial \mathbf{\Delta x}_\top} = AtE\frac{1.25-\nu}{1-\nu^2}\lambda\frac{\partial \lambda}{\partial \mathbf{\Delta x}_\top} \tag{259}$$

Here, A and t are the elemental area and axial thickness respectively, E is the Young's Modulus and ν is the Poisson's ratio. Equation (259) above can be written in the following form [24]:

$$\frac{\partial U}{\partial (\mathbf{\Delta x})_\top} = \mathbf{j}_\lambda + \mathbf{\Lambda \Delta x}_\top \tag{260}$$

The system of equations for a strongly coupled analysis then becomes:

$$\begin{bmatrix} \underline{\mathbf{K}} & \mathbf{\Lambda} \\ \mathbf{\Sigma} & \mathbf{K} \end{bmatrix} \begin{Bmatrix} \mathbf{\Delta a} \\ \mathbf{\Delta x}_\top \end{Bmatrix} = \begin{Bmatrix} \mathbf{j} - \mathbf{j}_\lambda \\ \mathbf{f} + \mathbf{f}_\lambda \end{Bmatrix} \tag{261}$$

D.4.3 The Method of Magnetostrictive Stress

The method of magnetostrictive stress is used to calculate equivalent nodal magnetostrictive forces [6]. This method uses measured data of magnetostrictive stress parallel to the direction of the magnetic field against flux density and stress. Assumptions are used to calculate the magnetostrictive stress in the direction perpendicular to the magnetic field. The calculated stress is shared across the nodes on the edge of each element and multiplied by the relevant area to get elemental nodal forces. The elemental nodal forces are summed to get the equivalent nodal forces for the whole structure.

D.4.4 Comparisons of Different Approaches

A common assumption that is used to calculate equivalent magnetostrictive forces is that magnetostrictive strain in a material remains within the isotropic range. The resultant deformation can therefore be estimated as

a quadratic function of flux density. In [28] Delaere *et al* investigated the effect of Maxwell forces and magnetostriction on the vibration spectra of an electrical machine. The authors used two isotropic magnetostriction curves to calculate magnetostrictive strain λ as a function of flux density b, these were $\lambda = 10^{-6}b^2$ and $\lambda = 10^{-6}(b^2 - 0.4b^4)$. The method of magnetostrictive stress was used to calculate the equivalent magnetostrictive forces. The principle of virtual work and weak coupling were used to solve the system of equations. The authors found that the acceleration spectra of the machine from magnetostriction alone was lower than that from Maxwell forces alone. The differences between the acceleration spectra from the two different magnetostriction curves were small [28].

A coupling method was developed by Belahcen in [6] in which both sets of field equations were included in a single set of matrix equations. The variables in these matrices were dependent on the solution. Iterations were needed to account for the non-linearity of the magnetic field and the dependence of the permeability on the magnetic field strength and mechanical stress. The magnetostrictive stress method and the virtual work method were both used and compared. The results of the calculations suggested that the magnetostrictive stress method was the best method for calculating magnetostrictive forces.

In [30] Delaere *et al* developed a 2D magnetic and undamped mechanical model of the stator of a synchronous machine. Weak coupling and the principle of virtual work were used to calculate the vibration spectrum of the stator from Maxwell, magnetostriction and Lorenz forces. In [31], Delaere *et al* used the principle of virtual work and strong coupling between magnetic and mechanical FE models to calculate local magnetic forces in a synchronous machine. In both papers the predicted frequency spectrum

of the stator of the machine was compared to a measured stator vibration spectrum and good correlation was found between the two.

D.4.5 Conclusion of the Methods Discussed

The literature review of magnetostriction analysis has shown that this is a complicated topic and measured magnetostriction values for materials are not readily available from the manufacturer. Magnetostrictive strain can sometimes be measured in the direction of the magnetic field. Otherwise analytical techniques exist for the estimation of magnetostriction parallel, perpendicular and at angles to the direction of the magnetic field. These techniques have proved to give reasonable results for magnetostriction analysis.

D.5 Approaches to Calculating Electromagnetic Torque

There are different methods suitable for calculating electromagnetic torque. These are mentioned only briefly here. The Maxwell stress method derives torque from an integral of Maxwell stress in the air gap. This method is used in this study and so is explained in section D.11 of this chapter.

- A Maxwell stress harmonic filter method derives the torque directly from values of magnetic potential [88].

- The virtual work method gives the torque for a linear system as the derivative of magnetic energy with respect to angle around the air gap [39] [90].

$$T = \frac{\partial W}{\partial \theta} \tag{262}$$

- The reference frame theory calculation of torque uses voltage equations for the rotor and stator. These equations can be transformed by well known transformations in electrical engineering onto a d/q reference frame or an α/β reference frame. The choice of reference frame

affects the calculation of torque. This method requires values for the rotor and stator current in each phase and these must be sinusoidal. The rotor and stator flux linkage in each phase and rotor and stator resistance are also required [4].

- The d/q reference frame averaged torque method gives torque as:

$$T = \frac{6n_{pp}}{4}(\psi_d j_q - \psi_d j_d) \tag{263}$$

Where n_{pp} is the number of pole pairs, ψ_d and ψ_q are the d and q flux linkages and j_d and j_q are d and q currents.

D.6 Part 2: The Electromagnetic Calculations used in this Study

The next sections lay out the calculations that were used in this study. The magnetic analysis of an electrical machine was undertaken in MATLAB with all scripts written by the author. The sections in this part of the chapter comprise:

- The central circle method.
- Magnetic flux density in the air gap.
- Maxwell forces which act across the air gap on the stator teeth.
- Equivalent magnetostriction forces in the stator iron.
- Electromagnetic torque.

Two features of the air gap between the rotor and the stator are important in this analysis. These are the *central circle* and the *middle circle* and these are introduced here:

In this study the rotor model and the stator model are created separately.

The rotor mesh is created in the rotor reference frame and the stator mesh is created in the stator reference frame. The stator reference frame remains static and the rotor reference frame rotates with respect to this by an angle ϕ as shown in figure 144. The *central circle* method is used to combine these models and this method requires a central circle to exist in the air gap between the rotor and stator models. The rotor model has a layer of elements adjacent to the rotor structure in the air gap between the rotor and the stator. The stator model also includes at least one layer of elements in the air gap adjacent to the stator structure. The boundary of the rotor model in the air gap lies on the boundary of the stator model in the air gap. This boundary is called the central circle. The circumferential positions of the nodes on the central circle of the stator model do not need to coincide with the circumferential positions of the nodes on the central circle of the rotor model. Figure 145 gives an illustration of the central circle and the air gap nodes.

The *middle* circle is distinct from the central circle and is important for the calculations of magnetic flux density, Maxwell force and torque. This is a circle that goes through the middle of a ring of elements in the air gap of either the rotor or stator model. A number of points are defined for each element on this circle in the reference coordinates of the element. In the reference coordinates these points are equally spaced and they start on the lower border of the element and finish on the upper border of the element see figure 146 for an illustration of this. Where there are two adjacent elements on the middle circle there are two points with the same coordinates in the stator reference frame on the mutual boundary of these elements.

D.7 The Central Circle Method

This section describes how the rotor and stator models are combined so that the rotation of the rotor with respect to the stator can be considered. Sections B.6 and B.8 show that the governing equation of a magnetic FE problem is:

$$\underline{\mathbf{K}}\mathbf{a} = \underline{\mathbf{j}} \tag{264}$$

In this study the magnetic stiffness matrix $\underline{\mathbf{K}}$ and excitation vector $\underline{\mathbf{j}}$ are created separately for the rotor and stator:

$$\underline{\mathbf{K}}_{\mathbf{r}}\mathbf{a}_{\mathbf{r}} = \underline{\mathbf{j}}_{\mathbf{r}} \quad \text{and} \quad \underline{\mathbf{K}}_{\mathbf{s}}\mathbf{a}_{\mathbf{s}} = \underline{\mathbf{j}}_{\mathbf{s}} \tag{265}$$

A method is required to combine the rotor and stator models so that the effect of the rotor field is imposed on the stator model and vice versa. This method must also allow for the rotation of the rotor model with respect to the stator model.

The method that has been chosen for this is called the central circle method [70]. The central circle method utilises two transformations. The first transformation approximates the potentials of the nodes on the central circle by a Fourier series. The second transformation provides for the rotation of the rotor reference frame.

The stiffness matrices for the rotor $\underline{\mathbf{K}}_{\mathbf{r}}$ and stator $\underline{\mathbf{K}}_{\mathbf{s}}$ are partitioned as shown:

$$\underline{\mathbf{K}}_{\mathbf{r}} = \begin{bmatrix} \mathbf{K}_{\mathbf{rrr}} & \mathbf{K}_{\mathbf{rrc}} \\ \mathbf{K}_{\mathbf{rcr}} & \mathbf{K}_{\mathbf{rcc}} \end{bmatrix} \qquad \underline{\mathbf{K}}_{\mathbf{s}} = \begin{bmatrix} \mathbf{K}_{\mathbf{sss}} & \mathbf{K}_{\mathbf{ssc}} \\ \mathbf{K}_{\mathbf{scs}} & \mathbf{K}_{\mathbf{scc}} \end{bmatrix} \tag{266}$$

The subscript **rrr** corresponds to the nodes in the rotor model, excluding those that lie on the central circle. The subscript **rcc** corresponds to the nodes in the rotor model that only lie on the central circle. Similarly, the

subscript **sss** corresponds to the nodes in the stator model, excluding those that lie on the central circle. The subscript **scc** corresponds to the nodes in the stator model which only lie on the central circle.

The excitation vectors and vectors of magnetic potential for the stator and rotor are divided in a similar manner:

$$\underline{\mathbf{j}}_{\mathbf{r}} = \left\{ \begin{array}{c} \underline{\mathbf{j}}_{\mathbf{rrr}} \\ \underline{\mathbf{j}}_{\mathbf{rcc}} \end{array} \right\}, \qquad \underline{\mathbf{j}}_{\mathbf{s}} = \left\{ \begin{array}{c} \underline{\mathbf{j}}_{\mathbf{sss}} \\ \underline{\mathbf{j}}_{\mathbf{scc}} \end{array} \right\} \tag{267}$$

$$\mathbf{a}_{\mathbf{r}} = \left\{ \begin{array}{c} \mathbf{a}_{\mathbf{rrr}} \\ \mathbf{a}_{\mathbf{rcc}} \end{array} \right\}, \qquad \mathbf{a}_{\mathbf{s}} = \left\{ \begin{array}{c} \mathbf{a}_{\mathbf{sss}} \\ \mathbf{a}_{\mathbf{scc}} \end{array} \right\} \tag{268}$$

The excitation applied to the central circle nodes is zero so:

$$\underline{\mathbf{j}}_{\mathbf{rcc}} = \underline{\mathbf{j}}_{\mathbf{scc}} = \mathbf{0} \tag{269}$$

but

$$\mathbf{a}_{\mathbf{rcc}} \neq \mathbf{a}_{\mathbf{scc}} \neq \mathbf{0} \tag{270}$$

The Fourier harmonics of the rotor and stator central circle potentials are $\mathbf{a}_{\mathbf{fr}}$ and $\mathbf{a}_{\mathbf{fs}}$ respectively. The transformation matrix that converts harmonics of potential into nodal potentials are $\mathbf{T}_{\mathbf{fr}}$ and $\mathbf{T}_{\mathbf{fs}}$:

$$\mathbf{a}_{\mathbf{rcc}} = \mathbf{T}_{\mathbf{fr}}\mathbf{a}_{\mathbf{fr}} \quad \text{and} \quad \mathbf{a}_{\mathbf{scc}} = \mathbf{T}_{\mathbf{fs}}\mathbf{a}_{\mathbf{fs}} \tag{271}$$

The number of columns in $\mathbf{T}_{\mathbf{fr}}$ and $\mathbf{T}_{\mathbf{fs}}$ is twice the number of harmonics in the Fourier series p. The number of rows in each is the number of nodes on

the central circle for either the rotor n_r or stator n_s:

$$\mathbf{T_{fr}} = \begin{bmatrix} \cos(\theta_{r1}) & \sin(\theta_{r1}) & \cdots & \cos(k\theta_{r1}) & \sin(k\theta_{r1}) & \cdots & \cos(p\theta_{r1}) & \sin(p\theta_{r1}) \\ \cos(\theta_{r2}) & \sin(\theta_{r2}) & \cdots & \cos(k\theta_{r2}) & \sin(k\theta_{r2}) & \cdots & \cos(p\theta_{r2}) & \sin(p\theta_{r2}) \\ \vdots & \vdots & \ddots & \vdots & \vdots & \ddots & \vdots & \vdots \\ \cos(\theta_{ri}) & \sin(\theta_{ri}) & \cdots & \cos(k\theta_{ri}) & \sin(k\theta_{ri}) & \cdots & \cos(p\theta_{ri}) & \sin(p\theta_{ri}) \\ \vdots & \vdots & \ddots & \vdots & \vdots & \ddots & \vdots & \vdots \\ \cos(\theta_{rn_r}) & \sin(\theta_{rn_r}) & \cdots & \cos(k\theta_{rn_r}) & \sin(k\theta_{rn_r}) & \cdots & \cos(p\theta_{rn_r}) & \sin(p\theta_{rn_r}) \end{bmatrix} \tag{272}$$

$$\mathbf{T_{fs}} = \begin{bmatrix} \cos(\theta_{s1}) & \sin(\theta_{s1}) & \cdots & \cos(k\theta_{s1}) & \sin(k\theta_{s1}) & \cdots & \cos(p\theta_{s1}) & \sin(p\theta_{s1}) \\ \cos(\theta_{s2}) & \sin(\theta_{s2}) & \cdots & \cos(k\theta_{s2}) & \sin(k\theta_{s2}) & \cdots & \cos(p\theta_{s2}) & \sin(p\theta_{s2}) \\ \vdots & \vdots & \ddots & \vdots & \vdots & \ddots & \vdots & \vdots \\ \cos(\theta_{si}) & \sin(\theta_{si}) & \cdots & \cos(k\theta_{si}) & \sin(k\theta_{si}) & \cdots & \cos(p\theta_{si}) & \sin(p\theta_{si}) \\ \vdots & \vdots & \ddots & \vdots & \vdots & \ddots & \vdots & \vdots \\ \cos(\theta_{sn_s}) & \sin(\theta_{sn_s}) & \cdots & \cos(k\theta_{sn_s}) & \sin(k\theta_{sn_s}) & \cdots & \cos(p\theta_{sn_s}) & \sin(p\theta_{sn_s}) \end{bmatrix} \tag{273}$$

Here k is an integer that increases from 1 to p for every pair of columns. θ_{r1}, θ_{ri} and θ_{rn_r} are the angles from the rotor reference frame to the 1st, ith and last node on the rotor central circle. θ_{s1}, θ_{si} and θ_{sn_s} are the angles from the stator reference frame to the 1st, ith and last node on the stator central circle. No zeroth harmonic has been included here because this would indicate a flow of flux around the central circle. There is no excitation present that would cause this to occur and so the zeroth harmonic has been omitted.

Substituting equation (271) into equation (265) and combining the rotor

and stator models into one set of matrix equations results in:

$$\left[\begin{array}{c|c|c|c} \mathbf{K_{rrr}} & \mathbf{K_{rrc}T_{fr}} & 0 & 0 \\ \hline \mathbf{T_{fr}^{\top}K_{rcr}} & \mathbf{T_{fr}^{\top}K_{rcc}T_{fr}} & 0 & 0 \\ \hline 0 & 0 & \mathbf{K_{sss}} & \mathbf{K_{ssc}T_{fs}} \\ \hline 0 & 0 & \mathbf{T_{fs}^{\top}K_{scs}} & \mathbf{T_{fs}^{\top}K_{scc}T_{fs}} \end{array}\right] \left\{\begin{array}{c} \mathbf{a_{rrr}} \\ \hline \mathbf{a_{fr}} \\ \hline \mathbf{a_{sss}} \\ \hline \mathbf{a_{fs}} \end{array}\right\} = \left\{\begin{array}{c} \underline{\mathbf{j}}_{\mathbf{rrr}} \\ \hline \mathbf{T_{fr}^{\top}}\underline{\mathbf{j}}_{\mathbf{rcc}} \\ \hline \underline{\mathbf{j}}_{\mathbf{sss}} \\ \hline \mathbf{T_{fs}^{\top}}\underline{\mathbf{j}}_{\mathbf{scc}} \end{array}\right\} \tag{274}$$

The second transformation provides the rotation of the rotor reference frame:

$$\mathbf{a_{fs}} = \mathbf{T}(\phi)\mathbf{a_{fr}} \qquad\qquad \underline{\mathbf{j}}_{\mathbf{fs}} = -\mathbf{T}(\phi)\underline{\mathbf{j}}_{\mathbf{fr}} \tag{275}$$

$\mathbf{T}(\phi)$ is a square matrix, of dimensions ($2p$ x $2p$):

$$\mathbf{T}(\phi) = \begin{bmatrix} \cos(\phi) & -\sin(\phi) & \cdots & 0 & 0 & \cdots & 0 & 0 \\ \sin(\phi) & \cos(\phi) & \cdots & 0 & 0 & \cdots & 0 & 0 \\ \vdots & \vdots & \ddots & \vdots & \vdots & \vdots & \vdots & \vdots \\ 0 & 0 & \cdots & \cos(k\phi) & -\sin(k\phi) & \cdots & 0 & 0 \\ 0 & 0 & \cdots & \sin(k\phi) & \cos(k\phi) & \cdots & 0 & 0 \\ \vdots & \vdots & \vdots & \vdots & \vdots & \ddots & \vdots & \vdots \\ 0 & 0 & \cdots & 0 & 0 & \cdots & \cos(p\phi) & -\sin(p\phi) \\ 0 & 0 & \cdots & 0 & 0 & \cdots & \sin(p\phi) & \cos(p\phi) \end{bmatrix} \tag{276}$$

The vector of potentials can be constrained:

$$\left\{\begin{array}{c} \mathbf{a_{rrr}} \\ \mathbf{a_{fr}} \\ \mathbf{a_{sss}} \\ \mathbf{a_{fs}} \end{array}\right\} = \left[\begin{array}{ccc} \mathbf{I} & 0 & 0 \\ 0 & 0 & \mathbf{I} \\ 0 & \mathbf{I} & 0 \\ 0 & 0 & \mathbf{T}(\phi) \end{array}\right] \left\{\begin{array}{c} \mathbf{a_{rrr}} \\ \mathbf{a_{sss}} \\ \mathbf{a_{fr}} \end{array}\right\} \tag{277}$$

$$\mathbf{L} = \begin{bmatrix} \mathbf{I} & 0 & 0 \\ 0 & 0 & \mathbf{I} \\ 0 & \mathbf{I} & 0 \\ 0 & 0 & \mathbf{T}(\phi) \end{bmatrix}$$

Substituting equation (277) into equation (274) and premultiplying by $\mathbf{L}^\top$ results in the combined system equation:

$$\left[\begin{array}{c|c|c} \mathbf{K_{rrr}} & 0 & \mathbf{K_{rrc}}\mathbf{T_{fr}} \\ \hline 0 & \mathbf{K_{sss}} & \mathbf{K_{ssc}}\mathbf{T_{fs}}\mathbf{T}(\phi) \\ \hline \mathbf{T_{fr}}^\top\mathbf{K_{rcr}} & \mathbf{T}(\phi)^\top\mathbf{T_{fs}}^\top\mathbf{K_{scs}} & \mathbf{T_{fr}}^\top\mathbf{K_{rcc}}\mathbf{T_{fr}} + \mathbf{T}(\phi)^\top\mathbf{T_{fs}}^\top\mathbf{K_{scc}}\mathbf{T_{fs}}\mathbf{T}(\phi) \end{array}\right] \left\{\begin{array}{c} \mathbf{a_{rrr}} \\ \hline \mathbf{a_{sss}} \\ \hline \mathbf{a_{fr}} \end{array}\right\} = \left\{\begin{array}{c} \underline{\underline{\mathbf{j_{rrr}}}} \\ \hline \underline{\underline{\mathbf{j_{sss}}}} \\ \hline 0 \end{array}\right\} \tag{278}$$

Equation (278) can be solved to find the non central circle rotor potentials, non central circle stator potentials and the harmonics of potential on the rotor central circle. The harmonics of potential on the stator central circle can be found from equation (275). The stator and rotor nodal central circle potentials can then be found from equation (271).

D.8 Magnetic Flux Density

In three dimensional magneto-static analysis, magnetic flux density $\mathbf{b}$ at any given point (x, y, z) is given by the curl of magnetic vector potential $\mathbf{a}$:

$$\mathbf{b} = \nabla \times \mathbf{a} \tag{279}$$

In two dimensional analysis this leads to:

$$\mathbf{b} = \left\{\begin{array}{c} b_x \\ b_y \end{array}\right\}, \qquad b_x = \frac{\partial \mathbf{a}}{\partial y}, \qquad b_y = -\frac{\partial \mathbf{a}}{\partial x} \tag{280}$$

Maxwell's third equation for a static electromagnetic field (explained in Appendix E) in differential form is:

$$\nabla \times \mathbf{h} = \mathbf{j} \tag{281}$$

$\mathbf{j}$ is a vector of current density. A required material equation for an unsaturated system is:

$$\mathbf{b} = \mu \mathbf{h} \tag{282}$$

$\mathbf{h}$ is the magnetic field strength. Incorporating equation (282) into equation (279) and equation (281) leads to:

$$\nabla \times (\nabla \times \mathbf{a}) = \mu \mathbf{j} \tag{283}$$

From vector calculus

$$\nabla \times (\nabla \times \mathbf{a}) = \nabla(\nabla \cdot \mathbf{a}) - \nabla^2 \mathbf{a} \tag{284}$$

$\nabla \cdot \mathbf{a} = 0$ and μ is assumed constant and so the formulation for a static magnetic field within one element is given by:

$$\nabla^2 \mathbf{a} = -\mu \mathbf{j} \tag{285}$$

The element flux density vector $\mathbf{b_e}$ is created in FE form from:

$$\mathbf{b_e} = \mathbf{J^{-1}} \mathbf{Z} \mathbf{a_e} \tag{286}$$

$\mathbf{Z} = \mathbf{Z}(\eta, \zeta)$ provides the derivatives of the shape functions with respect to reference coordinates. This study uses eight noded quadrilateral elements

and so $\mathbf{Z}$ is:

$$\mathbf{Z} = \begin{bmatrix} \frac{\partial N_1}{\partial \eta} & \frac{\partial N_2}{\partial \eta} & \frac{\partial N_3}{\partial \eta} & \frac{\partial N_4}{\partial \eta} & \frac{\partial N_5}{\partial \eta} & \frac{\partial N_6}{\partial \eta} & \frac{\partial N_7}{\partial \eta} & \frac{\partial N_8}{\partial \eta} \\ -\frac{\partial N_1}{\partial \zeta} & -\frac{\partial N_2}{\partial \zeta} & -\frac{\partial N_3}{\partial \zeta} & -\frac{\partial N_4}{\partial \zeta} & -\frac{\partial N_5}{\partial \zeta} & -\frac{\partial N_6}{\partial \zeta} & -\frac{\partial N_7}{\partial \zeta} & -\frac{\partial N_8}{\partial \zeta} \end{bmatrix} \quad (287)$$

Appendix B provides the Jacobian matrix $\mathbf{J} = \mathbf{J}(\eta, \zeta)$ in equation (125), the polynomials N_1 to N_8 in equation (115) and the ordering of the nodes in figure 124. The inverse of the Jacobian matrix, $\mathbf{J^{-1}}$, provides the transformation from reference coordinates to global coordinates. $\mathbf{a_e}$ holds the values of vector potential for each node in the element. The resulting flux density vector is in global (x, y) coordinates. This can be converted into radial and tangential coordinates by the rotation matrix $\mathbf{H}$ given in (174) in appendix B.

In the analysis of the electrical machine, the magnetic flux density is calculated at every point on the middle circle in the stator air gap. In order to achieve this the coordinates of each point on the middle circle for each element (η, ζ) are substituted into $\mathbf{Z}$ and $\mathbf{J}$ in equation (286). Global vectors of flux density are created. These hold the radial and tangential components of flux density for all of the points on the middle circle.

D.9 Maxwell Forces acting at the Tooth Tips

Radial and tangential Maxwell stresses σ_{RR} and $\sigma_{R\theta}$ are calculated from the radial and tangential component of flux density b_R and b_θ and the permeability of free space μ_0:

$$\sigma_{RR} = \frac{b_R^2 - b_\theta^2}{2\mu_0} \quad (288)$$

$$\sigma_{R\theta} = \frac{2 b_R b_\theta}{2\mu_0} \quad (289)$$

In the analysis of an electrical machine the radial and tangential Maxwell stresses are calculated for all points on the middle circle, for all time steps.

These values are stored in matrices $\boldsymbol{\sigma_{RR}}$ and $\boldsymbol{\sigma_{R\theta}}$. The rows of these matrices hold values for all points on the middle circle, the columns hold values for all time steps.

These matrices are used to calculate the nodal Maxwell forces that act on the tooth tips of the stator. This is done by considering the radial and tangential stress of the points on the middle circle within each bay. The average value of these points of bay k are taken as $\overline{\sigma}_{kRR}$ and $\overline{\sigma}_{kR\theta}$. These are multiplied by the length of the section of middle circle in the bay l (shown in figure 146 and the axial length of the air gap t. This gives the radial and tangential values of Maxwell force for the bay f_{MRk} and $f_{M\theta k}$ respectively.

$$f_{MRk} = \overline{\sigma}_{RRk} lt, \qquad f_{M\theta k} = \overline{\sigma}_{R\theta k} lt \tag{290}$$

These can be rotated to give Maxwell force values in the local Cartesian coordinates of the bay. A matrix of Maxwell forces $\mathbf{F_M}$ can be generated which has $2s$ rows and T columns where there are s bays and T time steps. The rows correspond to the local x and y DoFs of each tooth tip. The columns are populated with these values for each time step in the analysis.

In order to carryout an analysis of the effect of the different Fourier harmonics of Maxwell force the matrices of Maxwell stress or Maxwell force can be transformed into a 2D Fourier map. The coefficients of any required combinations of temporal and spatial harmonics can be extracted from the 2D Fourier map and expanded back into the temporal frequency domain. This procedure is explained in section B.16 of appendix B. If the matrices of Maxwell stress of every point on the middle circle are to be used for this then the Fourier decomposition treats the distribution of stress as a continuous function. The vectors of stress that are found in the temporal frequency domain will correspond to the radial and tangential values of

stress for every tooth tip in the stator. These values must be converted into values of force by multiplying by the axial and circumferential length of the air gap. These radial force values will then need to be rotated into the local Cartesian coordinates of the corresponding bay in order to be applied to the mechanical model.

If the matrices of nodal Maxwell force at the tooth tips are decomposed into the temporal frequency and spatial frequency domain then the vectors that are expanded back into the temporal frequency are force values in the local Cartesian coordinates of each bay and need no further transformations to be applied to the mechanical model.

D.10 Equivalent Magnetostriction Forces

Equivalent magnetostriction forces are calculated as the set of nodal forces that would cause the same strain in an element as magnetostriction would under the influence of an external magnetic field. A coordinate set is defined by (r, s), where r is the direction of the magnetic field and s is perpendicular to this. The magnetic model in this study is unsaturated and so the magnetostrictive strain is proportional to the square of flux density in the r and s directions. Two constants are required to calculate the magnetostrictive strain from the known magnetic flux density of every node in the stator core. These are α and β, these represent constants of proportionality in the r and s directions respectively. By assuming isotropic magnetostriction the strain in the s direction is half of the magnitude and has opposite sign to that in the r direction:

$$\beta = -\frac{\alpha}{2} \tag{291}$$

The magnetostrictive strain is:

$$\boldsymbol{\lambda_N} = \mathbf{b}^\top \mathbf{H}^\top \begin{bmatrix} \alpha & 0 \\ 0 & \beta \end{bmatrix} \mathbf{H}\mathbf{b} \tag{292}$$

$$\mathbf{b} = \begin{Bmatrix} b_x \\ b_y \end{Bmatrix} \tag{293}$$

The rotation matrix $\mathbf{H}$ in equation (292) transforms the magnetostrictive strain $\boldsymbol{\lambda_N}$ into the local (x, y) frame for the element [6]. $\mathbf{H}$ is explained in (174) in appendix B.

The magnetostrictive nodal force vector for a single element is described by $\mathbf{f_{\lambda e}}$:

$$\mathbf{f_{\lambda e}} = \int_{A_e} \mathbf{B}^\top \mathbf{D} \boldsymbol{\lambda_N} dA \tag{294}$$

Numerically this integral is calculated using Gaussian integration:

$$\mathbf{f_{\lambda e}} = \sum_{i=1}^{q} \sum_{k=1}^{q} w_i w_k \mathbf{B}(\zeta_i, \eta_k)^\top \mathbf{D} \boldsymbol{\lambda_N}(\zeta_i, \eta_k) |\mathbf{J}| \tag{295}$$

The matrices $\mathbf{B}$ and $\mathbf{D}$ are explained in section (B.4). The vector $\mathbf{f_{\lambda e}}$ has an entry for the x and y components of force for each node in the element [54].

The force vector for the whole mechanical structure is assembled by the same *merge and reduction* process that is used on the mass and stiffness matrices. This process is described in section B.12. The reduced vector of nodal forces is $\boldsymbol{f_{\lambda R}}$. A vector of magnetostriction forces is calculated for every time step.

In the electrical machine analysis, in order to analyse the effect of the mag-

netostrictive forces on the mechanical system, the reduced vectors of nodal force are decomposed into Fourier harmonics. In order to achieve this the cyclic symmetry of the structure must be preserved in $\boldsymbol{f_{\lambda R}}$. Thus in local coordinates of each bay, both DoFs are retained as masters for the same nodes in every bay in the stator. Each row of $\boldsymbol{f_{\lambda R}}$ corresponds to a master DoF in the stator.

For decomposition into a 2D Fourier map each master node per bay of $\boldsymbol{f_{\lambda R}}$ is considered in turn. The x and y components of force are separated from $\boldsymbol{f_{\lambda R}}$ and the components of force that correspond to the same node in each bay are also separated. If there are P nodes in a bay there will then be P vectors that hold the x component of force ($\mathbf{f}_{\boldsymbol{\lambda} x}$) for the same node in each bay of the stator. There will also be P vectors that hold the y component of force ($\mathbf{f}_{\boldsymbol{\lambda} y}$) for each node in each bay of the stator. These vectors are individually decomposed into a 2D Fourier map using the method described in section B.16 in appendix B for decomposition of a discrete function. The result of the decomposition is P two dimensional Fourier maps that hold the x coefficients of force and P two dimensional Fourier maps that hold the y coefficients of force for all temporal and spatial frequencies.

In order to analyse the effect of a certain combination of spatial and temporal harmonics (n and m), the relevant entries are extracted from all of the Fourier maps. The expansion of these coefficients into the temporal frequency domain is also described in section B.16 in appendix B. This expansion will lead to P vectors of equivalent magnetostriction forces for the local x and y DoFs in the structure. These can then be combined into a single vector with entries that correspond to each DoF in the model.

D.11 Electromagnetic Torque

The tangential component of Maxwell stress in the air gap of an electrical machine $\sigma_{R\theta}$ is given in equation (289) in section D.9. Net circumferential force acting on the stator f_{EM} is calculated from the line integral of the tangential component of Maxwell stress around the air gap. Electromagnetic torque T_{EM} is the product of the electromagnetic force and the radius to the path of integration r:

$$f_{EM} = \oint_l \sigma_{R\theta} dl \qquad\qquad T_{EM} = r \oint_l \sigma_{R\theta} dl \tag{296}$$

In this study the values of flux density of the points on the middle circle are used for the numerical calculation of torque using Simpson's rule. For a single element with unit axial depth, q middle circle points and average distance between each point h, the integral is:

$$r \int_{x_1}^{x_q} \sigma_{R\theta} dx = r \frac{h}{3} [\sigma_{R\theta 1} + 4(\sigma_{R\theta 2} + \sigma_{R\theta 4} + \ldots + \sigma_{R\theta q-1}) + \ldots$$
$$2(\sigma_{R\theta 3} + \sigma_{R\theta 5} + \ldots + \sigma_{R\theta q-2}) + \sigma_{R\theta q}] \tag{297}$$

D.12 Conclusion to the Chapter

The first part of this chapter has provided a literature review of techniques for magnetic finite element analysis. This is a vast topic and the literature review has given an overview of a few methods of analysis that other authors have used. The second part of this chapter has given the methods that were coded in MATLAB by the author in order to carryout magnetic FE analysis. The results of an investigation into a single stator tooth rig are presented in chapter 2 and for a large electrical machine in chapter 4.

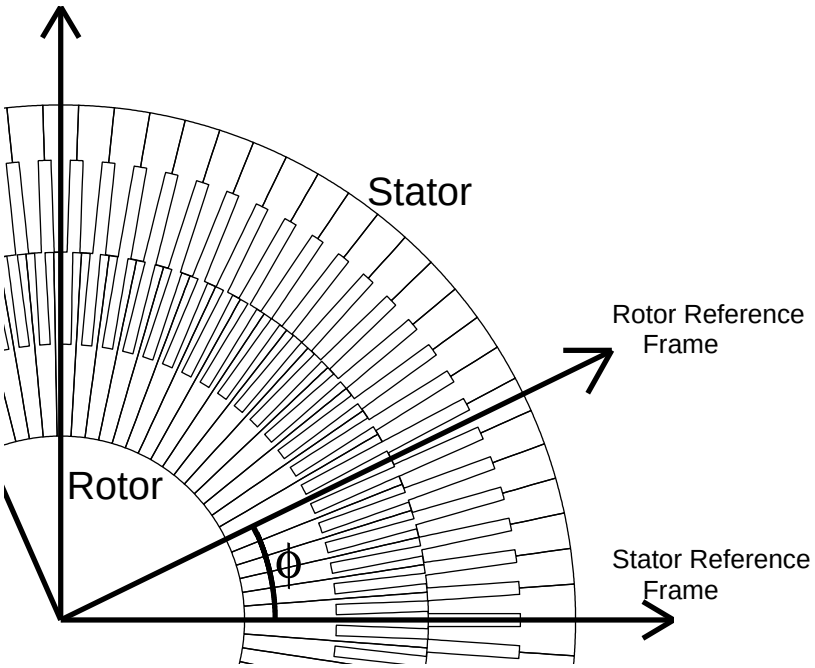

Figure 144: Stator and Rotor Reference Frames

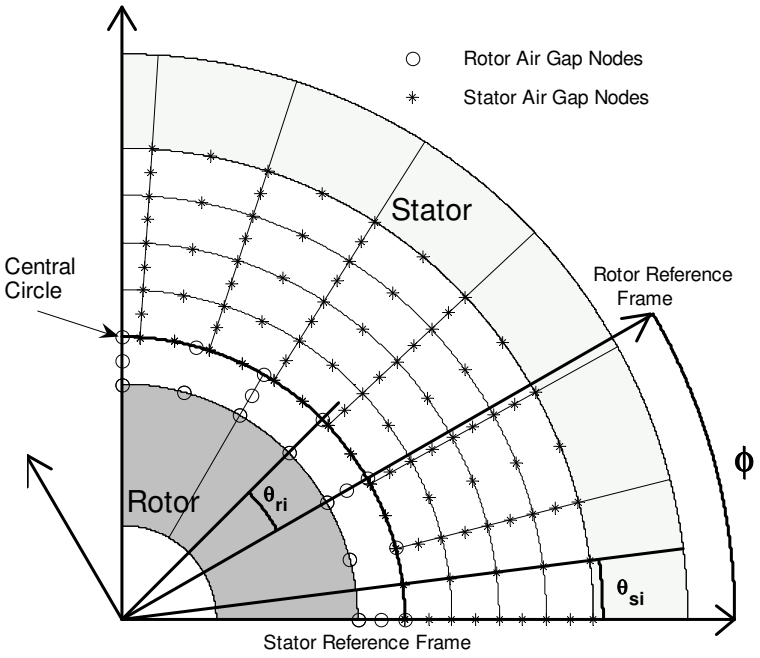

Figure 145: The Air Gap Between the Rotor and Stator Including the Central Circle

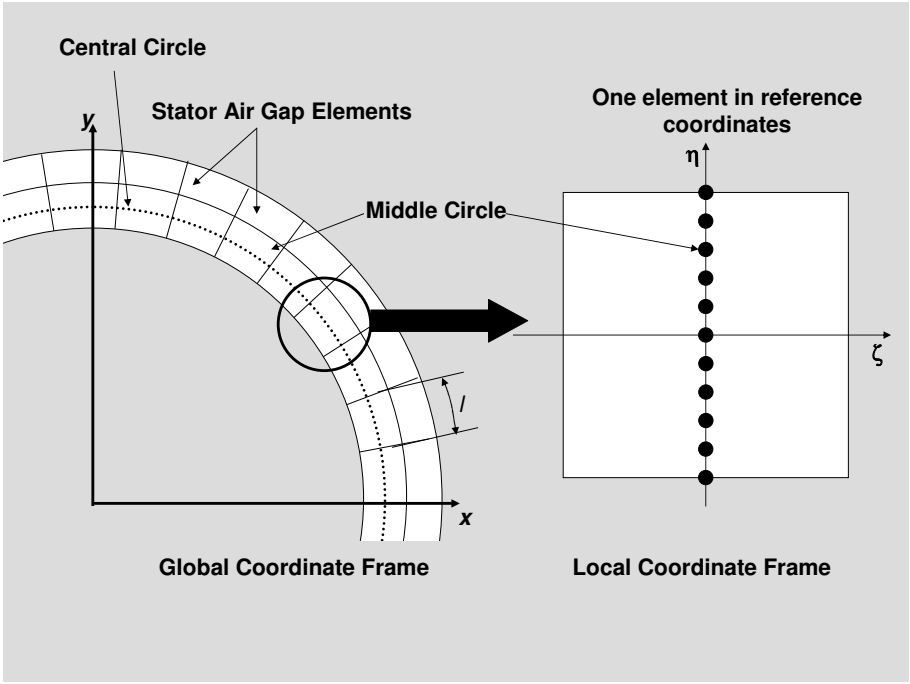

Figure 146: Stator Air Gap Elements in Global Coordinates and One Element in Local Coordinates

E Maxwell's Equations

Maxwell unified electromagnetic field theory by combining Ampere's law, Faraday's law and Gauss's law for electric and magnetic fields, he also added an extra term to Ampere's law. Maxwell's four equations govern the interaction of bodies which are magnetically or electrically charged, or both, for bodies and charges which are either stationary or varying with position or time. Maxwell's four equations are given below:

$$\nabla \cdot \mathbf{d} = \rho \qquad \oint_s \mathbf{d} ds = Q \tag{298}$$

$$\nabla \cdot \mathbf{b} = 0 \qquad \oint_s \mathbf{b} ds = 0 \tag{299}$$

$$\nabla \times \mathbf{h} = \mathbf{j} + \frac{\partial \mathbf{d}}{\partial t} \qquad \oint \mathbf{h} dl = \int_s \left(\mathbf{j} + \frac{\partial \mathbf{d}}{\partial t} \right) ds = I_{total} \tag{300}$$

$$\nabla \times \mathbf{e} = -\frac{\partial \mathbf{b}}{\partial t} \qquad \oint \mathbf{e} dl = -\int_s \frac{\partial \mathbf{b}}{\partial t} ds = \vartheta \tag{301}$$

Where $\mathbf{d}$ is electric flux density and $\mathbf{e}$ is electric field strength: $\mathbf{d} = \varepsilon_0 \varepsilon_r \mathbf{e}$. Q is total charge within an area s enclosed by a boundary l, $\mathbf{j}$ is current density and ρ is charge density, $\varepsilon_0 = 8.85 \times 10^{-12} Fm^{-1}$ is the permittivity of free space and ε_r is relative permittivity. $\mathbf{b}$ is magnetic flux density and $\mathbf{h}$ is magnetic field strength: $\mathbf{b} = \mu_0 \mu_r \mathbf{h}$. I_{total} is total current in s and ϑ is emf around l, $\mu_0 = 4\pi \times 10^{-7} Hm^{-1}$ is the permeability of free space and μ_r is relative permeability. The integrations are taken either over an enclosed surface s with ds representing an infinitesimal area on s, or over the boundary of the surface l where dl is an element of length on the surface, see figure 147.

Electrostatics

Maxwell's first equation (298) is taken from Gauss's law for electric fields. This law holds for static, time varying and motion varying electrical fields.

In differential form the divergence of electrical flux density gives the charge density which is causing the electric field. In integral form; the integral of electric flux density over the enclosed surface gives the total charge within the surface. If the charge is outside the surface, the right hand side of equation (298) goes to zero. In this case there is no net flux across the surface boundary because all lines of flux that enter the surface also leave the surface, see figure 148. For a surface which contains charge there is a resultant flux density across the surface which equals the total charge in the surface, see figure 149. This law is a necessary consequence of Coulomb's law (302) which states that an isolated charge q_1 surrounded by an electric field exerts a force $\mathbf{f}$ on a second charge q_2. The electric field is radial from the charge and q_2 is a distance r from q_1, the force decreases with the inverse square of distance from the charge.

$$\mathbf{f} = \frac{q_1 q_2}{4\pi\varepsilon_0\varepsilon_r r^2}\mathbf{r} \tag{302}$$

Magnetostatics

Maxwell's second equation (299) is taken from Gauss's law for magnetic fields. This law states that the total magnetic flux out of an enclosed surface is zero. Consequently, magnetic monopoles do not exist, magnetic poles only occur in pairs, lines of magnetic flux flow from the magnetic north to the magnetic south pole and the magnetic flux density is a solenoidal field vector. This means that all magnetic flux forms closed loops and so all lines which enter the surface s also leave the surface, see figure 150.

Varying Electric Field

Maxwell's third equation (300) is taken from Ampere's law. Ampere's law

is:

$$\nabla \times \mathbf{h} = \mathbf{j} \qquad \oint \mathbf{h} dl = \int_s \mathbf{j} ds = I_{total} \tag{303}$$

$$\nabla \cdot \mathbf{j} = -\frac{\partial \rho}{\partial t} \tag{304}$$

Equation (304) represents the continuity equation for electric charge. Ampere's law implies that $\nabla \cdot \mathbf{j} = 0$ and so $\frac{\partial \rho}{\partial t}$ is also zero. Therefore, Ampere's law applies only to steady currents; it explains that a steady current will produce a steady magnetic field.

Maxwell added an extra term to this law which allows for a time varying electric field. Replacing the right hand side of (303) with Maxwell's term results in:

$$\nabla \times \mathbf{h} = \frac{\partial \mathbf{d}}{\partial t} \qquad \oint \mathbf{h} dl = \int_s \frac{\partial \mathbf{d}}{\partial t} ds = I_{total} \tag{305}$$

This equation describes how an electric field which changes with time gives rise to a magnetic field which changes with position and time.

Equations (303) and (305) are both linear and therefore have superposable solutions; together they form Maxwell's third law (300) and describe how an electric field which changes with both position and time creates a magnetic field.

Varying Magnetic Field

Maxwell's fourth equation (301) is taken from Faraday's law. This law states that a magnetic field which changes with time gives rise to an electric field which varies with both position and time. The emf induced is given by the total electric field strength around a closed path. This is also

proportional to the rate of change of magnetic flux. The induced emf in turn induces a secondary current around the path. A steady magnetic field will not produce an electric field [96].

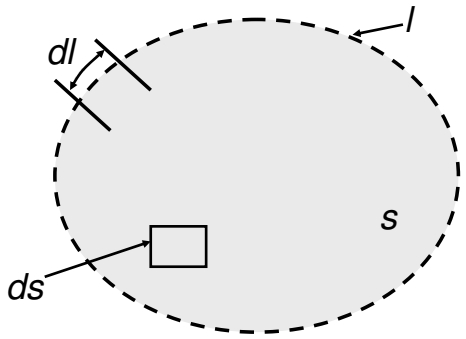

Figure 147: Integration Surface and Boundary for Maxwell's Equations

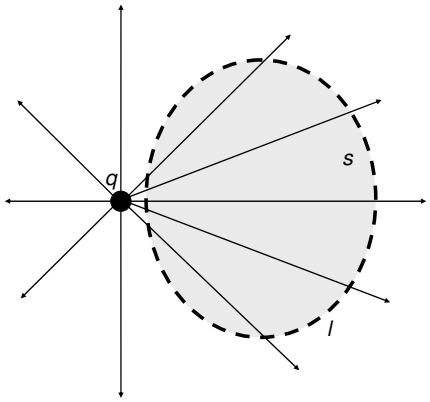

Figure 148: A Point Charge Outside of an Enclosed Boundary

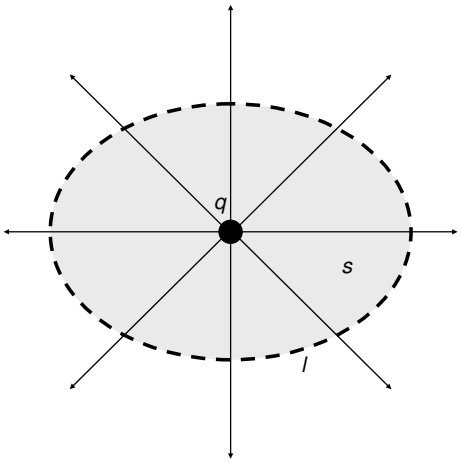

Figure 149: A Point Charge Within an Enclosed Boundary

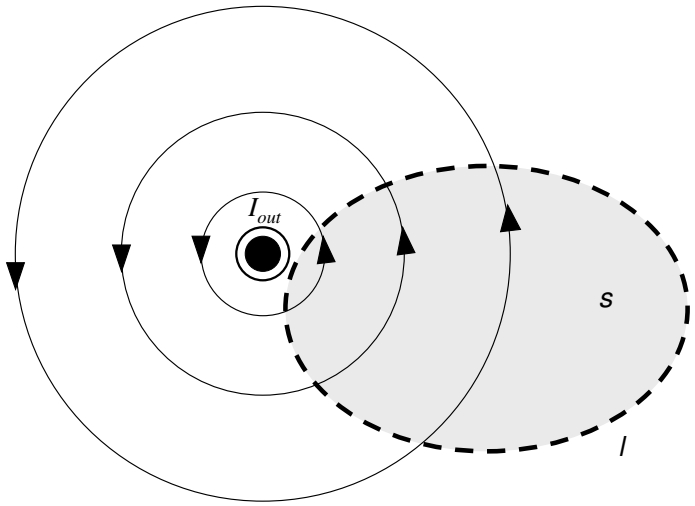

Figure 150: Closed Magnetic Field Lines around a Current Carrying Conductor

Robust Multi Degree of Freedom Hybrid Vibration Absorption

A Shahaj and S D Garvey
School of Mechanical, Materials and Manufacturing Engineering
University of Nottingham
University Park
Nottingham
NG7 2RD

ABSTRACT

A robust vibration absorber reduces vibrations of a system over a range of frequencies. Passive vibration absorption is achieved with a tuned mass and spring (known as a dynamic vibration absorber (DVA)). This is a simple, low cost method of reducing vibrations at a single frequency; however, in order to achieve robust absorption a heavy mass is required. Active vibration control is achieved with an actuator capable of applying a force to the system at any range of frequencies, but this method is expensive. Combining active and passive absorbers allows for robust absorption with minimum passive absorber mass. Various methods of combined absorption have already been proposed for systems with a single resonant frequency.

This paper investigates hybrid robust vibration control of a primary system with frequency components which are the first three harmonics of the excitation of the system. The hybrid absorber consists of a three mass-spring system. Passive absorption is achieved with three masses and joining springs, the active absorption is modelled as springs in parallel with the passive springs but with variable stiffness. Variations in frequency harmonics are proportional; absorption is maintained at a range of frequencies by altering the active spring stiffnesses.

1. INTRODUCTION

A dynamic vibration absorber (DVA) is a simple mass-spring system. When a primary system is subjected to a harmonic force, its vibration at a single frequency can be passively absorbed by attaching a tuned DVA [1]. The presence of the DVA causes an anti-resonance in the frequency response of the coupled system at the tuned resonant frequency of the absorber. The frequency range either side of the anti-resonant frequency where the primary system has a low response increases as the absorber mass increases, therefore in order to obtain a robust enough vibration absorber to provide vibration absorption in a finite frequency range, a large absorber mass is required which creates a heavy, undesirable system [2]. Robust vibration absorption is required in a number of situations, mainly where the excitation frequency of the primary system is variable, but also if the properties of the absorber system cannot be developed accurately or alter due to operating conditions causing an unpredictable absorber resonant frequency.

Active vibration absorption is provided in the form of actuators, which can include piezoelectric actuators, magnetostrictive actuators, electric motors or pneumatic springs, in conjunction with a control system. The active absorber can, theoretically, exert forces on the primary system at any range of frequencies so absorption is provided regardless of external factors which may affect system properties or operating speed. This type of absorption requires complex, expensive actuator and control arrangements [3].

Combining active absorption provision with a passive DVA enables a simple, low cost, robust absorber system to be developed. The combined absorber is capable of operating at a range of frequencies, without the need for a heavy absorber mass, and without the expense incurred from full active control [4].

Principles of vibration absorption can also be extended to consider absorbing the response of a primary system due to excitation forces with multiple frequencies. This is a concept that is useful in many situations as machinery

often experiences excitations that comprise of a fundamental frequency as well as integer harmonics of that frequency.

Combined active and passive robust absorption has been considered by Kidner et al. [5] who used a beam-like structure as a vibration absorber mounted on a primary system. Swept sinusoidal excitation was applied to the primary system initially at the passive tuned resonant frequency of the absorber; this was altered to equal the resonant frequency of the primary system. Robust absorption was provided by changing the beam geometry and consequently altering the beam stiffness and resonant frequency, fuzzy logic control enabled this geometry change to track the excitation frequency.

Hill et al. [6] developed a passive absorber which absorbed the response of the primary system at three excitation frequencies and in a small frequency range either side of these frequencies. The absorber consisted of two rods which each supported a mass either side of a centre section, mounted on the primary system. This configuration displayed six distinct, predictable mode shapes. The mass, material properties, rod diameters and lengths were tuned so that two absorber resonant frequencies occurred either side of each of the three excitation frequencies. This resulted in a passive absorber system which was slightly more robust than an absorber system would be if three absorber resonant frequencies were tuned exactly to the primary system excitation frequencies. Active absorption was attempted to enable absorption of a wider range of frequencies than the passive device alone would enable. Adaptive absorption was achieved with a stepper motor which wound the masses in and out and therefore changed the resonant frequencies of the absorber. In practice the presence of the motor increased the number of absorber resonances and decreased the effectiveness of the absorber at the required frequencies.

May et al. [7] developed an adaptive DVA to absorb the first, second, and third blade pass frequencies (BPFs) in a turboprop aircraft. The frequencies in question were 100Hz, 200Hz and 300Hz, the absorber was also required to exert 29N, 18N and 10N on the primary system at the three BPFs respectively. The authors developed an absorber with passive resonant frequency tuned to 100Hz; the fundamental frequency. The absorber acted actively over the range 50Hz to 400Hz using an active magnetostrictive rod and lever system.

This paper develops a multi degree of freedom (MDoF) DVA which satisfies the absorption requirements introduced in paper [7]: Absorption of the primary system is provided at the fundamental excitation frequency, 2nd harmonic and 3rd harmonic; nominally 100Hz, 200Hz and 300Hz. Modal participation factors are 29, 18 and 10 at the three excitation frequencies respectively.

In Section 2 of this paper the absorption and force requirements at all three excitation frequencies are provided by a 3 degree of freedom (3DoF) passive DVA. In Section 3 the concept of hybrid passive and active MDoF absorption is used. A static, active spring is used to provide vibration absorption when the three excitation frequencies vary in proportion to each other. This is effective over a small frequency range around the three nominal frequencies. Section 4 illustrates the characteristics and limitations of the active spring. Section 5 introduces a dynamic, active spring to provide robust vibration absorption over a wide frequency range around the three nominal frequencies when the frequencies vary in proportion to each other.

2. MULTI DEGREE OF FREEDOM PASSIVE ABSORBTION

A Three DoF DVA is developed to satisfy the following requirements:

- The first, second and third resonant frequencies occur at 100Hz, 200Hz and 300Hz respectively.
- The sum of the three masses is 1kg.
- The modal participation factors for mass3 are 29 in mode 1, 18 in mode 2 and 10 in mode 3.

The modal participation factors represent the force exerted by the absorber on the primary system in each of the three mode shapes of the absorber. These values are taken from the mass normalised mode vectors of each mode for mass 3.

The equations of motion for this system are:

$$[M_0]\ddot{x} + [K_o]x = f \tag{1}$$

$$x = \begin{Bmatrix} x_1 \\ x_2 \\ x_3 \end{Bmatrix} \quad [K_0] = \begin{bmatrix} K_{12} & -K_{12} & 0 \\ -K_{12} & K_{12}+K_{23} & -K_{23} \\ 0 & -K_{23} & K_{23}+K_3 \end{bmatrix} \quad f = \begin{Bmatrix} F_1 \\ F_2 \\ F_3 \end{Bmatrix} \quad [M_0] = \begin{bmatrix} M_1 & 0 & 0 \\ 0 & M_2 & 0 \\ 0 & 0 & M_3 \end{bmatrix}$$

The 3DoF DVA is shown in Figure 1

MatLab code was developed to solve this problem; the code required estimated values for the unknown parameters; M_1, M_2, M_3, K_{12}, K_{23}, K_3. The eigenvalue problem was solved with these values. The residuals of the calculated modal participation factors and resonant frequencies against the required values were found. The sensitivity of the residuals to changes in initial values was calculated and from this information numerical differentiation was carried out, which enabled values of the required parameters to be found to high precision.

The absorber system parameters were found to be:

M_1 = 0.0040606 kg	M_2 = 0.161353 kg	M_3 = 0.798040 kg
K_{12} = 82,355.016 Nm^{-1}	K_{23} = 329,265.970 Nm^{-1}	K_3 = 427,111.991 Nm^{-1}

Figure 2; the frequency response function for this system shows that the resonant peaks of the absorber system are extremely narrow, if this system was attached to a primary system, vibrations of the primary system would be absorbed only on the exact resonant frequencies of the absorber. A slight deviation in excitation frequency away from these frequencies could result in no absorption of the vibrations of the primary system or may even cause the system to vibrate at resonance; a case much worse than if no absorber were present.

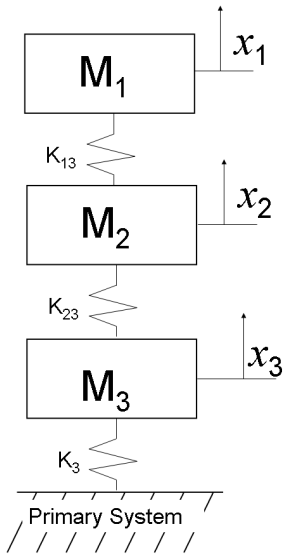

Figure 1: Three Degree of Freedom DVA

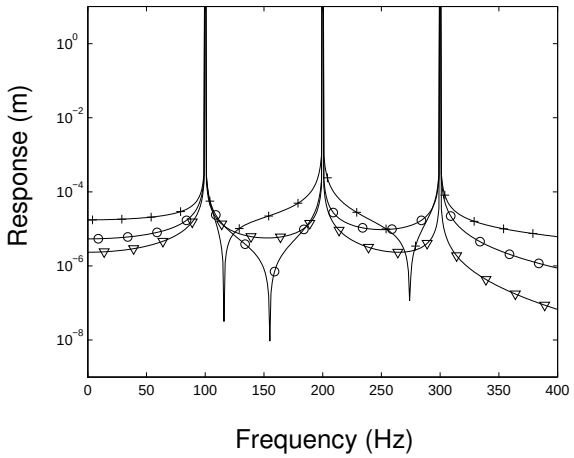

Figure 2: MDoF DVA Frequency Response Function
+ mass 1, o mass 2, ∇ mass 3

3. ROBUST HYBRID MULTI DEGREE OF FREEDOM VIBRATION ABSORPTION

This section illustrates how robust vibration absorption can be achieved by combining active vibration provision with the passive absorber system.

In a situation where a primary system experiences excitation which consists of a force with a fundamental frequency and integer harmonics of that frequency; variations in the fundamental excitation frequency cause proportional changes in the frequencies of the other harmonics.

A three mass-spring system must be developed to provide robust vibration absorption at and around all three nominal resonant frequencies. The three harmonics of excitation frequency of the primary system can vary in proportion to each other. The absorber maintains absorption of the resulting vibration of the primary system.

It is not possible for a mass-spring system to comply with the requirements that the resonant frequencies vary in proportion to each other and also maintain the modal participation factors required in Section 2.

For the absorber system to achieve robust absorption while complying with the constraint that the sum of all masses must be equal to 1kg; Passive absorption is required at the fundamental excitation frequency of the primary system and at the second and third harmonics. A small amount of active provision combined with the passive system enables the absorber properties to vary. Therefore the resonant frequencies of the absorber also vary. Frequency variations can be tuned to track the excitation frequencies of the primary system.

The active provision takes the form of a spring; the stiffness of this spring is variable by a factor σ. The overall stiffness of the active spring is denoted by (σ*dk*). This 'active' spring is placed in parallel with spring K_3, which joins mass 3 to the primary system.

The product σ*dk* represents the 'active' spring stiffness, *dk* is constant, σ is variable. When σ = 0, the resonant frequencies of the absorber are the nominal frequencies.

Altering the stiffness of the active spring alters the resonant frequencies of the absorber system; increasing the stiffness increases the resonant frequencies, decreasing the stiffness decreases the resonant frequencies. Therefore, variations in excitation frequency can be tracked by altering the active stiffness of the hybrid absorber system and vibration suppression can be maintained.

To comply with the requirement that all three resonant frequencies vary in proportion to each other, they must vary linearly with respect to σ. The rate of change of the natural frequencies with respect to σ is therefore:

$$\frac{df_1}{d\sigma}=1,\quad \frac{df_2}{d\sigma}=2,\quad \frac{df_3}{d\sigma}=3, \tag{2}$$

This is the equivalent of $\begin{bmatrix} U_1 & 0 & 0 \\ 0 & U_2 & 0 \\ 0 & 0 & U_3 \end{bmatrix}^T \begin{bmatrix} K_1 & 0 & 0 \\ 0 & K_1 & 0 \\ 0 & 0 & K_1 \end{bmatrix} \begin{bmatrix} U_1 & 0 & 0 \\ 0 & U_2 & 0 \\ 0 & 0 & U_3 \end{bmatrix} = c \begin{bmatrix} 1 & 0 & 0 \\ 0 & 4 & 0 \\ 0 & 0 & 9 \end{bmatrix}$ where $[K_1]=\begin{bmatrix} 0 & 0 & 0 \\ 0 & 0 & 0 \\ 0 & 0 & dk \end{bmatrix}$ (3)

U_1, U_2 and U_3 are mass normalised mode shape vectors. Equation (3) also gives the modal participation factors of the system, these are in direct contrast to the modal participation factors of the system designed in Section 2. The derivation of equation (3) is carried here:
Take [K] and [M] to be the mass and stiffness matrices of the hybrid passive and active system:

$$U^T[K]V=[\Lambda], \text{ where } [\mathrm{K}]=[\mathrm{K}_0]+\sigma[\mathrm{K}_1], \quad U^T[M]V=[I], \text{ where } [\mathrm{M}]=[\mathrm{M}_0]+\sigma[\mathrm{M}_1]. \tag{4a), (5a)}$$

U and V are mass normalised mode shape vectors and $[\Lambda]=\begin{bmatrix} \lambda_1 & 0 & 0 \\ 0 & \lambda_2 & 0 \\ 0 & 0 & \lambda_3 \end{bmatrix}$ $[I]=\begin{bmatrix} 1 & 0 & 0 \\ 0 & 1 & 0 \\ 0 & 0 & 1 \end{bmatrix}$.

Differentiate (4a) and (5a) with respect to σ and indicate this differentiation with dot notation:

$$\dot{U}[K]V+U^T\left[\dot{K}\right]V+U^T[K]\dot{V}=\left[\dot{\Lambda}\right], \qquad \dot{U}^T[M]V+U^T\left[\dot{M}\right]V+U^T[M]\dot{V}=0 \tag{4b), (5b)}$$

Define $B=V^{-1}\dot{V}$ and $A=U^{-1}\dot{U}$, (4b) and (5b) become: $A^T\Lambda+U^TK_1V+\Lambda B=\dot{\Lambda}$, $A^T+U^TM_1U+B=0$ (4c), (5c)

(4c) – λ_1(5c) simplifies to: $U^T[K_1]V=\left[\dot{\Lambda}\right]$ (6)

So if the rate of change of frequencies f_1, f_2 and f_3 with respect to σ are 1, 2, and 3; the rate of change of eigenvalues (λ_1, λ_2 and λ_3) are 1, 4 and 9. Substitute this information into (6) to get the result shown in (3).

Matlab code from section 2 was adapted to find a system that had:

- Resonant frequencies of 100Hz, 200Hz and 300Hz when $\sigma = 0$;
- $M_1+M_2+M_3$=1kg;
- $\frac{U_3^T[K_1]U_3}{U_1^T[K_1]U_1}=\frac{9}{1}$ and $\frac{U_2^T[K_1]U_2}{U_1^T[K_1]U_1}=\frac{4}{1}$

The resulting absorber parameters are:

M_1 = 0.194363 kg M_2 = 0. 333333kg M_3 = 0.472303 kg

K_{12} = 179,040.507 Nm^{-1} K_{23} = 435,068.433 Nm^{-1} K_3 = 870,135.921 Nm^{-1} dk = 0.944606 Nm^{-1}

This section searches for a linear solution to a non-linear problem, therefore the resulting system provides absorption which is approximate to the requirements.

Figures 3, 4 and 5 show the first, second and third resonant frequencies as σ changes. The dashed lines show the required frequencies and the solid lines are the resonant frequencies of the actual system with the above parameters.

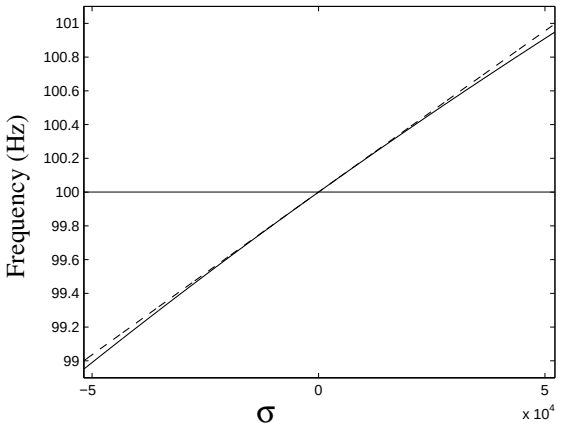

Figure 3: First Resonant Frequency v σ

— — — Required Frequency

——— Frequency of Resulting System

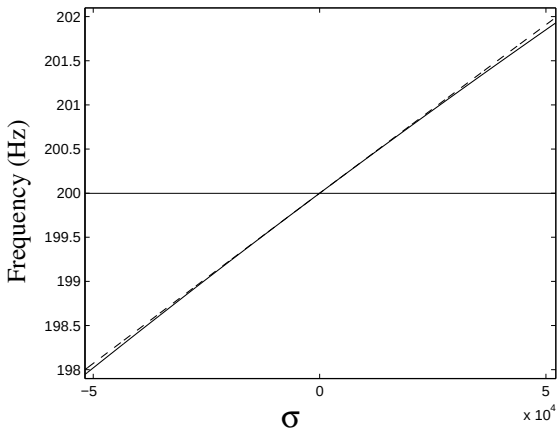

Figure 4: Second Resonant Frequency v σ

— — — Required Frequency

——— Frequency of Resulting System

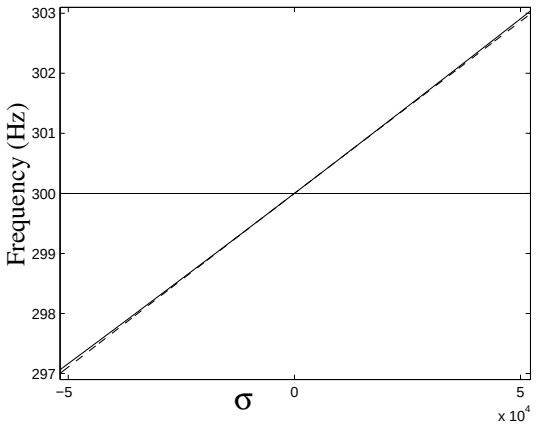

Figure 5: Third Resonant Frequency v σ

— — — Required Frequency

——— Frequency of Resulting System

Deviation	f = 100Hz	f = 200Hz	f = 300Hz
f - 0.1%	3.1031×10^{-4} %	1.1061×10^{-4}%	-3.6703×10^{-4}%
f + 0.1%	6.6933×10^{-4}%	4.7403×10^{-4}%	-1.6650×10^{-5}%
f - 1%	-0.04410%	-0.06249%	-0.10310%
f +1%	-0.04860%	-0.07003%	-0.12740%

Table 1: Error in Resonant Frequency with Deviation from Nominal Frequency

As the absolute value of σ increases; the error in system resonant frequencies increases. Table 1 shows that when the required frequency deviates by 0.1% from the nominal frequency, the error in resonant frequency of the designed system is only of magnitude $1x10^{-4}$%. When the deviation in resonant frequency is at 1% the magnitude of error in resonant frequency of the designed system is much larger; between 0.04% and 6.7%.

The results of this section show that robust vibration absorption is possible for a multi degree of freedom system with combined active and passive absorption, however all resonances cannot be controlled exactly proportionally with a single active spring for large variations from the nominal frequencies. Modal participation factors cannot be constrained in this case.

4. PROPERTIES OF A THREE DEGREE OF FREEDOM SYSTEM WITH AN ACTIVE SPRING

The resonant frequencies of the absorber system against values of the active spring denoted by K_C are plotted in Figure 6 and Figure 7. Here, K_C is equal to σdk in Section 3. These graphs can be separated into regions; in each region the response of the system is different and can be explained:

- $K_C << -K_3$

For large negative values of active stiffness, K_C, the value of the equivalent stiffness $K_3 + K_C$ is near zero. The first resonant frequency goes to zero and the system behaves like a 2DoF system, the second and third resonant frequencies are at their lowest values.

- $K_C \approx -K_3$

The response of the system changes abruptly from a 2DoF to a 3DoF system.

- $-K_3 < K_C < K_3$

This is a wide region where changes in K_C have little effect on the response of the system because the magnitude of K_C is much lower than the other spring stiffnesses.

- $K_C \approx K_3$

As the magnitude of K_C reaches the magnitude of the other springs in the system, the rate of change of frequencies with respect to K_C is high. Veering occurs: the mode shapes related to the second and third resonant frequencies switch over.

- $K_C >> K_3$

The third natural frequency goes to infinity with further increase in K_C. Infinite K_C is the equivalent of a rigid rod and so the system behaves like a 2DoF system again. Further increases in K_C have no effect on the 1st and 2nd resonant frequencies. The 1st and 2nd resonant frequencies in this region are at their maximum.

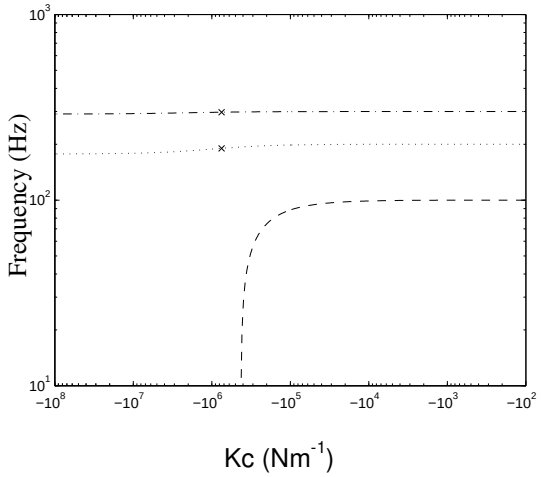

Figure 6: Resonant Frequencies v K_C, negative values of K_C
x: Frequency at the point where $K_C = -(K_{23} + K_3)$

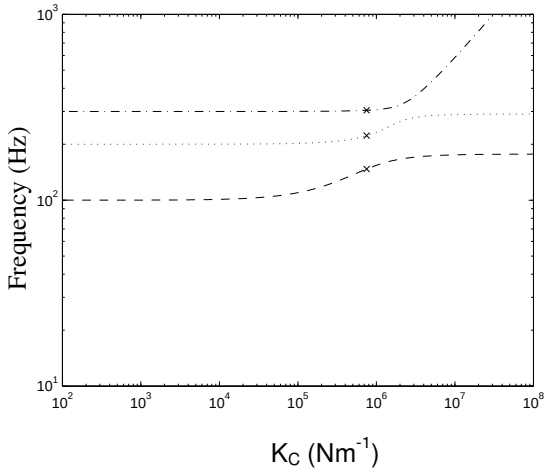

Figure 7: Resonant Frequencies v K_C, positive values of K_C
x: Frequency at the point where $K_C = K_{23} + K_3$

The resonant frequencies occur in the following ranges:
0Hz < f_1 < 177.16Hz, 177.17Hz < f_2 < 290.87Hz, 290.87Hz < f_3 < α Hz

The resonant frequency limits affect the effectiveness of this absorber system for use with a primary system which has excitation at a fundamental frequency and harmonics of this frequency that vary in proportion to each other.

The lower limit of the 3rd resonant frequency is 290.87Hz this is 3.04% of the nominal frequency. Decreases of 3.04% of the 2nd and 1st resonant frequency are 193.91Hz and 96.96Hz respectively. The upper limit for the whole system is given by the upper limit of the second resonant frequency, which is 290.87Hz. This is 45.44% of the nominal frequency. So, for the 1st, 2nd and 3rd resonances, the absorber can provide vibration absorption from 96.96Hz to 145.44Hz, from 193.91Hz to 290.87Hz and from 290.87Hz to 436.32Hz respectively.

5. DYNAMIC ACTIVE ABSORPTION PROVISION

In Section 3 the force exerted by the passive and active springs K_3 and σdk on the primary system is proportional to the extension of the springs. The active spring is described as static because the frequency of the system has no effect on the force that the active spring produces. This section uses a frequency dependent active spring. So for different modes, a different magnitude of force can be exerted by the spring.

The requirements of the combined passive and active absorber system in this section are that within the frequency limits found in Section 4, the resonant frequencies vary in proportion to each other.

The values of mass and the stiffness of the other springs are the same as in Section 2. When no active provision is exerted, the resonant frequencies of the system are 100Hz, 200Hz and 300Hz and the modal participation factors of mass three are 29, 18 and 10.

The addition of the frequency dependent spring adds two non-physical DoFs to the absorber system. The two DoFs have an inertia represented by 1kg in the mass matrix of the current system [M_2]. The stiffness matrix of the passive system is the same as [K_0] in Sections 2 and 3 but with two extra DoFs populated with zeros. The stiffness matrix for the active spring is [K_1].

$$[M_2]=\begin{bmatrix} M_1 & 0 & 0 & 0 & 0 \\ 0 & M_2 & 0 & 0 & 0 \\ 0 & 0 & M_3 & 0 & 0 \\ 0 & 0 & 0 & 1 & 0 \\ 0 & 0 & 0 & 0 & 1 \end{bmatrix},\quad [K_0]=\begin{bmatrix} K_{12} & -K_{12} & 0 & 0 & 0 \\ -K_{12} & K_{12}+K_{23} & -K_{23} & 0 & 0 \\ 0 & -K_{23} & K_{23}+K_3 & 0 & 0 \\ 0 & 0 & 0 & 0 & 0 \\ 0 & 0 & 0 & 0 & 0 \end{bmatrix},\quad [K_1]=\begin{bmatrix} 0 & 0 & 0 & 0 & 0 \\ 0 & 0 & 0 & 0 & 0 \\ 0 & 0 & K_C & K_{AC} & K_{BC} \\ 0 & 0 & K_{AC} & K_A & 0 \\ 0 & 0 & K_{BC} & 0 & K_B \end{bmatrix}$$

The overall stiffness of the system [K_2] is: $[K_2]=[K_0]+\sigma[K_1]$

The equation of motion for this system in the frequency domain is: $\left([K_2]-[M]\omega^2\right)x=F$, (7)

$$x=\begin{Bmatrix} x_1 \\ x_2 \\ x_3 \\ x_A \\ x_B \end{Bmatrix}, \text{ and } F=\begin{Bmatrix} F_1 \\ F_2 \\ F_3 \\ 0 \\ 0 \end{Bmatrix}$$

The presence of the extra DoFs within the frequency dependant spring enables the force that the spring exerts to alter for the three different mode shapes.

The static equivalent of this spring is the spring K_C used in Section 4 (now denoted K_{SC}). The relationship between the static and frequency dependent springs can be found by considering the force exerted. For the static spring the force exerted is:

$$F_3 = K_{SC}x_3 \quad (8)$$

For the frequency dependent spring, the static force exerted is found from the 3rd line in equation (7) when $\omega = 0$:

$$K_C x_3 + K_{AC} x_A + K_{BC} x_B = F_3 \quad (9)$$

For the frequency dependent spring, lines 4 and 5 in equation (7) expand to give:

$$x_A = -\frac{K_{AC} x_3}{K_A - \omega^2}, \text{ and } x_B = \frac{K_{BC} x_3}{K_B - \omega^2} \quad (10)$$

Substituting (10) back into (9) gives: $$F_3 = \left[K_C - \frac{{K_{AC}}^2}{K_A - \omega^2} - \frac{{K_{BC}}^2}{K_B - \omega^2} \right] x_3 \quad (11)$$

The three terms in the brackets of equation (11) are the equivalent of the static spring stiffness K_{SC}, equation (7).

The values of K_A and K_B represent the eigenvalues of the controller; the location of the controller resonant frequencies in the frequency response of the absorber determines the contribution from the active spring. For this example the values of K_A and K_B are set as linear functions of the fundamental excitation frequency (f_{ex}) of the primary system. The values of K_C, K_{AC} and K_{BC} are found so that the requirements of the absorber system are met. The functions of K_A and K_B are:

$$K_A = 10779 f_{ex} + 265459, \quad K_B = 56209 f_{ex} - 2110722 \quad (12), (13)$$

Figure 8 shows the values of K_C, K_{AB} and K_{BC} as excitation frequency changes. The above values for K_A, K_B, combined with values of K_C, K_{AC} and K_{BC} give resonant frequencies of the absorber system as shown in Figure 9. The errors in absorber resonant frequency at the limits of operation are given in Table 2. Table 2 clearly shows that the frequency dependent spring enables very accurate control of the absorber.

Deviation	f = 100Hz	f = 200Hz	f = 300Hz
f - 2%	3.25849×10^{-12}%	-1.23556×10^{-11}%	-5.36907×10^{-3}%
f +44%	5.92119×10^{-4}%	-7.89492×10^{-5}%	0%

Table 2: Error in Resonant Frequency with Deviation from Nominal Frequency

As the excitation frequency deviates from the nominal frequency, Figure 8 shows that the magnitude of control stiffness that is required for the absorber to track the frequency increases. At the upper limit of excitation frequency that can be absorbed, a very large value of K_C is required.

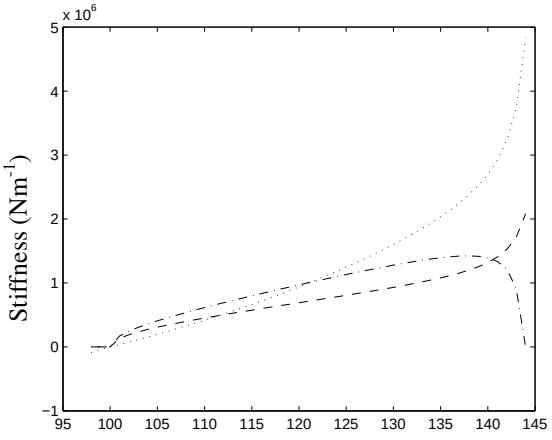

Figure 8: Controller Parameters v Fundamental Excitation Frequency

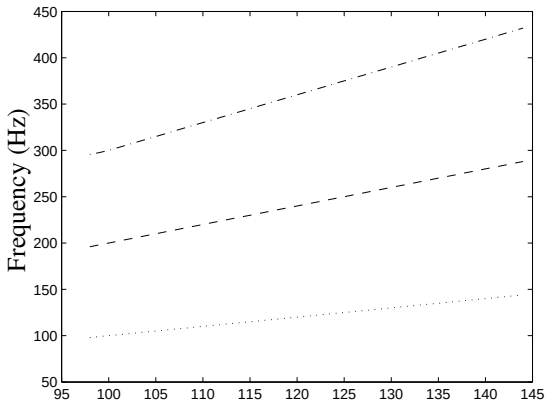

Figure 9: Absorber Resonant Frequency

- . - . -K_{BC}, ...K_C, - - - - K_{AC}

The magnitude of the mass and stiffness in the absorber system is linked to the cost of the absorber; heavier systems may be more expensive to run or may be unacceptable in the design requirements of the primary

system. Actuator cost can increase with frequency range. This is because actuator cost is related to reactive power. At the extremes of excitation frequency, in this example, actuator cost may be extremely high.

Reactive power is defined as: Reactive power = spring force x relative velocity (14)
Which is also; Reactive power = spring stiffness x (relative displacement)^2 x frequency (15)

Potential further development of the idea of hybrid absorption could be for a semi-active spring to be introduced into the system, in such a way that the change in fundamental excitation frequency could be tracked by altering a mechanical parameter. Only the higher harmonics would then require active control for total vibration suppression.

6. CONCLUSIONS

This paper has investigated multi degree of freedom absorption. For a passive system, the frequencies that require absorption and the force requirements at these frequencies can be achieved. However, to maintain minimum mass requirements, robustness is unattainable.

Introducing a static active spring enables system robustness. However, maintaining force requirements at frequencies away from the passively absorbed frequencies is not possible. Varying all absorber resonant frequencies in proportion to each other is possible for small deviations from the nominal frequencies.

The stiffness values of a frequency dependent active spring can be tuned so that absorber resonant frequencies can vary in proportion to each other over a wide frequency range. At the nominal, passively absorbed frequencies modal participation factors can be set.

7. REFERENCES

1. Liu, K. and J. Liu, *The Damped Dynamic Vibration Absorbers: Revisited and New Results.* Journal of Sound and Vibration, 2004. 284: p. 1181-1189.

2. Ryaboi, V.M., *Minimum Mass of Elastic-Inertial Vibration-Isolating Systems*. Mechanics of Solids, 1980. 15(4): p. 41-48.

3. Chen, Y.-D., C.-C. Fuh, and P.-C. Tung, *Application of Voice Coil Motors in Active Dynamic Vibration Absorbers*. IEEE Transactions on Magnetics, 2005. 41 no.3: p. 1149 - 1154.

4. Preumont, A., *Responsive Systems for Active Vibration Control*. NATO Science Series, ed. A. Preumont. Vol. 85. 2002, Amsterdam: IOS Press, Amsterdam Kluwer Academic Publishers. 394.

5. Kidner, M., R, F and M. Brennan, J, *Varying the Stiffness of a Beam-Like Neutralizer Under Fuzzy Logic Control*. Transactions of the ASME, 2002. 124(1): p. 90-99.

6. Hill, S., G and S. Snyder, D, *Design of an Adaptive Vibration Absorber to Reduce Electrical Transformer Structural Vibration*. Transactions of the ASME, 2002. 124(4): p. 606-611.

7. May, C., et al. *Magnetostrictive Dynamic Vibration Absorber (DVA) for Passive and Active Damping*. in Euronoise. 2003. Naples

Vibration Absorption for Quasi-Periodic Excitation – Methods and Two Renewable-Energy Applications.

S. D. Garvey, A. Shahaj
School of Mechanical, Materials and Manufacturing Engineering
The University of Nottingham, University Park, Nottingham, NG7 2RD. UK
email: **seamus.garvey@nottingham.ac.uk**

Abstract

In mechanical engineering applications, the predominant sources of vibration are usually close-to-periodic in the sense that the forcing vector, $\mathbf{f}(t)$, can be expressed compactly in the Fourier series form $\mathbf{f}(t)=\mathbf{f}_0(t)+\sum_{k=0}^{p}\left(\mathbf{f}_{kc}(t)\cos(k\theta(t))+\mathbf{f}_{ks}(t)\sin(k\theta(t))\right)$ where $\theta(t)=\int_{\tau=0}^{\tau=t}\Omega(\tau)d\tau$ and where the time-constants associated with the functions $\{a_k(t), b_k(t),\Omega(t)\}$ are all long compared with the inverse of $\overline{\Omega(t)}$. The specific format of the forcing allows effective vibration absorption to be proposed. By vibration absorption, we mean the introduction of additional (largely-)passive subsystems which serve to cancel the vibration close to its source or on a transmission path. Cases of such quasi-periodic forcing include inertial forces in all reciprocating/rotating machines, fluid-dynamic forces on bladed rotors and forces from cyclic manufacturing processes. Two renewable-energy applications are presented.

1 Introduction

This paper addresses the suppression of vibration on primary structures where the excitation is *quasi-periodic*. By *quasi-periodic*, we mean the correlation between $\mathbf{f}(t)$ and $\mathbf{f}(t + T_P)$ is close to unity for some fixed periodic time, T_P, where $\mathbf{f}(t)$ represents the vector of forcing applied to the structure. The correlation in this case is carried out over a number of periods T_P.

Quasi-periodic excitation can be decomposed into an approximate Fourier series as …

$$\mathbf{f}(t)=\mathbf{f}_0(t)+\sum_{k=0}^{p}\left(\mathbf{f}_{kc}(t)\cos(k\theta(t))+\mathbf{f}_{ks}(t)\sin(k\theta(t))\right) \tag{1}$$

with

$$\theta(t)=\int_{\tau=0}^{\tau=t}\Omega(\tau)d\tau \tag{2}$$

and where the time-constants associated with the functions $\{\mathbf{f}_0(t), \mathbf{f}_{kc}(t), \mathbf{f}_{ks}(t), \Omega(t)\}$ are all long relative to the inverse of $\overline{\Omega(\tau)}$.

Cases of such forcing include imbalance forcing in rotating machines, residual inertial forces in all reciprocating machines, aerodynamic forces on helicopter rotors and on propellers in a non-uniform flow field and cyclic production machinery of many different types such as industrial sewing machines, embossing presses, punches, shears and many other forms of production machinery.

When forcing arises from the cyclic movement of mass, it is sometimes straightforward to arrange counterbalance excitation by direct mechanical connections such that the net excitation is close to zero. Lancaster balancers for reciprocating machines are a classic instance.

Alternatively/additionally, if the excitation is absolutely periodic, then conventional undamped vibration absorbers can be used very effectively to react the inputs virtually completely [1]. The total mass of these vibration absorbers can often be low relative to the mass of the structure itself.

In many practical circumstances, it is neither possible to use some system of mechanical linkages to drive counterbalances nor to rely on the perfect periodicity of the original forcing. Examples include free-piston energy converters (e.g. [2]), aero-engine imbalance forcing (rotor speeds are not governed directly) and the two renewable energy applications discussed later as examples here: a *direct-compression* wind-turbine and a *tidal-ram*. Then a variety of different forms of solution may be sought including:

- Full active cancellation
- Damped vibration absorbers [3].
- *Flat-band Vibration Absorbers* – defined later in this paper.
- Hybrid passive/(semi-)active vibration absorber solutions [4],[5]
- Non-linear absorbers such as the "energy-pumping" systems [6],[7]

Full active cancellation requires that actively-controlled actuators are used to supply vibration cancellation forces to the structure. In the context of quasi-periodic excitation, the control algorithms can become very robust since an adaptive feedforward approach can be used to supply most of the correction force with little reliance on high-bandwidth closed-loop control. However, full active cancellation is still invariably very expensive because of actuator costs – even if the costs of sensing and control are small – and we do not consider these further here.

The other options are all considered in this paper in subsequent sections. Section 2 of the paper discusses a number of aspects of passive vibration absorbers – beginning with undamped and then damped single-degree-of-freedom (SDoF) absorbers and then progressing to multi-degree-of-freedom absorbers. Section 3 goes on to discuss what is believed to be a new discovery of this paper – *flat-band vibration absorbers.*

2 Passive Dynamic Vibration Absorbers.

2.1 SDoF Vibration Absorbers (Undamped).

The Single-Degree-of-Freedom (SDoF) dynamic vibration absorber is long established and is known to be an extremely effective measure for suppressing one frequency component of vibration at a single point on a *primary* structure. This absorber comprises a simple mass and spring subsystem and the principle of operation is that it presents an infinite dynamic stiffness to its point of application at one specific frequency which we will term the *design frequency*. For illustration purposes, the SDoF vibration absorber is depicted using a single discrete rigid mass and a connecting massless spring. In practice, the true SDoF absorber is a subsystem having one resonance frequency at exactly the design frequency when its attachment point is grounded and all other resonances relatively far away up the frequency spectrum.

The *combined* structure, comprising both the primary structure and the absorber, has an anti-resonance at the design frequency in its point-receptance function for the point where the absorber is fixed. Theoretically, the absorber may be arbitrarily small. Two factors combine to determine its minimum practicable size:

(a) The spring must be capable of exerting the requisite reaction force (the so-called *blocked-force* [8]) at the point of application to zero the vibration there at the design frequency without breaking or becoming unduly non-linear. This force is a property of the primary structure and forcing being applied to it.
(b) The anti-resonance must not be so "narrow" that real uncertainty in the excitation frequency will lead to a nearby resonance of the combined structure being excited significantly. This uncertainty has two sources; true variation in excitation frequency over a long time-duration and finite-time-duration effects

whereby for a time-span of length R it is impossible to distinguish frequencies which are closer together than $(1/R)$.

There are obvious reasons for making the absorber as small as it can be subject to the above two concerns. Larger absorbers are less likely to break as a result of the blocked force, less likely to exhibit significant non-linearity (because deformations will remain small in proportion to the actual scale of the absorber) and have "wider" anti-resonance troughs. Figure 1a illustrates a *primary* structure to which a SDoF absorber has been fitted. Figure 1b shows the auto-point frequency response function for the primary system alone and for the combined system for the three cases where the absorber mass is 5%, 10% and 15% respectively of the primary system mass and where the design frequency is below a major resonance of the primary system. Figure 1c shows the same four auto-point frequency response functions where the design frequency is above the major resonance frequency.

Figures 1b and 1c amply illustrate the point that the "width" of the anti-resonance peak is broader as the absorber mass increases as a proportion of the effective mass of the primary system. These figures also contrast the effect of a vibration absorber when the effective dynamic stiffness of the primary system is positive (Fig. 1b) or negative (Fig. 1c) in the vicinity of the absorber design frequency. In both cases, resonances are present in the spectrum of the combined system which are close to the design frequency (below it and above it respectively).

In Figures 1b and 1c, the dynamic stiffness of the primary system has been relatively insensitive to frequency in the vicinity of the absorber design frequency. Throughout the rest of this paper, we will assume that this remains the case and we will rely upon that.

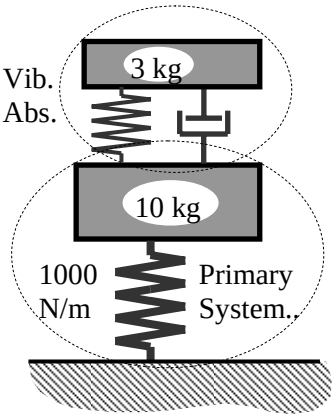

Figure 1a. SDoF Absorber.

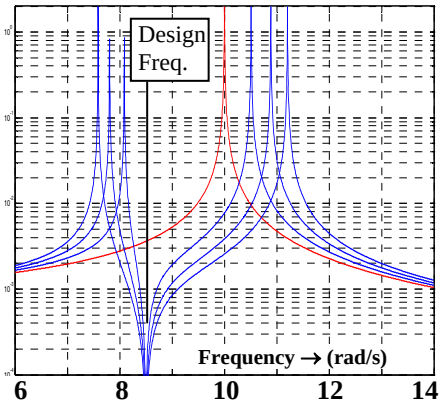

Figure 1b. Response vs. freq.

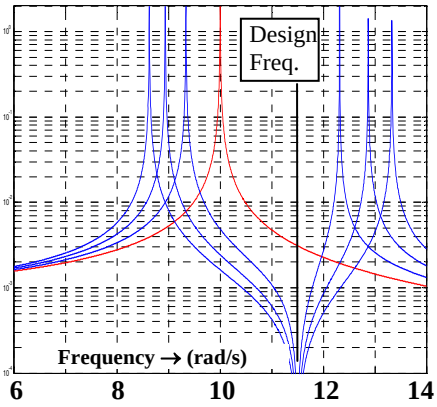

Figure 1c. Response vs. freq.

2.2 SDoF Vibration Absorbers (Damped).

Adding damping to the vibration absorber has a double effect. On the one hand, it suppresses the peak response of resonances by contributing some damping to modes of the combined structure whose resonances are near to the design frequency. On the other hand, it transforms a sharp anti-resonance in the magnitude of frequency-response at the design frequency into a round-bottomed local minimum. Figures 2a and 2b each show the frequency-response function of the same primary system used in Figures 1. Three other curves are superimposed with various levels of damping: 0%, 2% and 4%. The same absorber mass is used in all cases here – 15% of primary system mass. In Figure 2a, the design frequency is 8.5 rad/s. In Figure 2b, it is 11.5 rad/s. In both cases, the first (and only) primary system resonance is 10 rad/s.

Figures 2a and 2b transmit a clear message: damping in (SDoF) vibration absorbers must be aimed at applications where the band of frequencies of interest is quite broad. The range of frequencies where the response of the combined system is lower than the response of the primary system is almost totally independent of the level of damping. Within this range, the magnitude of the response of the combined system is increased by the presence of damping.

In the context of systems excited by quasi-periodic forcing as described above, the range of frequencies may indeed be quite broad but over any one time interval spanning a relatively small number of periods, it will be small. If we admit the possibility of semi-active control to allow the absorber design frequency to track the excitation frequency (or frequencies), the case for including substantial damping in the vibration absorber is clearly weak. From this point forward in this paper, we dismiss the possibility of substantial damping in the absorber subsystem.

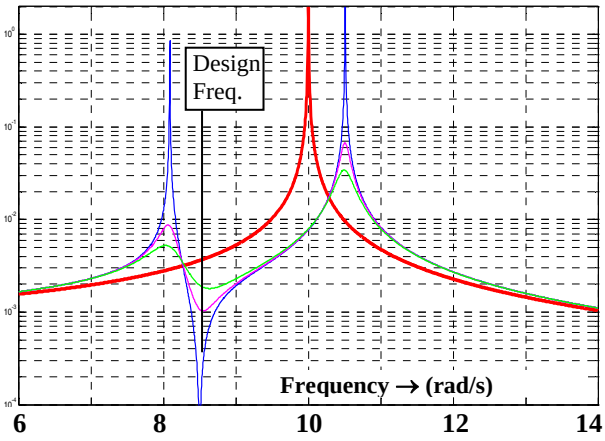

Figure 2a. Damped absorbers: |resp.| vs. f.

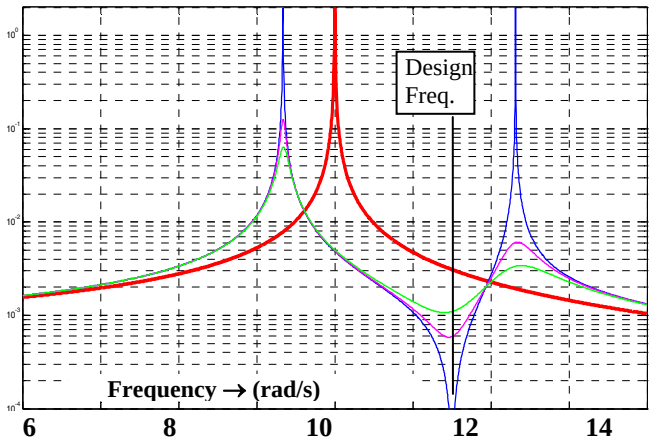

Figure 2b. Damped absorbers: |resp.| vs. f.

2.3 MDoF Vibration Absorbers.

In some senses, Multi-Degree-of-Freedom (MDoF) dynamic vibration absorbers are trivial extensions of SDoF absorbers. Very general definitions are possible – including cases where vibration is suppressed at more than a single degree of freedom on the primary structure. In this paper, we restrict attention completely to the case where vibration is to be suppressed only at a single location.

Conceptually, the simplest MDoF dynamic vibration absorber comprises a set of decoupled SDoF absorbers in parallel as Figure 3a illustrates. By tuning each individual SDoF absorber to a different design frequency, it is possible to react numerous distinct frequency-components. To any one SDoF absorber in this system, the combination of the actual primary structure and all of the remaining SDoF absorbers is, in effect, simply a complex primary structure. If the primary structure here is held still in space, then collectively, the set of all SDoF absorbers is simply a MDoF system having resonances at each one of the several design frequencies.

Figure 3b shows the auto-point frequency response function of a primary structure and that of the combined structure where an MDoF absorber has been fitted comprising three parallel SDoF absorbers. The primary system is formed from a mass of 10kg and a spring of stiffness 1000 N/m – as it was in all cases previously. The three SDoF absorbers contain masses of 0.5 kg, 1 kg and 1.5 kg and their springs have stiffness 32 N/m, 72.25 N/m and 121.5 N/m respectively – chosen such that the design frequencies are 8 rad/s, 8.5 rad/s and 9 rad/s respectively. Figure 3b shows that the widths of the three anti-resonances are indeed “proportional” to the individual SDoF absorber masses.

Figure 3c presents the auto-point frequency response functions of the primary structure and the combined structure where three SDoF absorbers have once again been fitted. This time, the absorber masses are 0.5 kg, 1 kg and 1.5 kg as before but the corresponding springs have stiffness 60.5 N/m, 132.25 N/m and 144 N/m respectively – chosen such that the design frequencies are 11 rad/s, 11.5 rad/s and 12 rad/s respectively. Figure 3c confirms again that the widths of the three anti-resonances are indeed “proportional” to the individual SDoF absorber masses.

Figures 3b and 3c already suggest one main result of this paper. Note that in each case the frequency response of the combined system has only two “major” resonances. For frequencies between the lowest and highest design frequencies the response is almost everywhere diminished. We extend this idea later.

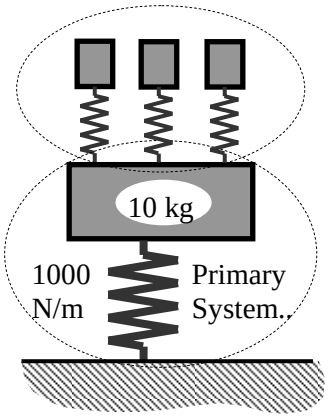

Fig 3a. MDoF Absorber.

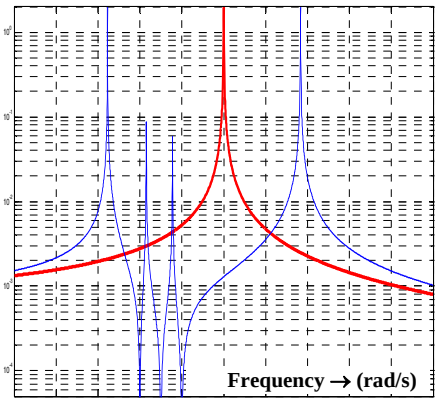

Fig. 3b. Resp. vs. f, (3DoF Absrbr)

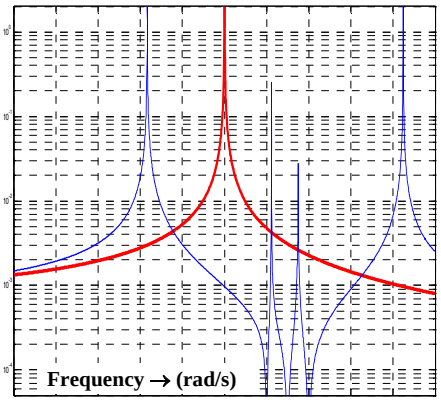

Fig. 3c. Resp. vs. f, (3DoF Absrbr)

2.4 Equivalence Classes of MDoF Vibration Absorbers.

The practicality of lining up a number of SDoF absorbers in parallel at a single point is, of course, rather limited. We are prompted, therefore, to consider the concept of *equivalence classes* of MDoF vibration absorbers. We restrict attention to the set of MDoF absorbers which act to suppress vibration at a single point only. Two MDoF vibration absorbers are *equivalent* if, for all frequencies, the same dynamic stiffness is added by the two absorbers to the point on the primary structure.

To identify the class of all equivalent absorbers, consider first that the set of generalized coordinates for the absorber comprises one *massless* coordinate corresponding to motion of the point of attachment and a further N generalized coordinates describing those movements of the absorber which involve non-zero kinetic energy. In general, the equation of motion for the absorber can be written

$$\left(\begin{bmatrix} k_{xx} & \mathbf{k}_{xn} \\ \mathbf{k}_{nx} & \mathbf{K}_{nn} \end{bmatrix} + j\omega\begin{bmatrix} d_{xx} & \mathbf{d}_{xn} \\ \mathbf{d}_{nx} & \mathbf{D}_{nn} \end{bmatrix} - \omega^2\begin{bmatrix} 0 & 0 \\ 0 & \mathbf{M}_{nn} \end{bmatrix}\right)\begin{bmatrix} q_x \\ \mathbf{q}_n \end{bmatrix} = \begin{bmatrix} f_x \\ \mathbf{f}_n \end{bmatrix} = \begin{bmatrix} f_x \\ \mathbf{0} \end{bmatrix}. \tag{6}$$

In (6), $\mathbf{f}_n$ is set to zero since no external forces are applied to the degrees of freedom of an absorber. For the special case where the MDoF absorber comprises N different SDoF absorbers in parallel, $\{(k_1, d_1, m_1), (k_2, d_2, m_2), (k_3, d_3, m_3) \ldots (k_N, d_N, m_N)\}$, the forms of the vector and matrix quantities of equation (7) are as follows:

$$\mathbf{k}_{xn} = \begin{bmatrix} -k_1 & -k_2 & -k_3 & .. & -k_N \end{bmatrix} = \mathbf{k}_{nx}{}^T \tag{7}$$

$$\mathbf{d}_{xn} = \begin{bmatrix} -d_1 & -d_2 & -d_3 & .. & -d_N \end{bmatrix} = \mathbf{d}_{nx}{}^T \tag{8}$$

$$\mathbf{K}_{nn} = diag\left(\begin{bmatrix} k_1 & k_2 & k_3 & .. & k_N \end{bmatrix}^T\right) \tag{9}$$

$$\mathbf{D}_{nn} = diag\left(\begin{bmatrix} d_1 & d_2 & d_3 & .. & d_N \end{bmatrix}^T\right) \tag{10}$$

$$\mathbf{M}_{nn} = diag\left(\begin{bmatrix} m_1 & m_2 & m_3 & .. & m_N \end{bmatrix}^T\right) \tag{12}$$

The dynamic stiffness of the vibration absorber is its key property and this can be deduced as:

$$\left(\frac{f_x}{q_x}\right)(\omega) = \left((k_{xx} + j\omega d_{xx}) - (\mathbf{k}_{xn} + j\omega\mathbf{d}_{xn})(\mathbf{K}_{nn} + j\omega\mathbf{D}_{nn} - \omega^2\mathbf{M}_{nn})^{-1}(\mathbf{k}_{nx} + j\omega\mathbf{d}_{nx})\right) \tag{13}$$

Inserting two identity matrices, ($\mathbf{T}_R\mathbf{T}_R^{-1}$) and ($\mathbf{T}_L^{-1}\mathbf{T}_L$) into the product in (13) leads to:

$$\left(\frac{f_x}{q_x}\right)(\omega)=\left(\left(k_{xx}+j\omega d_{xx}\right)-\left(\mathbf{k}_{xn}+j\omega\mathbf{d}_{xn}\right)\left(\mathbf{T}_R\mathbf{T}_R^{-1}\right)\left(\mathbf{K}_{nn}+j\omega\mathbf{D}_{nn}-\omega^2\mathbf{M}_{nn}\right)^{-1}\left(\mathbf{T}_L^{-1}\mathbf{T}_L\right)\left(\mathbf{k}_{nx}+j\omega\mathbf{d}_{nx}\right)\right) \quad (14)$$

We can immediately conclude that two different MDoF absorbers (distinguished by the additional subscripts 0 and 3 for compatibility with the next subsection) are *equivalent* if for some invertible matrices $\{\mathbf{T}_L, \mathbf{T}_R\}$:

$$\mathbf{k}_{xn3}=\mathbf{k}_{xn0}\mathbf{T}_R \quad , \quad \mathbf{d}_{xn3}=\mathbf{d}_{xn0}\mathbf{T}_R\,. \quad (15)$$

$$\mathbf{k}_{nx3}=\mathbf{T}_L^{\,T}\mathbf{k}_{xn0} \quad , \quad \mathbf{d}_{nx3}=\mathbf{T}_L^{\,T}\mathbf{d}_{nx0} \quad (16)$$

$$\mathbf{K}_{nn3}=\mathbf{T}_L^{\,T}\mathbf{K}_{nn0}\mathbf{T}_R \quad , \quad \mathbf{D}_{nn3}=\mathbf{T}_L^{\,T}\mathbf{D}_{nn0}\mathbf{T}_R \quad , \quad \mathbf{M}_{nn3}=\mathbf{T}_L^{\,T}\mathbf{M}_{nn0}\mathbf{T}_R \quad (17)$$

Thus the set of all equivalent MDoF vibration absorbers is spanned by pairs of invertible matrices $\{\mathbf{T}_L, \mathbf{T}_R\}$. We use this fact in the following section to devise vibration absorbers which are *chain-structured* having known properties equivalent to the properties of a given set of parallel SDoF vibration absorbers.

2.5 Transforming from multiple parallel SDoFs to "chain-structure" absorber.

The properties of a MDoF vibration absorber are very conveniently defined in terms of a multiplicity of SDoF absorbers in parallel. However, this form is not generally practicable and it is relevant to consider equivalent absorbers of more convenient structure. Any structure having the form of Figure 4 is said to have *chain structure* – provided that the choice of generalized coordinates is the same as that indicated.

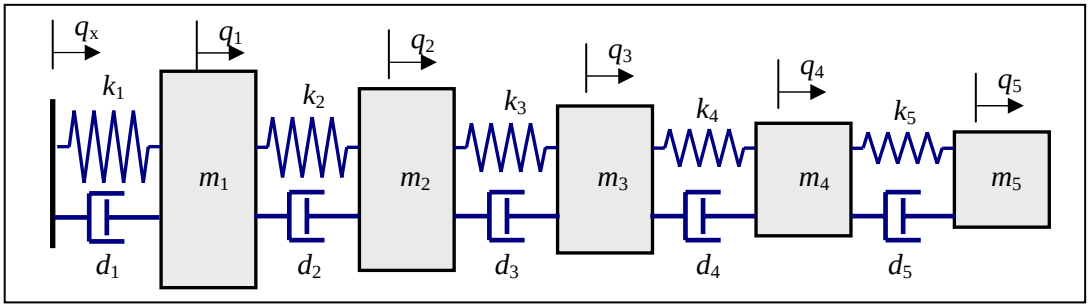

Fig. 4. A chain-structure MDoF absorber

The stiffness, damping and mass matrices describing such a structure are as follows (for N=5):

$$\mathbf{K}_A=\begin{bmatrix} k_1 & -k_1 & 0 & 0 & 0 & 0 \\ -k_1 & (k_1+k_2) & -k_2 & 0 & 0 & 0 \\ 0 & -k_2 & (k_2+k_3) & -k_3 & 0 & 0 \\ 0 & 0 & -k_3 & (k_3+k_4) & -k_4 & 0 \\ 0 & 0 & 0 & -k_4 & (k_4+k_5) & -k_5 \\ 0 & 0 & 0 & 0 & -k_5 & k_5 \end{bmatrix} \quad (18)$$

$$\mathbf{D}_A=\begin{bmatrix} d_1 & -d_1 & 0 & 0 & 0 & 0 \\ -d_1 & (d_1+d_2) & -d_2 & 0 & 0 & 0 \\ 0 & -d_2 & (d_2+d_3) & -d_3 & 0 & 0 \\ 0 & 0 & -d_3 & (d_3+d_4) & -d_4 & 0 \\ 0 & 0 & 0 & -d_4 & (d_4+d_5) & -d_5 \\ 0 & 0 & 0 & 0 & -d_5 & d_5 \end{bmatrix} \quad (19)$$

$$\mathbf{M}_A = diag\left(\begin{bmatrix} 0 & m_1 & m_2 & m_3 & m_4 & m_5 \end{bmatrix}^T\right) \tag{20}$$

Devising transformation matrices $\{\mathbf{T}_L, \mathbf{T}_R\}$ to effect the transformations from a vibration absorber of the (multiple SDoF systems) form to one of chain-structure is straightforward if the dampers of the multiple SDoF system were each related to the corresponding stiffness by a constant multiplier, ω_{damp} through

$$d_i = \frac{k_i}{\omega_{damp}} \quad \text{for all } i. \tag{21}$$

In most cases $\mathbf{T}_L = \mathbf{T}_R = \mathbf{T}$ and only this symmetric case is catered for here. The extension to the general case is relatively trivial. The transformation takes place in 3 main stages.

$$\mathbf{T} = \mathbf{T}_1\, \mathbf{T}_2\, \mathbf{T}_3 \tag{22}$$

The first of these transformation stages, $\mathbf{T}_1$, transforms $\mathbf{M}_{nn}$ for the absorber to be the ($N \times N$) identity matrix. Invariably, $\mathbf{T}_1$ is simply a diagonal matrix. The second transformation stage, $\mathbf{T}_2$, preserves the fact that $\mathbf{M}_{nn} = \mathbf{I}$ whilst transforming the stiffness matrix to symmetric tridiagonal form. This step is based on *Householder reflections* (symmetric orthogonal matrices) and it is a very well-established, stable and widely-used process. The third stage of the transformation, $\mathbf{T}_3$ is again a diagonal matrix. The other diagonal entries of $\mathbf{T}_3$ are found very easily by solving a (tridiagonal) set of simultaneous linear equations.

The transformation process is illustrated using the absorber system used for Figure 3b. This comprised three parallel SDOF absorbers having individual masses, 0.5 kg, 1.0 kg and 1.5 kg respectively and having absorber design frequencies of 8 rad/s, 8.5 rad/s and 9 rad/s. This absorber system is characterized by:

$$k_{xx0} = 225.75 \ \text{(N/m)} \quad \text{and} \quad \omega_{damp} = \infty \tag{23}$$

$$\mathbf{k}_{xn0} = -\begin{bmatrix} 32 & 72.25 & 121.5 \end{bmatrix} \text{(N/m)} = \mathbf{k}_{nx0}{}^T \tag{24}$$

$$\mathbf{K}_{nn0} = \begin{bmatrix} 32 & 0 & 0 \\ 0 & 72.25 & 0 \\ 0 & 0 & 121.5 \end{bmatrix} \text{(N/m)}, \quad \mathbf{M}_{nn0} = \begin{bmatrix} 0.5 & 0 & 0 \\ 0 & 1.0 & 0 \\ 0 & 0 & 1.5 \end{bmatrix} \text{(kg)}, \tag{25}$$

None of the transformations ever affects k_{xx}. Thus, $k_{xx3} = k_{xx0} = 225.75$ (N/m). After the first stage, we have

$$\mathbf{k}_{xn1} = -\begin{bmatrix} 45.2548 & 72.25 & 99.2043 \end{bmatrix} \text{(N/m)} = \mathbf{k}_{nx1}{}^T \tag{26}$$

$$\mathbf{K}_{nn1} = \begin{bmatrix} 64 & 0 & 0 \\ 0 & 72.25 & 0 \\ 0 & 0 & 81 \end{bmatrix} \text{(N/m)}, \quad \mathbf{M}_{nn1} = \begin{bmatrix} 1 & 0 & 0 \\ 0 & 1 & 0 \\ 0 & 0 & 1 \end{bmatrix} \text{(kg)} \tag{27}$$

After the second stage, we have

$$\mathbf{k}_{xn2} = -\begin{bmatrix} 130.8035 & 0 & 0 \end{bmatrix} \text{(N/m)} = \mathbf{k}_{nx2}{}^T \tag{28}$$

$$\mathbf{K}_{nn2} = \begin{bmatrix} 76.2955 & -5.98497 & 0 \\ -5.98497 & 71.1919 & -4.96549 \\ 0 & -4.96549 & 69.7626 \end{bmatrix} \text{(N/m)}, \quad \mathbf{M}_{nn2} = \begin{bmatrix} 1 & 0 & 0 \\ 0 & 1 & 0 \\ 0 & 0 & 1 \end{bmatrix} \text{(kg)} \tag{29}$$

The non-zeros in the diagonal matrix, $\mathbf{T}_3$, are determined from the equation:

$$\mathbf{K}_{nn2}\mathbf{T}_3 + \mathbf{k}_{nx2} = \mathbf{0} \tag{30}$$

Using this transformation, the absorber quantities after the third transformation are

$$\mathbf{k}_{xn2} = -\begin{bmatrix} 225.75 & 0 & 0 \end{bmatrix} \text{(N/m)} = \mathbf{k}_{nx2}{}^T \tag{31}$$

$$\mathbf{K}_{nn3} = \begin{bmatrix} 227.256 & -1.5062 & 0 \\ -1.5062 & 1.5137 & -7.5146\text{E-}3 \\ 0 & -7.5146\text{E-}3 & 7.5146\text{E-}3 \end{bmatrix} \text{(N/m)}, \qquad \mathbf{M}_{nn3} = diag\left(\begin{bmatrix} 2.9786 \\ 2.1262\text{E-}2 \\ 1.0772\text{E-}4 \end{bmatrix} \right) \text{(kg)} \tag{32}$$

Two important observations are immediately obvious from this example:

(a) The first stiffness in the chain-structured absorber is identical to the sum of the stiffnesses of the individual SDoF absorbers in the parallel arrangement. This must always be so since the added dynamic stiffness of the absorbers must be identical at very high frequencies (well above design frequencies).

(b) The total amount of mass in the chain-structured absorber is identical to the sum of the masses of the individual SDoF absorbers in the parallel arrangement. This must also be true always since the additional dynamic stiffness of the two absorbers must be identical at very low frequencies (well below the design frequencies).

We will make strong use this transformation from sets of parallel SDoF absorbers and chain-structured MDoF absorbers. The parallel-SDoF absorbers provide a very convenient means by which to specify the performance of the absorbers. In fact, we will consider that this is the *canonical form* for any given equivalence class of MDoF absorbers. However, the chain-structured absorbers produce a very practical means of implementation. The first spring (coupling the entire absorber to the primary structure) obviously carries all of the absorber force in this case and it seems natural that this should also be the highest-stiffness spring.

2.6 Flat-Band Vibration Absorbers.

Figure 3b shows the response of a primary system and a combined system involving the primary system and a three-degree-of-freedom vibration absorber whose total mass was 3kg. In the range of the absorber design frequencies (8 rad/s to 9 rad/s), the response of the combined system is nearly always much lower than the response of the primary system. This plot prompts a relatively obvious question: *what would happen if the total absorber mass of 3kg were to be divided between, say, 40 different parallel SDoF absorbers having design frequencies equally spaced (geometrically) between 8 rad/s and 9 rad/s ?*

Figure 5a answers that question. This Figure also displays the response of the combined system obtained if a single SDoF absorber with mass 3 kg and design frequency 8.43 rad/s were fitted to the primary system. The combined system has two major resonances in it having very similar peak amplitudes and resonance frequencies for the two different absorber arrangements. This is entirely to be expected. The design frequency of this SDoF absorber was chosen deliberately to maximize this similarity in order to stress the fact that the major difference between the behaviour of the simple SDoF absorber and a *flat-band vibration absorber* (FBVA) having similar (central) design frequency and the same total mass occurs in the region of the (flattened) “anti-resonance” – in the design frequency region. Figure 5a indicates a finding that is borne out by experience with other situations where the primary system does not have a resonance within the frequency band of interest; if it is important to maintain response of the combined system beneath some target value over some range of frequencies using some given total amount of absorber mass, then in general this band will be roughly 1.6 times broader using a FBVA than it would be using a simple SDoF absorber.

For both vibration absorber arrangements, a very small amount of damping has been added - the dampers are proportional to the corresponding stiffnesses according to equation (21) with ω_{damp} = 1000 rad/s. In other words the damping factors of the individual SDoF absorbers vary between (16/1000) and (18/1000) – all less than 2%. The only significance of the damping here is to provide sufficient *modal-overlap* between the individual SDoF resonances. The primary purpose of this damping is <u>not</u> to reduce the response of the combined system at its two major resonances. Note that if 200 absorbers had been used rather than 40, the damping values could be reduced to less than 0.4%. Note also that in this case, the resonances of the combined system in the frequency range of interest (8 rad/s to 9 rad/s) are so close that damping would be entirely irrelevant anyway if the excitation frequency was varying with time-constants less than about 200 s.

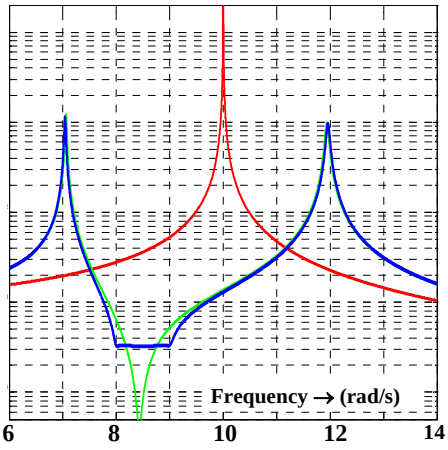

Fig. 5a. Resp. vs. f, (FBVA)

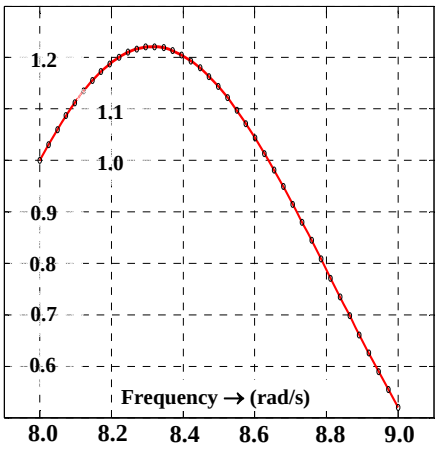

Fig. 5b. Mass Ratios vs f.

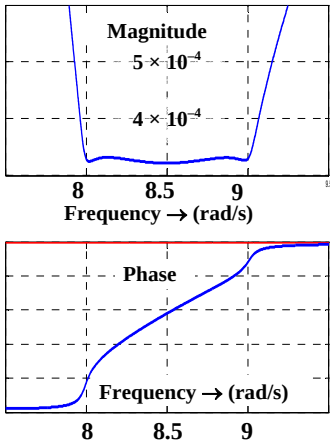

Fig. 5c. FBVA resp. zoomed

In the FBVA arrangement modelled, the mass of each absorber is not identical. Figure 5b shows the ratios used in this case to provide a relatively flat-bottomed combined system response. Figure 5c shows the magnitude and phase of the frequency response of the combined system with the FBVA in place. The magnitude varies within a range of ±2% of the mean response value. The phase climbs fairly-steadily from $-\pi$ to 0 between frequencies 8 rad/s and 9 rad/s.

The relevance of the FBVA to the context of quasi-periodic excitation is quite obvious: if we require to suppress vibration over specific frequency bands (whose centres are integer multiples of some nominal fundamental frequency, then it may be much better to use one FBVA for each band rather than using (in effect) one SDoF absorber for each band.

2.7 Chain-structure Formats of Flat-Band Vibration Absorbers.

A FBVA can be designed initially in the format of a combination of many parallel SDoF absorbers. The design frequencies of these absorbers are spaced apart regularly within the frequency band of interest and these design frequencies determine the ratios between individual springs and masses. Exact geometric spacing is suggested. A value is then chosen for ω_{damp} which will relate all individual dampers to the corresponding spring through equation (21). A value of around $(50{,}000 \times \Delta f)$ is suggested – where Δf is a representative frequency gap between consecutive resonances of the absorber. The sum of all of the absorber masses is a fixed quantity decided a-priori by the designer. Some smooth distribution of the absorber masses over the frequency band of interest is selected – such as Fig. 5b illustrates. Concentrating more mass in a particular region of the frequency-band of interest tends to reduce the response of the combined system in that region and this freedom to spread the absorber mass arbitrarily across the frequency band of interest makes it possible to achieve the very flat response.

Having developed a FBVA in the (canonical) format of multiple parallel SDoF absorbers, it is useful, often, to transform it to a chain-structured format. We do this for the case of the 40 DoF FBVA reported in the previous section. Figures 6a and 6b shows the mass and stiffness values associated with individual parts of the chain-structured absorber. See Figure 4 to interpret the numbering.

The corresponding numerical values are given in table 1 below. What is striking from Figures 6a and 6b is how rapidly the mass and stiffness values diminish – and how relatively constant is that diminishing.

	i=1	i=2	i=3	i=4	i=5	i=6
k_i (N/m)	213.93	0.91032	3.6205E–3	1.3596E–5	4.9955E–8	1.8126E–10
m_i (kg)	2.9874	1.2589E–2	5.0929E–5	1.8814E–7	6.9135E–10	2.5088E–12

Table 1: Properties of the Chain-Structured FBVA.

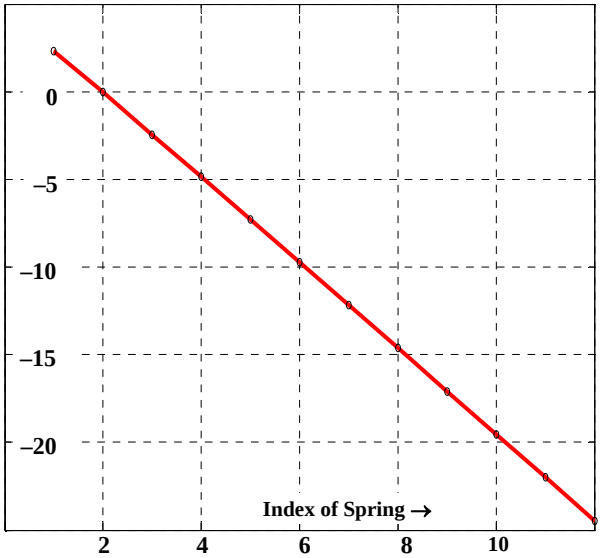

Fig. 6a. $\log_{10}(k_i)$ vs. i for chain-structured FBVA

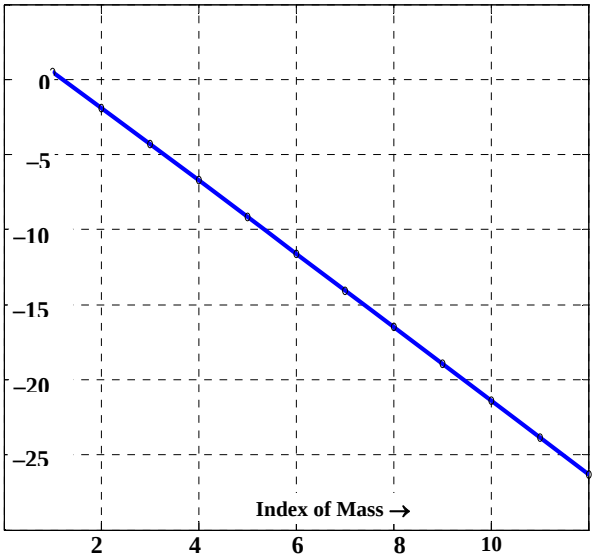

Fig. 6b. $\log_{10}(m_i)$ vs. i for chain-structured FBVA

Because of factors relating to numerical resolution, values of k_i and m_i for $i > 12$ cannot be computed accurately using the straightforward procedure described. For $i < 12$, the ratio $(k_i/(m_i))$ varies away from its average value by less than 1%. Moreover, the ratio $(k_i/k_{(i+1)})$ varies about its mean value, 274.5, by only relatively little. Considering a practical implementation of this FBVA, it is inconceivable that more than three DoFs would be attempted and it is also fairly hard to imagine that omitting the remainder of the system would cause any noticeable difference.

3 Active and Semi-active Absorber Approaches

3.1 Active / Semi-Active Vibration Absorption.

In all passive vibration absorption schemes, forces are exerted at one or more points which provide most of the force necessary at those points to suppress motion – at least for specific frequency bands. The magnitudes of the forces applied are determined by the primary structure and its excitation and they may often be large. In broad terms, this presents two distinct issues: (a) how to transmit the force and (b) how to react it. The former issue is generally simple and the latter one challenging. If we could simply tie our structures to *ground* at the points of interest by introducing some elements in direct tension/compression, most vibration problems could be resolved easily – e.g. the so-called *sky-hook damper* of vehicle dynamics. In general, we can only couple points on the same flexible structure or introduce additional mass to provide seismic reaction. Unfortunately, the forces used for vibration suppression on the primary structure cause significant movements of the seismic mass. Thus, there are power-flows to and from the seismic masses and if the absorption scheme is to be anything other than simple added mass, then substantial proportions of those power-flows arise in connection with the control forces themselves.

Fully active vibration absorption requires the inclusion of actuators of some description into the primary structure which can account for power flows which are significant in comparison to the vibration energy of the primary structure. They are invariably very expensive and difficult to implement. Semi-active or hybrid vibration absorption, in contrast, may be relatively inexpensive and can provide a substantial improvement over purely passive measure. A particular feature is that the design frequencies (or frequency bands) for absorption can be adapted in time. Here, “semi-active” vibration absorbers are considered to be those whose passive stiffnesses can be modified directly (e.g. [4]) and “hybrid” absorbers involve actuators in parallel with the springs of a passive absorber such as in [5]. Hybrid absorbers are generally more expensive and more versatile but will often have the same effect as semi-active ones (ability to tune absorber frequencies) so we concentrate on the latter.

The key properties of semi-active absorption are (i) the extent to which the absorber frequencies can be modified, (ii) the rate at which they can be modified and (iii) the degree to which different absorber frequencies may be modified independently. In the class of cases of interest here (quasi-periodic excitation), there is no call for independent control of different absorber frequencies.

We illustrate semi-active absorption by applying the force $f(t)$ to a simple SDoF primary structure comprising mass 10 kg and stiffness 1000 N/m over a period of 800 seconds.

$$f(t)=\sin(\theta) \quad \text{where} \quad \dot{\theta}=\left(10-\tfrac{1}{80}|t-400|+p\cos(t/4)\right) \tag{33}$$

Initially we set p=0 and then $f(t)$ is "sinusoidal" with a frequency which varies linearly from 5 rad/s to 10 rad/s and back again. Subsequently, we set p=0.4 rad/s which adds some frequency "dither". Three cases of vibration absorption are considered: (i) no absorption, (ii) a semi-active SDoF absorber of mass 2 kg which is tuned to $\left(10-\tfrac{1}{80}|t-400|\right)$ and (iii) a semi-active FBVA with total mass 2kg tuned to have a centre frequency $\left(10-\tfrac{1}{80}|t-400|\right)$ and a band-width of 0.8 rad/s. Figures 7a – 7c show the envelopes of magnitudes of the primary system mass. In each case the red curve is the outcome when p=0, (no frequency dither) and the blue curve applies when p=0.4 rad/s.

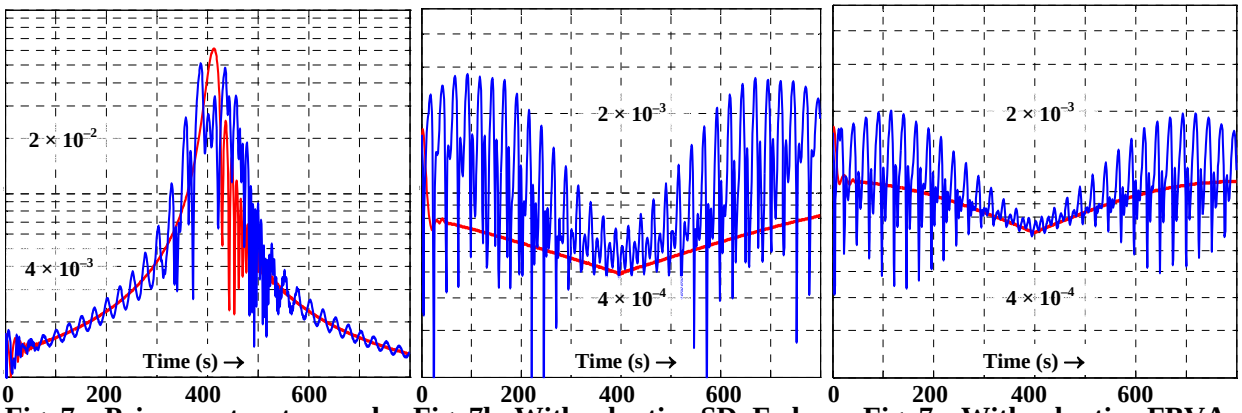

Fig. 7a. Primary structure only **Fig. 7b. With adaptive SDoF abs.** **Fig. 7c. With adaptive FBVA.**

The outcomes are mostly consistent with expectation. Firstly, the primary structure without absorption responds with peak amplitude much higher than that obtained with absorption – around 20 times higher. Secondly, the adaptively tuned SDoF behaves better than the adaptively-tuned FBVA when there is no frequency dither present. The ratio here is around 1.4. Thirdly, and most importantly, the FBVA behaves rather better than the SDoF system when there is frequency dither present. The ratio is again around 1.4.

4 A Renewable-Energy Application with Quasi-Periodic Excitation

In terms of wind-turbine economics, "larger is better". Large diameter machines tap into a higher mean wind-speed and require a smaller proportion of total cost for installation and maintenance. Consideration of the scaling laws for wind-turbines shows that (a) the main-shaft torque rises in proportion to D^3 (where D is turbine tip-diameter) and (b) that gravitational forces dominate over aerodynamic forces for large D.

The cost of gearboxes or direct-driven generators rises with input torque ($\propto D^3$) but the value of a wind-turbine is proportional only to D^2. Evidently, as diameter increases further, some fundamental change in the nature of wind-turbine power-extraction is inevitable. One suggestion is that the power extracted from the wind in very large turbines might be converted within the turbine rotor itself by allowing free-moving masses within the blades of the turbine to travel relative to the blade under the influence of gravity as Figure 8a illustrates. The motion of the masses relative to the blade can be converted into some transportable power in numerous different ways but one obvious way, considered here, is to allow the masses to be pistons and to extract their energy in the form of compressed air.

The concept is illustrated by a 200m tip-diameter 4-blade machine with rated wind-speed 15m/s and rated power 18MW. This turbine has a mass (piston) of 55,000kg in each blade. The centre of gravity of this piston is capable of falling from a radius of 85m to a radius of 20m. The pistons in diametrically-opposite blades are connected by stiff ties such that the effect of centrifugal force on the piston in the rising blade is alleviated. Rated rotational speed of the machine is 0.540 rad/s – meaning that it takes 11.64 seconds to complete a single cycle. When the wind-speed is equal to rated wind-speed (15 m/s) or above, the machine turns at 0.54 rad/s except that in very strong winds, the turbine shuts down (like all turbines). The energy converted in each half-cycle of the blade is 26.22 MJ and if the pressure-ratio is 70:1, then the volume of new atmospheric air compressed and discharged in each half-cycle (per blade) should be 31.62 m^2.

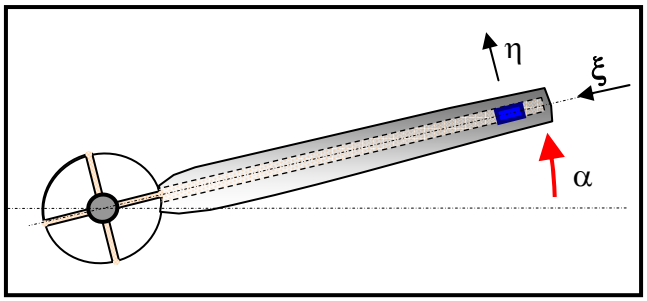

Fig. 8a. Energy conversion within the blades.

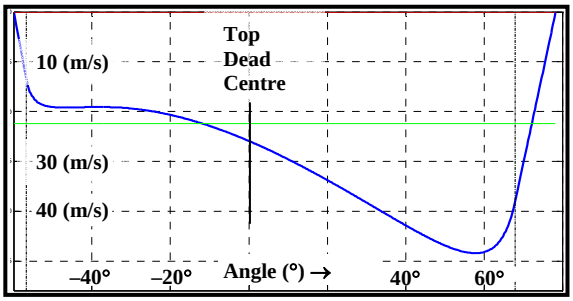

Fig. 8b. Radial Piston Velocity (m/s).

If the pistons in two diametrically-opposite blades are considered together, the centrifugal acceleration associated with the centre of mass has a maximum of $0.5 \times (85 - 20) \times 0.54^2 = 9.477$ m/s^2. Evidently, the pair of masses will at least begin to *commutate* naturally. However, the net inward acceleration is too small to cause the pistons to travel 65m in under 5 seconds. To assist in the extraction of energy, high-pressure air is re-inducted to accelerate a pair of pistons away from the "high" position in their half-cycle. In the present case, a cylinder internal cross-sectional-area of 0.548 m^2 is selected. High pressure air is re-inducted. Figure 8b presents the radial velocity profile of a piston CoG falling from its maximum radius of 85m (starting at 60° before top-dead-centre) to its minimum radius of 20m (at 78.3° after top-dead-centre). Dashed lines indicate where induction of high pressure air ends and where expulsion begins. During the induction and expulsion phases, piston accelerations of around 7g are obtained. At these times, there is a high net horizontal force applied to the rotor hub. If this is not largely absorbed within the rotor, it will cause large stresses in the main bearing and will also excite the tower substantially. Figure 9a shows the trajectory of the centre of mass of the movable pistons (cycled 4 times per rotor revolution) and Figure 9b shows the plot of horizontal force which would be exerted on the tower over one rotor revolution.

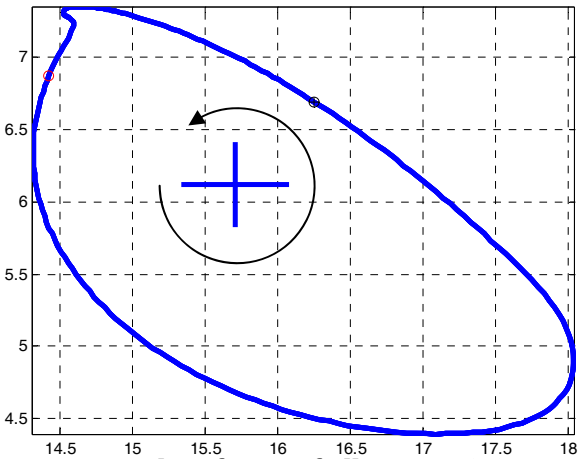

Fig. 9a. Orbit of CoG of all Pistons (m).

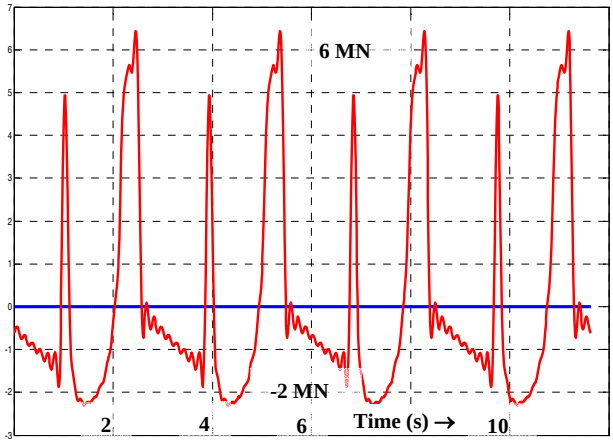

Fig. 9b. Net horizontal force on main shaft.

A reduced-dimension model of the tower (including the main rotor mass) takes the following form:

$$\mathbf{K}_{TW} = diag\left(\begin{bmatrix} 3.108\times10^{6} \\ 94.76001 \\ 853.8226 \end{bmatrix}\right) \text{(N/m)} \quad , \quad \mathbf{M}_{TW} = \begin{bmatrix} 1.0917\times10^{6} & -386.330 & 208.828 \\ -386.330 & 1 & 0 \\ 208.828 & 0 & 1 \end{bmatrix} \text{(kg)} \tag{34}$$

The first degree of freedom here coincides exactly with the horizontal translation of the main turbine shaft. Craig-Bampton reduction was used. The natural frequencies are 0.2679 Hz, 1.6701 Hz and 4.7647 Hz. Of the 1092 tonnes of mass associated with lateral movement of main-shaft, 691 tonnes belong to the rotor.

The fundamental forcing frequency is 0.34377 Hz (four times rotational frequency). Table 2 gives the magnitudes of the first five forcing harmonics together with the magnitudes of displacement response.

	i=1	*i*=2	*i*=3	*i*=4	*i*=5
Frequency (Hz)	0.34377	0.68754	1.03132	1.37510	1.71887
Force Harm. Magn. (MN)	1.7165	2.1481	1.0217	1.0573	0.73642
Disp. Harm. Magn. (m)	0.84869	0.11955	0.02136	0.00880	0.02278
Brng. Force Harmonics (MN)	1.0185	0.6071	0.4021	0.6034	1.0990

Table 2: Magnitudes of harmonics of horizontal forcing, displacement & bearing reaction.

We now consider an FBVA applied to this. The FBVA is allowed a total mass of 108 tonnes and this mass is split between the 5 harmonics in the proportions 5:3:2:3:5. In the initial FBVA design, 3 SDoF absorbers with masses are dedicated to each harmonic, at frequencies of 99%, 100%, 101% of the nominal harmonic. A value ω_{damp}=80 rad/s is chosen throughout. Table 3 summarises the SDoF absorber masses used and Fig. 10 shows the tower response to unit horizontal excitation with and without the FBVA.

Harm	m_1(kg)	m_2(kg)	m_3(kg)
1	4000	11000	15000
2	3000	6000	9000
3	2000	4000	6000
4	3000	6000	9000
5	8000	10000	12000

Table 3. SDoF Absorber masses.

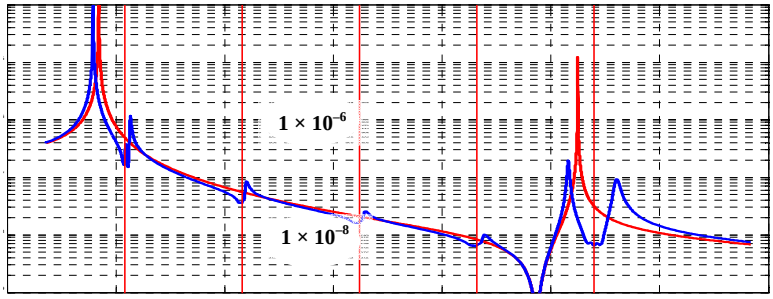

Fig. 10. Tower-top response with and without absorbers

The effectiveness of the absorbers in this case is quite limited except at the fifth harmonic where a reduction by a factor greater than 4 has occurred. In the vicinity of fundamental frequency, reductions of a factor of around 2 are found. The resonance frequencies in this vicinity could be smoothed out with higher damping but the presence of some frequency dither would have this effect automatically. With additions of mass which are (at most) <3% of the total tower-top mass, only modest reductions can be expected if ±1% of frequency "dither" is to be managed. The capability to adapt the absorber could be provided conveniently here using air-springs. This FBVA can be transformed into a chain-structured form. The sequence of masses then begins as: 63315kg, 18402kg, 11989kg, 6700.4kg, 3016.0kg, 4472.8kg, 88.676kg, 6.2029kg, 4.1562kg, 3.9073kg, 1.0805kg. The remaining five masses are less than 1kg and the final mass is only 0.194 gr.

5 A Second Renewable-Energy Applicat[n] and Non-Linear Absorbers

One possible means of extracting tidal power is to harvest that power also in the form of compressed air. Rotary machines are possible but because tidal flows are slow and because the same "optimal tip-speed ratio" concept applies to wind-turbines and water-turbines, rotational speeds are correspondingly slow. A very old engineering concept (the *hydraulic ram* pioneered by Joseph Montgolfier in 1796) finds new life here as the *tidal ram*. The hydraulic ram operates by allowing a column of water to accumulate velocity in a fixed and rigid tube and then closing a valve suddenly. The kinetic energy of the contained moving water is then converted into potential energy – usually by compressing a fixed volume of air – and this potential energy can then be exploited to drive a quantity of water up to a height much larger than the original head. The hydraulic ram requires some key customizations to become suited to tidal applications: (a) it must be self-starting, (b) it must deal with a range of flow speeds (the highest of which will be around 3m/s), (c) it must compress air directly (rather than propelling water up to a height), (d) for economic reasons it must be realizable at scales where many tonnes of moving water are decelerated within the tube, (e) it must be installed in such a way that it can extract energy from both directions of a fully-reversing flow and (f) the oscillatory component of the net force exerted by the water on the device must be reacted internally within the device – some kind of vibration absorption is intrinsically required. The imperative for (f) is obvious only when (d) and (e) are considered together. Consideration (e) means that the device must be tethered to a fixed mooring point and held elevated by some buoyant provisions breaking the sea surface and consideration (d) then indicates that the cost of the mooring point will be very large if the oscillatory forces are to be transferred to the sea-bed. Figure 11a shows a schematic of a possible design for one *tidal ram*. The blue curve (comprising three near-straight segments) in Figure 11b shows a typical *force-pulse* exerted on the device when the main water valve (7) is closed. The red curve is a linear combination of the functions $\{\sin(\pi(t-t_0)/T_1), \sin(3\pi(t-t_0)\ \pi\ /T_1), \sin(5\pi(t-t_0)/T_1), \sin(7\pi(t-t_0)/T_1), \sin(9\pi(t-t_0)/T_1)\ \}$ with t_0=0.02s and T_1=0.428s and it approximates the blue curve.

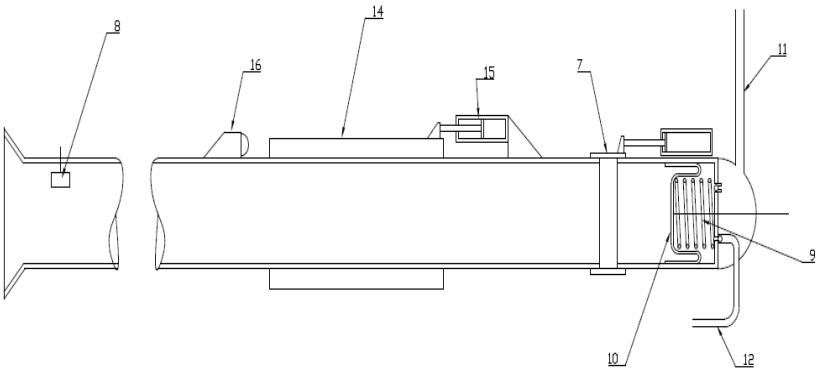

Fig. 11a. One implementation of *Tidal Ram*.

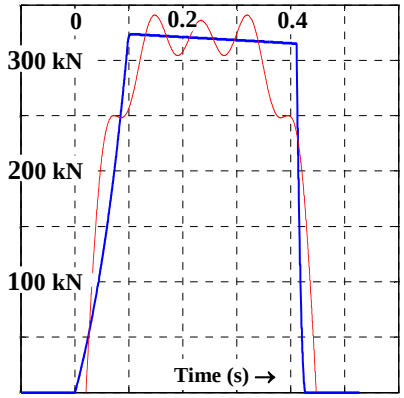

Fig. 11b. Force pulse at valve closure

The contained water column has 2m diameter and 7m long. Its velocity when valve closes is 5m/s. The energy extracted in one pulse is 280kJ. This energy can compress an initial volume of 3.77 m^2 of air up to 2 bar and discharge it into a high pressure reservoir. A *flow-concentrator* at the front (only partly shown) has an effective mouth area of 80m^2 (~5m radius). At a full tidal flow of 3m/s, the device will pulse with frequency 0.511 Hz. In flows of {2.8, 2.6, 2.4, 2.2, 2.0} (m/s) it will pulse at frequencies of {0.378, 0.233, 0.114, 0.040, 0.013} (Hz) respectively. It does not operate at all for flows below 2.0 m/s.

Each individual pulse is identical and even at the fastest pulsing rate of 0.511 Hz, the duration of the force pulse, 0.428 s, is significantly shorter than even the shortest periodic time of 1.95s. This feature inherently lends itself to some form of non-linear absorption where the vibration absorption focuses on reacting the individual pulses in turn rather than focusing on the trying to suppress harmonics in the frequency domain. The *energy-pumping* ideas of Vakakis and co-workers [6],[7] provide one potentially-promising solution.

A different approach is adopted here. Item (14) of Fig. 11a schematically indicates a linear dynamic subsystem which may be caused to impinge on the main body of the tidal ram at point (16) at around the same instant that the main valve closes. Some restoring provision represented (inaccurately) by (15) reverses the velocity of this linear subsystem after an impingement without deforming it. The core concept here is that the subsystem has no internal strain energy before an impingement or after it – we require it to *bounce* off point (16) in such a way that if all initial velocities of the component masses were identical before impingement, then they would also be identical afterwards – all reversed by the impingement.

The equivalence classes of absorbers provide the perfect resource. The linear subsystem has the chain-structure form of Fig. 4. The requirement for perfect bounce is very simply expressed: all resonances of the structure (with q_x=0) must be odd multiples of the lowest resonance, f_{n1} (= (0.5/0.4275) Hz here). We represent the absorber first in the canonical form of five parallel SDoF absorbers with resonances of 1.1905 Hz × {1,3,5,7,9}. Total mass is chosen such that the water column momentum can be reacted without very large velocity changes. Individual SDoF masses are proportional to the multipliers of the sinusoidal functions listed above Fig. 11: {65.59, 14.24, 4.923, 4.217, 5.027} tonnes respectively. Provided that the valve-closure is synchronized properly with the absorber impacts, the smooth force pulse of Fig. 11b is provided by the absorber as a reaction to the force pulse exerted by the water.

6 Conclusions

This paper introduces *flat-band vibration absorbers* – linear absorber subsystems which present an additional dynamic stiffness to primary structure which is high and relatively-constant over a frequency band. Through the concept of *equivalence* of vibration absorbers, it shows how these may be designed as multiplicities of parallel SDoF absorbers and transformed subsequently into chain structure. A set of these is illustrated for the case of a large wind-turbine with integral air compression in its rotor. It then considers non-linear absorbers for reacting shaped impulses – motivated by the application of a very simple tidal-powered compressor. The equivalence classes for vibration absorbers enables suitable bouncing counter-measures to be designed directly.

References

[1] D. J. Inman. *Engineering Vibration*. Edition 3. Prentice-Hall. New Jersey. 2007.

[2] J.B.Wang, M. West, D. Howe, H.Z.D. LaParra, W.M. Arshad, *Design and Experimental Verification of a Free-Piston Energy Converter*. IEEE Trans. on Energy Conversion. Vol. 22(2). pp299-306

[3] K. Liu, J. Liu, *Damped Dynamic Vibration Absorbers: Revisited and New Results.* Journal of Sound and Vibration, Vol. 284, Academic Press (2004), pp. 1181-1189.

[4] M. J. Brennan. *Vibration Control Using a Tunable Vibration Neutraliser*. Proc. Inst. Mech. Engrs. Part C. Journal of Mechanical Engineering Science. Vol. 211. (1997) pp 91-108

[5] A. Shahaj, S.D. Garvey, *Robust Multi-Degree-of-Freedom Hybrid Vibration Absorption*. Int. Modal Analysis Conf. (IMAC XXII), Soc. for Experimental Mechanics, Orlando, Feb. 4 – Feb. 8, 2008.

[6] A. F. Vakakis. *Inducing Passive Nonlinear Energy Sinks in Vibrating Systems*. Trans. ASME, Journal of Vibration and Acoustics, Vol. 123, (2001), pp. 324 – 332.

[7] D. M. McFarland, G. Kerschen, J. J. Kowtko, Y. S. Lee, L. A. Bergman, A. F. Vakakis. *Experimental Investigation of Targeted Energy Transfers in Strongly and Nonlinearly Coupled Oscillators.* J. Acoust. Soc. Am. Vol. 118(2), (2005), pp. 791-799

[8] A. H. Von Flotow. *An Exposition Overview of Active Control of Machinery Mounts*. Proceedings of the 27th Conference on Decision and Control, Texas, USA, pp 2029-2032. 1988.